Journal of Applied Mechanics

Published Bimonthly by ASME

VOLUME 75 • NUMBER 4 • JULY 2008

RESEARCH PAPERS

041001 Slow Steady Viscous Flow of Newtonian Fluids in Parallel-Disk Viscometer With Wall Slip
Y. Leong Yeow, Yee-Kwong Leong, and Ash Khan

041002 Marginal Instability and Intermittency in Stochastic Systems—Part I: Systems With Slow Random Variations of Parameters
M. F. Dimentberg, A. Hera, and A. Naess

041003 Effect of Specimen Size on the Dissipated Energy Density in Compression
Giuseppe Ferro and Alberto Carpinteri

041004 Parametric Instability of an Axially Moving Belt Subjected to Multifrequency Excitations: Experiments and Analytical Validation
Guilhem Michon, Lionel Manin, Didier Remond, Regis Dufour, and Robert G. Parker

041005 Nonlinear Buckling of Compressed FRP Cylindrical Shells and Their Imperfection Sensitivity
Seishi Yamada, James G. A. Croll, and Nobuhisa Yamamoto

041006 Experimental Investigation of the Painlevé Paradox in a Robotic System
Zhen Zhao, Caishan Liu, Wei Ma, and Bin Chen

041007 Stability and Vibration Behavior of Composite Cylindrical Shell Panels Under Axial Compression and Secondary Loads
J. Girish and L. S. Ramachandra

041008 Vibration Analysis of a Floating Roof Taking Into Account the Nonlinearity of Sloshing
M. Utsumi and K. Ishida

041009 Optimal Winding Conditions of Flat Steel Ribbon Wound Pressure Vessels With Controllable Stresses
Chuanxiang Zheng and Shaohui Lei

041010 Stability Analysis of an Inflatable Vacuum Chamber
Sean A. Barton

041011 Evaluation of Planar Harmonic Impedance for Periodic Elastic Strips of Rectangular Cross Section by Plate Mode Expansion
Eugene J. Danicki

041012 Modeling of Hydraulic Pipeline Transients Accompanied With Cavitation and Gas Bubbles Using Parallel Genetic Algorithms
Songjing Li, Chifu Yang, and Dan Jiang

041013 Elastic Stress and Magnetic Field Concentration Near the Vertex of a Soft-Ferromagnetic 2D Compound Wedge
Davresh Hasanyan, Zhanming Qin, and Liviu Librescu

041014 An Adaptive Meshless Method for Analyzing Large Mechanical Deformation and Contacts
Qiang Li and Kok-Meng Lee

(Contents continued on inside back cover)

Transactions of the ASME, Journal of Applied Mechanics (ISSN 0021-8936) is published bimonthly (Jan., Mar., May, July, Sept., Nov.) by The American Society of Mechanical Engineers, Three Park Avenue, New York, NY 10016. Periodicals postage paid at New York, NY and additional mailing offices. POSTMASTER: Send address changes to Transactions of the ASME, Journal of Applied Mechanics, c/o THE AMERICAN SOCIETY OF MECHANICAL ENGINEERS, 22 Law Drive, Box 2300, Fairfield, NJ 07007-2300.
CHANGES OF ADDRESS must be received at Society headquarters seven weeks before they are to be effective. Please send old label and new address.

Canadian Goods & Services Tax Registration #126148048.

This journal is printed on acid-free paper, which exceeds the ANSI Z39.48-1992 specification for permanence of paper and library materials. ♾™
♻ 85% recycled content, including 10% post-consumer fibers.

(Contents continued)

Journal of Applied Mechanics Volume 75, Number 4 JULY 2008

041015 The Dynamic Compressive Response of Open-Cell Foam Impregnated With a Newtonian Fluid
M. A. Dawson, G. H. McKinley, and L. J. Gibson

041016 Almost Sure Stability of a Moving Elastic Band
Ratko Pavlović, Predrag Rajković, and Ivan Pavlović

041017 Jumps Across an Outgoing Spherical Shock Wave Front
Yukio Sano and Tomokazu Sano

041018 Experimental Data Have to Decide Which of the Nonprobabilistic Uncertainty Descriptions—Convex Modeling or Interval Analysis—to Utilize
Xiaojun Wang, Isaac Elishakoff, and Zhiping Qiu

041019 Screw Dislocations in a Three-Phase Composite Cylinder Model With Interface Stress
Q. H. Fang, Y. W. Liu, and P. H. Wen

041020 Post-buckling and Snap-Through Behavior of Inclined Slender Beams
Jian Zhao, Jianyuan Jia, Xiaoping He, and Hongxi Wang

041021 Independent Meshing of Contact Surfaces in 3D Boundary Element Method Contact Analysis
A. Sahli, M. B. Guemmour, S. Kebdani, D. Boutchicha, and O. Rahmani

041022 An Alternative to F. Y. M. Wan's Single Equation for an Elastic Right Circular Conical Shell
J. G. Simmonds

041023 Aeroelastic Stability of Wide Webs and Narrow Ribbons in Cross Flow
Rahul A. Bidkar, Arvind Raman, and Anil K. Bajaj

041024 Snapping of a Planar Elastica With Fixed End Slopes
Jen-San Chen and Yong-Zhi Lin

041025 A Micromechanics Model for the Thermal Conductivity of Nanotube-Polymer Nanocomposites
Gary D. Seidel and Dimitris C. Lagoudas

TECHNICAL BRIEFS

044501 Analytical Solutions for the Modeled *k* Equation
Rafik Absi

044502 Stationary Response of MDOF Dissipated Hamiltonian Systems to Poisson White Noises
Y. Wu and W. Q. Zhu

044503 An Alternative Two-Variable Model for Bending Problems of Multilayered Beams
Neng-Hui Zhang and Jian-Zhong Chen

044504 Transient Response of Submerged Plates Subject to Underwater Shock Loading: An Analytical Perspective
Zhanke Liu and Yin L. Young

DISCUSSIONS

045501 Discussion: "A Greenwood–Williamson Model of Small-Scale Friction" (Jones, R. E., 2007, ASME J. Appl. Mech., 74, pp. 31–40)
Izhak Etsion

045502 Closure to "Discussion of 'A Greenwood–Williamson Model of Small-Scale Friction' " (2008, ASME J. Appl. Mech., 75, p. 045501)
Reese Jones

045503 Discussion: "New First-Order Shear Deformation Plate Theories" (Shimpi, R. P., Patel, H. G., and Arya, H., 2007, ASME J. Appl. Mech., 74, pp. 523–533)
J. G. Simmonds

045504 Closure to "Discussion of 'New First-Order Shear Deformation Plate Theories' " (2008, ASME J. Appl. Mech., 75, p. 045503)
R. P. Shimpi, H. G. Patel, and H. Arya

(Contents continued on facing page)

Journal of Applied Mechanics **Volume 75, Number 4** **JULY 2008**

ERRATA

047001 **Erratum: "Reynolds-Stress Modeling of Three-Dimensional Secondary Flows With Emphasis on Turbulent Diffusion Closure" [Journal of Applied Mechanics, 2007, 74(6), pp. 1142–1156]**
I. Vallet

The ASME Journal of Applied Mechanics is abstracted and indexed in the following:

Alloys Index, Aluminum Industry Abstracts, Applied Science & Technology Index, Ceramic Abstracts, Chemical Abstracts, Civil Engineering Abstracts, Compendex (The electronic equivalent of Engineering Index), Computer & Information Systems Abstracts, Corrosion Abstracts, Current Contents, EEA (Earthquake Engineering Abstracts Database), Electronics & Communications Abstracts Journal, Engineered Materials Abstracts, Engineering Index, Environmental Engineering Abstracts, Environmental Science and Pollution Management, Fluidex, Fuel & Energy Abstracts, GeoRef, Geotechnical Abstracts, INSPEC, International Aerospace Abstracts, Journal of Ferrocement, Materials Science Citation Index, Mechanical Engineering Abstracts, METADEX (The electronic equivalent of Metals Abstracts and Alloys Index), Metals Abstracts, Nonferrous Metals Alert, Polymers Ceramics Composites Alert, Referativnyi Zhurnal, Science Citation Index, SciSearch (Electronic equivalent of Science Citation Index), Shock and Vibration Digest, Solid State and Superconductivity Abstracts, Steels Alert, Zentralblatt MATH

Slow Steady Viscous Flow of Newtonian Fluids in Parallel-Disk Viscometer With Wall Slip

Y. Leong Yeow[1]
Department of Chemical
and Biomolecular Engineering,
The University of Melbourne,
Victoria, Australia 3010
e-mail: yly@unimelb.edu.au

Yee-Kwong Leong
School of Mechanical Engineering,
The University of Western Australia,
Crawley, Western Australia, Australia 6009

Ash Khan
Department of Civil
and Chemical Engineering,
RMIT University,
Victoria, Australia 3000

The parallel-disk viscometer is a widely used instrument for measuring the rheological properties of Newtonian and non-Newtonian fluids. The torque-rotational speed data from the viscometer are converted into viscosity and other rheological properties of the fluid under test. The classical no-slip boundary condition is usually assumed at the disk-fluid interface. This leads to a simple azimuthal flow in the disk gap with the azimuthal velocity linearly varying in the radial and normal directions of the disk surfaces. For some complex fluids, the no-slip boundary condition may not be valid. The present investigation considers the flow field when the fluid under test exhibits wall slip. The equation for slow steady azimuthal flow of Newtonian fluids in parallel-disk viscometer in the presence of wall slip is solved by the method of separation of variables. Both linear and nonlinear slip functions are considered. The solution takes the form of a Bessel series. It shows that, in general, as a result of wall slip the azimuthal velocity no longer linearly varies in the radial direction. However, under conditions pertinent to parallel-disk viscometry, it approximately remains linear in the normal direction. The implications of these observations on the processing of parallel-disk viscometry data are discussed. They indicate that the method of Yoshimura and Prud'homme (1988, "Wall Slip Corrections for Couette and Parallel-Disk Viscometers," J. Rheol., ***32****(1), pp. 53–67) for the determination of the wall slip function remains valid but the simple and popular procedure for converting the measured torque into rim shear stress is likely to incur significant error as a result of the nonlinearity in the radial direction.* [DOI: 10.1115/1.2910901]

Keywords: parallel-disk viscometer, wall slip, slow viscous flow, Navier slip law, Bessel series

1 Introduction

The parallel-disk viscometer is employed by rheologists to measure the shear properties of a wide range of fluids. In a typical steady-shear measurement, the gap between the two parallel disks is filled with the fluid under test. The upper disk is rotated at a steady angular speed ω while the lower disk is held stationary. The torque Γ is recorded for a series of rotational speeds. These Γ-ω data are then converted into material properties of the fluid. The no-slip boundary condition is assumed at the disk-fluid boundaries. Under the normal conditions of parallel-disk viscometry, the inertia terms in the equation of motion are small and can be ignored. It is also observed that the stress-free fluid surface at the rim of the disks essentially remains flat in the vertical direction. As a consequence, the flow field inside the gap is approximately unidirectional and the cylindrical polar velocity components in the r and z directions can be ignored. The azimuthal component v_θ also takes on a particularly simple form. The v_θ that satisfies the equation of motion and the no-slip boundary condition is

$$v_\theta(r,z) = \left(\frac{1}{2} + \frac{z}{h}\right)\omega r, \quad 0 \leqslant r \leqslant R \text{ and } -h/2 \leqslant z \leqslant h/2 \quad (1)$$

where R is the disk radius and h ($\ll R$) is the disk gap. In Eq. (1), $z=0$ is the midplane between the disks. This $v_\theta(r,z)$ is linear in r and z. At the midplane, it is exactly half the speed of the upper disk. $v_\theta(r,z)$ is antisymmetric about the midplane velocity. Equation (1) is assumed by many of the commercial software that accompany the current generation of parallel-disk viscometers for converting the measured Γ-ω data into rheological properties. When the shear stress at the disk surfaces is sufficiently high, some fluids may no longer adhere to the disk and begin to exhibit wall slip. When this happens, the rheological properties derived from the Γ-ω data becomes gap dependent and are no longer genuine properties of the fluid under test. This gap dependence is, in fact, used as an indicator of wall slip [1]. In fluids with suspended particles or droplets, shear-induced segregation may result in the formation of a thin layer of low viscosity fluid next to the disk surfaces. This low viscosity layer then acts as a lubricating film resulting in high velocity gradient next to the disk surfaces. While there is no genuine breakdown of the no-slip boundary condition, this shear-induced inhomogeneity will again result in gap-dependent rheological properties. This is often referred to as apparent wall slip. In either real or apparent slip, an additional material property function, the slip function $S(v_{\text{slip}})$ is often introduced to relate the slip velocity v_{slip} to the wall shear stress $\tau_w = S(v_{\text{slip}})$. The slip velocity is defined by $v_{\text{slip}} \equiv v_{\text{disk}} - v_{\text{fluid}}$ at the disk surface. Yoshimura and Prud'homme [1] have developed a procedure in which two sets of Γ-ω data for two different gaps are used to obtain $S(v_{\text{slip}})$. This procedure is now routinely used to obtain this additional material property function [2–4].

When wall slip is present, it is not immediately clear that the simple kinematics represented by Eq. (1) is still valid within the disk gap. There have been a number of investigations into this issue—both for genuine and for apparent slip [5,6]. The general consensus is that while the analysis of Yoshimura and Prud'homme [1] is not exact, it is an acceptable approximation—particularly when the $h:R$ ratio is small. In this investigation, a series solution for $v_\theta(r,z)$ is obtained for Newtonian fluids that

---

[1] Corresponding author.

Contributed by the Applied Mechanics Division of ASME for publication in the JOURNAL OF APPLIED MECHANICS. Manuscript received April 3, 2006; final manuscript received March 3, 2008; published online May 9, 2008. Review conducted by Bassam A. Younis.

exhibit wall slip. The solution is applicable to linear and nonlinear $S(v_{\text{slip}})$. This series solution is used to investigate the nature of the flow field within the disk gap and to verify some of the assumptions inherent in the procedure of Yoshimura and Prud'homme [1].

2 Equation of Motion

For a Newtonian fluid under the normal conditions of parallel-disk viscometery, the azimuthal equation of motion reduces to [7]

$$\frac{\partial^2 v_\theta}{\partial r^2} + \frac{1}{r}\frac{\partial v_\theta}{\partial r} - \frac{v_\theta}{r^2} + \frac{\partial^2 v_\theta}{\partial z^2} = 0 \tag{2}$$

The inertia term has been ignored and the flow is assumed to be axisymmetric so that the azimuthal velocity is a function of r and z only, i.e., $v_\theta(r,z)$. It is further assumed that wall slip occurs to the same extent at the upper and lower disks and consequently $v_\theta(r,z)$ remains antisymmetric about the midplane. This more general form of $v_\theta(r,z)$ replaces that given by Eq. (1).

At the disk surfaces, the no-slip boundary condition is replaced by

$$\tau_w(r,h/2) = \tau_w(r,-h/2) = S(\omega r - v_\theta(r,h/2)) = S(v_\theta(r,-h/2)) \tag{3}$$

These expressions equate the viscous shear stress τ_w generated by the steady shear of the fluid next to the disk surfaces with that generated by slippage. In addition to Eq. (3), $v_\theta(r,z)$ also has to satisfy the stress-free condition at the rim of the disk, i.e., $\tau_{r\theta}=0$. In terms of $v_\theta(r,z)$, this takes the form [7]

$$\frac{\partial(v_\theta/r)}{\partial r} = 0 \quad \text{at } r = R \tag{4}$$

The method of separation of variables will be used to construct a solution for Eq. (2) subject to Eqs. (3) and (4).

3 Separable Solution

To cope with wall slip, instead of Eq. (1), $v_\theta(r,z)$ will be assumed to be of the form

$$v_\theta(r,z) = \frac{\omega r}{2} + \alpha_0 rz + V(r,z) = \frac{\omega r}{2} + \alpha_0 rz + F(r)G(z) \tag{5}$$

where α_0 is a constant and $V(r,z)$ is a function to be determined. The first two terms in this representation of $v_\theta(r,z)$ automatically satisfy Eq. (2). Equation (5) reduces to Eq. (1), i.e., $\alpha_0 \to \omega/h$ and $V(r,z)\to 0$, when the no-slip boundary condition applies. In the solution scheme to be developed, it is further assumed that the r and z in $V(r,z)$ are separable so that $V(r,z)=F(r)G(z)$. Substituting Eq. (5) into Eq. (2) leads to

$$\frac{1}{F(r)}\left[\frac{d^2F(r)}{dr^2} + \frac{1}{r}\frac{dF(r)}{dr} - \frac{F(r)}{r^2}\right] = -\frac{1}{G(z)}\frac{d^2G(z)}{dz^2} = -\lambda^2 \tag{6}$$

or

$$\frac{d^2F(r)}{dr^2} + \frac{1}{r}\frac{dF(r)}{dr} + \left\{\lambda^2 - \frac{1}{r^2}\right\}F(r) = 0 \tag{7a}$$

$$\frac{d^2G(z)}{dz^2} = \lambda^2 G(z) \tag{7b}$$

where $-\lambda^2$ is the separation constant and λ is taken to be real and positive. Equation (7a) is a first order Bessel equation and its solution is $J_1(\lambda r)$—Bessel function of the first kind of order 1. The other linearly independent solution is the corresponding Bessel function of the second kind $Y_1(\lambda r)$. Since $Y_1(\lambda r)$ is singular at $r=0$, it is discarded. The solution to Eq. (7b) is $\sinh(\lambda r)$. The second solution is $\cosh(\lambda r)$. This second solution also has to be discarded as it is symmetric about the midplane while physical considerations require $v_\theta(r,z)$ to be antisymmetric.

The admissible values of λ are determined by Eq. (4). In terms of $J_1(\lambda r)$, this takes the form

$$\frac{d(J_1(\lambda r)/r)}{dr} = 0 \quad \text{at } r = R \tag{8a}$$

From the relationships between Bessel functions of different orders, this boundary condition reduces to [8]

$$J_2(\lambda R) = 0 \tag{8b}$$

This equation has infinitely many solutions. The first ten of these are $\lambda R=\{5.13562, 8.41724, 11.6198, 14.796, 17.9598, 21.117, 24.2701, 27.4206, 30.5692, 33.7165\}$. These were obtained by numerically solving Eq. (8b). The $\alpha_0 rz$ term in Eq. (5) can be regarded as the solution associated with $\lambda R=0$. This term together with the $J_1(\lambda_i r)$ terms forms an orthogonal basis that can be used to construct a generalized Fourier series to represent most well behaved functions [8]. The series solution for $v_\theta(r,z)$ can thus be written as

$$v_\theta(r,z) = \omega r/2 + \alpha_0 rz + \sum_{i=1}^{\infty} \alpha_i J_1(\lambda_i r)\sinh(\lambda_i z) \tag{9}$$

where $\alpha_0, \alpha_1, \alpha_2, \alpha_3, \ldots$ are the coefficients yet to be determined.

4 Matching Slip Boundary Condition

In terms of Eq. (9), the slip velocity at the upper disk is

$$v_{\text{slip}}(r,h/2) = \omega r - \left[\omega r/2 + \alpha_0 rh/2 + \sum_{i=1}^{\infty} \alpha_i J_1(\lambda_i r)\sinh(\lambda h/2)\right] \tag{10}$$

From Eq. (3), τ_w at the upper disk is

$$\tau_w = S\left(\omega r/2 - \alpha_0 rh/2 - \sum_{i=1}^{\infty} \alpha_i J_1(\lambda_i r)\sinh(\lambda_i h/2)\right) \tag{11}$$

Because of the anti-symmetric nature of Eq. (9), Eq. (11) also applies at the lower disk. At the upper disk, for a Newtonian fluid with viscosity η, τ_w is also given by

$$\tau_w = \eta \left.\frac{\partial v_\theta(r,z)}{\partial z}\right|_{h/2} = \eta\alpha_0 r + \eta\sum_{i=1}^{\infty} \lambda_i \alpha_i J_1(\lambda_i r)\cosh(\lambda_i h/2) \tag{12}$$

Again this expression also applies at the lower disk. Equating the two expressions for τ_w gives

$$\eta\alpha_0 r + \eta\sum_{i=1}^{\infty} \lambda_i \alpha_i J_1(\lambda_i r)\cosh(\lambda_i h/2) = S\left(\omega r/2 - \alpha_0 rh/2 - \sum_{i=1}^{\infty} \alpha_i J_1(\lambda_i r)\sinh(\lambda_i h/2)\right) \tag{13}$$

The coefficients $\alpha_0, \alpha_1, \alpha_2, \alpha_3, \ldots$ are determined so that this condition is met for $0 \leq r \leq R$ or approximately satisfied at a large number of collocation points for r in this range. The values of $\alpha_0, \alpha_1, \alpha_2, \alpha_3 \ldots$ and the way they are obtained depend on the form of $S(v_{\text{slip}})$, as will be demonstrated in the next section.

5 Results

5.1 Linear Slip Law. In the boundary condition proposed by Navier in 1823, the wall shear stress is assumed to be a linear function of the slip velocity, i.e., $\tau_w = k_1 v_{\text{slip}}$ [9]. Substituting this into Eq. (13) leads to

$$\eta\alpha_0 r + \eta\sum_{i=1}^{\infty}\lambda_i\alpha_i J_1(\lambda_i r)\cosh(\lambda_i h/2) = k_1\left[\omega r/2 - \alpha_0 rh/2 - \sum_{i=1}^{\infty}\alpha_i J_1(\lambda_i r)\sinh(\lambda_i h/2)\right], \quad 0 \leqslant r \leqslant R \tag{14}$$

Linearity of the slip function means that all the coefficients of the Bessel series are identically zero and the unknown α_0 is given by

$$\frac{R\alpha_0}{\omega} = 1 \bigg/ \left(\frac{2\eta}{k_1 R} + \frac{h}{R}\right) \tag{15}$$

Equation (15) gives the dimensionless parameter $R\alpha_0/\omega$ in terms of the dimensionless group η/k_1R and the gap ratio h/R. η/k_1R is a measure of the relative importance of the viscous shear stress and the slippage shear stress. h/R is the key geometric parameter of the viscometer. The resulting $v_\theta(r,z)$ is

$$\frac{v_\theta(r,z)}{\omega R} = \frac{1}{2}\left(\frac{r}{R}\right) + \left(\frac{r}{R}\right)\left(\frac{z}{R}\right) \bigg/ \left(\frac{2\eta}{k_1 R} + \frac{h}{R}\right) \tag{16}$$

Equation (16) clearly shows that, in the presence of linear slip, the velocity remains linear in r and in z. When $k_1 \gg \eta/h$, corresponding to negligible wall slip, Eq. (16) reduces to Eq. (1).

Based on Eq. (16), the wall shear stress is given by

$$\frac{\tau_w}{\eta\omega} = \left(\frac{r}{R}\right) \bigg/ \left[\frac{2\eta}{k_1 R} + \frac{h}{R}\right] \tag{17}$$

Thus, for a Newtonian fluid that follows the linear slip law, the wall shear stress remains a linear function of r as is observed when the no-slip boundary condition applies. The shear stress within the disk gap is independent of z—a condition observed for all fluids when the no-slip boundary condition applies [1].

Typical $v_\theta(r,z)$ profiles for the linear slip law are shown in Fig. 1. These results are for $k_1R/\eta=5$ and $h/R=0.15$. U, M, and L in Fig. 1(*a*) refer to the upper disk, the midplane, and the lower disk, respectively. These curves reveal very significant wall slip. For example, at the rim of the disks, v_{slip} is as high as 36.4% of the rim speed of the upper disk. Figure 1(*b*) shows the velocity profiles across the gap at different radial positions. Wall slip has greatly reduced the slope of these curves. The maximum shear rate is only $(100-2\times 36.4)=27.2\%$ of that given by Eq. (1) when there is no slip.

The linear relationship between shear stress and r, as described by Eq. (17), is shown in Fig. 2 by the straight line "ln." This stress is independent of z. The line "ns" on the same plot is the corresponding stress for a Newtonian fluid with the same viscosity but does not exhibit wall slip. Because of wall slip, the stress on ln is only 27.2% of that on ns. For ease of comparison, the stress curves for all the $S(v_{\text{slip}})$ subsequently investigated are summarized in Fig. 2.

5.2 Square Dependence on Slip Velocity. The linear slip function considered in Sec. 5.1 does not test the numerical performance of the Bessel series solution. In this example, the linear slip law of Navier is generalized to $\tau_w=k_2v_{\text{slip}}^2$. Substituting this into Eq. (13) yields

$$\eta\alpha_0 r + \eta\sum_{i=1}^{\infty}\lambda_i\alpha_i J_1(\lambda_i r)\cosh(\lambda_i h/2) = k_2\left[\omega r/2 - \alpha_0 rh/2 - \sum_{i=1}^{\infty}\alpha_i J_1(\lambda_i r)\sinh(\lambda_i h/2)\right]^2, \quad 0 \leqslant r \leqslant R \tag{18}$$

The nonlinear nature of Eq. (18) does not permit the exploitation of the orthogonal properties of $J_1(\lambda_i r)$ to determine the unknown coefficients $\alpha_0,\alpha_1,\alpha_2,\alpha_3,\ldots$. Instead, they are determined by least-squares minimization of the difference between the left hand side (LHS) and right hand side (RHS) of Eq. (18) at a set of preselected collocation points. Typically, 150–200 collocation points uniformly spaced between $0.02\leqslant r/R\leqslant 1$ are included in the minimization process. The region $0\leqslant r/R\leqslant 0.02$ has been arbitrarily excluded as $v_\theta(r,z)$ and τ_w there are too small to be accurately evaluated. In the least-squares minimization process, the series representation of $v_\theta(r,z)$ is terminated after N terms, typically $N=10-20$. N is adjusted so that the average difference

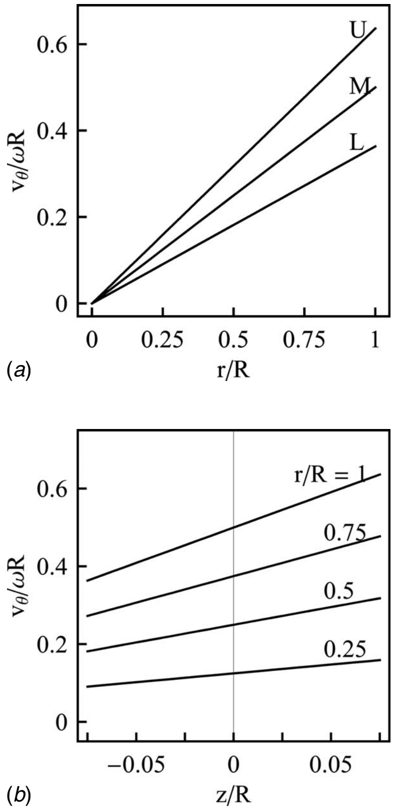

Fig. 1 Linear slip law. (*a*) Variation of azimuthal velocity with radius at the upper disk (U), midplane (M), and lower disk (L). (*b*) Variation of azimuthal velocity with axial coordinate at different radial positions.

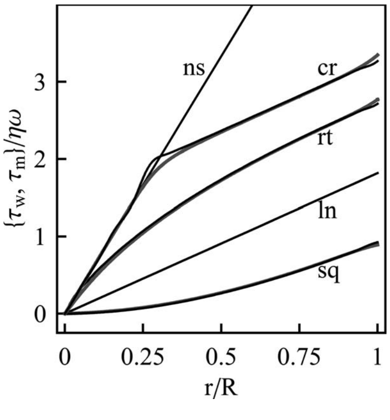

Fig. 2 Radial variation of shear stress for no slip (ns), linear slip (ln), square dependence (sq), square-root dependence (rt), and linear slip with critical wall shear stress (cr). The darker curves are for the stress at the disk surfaces and the lighter curves are for the stress at the midplane.

between the LHS and RHS of Eq. (18) is less than about 1%. As expected in the neighborhood of $r=0$, the difference can be as large as 10–15%. However, this does not appear to have a great influence on the behavior of $v_\theta(r,z)$.

The search of the $\alpha_0, \alpha_1, \alpha_2, \ldots, \alpha_N$ that minimize the least-squares difference was performed using the commercial software MATHEMATICA® [10]. The computation starts with a relatively small N, typically $N=5-6$, and this is progressively increased using the previously obtained coefficients as the starting point. To avoid being trapped by local minima, the minimization computation was repeated with slightly modified starting values of the coefficients and also by using different minimization strategies provided by the commercial software. No numerical difficulties were encountered in this and in the subsequent examples.

Results for the slip law $\tau_w = k_2 v_{\text{slip}}^2$ with $k_2 \omega R^2/\eta = 5$ and $h/R = 0.15$ are summarized in Figure 3. Figure 3(*a*) shows that, except at the midplane, $v_\theta(r,z)$ is clearly no longer linear in r. The three velocity profiles are also much closer to one another compared to that in Fig. 1(*a*), indicating increased wall slip. For example, the velocity of the fluid at the rim of the upper disk is only 56.8% of the rim speed giving a v_{slip} of 43.2%. With this v_{slip}, the maximum shear rate attained is only $(100-2\times 43.2)\% = 13.6\%$ of that given by Eq. (1) when the no-slip boundary condition applies. The velocity profiles in Fig. 3(*b*) show that $v_\theta(r,z)$ approximately remains linear in z for all r. The slight deviation from linearity can only be observed by plotting $(\partial v_\theta/\partial z)_r$ against z at different radial positions, see Fig. 3(*c*). In general, for a fixed r, $(\partial v_\theta/\partial z)_r$ varied by less than 3.5% for $-1/2 < z/h \leqslant 1/2$. The two curves marked "sq" in Fig. 2 show the nonlinear variation of the shear stress with r as a consequence of the square dependence on v_{slip}. The shear stress at the disk surfaces τ_w (darker curve) and that at the midplane τ_m (lighter curve) are very close together, reflecting the small variation of shear rate with z. These curves also show the very significant reduction in shear stress brought about by wall slip.

5.3 Square-Root Dependence on Slip Velocity. The computation in Sec. 5.2 is repeated for $\tau_w = k_{1/2} v_{\text{slip}}^{1/2}$ as an example where the wall shear stress increases less than linearly with v_{slip}. Substituting this into Eq. (13) resulted in

$$\eta\alpha_0 r + \eta\sum_{i=1}^{\infty} \lambda_i \alpha_i J_1(\lambda_i r)\cosh(\lambda_i h/2) = k_{1/2}\left[\omega r/2 - \alpha_0 r z_w - \sum_{i=1}^{\infty} \alpha_i J_1(\lambda_i r)\sinh(\lambda_i h/2)\right]^{1/2}, \quad 0 \leqslant r \leqslant R \tag{19}$$

Least-squares minimization is again used to determine $\alpha_0, \alpha_2, \ldots, \alpha_N$. The same set of collocation points in Sec. 5.2 was used. It was found that, for this slip law, a slightly larger number of terms, $25 < N < 30$, of the Bessel series was required to keep the average difference between the LHS and RHS of Eq. (19) to around 1%.

Plots of the variation of $v_\theta(r,z)$ with r for this slip law, for $k_{1/2}(R/\omega)^{1/2}/\eta = 5$ and $h/R = 0.15$, are shown in Fig. 4(*a*). $v_\theta(r,z)$, for $z \neq 0$, is now even more nonlinear in r. This may explain the increase in N required to represent $v_\theta(r,z)$ to the same degree of accuracy as before. A reduction in wall slip, compared to the linear slip law, is observed. The maximum v_{slip} is reduced from 36.4% to 29.3% of the rim speed, see Fig. 4(*a*). Consequently, the maximum shear rate experienced by the Newtonian fluid is now about 41.4% of that when there is no slip. As in the previous examples, Fig. 4(*b*) shows that $v_\theta(r,z)$ approximately remains linear in z. The slight deviation from linearity is shown in the plots of $(\partial v_\theta/\partial z)_r$ against z in Fig. 4(*c*). The maximum variation, at $r/R=1$, is about 2.0%.

The general lowering of v_{slip}, compared to Secs. 5.1 and 5.2, for the square-root dependent $S(v_{\text{slip}})$ means that the shear stress is correspondingly higher. This can be observed from the stress curves "rt" in Fig. 2. The stress at the disk surfaces (darker curve) and that for the midplane (lighter curve) are again very close together confirming that the variation of shear rate with z can be ignored. The shear stress is again nonlinear in r.

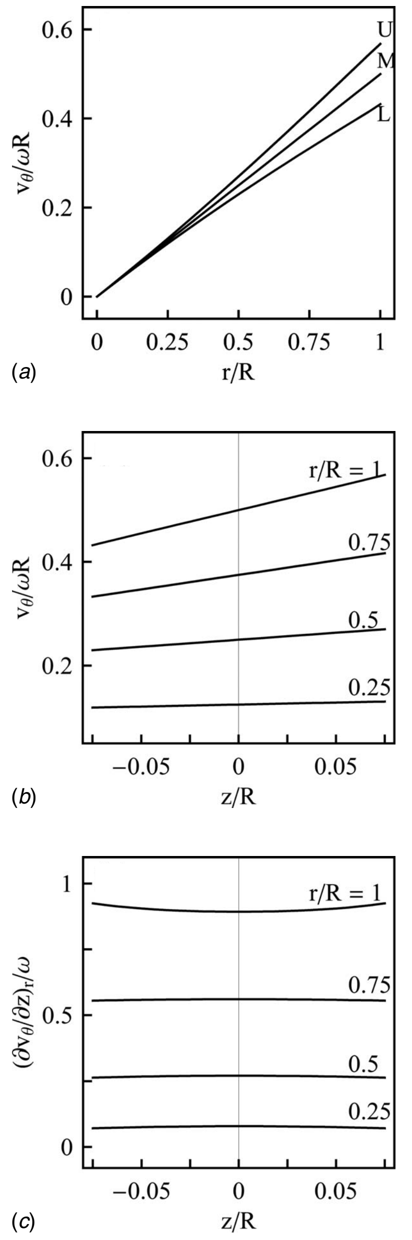

Fig. 3 Square dependence wall slip. (*a*) Variation of azimuthal velocity with radius at the upper disk (U), mid plane (M), and lower disk (L). (*b*) Variation of azimuthal velocity with axial coordinate at different radial positions. (*c*) Variation of shear rate with axial coordinate at different radial positions.

5.4 Fluid With Critical Wall Shear Stress. Materials, such as polymer melts, do not exhibit wall slip at low wall shear stress. Wall slip often only becomes noticeable when τ_w has exceeded some threshold value. To model this observation, the linear slip law is modified to

$$v_{\text{slip}} = 0 \quad \text{for } \tau_w \leqslant \tau_{w\text{crit}}$$

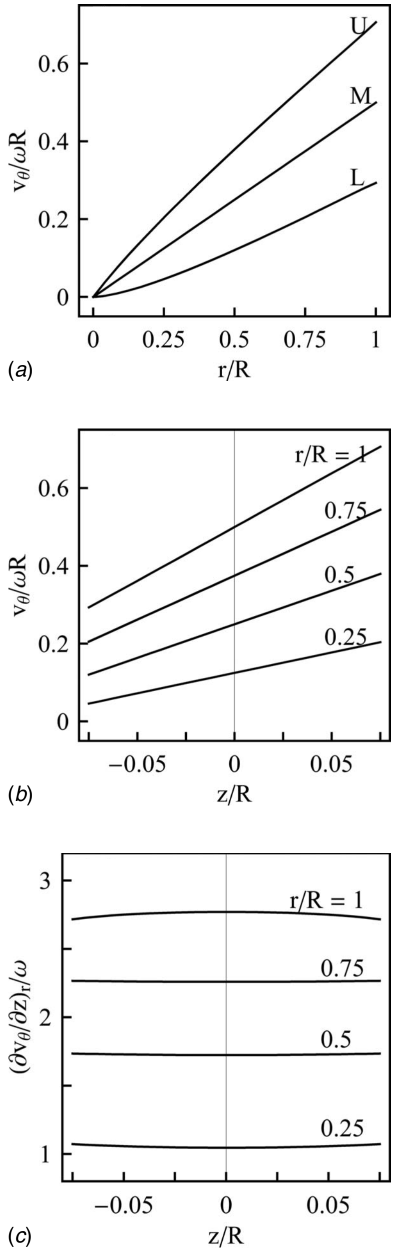

Fig. 4 Square-root dependence wall slip. (*a*) Variation of azimuthal velocity with radius at the upper disk (U), midplane (M), and lower disk (L). (*b*) Variation of azimuthal velocity with axial coordinate at different radial positions. (*c*) Variation of shear rate with axial coordinate at different radial positions.

$$\tau_w = \tau_{w\text{crit}} + k_Y v_{\text{slip}} \quad \text{for } \tau_w > \tau_{w\text{crit}} \tag{20}$$

where $\tau_{w\text{crit}}$ is the critical wall shear stress below which the classical no-slip boundary condition is observed. k_Y plays the same role as k_1 in Sec. 5.1. For this generalized $S(v_{\text{slip}})$, the matching of boundary condition at the rotating disk takes the form

$$\omega r/2 + \alpha_0 r h/2 + \sum_{i=1}^{\infty}\alpha_i J_1(\lambda_i r)\sinh(\lambda_i h/2) = \omega r \quad \text{for } \tau_w \leqslant \tau_{w\text{crit}} \tag{21a}$$

$$\eta\alpha_0 r + \eta\sum_{i=1}^{\infty}\lambda_i\alpha_i J_1(\lambda_i r)\cosh(\lambda_i h/2) = \tau_{w\text{crit}} + k_Y\left[\omega r/2 - \alpha_0 r h/2 - \sum_{i=1}^{\infty}\alpha_i J_1(\lambda_i r)\sinh(\lambda_i h/2)\right]$$
$$\text{for } \tau_w > \tau_{w\text{crit}} \tag{21b}$$

Because of the antisymmetric nature of $v_\theta(r,z)$, Eqs. (21*a*) and (21*b*) ensure that Eq. (20) is automatically met at the stationary disk. As in the last two examples, the coefficients $\alpha_0,\alpha_1,\alpha_2,\ldots,\alpha_N$ are determined by least-squares minimization of the difference between the LHS and RHS of Eqs. (21*a*) and (21*b*) over a set of regularly spaced collocation points. In computing the least-squares deviation, Eq. (21*a*) applies for $0 < r \leqslant r_{\text{crit}}$ and Eq. (21*b*) for $r_{\text{crit}} < r \leqslant R$, where r_{crit} is the radial position for the onset of wall slip. For a Newtonian fluid with viscosity η, it is given by

$$r_{\text{crit}} = \tau_{w\text{crit}} h/(\eta\omega) \tag{22}$$

This expression is based on the assumption that the no-slip boundary condition for $r \leqslant r_{\text{crit}}$ is sufficient to ensure that the velocity is linear in z and hence the wall shear stress is given by $\eta\omega r/h$. If the velocity profiles given by the Bessel series indicate significant deviation from linearity, then an iterative procedure will have to be adopted to evaluate r_{crit}. In the least-squares minimization process, typically, the span $0 < r \leqslant r_{\text{crit}}$ is divided into 100–150 collocation points and that for $r_{\text{crit}} < r \leqslant R$ into 200–300 points.

Typical results for a Newtonian fluid with $\tau_{w\text{crit}}$ are shown in Fig. 5. These results are for $\tau_{w\text{crit}}/\eta\omega = 2$, $k_Y R/\eta = 5$ and $h/R = 0.15$. The corresponding $r_{\text{crit}}/R = 0.3$. Figure 5(*a*) shows the distinct change in the slope of the $v_\theta(r,z)$ curves at $r = r_{\text{crit}}$ as the fluid begins to slip at the disk surfaces. As expected, at the lower disk, $v_\theta(r,-h/2) = 0$ for $r \leqslant r_{\text{crit}}$. The $v_\theta(r,-h/2)$ given by the series solution shows small fluctuations about 0 for $r \leqslant r_{\text{crit}}$ but these fluctuations do not show up in the scales of Fig. 5(*a*). As in the previous examples, $v_\theta(r,z)$ again appears to be approximately linear in z, see Fig. 5(*b*). The $(\partial v_\theta/\partial z)_r$ plots in Fig. 5(*c*) reveal the small deviation from linearity in z and, in particular, they show that the most significant deviation is in the neighborhood of $r = r_{\text{crit}}$. There the maximum difference in $(\partial v_\theta/\partial z)_r$ is around 7.65%. At $r = R$, the maximum difference is reduced to 2.34% (in the opposite direction). These were not considered as sufficiently large to warrant the iterative recalculation of r_{crit}. The $\tau_{w\text{crit}}$ has imparted a very distinctive shape on the shear stress versus r plots. See the "cr" curves for τ_w (darker curve) and τ_m (lighter curve) in Fig. 2. These curves are highly nonlinear. As expected, they closely follow the no-slip line ns for $r < r_{\text{crit}}$. As wall slip sets in at $r = r_{\text{crit}}$, these curves sharply change slope. As in the previous examples, the close proximity of the τ_w and τ_m curves confirms that the variation of shear rate with z can be ignored.

Discussion

For the $S(v_{\text{slip}})$ investigated, the numerical performance of the Bessel series representation of $v_\theta(r,z)$ appears to be satisfactory. The method of separation of variables adopted here can, in principle, be extended to even more general slip behaviors. For example, if the slip behavior of a real fluid can be approximated by a low order polynomial of the form

$$\tau_w = \beta_1 v_{\text{slip}} + \beta_2 v_{\text{slip}}^2 + \beta_3 v_{\text{slip}}^3 \tag{23}$$

where $\beta_1, \beta_2 \ldots$ are known empirical coefficients, then the procedure described above can be applied to obtain the series representation of $v_\theta(r,z)$.

Similarly, the treatment of $S(v_{\text{slip}})$ with a $\tau_{w\text{crit}}$ can be extended to a more general form of the slip function. However, for such materials, it is probably more convenient to inverse the relationship between v_{slip} and τ_w and to express it in the form

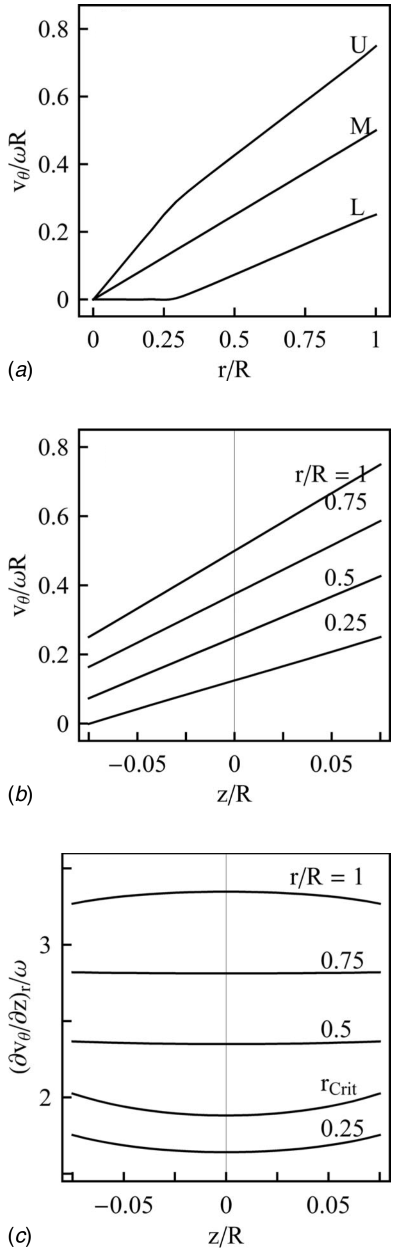

Fig. 5 Linear slip with critical wall shear stress. (*a*) Variation of azimuthal velocity with radius at the upper disk (U), midplane (M), and lower disk (L). (*b*) Variation of azimuthal velocity with axial coordinate at different radial positions. (*c*) Variation of shear rate with axial coordinate at different radial positions.

$$v_{\text{slip}} = 0 \quad \text{for } \tau_w \leqslant \tau_{w\text{crit}}$$

$$v_{\text{slip}} = T(\tau_w) \quad \text{for } \tau_w > \tau_{w\text{crit}} \tag{24}$$

where $T(\tau_w)$ is a general function of the wall shear stress. For this type of slip function, a boundary velocity matching condition, similar to the stress matching condition in Eq. (13), can be developed. The main issue here is the numerical performance of this new matching condition. This has not been investigated.

The present investigation only dealt with Newtonian fluids exhibiting wall slip. Most real fluids that exhibit wall slip are likely to simultaneously exhibit one or more non-Newtonian behaviors. It is therefore of practical interest to extend this slip investigation to non-Newtonian fluids. Unfortunately, the non-Newtonian equivalent of Eq. (2) that forms the starting point of this investigation is nonlinear and the standard method of separation of variables becomes inapplicable. For this class of more general problems, it is more efficient to resort to finite element computation. This is currently under progress. The Newtonian results reported here can then be used as a special case in the validation of the finite element method (FEM) results.

As mentioned above, the method of Yoshimura and Prud'homme [1] is now widely used in the determination of $S(v_{\text{slip}})$. One of the key assumptions in this method is that the shear rate in the gap is function of r only and is independent of z. The shear rate plots in Figs. 3(*c*), 4(*c*), and 5(*c*) show that, for the $S(v_{\text{slip}})$ investigated, the shear rate is not exactly independent of z. However, as the variation is generally less than 10%, this small variation can most probably be ignored. Similarly, only small variations in shear rate were observed for $h:R$ as large as 0.2 (not shown). Since in most parallel-disk viscometry measurements $h:R<0.2$, one is therefore justified to apply the method of Yoshimura and Prud'homme to determine wall slip.

For the case of linear wall slip, the shear stress remains linear in r as is expected of a Newtonian fluid. From the shear stress plots in Fig. 2, it is clear that, even for a Newtonian fluid, this stress is no longer linear in r for a general $S(v_{\text{slip}})$. This has an important practical implication on the processing of the Γ-ω data of parallel-disk viscometry. The measured torque Γ is often converted into shear stress τ_R at the rim of the disks using the simple expression

$$\tau_R = 2\Gamma/(\pi R^3) \tag{25}$$

This is the expression implemented in many of the software that accompany the current generation of parallel-disk viscometers. Equation (25) is an approximation and is strictly valid only when the shear stress is linear in r as is in the case of a Newtonian fluid that does not exhibit wall slip. The exact expression relating τ_R to Γ is [7]

$$\tau_R = \frac{\Gamma}{2\pi R^3}\left[3 + \frac{d\log_e \Gamma}{d\log_e \dot{\gamma}_R}\right] \tag{26}$$

where $\dot{\gamma}_R = \omega R/h$ is the shear rate at the rim of the disks. The main reason for adopting the approximate equation (25) instead of the exact equation (26) is that the evaluation of the derivative term on the RHS of Eq. (26) is difficult and is likely to amplify the noise in the Γ-ω data. For Newtonian fluid with nonlinear wall slip and certainly for non-Newtonian fluids with or without wall slip, the use of Eq. (25) is likely to lead to significant error and is therefore not recommended [11].

Conclusion

The method of separation of variables gave a reliable series representation of the azimuthal velocity for Newtonian fluids in steady parallel-disk flow in the presence of wall slip. The solution shows that the azimuthal velocity approximately remains linear in z and hence justifies the use of the procedure of Yoshimura and Prud'homme for the determination of the wall slip function. As a consequence of wall slip, the wall shear stress, even for a Newtonian fluid, is no longer linear in r. This is not consistent with the key assumption of the simple but very popular method for converting the measured torque into rim shear stress.

References

[1] Yoshimura, A., and Prud'homme, R. K., 1988, "Wall Slip Corrections for Couette and Parallel-Disk Viscometers," J. Rheol., **32**(1), pp. 53–67.
[2] Yilmazer, U., and Kalyon, D. H., 1989, "Slip Effects in Capillary and Parallel Disk Torsional Flows of Highly Filled Suspensions," J. Rheol., **33**(8), pp. 1197–1212.
[3] Hartman Kok, P. J. A., Kazrian, S. G., Lawrence, C. J., and Briscoe, B. J., 2002, "Near-Wall Particle Depletion in a Flowing Colloidal Suspension," J. Rheol., **46**(2), pp. 481–493.
[4] Bertola, V., Bertrand, F., Tabuteau, H., Bonn, D., and Coussot, P., 2003, "Wall Slip and Yielding in Pasty Materials," J. Rheol., **47**(5), pp. 1211–1226.
[5] Brunn, P. S., 1994, "A Note on the Slip Velocity Concept for Purely Rotational Viscometric Flows," Rheol. Acta, **37**(2), pp. 196–197.

[6] Wein, O., 2005, "Viscometric Flow under Apparent Wall Slip in Parallel-Plate Geometry," J. Non-Newtonian Fluid Mech., **126**(2–3), pp. 105–114.

[7] Bird., R. B., Armstrong, R. C., and Hassager, O., 1987, *Dynamics of Polymeric Liquids*, 2nd ed., Wiley-Interscience, New York, Vol. 1, Chap. 10.

[8] Andrews, L. C., 1986, *Special Functions for Engineers and Applied Mathematicians*, Macmillan, New York, Chap. 6.

[9] Piau, J. M., and Piau, M., 2005, "Letter to the Editor: Comment on "Origin of Concentric Cylinder Viscometry" [J. Rheol. **49**, 807–818 (2005)]. The Relevance of the Early Days of Viscosity, Slip at the Wall, and Stability in Concentric Cylinder Viscometry," J. Cryst. Growth, **49**(6), pp. 1539–1550.

[10] Wolfram Research, 2002, MATHEMATICA® 4.2, Wolfram Research, Champaign.

[11] Yeow, Y. L., Leong, Y.-K., and Khan, A., 2007, "Error Introduced by a Popular Method of Processing Parallel-Disk Viscometery Data," Appl. Rheol., **17**(6), pp. 66415/1–66415/6.

Marginal Instability and Intermittency in Stochastic Systems—Part I: Systems With Slow Random Variations of Parameters

M. F. Dimentberg
Mechanical Engineering Department,
Worcester Polytechnic Institute,
100 Institute Road,
Worcester, MA 01609

A. Hera
Information Technology Division,
Worcester Polytechnic Institute,
100 Institute Road,
Worcester, MA 01609

A. Naess
Centre for Ships and Ocean Structures,
and Department of Mathematical Sciences,
Norwegian University of Science and Technology,
NO-7491 Trondheim, Norway

Dynamic systems with lumped parameters, which experience random temporal variations, are considered. The variations may "smear" boundary between the system's states, which are dynamically stable and unstable in the classical sense. The system's response within such a "twilight zone" of marginal instability is found to be of an intermittent nature, with alternating periods of zero (or almost-zero) response and rare short outbreaks. As long as it may be impractical to preclude completely such outbreaks for a designed system, subject to highly uncertain dynamic loads, the corresponding system's response should be analyzed. Results of such analyses are presented for cases of slow and rapid (broadband) parameter variations in Parts I and II, respectively. In the former case, the "nominal" system—one without variations of parameter(s)—is stable in the classical sense. Its transient response during the "slow" short-term excursions of the parameter(s) into the instability domain is described by a linear model. The analysis is based on Krylov–Bogoliubov averaging over "rapid" time within the response period together with parabolic approximation for the parameter variations in the vicinity of their peaks (so-called Slepian model). Solution to the resulting deterministic transient response problem with random initial condition(s) at the instant of upcrossing the stability boundary yields a relation between peak value(s) of the response(s) and that of the parameter(s); in this way, reliability study for the system is reduced to a probabilistic analysis of the parameter variations. The solutions are obtained for the cases of negative-damping-type instability in a SDOF system and for TDOF systems with potential dynamic instability due to coalescing or merging of natural frequencies; the illustrating examples of applications are rotating shafts with internal damping, two-dimensional galloping of a rigid body in a fluid flow and a row of tubes in a cross flow of fluid. The response is of the intermittent nature due to the way it is generated, with alternating relatively long periods of zero (or almost-zero) response and short outbreaks due to temporary excursions into the instability domain. [DOI: 10.1115/1.2910900]

1 Introduction

Classical definitions of stability and instability deal with long-term behavior of dynamic systems, that is, behavior as time $t \to \infty$. These definitions are quite adequate for numerous engineering applications, where long-term operation of the systems is indeed required. However, they may become not perfectly appropriate for applications with limited service life, such as missiles, projectiles, etc. In such applications, a system may sometimes be qualified as acceptable in spite of being unstable in the classical sense as long as its deviations from the design state are small enough for successful and safe operation. Thus, design of such marginally unstable systems may be based on analysis of their transient response within limited service life.

The classical definitions of stability and instability may also prove to be not perfectly adequate for another class of dynamic systems—those that may be intended for long-term operation. Such systems are designed, as a rule, to operate within their stability domain in the classical sense as long as their "nominal" design parameters are considered. However, if the system's parameters may experience random temporal variations around their nominal or expected values, the system may become "temporary unstable" occasionally whenever the "classical" instability boundary is crossed. Whenever complete elimination of such excursions of the system out of its stability domain may lead to impossible or impractical design, the corresponding short-time outbreaks in response should be analyzed to evaluate the system's reliability.

The resulting dynamic response of a system may be expected to be of an intermittent nature, whereby relatively long periods of zero or almost-zero response are alternating with relatively rare spontaneous short-period high-level outbreaks. The name "intermittency" is used in Fluid Mechanics for transitional regimes between laminar and turbulent flows. The complete transition usually requires *finite* change in the basic control parameter, such as the Reynolds number, and within the transitional range sporadic alternations or on/off switching between laminar and turbulent flow patterns can be observed. More recently, the name was applied, by analogy, to dynamic systems with lumped parameters that exhibit potential for such "noninstantaneous" transition to chaos—with sporadic outbreaks in chaotic response within the transitional zone and zero or almost-zero response between the outbreaks; for an extensive survey of the topic, see Ref. [1].

In this paper, analytical studies are presented for intermittency in systems with lumped parameters subject to *externally imposed random variations of parameters*. These variations may "smear"

Contributed by the Applied Mechanics Division of ASME for publication in the JOURNAL OF APPLIED MECHANICS. Manuscript received July 5, 2006; final manuscript received November 13, 2007; published online May 9, 2008. Review conducted by Igor Mezic.

the stability boundary of a given system, that is, expand it into the transitional *zone*; the system may then be become marginally unstable in the classical sense. Within such a zone, spontaneous high-level and relatively rare outbreaks alternate with periods of almost-zero response. This behavior of the response may also be qualified as being intermittent indeed. Its analysis may be of importance for engineering as long as it may be impractical for some applications to completely preclude the system's operation within the transitional zone; this may be the case, for example, with a structure subject to wind loads due to hurricanes and/or ocean wave loads in severe storms. Thus, problems of first-passage failure and/or of low-cycle fatigue may be of concern for a system operating within the transitional state. These problems can be treated by existing methods for analysis of random vibrations, which provide possibility for estimating system's reliability in the *design analysis*. Furthermore, relevant dynamic studies may also be of importance for *interpretation* of test results for a machine or structure, where intermittent behavior of the response is observed.

This paper presents results of such dynamic response analyses for two distinctly different types of intermittent response in systems with randomly varying parameters. The first type, as considered in this Part I, corresponds to systems with slow stationary random temporal variations of parameters compared to the system's natural frequency(frequencies). The systems considered clearly operate *within classical stability domain* for the mean or nominal system, i.e., one without parameter variations. Therefore, the system's response is zero as long as random variations of parameter(s) do not make the system temporary unstable. On the other hand, any brief excursion beyond the instability threshold would lead to growth of the system's response. The growth is assumed to be limited as long as the system quickly returns back into the stability domain. The response would be seen then as a set of spontaneous brief outbreaks alternating with intervals of zero response. Thus, it is the case of intermittency. Basically, the response is transient during each outbreak and the system just "does not have time to escape into infinity." Therefore, *linear* model of the system may be adequate at least qualitatively (if not quantitatively). The method for analysis as used in this paper is based on parabolic approximation for temporal variation(s) of parameter(s) during its (their) brief excursions into instability domain [2], which is also called asymptotic theory of the so-called Slepian model for the process [3]. In this way, the problem of random vibration is reduced to a transient problem with *random initial conditions* rather than with random excitation. Moreover, as long as solution to the transient problem is obtained—either by approximate analytical approach as in Refs. [4,5], or numerically—the whole problem of response analysis is reduced to statistical analysis of the random variations in the system's parameter(s)—more specifically in bifurcation parameter, which defines magnitude of nonconservative force(s) responsible for potential dynamic instability; theory of excursions of random processes is essentially involved in this analysis. Results are presented for a single-degree-of-freedom (SDOF) system with randomly varying damping and for two-degrees-of-freedom (TDOF) systems with bifurcation due to coalescing or merging of the system's natural frequencies. Specific potential examples of application are rotating shaft with temporal variations in its apparent internal damping, two-dimensional galloping of a rigid body in a flow with temporal variations of flow speed, and TDOF flutter in a row of tubes in a cross flow of fluid with temporal variations of flow speed.

Another type of marginal instability and intermittency will be considered in Part II, where the parameters' variations are assumed to be broadband with respect to the system. The systems with such parameter variations operate *within the domain of stochastic instability* although very close to the corresponding instability threshold; the adequate modeling for their steady-state response clearly requires the system's *nonlinearity* to be accounted for. Analysis of these marginally unstable systems is based on the theory of Markov processes and solutions to the Fokker-Planck-Kolmogorov (FPK) equations for the response probability density function (PDF).

The Slepian model of a stationary zero-mean random process $g(t)$ with unit standard deviation implies its parabolic approximation in the vicinity of its peak, which exceeds a given level u [3]—that is during upcrossing level u that starts at time instant $t=0$

$$\begin{aligned} g(t/u) &\cong u + (1/u)(\varsigma t - \lambda^2 t^2/2) \\ &\quad \text{so that } g(t) \cong u + \varsigma t - (u/2)(\lambda t)^2 \\ &\quad \text{for } t \in [0, 2\varsigma/\lambda^2 u] \quad \text{and} \\ &\quad \max_t g(t) = g(\varsigma/\lambda^2 u) = g_p = u + \varsigma^2/2\lambda^2 u \end{aligned} \tag{1}$$

Here, subscript p will be used for peak values of random processes, ς is the random slope of $g(t)$ at the instant of upcrossing, and $\lambda^2=\sigma_{\dot{g}}^2=\int_{-\infty}^{\infty}\omega^2\Phi_{gg}(\omega)d\omega$, where $\Phi_{gg}(\omega)$ is power spectral density (PSD) of $g(t)$ so that λ is a mean frequency of $g(t)$. Thus, according to the parabolic approximation (1), the random process $g(t)$ is regarded as deterministic within the high-level excursion of duration $\tau_f=\lambda t_f=2\varsigma/\lambda u$ above level u, depending just on its initial slope ς at the instant of upcrossing. This slope is regarded as a random *variable* for the excursion; in particular, it has a Rayleigh PDF in case of a Gaussian $g(t)$ [2,3]. Furthermore, the instant of downcrossing τ_f is clearly obtained as a second root of equation $g(t)=u$, the first one being $t=0$. This probabilistic description may be used together with the solution for the transient response within the instability domain.

2 SDOF System With Potential Instability of the Negative-Damping Type

The equation of motion of the SDOF system is

$$\ddot{X} + 2(\alpha - q(t))\dot{X} + \Omega^2 X = 0 \tag{2}$$

where $q(t)$ is a zero-mean stationary random process with PSD (the actual mean value $\langle q \rangle$ of the additional negative damping coefficient due to an external nonconservative force may be just deducted from the coefficient of structural damping α_s so that $\alpha=\alpha_s-\langle q \rangle$). The total mean damping coefficient α is assumed to be positive so that the system is dynamically stable (asymptotically) in the mean and its response should be zero as long as the total damping coefficient $\alpha - q(t)$ remains positive. However, if this randomly varying damping coefficient may occasionally cross the zero level, the outbreaks in response would be observed within finite time intervals. Denoting

$$q(t) = \sigma_q g(t) \quad \text{and } u = \alpha/\sigma_q \tag{3}$$

where σ_q is standard deviation of the process $q(t)$, we may substitute the parabolic approximation (1) into the stochastic equation of motion (2), thereby reducing it to an ordinary differential equation (ODE) with a single random parameter ς. This ODE for a certain representative crossing should be integrated starting from the instant of upcrossing denoted by t_u; the final instant for integration should correspond (at least) to the peak of the response $X(t)$ for a given outbreak.

The problem of transient response can be solved analytically for the present case using the asymptotic Krylov–Bogoliubov (KB) method of averaging over the response period for the quite common case of a lightly damped system (1) with slow temporal variations of the damping coefficient: $|\alpha - q(t)| \ll \Omega$, $\lambda \ll \Omega$ [4]. With these assumptions being adopted, the solution may be approximated by that for the undamped system, namely,

$$X(t) = A \sin \psi, \quad \dot{X}(t) = \Omega A \cos \psi, \quad \psi = \Omega t + \phi \tag{4}$$

where $A(t)$ and $\phi(t)$ are now slowly varying functions. The procedure results in a simple ODE for the new state variable $\nu = \ln A$ [4] as follows:

$$\nu' = (\sigma_q/\lambda)[(\varsigma/\lambda)\tau - u\tau^2/2] \tag{5}$$

where primes denote differentiation over nondimensional local time $\tau = \lambda(t - t_u)$ with origin at the upcrossing instant t_u. Integrating this ODE yields, finally,

$$A(\tau) = A_0 \exp\{(\sigma_q/\lambda)[(\varsigma/\lambda)(\tau^2/2) - u\tau^3/6]\} \quad \text{where } A_0 = \exp(\nu(0)) \tag{6}$$

It is clear that response outbreaks are possible only with a nonzero value of the initial response amplitude A_0, which should be estimated somehow from a subcritical response analysis. On the other hand, whenever the inverse problem of interpreting measured response is considered, a simple formula as presented later may be used for estimating A_0 from the observed signal.

It can be seen from the above analysis that the peak value of the response amplitude is attained precisely at the final instant of the excursion into the instability domain $\tau_f = 2\varsigma/\lambda u$; at this instant, the right-hand side (RHS) of the ODE (5) becomes equal to zero once again. The peak amplitude as found from solution (6) is

$$A_p = A(\tau_f) = A_0 \exp(2\delta) \quad \text{where } \delta = (\sigma_q/3\lambda u^2)(\varsigma/\lambda)^3 \tag{7}$$

This solution together with Eq. (1) define in parametric form the relation between $\bar{A}_p = A_p/A_0$ and g_p—which is between peak values of the amplitude ratio and of $g(t)$—as long as both these peak values are obtained as functions of the random nondimensional slope ς/λ of the damping coefficient variation at the instant of the excursion. The explicit relation can be simply derived by excluding ς/λ. Let $\bar{A}_p = h(g_p)$ for $g_p \ge u$. Then, the function inverse to h (denoted by superscript "−1") can be obtained as

$$g_p = u + (\varsigma/\lambda)^2(1/2u) = h^{-1}(\bar{A}_p) = u + (1/2u)[(3\lambda u^2/2\sigma_q)\ln \bar{A}_p]^{2/3} \tag{8}$$

These relations open the way to predicting reliability for system (1) based on relevant statistics of $g(t)$. Thus, the first-passage problem for $A(t)$ with barrier A_* is reduced to that for $g(t)$ with barrier $g_* = h^{-1}(\bar{A}_*)$, as evaluated by using relation (8). Furthermore, the PDF of $g(t)$ can be used to obtain the PDF of $\bar{A}_p$ and thus of the local peaks of $X(t)$ within the cluster of response cycles with peak amplitude A_p; this may be of importance for evaluating low-cycle fatigue life for a system subject to the short-term dynamic instability. The derivation includes two steps. First, the PDF $p_g(g_p)$ of *peaks* of $g(t)$ is obtained from that of the $g(t)$ itself as described in Refs. [2,3]; then, the basic relation for the PDF of a nonlinear function of a random variable is applied as follows:

$$p(\bar{A}_p) = p_g(h^{-1}(\bar{A}_p))|dh^{-1}/d\bar{A}_p| \tag{9}$$

It should be just kept in mind that this PDF is nonzero for $\bar{A}_p \ge 1$ rather than for $\bar{A}_p \ge 0$, as long as the subcritical response amplitude A_0 has been introduced. Furthermore, according to relations (8) and (9), this PDF has a singularity at $\bar{A}_p = 1$. It goes without saying that the *unconditional* PDF $p(\bar{A}_p)$ is normalized not to unity but to $\text{Prob}\{g_p > u\}$. Its direct use for predicting reliability in engineering applications is possible as long as some information on the most probable actual subcritical response amplitude A_0 is available.

The corresponding prediction of the PDF of the actual (nonscaled) response amplitude and/or its peaks may be improved if PDF $p(A_0)$ of the random variable A_0 is known. Thus, assuming random variables A_0 and ς to be independent, one can write

$$p(A_p) = \int_0^\infty p(A_p/A_0)p(A_0)dA_0 \tag{10}$$

The solution (9) has been verified in Ref. [4] by direct numerical simulation of the basic equation (1) with Gaussian $q(t)$ and with small Gaussian white noise being added to its RHS in order to provide nonzero initial response amplitudes for each upcrossing of the level α by $q(t)$. This external excitation used to be turned off immediately upon each upcrossing and brought back upon the corresponding downcrossing. Therefore, this procedure provided really free motion during short-term instability, as assumed in the theory, and it was found to be very important indeed for achieving good accuracy of the estimated PDFs—particularly in view of difficulties in dealing with rare upcrossings. The initial amplitudes A_0 have been measured directly from the response sample $X(t)$ for every upcrossing and in the original simulation runs [4] were used to calculate the relative amplitudes and their peak values $\bar{A}_p = A_p/A_0$ (calculation of amplitudes has been based on the Hilbert transform). These simulations [4] demonstrated good agreement between the theoretical relation (9) and the direct numerical estimate for $p(\bar{A}_p)$ except for very high-amplitude range, where the observed peaks were extremely rare indeed (only three excursions were observed at the level $\bar{A}_p = 5$ with sample length of 142 h and only one or two excursions at each of the higher levels of $\bar{A}_p$).

Figure 1 illustrates new simulation results for the same system parameters and setup as in Ref. [4], which now provide verification for theoretical solution (10) for the PDF of "physical," i.e., nonscaled peak amplitudes (see short part of the sample of $X(t)$ in Fig. 1(*a*) where for convenience this process has been scaled to its standard deviation whereas total processed sample contained about 300,000 periods of $X(t)$). Theoretical expression for $p(\bar{A}_p)$ is compared with the corresponding histogram in Fig. 1(*b*). The former one has been normalized here to its theoretical value for Rayleigh-distributed peaks of the Gaussian process, that is, $\text{Prob}\{g_p(t) > u\} = \exp(-u^2/2)$, which equals 0.1353 for $u = 2$, whereas the histogram has been normalized to direct estimate of this probability calculated as the ratio of upcrossings of the level u to that of the zero level. The present procedure for processing data included compiling values of A_0 at each upcrossing and estimating their PDF $p(A_0)$. The resulting histogram is shown in Fig. 1(*c*) together with the curve of its best fit by Rayleigh PDF with parameter 1.32 (standard deviation of the corresponding Gaussian process), which is seen to provide close analytical approximation for $p(A_0)$. This expression was substituted into the theoretical solution (10), which is seen to be in good agreement with directly measured $p(A_p)$, as shown in Fig. 1(*d*).

In concluding this section, a procedure should be mentioned for identification of system (2) from its observed intermittent response with nonoverlapping outbreaks [4]. It is based on the analytical solution (6) for amplitude, which is applied to the instants of peak amplitude and those of corresponding inflexion points of the curves $\ln A(t)$ at the parts of outbreaks with increasing amplitude. The procedure based on averaging over all observed outbreaks provides estimates for mean frequency and standard deviation λ, σ_q of the parameter variations together with the total nominal or expected damping factor $u\sigma_q$.

3 TDOF Systems With Axial Symmetry

In this section, the basic approach is applied to a special class of TDOF systems with certain symmetry properties that make them amenable to analytical solution for the transient response through the use of a single complex state variable. The first example of such a system is a simple axisymmetric Jeffcott rotor

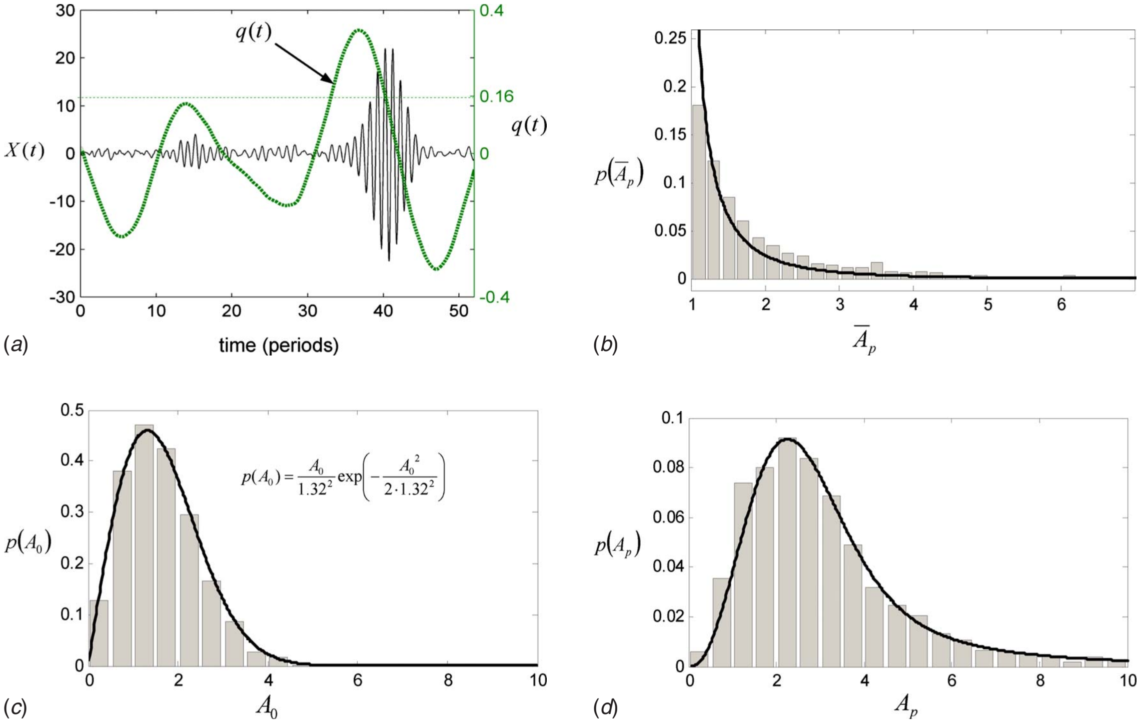

Fig. 1 Short-term single-mode dynamic instability: comparison of theory with direct numerical simulation equation (2) for cases $\Omega=2.0\ \mathrm{s}^{-1}$, $\alpha=0.16\ \mathrm{s}^{-1}$, $\lambda=0.1\ \mathrm{s}^{-1}$, and $u=2$. (*a*) A short sample of $q(t)$ illustrating "outbreak" in $X(t)$ corresponding to upcrossing level 0.16 (nonzero response within stability domain is due to additional random RHS in the equation, which is needed to provide initial conditions for transients due to instability); (*b*) theoretical PDF of scaled amplitude $\bar{A}_p=A_p/A_0$ and corresponding histogram as obtained from sample of $X(t)$; (*c*) histogram of directly measured initial amplitudes—values at the instants of upcrossing—and the corresponding curve of Rayleigh PDF, which provides the best fit of the data; and (*d*) PDF of "physical"—nonscaled—peak response amplitude as calculated according theoretical solution based on theoretical Rayleigh PDF of initial amplitudes and corresponding histogram of directly measured peak response amplitudes.

with both external, or "nonrotating" and internal or "rotating" viscous damping; the latter is assumed to contain component(s) due to nonconservative fluid and/or magnetic forces, which may experience temporal random variations. The analytical solution for PDF of the rotor's translational vibrations during short-term excursions into the instability domain has been obtained in Ref. [5] according to the same procedure as described in Sec. 2. This was found to be possible through the use of a single complex variable $z=x+iy$ for lateral displacements x, y of the rotor's disk into two perpendicular directions; an explicit expression for the shaft's radius of whirl $r(t)=\sqrt{x^2+y^2}$ has been derived accordingly. Similar approach is presented in this section for the case of angular vibrations (tilting) of the disk.

We consider another simple TDOF rotor, which also has a disk at midspan of a weightless shaft similarly to the basic Jeffcott rotor. In the present case, however, the bearings impose complete restraint of lateral transverse displacements of the disk while permitting angular oscillations or tilting of the disk around its transverse axes x and y. (This constraint is visualized in Ref. [6] as being provided by a thin circular plate normal to the shaft's axis, which has infinite in-plane stiffness and finite stiffness in bending). Denoting by ϕ_x, ϕ_y the corresponding rotating (tilting) angles and by K the total apparent rotational stiffness as provided by shaft and/or bearings one can write the following pair of the equations of motion [6]:

$$\ddot{\phi}_x+2\kappa\dot{\phi}_x+\Omega^2\phi_x+\rho\nu\dot{\phi}_y+2\beta\nu\phi_y=0$$

$$\ddot{\phi}_y+2\kappa\dot{\phi}_y+\Omega^2\phi_y-\rho\nu\dot{\phi}_x-2\beta\nu\phi_x=0 \tag{11}$$

Here, ν is rotation speed whereas $\Omega=\sqrt{K/J}$ and $\rho=J_p/J$ where J and J_p are mass moments of inertia of the rotor about anyone of transverse axes and about rotation axis, respectively. Furthermore, $\kappa=\alpha+\beta$ where $\alpha=c_n/2J$, $\beta=c_i/2J$, and c_n, and c_r are, respectively, coefficients of external, or nonrotating and internal or rotating linear viscous damping. It should be noted that except for the "gyroscopic" term, i.e., one with polar moment of inertia, Eq. (11) possesses complete similarity with the equations of translational lateral displacements. Namely, the latter may be written in the form (11) with $\rho=0$ and ϕ_x, ϕ_y replaced by x, y, respectively, whereas the disk's mass m should be substituted for its moment of inertia J [5] (and it goes without saying that relevant damping coefficients c for translational rather than tilting motions should be used). Thus, in case $\rho\to 0$, the present analytical solution for transient response has the same form as the one obtained in Ref. [5] for translational vibrations.

Introducing complex rotation angle $\phi=\phi_x+i\phi_y$, where $i=\sqrt{-1}$, one can replace the two differential equations (11) by the following equivalent single equation:

$$\ddot{\phi}+2\kappa\dot{\phi}+\Omega^2\phi-i\rho\nu\dot{\phi}-2i\beta\nu\phi=0 \tag{12}$$

Now let the internal damping coefficient be time variant so that $\beta(t)=\langle\beta\rangle+q(t)$, where angular brackets denote probabilistic averaging; for its zero-mean part $q(t)$, we shall use corresponding process $g(t)$ with unit standard deviation (see relation (3)), which will be approximated by the Slepian model (1). Assume now that both damping ratios in Eq. (12) are small and temporal variations are slow (as in Sec. 2): $\alpha/\Omega \ll 1$, $\beta/\Omega \ll 1$, and $\lambda \ll \Omega$. Equation (12) may then be analyzed by asymptotic KB averaging over the period. The following change of variables is introduced accordingly.

$$\phi = A_+ \exp(i\Lambda_+ t) + A_- \exp(-i\Lambda_- t),$$

$$\dot{\phi} = i\Lambda_+ A_+ \exp(i\Lambda_+ t) - i\Lambda_- A_- \exp(-i\Lambda_- t)$$

$$\Lambda_\pm = \sqrt{\Omega^2 + (\rho\nu/2)^2} \pm \rho\nu/2 \quad \text{so that } \Lambda_+ - \Lambda_- = \rho\nu, \tag{13}$$

$$\Lambda_+ \cdot \Lambda_- = \Omega^2$$

Here, subscripts "plus" and "minus" are used for the forward and backward whirls, respectively. The corresponding two whirl speeds, Λ, which are seen to be different due to gyroscopic effect, have been obtained here as "generating" solutions to Eq. (12) with $\alpha=0$, $\beta=0$. The amplitudes A of the forward and backward whirls would be slowly varying functions of time under the above assumptions. Thus, resolving relation (13) for A_+ and differentiating yield

$$\begin{aligned}
\dot{A}_+ &= \frac{\Lambda_-}{\Lambda_+ + \Lambda_-}\frac{d}{dt}[(\phi + \dot{\phi}/i\Lambda_-)\exp(-i\Lambda_+ t)] \\
&= \frac{\Lambda_-}{\Lambda_+ + \Lambda_-}(\dot{\phi} - (\Lambda_+/\Lambda_-)\dot{\phi} - i\Lambda_+\phi + \ddot{\phi}/i\Lambda_-)\exp(-i\Lambda_+ t) \\
&= (\Lambda_+ + \Lambda_-)^{-1}[-\rho\nu\dot{\phi} - i(\ddot{\phi} + \Omega^2\phi)]\exp(-i\Lambda_+ t) \\
&= (\Lambda_+ + \Lambda_-)^{-1}(2i\kappa\dot{\phi} + 2\beta\nu\phi)\exp(-i\Lambda_+ t) \\
&\cong 2A_+(\Lambda_+ + \Lambda_-)^{-1}(-\kappa\Lambda_+ + \nu\beta)
\end{aligned} \tag{14}$$

The last approximate equality is obtained by substituting expression (13) for ϕ_x and ϕ_y and applying KB averaging, which implies just neglecting terms with complex exponents; slowly varying function $\beta(t)$ is regarded as fixed throughout this averaging over the "fast" time [7]. The resulting asymptotic equation for the amplitude of forward whirl is seen to be uncoupled from that of backward whirl. The latter can be derived similarly but it is not needed here since dynamic instability is possible only in the forward whirl mode; it happens whenever the cofactor in the utmost right parentheses in the RHS of Eq. (14) is positive.

Equation (14) is now brought into the format of the basic procedure by introducing once again scaled nominal stability margin u, which is now defined as

$$u = \frac{1}{\sigma_q}(\beta_* - \langle\beta\rangle) \quad \text{where } \beta_* = \frac{\alpha}{\nu/\Lambda_+ - 1} \tag{15}$$

Introducing now the same nondimensional local time $\tau=\lambda(t-t_u)$ as before, with origin at the instant for upcrossing level u by $g(t)$ and applying parabolic approximation for the latter, we obtain from Eq. (14) the following first-order ODE for the state variable $v=\ln A$ (the subscript "plus" is dropped hereafter in this section as long as backward whirl is not involved at all):

$$\begin{aligned}
v' = dv/d\tau &= (\mu\sigma_q/\lambda)[(\varsigma/\lambda)\tau - u\tau^2/2] \\
\text{where } \mu &= 2(\nu - \Lambda_+)/(\Lambda_+ + \Lambda_-) \\
&= \nu(1-\rho/2)/\sqrt{\Omega^2 + (\rho\nu/2)^2} - 1
\end{aligned} \tag{16}$$

It should be noted that this ODE is only valid provided that $\mu > 0$ or $\nu > \Lambda_+$; otherwise, upcrossing the instability threshold by $\beta(t)$ would not be possible at all. This condition can be rewritten as $\nu > \Omega/\sqrt{1-\rho}$, which indicates that instability in tilting is possible only for shafts with moments-of-inertia ratio less than unity. In the limiting case of diminishing gyroscopic effect, $\rho \to 0$, we have $\mu=\nu/\Omega-1$, and the ODE (16) is reduced, as suggested earlier, to the one obtained in Ref. [5] for the case of translational vibrations.

Integrating the ODE (16), we obtain the following analytical solution for the amplitude of forward whirl (compare with Eq. (6))

$$\begin{aligned}
A(\tau) &= A_0 \exp\{(\mu\sigma_q/\lambda)[(\varsigma/\lambda)(\tau^2/2) - u\tau^3/6]\} \\
&\text{where } A_0 = \exp(v(0))
\end{aligned} \tag{17}$$

This solution may be used to obtain the PDF of peaks of $A(t)$ in terms of that of peaks of $g(t)$, as illustrated in Sec. 2; similarly, first-passage problems for $A(t)$ may also be reduced to those for $g(t)$.

4 General TDOF Systems

General case of marginally unstable TDOF system will be considered in this section using the same procedure that relies on parabolic approximation for slow temporal random variations of the bifurcation parameter. However, contrary to the special case studied in Sec. 3, the equations of transient motion during short-term instability cannot be reduced now to a single state variable. Thus, two coupled response variables (amplitudes) remain after KB averaging for the case of lightly damped system, thereby requiring numerical integration for the two ODEs of slow motion from starting point of the response outbreak till the instant when both response variables pass their peaks. Then, as long as relation is established (numerically) between peak value(s) of response(s) and that of scaled zero-mean part $g(t)$ of the bifurcation parameter, the basic procedure can be applied for predicting response PDF. Several examples of such analysis are presented in the following.

4.1 Rotating Shaft With Anisotropy in Support Stiffness. We consider translational transverse vibrations of a rotating Jeffcott rotor with disk of mass m. Because of anisotropy in the stiffness properties of the shaft's supports, the total apparent stiffnesses of the shaft are not symmetric (the case of nonrotating anisotropy [8]). Let k_x and k_y be principal stiffnesses corresponding to directions x and y, respectively. Introducing complex displacement $z=x+iy$ to represent 2D vector of the disk's transverse displacements, one may write the following single complex differential equation of motion [8]:

$$\ddot{z} + 2\kappa\dot{z} + \Omega^2 z + \sigma\Omega^2\bar{z} - 2i\beta\nu z = 0 \tag{18}$$

Here, the bar denotes complex conjugate of z and

$$\Omega = \sqrt{k_m/m}, \quad k_m = \frac{1}{2}(k_x + k_y), \quad \sigma = \frac{k_x - k_y}{k_x + k_y},$$

$$\kappa = \alpha + \beta \quad \text{where } \alpha = c_n/2m, \quad \beta = c_i/2m$$

Here, c_n and c_r are, respectively, coefficients of external or nonrotating, and internal or rotating linear viscous damping (with corresponding damping forces being related to translational motion).

For the case of zero "mistuning factor" σ, Eq. (18) reduces to the one solved explicitly in Ref. [5]. The general case of nonzero σ will be studied in the following by KB averaging assuming this factor to be small; assumptions of small damping ratios and slow temporal variations of the internal damping coefficient, similar to those used in Sec. 3, will be adopted here as well.

We introduce now amplitudes of forward and backward whirls $z_+(t)$ and $z_-(t)$, respectively, as new state variables according to relations

$$z = z_+ \exp(i\Omega t) + iz_- \exp(-i\Omega t),$$

$$\dot{z} = i\Omega z_+ \exp(i\Omega t) + \Omega z_- \exp(-i\Omega t) \tag{19}$$

These relations are resolved for slowly varying functions $z_+(t)$ and $z_-(t)$ and resulting expressions are differentiated. The RHSs of the resulting two first-order ODEs are found to be proportional to a small parameter in view of the assumptions adopted. Thus, KB averaging over response period $2\pi/\Omega$ can be applied [7], which reduces to neglecting terms with complex exponents of fast time; the slowly varying internal damping factors are once again regarded as constant in the fast time (but not in the slow time). This results in the following set of real reduced ODEs, which are found to be coupled through the mistuning of the natural frequencies in the x and y directions:

$$\dot{z}_+ = [-\alpha + \beta(\nu/\Omega - 1)]z_+ + (\sigma\Omega/2)z_-$$
$$\dot{z}_- = -(\sigma\Omega/2)z_+ - [\alpha + \beta(\nu/\Omega + 1)]z_- \tag{20}$$

System (20) is asymptotically stable as long as its determinant is positive. Equating the determinant to zero yields condition for neutral stability resulting in quadratic equation for instability threshold in terms of critical value of the internal damping factor. This critical value as denoted by a star subscript is found to be

$$\beta_* = \frac{\alpha + \sqrt{(\alpha\nu/\Omega)^2 + [(\nu/\Omega)^2 - 1](\sigma\Omega/2)^2}}{[(\nu/\Omega)^2 - 1]} \tag{21}$$

Now, for the process $\beta(t) = \langle\beta\rangle + q(t)$, we introduce once again its scaled zero-mean part $g(t) = q(t)/\sigma_q$, where σ_q is standard deviation of $q(t)$, whereas scaled positive stability margin u of the mean or nominal rotor is still defined by basic formula (15) but with expression (21) for the instability threshold. The ODEs (20) may now be applied to describe the response outbreak after upcrossing instability threshold at time instant $t = t_u$. Using the introduced definitions in Eq. (20) and applying parabolic approximation for $g(t)$ yield the final set of ODEs in the transformed local time

$$\lambda z_+' = \{-\alpha + \beta_*(\nu/\Omega - 1) + \sigma_q[(\varsigma/\lambda)\tau - u\tau^2/2](\nu/\Omega - 1)\}z_+ + (\sigma\Omega/2)z_-$$
$$\lambda z_-' = -(\sigma\Omega/2)z_+ - \{\alpha + \beta_*(\nu/\Omega + 1) + \sigma_q[(\varsigma/\lambda)\tau - u\tau^2/2](\nu/\Omega + 1)\}z_- \tag{22}$$

These ODEs should be integrated starting from initial values of response amplitudes at $\tau = 0$. An example with Gaussian $q(t)$ and $\Omega = 1\ \text{s}^{-1}$, $\alpha = 0.02\ \text{s}^{-1}$, $\lambda = 0.01\ \text{s}^{-1}$, and $\nu = 1800$ rpm has been considered for various values of the mistuning parameter σ with parameters of $\beta(t)$ being kept fixed. The case $\sigma = 0.001$, $u = 2$ has been chosen as the reference one and relation $\langle\beta\rangle = 0.5\beta_*$ has been imposed for this case; values of u have been calculated for other cases accordingly as $u = 2.12$, 2.46, and 4.38 for $\sigma = 0.01$, 0.02, and 0.05, respectively.

Numerical solutions for z_+ and z_- were obtained for initial conditions (ICs) with imposed ratio of these state variables as defined by eigenvector of the matrix in the RHS of the ODEs (20) (that is, the same ratio as at the neutral stability boundary). Amplitude or rather whirl radius $A = \sqrt{z_+^2 + z_-^2}$, which is proportional to its initial value $A_0 = A(0)$, has been calculated then as a function of nondimensional local time τ. Peak values of $A(\tau)$ were identified from the numerical solution and ratios $\bar{A}_p = A_p/A_0$ were used to calculate their PDFs, as presented in Fig. 2. It should be noted that the upper curve—one for the reference case with very small $\sigma = 0.001$—practically coincides with the corresponding analytical solution for $\sigma = 0$ [4]. Figure 2 clearly illustrates reduction of transient responses with increasing mistuning between the shaft's natural frequencies in two directions.

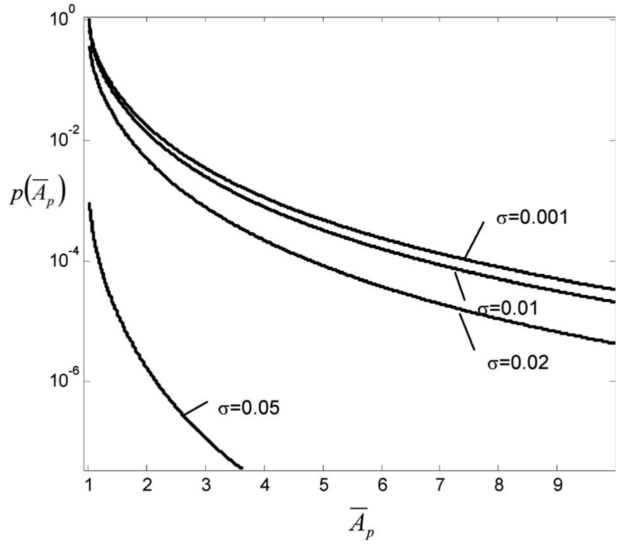

Fig. 2 Theoretical PDFs of scaled peak radius of whirl of rotating shaft with temporal random variations of the internal damping for different values of mistuning factor

4.2 Two-Dimensional Galloping of a Rigid Body in a Fluid Flow. As another example, we consider an infinite rigid horizontal cylinder with blunt cross section. The cylinder is mounted on elastic suspension springs and is subject to a fluid cross flow. The name "galloping" was introduced in first studies initiated in 1930s with applications to cross-flow (vertical) response of ice-covered transmission power lines excited by wind. Basic SDOF model was used and their potential single-mode instability had been established by Den-Hartog [9] for cross-sectional shapes with negative rather than positive slope of lift curve (versus angle of attack). This case can clearly be handled by the procedure of Sec. 2 (see also Ref. [4]) whenever the speed of wind is subject to temporal random variations.

More recent studies indicate, however, that horizontal vibrations (along flow) very often may also be present, which are coupled with the vertical ones and should not be ignored (see Ref. [10] and references cited there in). Thus, the same TDOF model as in Ref. [10] will be considered (with certain obvious changes in notation) with full two-by-two aerodynamic damping matrix **B** but for special case of identical stiffnesses of suspension springs in directions x (horizontal) and y (vertical). Two differential equations for displacements in these directions may be written as

$$\ddot{x} + 2\alpha\dot{x} + \Omega^2 x + \mu(t)(\beta_{xx}\dot{x} + \beta_{xy}\dot{y}) = 0$$
$$\ddot{y} + 2\alpha\dot{y} + \Omega^2 y + \mu(t)(\beta_{yx}\dot{x} + \beta_{yy}\dot{y}) = 0 \tag{23}$$

Here, four coefficients β, which are elements of the aerodynamic damping matrix **B**, depend on lift and drag factors and their derivatives over angle of attack according to the relations that are presented in Ref. [10] together with expression for scaled flow speed μ. The latter is assumed here to experience slow temporal variations. System (23) has only one natural frequency due to the assumption of equal stiffnesses in x and y directions, whereas α is an equivalent viscous damping of the cylinder assumed to be identical in two directions.

The case of lightly damped system (23) has been analyzed in Ref. [10] by perturbational approach that leads to interesting explicit expressions for periodic oscillations. The same assumption of small damping ratios will be adopted here for analysis by the KB averaging [7], which provides similar reduction for transient problems. For this application, it may seem preferable to deal with real rather than complex quantities, so that solution to Eq. (23) is sought in the form $x = x_c \cos \Omega t + x_s \sin \Omega t$, $\dot{x} = \Omega(-x_c \sin \Omega t + x_s \cos \Omega t)$ together with similar change of variables y and $\dot{y}$. Resolving these relations for new slow state variables and differentiating, we obtain four first-order ODEs with small parameter in their RHSs. Thus, averaging over the response period $2\pi/\Omega$ in rapid time can be applied, once again with fixed bifurcation parameter μ in rapid time. This results in two identical

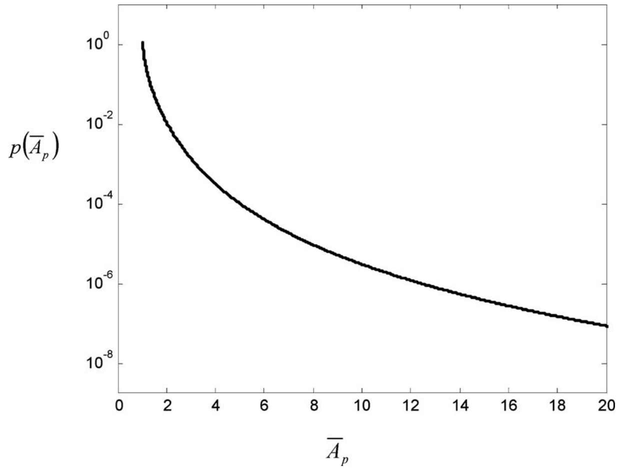

Fig. 3 Theoretical PDF of scaled peak vertical response of a rigid body in a 2D galloping

uncoupled equations for 2D vectors: $\mathbf{z}_c=[x_c,y_c]^T$ and $\mathbf{z}_s=[x_s,y_s]^T$, where superscript T denotes transposed vector

$$\dot{\mathbf{z}}_c=\left\{-\alpha\mathbf{I}-\frac{1}{2}\mu(t)\mathbf{B}\right\}\mathbf{z}_c \quad \text{and} \quad \dot{\mathbf{z}}_s=\left\{-\alpha\mathbf{I}-\frac{1}{2}\mu(t)\mathbf{B}\right\}\mathbf{z}_s \tag{24}$$

where $\mathbf{I}$ is identity matrix.

Condition for neutral stability of zero solution to any one of the ODE's (24) is that of zero determinant of the matrix in braces. Imposing this condition yields a quadratic equation for critical value of the bifurcation parameter which, will be denoted by a star subscript. For the example to be presented, we assume that $\text{Tr}\,\mathbf{B}\equiv\beta_{xx}+\beta_{yy}>0$, $\text{Det}\,\mathbf{B}\equiv\beta_{xx}\beta_{yy}-\beta_{xy}\beta_{yx}<0$. Then,

$$\mu_*=-\frac{\alpha}{\text{Det}\,\mathbf{B}}[\text{Tr}\,\mathbf{B}+\sqrt{(\text{Tr}\,\mathbf{B})^2-4\,\text{Det}\,\mathbf{B}}] \tag{25}$$

The parabolic approximation for $g(t)$ may be applied once again, thereby reducing the problem to solution of any one of the vector ODEs (24) with

$$\mu(t)\equiv\langle\mu\rangle+\sigma_q g(t)=\mu_*-\sigma_q(u-g(t))$$

$$=\mu_*+\sigma_q[\varsigma t-(u/2)(\lambda t)^2], \quad \text{where } u=(\mu_*-\langle\mu\rangle)/\sigma_q$$

and μ_* as defined by expression (25). Numerical integration has been performed for cases $\Omega=1\ \text{s}^{-1}$, $\alpha=0.007\ \text{s}^{-1}$, and $\lambda=0.01\ \text{s}^{-1}$ and the same aerodynamic damping matrix as in one of the examples presented in Ref. [10], namely,

$$\beta_{xx}=2.14, \quad \beta_{xy}=0.46, \quad \beta_{yx}=1.2,$$

$$\beta_{yy}=-0.32 \quad \text{so that } \mu_*=0.0266$$

Figure 3 shows PDF $p(\bar{A}_p)$ of $\bar{A}_p=A_p/A_0$. Here, A_p is peak value of $y_c(\tau)$ in this case whereas $A_0=y_c(0)$ and $x_c(0)$ has once again been assigned according to the same eigenvector condition as in Sec. 4.1.

4.3 TDOF Flutter of a Tube Row in a Cross Flow of Fluid.

A certain flutter-type mechanism of dynamic instability due to nonconservative fluid forces has been proposed and studied in Ref. [11] and extended in Ref. [12] for a tube row in a cross flow of fluid. It is related to proximity effect and corresponding cross stiffnesses of two neighboring circular cylinders (tubes). Each tube is assumed to have two DOFs corresponding to motions along and across the flow with displacements x_j and y_j, respectively, where j is number of tube (single spanwise mode may be considered for each direction in case of elastic tubes). General equations of motion of the row of identical tubes accounting for linearized fluid forces are presented in Sec. 5.2 of Ref. [12] and their stability analysis is presented for two neighboring tubes under assumption that only two certain cross-stiffness coefficients are involved in dynamic instability. Thus, it is the case of a TDOF flutter indeed and the equations of motion of tube j along the flow and tube $j+1$ perpendicular to flow are

$$\ddot{x}_j+2\alpha\dot{x}_j+\Omega^2x_j=(\gamma C_x/m)y_{j+1} \quad \text{and}$$

$$\ddot{y}_{j+1}+2\alpha\dot{y}_{j+1}+\Omega^2y_{j+1}=-(\gamma K_x/m)x_j \tag{26}$$

Here, $\gamma=\rho U^2/2$ and $\Omega=\sqrt{k/m}$, where U is flow speed, m is mass of tube, and k is its stiffness; the latter is assumed in this paper to be the same for both directions x and y as well as the structural damping factor α (stability analysis for this special case of Eqs. (5-14) and (5-15) of Ref. [12] had been presented in Ref. [11]); C_x and K_y are fluidelastic coefficients, which are involved in the TDOF flutter that leads to whirling motion that is observed in tests (see references in Ref. [12]), whereas two other fluidelastic coefficients C_y and K_x are neglected.

Assuming now that flow speed U is subject to (relatively slow) temporal random variations, we may apply the basic procedure for stochastic analysis. Introducing complex coordinate $z=x_j+y_{j+1}$, we may replace two real equations (26) by a single complex equation

$$\ddot{z}+2\alpha\dot{z}+\Omega^2z+i\gamma\Lambda^2(z+\sigma\bar{z})=0$$

$$\text{where } K_y+C_x=2\Lambda^2, \quad K_y-C_x=2\sigma\Lambda^2 \tag{27}$$

To apply KB averaging for the case of lightly damped system, we introduce change of variables

$$z=z_+\exp(i\Omega t)+z_-\exp(-i\Omega t),$$

$$\dot{z}=i\Omega[z_+\exp(i\Omega t)-z_-\exp(-i\Omega t)] \tag{28}$$

(which is seen to be similar to Eq. (19) but without cofactor i in the expression for z; this transformation yields real final ODEs for two new state variables). Similarly to derivation in Sec. 4.1, relation (28) is resolved for $z_+(t)$ and $z_-(t)$ and the resulting expressions are differentiated. Subsequent application of the KB averaging yields then

$$\dot{z}_+=-(\alpha+\gamma\Lambda^2/2\Omega)z_+-(\gamma\sigma\Lambda^2/2\Omega)z_-$$

$$\dot{z}_-=(\gamma\sigma\Lambda^2/2\Omega)z_++[-\alpha+\gamma\Lambda^2/2\Omega]z_- \tag{29}$$

Condition for neutral stability of this system, which is that of vanishing determinant of the RHS of this ODE set, yields the corresponding critical value of γ as denoted by a star subscript as follows:

$$\gamma_*=2\alpha\Omega/(\Lambda^2\sqrt{1-\sigma^2}) \tag{30}$$

This condition for neutral stability clearly coincides with the exact one as obtained in Ref. [12] by direct application of the Routh–Hurwitz criterion to the original equation (26).

Direct numerical integration of the ODEs (29) may now be applied for the case where parabolic approximation is used for zero-mean part of $\gamma(t)$. It may happen, however, that data on fluidelastic coefficients C_x and K_y are available only from stability tests. As can be seen from formula (30), critical flow speed depends only on product of these coefficients (these kinds of data are presented in Ref. [11]). As long as individual values of C_x and K_y are not known, it would be reasonable to consider "the worst case"—one with smallest critical speed. As can be seen from Eq. (30), it is the case where $C_x=K_y$ or $\sigma=0$. Moreover, in this special case, two ODEs (29) are uncoupled so that we may consider only the second of these, which is prone to short-term instability and apply analytical solution of Sec. 2.

5 Conclusions

Dynamic systems have been considered with random temporal variations in a parameter of nonconservative force(s), or bifurcation parameter. While mean or expected value of this parameter lies within the stability domain of the corresponding "nominal" system, its random variations may occasionally bring the system into the domain of dynamic instability for brief periods. As long as it may be impossible or impractical to preclude completely the corresponding response outbreaks in designing such "marginally unstable" systems, this random response should be studied to evaluate the system's reliability. This response may be of an intermittent nature just because of the way it is generated, with alternating relatively long periods of zero or almost-zero response and relatively brief and rare violent outbreaks.

A procedure for analysis of response of this kind has been described in this paper for the case where expected frequency of the (bifurcation) parameter variations is small compared with the system's lowest natural frequency. It is based on parabolic approximation of the variation process in the vicinities of its peaks, or the so-called Slepian model. The approximation reduces the problem of random vibration to one of deterministic transient vibration with random initial conditions; in this way, probabilistic analysis of the intermittent response is reduced to that of the bifurcation parameter variation process. Thus, the PDF of the response peaks may be predicted, which is important for evaluating damage accumulation in low-cycle fatigue; first-passage analysis for response is also reduced to that for the bifurcation parameter.

The resulting ODE(s) of transient motion during the short-term or temporary dynamic instability has(ve) been reduced by the KB averaging over "fast" time for the important case of highly damped system. Cases of single-mode instability of the negative-damping type and of two-mode flutter-type instability have been considered. Analytical solutions for the former case have been obtained for transient response outbreak and thus for PDF of response peaks. This analysis has been extended to certain TDOF systems with special symmetry properties. General TDOF systems have been studied using numerical solution for the transient response problem. Specific examples of applications considered include rotating shafts with temporal variations in apparent "rotating" damping and 1D or 2D galloping of a rigid body in a fluid flow with randomly varying speed.

Acknowledgment

M.F.D. contributed to this work during his stay at the Centre for Ships and Ocean Structures (CeSOS) of the Norwegian University of Science and Technology (NTNU). The financial support provided by CeSOS is most highly appreciated.

References

[1] Nayfeh, A. H., and Balachandran, B., 1995, *Applied Nonlinear Dynamics*, Wiley, New York.
[2] Stratonovich, R. L., 1967, *Topics in the Theory of Random Noise*, Gordon and Breach, New York, Vol. II.
[3] Leadbdetter, M. R., Lindgren, G., and Rootzen, H., 1983, *Extremes and Related Properties of Random Sequences and Processes*, Springer-Verlag, New York.
[4] Dimentberg, M., and Naess, A., 2006, "Short-Term Dynamic Instability of a System With Randomly Varying Damping," J. Vib. Control, **12**, pp. 495–508.
[5] Dimentberg, M., 2005, "Vibration of a Rotating Shaft With Randomly Varying Internal Damping," J. Sound Vib., **285**, pp. 759–765.
[6] Dimentberg, M., Ryzhik, B., and Sperling, L., 2005, "Random Vibrations of a Damped Rotating Shaft," J. Sound Vib., **279**, pp. 275–284.
[7] Bogoliubov, N. N., and Mitropolsky, Y. A., 1961, *Asymptotic Methods in the Theory of Nonlinear Oscillations*, Gordon and Breach, New York.
[8] Genta, G., 1995, *Vibrations of Structures and Machines*, Springer, New York.
[9] Den Hartog, J. P., 1985, *Mechanical Vibrations*, Dover, New York.
[10] Luongo, A., and Piccardo, G., 2005, "Linear Instability Mechanisms for Coupled Translational Galloping," J. Sound Vib., **288**, pp. 1027–1047.
[11] Connors, H. G., 1970, "Fluidelastic Vibration of Tube Arrays Excited by Cross Flow," *Symposium on Flow-Induced Vibration in Heat Exchangers, ASME Winter Annual Meeting*.
[12] Blevins, R. D., 1994, *Flow-Induced Vibration*, Krieger, Malabar, FL.

Giuseppe Ferro[1]
e-mail: ferro@polito.it

Alberto Carpinteri

Department of Structural Engineering
and Geotechnics,
Corso Duca degli Abruzzi 24,
Politecnico di Torino,
10129 Torino, Italy

Effect of Specimen Size on the Dissipated Energy Density in Compression

The size effects in compression on drilled cylindrical concrete specimens obtained from a unique concrete block over a large scale range (1:19) are analyzed. The experimental results show scale effects on dissipated energy density rather than on the compressive strength. A theoretical explanation for such a phenomenon is presented, assuming a noninteger physical dimension of the subdomain where dissipation occurs. A comparison between experimental and theoretical values is discussed and a renormalization procedure to obtain a scale-independent constitutive law is presented.
[DOI: 10.1115/1.2910899]

Keywords: compression test, concrete, dissipated energy density, size effects, microstructural disorder, fractals

Introduction

Scale effects have received a strong interest in the past few decades. With the term *scale effects*, both the variation of mechanical parameters and the variation of failure mode by varying the characteristic structural dimension (ductile to brittle transition) are considered. Very interesting results have been achieved by the second author in defining brittleness numbers, which easily determine the failure behavior: the static [1,2], the energetic [3–5], and the composite [6] brittleness number. In tension, the phenomenon has been deeply discussed and important conclusions have been set. In particular, the variation of tensile strength was considered with the formulation of different laws. Bažant [7] defined the so-called size effect law in the hypothesis of the presence of an initial crack of length proportional to the specimen size. This law has been often used in the literature. Successively, Carpinteri [8,9] and Carpinteri et al. [10] proposed the multifractal scaling law, valid for initially integer specimens and components. On the other hand, the compression failure is more complex and the related size effects are less understood.

The brittle failure in compression has been widely studied over the past decades. The phenomenon of axial splitting in the absence of confinement, as well as the related phenomena of exfoliation or sheet fracture, has been analyzed by Holzhausen and Johnson [11], by Nemat-Nasser and Horii [12], and by Ashby and Hallam [13]. Horii and Nemat-Nasser [14] have modeled the transition from brittle failure to ductile flow under very high confining pressures, by considering possible zone of plastically deformed materials at high shear-stress region around preexisting flaws. An interesting overview of brittle failure in compression can be found in Ref. [15].

Bažant and Xiang [16] proposed a simplified model of compression failure of quasibrittle columns, with the propagation of a band of axial splitting cracks in a direction parallel or inclined with respect to the column axis, predicting in that case the size effect on nominal strength. Rossi et al. [17], in order to explore the possibilities for the numerical modeling of concrete behavior, considered the failure of concrete in compression as the sequence of two-stage crack mechanisms. At the first stage, cracks parallelly open to the direction of loading, leading to the formation of slender columns in the material. At the second stage, these columns bend because of eccentric compressive loading and an oblique cracking mechanism starts at a scale smaller than the one of the columns. A softening branch is observed and, as a consequence, the multiscale heterogeneity of the material is proved to affect also the postpeak behavior. Markeset and Hillerborg [18] proposed the compressive damage zone model based on the hypothesis of compression failure mode as a combination of distributed axial splitting and localized deformation within a zone of limited length. Slate et al. [19] observed how the tensile mechanism is the most relevant crack mechanism controlling failure of concrete in uniaxial compression. In normal-strength concretes, they found highly irregular failure surfaces including a large amount of bond failure. In high-strength concretes, instead, the failure mode is that typical of nearly homogeneous materials in which failure occurs suddenly in a vertical, nearly flat plane passing through aggregates and mortar. This result can be easily explained by the model by Carpinteri and Chiaia [20], in which the fractal dimension of the fracture surface is presented as a function of aggregates and mortar characteristics.

The variation of the compressive strength with size and height-diameter (or slenderness) ratio is relevant when the rigid test machine platens are in direct contact with the concrete specimen, the lateral deformation of concrete being restrained at the specimen ends. In this context, a wide investigation has been carried out by Carpinteri et al. [21]. When, instead, the friction at the specimen ends is reduced, the strength variation is less evident.

Van Vliet and van Mier [22], using improved experimental techniques of axial displacement control and lubricated end platens as well as variable height to diameter ratios, observed that postpeak data from uniaxial compression experiments on plain concrete suggest a stress-displacement rather than a stress-strain relation. To obtain a unique empirical stress-displacement relationship, they suggested a functional dependence of the axial stress on the axial displacement, which turns out to be more or less insensitive to the height of the specimen.

An experimental investigation on geometrically similar cylindrical concrete specimens, obtained by a unique concrete block in compression over a very large scale range (1:19), will be briefly reported [23] and the obtained scale effects will be herein discussed. It will be shown how, avoiding friction, the strength is almost independent of specimen dimension while strong variations are observed for dissipated energy density. This phenomenon can be interpreted by considering the fragmentation and the com-

---

[1] Corresponding author.

Contributed by the Applied Mechanics Division of ASME for publication in the Journal of Applied Mechanics. Manuscript received August 9, 2006; final manuscript received September 11, 2006; published online May 9, 2008. Review conducted by Robert M. McMeeking.

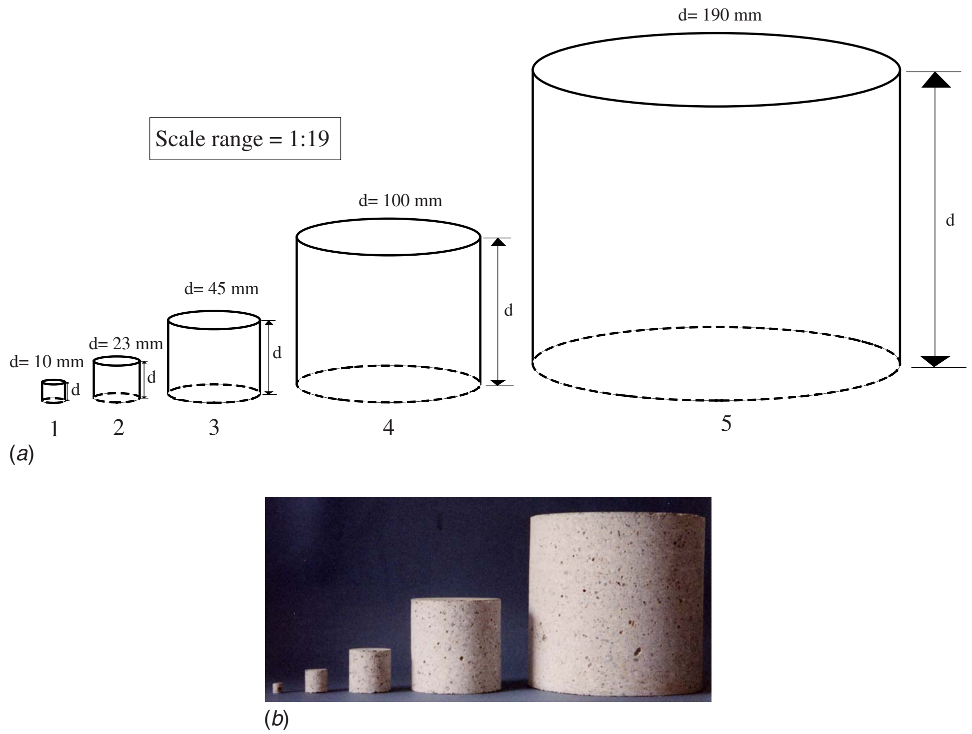

(*a*)

(*b*)

Fig. 1 (*a*) Geometries of the five different concrete specimens; (*b*) overall view of the five specimen sizes

minution theories. In this field, fractal geometry represents a very helpful tool to explain such a phenomenon. Turcotte [24] proposed a very interesting fractal approach for fragmentation. He affirmed that, if the fragments are produced over a wide range of sizes and if natural scales are not associated with the fragmented material, a fractal distribution of number versus size would seem to be expected.

In this context, a theoretical explanation, recently proposed by Carpinteri and Pugno [25,26], for the scale effects on the dissipated energy density in compression, is discussed and applied to the experimental results. From the theory, it can be evidenced how, in the scale range of the tested specimens, the energy dissipation occurs in a subdomain with a noninteger physical dimension.

In the last section, a scale-independent constitutive law in compression is put forward, which permits to define a unique relationship for softening in concrete. This goal is achieved by defining a fractal strain (or dilatation) whose fractal dimension is related to the subdomain in which energy dissipation occurs.

Experimental Evidence

In this section, the experimental tests performed at the Politecnico di Torino are briefly presented. As pointed out in the Introduction, all the cylinder were obtained on drilling from a unique concrete block with sizes $800 \times 500 \times 200$ mm^3. The microconcrete used for the specimens is characterized by a maximum aggregate size of 4 mm, with a compression strength, obtained by cubes ($150 \times 150 \times 150$ mm^3) after 28 days, equal to 33 N/mm^2. The water-cement ratio was equal to 0.65.

Five different diameters were considered in relation to the disposable drilling core bits in a scale range of 1:19. The specimens were cylinders with a height-diameter ratio $h/d=1$ and d chosen as characteristic dimension equal to 10 mm, 23 mm, 45 mm, 100 mm, 190 mm, respectively. Six specimens have been tested for $d=10$ mm, 23 mm, and 45 mm and four specimens for $d=100$ mm and 190 mm. The geometries of the tested specimens are presented in Fig. 1(*a*), while an overview of all the specimen sizes is reported in Fig. 1(*b*). Each specimen is individuated by a label formed by a letter C (compression) and by two numbers. The first number is related to the specimen dimension (1 for $d=10$ mm, 2 for $d=19$ mm, and so on) as reported in Fig. 1. The second number indicates the specimen.

For the three smallest sizes, the tests were carried out on a uniaxial compression machine with a capacity of 100 kN. The machine was controlled by a closed-loop servo-hydraulic system. All compression tests with this machine have been performed under displacement control, by imposing a constant rate of the displacement of the upper loading platen.

For the two remaining specimen sizes, $d=100$ mm (C4) and 190 mm (C5), a manual load controlled uniaxial compression machine with a capacity of 3000 kN was used. The choice of this kind of machine was necessary as the peak load for these specimens exceeded the maximum load of the other displacement controlled machines available in the laboratory. In addition, the height of the specimens did not permit the control of the postpeak load-displacement diagram, due to the more brittle structural behavior, unless a very sophisticated control system could be available, as performed by van Vliet and van Mier [22].

For these two larger sizes, loading cycles around the peak load were performed in order to capture the postpeak branch and to plot the entire curve. Unfortunately, as should have been easy to predict, only for one specimen (C44), we were able to capture the softening part.

The system adopted in the present compression tests for reducing friction at the ends of the specimens comes out from the analysis of the RILEM Technical Committee 148 SSC results [27]. These results suggested us to use two Teflon layers of 150 μm thickness with oil in between and a specimen slenderness equal to one.

The experimental load versus displacement diagrams can be found in Ref. [23]. Only one stress-deformation curve for each of the four sizes of concrete loaded in uniaxial compression is plotted in Fig. 2. These curves, as the load versus displacement ones, show a steadily initial increasing slope, due to the lower stiffness

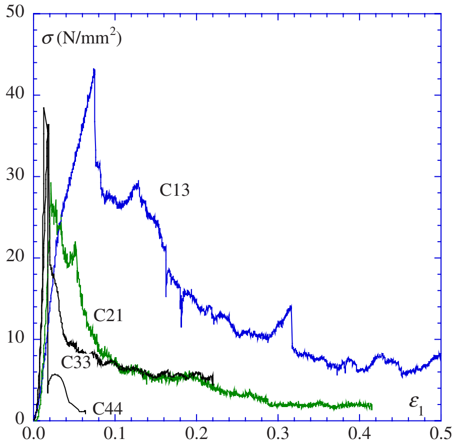

Fig. 2 Stress-strain curves for four different cylindrical specimen sizes

at the beginning of the test, i.e., to the adjustment of the loading platens to the specimen surfaces and to the compressibility of the Teflon interlayers.

After this initial part, the stress-strain path is nearly linear and this linear part is as more pronounced as larger the specimen is (Fig. 2). The smaller the specimen, the more pronounced prepeak nonlinearities are. After the peak stress, a gradually descending branch has been detected. As it can be deduced from Fig. 2, the stress-strain curve for different specimens are almost the same in the prepeak regime, but, beyond the peak, the slope of the descending branch decreases with decreasing specimen height. Van Mier [28] plotted the normalized stress versus postpeak displacement diagrams, in which the displacements are calculated as

$$\delta = (\epsilon - \epsilon_{\text{peak}})h \tag{1}$$

and obtained nearly overlapping curves. He concluded that, as the same displacement is needed to fracture the specimens, the postpeak deformation must be localized in a small zone, and cannot be interpreted as an average strain. This fracture localization of concrete uniaxial compression implies that strain cannot be used as state variable in constitutive laws. The dimensionless stress versus postpeak deformation diagrams for four cylindrical specimen sizes are plotted in Fig. 3. It can be effectively evidenced that these curves are close to each other, even if different initial slopes, indicating an increase of brittleness with size, are present.

The values of the peak stresses, which are commonly called *compressive strength*, are reported in Fig. 4 by varying the specimen sizes. It can be noticed how, reducing friction, a marked size effect does not come out, as instead can be evidenced in tension [10,29,30] or in compression when localization is present [21]. The same results were obtained experimentally by the RILEM Committee 148 [27] and numerically by Carpinteri et al. [31,32] by simulations with a boundary element approach. The scatter in the results is not pronounced and even for the smallest size the values are comparable to the compressive strength of standard cubes. This permits to affirm that, if friction is avoided or drastically reduced, the compressive strength of an existing concrete structure can be evaluated using very small drilling core specimens.

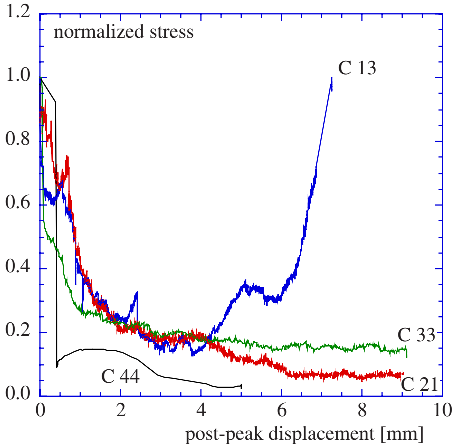

Fig. 3 Normalized stress versus postpeak displacement for four different cylindrical specimen sizes

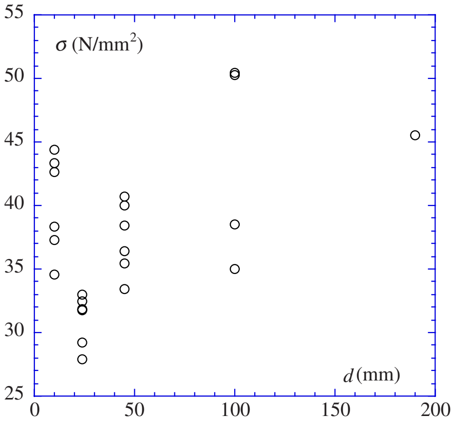

Fig. 4 Peak stresses by varying specimen size

The dissipated energy density can be evaluated by considering the area under the $P-\delta$ curve divided by the volume of the specimen. This is equivalent to consider the area under the stress-strain curve. The values of the dissipated energy density are plotted versus the characteristic specimen size in Fig. 9 in bilogarithmic plane. They undergo severe scale effects. The trend is a decrease by increasing the specimen dimension. This interesting result is discussed in the next section and a theoretical explanation is presented, based on a fractal hypothesis for the fragment size distribution generated during the compression test.

Fractal Explanation of Size Effect on Dissipated Energy Density in Compression

Monofractal Approach. The performed compression tests have shown an evident decrease of dissipated energy density with increasing specimen dimension (Fig. 9). This interesting phenomenon can be interpreted by considering the fragmentation and the comminution theories. In this field, fractal geometry represents a very helpful tool. Fragmentation involves initiation and propagation of fractures. Fracture propagation is a highly nonlinear process requiring complex models even for the simplest configuration. Fragmentation involves the interaction between fractures over a wide range of scales. If fragments are produced over a wide range of sizes and if natural scales are not associated with the fragmented material, fractal distribution of number versus size would seem to be expected. The statistical number-size distribution for a large number of objects can be fractal [24,33].

Let us consider a concrete specimen, which undergoes a compression test. In the postpeak softening regime, the specimen is characterized by the generation of a large number of fragments. After fragmentation, the number of fragments N with a characteristic linear dimension greater than r should satisfy the relation

$$N = \frac{B}{r^D} \tag{2}$$

where B is a constant of proportionality, and D is the fractal

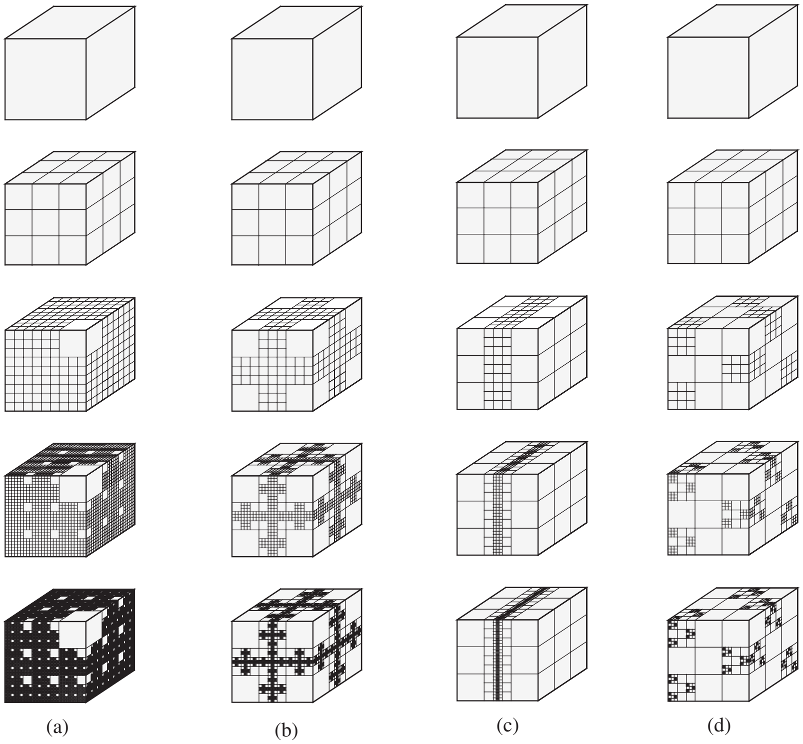

Fig. 5 Physical meaning of exponent D; (a) at each step, only one cube is retained, while all the others are divided into 27 equalsized cubes with $r_n = \frac{1}{3} r_{n-1}$ (D=2.93), very close to a volumetric fragmentation; (b) at each step, the eight angular cubes are retained, while all the others 19 are divided into 27 equal-sized cubes with $r_n = \frac{1}{3} r_{n-1}$ (D=2.70); (c) and (d) at each step, the nine cubes are divided into 27 equal-sized cubes with $r_n = \frac{1}{3} r_{n-1}$, while the others 18 are retained (D=2.00), showing a localization of the dissipation energy

dimension.

In order to describe the mechanical meaning of the fractal exponent D, in Fig. 5 some examples of discrete fragmentation model are presented, where fragmentation is a scale-invariant process that leads to a fractal distribution of chip sizes. We consider a fractal cube and use it as the basis for a fragmentation model. The fragmentation is such that some blocks are retained at each scale but others are fragmented. In order to determine D, Eq. (2) can be written as

$$D = \frac{\log(N_{n+1}/N_n)}{\log(r_n/r_{n+1})} \tag{3}$$

and then we can find for the three cases $D = \log 25/\log 3 = 2.93$ (Fig. 5(a)), $D = \log 19/\log 3 = 2.68$ (Fig. 5(b)), and $D = \log 9/\log 3 = 2.00$ (Figs. 5(c) and 5(d)), respectively. This is the fractal distribution of a discrete set. The cumulative number of blocks larger than a specified size for the three highest orders are $N_{1c}=2$ for $r_1 = h/3$, $N_{2c}=52$ for $r_2 = h/9$, and $N_{3c}=1302$ for $r_3 = h/27$, obtaining a value $D=2.95$ for the first example; $N_{1c}=8$, $N_{2c}=160$, $N_{3c}=3048$, and $D=2.70$ for the second example; $N_{1c}=18$, $N_{2c}=180$, $N_{3c}=1638$, and $D=2.05$ for the last two (Fig. 6). The fractal dimensions for the discrete set and for the cumulative statistics are nearly equal.

Considering W as the global dissipated energy measured by the experimental setup, $\mathcal{G}$ as the elastic energy release rate or the specific energy necessary to generate the unit area of fracture, which is by hypothesis invariant with respect to the scale of observation, we have

$$W = \mathcal{G}A \text{ and then } \mathcal{G} = \frac{W}{A} = \frac{SV}{A} = \frac{Sl^3}{l^2} = Sl \tag{4}$$

If we consider a sequence of scale of observation, we have

$$\mathcal{G} = S_1 l_1 = \ldots = S_{n-1} l_{n-1} = S_n l_n = S_{n+1} l_{n+1} = \ldots = S_\infty l_\infty \tag{5}$$

where the first scale of observation could be the macroscopic one, with $S_1 l_1 = Sl$, l being the characteristic linear dimension of the specimen, and the asymptotic scale of observation could be the

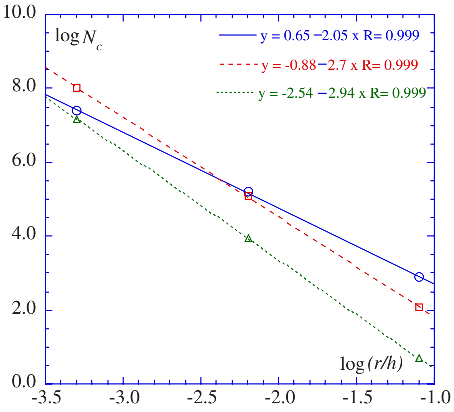

Fig. 6 Cumulative statistics for the proposed fragmentation models

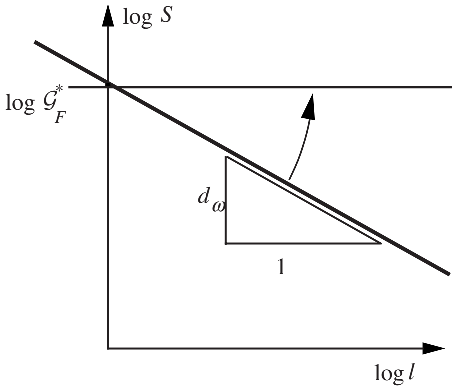

Fig. 7 Size effect on dissipated energy density in compression

microscopic one, with $S_\infty l_\infty = \mathcal{G}_F^* l^*$, l^* being the measure of the fractal set representing the fragmented configuration. From the equality between the extreme members, we can write

$$S = \mathcal{G}_F^* \left(\frac{l^*}{l} \right) \quad \text{or } S = \mathcal{G}_F^* \left(\frac{l^{1-d_\omega}}{l} \right) \tag{6}$$

where $0 < d_\omega < 1$ is the decrement of the topological dimension due to the nonhomogeneous fragmentation. Taking the logarithms of both members of Eq. (6), we obtain

$$\log S = \log \mathcal{G}_F^* - d_\omega \log l \tag{7}$$

where $d_\omega = 3 - D$ can be considered as the decrement of the topological dimension of the set in which energy dissipation occurs. Equation (7) represents a straight line with slope $(D-3)$ in the $\log S$ versus $\log l$ plane (Fig. 7). If $D=2$, the slope is -1, as well as $D=3$ implies a vanishing slope. For $D=2$ (localization) $d_\omega = 1$; for $D=3$ (volumetric dissipation) $d_\omega = 0$.

The two extreme cases are $D=2$, surface theory [34], when the dissipation really occurs on a surface ($W \propto V^{2/3}$), and by $D=3$, volume theory [35], when the dissipation occurs in a volume ($W \propto V$). In this case, $\mathcal{G}_F^*$ presents the following physical dimensions:

$$[\mathcal{G}_F^*] = \frac{[F][L]^{-1}}{[L]^{D-2}} = [F][L]^{1-D} \tag{8}$$

For $D=2 \rightarrow [\mathcal{G}_F^*] = [F][L]^{-1}$, which is the canonical dimension for fracture energy, while for $D=3 \rightarrow [\mathcal{G}_F^*] = [F][L]^{-2}$, which is the physical dimension of stress. The experimental cases of fragmentation are usually intermediate ($D \cong 2.5$) [24], as well as the size distribution for concrete aggregates due to Fuller [36].

The fractal nature of the fragments generated by the compressive test emerges very clearly at the size scale of the specimens [37]. Momber [38] applied fragmentation theory to the study of compression and analyzed the fragments, determining a fractal exponent D close to 2. On the other hand, the property of self-similarity is very likely to vanish or change at higher or lower scales, owing to the limited characteristic of the particle size curve. The price to pay for obtaining a constant value is the loss of the classical physical dimensions for dissipated energy density. It is obviously very difficult to use these results in a structural analysis, a non-Euclidean (or fractal) mechanics being not yet available, even if very important steps have been moved forward by Carpinteri et al. [39].

Multifractal Approach. The monofractal hypothesis provides a dissipated energy density $S = W/V \rightarrow 0$ for $l \rightarrow \infty$. Due to the limited validity of the self-similarity property, this is of course a physical nonsense. The same trend has been obtained in traction [9,40], where the monofractal hypothesis was considered for cross-sectional ligaments. In that case, the geometrical multifractality of the cross-sectional material ligament [8,10] permitted to determine the multifractal scaling law for tensile strength, as well as for fracture energy [20,41] whenever the geometrical multifractality for fracture surface is assumed. The topological concept of geometrical multifractality, which can be also considered as an extension of the concept of self-affinity, may explain the inconsistencies shown in the preceding section. A self-affine fractal [42] is a fractal showing a different scaling law with respect to self-similarity, in the sense that a (statistically) similar morphology can be obtained only if the lengths are rescaled by direction-dependent factors. Such a fractal set can be identified by two different values of the fractal dimension: a local fractal dimension, in the limit of scales tending to zero, strictly equal to the Hausdorff topological dimension, and a global fractal dimension, corresponding to the largest scales, equal to the (integer) topological dimension.

On the other hand, as is shown in Fig. 8, it appears more consistent to deal with a continuous variation of the fractal dimension against the observation scale length (i.e., geometrical multifractality), than to consider only two limit values of the fractal dimension.

If a cube is fragmented in a recursive process into eight cubes (of $\frac{1}{2}$ linear dimension), at each step with probability f, the volume of each fragment and the number of fragments (cubes) at the nth step will be

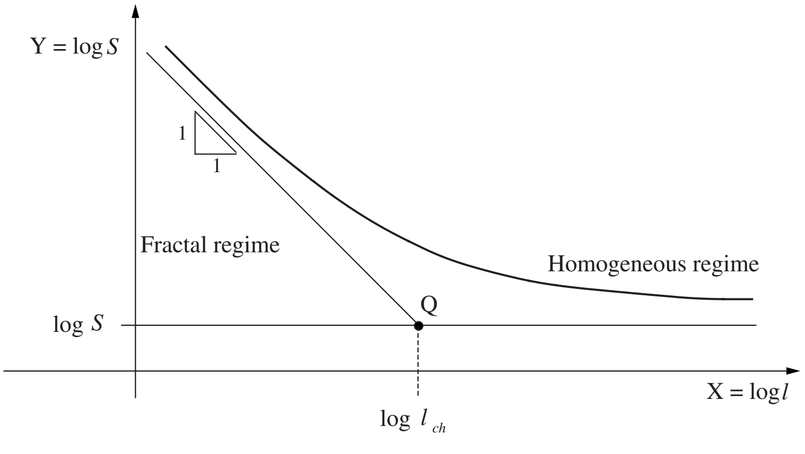

Fig. 8 Multifractal scaling law for volumetric energy dissipation versus size scale

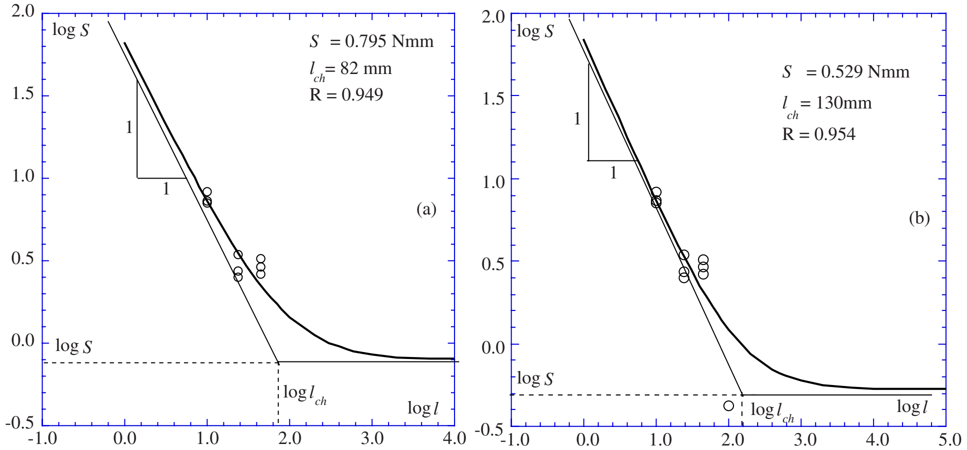

Fig. 9 Bilogarithmic diagrams of dissipated energy density versus size: (*a*) three sizes; (*b*) four sizes

$$V_n = \frac{1}{8^n}V_0 \tag{9}$$

$$N_n = (8f)^n N_0 \tag{10}$$

where V_0 is the volume of the N_0 original cubes. Taking the natural logarithms of both Eqs. (9) and (10) and eliminating n from them:

$$\frac{N_n}{N_0} = \left(\frac{V_n}{V_0}\right)^{-\ln 8f/\ln 8} \tag{11}$$

If a fragmented cube produces at each step a generic integer number V_0/V_1 of cubes, and noting that $V_n = r_n^3$, Eq. (11) can be generalized as

$$\frac{N_n}{N_0} = \left(\frac{r_n}{r_0}\right)^{-3\ \ln(V_0/V_1)f/\ln(V_0/V_1)} \tag{12}$$

From the comparison with the well-known definition of fractal distribution

$$N_n = \frac{B}{r_n^D} \tag{13}$$

it is possible to write

$$D = 3\frac{\ln \dfrac{V_0}{V_1}f}{\ln \dfrac{V_0}{V_1}} \tag{14}$$

From Eq. (14), we deduce the probability of fragmentation f (in any case greater than V_1/V_0):

$$f = \left(\frac{r_1}{r_0}\right)^{3-D} \tag{15}$$

In other words, assuming a constant probability f, we can describe a self-similar process and obtain a constant fractal exponent D. Carpinteri and Pugno [43] proposed the existence of a *material quantum* as a lower limit for chip size. This quantum is strictly related to the type of concrete considered. As affirmed by Slate et al. [19] for normal-strength concrete, it can be the aggregate, the fractures being irregular and only in the mortar or the interfaces mortar aggregate. For high-strength concrete, the quantum can be the sand grain, the fracture being more flat. This different quantum size justifes the translation of the law in Fig. 10. The probability of fragmentation should increase with fragment size and the corresponding exponent D should also increase according to Eq. (14). A nonconstant exponent D in Eq. (13) permits to describe a multifractal law [9]. The rupture of self-similarity in the fragmentation process should be due to the existence of the material quantum and represents the physical reason of the multifractal character. Carpinteri and Pugno [25,26,43] set that

$$D_{\min} = D(r = r_{\min}) \approxeq 2, \quad D_{\max} = D(r \rightarrow \infty) \approxeq 3 \tag{16}$$

as well as the corresponding probabilities are (Eq. (15))

$$f_{\min} = f(r = r_{\min}) = \frac{r_1}{r_0}, \quad f_{\max} = f(r \rightarrow \infty) = 1 \tag{17}$$

The simplest expression for f satisfying conditions (17) is

$$f(r) = \left(\frac{r_1}{r_0}\right)^{r_{\min}/r} \tag{18}$$

so that the following variation of D was obtained [25,26,43]:

$$D(r) = 3 - \frac{r_{\min}}{r} \tag{19}$$

allowing $D(r) \rightarrow 2$ for $r \rightarrow r_{\min}$, whereas $D(r) \rightarrow 3$ for $r \rightarrow \infty$.

According to the previous considerations, the following multifractal scaling law for dissipated energy density (Fig. 8) can be proposed [8,10,30]:

$$S = S_\infty\left(1 + \frac{l_{\text{ch}}}{l}\right) \tag{20}$$

where the two material constants S_∞ and l_{ch} can be obtained from fitting the experimental results. The physical requirements previously exposed are thus respected

$$\lim_{l \rightarrow +\infty} S_\infty\left(1 + \frac{l_{\text{ch}}}{l}\right) = S_\infty \tag{21}$$

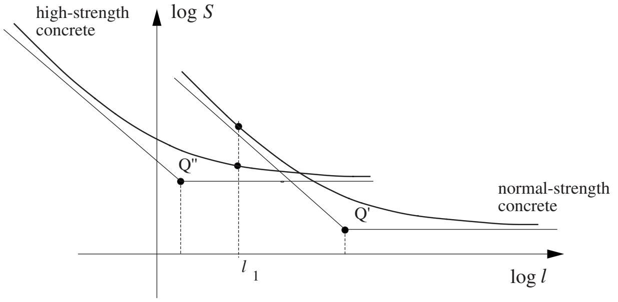

Fig. 10 Multifractal scaling law for two different material microstructures

$$\lim_{l\to 0^+} S_\infty\left(1+\frac{l_{\mathrm{ch}}}{l}\right)=+\infty \tag{22}$$

In the bilogarithmic diagram shown in Fig. 8 ($X=\log l; Y=\log S$), the analytical expression becomes

$$Y(X)=\log S_\infty+\log\left(1+\frac{l_{\mathrm{ch}}}{10^X}\right) \tag{23}$$

The asymptotes in the bilogarithmic plot present peculiar physical meanings (Fig. 8). The horizontal asymptote, corresponding to the larger sizes (*homogeneous* regime), presents the following expression:

$$H_1(X)=\log S_\infty \tag{24}$$

while the oblique asymptote, which corresponds to the macroscopic dimension l tending to zero (i.e., $X\to-\infty$) and governs the *disordered* or *fractal* regime, presents the following expression:

$$H_2(X)=-X+\log\sqrt{l_{\mathrm{ch}}} \tag{25}$$

Point Q is the intersection of the two asymptotes (Fig. 8) and its horizontal coordinate is given by

$$X_Q=\log l_{\mathrm{ch}} \tag{26}$$

where l_{ch} is a characteristic length. Point Q ideally separates the disordered regime, where fragmentation is not homogeneous, from the ordered (homogeneous) regime. The microstructural characteristic size l_{ch}, in the case of normal-strength concrete, could be proportional to the maximum aggregate size $d_{\max}$:

$$l_{\mathrm{ch}}=\alpha d_{\max} \tag{27}$$

It is reasonable to suppose that for finer grained brittle materials (rocks, high-strength concrete), this value should be considerably smaller than in the case of normal-strength concrete, thus providing the curve to horizontally shift to the left in the bilogarithmic diagram (Fig. 10). Given a particular size l_1, for example, a normal-strength concrete specimen could behave according to the fractal disordered regime, whereas a rock or high-strength concrete specimen of the same size could be set in the (nearly) horizontal branch (Fig. 10), thus showing a homogeneous macroscopic behavior, characterized by a large and ordered distribution of microfractures.

The process shows two asymptotes. At the smallest scales, the dissipation occurs over a domain very close to a surface ($D=2$), whereas at the largest scales the dissipation occurs over a domain close to a volume ($D=3$).

Conclusions

The uniaxial compression tests performed under displacement control on drilled cylindrical specimens obtained by a unique concrete block over a very large scale range (1:19) have confirmed as that scale effect on compressive strength is not as evident as in traction. The experimental results have instead manifested a strong scale effect on dissipated energy density, showing a sharp decrease of that quantity by increasing specimen size.

The hypothesis of energy dissipation in a subdomain with physical dimension between 2 and 3 can be effective to justify such a phenomenon. It can be observed how, when energy dissipation occurs in the volume ($D=3$), no scale effects are present, whereas when energy dissipation occurs over an area ($D=2$), the scale effects are characterized in the bilogarithmic diagram $\log S$ versus $\log l$ by a linear law with slope equal to -1. By fitting the experimental values, we obtain an intermediate case, and a renormalized value for dissipated energy density, invariant with scale, can be obtained. This scale-invariant value is characterized by noninteger physical dimensions. This hypothesis works very well in the size range of the tested specimens.

In order to extend the trend of the dissipated energy density to all the size scales, a multifractal law has been proposed, from which comes out how at small scales the failure is dominated by a fragmentation process ($D=2$) with severe scale effect, while at large scales the energy dissipation occurs in the volume ($D=3$) and the related scale effect vanishes.

A renormalization procedure for strain (or dilation) has been eventually proposed in order to obtain a scale-invariant stress versus renormalized strain diagram.

Acknowledgment

The present research was carried out with the financial support of the Ministry of University and Scientific Research (MIUR) under the Grant No. PRIN 2003 “Damage mechanics and durability of ordinary and high performance concrete.”

References

[1] Carpinteri, A., 1981, “Static and Energetic Fracture Parameters for Rocks and Concretes,” Mater. Constr. (Paris), **14**, pp. 151–162.
[2] Carpinteri, A., 1982, “Notch Sensitivity in Fracture Testing of Aggregative Materials,” Eng. Fract. Mech., **16**, pp. 467–481.
[3] Carpinteri, A., 1985, “Interpretation of the Griffith Instability as a Bifurcation of the Global Equilibrium,” *Application of Fracture Mechanics to Cementitious Composites*, S. P. Shah, ed., Martinus Nijhoff, Dordrecht, pp. 287–316.
[4] Carpinteri, A., 1989, “Cusp Catastrophe Interpretation of Fracture Instability,” J. Mech. Phys. Solids, **37**, pp. 567–582.
[5] Carpinteri, A., 1989, “Size Effects on Strength, Toughness and Ductility,” J. Eng. Mech., **115**, pp. 1375–1392.
[6] Carpinteri, A., 1984, “Stability of Fracturing Process in R.C. Beams,” J. Struct. Eng., **110**, pp. 544–558.
[7] Bažant, Z. P., 1984, “Size Effect in Blunt Fracture: Concrete, Rock, Metal,” J. Eng. Mech., **110**, pp. 518–535.
[8] Carpinteri, A., 1994, “Scaling Laws and Renormalization Groups for Strength and Toughness of Disordered Materials,” Int. J. Solids Struct., **31**, pp. 291–302.
[9] Carpinteri, A., 1994, “Fractal Nature of Material Microstructure and Size Effects on Apparent Mechanical Properties,” Mech. Mater., **18**, pp. 89–101.
[10] Carpinteri, A., Chiaia, B., and Ferro, G., 1995, “Size Effects on Nominal Tensile Strength of Concrete Structures: Multifractality of Materials Ligaments and Dimensional Transition From Order to Disorder,” Mater. Struct., **28**, pp. 311–317.
[11] Holzhausen, G. R., and Johnson, A. M., 1979, “Analyses of Longitudinal Splitting of Uniaxially Compressed Rock Cylinders,” Int. J. Rock Mech. Min. Sci. Geomech. Abstr., **16**, pp. 163–177.
[12] Nemat-Nasser, S., and Horii, H., 1982, “Compression-Induced Nonplanar Crack Extension With Application to Splitting, Exfoliation and Rockburst,” J. Geophys. Res., **87**, pp. 6805–6821.
[13] Ashby, M. F., and Hallam, D., 1986, “The Failure of Brittle Solids Containing Small Cracks Under Compressive Stress States,” Acta Metall., **34**, pp. 497–510.
[14] Horii, H., and Nemat-Nasser, S., 1986, “Brittle Failure in Compression: Splitting, Faulting and Brittle-Ductile Transition,” Philos. Trans. R. Soc. London, **319**, pp. 337–374.
[15] Nemat-Nasser, S., and Hori, M., 1993, *Micromechanics: Overall Properties of Heterogeneous Materials*, North-Holland, Amsterdam.
[16] Bažant, Z. P., and Xiang, Y., 1997, “Size Effect in Compression Fracture: Splitting Crack Band Propagation,” J. Eng. Mech., **123**, pp. 162–172.
[17] Rossi, P., Ulm, F. J., and Hachi, F., 1996, “Compressive Behaviour of Concrete: Physical Mechanisms and Modeling,” J. Eng. Mech., **122**, pp. 1038–1043.
[18] Markeset, G., and Hillerborg, A., 1995, “Softening of Concrete in Compression-Localization and Size Effects,” Cem. Concr. Res., **25**, pp. 702–708.
[19] Slate, F. O., Nilson, A. N., and Martinez, S., 1986, “Mechanical Properties of High-Strength Lightweight Concrete,” J. Am. Concr. Inst., **77**, pp. 606–613.
[20] Carpinteri, A., and Chiaia, B., 1995, “Multifractal Nature of Concrete Fracture Surfaces and Size Effects on Nominal Fracture Energy,” Mater. Struct., **28**, pp. 435–443.
[21] Carpinteri, A., Ferro, G., and Monetto, I., 1999, “Scale Effects in Uniaxially Compressed Concrete Specimens,” Mag. Concrete Res., **51**, pp. 217–225.
[22] van Vliet, M. R. A., and van Mier, J. G. M., 1996, “Experimental Investigation of Concrete Fracture Under Uniaxial Compression,” Mech. Cohesive-Frict. Mater., **1**, pp. 115–127.
[23] Ferro, G., 2006, “Scale Effects on Compressive Tests for Concrete Specimens,” Eng. Fract. Mech., **79**, pp. 1510–1530.
[24] Turcotte, D. L., 1992, *Fractals and Chaos in Geology and Geophysics*, Cambridge University Press, Cambridge.
[25] Carpinteri, A., and Pugno, N., 2002, “A Fractal Comminution Approach to Evaluate the Drilling Energy Dissipation,” Int. J. Numer. Analyt. Meth. Geomech., **26**, pp. 499–513.
[26] Carpinteri, A., and Pugno, N., 2003, “A Multifractal Comminution Approach for Drilling Energy Dissipation,” Powder Technol., **131**, pp. 93–98.
[27] van Mier, J. G. M., et al., 1997, “Report of the Round Robin Test Carried Out by RILEM TC 148-Ssc: Strain-Softening of Concrete in Uniaxial Compres-

sion," Mater. Struct., **30**, pp. 195–209.

[28] van Mier, J. G. M., 1986, "Multiaxial Strain-Softening of Concrete-Part 1: Fracture and Part II: Load-Histories," Mater. Struct., **19**, pp. 179–200.

[29] Ferro, G., 1994, "Effetti di Scala Sulla Resistenza a Trazione dei Materiali," Ph.D. thesis, Politecnico di Torino.

[30] Carpinteri, A., Chiaia, B., and Ferro, G., 1997, "A New Explanation for Size Effects on the Flexural Strength of Concrete," Mag. Concrete Res., **49**, pp. 45–53.

[31] Carpinteri, A., Ciola, F., and Pugno, N., 2001, "Boundary Element Method for the Strain-Softening Response of Quasi-Brittle Materials in Compression," Comput. Struct., **51**, pp. 389–401.

[32] Carpinteri, A., Ciola, F., Pugno, N., Gobbi, M. E., and Ferrara, G., 2001, "Size-Scale and Slenderness Influence on the Compressive Strain-Softening Behavior of Concrete," Fatigue Fract. Eng. Mater. Struct., **24**, pp. 441–450.

[33] Turcotte, D. L., 1986, "Fractals and Fragmentation," J. Geophys. Res., **91**, pp. 1921–1926.

[34] Rittinger, P. R., 1937, Lehrbuch der aufbereitungskunde. Berlin.

[35] Kick, F., 1885, Das gesetz der proportionalen widerstande. Leipzig.

[36] Stroeven, P., 1991, "Fractals and Fractography in Concrete Technology," *International Symposium on Brittle Matrix Composities*, Warsaw, Poland, pp. 1–10.

[37] Lee, Y.-H., and Willam, K., 1997, "Mechanical Properties of Concrete in Uniaxial Compression," ACI Mater. J., **94**, pp. 457–471.

[38] Momber, A. W., 2000, "The Fragmentation of Standard Concrete Cylinders Under Compression: The Role of Secondary Fracture Debris," Eng. Fract. Mech., **67**, pp. 445–459.

[39] Carpinteri, A., Chiaia, B., and Cornetti, P., 2001, "Static-Kinematic Duality and the Principle of Virtual Work in the Mechanics of Fractal Media," Comput. Methods Appl. Mech. Eng., **191**, pp. 3–19.

[40] Carpinteri, A., and Ferro, G., 1994, "Size Effects on Tensile Fracture Properties: A Unified Explanation Based on Disorder and Fractality of Concrete Microstructure," Mater. Struct., **27**, pp. 563–571.

[41] Carpinteri, A., and Chiaia, B., 1996, "Size Effects on Concrete Fracture Energy: Dimensional Transition From Order to Disorder," Mater. Struct., **29**, pp. 259–266.

[42] Mandelbrot, B. B., 1985, "Self-Affine Fractals and Fractal Dimension," Phys. Scr., **32**, pp. 257–260.

[43] Carpinteri, A., and Pugno, N., 2002, "Fractal Fragmentation Theory for Shape Effects of Quasi-Brittle Materials in Compression," Mag. Concrete Res., **54**, pp. 473–480.

Guilhem Michon
Université de Toulouse,
ISAE DMSM,
10 Avenue Edouard Belin,
31055 Toulouse, France
e-mail: guilhem.michon@isae.fr

Lionel Manin
e-mail: lionel.manin@insa-lyon.fr

Didier Remond
e-mail: didier.remond@insa-lyon.fr

Regis Dufour
e-mail: regis.dufour@insa-lyon.fr

LaMCoS,
INSA-Lyon,
CNRS UMR5259,
F69621, France

Robert G. Parker
Department of Mechanical Engineering,
The Ohio State University,
650 Ackerman Road,
Columbus, OH 43202
e-mail: parker.242@osu.edu

Parametric Instability of an Axially Moving Belt Subjected to Multifrequency Excitations: Experiments and Analytical Validation

This paper experimentally investigates the parametric instability of an industrial axially moving belt subjected to multifrequency excitation. Based on the equations of motion, an analytical perturbation analysis is achieved to identify instabilities. The second part deals with an experimental setup that subjects a moving belt to multifrequency parametric excitation. A data acquisition technique using optical encoders and based on the angular sampling method is used with success for the first time on a nonsynchronous belt transmission. Transmission error between pulleys, pulley/belt slip, and tension fluctuation are deduced from pulley rotation angle measurements. Experimental results validate the theoretical analysis. Of particular note is that the instability regions are shifted to lower frequencies than the classical ones due to the multifrequency excitation. This experiment also demonstrates nonuniform belt characteristics (longitudinal stiffness and friction coefficient) along the belt length that are unexpected sources of excitation. These variations are shown to be sources of parametric instability. [DOI: 10.1115/1.2910891]

Keywords: automotive belt, parametric instabilities, multifrequency excitation, experimental investigation, angular sampling

1 Introduction

Instead of classical V belts, serpentine drives are used in front end accessory drives (FEADs). They use flat and multiribbed belts running over multiple accessory pulleys, leading to simplified assembly and replacement, longer belt life, and compactness [1]. Numerous mechanical phenomena occur in this application: rotational vibrations [2], hysteretic behavior of belt tensioner [3], nonlinear transverse vibration due to the existence of pulley eccentricity [4], dry friction tensioner behavior [5], or parametric excitation.

Commonly known under the category of axially moving media, belt spans are subjected to parametric excitation from their operating environment as studied by Zhang [6]. A theoretical nonlinear dynamic analysis is also analyzed by Mockenstrum et al. [7,8]. However, only Pellicano et al. [9,10] present a coupled theoretical and experimental investigation, where the excitation comes from pulley eccentricity, which causes simultaneous direct and parametric excitation.

Widely used in automotive engines, belt spans experience multifrequency excitation caused by engine firing and accessory variable torques [11]. Belt parametric instability occurs as transverse vibration in these applications, where the problems are noise and belt fatigue.

This paper builds on a previous work of Parker and Lin [12] as an experimental illustration and model validation. First, it deals with the general moving belt model subjected to multifrequency tension and speed fluctuations. Then a specific test bench is presented, which produce this kind of excitation. Data acquisition is based on the principle of pulse timing method and leads to angular sampling for frequency analysis [13]. This method is applied here for the first time on a nondiscrete geometry. The theoretical results from perturbation analysis are compared to the experimental ones. An unexpected source of parametric excitation is also highlighted.

2 Mathematical Model

A mathematical model of an axially moving beam subjected to multifrequency tension and speed parametric excitation is used to establish the parametric instability region transition curves. The equation of motion for transverse vibration of a beam of length L moving with time dependent transport velocity $c(T)$ is governed by [14]

$$\rho A(V_{,TT}+c_{,T}V_{,X}+2cV_{,TX}+c^2V_{,XX})-(P_s+P_d(T))V_{,XX}+EIV_{,XXXX} = 0 \qquad (1)$$

where ρA is the mass per unit length, EI the bending stiffness, V the transverse displacement, P_s the mean belt tension, $P_d(T)$ the dynamic tension, and T and X the independent time and spatial variables. The dynamic tension results from longitudinal motion of the endpoints as a result of pulley oscillations and quasistatic midplane stretching from transverse deflection, and is given by

$$P_d(T)=\frac{EA}{L}\left[U(L,T)-U(0,T)+\frac{1}{2}\int_0^L V_{,X}^2 dX\right] \qquad (2)$$

EA is the longitudinal stiffness modulus and U the longitudinal displacement. With the dimensionless parameters,

$$x,v,u=\frac{X,V,U}{L}, \quad t=T\sqrt{\frac{P_s}{\rho AL^2}}, \quad \gamma=c\Bigg/\sqrt{\frac{P_s}{\rho A}}$$

Contributed by the Applied Mechanics Division of ASME for publication in the Journal of Applied Mechanics. Manuscript received November 15, 2006; final manuscript received March 3, 2008; published online May 13, 2008. Review conducted by Igor Mezic.

$$\zeta = \frac{EA}{P_s}, \quad \mu = \frac{EI}{P_s L^2}, \quad \Omega_i = \sqrt{\frac{\rho A L^2}{P_s}}\tilde{\Omega}_i \tag{3}$$

Equation (1) becomes

$$v_{,tt} + 2\gamma v_{,tx} + \gamma_{,t} v_{,x} - (1-\gamma^2)v_{,xx} + \mu v_{,xxxx} - \zeta\left[u(1,t) - u(0,t) + \frac{1}{2}\int_0^1 v_{,x}^2 dx\right]v_{,xx} = 0 \tag{4}$$

The belt tension and speed fluctuations are, respectively,

$$\zeta[u(1,t) - u(0,t)] = \sum_{i=1}^{k} \varepsilon_i \cos(\Omega_i t + \theta_i) \tag{5}$$

$$\gamma = \gamma_0 + \sum_{i=1}^{k'} \varepsilon_i' \cos(\Omega_i' t + \theta_i') \tag{6}$$

where $\varepsilon_i = EAu_i / P_s < 1$ represents the ratio of the ith spectral component of the dynamic tension fluctuation to the mean span tension.

As investigated in Ref. [12], the boundaries of the instability regions can be obtained on the basis of Floquet theory and perturbation analysis.

Linearizing Eq. (4) and writing in state-space form gives [12]

$$AW_t + BW + \sum_{i=1}^{k'} \varepsilon_i'\{\sin(\Omega_i' t + \theta_i')C + \Omega_i' \cos(\Omega_i' t + \theta_i')D\}W - \sum_{i=1}^{k} \varepsilon_i \cos(\Omega_i t + \theta_i)EW + \left(\sum_{i=1}^{k'} \varepsilon_i' \sin(\Omega_i' t + \theta_i')\right)^2 EW = 0 \tag{7}$$

where

$$A = \begin{bmatrix} 1 & 0 \\ 0 & -(1-\gamma_0^2)\frac{\partial^2}{\partial x^2} + \alpha\frac{\partial^4}{\partial x^4} \end{bmatrix},$$

$$B = \begin{bmatrix} 2\gamma_0 \frac{\partial}{\partial x} & -(1-\gamma_0^2)\frac{\partial^2}{\partial x^2} + \alpha\frac{\partial^4}{\partial x^4} \\ (1-\gamma_0^2)\frac{\partial^2}{\partial x^2} - \alpha\frac{\partial^4}{\partial x^4} & 0 \end{bmatrix}$$

$$C = \begin{bmatrix} 2\frac{\partial}{\partial x} & 2\gamma_0\frac{\partial^2}{\partial x^2} \\ 0 & 0 \end{bmatrix}, \quad D = \begin{bmatrix} 0 & \frac{\partial}{\partial x} \\ 0 & 0 \end{bmatrix}, \quad E = \begin{bmatrix} 0 & \frac{\partial^2}{\partial x^2} \\ 0 & 0 \end{bmatrix},$$

$$W = \begin{bmatrix} v_{,t} \\ v \end{bmatrix} \tag{8}$$

The inner product in the state space is $\langle W, V\rangle = \int_0^1 W^T \bar{V} dx$, where overbar denotes the complex conjugate and superscript T denotes the transpose. The Galerkin basis consists of the state-space eigenfunctions of the nonparametrically excited moving string ($\mu=0$) system [15]

$$\Phi_n = \begin{bmatrix} j\omega_n \psi_n \\ \psi_n \end{bmatrix} = \begin{bmatrix} \lambda_n \psi_n \\ \psi_n \end{bmatrix} \tag{9}$$

where ψ_n are the complex eigenfunctions of Eq. (4) and ω_n the natural frequencies

$$\psi_n = \frac{1}{n\pi\sqrt{1-\gamma_0^2}} e^{jn\pi\gamma_0 x}\sin(n\pi x), \quad \lambda_n = jn\pi(1-\gamma_0^2) \tag{10}$$

Let us define $E_{nm} = \langle E\Phi_n, \Phi_m\rangle$ and $E_{\bar{n}m} = \langle E\bar{\Phi}_n, \Phi_m\rangle$, with similar relations for the C and D operators.

Using perturbation analysis to consider speed and tension fluctuations, primary instability occurs when

$$\Omega_l = \Omega_l' = 2\omega_n \pm \sqrt{(\varepsilon_l'|-jC_{\bar{n}n} + 2\omega_n D_{\bar{n}n}|)^2 + (\varepsilon_l|E_{\bar{n}n}|)^2} - |E_{\bar{n}n}|^2 \times\left[-\sum_{i=1,i\neq l}^{k} \varepsilon_i^2 \frac{2\omega_n}{\Omega_i^2 - 4\omega_n^2} + \frac{\varepsilon_l^2}{8\omega_n}\right] - |-jC_{\bar{n}n} + 2\omega_n D_{\bar{n}n}|^2 \times\left[-\sum_{i=1,i\neq l}^{k'} \varepsilon_i'^2 \frac{2\omega_n}{\Omega_i'^2 - 4\omega_n^2} + \frac{\varepsilon_l^2}{8\omega_n}\right] + \sum_{i=1}^{k'}\left(\frac{\varepsilon_i'}{2}\right)^2 |E_{nn}| \tag{11}$$

and secondary instability occurs when

$$\Omega_l = \Omega_l' = \omega_n \pm \sqrt{\left(\frac{\varepsilon_l^2}{\omega_n}\operatorname{Im}(E_{nn})|E_{\bar{n}n}|\right)^2 \left(\frac{\varepsilon_l'^2}{\omega_n}\operatorname{Im}(-jC_{nn} + \omega_n D_{nn})|-jC_{\bar{n}n} + \omega_n D_{\bar{n}n}|\right)^2} - |E_{\bar{n}n}|^2\left[-\sum_{i=1,i\neq l}^{k} \varepsilon_i^2 \frac{\omega_n}{\Omega_i^2 - 4\omega_n^2} + \frac{\varepsilon_l^2}{3\omega_n}\right] - |-jC_{\bar{n}n} + \omega_n D_{\bar{n}n}|^2\left[-\sum_{i=1,i\neq l}^{k'} \varepsilon_i'^2 \frac{\omega_n}{\Omega_i'^2 - 4\omega_n^2} + \frac{\varepsilon_l^2}{3\omega_n}\right] + \sum_{i=1}^{k'}\left(\frac{\varepsilon_i'}{2}\right)^2 |E_{nn}| \tag{12}$$

3 Experimental Setup

In industrial applications, excitation sources are not at a single frequency, especially in an automotive engine. Engine firing and driven accessories cause multifrequency speed and tension fluctuations. Furthermore, practical belt speeds are such that they impact the dynamics and must be included. The following experiment examines parametric instabilities from this kind of excitation in a moving belt system.

3.1 Belt Drive Description. The studied transmission consists of four pulleys linked together by an automotive multiribbed belt, as shown in Fig. 1. The input shaft speed (from 0 rpm to 2000 rpm) is controlled by a 60 kW electric motor. The driven shaft is connected to a hydraulic pump. The output pressure of the fluid is controlled to apply a mean torque on the driven pulley. Due to its design, however, the pump generates torque fluctuations of order 2 (i.e., 2 pulses/rev) around the mean value. These fluctuations cause tension variations that parametrically excite the moving belt.

Due to the rotation direction, the upper span is tight and the lower one is slack. As these two spans have approximately the same length, the instability will appear in the slack span for the lowest excitation frequencies. Figure 2 shows an example of transverse vibration of the lower span.

3.2 Measurement Devices. Angular positions are measured by optical encoders mounted on Pulleys 1, 2, and 3 (respectively,

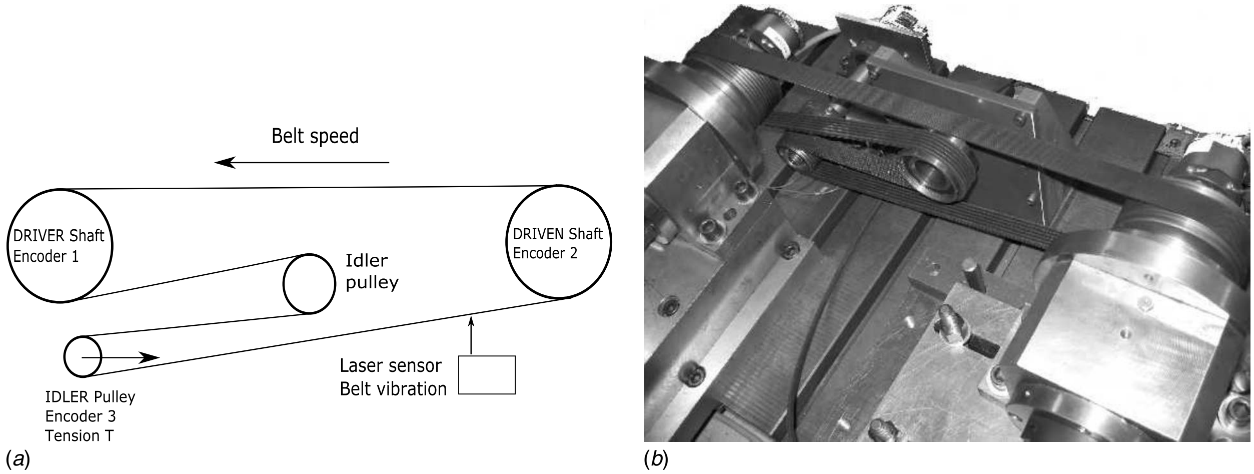

Fig. 1 Experimental setup for parametrically excited moving belt drive

2048 pulses/rev, 2048 pulses/rev, and 2500 pulses/rev). Belt tension is measured by a piezoelectric sensor on the Pulley 3 support and belt lateral vibration by a laser displacement sensor (0.02 m range, 10 μm dynamic resolution).

The data acquisition system is custom made with a PXI frame including classical data acquisition boards and a four-channel counterboard permitting the use of the pulse timing method. Each optical encoder delivers a square signal (TTL) as it rotates. Between two rising edges of this signal, a counter records the number of pulses given by a high frequency clock (80 MHz), see Fig. 3. For each encoder, it is therefore possible to build a time vector that contains the times of occurence of the TTL signal's rising edges. Hence, the total rotation angle of each shaft is determined and instantaneous rotation speed and acceleration are deduced. In this application, measurement is triggered on the reference encoder mounted on the driving shaft and analog signals are acquired at each instant of the reference encoder's rising edge. Obviously, when an analog signal is sampled in the angular domain, the speed conditions are taken into account in order to set the cutoff frequency of antialiasing filters. An important characteristic of this measurement principle is to separate resolution and precision. Resolution is given by the number of pulses/rev, and the theoretical angular precision is proportional to the ratio between rotation speed and counterclock frequency. The grating quality of the optical encoder disk, as well as the electronic signal conditioning and processing, may also affect the practical accuracy.

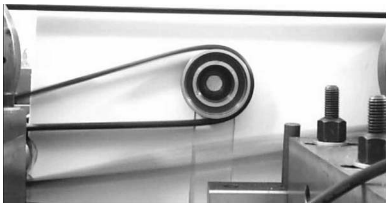

Fig. 2 Example of instability in slack belt span

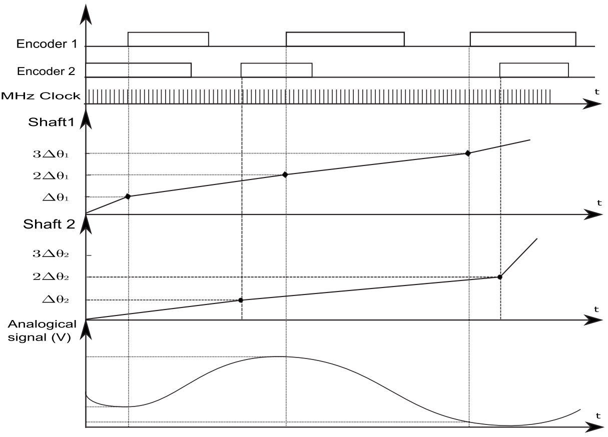

Fig. 3 Angular sampling principle

3.3 Angular Sampling Benefits. Compared to classical acquisition [16], data are resampled based on the angular rotation of a chosen encoder, which is not necessarily the reference one. It consists in calculating the angular rotations of the other encoders at the times corresponding to the rising edges of the sampling encoder. Hence, if angular sampling is performed on encoder i, the angular positions of each of the slave encoders are computed from linear interpolation at the times corresponding to the encoder i rising edge locations, see Fig. 4(*a*).

For the analog signals, the same method is applied and they are recorded at the angular frequency of the reference encoder. This method is called angular sampling and is detailed in Ref. [13]. It is mainly applied in rotating machines with synchronous transmission elements, such as gears or timing belts. Its application to a transmission in the presence of belt slip is novel and provides important advantages as described below. This technique is especially useful for systems with variable speed because the position of the sampling points and the angular resolution remain exactly the same when the speed fluctuates.

As the angular sampling frequency is constant based on the encoder resolution, instead of performing the fast Fourier transform (FFT) analysis in the time domain, this is performed in the angular domain. In other words, the measured signals are treated as functions of the angular position of the sampling encoder. The sampling encoder's position plays the role typically filled by time in classical FFT analysis.

The spectral data are a function of angular frequency, which has units of rad^{-1}. The maximum angular frequency is $1/\delta\theta$, where $\delta\theta=2\pi/N_g$ is the angular resolution of the sampling encoder based on N_g gratings. Increments on the angular frequency axis are spaced at $\delta f=1/N\delta\theta$, where N is the number of sampling encoder rising edges in the collected data. Examples of classical Campbell and angular frequency diagrams are compared in Fig. 5. On Fig. 5(*a*), natural frequencies are located at a constant frequency when speed increases while speed-dependent frequency orders linearly increase. In the angular frequency domain, however, natural frequencies appear as hyperbola $(f=\omega(1/\theta))$ and

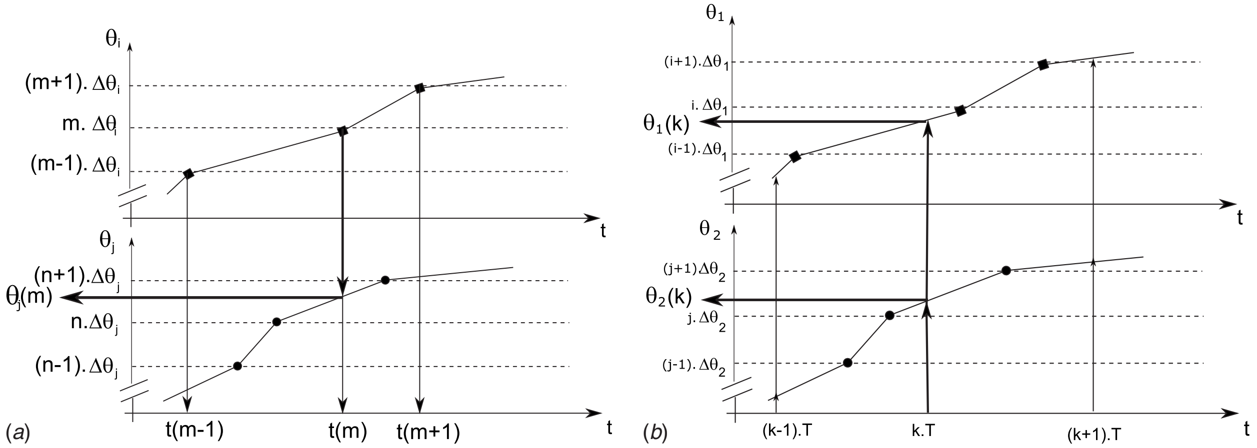

Fig. 4 Angular resampling method (*a*) and time resampling method (*b*)

speed-dependent frequency orders are located at a constant angular frequency ($f=a\cdot\omega$ leads to $1/\theta=a$), vertical lines parallel to the speed axis, see Fig. 5(*b*).

Thus, the main advantages of performing angular sampling in this application are as follows:

- Sampling points are exactly located in reference to the geometry of the rotating machine, even when speed varies. It permits to compare several measurement results based on the same sampling conditions.
- Spectral analysis is always performed with the same accuracy and the same resolution. Angular sampling also ensures that the magnitude of harmonic components are exactly estimated [13].
- By choosing Encoder 3 as reference, and assuming that no slip occurs between belt and the idler pulley since no torque is being transmitted, the sampling points are attached to the belt.

  Therefore, it is more convenient to identify speed-dependent frequency components on a graph with an angular frequency axis related to a chosen reference encoder.

For standard Fourier analysis, it is necessary to get the measurements as a function of one single time vector with equally spaced intervals. This requires a time resampling of the data using linear interpolation, as shown in Fig. 4(*b*).

3.4 Phase Difference Measurement. This angular sampling method has already been used for many synchronous transmission studies (gearbox, timing belt drive) but never for nonsynchronous transmissions, such as serpentine multiribbed belt drives. The transmission error ϵ is defined as the angular rotation difference between shaft i and shaft j,

$$\epsilon=\theta_i-\eta\cdot\theta_j \tag{13}$$

where η and $\theta_{i,j}$ are, respectively, the transmission ratio and the angular positions of shaft i, j.

In the case of nonsynchronous belt drive systems, some creep occurs between the belt and the pulleys due to the power transmission by friction [17,18]. Indeed, the creep corresponds to the relative slip between the belt and the driven pulley as the belt elongates on the pulley contact arc as its tension increases. Here, the transmission error between Pulleys 3 and 2 is considered.

The rotation of Pulley 3 is not totally transmitted to Pulley 2 due to the belt stretching on Pulley 2, which causes a delay. Therefore, the mean value of the transmission error is not zero as it is for a synchronous drive, but rather always increases (Fig. 6). In our application, analysis permits decomposition of the observed transmission error as the sum of a linear function of time representing the transmission error due to the pulley belt creep ϵ_{creep}, and the residual transmission error ϵ_{res} due to the system dynamic as in synchronous transmission.

$$\epsilon=\theta_3-\eta\cdot\theta_2=\epsilon_{\text{res}}+\epsilon_{\text{creep}} \tag{14}$$

where ϵ_{creep} is identified from ϵ as a linear regression of time assuming a constant mean rotation speed. Removing the linear part ϵ_{creep} from the transmission error ϵ yields the zero-mean pe-

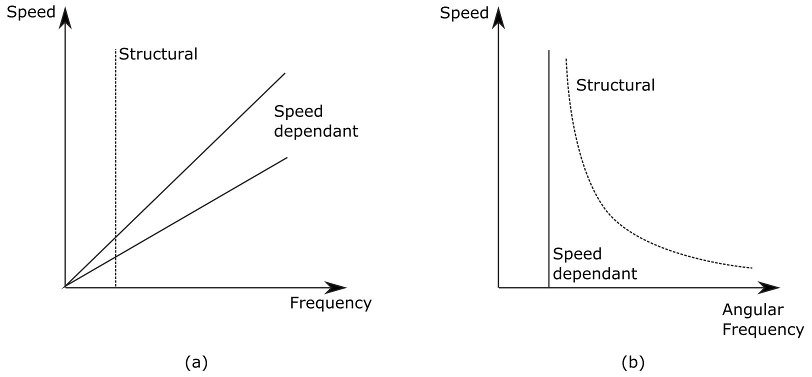

Fig. 5 Campbell diagrams in (*a*) time and (*b*) angular frequency domain

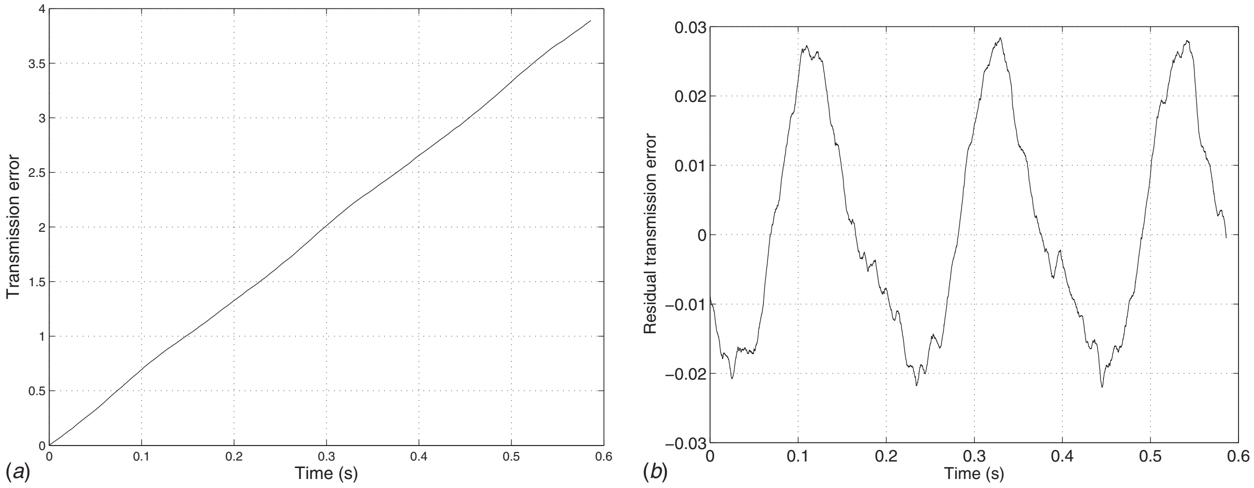

Fig. 6 Total (*a*) and residual (*b*) transmission error versus time

riodic residual transmission error ϵ_{res} (Fig. 6).

As mentioned in the theoretical model description, the dynamic belt tension can be expressed as the difference of the endpoint positions and midplane stretching from transverse vibration, see Eq. (2). Considering the belt span that connects Pulleys 3 and 2, and taking into account the belt translation direction, $U(L,T)$ and $U(0,T)$ correspond, respectively, to the belt unseating point on Pulley 3 and to the belt seating point on Pulley 2. These two points are not fixed in space since pulley rotations oscillate around the linearly increasing angles $w_3 t$ and $w_2 t$. Assuming a no-slip condition at these two points, $U(L,T)$ and $U(0,T)$ can be estimated from pulley angle oscillations multiplied by the respective pulley pitch radius. Finally, the difference between $U(L,T)$ and $U(0,T)$ corresponds to the residual transmission error at time T. Therefore, residual transmission error and belt tension fluctuation are related. Figure 7 presents the measured progression of belt tension and residual transmission error angular waterfall analysis with change in rotation speed (note that all waterfall plots are top views). The same frequency components appear on each graph and prove that the measurement system with optical encoders and angular sampling permits evaluation of belt tension fluctuation. Finally, this analysis shows that the transmission error includes the pulley belt creep plus the system dynamic.

3.5 Nonuniform Belt Characteristic Identification and Consequences.

The low modulation observed on the dynamic transmission error (Fig. 6) corresponds to the belt traveling frequency and demonstrates that there are nonuniform belt characteristics. In order to check this nonuniformity, a belt has been cut in ten equal parts. Each part has been tested to determine longitudinal rigidity modulus k and damping C. Each belt sample is clamped at one end and has a mass m suspended at the other, see Fig. 8. This system is excited via a shock hammer. The free response is recorded via an accelerometer and postprocessed to ob-

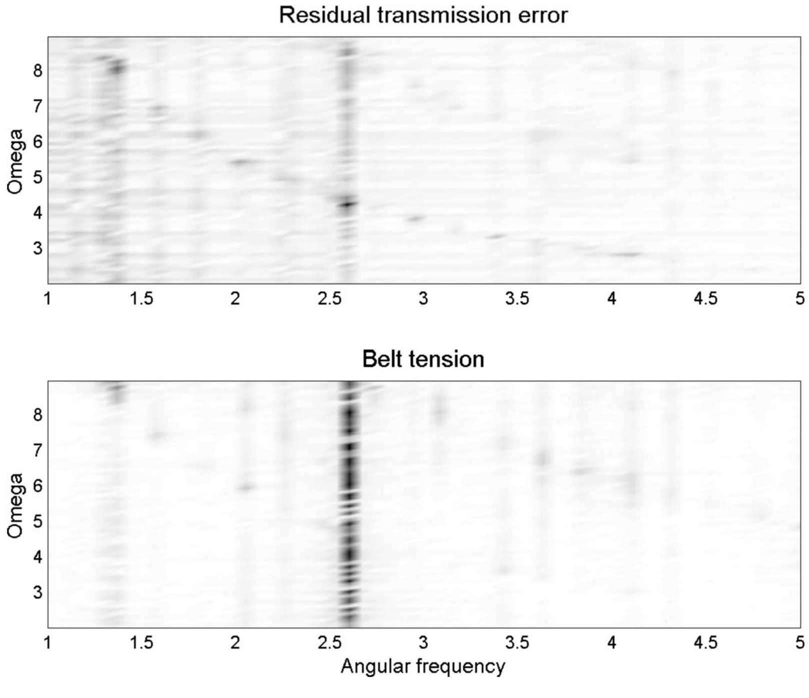

Fig. 7 Belt tension and transmission error angular top-view waterfall as a function of rotation speed

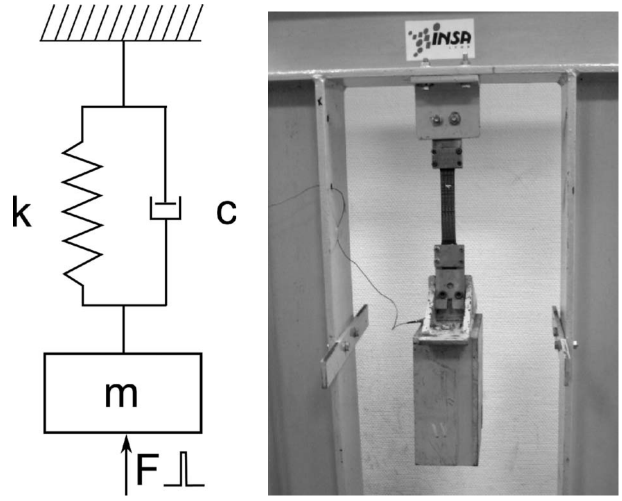

(*a*) (*b*)

Fig. 8 Experimental setup for the local belt characteristics identification

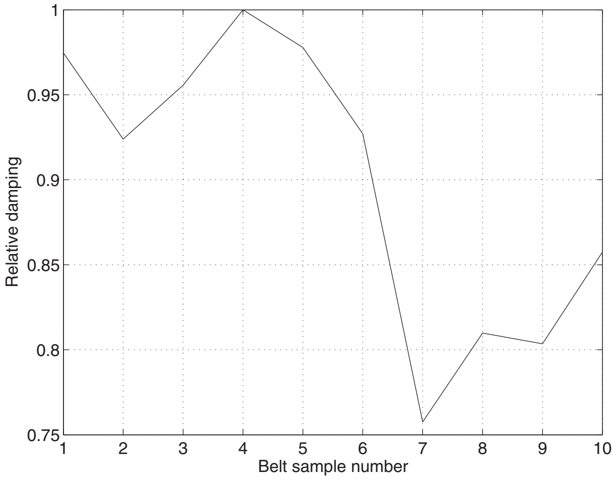

Fig. 9 Dimensionless damping evolution along the belt length $C_i/C_{\max}$

tain belt longitudinal stiffness and damping. Longitudinal damping coefficients of belt samples, normed by the maximum measured value, are plotted versus belt sample number in Fig. 9. Non-negligible variation is observed for C while local stiffness, and therefore EA, is constant. This irregularity is probably due to the manufacturing process (printing, cord winding, cutting). The low frequency modulation observed is shown to be a parametric excitation source next.

4 Belt Span Instability Analysis

4.1 Experimental Investigation. On the global experimental setup for a given initial belt tension and mean torque, a speed sweep of the driving shaft is performed from 532 rpm to 1512 rpm in 14 rpm increments (70 tests). The experimental results are presented in Fig. 10 as a top-view waterfall in the angular frequency domain for (*a*) the transverse vibration, (*b*) belt tension, and (*c*) belt speed. All parameters are dimensionless as defined in Sec. 2 (waterfall FFT in the time-frequency domain are given in Appendix).

The belt tension angular waterfall, Fig. 10(*b*), exhibits lines parallel to the speed axis, which proves a speed-dependent excitation. The belt transverse vibration angular waterfall is presented on Fig. 10(*a*). The instabilities are represented by the black spots located on a hyperbola. which proves parametric instability. The system is unstable for numerous frequencies.

4.2 Main Instability Regions. The main excitation of the system comes from the pump design, which creates torque fluctuations of order 2, inducing speed and tension fluctuations. Regarding belt instability, speed variation is a negligible source of excitation compared to the tension fluctuation. The latter is observed to be the principle source of parametric excitation and is located on the angular frequency waterfall graph at abscissa 2.60 as a vertical line. Primary and secondary instability regions, circled on Fig. 10(*a*), are the response to this torque excitation.

Experimentally, the primary instability occurs for $\Omega_1 \in [7.9, 8.8]$. This region is classically wider than the corresponding secondary region (which occurs for $\Omega_1 \in [4.1, 4.5]$), but also shifted of 0.3 from $2\omega_1$ toward lower frequencies due to the multifrequency excitation.

Considering the small transverse rigidity modulus and the large span length in this application, the bending stiffness modulus is neglected. Therefore, in the following, the belt span is considered as a string ($\mu=0$). Thus, using Eqs. (7) and (8) and $C_{\bar{n}n}=(1-e^{-2jn\pi\gamma_0})/2$, $D_{\bar{n}n}=0$, $E_{\bar{n}n}=(1-e^{-2jn\pi\gamma_0})/(4\gamma_0)$, and $E_{nn}=jn\pi(1+\gamma_0^2)/2$. The experimental parameters introduced in the model are $\gamma_0=0.5$, $\omega_1=4.3$, $\Omega_2=8$, $\Omega_2'=8$, $\varepsilon_1'=0.001$, $\varepsilon_2=0.3$, $\varepsilon_2'=0.001$. For $\varepsilon_1=0.7$, the instability region occurs for $\Omega_1 \in [7.8\ 9.2]$.

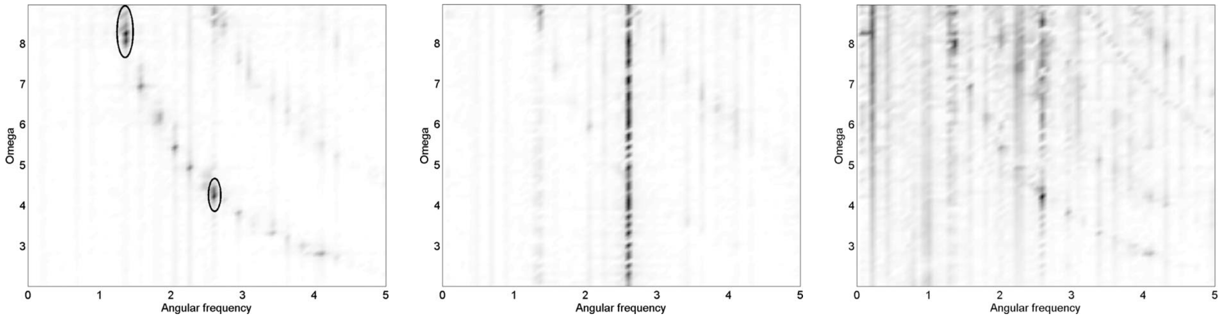

(*a*) (*b*) (*c*)

Fig. 10 Experimental angular top-view waterfall: (*a*) transverse vibration, (*b*) belt tension fluctuation, (*c*) belt speed fluctuation

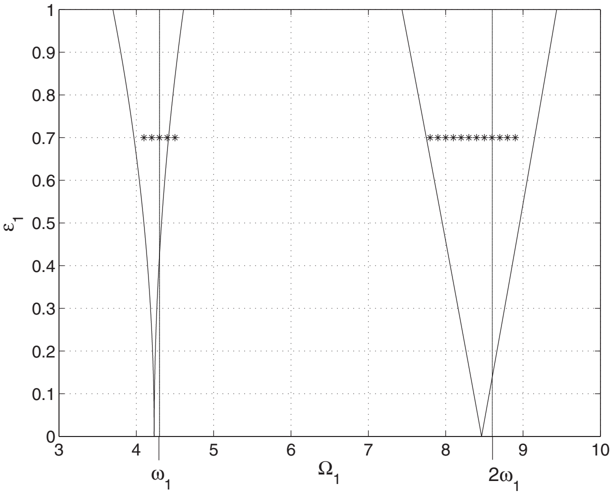

Fig. 11 Instability region. Model (solid line) and experiment (stars).

The instability region boundaries are plotted as a function of the excitation amplitude ε_1 in Fig. 11. When $\Omega_2 < 2\omega_1$, the second source of excitation shift the instability region to lower frequencies. While this phenomenon is not classical, the experimental observations confirm the theoretical results of Ref. [12].

4.3 Low Amplitude Instability Region. The low frequency modulation observed on the residual transmission error due to the belt characteristic irregularity highlighted in Sec. 3.5 is a source of parametric excitation. It appears on the waterfall plot of the tension fluctuation as low level parallel lines separated by 0.20, that is, the belt traveling frequency. This irregularity explains the peripheral instabilities presented on Fig. 10(*a*).

5 Conclusion

This paper focuses on an experimental investigation of an industrial axially moving belt subjected to multifrequency excitation. Comparison with analytical results from a perturbation analysis is presented and permits to validate theoretical instabilities. The main conclusion are as follows:

- Parametric instabilities occur in experimental system such as belt drive.
- Measurement system based on angular sampling is shown to be an efficient tool for instability analysis in belt drive systems.
- Irregular belt characteristics have been detected and highlighted as unexpected source of parametric excitation.
- Instability regions are shifted when subjected to multifrequency excitation.
- Experimental observations confirm the theoretical results.

Further analysis will focus on the role of the hysteretic behavior of the belt tensioners on these instabilities.

Appendix

Figure 12 represents the top-view waterfall in the classical Campbell-like diagram.

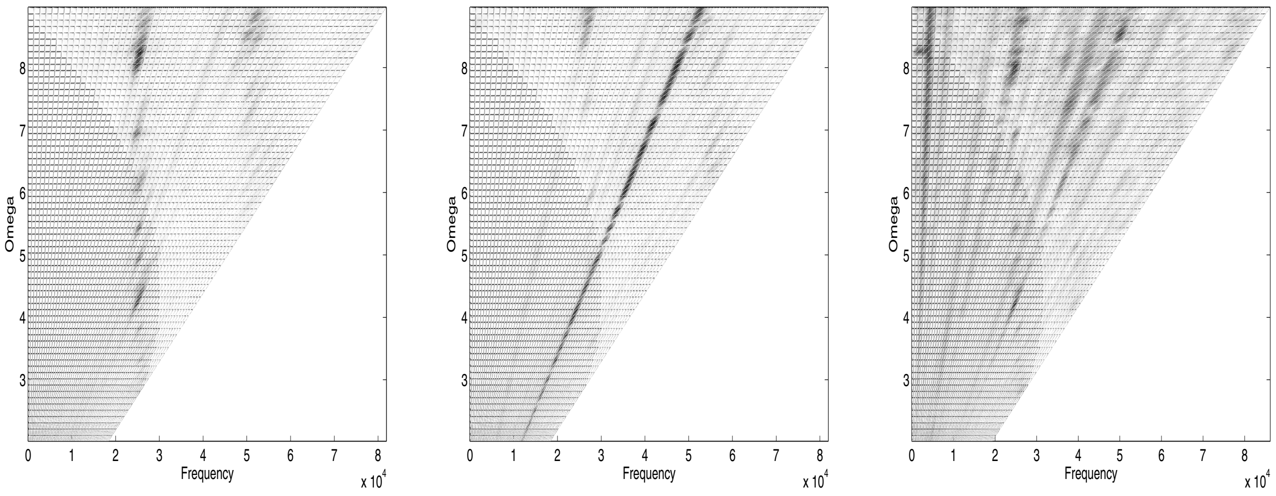

(a)

(b)

(c)

Fig. 12 Experimental classical Campbell-like diagram top-view waterfall: transverse vibration (*a*), belt tension fluctuation (*b*), belt speed fluctuation (*c*)

References

[1] Gerbert, G., 1981, "Some Notes on V-Belt Drives," ASME J. Mech. Des., **103**, pp. 8–18.

[2] Hwang, S. J., Perkins, N. C., Ulsoy, A., and Meckstroth, R. J., 1994, "Rotational Response and Slip Prediction of Serpentine Belt Dirve Systems," ASME J. Vibr. Acoust., **116**, pp. 71–78.

[3] Michon, G., Manin, L., and Dufour, R., 2005, "Hysteretic Behavior of a Belt Tensioner, Modeling and Experimental Investigation," J. Vib. Control, **11**(9), pp. 1147–1158.

[4] Wickert, J. A., 1992, "Non-Linear Vibration of a Traveling Tensioned Beam," Int. J. Non-Linear Mech., **27**(3), pp. 503–517.

[5] Leamy, M. J., and Perkins, N. C., 1998, "Nonlinear Periodic Response of Engine Accessory Drives With Dry Friction Tensioners," ASME J. Vibr. Acoust., **120**, pp. 909–916.

[6] Zhang, L., and Zu, J. W., 1999, "One-to-One Auto-Parametric Resonance in Serpentine Belt Drive Systems," J. Sound Vib., **232**, pp. 783–806.

[7] Mockensturm, E., Perkins, N., and Ulsoy, A., 1996, "Stability and Limit Cycles of Parametrically Excited, Axially Moving Strings," ASME J. Vibr. Acoust., **118**, pp. 346–351.

[8] Mockensturm, E. and Guo, J., 2005, "Nonlinear Vibration of Parametrically Excited Viscoelastic Axially Moving Media," ASME J. Appl. Mech., **72**, pp. 374–380.

[9] Pellicano, F., Catellani, G., and Fregolent, A., 2004, "Parametric Instability of Belts, Theory and Experiments," Comput. Struct., **82**, pp. 81–91.

[10] Pellicano, F., Fregolent, A., Bertuzzi, A., and Vestroni, F., 2001, "Primary and Parametric Non-Linear Resonances of a Power Transmission Belt: Experimental and Theoretical Analysis," J. Sound Vib., **244**, pp. 669–684.

[11] Cheng, G., and Zu, J. W., 2003, "Nonstick and Stick-Slip Motion of a Coulomb-Damped Belt Drive System Subjected to Multifrequency Excitations," ASME J. Appl. Mech., **70**, pp. 871–884.

[12] Parker, R., and Lin, Y., 2001, "Parametric Instability of Axially Moving Media Subjected to Multifrequency Tension and Speed Fluctuation," ASME J. Appl. Mech., **68**, pp. 49–57.

[13] Remond, D., and Mahfoudh, J., 2005, "From Transmission Error Measurements to Angular Sampling in Rotating Machines With Discrete Geometry," Shock Vib., **9**, pp. 1–13.

[14] Thurman, A. L., and Mote, C. D., Jr., 1969, "Free, Periodic, Non-Linear Oscillation of an Axially Moving String," ASME J. Appl. Mech., **36**, pp. 83–91.

[15] Jha, R., and Parker, R., 2000, "Spatial Discretization of Axially Moving Media Vibration Problems," ASME J. Vibr. Acoust., **122**, pp. 290–294.

[16] Houser, D. R., and Blankenshio, G. W., 1989, "Methods for Measuring Transmission Error Under Load and at Operating Speeds," SAE Trans., **98**(6), pp. 1367–1374.

[17] Gerbert, G., and Sorge, F., 2002, "Full Sliding Adhesive-Like Contact of V-Belts," ASME J. Mech. Des., **124**, pp. 706–712.

[18] Betchel, S. E., Vohra, S., Jacob, K. I., and Carslon, C. D., 2000, "The Stretching and Slipping of Belts and Fibers on Pulleys," ASME J. Appl. Mech., **67**, pp. 197–206.

Nonlinear Buckling of Compressed FRP Cylindrical Shells and Their Imperfection Sensitivity

Seishi Yamada
Professor
Department of Civil Engineering,
Toyohashi University of Technology,
Toyohashi 441-8580, Japan

James G. A. Croll
Professor
Department of Civil Engineering,
University College London, Gower Street,
London WC1E 6BT, UK

Nobuhisa Yamamoto
Graduate Student
Department of Civil Engineering,
Toyohashi University of Technology,
Toyohashi 441-8580, Japan

An elastic, nonlinear, Ritz analysis has been developed to allow investigation of the imperfect behavior of axially compressed orthotropic fiber reinforced polymer cylindrical shells. In a particular mode, buckling loads are shown to be strongly influenced by the constitutive material coefficients and are sensitive to initial geometric imperfections. Just as for the previously analyzed isotropic cylindrical shells, the reduced stiffness criteria are shown to provide close lower bounds to the imperfection sensitive elastic buckling loads. The potential benefits in the use of the reduced stiffness theoretical results to allow specification of the optimal designs are illustrated. [DOI: 10.1115/1.2839894]

Keywords: fiber reinforced polymer, cylindrical shell, spherical shell, imperfection sensitivity, elastic buckling

1 Introduction

The constant demand and necessity for lightweight efficient structures continue to encourage engineers to the field of structural optimization and simultaneously to the use of nonconventional materials. In many situations, fiber reinforced polymeric (FRP) matrix composites provide opportunities for enhanced efficiency, primarily because of their high strength-to-weight ratios. There exists a large activity in the area of material characterization, analysis, fabrication, and design of composite structures [1–10]. The lightweight and high corrosion resistance of FRP composites make them particularly suitable for bridges, aerospace components, storage tanks, and pressure vessel, or large-span structural members. In this paper, the FRP structural members that are modeled are thin-walled orthotropic cylindrical shells and it is their elastic buckling performance under axial compression forces that provides the major focus. It is well known that axially compressed cylindrical shells have a buckling behavior, which is very sensitive to initial geometric imperfections [11]. The price paid for utilizing the optimal characteristics of the shell are that any small deviations from the idealized, or perfect, geometry result in very severe reductions in the load carrying capacity. Indeed, the stronger is the optimum the more sensitive are the buckling loads to small changes in geometric form. This characteristic of shell buckling is more conventionally referred to as imperfection sensitivity. Viewed in this way, optimization and imperfection sensitivity are seen to be different sides of the same coin. For increasing amplitudes of initial imperfection, the reduced buckling loads are commonly referred to as imperfection sensitive buckling behavior.

The present paper investigates the nonlinear buckling behavior of the FRP composite cylindrical shells having material properties similar to those of columns that were recently studied experimentally by Yamada and Komiya [12,13]. From accurate solutions of the nonlinear shell equations, it will be demonstrated that for increasing amplitudes of initial imperfections the elastic buckling loads exhibit well defined lower bounds. Moreover, an extension of classical buckling theory [14–16] to provide what has became known as “reduced stiffness” theory, in the same as way as for related isotropic cylinders [17,18], is shown to provide analytical predictions of these lower bound buckling loads.

2 Nonlinear Buckling Analysis

For an imperfect thin-walled circular cylinder of longitudinal length L, wall thickness t, and radius R, shown in Fig. 1, the change in the total potential energy, consequent upon the application of a uniform axial compression stress of σ, may be written as

$$\Pi = U_M + U_B + V_\lambda \tag{1}$$

where U_M are the various contributions to the membrane strain energies, U_B the bending energies, and V_λ the increase in load potential. Under the action of an axial compressive stress of σ, these energy contributions are given as

$$U_M = \frac{1}{2}\int_0^{2\pi R}\int_0^L (n_x\varepsilon_x + n_y\varepsilon_y + 2n_{xy}\varepsilon_{xy})dxdy \tag{2a}$$

$$U_B = \frac{1}{2}\int_0^{2\pi R}\int_0^L (m_x\kappa_x + m_y\kappa_y + 2m_{xy}\kappa_{xy})dxdy \tag{2b}$$

$$V_\lambda = -\sigma t\int_0^{2\pi R}\int_0^L \left(-\frac{\partial u}{\partial x}\right)dxdy \tag{2c}$$

In these expressions, (n_x, n_y, n_{xy}) and (m_x, m_y, m_{xy}) are the total bending and membrane stress resultants, and $(\varepsilon_x, \varepsilon_y, \varepsilon_{xy})$ and $(\kappa_x, \kappa_y, \kappa_{xy})$ are the corresponding strains associated with displacements (u, v, w) from an imperfect but stress-free unloaded state.

Total bending and membrane stress resultants are related to strains through the orthotropic constitutive equations:

$$\begin{gathered} n_x = A_{11}\varepsilon_x + A_{12}\varepsilon_y, \quad n_y = A_{12}\varepsilon_x + A_{22}\varepsilon_y, \quad n_{xy} = 2A_{66}\varepsilon_{xy} \\ m_x = D_{11}\kappa_x + D_{12}\kappa_y, \quad m_y = D_{12}\kappa_x + D_{22}\kappa_y, \quad m_{xy} = 2D_{66}\kappa_{xy} \end{gathered} \tag{3}$$

For deformations from an initial imperfection, w^0, the strain-displacement relations are taken to be of the Donnell–Mushtari–Vlasov type for shallow shells [14–16], for which

---

Contributed by the Applied Mechanics Division for Publication in the JOURNAL OF MECHANICAL DESIGN. Manuscript received August 7, 2006; final manuscript received August 27, 2007; published online May 13, 2008. Review conducted by Edmundo Corona.

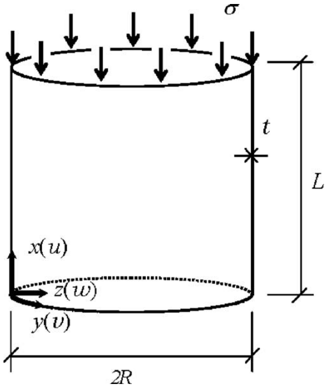

Fig. 1 Notation used for cylindrical shell

$$\varepsilon_x = \frac{\partial u}{\partial x} + \frac{\partial w^0}{\partial x}\frac{\partial w}{\partial x} + \frac{1}{2}\left(\frac{\partial w}{\partial x}\right)^2 \tag{4a}$$

$$\varepsilon_y = \frac{\partial v}{\partial y} - \frac{w}{R} + \frac{\partial w^0}{\partial y}\frac{\partial w}{\partial y} + \frac{1}{2}\left(\frac{\partial w}{\partial y}\right)^2 \tag{4b}$$

$$\varepsilon_{xy} = \frac{1}{2}\left(\frac{\partial u}{\partial y} + \frac{\partial v}{\partial x} + \frac{\partial w^0}{\partial x}\frac{\partial w}{\partial y} + \frac{\partial w^0}{\partial y}\frac{\partial w}{\partial x} + \frac{\partial w}{\partial x}\frac{\partial w}{\partial y}\right) \tag{4c}$$

$$\kappa_x = -\frac{\partial^2 w}{\partial x^2}, \quad \kappa_y = -\frac{\partial^2 w}{\partial y^2}, \quad \kappa_{xy} = -\frac{\partial^2 w}{\partial x \partial y} \tag{4d}$$

End boundaries are assumed to be supported in such a way as to conform with the classical simple support, corresponding with the conditions,

$$w = 0, \quad \frac{\partial^2 w}{\partial x^2} = 0, \quad \frac{\partial u}{\partial x} = 0, \quad v = 0 \quad \text{at } x = 0, L \tag{5}$$

By taking displacement functions u, v, and w as linear combinations of the harmonic expressions

Table 1 Lamination details

	V_y/V	Laminate configuration
C20T	0.2	$90_4/0_{32}/90_4$
C50T	0.5	$90_{10}/0_{20}/90_{10}$
C80T	0.8	$90_{16}/0_8/90_{16}$
C50L	0.5	$0_{10}/90_{20}/0_{10}$

$$u = \sum_i \sum_j^{J_i^u} u_{i,j} \cos(iy/R)\cos(j\pi x/L) \tag{6a}$$

$$v = \sum_i \sum_j^{J_i^v} v_{i,j} \sin(iy/R)\sin(j\pi x/L) \tag{6b}$$

$$w = \sum_i \sum_j^{J_i^w} w_{i,j} \cos(iy/R)\sin(j\pi x/L) \tag{6c}$$

these boundary conditions will be exactly satisfied since each separate component satisfies the boundary conditions of Eq. (5). In these expressions, i and j are the circumferential full-wave and the longitudinal half-wave numbers; $u_{i,j}, v_{i,j}, w_{i,j}$ are the amplitudes of each harmonic function. The initial geometric imperfection is taken to consist of a harmonic

$$w^0 = w^0_{b,f} \cos(by/R)\sin(f\pi x/L) \tag{7}$$

in which b and f represent the circumferential full-wave and longitudinal half-wave numbers. To provide convergence of the nonlinear postbuckling response, extensive numerical experiments have established that a total choice of 64 (=28+17+19) modes are required in Eqs. (6a)–(6c), for a particular imperfection mode adopted as follows. For u, a total of 28 degrees of freedom,

$$J_0^u = 21 \quad \text{for } i = 0 \quad \text{and } j = 1,3,5,7,9,11,13,15,17,19,21$$

$$J_b^u = 15 \quad \text{for } i = b \quad \text{and } j = 1,3,5,7,9,11,13,15$$

$$J_{2b}^u = 11 \quad \text{for } i = 2b \quad \text{and } j = 1,3,5,7,9,11$$

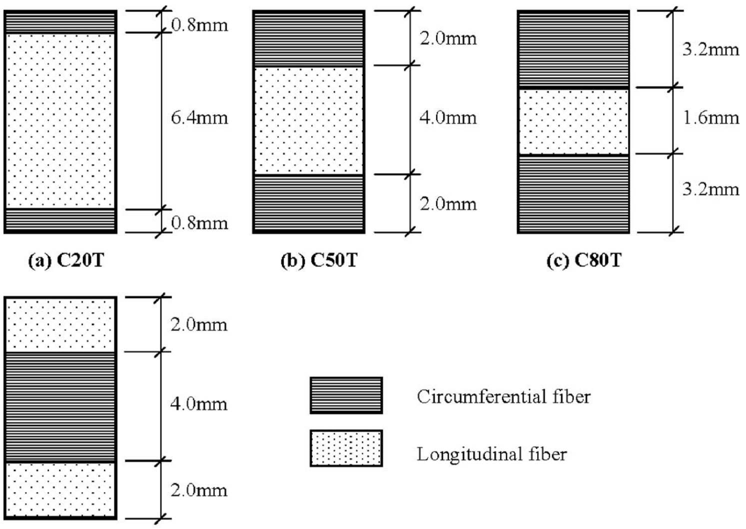

(a) C20T **(b) C50T** **(c) C80T**

(d) C50L

Fig. 2 Lamination details

Table 2 Coefficients in Eq. (3)

	A_{11}	A_{12}	A_{22}	A_{66}	D_{11}	D_{12}	D_{22}	D_{66}
		(MN/m)				(N m)		
C20T	312	15.0	125	23.9	1180	80.0	1150	128
C50T	218	15.0	218	23.9	541	80.0	1790	128
C80T	125	15.0	312	23.9	347	80.0	1980	128
C50L	218	15.0	218	23.9	1790	80.0	541	128

$$J_{3b}^{u}=5 \quad \text{for } i=3b \quad \text{and } j=1,3,5 \tag{8a}$$

For v, a total 17 of degrees of freedom,

$$J_{b}^{v}=15 \quad \text{for } i=b \quad \text{and } j=1,3,5,7,9,11,13,15$$

$$J_{2b}^{v}=11 \quad \text{for } i=2b \quad \text{and } j=1,3,5,7,9,11$$

$$J_{3b}^{v}=5 \quad \text{for } i=3b \quad \text{and } j=1,3,5 \tag{8b}$$

For w, a total of 19 degrees of freedom,

$$J_{0}^{w}=15 \quad \text{for } i=0 \quad \text{and } j=1,3,5,7,9,11,13,15$$

$$J_{b}^{w}=11 \quad \text{for } i=b \quad \text{and } j=1,3,5,7,9,11$$

$$J_{2b}^{w}=9 \quad \text{for } i=2b \quad \text{and } j=1,3,5,7,9 \tag{8c}$$

Since only buckling that is symmetric about the midlength of the shell is being considered, just odd values of j are included.

The sets of nonlinear algebraic equations are obtained through the stationarity of the total potential energy with respect to each of the displacement degrees of freedom included in Eqs. (6*a*)–(6*c*). Solution of these sets of nonlinear equation is achieved using a step-by-step process in which either load or a suitable displacement is used as the control parameter. At each step, a Newton–Raphson iteration is used to provide convergence to an acceptable level of precision. A more complete description of the theoretical model for the related isotropic cylinders is included in Yamada and Croll [17], which lists the integration coefficients for all terms up to and including the quartic (fourth-power) energy terms. Appropriate numbers of Newton–Raphson iterations and the choice of a suitable control parameter depend on the nature of the local nonlinearities of the equilibrium path [18].

3 Axisymmetric Buckling Load and Structural Modeling

For understanding the fundamental buckling load carrying capacity of orthotropic cylindrical shells, it is helpful to obtain the axisymmetric buckling loads since these allow comparisons with the well-known classical buckling loads for the associated isotropic shells. If we adopt just $i=0$ in Eqs. (6*a*)–(6*c*), an eigenvalue equation will result for the linear buckling problem if it is assumed that the prebuckling membrane stress state is uniform. Using ($n_x=-\sigma t$, $n_y=0$, $n_{xy}=0$), the lowest axisymmetric critical load and its associated critical wave number in the axial direction are given by

$$\sigma_s=\frac{2}{Rt}\sqrt{\frac{D_{11}(A_{11}A_{22}-A_{12}^2)}{A_{11}}} \tag{9a}$$

$$j_s=\frac{L}{\pi}\left(\frac{A_{11}A_{22}-A_{12}^2}{D_{11}A_{11}R^2}\right)^{1/4} \tag{9b}$$

For isotropic cylinders having Poisson's ratio ν, $\sigma_s=\sigma_{cl}=Et/(R\sqrt{3(1-\nu^2)})$ is the well-known classical buckling stress and $j_{s,iso}=j_{cl}=L[12(1-\nu^2)]^{1/4}/(\pi\sqrt{Rt})$. For convenience, the compressive stress may be expressed as a nondimensional load parameter Λ or $\bar{\lambda}$ defined as

$$\Lambda=\sigma/\sigma_s, \quad \bar{\lambda}=\sigma/E_x \tag{10}$$

where E_x is effective axial Young's modulus, which, from Eq. (3), takes the form

$$E_x=(A_{11}A_{22}-A_{12}^2)/(tA_{22}) \tag{11}$$

In the following analytical studies, a commercially available unidirectional glass fiber lamina unit with a 0.2 mm thickness has been adopted for a shell consisting of 40 laminations. This lamina unit is used to develop four types of orthotropic cylindrical shell arranged with three layers having a total thickness $t=8$ mm and arranged symmetrically about the midsurface as listed in Table 1; fiber orientations are relative to the axial direction. Total volume of fiber has been fixed at $V=60\%$, and the fiber volume ratio in the circumferential direction V_y is adopted as the variable parameter in this study. Lamination details are represented in Table 1

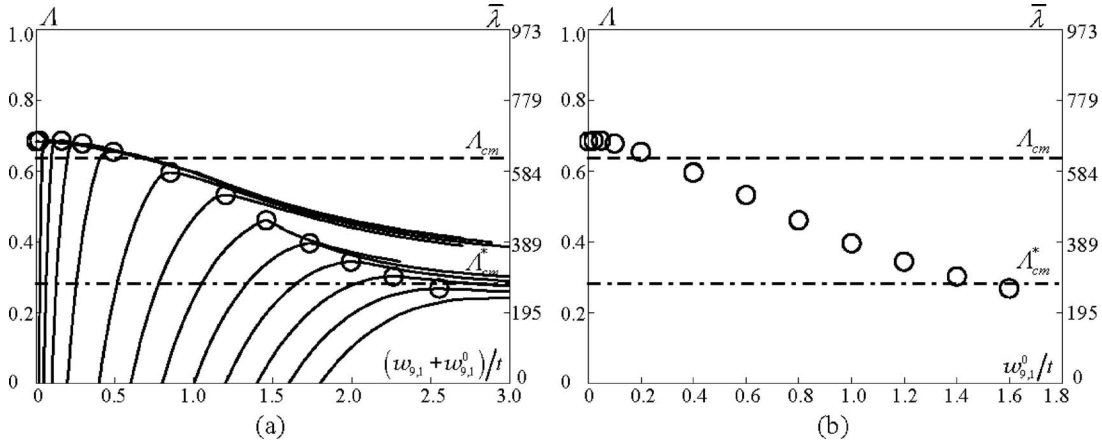

Fig. 3 Selected results for shell C50T (b=9) showing (a) load against deflection responses and (b) imperfection sensitivity

and Fig. 2. Table 2 shows the coefficients in Eq. (3) obtained from the classical lamination theory and related by coupon tests in Yamada and Komiya [12,13].

4 Nonlinear Analytical Results for the Pre- and Postbuckling Behaviors of Imperfect Shells

Due to the limitations of space, this paper considers only the results for shells having the geometric parameter $Z = 0.942L^2/(Rt) = 100$. It is well known that for complete, isotropic, cylinders, this parameter, often referred to as the Batdorf parameter, is sufficient to characterize the classical critical behavior when the shallow shell assumptions (DMV formulation) are used. This means that the linearized governing equations can be normalized in terms of the single independent geometric parameter Z. In the present study, the radius thickness ratio $R/t=405$ has been selected to conform with previous studies [11,17], so that for $Z = 100$ it follows that in all cases $L/R=0.512$. In the nonlinear postbuckling behavior, however, other independent geometric parameters are needed for both isotropic and the present orthotropically shells.

Included in Fig. 3(*a*) are the representative imperfect equilibrium paths for shell C50T having initial geometric imperfections with a single axial half-wave $f=1$ and circumferential wave number $b=9$. The horizontal axis in Fig. 3(*a*) represents the total displacement component in this same mode. It is apparent that the buckling behavior has two distinct forms. For small imperfections, those having $w_{9,1}^0/t < 0.2$, the buckling loads are effectively independent of imperfection amplitude for the mode. In Fig. 3(*b*), the horizontal axis represents the amplitude of initial imperfection, and the vertical axis is the buckling loads; the buckling loads for $b=9$ are shown to be clustered at $\Lambda=0.65$ when $w_{9,1}^0/t < 0.2$. To help interpret this change in behavior as imperfection levels are increased, Figs. 4 and 5 show the incremental displacement at the buckling points for imperfection having amplitude $w_{9,1}^0/t=0.10$

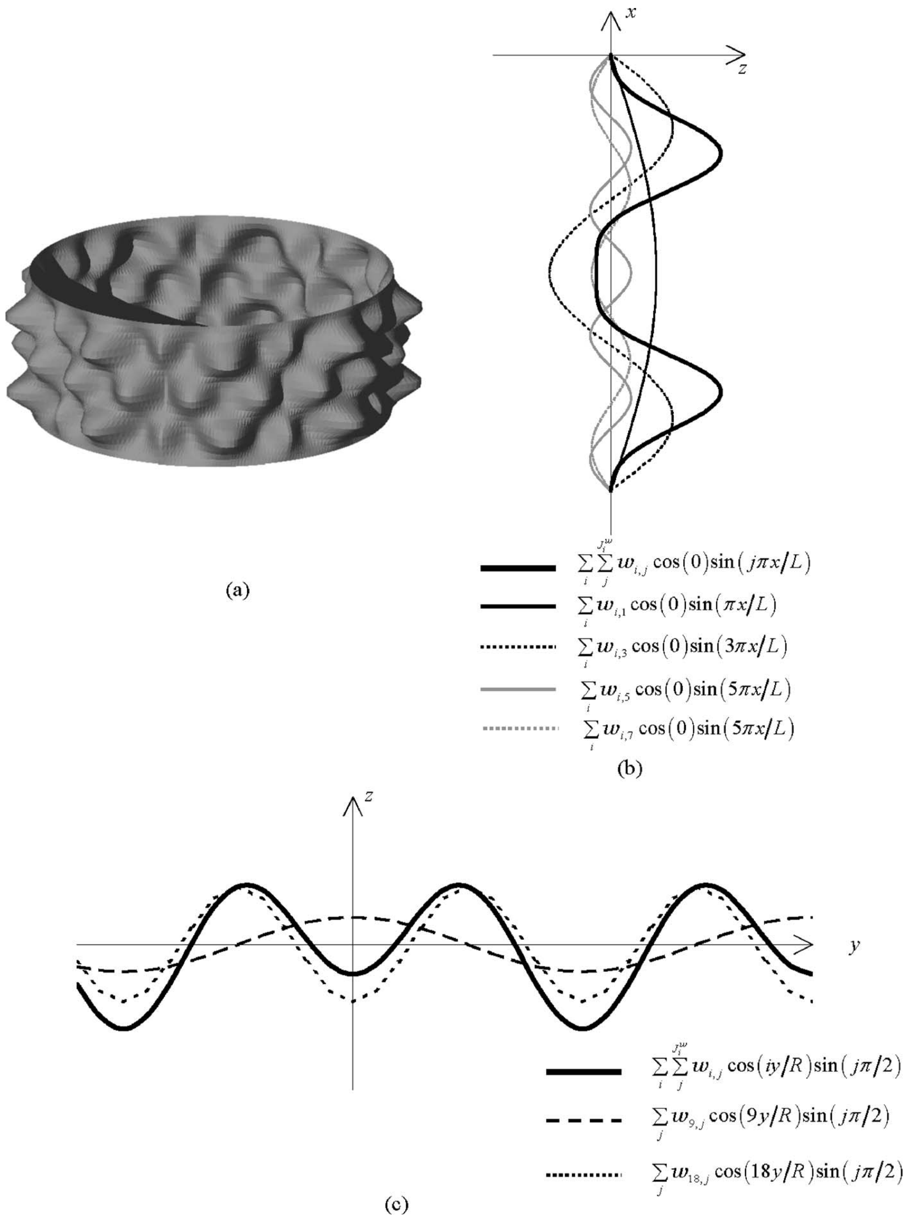

Fig. 4 Incremental displacement modes at the buckling points for small imperfection $w^0/t=0.10$ in shell C50T ($b=9$) showing (*a*) shape, (*b*) axial profile at $y=0$, and (*c*) circumferential profile at $x=L/2$

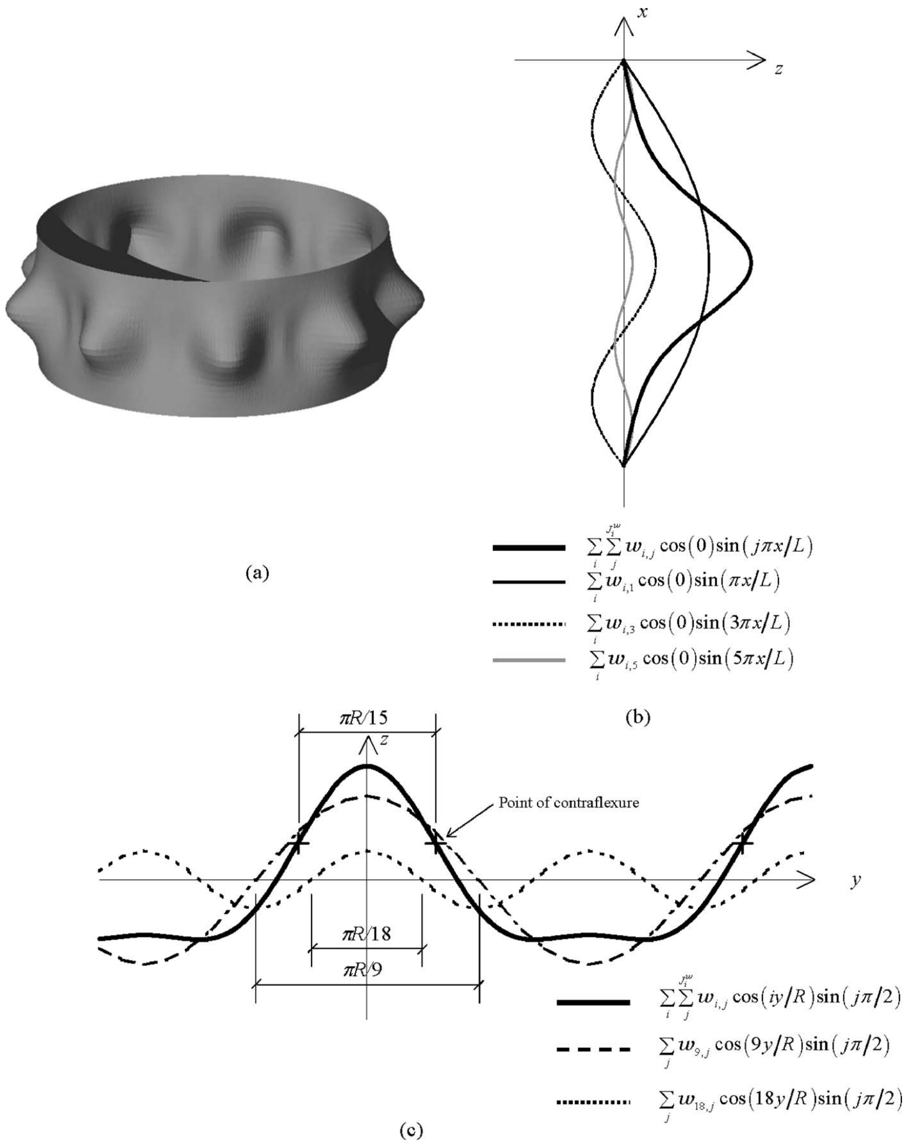

Fig. 5 Incremental displacement modes at the buckling points for a large imperfection $w^0/t=1.60$ in shell C50T ($b=9$) showing (*a*) shape, (*b*) axial profile at $y=0$, and (*c*) circumferential profile at $x=L/2$

and 1.60, respectively. As is shown in relation to Fig. 4, the incremental deformation at the buckling load, for a typical example of one of these small imperfections, exhibits a mode shape, which has a circumferential wave number dominated by $i=18$ and a mixture of both $j=3$ and 5 axial half-waves. As shown in Fig. 6(*b*), it is this mode that exhibits the lowest classical critical load Λ_c for the three modes $i=0,9,18$ taken into account for the present nonlinear studies. In mode $i=18$, the critical load is just a little higher than the minimum Λ_{cm} occurring in $j=4$ and $i=17$. For larger imperfections, those having $w_{9,1}^0/t>0.2$, Fig. 3 also shows that there is a relatively high degree of sensitivity of buckling loads to changes in imperfection amplitude. Figure 5 shows that the incremental deformation at the buckling load, for a typical case of these larger imperfections, exhibits a mode having a circumferential wave number close to that predicted by the reduced stiffness model. A combination of $i=9$ and 18 results in a compound circumferential mode shape that is shown in Fig. 5(*c*) to have a localized circumferential wavelength that is close to $i=15$. A coupling with shorter axial wavelength $j=3,5$ results in the axial mode shape of the incremental deformation at buckling being close to $j=3$. This coupling in the postbuckling response will be discussed further in relation to the reduced stiffness model in the next section. Here as elsewhere we use the term "incremental displacement" to represent small changes occurring at the buckling loads; these often differ significantly from the "total deformation." It is these incremental displacements that provide a better guide to the stiffness distributions at the instant of buckling.

Imperfections having different circumferential wave numbers exhibit very similar forms of behavior. However, it is noticeable in the summarized results of Fig. 6 that at moderate levels of imperfection the wave number b, displaying the highest level of imperfection sensitivity, is generally that for which in mode $j=1$ the shell has the lowest classical critical load. For a given amplitude of imperfections having moderate amplitudes, $w_{b,1}^0/t>0.2$, it is when b is between 12 and 13 in Fig. 6(*a*) that the shell C20T experiences the lowest buckling loads. It is also around $i=12-13$ that the lowest classical critical load Λ_c occurs in mode $j=1$. For shell C50L shown in Fig. 6(*d*), these minima both occur at around $i=b=13-14$. In each of the cases shown in Fig. 6, there are also well defined minimal buckling loads. These are summarized in Table 3. For shell C20T, this minimum occurs in mode $b=11$ at a load level $\Lambda^N=0.230$. In this mode, an imperfection

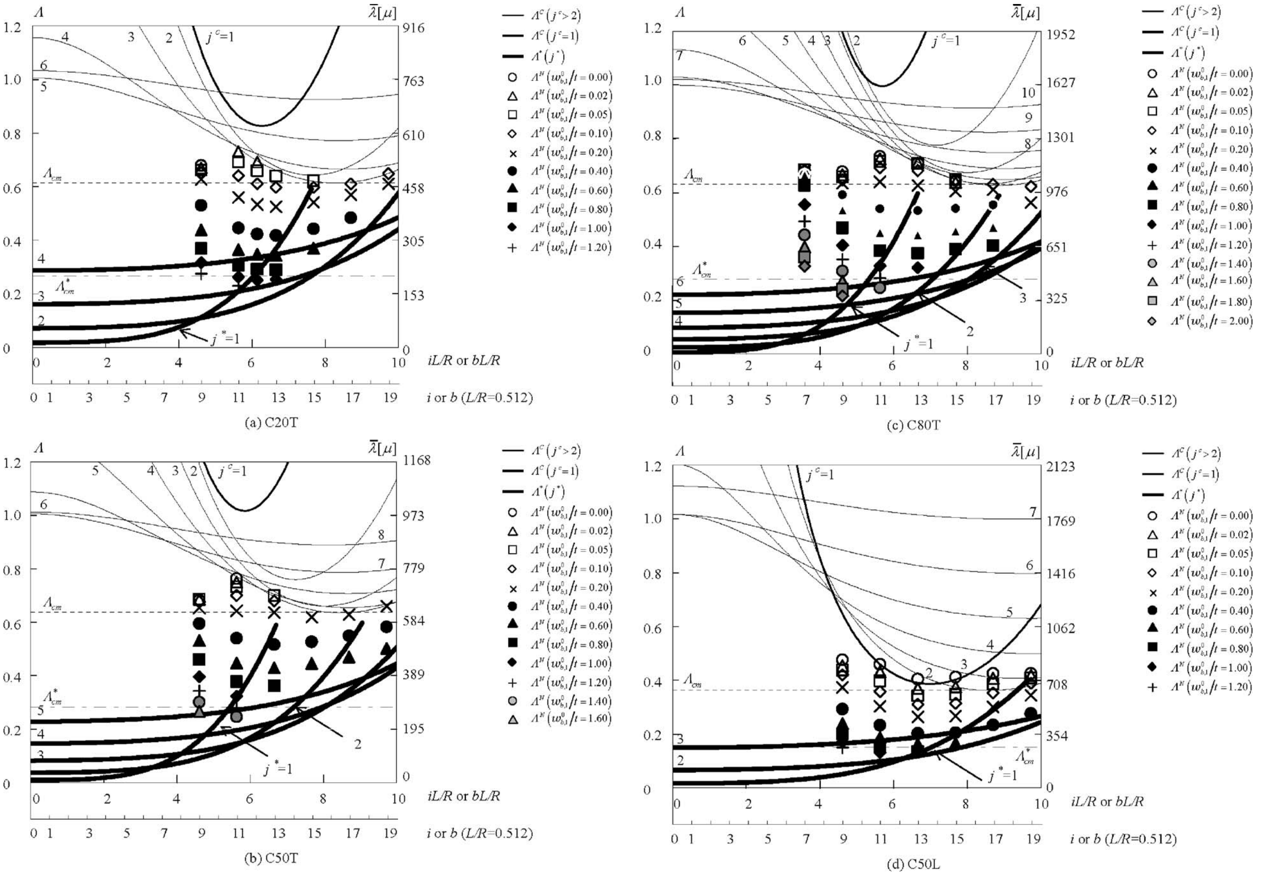

(a) C20T

(c) C80T

(b) C50T

(d) C50L

Fig. 6 Plots of nonlinear buckling loads for various imperfection amplitudes and circumferential wave number *b* with single axial number compared with the linear buckling loads or the reduced stiffness buckling loads

having an amplitude $w^0_{9,1}/t > 1.2$ would not exhibit a maximum, buckling, load and the equilibrium path would monotonically approach from below this same level of load $\Lambda^N = 0.230$. In a similar way for other imperfection wave numbers b, the absence of a buckling load above a certain threshold level of imperfection, in all the studies shown in Fig. 6, also implies that there is no maximum, buckling, load exhibited at that level of imperfection.

It would be of considerable practical advantage if simple analysis could predict the levels of these lowest imperfection sensitive buckling loads.

5 Buckling Lower Bounds and the Reduced Stiffness Method

In previous studies, it has been shown that the lower bounds to the scatter of imperfect experimental and numerically simulated buckling loads are reliably predicted by the reduced stiffness method (see, for example, Refs. [17–20]). For a particular shell buckling problem, this method has the great advantage of being based upon a very simple extension of a classical bifurcation analysis. It argues that of the various shell energy components that provide the resistance within the various possible critical buckling modes, it will be the membrane components that are lost as a result of the nonlinear mode couplings occurring in the postbuckling range. As a lower bound to the buckling into these modes will be an equivalent bifurcation analysis from which these at risk membrane energy components have been eliminated. From this perspective, it becomes clear that all the potential loss of stiffness and associated imperfection sensitivity within a given buckling mode is contained within an appropriate interpretation of the classical linear bifurcation analysis. Both upper and lower bounds to imperfection sensitive buckling loads therefore become possible from just a linear bifurcation analysis.

The classical bifurcation analysis for a prospective buckling deformation i,j from a uniform prebuckling stress and strain state could be represented in terms of energy as

$$U_{2B} + U_{2M} + \Lambda_C\left(\frac{\partial V^x_{2M}}{\partial \Lambda} + \frac{\partial V^y_{2M}}{\partial \Lambda}\right) = 0 \tag{12}$$

In this equation, the subscripts 2 for all terms imply, that they belong to the quadratic form; U_{2B} is the linear bending energy; U_{2M} is the linear membrane energy; V^x_{2M} and V^y_{2M} are the linearized membrane energy components associated with, respectively,

Table 3 Lower limits for nonlinear buckling

	Λ^N_{cm}	$b(bL/R)$	$w^0_{b,1}/t$	$\Lambda^*_{\mathrm{cm}}\ (i,j)$	$\Lambda_{\mathrm{cm}}\ (i,j)$
C20T	0.230	11(5.63)	1.20	0.267(15,2)	0.615(16,3)
C50T	0.247	11(5.63)	1.40	0.283(16,3)	0.637(17,4)
C80T	0.216	9(4.61)	2.00	0.278(16,3)	0.631(17,5)
C50L	0.131	11(6.65)	1.00	0.151(14,1)	0.363(17,2)

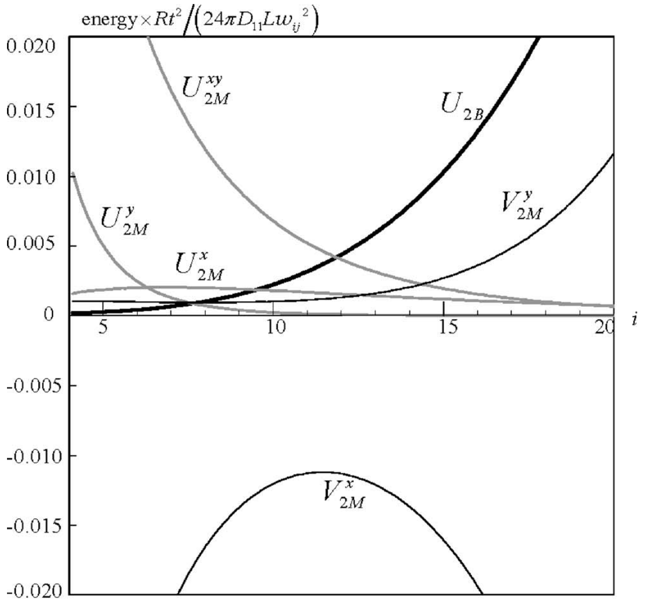

(a) C50T for $j^c=1$

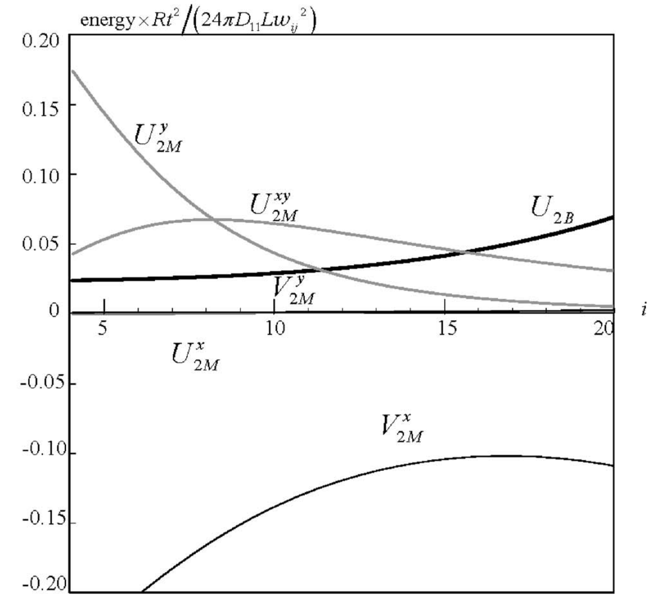

(b) C50T for $j^c=4$

Fig. 7 Energy components

the axial and circumferential directions. Here as elsewhere (see, for example, in Refs. [18,19]), "linear" is used in the sense of being derived from the linear strain-displacement relationships in the incremental critical deformations, while "linearized" implies an interaction between the fundamental membrane state and the quadratic contributions to the membrane strain-displacement relationships. Solution of Eq. (12) will result in the spectra Λ_c shown by the lighter solid curves in Fig. 6. As in Ref. [17], i_{cm} is defined to be the circumferential full-wave number associated with the lowest classical linear critical loads Λ_{cm}.

For the C50T shell, Fig. 7 shows for selected modes the breakdown of the incremental quadratic components of the energy, where the energies are normalized by $24\pi w_{i,j}{}^2 D_{11} L/(R/t^2)$. It can be seen that V_{2M}^x provides the negative destabilizing contributions to the critical loads Λ^c. Both the linear bending U_{2B} and membrane U_{2M} energies contribute to the stabilization, as does the linearized circumferential component V_{2M}^y.

In Refs. [17,18], it has been demonstrated that for pressure and axially loaded isotropic cylinders, both the linear membrane, U_{2M}, and linearized circumferential, V_{2M}^y, energies are with increasing imperfection eventually eliminated at buckling. It is suggested that similar behavior will occur for FRP cylinders. Based upon a reduced energy, the critical load, Λ^*, may be obtained by solving the equation for the prospective buckling deformation i and j, as follows:

$$U_{2B} + \Lambda_C^* \frac{\partial V_{2M}^x}{\partial \Lambda} = 0 \tag{13}$$

For the present orthotropic cylinders, this equation gives an explicit expression for the reduced stiffness criterion as

$$\Lambda_C^* = \frac{R}{L^2}\sqrt{\frac{A_{11}(A_{11}A_{22}-A_{12}^2)}{D_{11}}} \times \frac{D_{11}(j\pi)^4 + 2(D_{12}+2D_{66})(j\pi)^2(iL/R)^2 + D_{22}(iL/R)^4}{(2A_{11}A_{22}-A_{12}^2)(j\pi)^2 + A_{12}A_{22}(iL/R)^2} \tag{14}$$

Reduced stiffness spectrum curves for selected j values, obtained from Eq. (14), are shown in Fig. 6 by the heavy solid curves.

Through extensive numerical simulation and direct experimental observation, it has been shown that for a particular value of axial half-wave j, it will be that circumferential mode i_{cm}, which corresponds with the minimum classical critical load, into which the buckling will be biased. A lower bound to the buckling into this mode will be the associated reduced stiffness critical load, Λ_{cm}^*. Depending on the disposition of the fiber reinforcement, the lowest reduced stiffness critical load Λ_{cm}^* will be associated with different axial wavelengths. For isotropic shells, the classical critical minimum Λ_{cm} occurs for a wide range of j values but it is $j=1$ that produces the lowest value for Λ_{cm}^* (see, for example, Ref. [18]). Figure 6 shows that the lowest values of both Λ_{cm} and Λ_{cm}^* depend on the particular properties of the fiber lay-ups. For shell C50T, the minimum classical critical load is $\Lambda_{\mathrm{cm}}=0.637$ occurring in the mode $(i_{\mathrm{cm}}, j_{\mathrm{cm}})=(17,4)$. For this same shell, the minimum reduced stiffness critical load $\Lambda_{\mathrm{cm}}^*=0.283$ can be seen in Fig. 6(*b*) to be associated with the mode $(i_{\mathrm{cm}}^*, j_{\mathrm{cm}}^*)=(16,3)$. For the shell C50L, Fig. 6(*d*) shows that $\Lambda_{\mathrm{cm}}=0.363$ in mode $(i_{\mathrm{cm}}, j_{\mathrm{cm}})=(17,2)$ and $\Lambda_{\mathrm{cm}}^*=0.151$ in mode $(i_{\mathrm{cm}}^*, j_{\mathrm{cm}}^*)=(14,1)$. In these and all other cases considered, the values of the reduced stiffness critical load have a close correspondence with the lowest recorded numerically predicted buckling loads.

To provide additional confirmation of the lower boundedness of the present reduced stiffness critical load Λ_{cm}^*, the lower limits of the nonlinear analytical buckling loads plotted by various dots in Fig. 6 have been compared with the present reduced stiffness analytical results. The many dots in Fig. 6, for example, show the buckling loads for imperfections in modes $7 \leq b \leq 19$ $(3.58 \leq bL/R \leq 9.73)$ and $f=1$. For shell C50T, the minimum buckling load $\Lambda_{\mathrm{cm}}^N=0.230$ occurs for the imperfection having wavelength $(b,f)=(11,1)$. Although the initial imperfection has a shape that does not correspond to the wavelength associated with Λ_{cm}^*, the incremental mode shape at the buckling load, shown in Fig. 8, is as close to that of the reduced stiffness mode shape as the limitations in the degrees of freedom for the present analysis would allow. Through a combination of modes $i=11$ and 22, the circumferential wavelength of the incremental displacement at the minimum buckling load shown at midlength in Fig. 8(*c*) can, at the location where the maximum displacement occurs, be seen to have an effective length close to $\pi R/15$. This is close to $i_{\mathrm{cm}}^*=16$ that characterizes the reduced stiffness prediction. Through a combination of the modes $j=1-5$, the axial half wavelength associated with the lowest imperfect buckling load can be seen in Fig. 8(*b*) to be close $j=3$. As shown in Fig. 6(*b*), the reduced stiffness

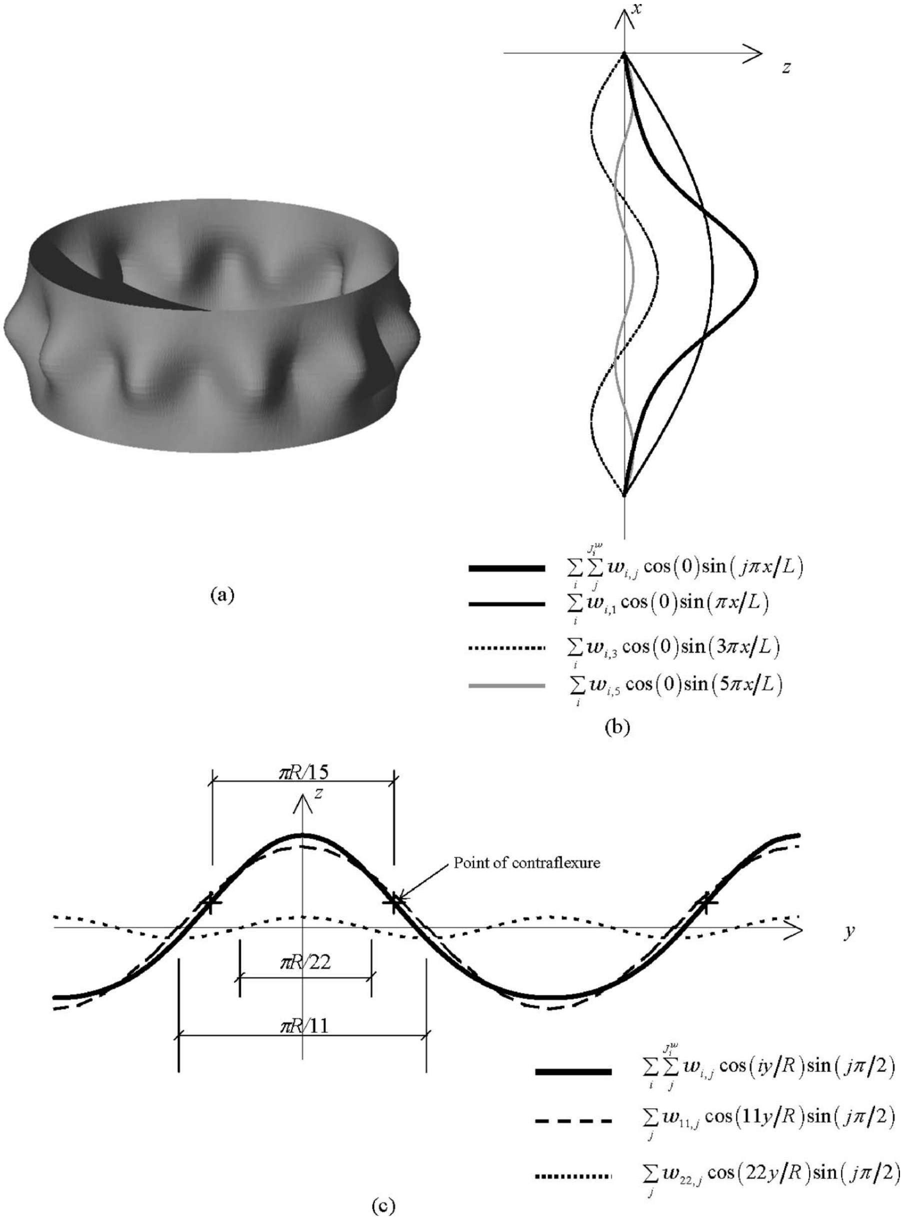

Fig. 8 Incremental displacement modes at the buckling points for a large imperfection $w^0/t=1.40$ in shell C50T ($b=11$) showing (*a*) shape, (*b*) axial profile at $y=0$, and (*c*) circumferential profile at $x=L/2$

loads Λ^*_{cm} are almost equal for modes $j=2$ and 3. It is worth remembering that for the current choice of degrees of displacement freedom, included in the nonlinear analyses of Eqs. (6*a*)–(6*c*), precludes consideration of buckling into a mode $j=2$. Figure 5 shows the nature of the incremental displacements at the lowest buckling load for the imperfection $w^0/t=1.6$ having $b=9$. Again, an imperfection having a very different form to the mode associated with Λ^*_{cm} can be seen to eventually buckle into a deformation that is very close to $(i^*_{\mathrm{cm}}, j^*_{\mathrm{cm}})=(16,3)$. Other shells can be seen in Fig. 6 to show very similar levels of agreement between the lower bound to the nonlinear buckling studies and the predictions of lower bounds using the reduced stiffness approach. They also show how the incremental buckling deformations at the lowest buckling loads are close to those predicted by the reduced stiffness method, even though the shapes of the initial imperfection may be very different.

Figure 9 shows how the sensitivity of buckling loads for the present FRP shells compares with that of the related isotropic shell [18] in those modes that display the most extreme imperfection sensitivity. For the present cases of FRP shells, the knockdown factors are somewhat less than for the isotropic shell having the same geometric parameters. For each case, it is clear that the lower limit to the imperfection generated knockdown is approximated by the associated reduced stiffness predictions shown in Fig. 6.

Figure 10 shows the variations of the classical critical loads σ_{cm} and reduced stiffness prediction σ^*_{cm} for variation in the circumferential fiber volume fraction V_y/V. It is clear that the axial wavelengths for both the minimum classical and reduced stiffness critical loads depend on the distribution of fiber between the axial and hoop directions, but perhaps not as much as might have been expected. It can be seen that the axial wave numbers associated with σ^c_{cm}, σ^*_{cm} increase as the ratio V_y/V becomes larger. Associated with this increase in j_{cm} and j^*_{cm} is a shortening of the critical circumferential wavelength indicated by an increase in i_{cm} and

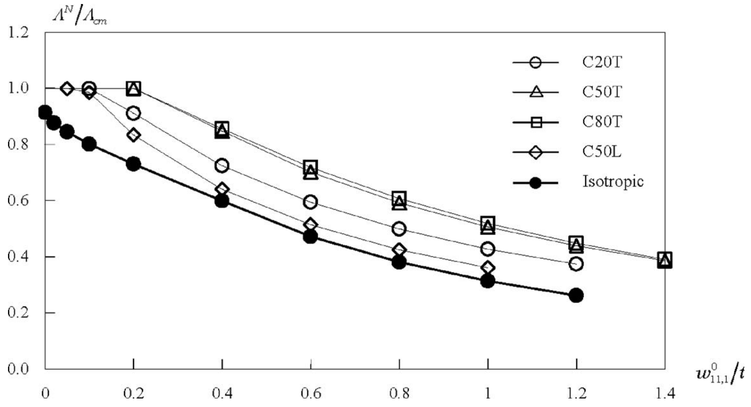

Fig. 9 Comparison of initial imperfection sensitivity

i^*_{cm}. The maximum of σ^c_{cm} is obtained when $V_y/V=0.15$ for T series and $V_y/V=0.80$ for L series, with both occurring at very similar stress levels. Maximum safe loads carrying capacities, as measured by σ^*_{cm}, are likewise relatively insensitive to the circumferential fiber volume fraction. However, Fig. 10 shows that σ^*_{cm} reaches its maximum value for V_y/V around 0.1 for the T series and 0.9 for the L series.

6 Conclusions

In the present study, an elastic, nonlinear, Ritz analysis has been developed to allow investigation of the imperfect behavior of axially compressed orthotropic FRP cylindrical shells. In a particular mode, buckling loads are shown to be strongly influenced by the constitutive material coefficients and are sensitive to initial geometric imperfections. However, the lower bounds to imperfection generated knockdown in buckling loads are remarkably insensitive to the particular distribution of fiber reinforcement. Just as for the previously analyzed isotropic cylindrical shells, the reduced stiffness criteria are shown to provide close lower bounds to the imperfection sensitive elastic buckling loads for imperfect orthotropic cylindrical shells. The potential benefits in the use of the reduced stiffness theoretical results to allow specification of the optimal designs of these classes of complicated composite structures are illustrated through the determination of the values of the circumferential fiber volume ratio producing maximum safe load capacities.

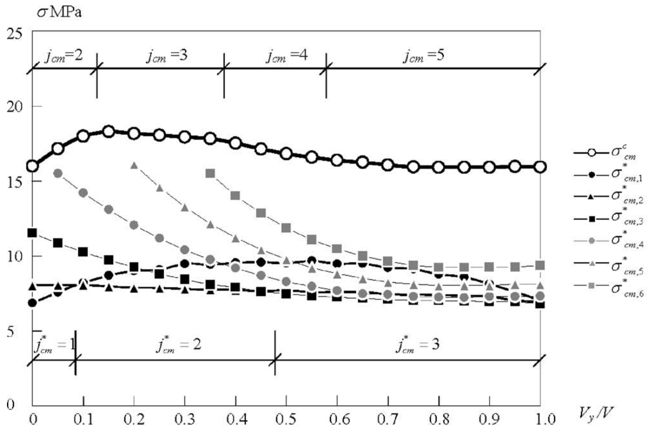

(a) T-series

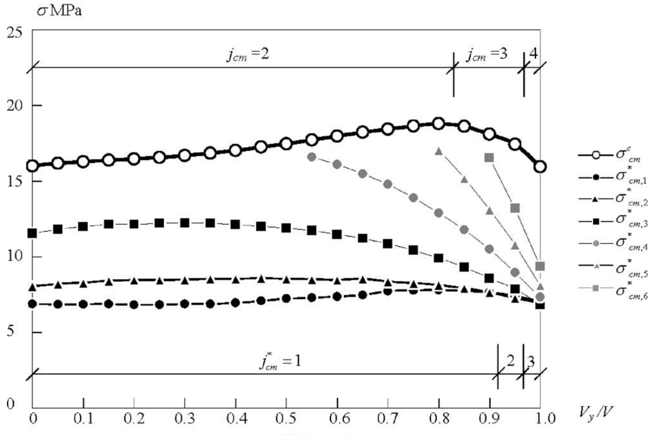

(b) L-series

Fig. 10 Effects of the ratio V_y/V on the buckling loads

References

[1] Vinson, J. R., and Sierakowski, R. L., 1986, *The Behavior of Structures Composed Materials*, Martinus Nijhoff, Dordrecht.

[2] Singer, J., Arbocz, J., and Weller, T., 2002, "Composite Structures," *Buckling Experiments*, Vol. 2, Wiley, pp. 1164–1242.

[3] Samuelson, L. A., and Eggwertz, S., 1992, "Shells of Composite Materials," *Shell Stability Handbook*, Elsevier, New York, pp. 222–227.

[4] Tennyson, R. C., and Hansen, J. S., 1983, "Optimum Design for Buckling of Laminated Cylinders," *Collapse: The Buckling of Structures in Theory and Practice*, Cambridge University Press, Cambridge, pp. 409–430.

[5] Johns, R. M., and Morgan, S., 1975, "Buckling and Vibration of Cross-Ply Laminated Circular Cylindrical Shells," AIAA J., **13**, pp. 664–671.

[6] Kobayashi, S., Koyama, K., Seko, H., and Hirose, K., 1982, "Compressive Buckling of Graphite-Epoxy Composite Circular Cylindrical Shells," *ICCM-IV*, pp. 555–564.

[7] Card, M. F., 1966, "Experiments to Determinate the Strength of Filament Wound Cylinders Loaded in Axial Compression," Report No. NASA TN D-3522.

[8] Tennyson, R. C., and Muggeridge, D. B., 1973, "Buckling of Laminated Anisotropic Imperfect Circular Cylinders Under Axial Compression," J. Spacecr. Rockets, **10**, pp. 143–148.

[9] Tennyson, R. C., and Muggeridge, D. B., 1971, "Buckling of Circular Cylindrical Shells Having Axisymmetric Imperfection Distributions," AIAA J., **9**, pp. 924–930.

[10] Geir, B., Klein, H., and Zimmermann, R., 1991, "Buckling Tests With Axially Compressed Unstiffened Cylindrical Shells Made From CFRP," *Buckling of Shell Structures, on Land, in the Sea and in the Air*, Elsevier, New York, pp. 498–507.

[11] Yamaki, N., 1984, *Elastic Stability of Circular Cylindrical Shells*, North-Holland, Amsterdam.

[12] Yamada, S., and Komiya, I., 1996, "Elastic Deflection Behavior of a Box-Shaped Pultruded Composite Member and its Collapse, Fiber Composites in Infrastructure," *ICCI'96*, University of Arizona, Tucson, pp. 699–707.

[13] Yamada, S., Takashima, H., Tadaka, R., and Komiya, I., 1998, "Experiments on the Buckling and Collapse of Pultruded Composite Columns Under Axial Compression," *Fiber Composites in Infrastructure, ICCI'98*, Arizona, Tucson, Vol. 2, pp. 236–247.

[14] Donnell, L. H., 1934, "A New Theory for the Buckling of Cylinders Under Axial Compression and Bending," Trans. ASME, **56**, pp. 795–806.

[15] Koiter, W. T., 1945, *The Effects of Axisymmetric Imperfections on the Buckling of Cylindrical Shells Under Axial Compression*, Lockhead Missile and Space Co., Sunnyvale.

[16] Yamada, S., and Croll, J. G. A., 1989, "Buckling Behavior of Pressure Loaded Cylindrical Panels," J. Eng. Mech., **115**(2), pp. 327–344.

[17] Yamada, S., and Croll, J. G. A., 1993, "Buckling and Postbuckling Characteristics of Pressure Loaded Cylinders," ASME J. Appl. Mech., **60**, pp. 290–299.

[18] Yamada, S., and Croll, J. G. A., 1999, "Contributions to Understanding the Behavior of Axially Compressed Cylinders," ASME J. Appl. Mech., **66**, pp. 299–309.

[19] Batista, R. C., 1979, "*Lower Bound Estimates for Cylindrical Shell Buckling*," Ph.D. thesis, UCL, University of London.

[20] Ellinas, C. P., and Croll, G. G. A., 1983, "Experimental and Theoretical Correlations for Elastic Buckling of Axially Compressed Ring Stiffened Cylinders," J. Strain Anal., **18**, pp. 81–93.

Experimental Investigation of the Painlevé Paradox in a Robotic System

Zhen Zhao

Caishan Liu
e-mail: lcs@mech.pku.edu.cn

Wei Ma

Bin Chen

State Key Laboratory for Turbulence
and Complex Systems,
College of Engineering,
Peking University,
Beijing 100871, P.R.C.

This paper aims at experimentally investigating the dynamical behaviors when a system of rigid bodies undergoes so-called paradoxical situations. An experimental setup corresponding to the analytical model presented in our prior work Liu et al. [2007, "The Bouncing Motion Appearing in a Robotic System With Unilateral Constraint," Nonlinear Dyn., ***49****(1–2), 217–232] is developed, in which a two-link robotic system comes into contact with a moving rail. The experimental results show that a tangential impact exists at the contact point and takes a peculiar property that well coincides with the maximum dissipation principle stated in the work of Moreau [1988, "Unilateral Contact and Dry Friction in Finite Freedom Dynamics," Nonsmooth Mechanics and Applications, Springer-Verlag, Vienna, pp. 1–82] the relative tangential velocity of the contact point must immediately approach zero once a Painlevé paradox occurs. After the tangential impact, a bouncing motion may be excited and is influenced by the speed of the moving rail. We adopt the tangential impact rule presented by Liu et al. to determine the postimpact velocities of the system, and use an event-driven algorithm to perform numerical simulations. The qualitative comparisons between the numerical and experimental results are carried out and show good agreements. This study not only presents an experimental support for the shock assumption related to the problem of the Painlevé paradox, but can also find its applications in better understanding the instability phenomena appearing in robotic systems.* [DOI: 10.1115/1.2910825]

Keywords: Painlevé paradox, robotic system, instability phenomenon, impulsive dynamics

1 Introduction

It is well known that the rigid body model for mechanical systems with unilateral constraints and friction may possess some singularities, at which the dynamical equations will have multiple solutions or even no solution at all. The classical Painlevé example, where a planar slender rod slides on a rough surface, represents the simplest system with such singularities. Recently, the interest in understanding the physical phenomena corresponding to the singular situations has witnessed a substantial increase [1–30]. Rich information and a good overview on the subject can be found in the excellent book written by Brogliato [5], which contains a wide variety of the problem of interest and a long list of references.

When Coulomb friction is coupled to unilateral constraints, rigid body models may have no solution for certain configurations. An important viewpoint adopted by many authors is that a shock should then exist at the contact point. Since the shock occurs in a special situation without normal velocity and friction is considered to be the main cause for its occurrence, different nomenclatures can be found in the literature, such as the impact without collision (IW/OC), frictional catastrophe, or tangential impact [11,12,16,19]. According to the shock assumption, some crucial results can be deduced and the problem of the Painlevé paradox seems to be solvable. For example, recent development related to the time-stepping numerical method indicates that the singularity of rigid body model can be successfully avoided if the contact forces are allowed to be impulsive [24,25,30,31], thus confirming a fact observed numerically in Refs. [11,28]. Obviously, the shock assumption is fundamental for the problem of Painlevé paradox, and the validation from experiments should be introduced. One aim of this paper is to develop an experimental method to support the shock assumption.

The Painlevé phenomenon was firstly discovered in the classical Painlevé example (a slender rod that slides on a rough plane), and many excellent theoretical results are motivated from the simple system. However, using the example to serve as the experimental model creates a lot of difficulties. For instance, the coefficient of friction in the system has to be greater than $4/3$ for the occurrence of the Painlevé paradox, a large value rarely found in practical materials [16]. Meanwhile, the sliding of a rod under gravity is also difficult to be implemented in practice. Therefore, it is crucial to search for a new example that can involve the paradox and can be easily implemented by experiments. Such examples have been presented in Refs. [15,28], where it has been shown that the Painlevé paradoxes may occur for arbitrarily small values of the coefficient of friction.

Recent studies have indicated that the Painlevé paradox may be a common phenomenon and could be found in a variety of different applications such as robotic manipulation, legged locomotion, and vehicle braking systems [15,26–28]. Especially, according to our recent work for a robotic system that comes into contact with a moving belt [28], the Painlevé paradox will appear even though the coefficient of friction takes a very small value. In this paper, we will use the analytical model presented in Ref. [28] to develop an experimental setup for the demonstration of the dynamical behaviors associated with the Painlevé paradox.

According to the theoretical analysis shown in Ref. [28], the Painlevé paradox can be found by setting the robotic system within a paradoxical configuration, which depends on the practical value of the coefficient of friction. By conducting the shock assumption into the paradoxical situation of the robotic system, and

---

Contributed by the Applied Mechanics Division of ASME for publication in the JOURNAL OF APPLIED MECHANICS. Manuscript received November 26, 2006; final manuscript received December 2, 2007; published online May 13, 2008. Review conducted by N. Sri Namachchivaya.

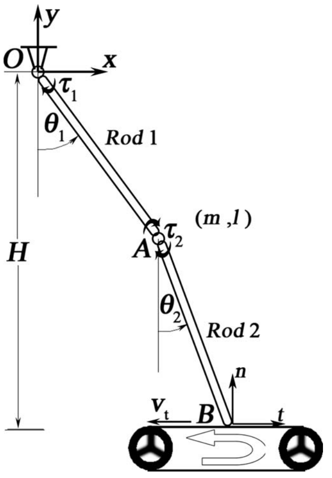

Fig. 1 Two-link manipulator contacting with a constantly moving belt

using the Darboux–Keller's method [21,32–37], it is also shown that the tangential impact will take a peculiar property; the relative motion of the contact point *must* be immediately brought into a stick in tangential direction. Therefore, the shock assumption can be verified by observing whether there is a tangential stick in paradoxical situations. In our experiments, two laser vibrometers with precise accuracy will be used to carefully measure the changes of the contact relative velocities of the robotic system.

Using numerical methods to reproduce the dynamical behaviors is significant for the analysis of mechanical systems. It is obvious that a jump rule related to the tangential impact should be provided for systems involving paradoxical situations. Since the tangential impact will excite a bouncing motion that can make the system contain different modes of motion such as slipping phases, collisions with friction, and flying without contact, an event-driven algorithm will be used to perform the numerical simulations. Qualitative comparisons between the numerical and experimental results are carried out.

Based on the numerical analysis and the experimental observation, two instability phenomena exhibited in robotic systems are discovered: one that is the bouncing motion induced by a tangential impact, and the other that is related to a slip-stick motion that appears in the robotic system without the occurrence of the Painlevé paradox. The first case indicates that the problem of the Painlevé paradox will extremely influence the controllability of the robotic system, as pointed out by Brogliato [4]. The second case shows that the stick-slip motion is periodic when the rail moves with a constant velocity.

The organization of thus study is as follows. Section 2 presents the description of the model for a two-link manipulator. The key theoretical results developed in Ref. [28] for the paradoxical situation will be reviewed in Sec. 3. The experimental setup and the phenomena associated with the paradoxical situations will be exhibited in Sec. 4. Section 5 provides the comparison between the numerical and experimental results. We conclude in Sec. 6 with a summary and the potential application of our study.

2 Two-Link Manipulator With Unilateral Constraint

This section will first conduct the model of a two-link robotic system, and then find the condition for the occurrence of the Painlevé paradox by using a linear complementarity problem (LCP) method, a theory for nonsmooth dynamics established by Moreau [38,39] and then extended into the multibody systems by Pfeiffer and Glocker [2].

The manipulator is shown in Fig. 1, which consists of two identical rods with length l and mass m and comes into contact with a moving belt with velocity v_t. The external torques τ_1 and τ_2 are applied on Joints O and A. H is the height from the Fixed Point O to the rough surface. The joint angles θ_1 and θ_2 are selected as the generalized coordinates of the system when unconstrained by contact, and their positive values are assigned along the counterclockwise direction.

We set an inertial coordinate frame Oxy attached at Joint O, and suppose that a local inertial coordinate frame (B,t,n) with origin located at Contact Point B, is defined such that n is normal to the contact surface and (t,n) forms a right-handed coordinate system. (F_t,F_n) represent the contact forces in the tangential and normal directions. The components in Oxy for the Contact Point B can be expressed by the generalized coordinates.

$$\mathbf{x}=\begin{bmatrix} x_t \\ x_n \end{bmatrix}=\begin{bmatrix} l(\sin\theta_1+\sin\theta_2) \\ -l(\cos\theta_1+\cos\theta_2) \end{bmatrix} \tag{1}$$

These kinematics can yield the contact Jacobian matrix $\mathbf{K}$ that relates velocities and accelerations of the Contact Point B to the generalized coordinates through the relations

$$\dot{\mathbf{x}}=\mathbf{K}^{\mathbf{T}}\dot{\mathbf{q}} \tag{2}$$

$$\ddot{\mathbf{x}}=\mathbf{K}^{\mathbf{T}}\ddot{\mathbf{q}}+\mathbf{S} \tag{3}$$

where

$$\mathbf{K}=\begin{bmatrix} K_1 \\ K_2 \end{bmatrix}=\begin{bmatrix} l\cos\theta_1 & l\sin\theta_1 \\ l\cos\theta_2 & l\sin\theta_2 \end{bmatrix}$$

$$\mathbf{S}=\begin{bmatrix} S_1 \\ S_2 \end{bmatrix}=\begin{bmatrix} -l(\dot{\theta}_1^2\sin\theta_1+\dot{\theta}_2^2\sin\theta_2) \\ l(\dot{\theta}_1^2\cos\theta_1+\dot{\theta}_2^2\cos\theta_2) \end{bmatrix}$$

The governing equations for the system with persistent contact can be written as

$$\ddot{\mathbf{q}}=\mathbf{M}^{-1}\mathbf{K}\mathbf{F}+\mathbf{M}^{-1}(-\mathbf{R}+\mathbf{W}) \tag{4}$$

where

$$\mathbf{M}=\begin{bmatrix} 4ml^2/3 & ml^2\cos(\theta_1-\theta_2)/2 \\ ml^2\cos(\theta_1-\theta_2)/2 & ml^2/3 \end{bmatrix},$$

$$\mathbf{F}=\begin{bmatrix} F_t \\ F_n \end{bmatrix},\quad \ddot{\mathbf{q}}=\begin{bmatrix} \ddot{\theta}_1 \\ \ddot{\theta}_2 \end{bmatrix}$$

$$\mathbf{W}=\begin{bmatrix} \tau_1-\tau_2-3mgl\sin\theta_1/2 \\ \tau_2-mgl\sin\theta_2/2 \end{bmatrix},\quad \mathbf{R}=\begin{bmatrix} ml^2\dot{\theta}_2^2\sin(\theta_1-\theta_2)/2 \\ ml^2\dot{\theta}_1^2\sin(\theta_1-\theta_2)/2 \end{bmatrix}$$

The substitution of Eq. (3) into Eq. (4) leads to

$$\ddot{\mathbf{x}}=\mathbf{Q}\mathbf{F}+\mathbf{K}^{\mathbf{T}}\mathbf{M}^{-1}(-\mathbf{R}+\mathbf{W})+\mathbf{S} \tag{5}$$

where

$$\mathbf{Q}=\mathbf{K}^{\mathbf{T}}\mathbf{M}^{-1}\mathbf{K}=\begin{bmatrix} Q_{11} & Q_{12} \\ Q_{21} & Q_{22} \end{bmatrix} \tag{6}$$

is a matrix that depends only on the configuration of the system.

Fact 1. $\mathbf{Q}$ is a symmetric and positive definite matrix, since $\mathbf{M}$ is a symmetric positive matrix and $\mathbf{K}$ is full rank in most cases (i.e., $\mathbf{K}$ may have singularities only in some extreme configurations).

The relative velocity between the contact point and the belt is

$$\dot{x}_r=x_t-v_t=l(\dot{\theta}_1\cos\theta_1+\dot{\theta}_2\cos\theta_2)-v_t \tag{7}$$

If $\dot{x}_r\neq 0$, the manipulator will slip on the moving belt; otherwise, the tip sticks on the belt. Defining a velocity-dependent coefficient of friction μ, in which $\mu=\mu_0$ for $\dot{x}_r<0$ and $\mu=-\mu_0$ for $\dot{x}_r>0$, the relationship between the tangential and the normal contact force by Coulomb's frictional law can be expressed as

$$F_t=\mu\cdot F_n \tag{8}$$

During the slip mode, the dynamical equations in tangential and normal directions take the following form:

$$\ddot{x}_n = A(\mathbf{q},\mu)\cdot F_n + B(\mathbf{q},\dot{\mathbf{q}}) \tag{9}$$

$$\ddot{x}_t = C(\mathbf{q},\mu)\cdot F_n + D(\mathbf{q},\dot{\mathbf{q}}) \tag{10}$$

where

$$A(\mathbf{q},\mu) = \mu Q_{21} + Q_{22}, \quad B(\mathbf{q},\dot{\mathbf{q}}) = \mathbf{K}_2^T\mathbf{M}^{-1}(-\mathbf{R}+\mathbf{W}) + S_2$$

$$C(\mathbf{q},\mu) = \mu Q_{11} + Q_{12}, \quad D(\mathbf{q},\dot{\mathbf{q}}) = \mathbf{K}_1^T\mathbf{M}^{-1}(-\mathbf{R}+\mathbf{W}) + S_1$$

Combining the Signorini complementarity condition ($\ddot{x}_n \geq 0$, $F_n \geq 0$ and $\ddot{x}_n \cdot F_n = 0$) with Eq. (9) gives the standard formulation of a LCP whose unknown is F_n and whose matrices (here a scalar) are $A(\mathbf{q},\mu)$ and $B(\mathbf{q},\dot{\mathbf{q}})$. Obviously, negative values of A will make this LCP possess multiple solutions or no solution at all. As illustrated by many authors, a so-called impact without collision occurs because of the configurations in which $A<0$ and $B<0$.

More interestingly, by observing the ingredients of the coefficient A, we can find that the paradoxical situation just depends on the configuration of the system and the velocity-dependent coefficient of friction. Therefore, for a given coefficient of friction, the Painlevé paradox is allowed to occur only when the system takes the paradoxical configurations, for which $A<0$. In other words, we can rely on the practical value of the coefficient of friction to determine the initial configuration that can make the Painlevé paradox appear.

3 Properties of the Tangential Impact and the Impact Rule

By conducting the shock assumption into the paradoxical situations, the theoretical description related to the properties of the tangential impact and the impact rule for the robotic system have been presented in Ref. [28]. In this section, some key results will be introduced.

3.1 Properties of the Tangential Impact. In order to consider the coupling between normal and tangential motions, the experience of an impact with friction must be carefully investigated. By assigning to the impact duration a very short but not infinitesimal time, Darboux [37] and Keller [34] developed a method that yields a set of differential equations with respect to the normal impulse, a "time like" independent variable. These nonlinear differential equations describe the impulsive behaviors (the impact dynamics), such that the singularities of impacts due to friction can be successfully avoided [35,36]. This method has been extended for the investigation of the properties of the tangential impact [28].

Let us set the impact duration as $[t_0, t_f]$ and divide this short time into much smaller intervals $[t_i, t_{i+1}]$. Integrating Eq. (5) and ignoring the contribution of the finite forces on $[t_i, t_{i+1}]$ yield the following differential equations of motion:

$$d\dot{x}_t = Q_{11}dP_t + Q_{12}dP_n$$

$$d\dot{x}_n = Q_{21}dP_t + Q_{22}dP_n \tag{11}$$

where

$$dP_t = \int_{t_i}^{t_{i+1}} F_t dt, \quad dP_n = \int_{t_i}^{t_{i+1}} F_n dt$$

are the changes of tangential and normal impulses on $[t_i, t_{i+1}]$, respectively.

Now, applying the relationship $dP_t/dP_n = \mu$ defined by Coulomb's frictional law into Eq. (11) directly leads to

$$d\dot{x}_t = (\mu Q_{11} + Q_{12})dP_n$$

$$d\dot{x}_n = (\mu Q_{21} + Q_{22})dP_n \tag{12}$$

where

$$d\dot{x}_t = \int_{t_i}^{t_{i+1}} \ddot{x}_t dt, \quad d\dot{x}_n = \int_{t_i}^{t_{i+1}} \ddot{x}_n dt$$

are the changes of the tangential and normal velocities, respectively.

During the interval $[t_i, t_{i+1}]$, the normal impulse is a strictly monotone function of time. This permits us to think of it as a time like independent variable, and to perform a time scale of the shock dynamics. Thus, Eq. (12) is a set of first order ordinary differential equations with respect to dP_n, which varies like a time variable. Combining Eq. (12) with the condition for the occurrence of the Painlevé paradox, we can deduce the property of the tangential impacts, which is elucidated by the following theorem.

Theorem 1. *The impulsive process induced by the Painlevé paradox will first result in a normal compressional process, and then immediately bring the relative tangential velocity of the contact point to zero. After that, the tangential motion of the contact point will stick on the contact surface, while the normal motion of the contact point will continue to be compressional until the normal velocity equals zero. Then, an expansion phase in the normal direction is carried out to make the impact finish.*

Proof. We will use Fact 1 for the properties of matrix Q, the condition for the occurrence of Painlevé paradox, and Coulomb's frictional law to prove the property of the tangential impact.

Matrix Q can be thought of as a constant matrix due to the little change of the configuration in an impulsive process. So the elements in Q satisfy the following relationships based on Fact 1:

$$Q_{22} > 0, Q_{11} > 0, \quad Q_{11}Q_{22} > Q_{21}^2$$

During the slip mode, the condition for the occurrence of Painlevé paradox permits us to write that

$$A = \mu Q_{21} + Q_{22} < 0, \quad -\mu Q_{21} > Q_{22}$$

In the case $\dot{x}_t < 0$, we have $\mu = \mu_0 > 0$, so $Q_{21} < 0$. Therefore,

$$-\mu Q_{21}Q_{11} > Q_{22}Q_{11} > Q_{21}^2$$

and

$$(\mu Q_{11} + Q_{12}) > 0$$

Similarly, if $\dot{x}_t > 0$, we can obtain the following inequality:

$$(\mu Q_{11} + Q_{12}) < 0$$

Thus, these two cases ($\dot{x}_t > 0$ and $\dot{x}_t < 0$) can be expressed by using a uniform inequality

$$\dot{x}_t(\mu Q_{11} + Q_{12}) < 0$$

The above inequality indicates that the magnitude of the tangential velocity always decreases when the sliding friction is sustained. Since the condition $A<0$ cannot be removed if the tangential velocity is not set to zero, the tangential motion of the contact point must reach the point of slip stopping.

Before slip stops, we can find from the second equation of Eq. (12) that the contact point will take a normal velocity penetrating into the contact surface, with an increment for its magnitude ($A < 0$ and the initial value equal to zero). Due to the coupling between the normal and tangential impulses, a compressional process in the normal direction is generated once the paradox appears. Before slip stopping, $A<0$ is always satisfied, so that the magnitude of the normal velocity will continue to increase. So the tangential slip at the contact point stops in the compressional process where the normal velocity is not equal to zero.

Once the tangential speed vanishes, the tangential motion might stick on the contact surface or continue to slip, depending on the property of dry friction. Setting $d\dot{x}_t = 0$ in Eq. (11), one can obtain the following inequality:

$$|dP_t/dP_n| = |Q_{12}/Q_{11}| < \mu_0$$

Usually, the static coefficient of friction, μ_s, is larger than the sliding coefficient, μ_0. The above inequality indicates that contact forces must enter into the interior of the friction cone once the tangential velocity disappears. So stick should occur at the instant when the tangential velocity vanishes. During the tangential impact, no other additional impulses are applied on the system. The stick mode can be preserved until the impulsive process finishes. Therefore, we can conclude that the relative tangential speed after tangential impact must equal zero. This well coincides with the maximum dissipation principle stated in Ref. [11] by Moreau.

Once stick occurs, dP_n and dP_t cannot be connected linearly by the coefficient of friction μ, and must satisfy the relationship defined by the first equation in Eq. (11) by setting $d\dot{x}_t=0$. This relationship can make the normal velocity of the contact point decrease and reach zero. After that, an expansion phase will occur in order to release the energy accumulated in the compressional phase. The expansion phase can be governed by an impact law such as Poisson's or Stronge's laws [33]. □

We can summarize the process of the tangential impact as follows: The friction will first result in a compressional motion in the normal direction and then bring the relative tangential motion from slip to stick. Then, sticking motion will persist until the contact constraint is released. The normal motion at the contact point will continue to be compressional from the instant of stick appearance to the time when the normal velocity vanishes. After that, an expansion phase is carried out to make the impact terminate.

3.2 Impact Rule for the Tangential Impact.

Assigning a duration $[t_0, t_f]$ to the tangential impact, we can split such an impulsive process into three periods. The first one is a *sliding compressional period* denoted as $[t_0, t_1]$, where t_1 is related to the instant of stick appearing. The second one is a *sticking compressional period* denoted as $[t_1, t_2]$, where t_2 corresponds to the instant when the normal velocity vanishes. The third one is a *sticking restitution period* denoted as $[t_2, t_f]$, which describes the expansion process of the normal motion, defined by using the Poisson's law for normal impact.

Sliding Compressional Period, $[t_0, t_1]$. Let us set $\dot{x}_t^0$ as the initial speed of slip at t_0. At $t=t_1$, the tangential velocity $\dot{x}_t^1$ will be equal to zero. Thus, the change of the normal impulse can be obtained by integrating the first equation of Eq. (12) as follows:

$$P_n^1 = -\frac{\dot{x}_t^0}{\mu Q_{11} + Q_{12}} \tag{13}$$

By considering the initial value of the normal velocity $\dot{x}_n^0=0$, we can obtain the normal velocity $\dot{x}_n^1$ at t_1 by integrating the second equation in Eq. (12) and by using expression (13) as folllows:

$$\dot{x}_n^1 = (\mu Q_{21} + Q_{22})P_n^1 = -\frac{\mu Q_{11} + Q_{12}}{\mu Q_{21} + Q_{22}}\dot{x}_t^0 \tag{14}$$

Sticking Compressional Period, $[t_1, t_2]$. The stick at the contact point implies the following relationship:

$$d\dot{x}_t = 0, \quad dP_t/dP_n = -(Q_{12}/Q_{11}) \tag{15}$$

Combining Eq. (15) with the second equation of Eq. (11), one can deduce the differential equation for the normal motion in the stick mode as follows:

$$d\dot{x}_n = \left(-\frac{Q_{12}^2}{Q_{11}} + Q_{22}\right)dP_n \tag{16}$$

Due to $\dot{x}_n^2=0$ at the end of this period, we can easily obtain the change of the normal impulse P_n^2 at t_2 as follows:

$$P_n^2 = \frac{Q_{11}\dot{x}_n^1}{Q_{12}^2 - Q_{11}Q_{22}} = -\frac{Q_{11}(\mu Q_{11} + Q_{12})}{(Q_{12}^2 - Q_{11}Q_{22})(\mu Q_{21} + Q_{22})}\dot{x}_t^0 \tag{17}$$

Sticking Restitutional Period, $[t_2, t_f]$. This period represents an expansion process of the normal motion. The expansion impulse P_n^r can be obtained by using Poisson's coefficient e_p as

$$e_p = \frac{P_n^r}{P_n^c}$$

where $P_n^c = P_n^1 + P_n^2$ is the compressional impulse in the normal direction. So we have

$$P_n^r = e_p P_n^c = e_p(P_n^1 + P_n^2)$$

At the beginning of this period, the normal speed $\dot{x}_n^2=0$. Meanwhile, the normal motion during this period will be governed by Eq. (16) since stick in tangential direction is preserved. Thus, at the end of this period, the normal speed $\dot{x}_n^f$ can be expressed as

$$\dot{x}_n^f = \left(-\frac{Q_{12}^2}{Q_{11}} + Q_{22}\right)P_n^r \tag{18}$$

Clearly the postimpact velocity in the normal direction, $\dot{x}_n^f$, is not equal to zero except for $e_p=0$ for the tangential impact without any initial normal velocity. In other words, after the tangential impact, the contact point will leave the contact surface with a certain velocity in the normal direction. Nevertheless, the tangential velocity at the contact point $\dot{x}_t^f$ must be equal to zero when the tangential impact finishes.

By integrating Eq. (4) and neglecting the contribution of the finite forces, the changes of the generalized velocities of the system due to the tangential impact can also be calculated as follows:

$$\begin{bmatrix} \Delta\dot{\theta}_1 \\ \Delta\dot{\theta}_2 \end{bmatrix} = M^{-1}K\begin{bmatrix} P_t \\ P_n \end{bmatrix} \tag{19}$$

where $\Delta\dot{\theta}_1$ and $\Delta\dot{\theta}_2$ represent the changes of the generated velocities, respectively. P_t and P_n are the total impulses in the tangential and normal directions.

4 Dynamical Behavior Related to the Paradoxical Situation

In this section, we will present the experimental setup for the robotic system that corresponds to the analytical model described in the above section. According to the coefficient of friction estimated from experiments, we will firstly determine the paradoxical configuration that can make the Painlevé paradox appear. By setting the system with the paradoxical configuration and initially establishing a contact constraint, we can observe the dynamical behavior associated with the paradoxical situation. The paradoxical phenomena will be demonstrated by showing the velocities of the contact point. The influence of the rail's speed on the bouncing motion generated due to the tangential impact will be exhibited. In addition, how the dynamical behaviors of the robotic system evolve into a shock from a normal configuration to the singular one will be demonstrated experimentally, and the stick-slip phenomena appearing in the robotic system will be investigated.

4.1 Description of Experiment.

The experimental setup of the robotic system is formed by using two identical aluminum cylindrical bars ($m=0.12kg, l=0.21m$) connected with revolute joints, see Fig. 2. The upper revolute joint is used to connect the system with a fixed bracket that contains a slot to make the height of the system adjustable. A semispherical head made of plastic material is installed on the contact end in order to make the contact achieve relatively uniform conditions during the motion. The belt used in the analytical model is replaced by a steel rail, which moves along the horizonal direction, dragging a rope by hand.

A passive torque is provided by a torsional spring mounted at

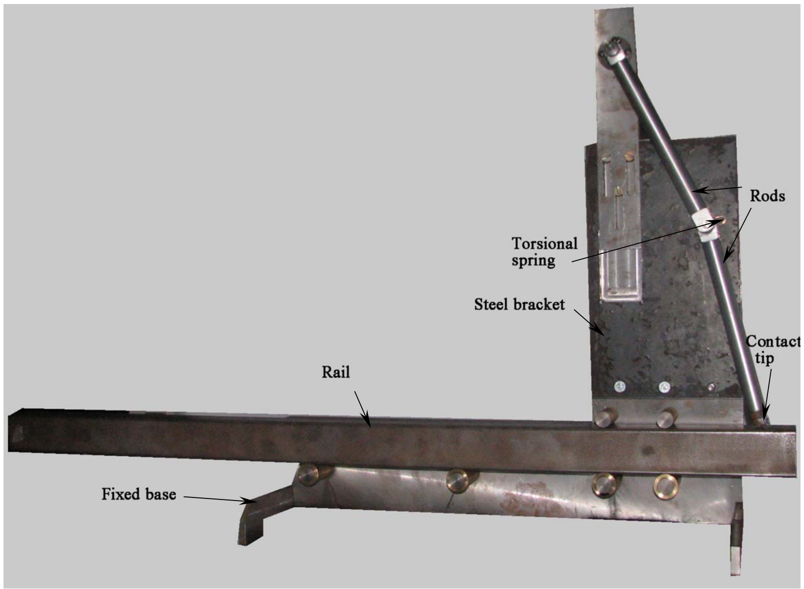

Fig. 2 The physical model of the experimental setup

the middle revolute joint. To consider the effects of joint friction, we use a uniform coefficient c to represent the damping torques acting on the two identical revolute joints. So the torques τ_1 and τ_2 at the revolute joints can be approximated as

$$\tau_1 = -c\dot{\theta}_1 \tag{20}$$

$$\tau_2 = k(\theta_1 - \theta_2 - \alpha_0) + c(\dot{\theta}_1 - \dot{\theta}_2) \tag{21}$$

where k is the stiffness of the torsional spring, and α_0 is the initial angle of the spring.

Two laser-Doppler vibrometers (OFV-303-353) with a controller (OFV-3001) are used to measure the rail speed and the velocity of the contact point, in which laser signals are sent to track the movements of the sensitive papers attached in the rail and the contact head. The experimental signals are transferred into a laptop through an analog-to-digtal (A\D) card with 10 kHz sample rate. The sketch of the experimental system is depicted in Fig. 3.

By using a simple slide experiment for the homogenous contact surface, we estimate the coefficient of friction as μ=0.6. Meanwhile, the contact constraint will allow the following geometric relationship to exist:

$$l(\cos\theta_1 + \cos\theta_2) = H$$

where H is the height of the system (see Fig. 1), and θ_1 and θ_2 are the angles related to the upper joint and the middle joint, respectively.

Based on the above relationship and the condition $A<0$, a function of θ_1 with respect to H and μ can be obtained for the occurrence of the Painlevé paradox. For the given coefficient of friction μ=0.6 with a different value of H, Table 1 presents the allowable scope of θ_1 for the occurrence of the Painlevé paradox.

Since the paradoxical situations appear under the condition that the robotic system should be in a paradoxical configuration with an initial condition of slip, we can release the tip of the system with an approximately zero height on the moving rail in order to generate the slip mode. In this case, the absolute value of the velocity of the tip is equal to zero, such that a relative slip between the tip and the rail can be established. According to the property of the tangential impact, the absolute tangential velocity of the tip should immediately approach the one of the moving rail if a shock exists. In the following, we will present the experimental results for the robotic system with different configurations by changing the joint angles and the height of the system. In particular, the observation of the stick phenomena associated with the paradoxical situations will be emphasized.

4.2 Experimental Results.

Let us set the robotic system with a fixed height H=0.3775 m, then repeat experiments for the system with joint angle θ_1 that takes different values among the scope of $\theta_1 \in (-37\text{ deg}, 37\text{ deg})$ (the possible values that can make the tip of the robotic system touch on the moving rail). The negative value of θ_1 corresponds to the situation where Rod 1 slopes to the left side against the vertical line passing through the fixed revolute

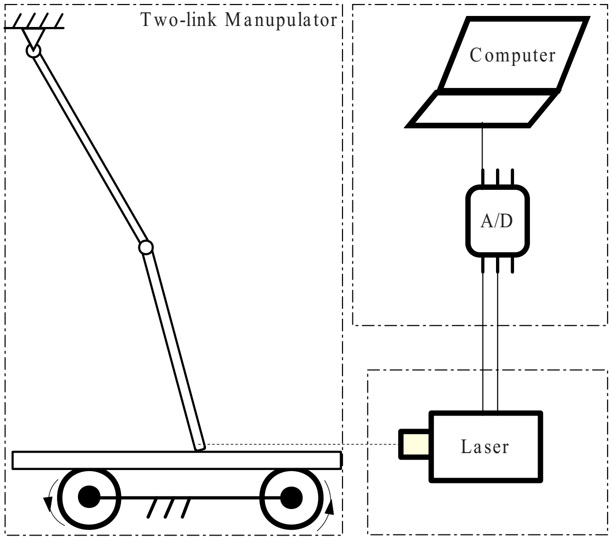

Fig. 3 The sketch of the experimental system

Table 1 The paradoxical configurations in different heights

	The coefficient of friction μ=0.6			
θ_1 (deg)	None	41.5–48.5	33–42.5	22.7–34.9
H (m)	0.21	0.331	0.35	0.3775

Table 2 The configurations investigated in experiments

	The height $H=0.3775$ m						
θ_1 (deg)	−15	7	15	21	25	30.5	32
Paradox	N	N	N	N	Y	Y	Y

joint. Table 2 presents the configurations of the system that are investigated in experiments, in which "Y" represents the paradoxical configurations, while "N" represents the ones of nonparadox appearing.

Figure 4 shows the experimental curves for the rail's speed and the tangential velocity of the contact point for the system with a paradoxical configuration of $\theta_1=32$ deg. When the tip touches the moving rail with zero velocity at $t=4.84$ s, the first vertical line shown in Fig. 4 indicates that the tip immediately approaches the value of the rail speed. This is related to a sticking phenomenon corresponding to a tangential impact appearing in the paradoxical configuration. After this event, the tip bounces on the moving rail and sequential collisions appear at $t=4.92$ s, 5.02 s, 5.10 s, etc.

We also found from experiments that the magnitude of the bouncing motion will be significantly influenced by the rail's speed. Figure 5 presents the experimental results by setting the robotic system in the same configuration as in the previous experiments, while the rail's speed is changed to $v_t=-0.5$ m/s. A tangential impact appears at the measure time $t=2.12$ s when the tip touches the rail, and then the subsequent impacts occur at the instant $t=2.21, 2.29, \ldots$. The comparison between Figs. 4 and 5 clearly shows that the magnitude of the tangential velocity is enlarged due to the increase of the rail's speed.

If the rail moves slowly, the bouncing motion induced by the tangential impact will be of low magnitude and even disappear when the velocity of the rail is lower than a certain threshold. Figure 6 shows the experimental results for the robotic system with the same configurations as the previous two experiments, while setting the rail moving with $v_t=-0.075$ m/s. Clearly after the tangential impact, the tip of the robotic system will stick on the moving rail, even though there is a peak in the curve of the tangential velocity because of the tangential impact.

This phenomenon can be elucidated from the viewpoint of the system's energy. According to Eqs. (18) and (19), the normal and tangential impulses are proportional to the rail's speed. So the robotic system can gain more energy from the tangential impact in the situation of the rail moving fast. Thus, the sequential collisions can be enlarged to make the magnitude of the bouncing motion increase. If the rail moves much more slowly, the robotic system cannot gain enough energy to overcome the contact force generated by the gravity and the torsional spring. In this case, the bouncing motion cannot be observed experimentally.

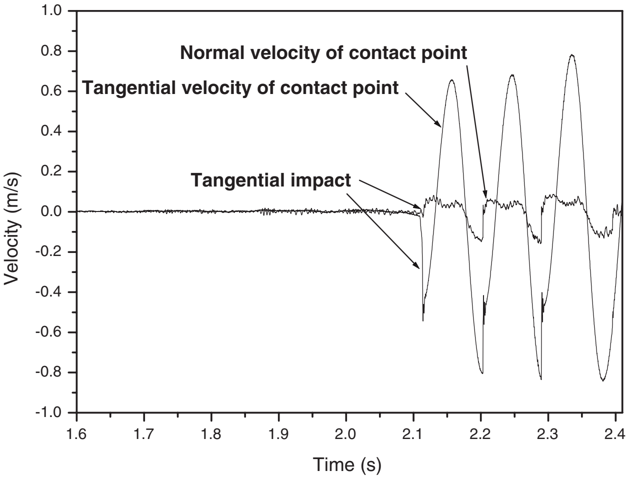

Fig. 5 The tangential velocity of the contact point ($H=0.3775$ m, $\theta_1=32$ deg, and $v_t=-0.075$ m/s)

For the system with the configuration of $\theta_1=30.5$ deg, the bouncing motion due to the tangential impact can also be observed by experiments when the rail takes a relatively high speed (as shown in Fig. 17). The experimental results related to the two cases of the system with $\theta_1=30.5$, 32 deg will be used in the following section to verify the numerical simulations.

When $\theta_1<29$ deg, the joint angle θ_2 will be greater than θ_1 if the tip can touch on the rail for the system with height $H=0.3775$ m, so that the initial torque of the torsional spring applied at the middle joint will change its direction and then influence the dynamical behavior of the system. Figure 7 presents the experimental results for the system with a paradoxical configuration by setting joint angle $\theta_1=25$ deg. When contact is established, a tangential impact appears at the contact point (the tangential velocity of the tip immediately approaches the one of the rail), and then an oscillation for the tangential motion is induced. However, the contact point does not leave away from the rail surface after the tangential impact and no bouncing motion can be observed. The reason for that is because the system with the configurations of $\theta_2>\theta_1$ can only obtain very little energy from the

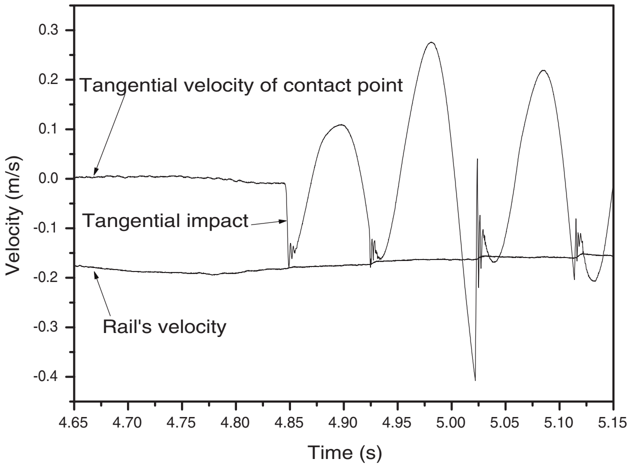

Fig. 4 The relative velocity of the contact point in tangential direction ($H=0.3775$ m, $\theta_1=32$ deg, and $v_t=-0.16$ m/s)

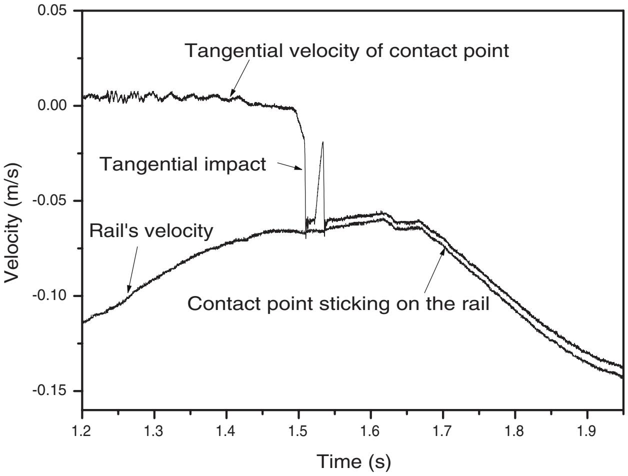

Fig. 6 The tangential velocity of the contact point ($H=0.3775$ m, $\theta_1=32$ deg, and $v_t=-0.075$ m/s)

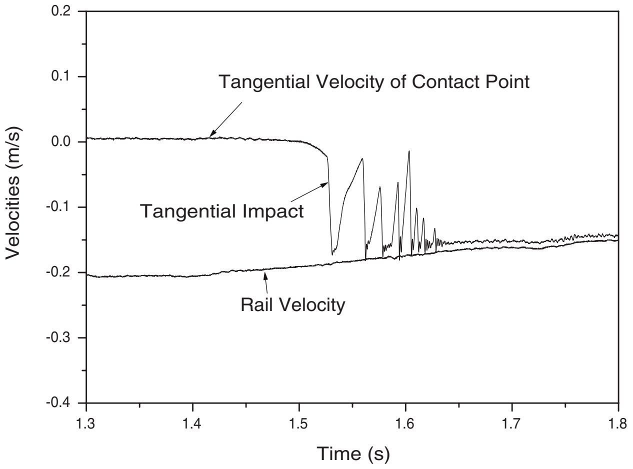

Fig. 7 The tangential velocity of the tip with $H=0.3775$ m and $\theta_1=25$ deg

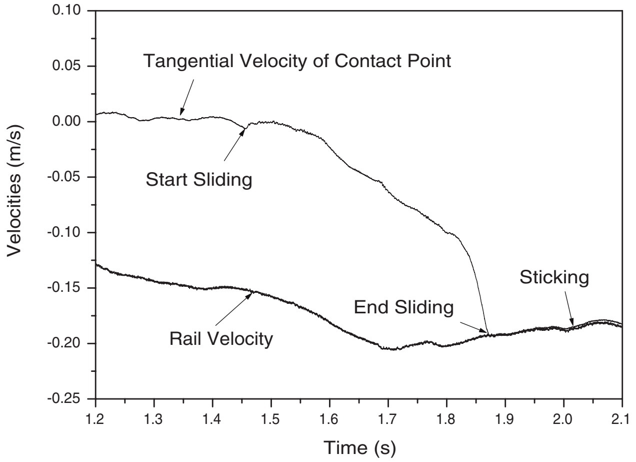

Fig. 9 The tangential velocity of the tip with $H=0.3775$ m and $\theta_1=7$ deg

tangential impact that is not enough to overcome the effects of the gravity and the torsional spring. Therefore, the contact point will stick on the moving rail.

It may be interesting to investigate how the tangential motion at contact point evolves into a shock by gradually changing the system from a normal configuration to a paradoxical configuration. Figures 8–11 present the experimental results obtained by setting the system with $\theta_1=-15$ deg, 7 deg, 15 deg, 21 deg, respectively. This corresponds to the situation where the initial configuration of the system gradually approaches the boundary of the singular region. From the experimental curves (except for the case of $\theta_1=-15$ deg), we can find that friction will decrease the slip velocity and finally bring the contact point to stick on the moving rail. In particular, the duration from the beginning of slip to the occurrence of sticking becomes shorter when the configuration of the system is near to the paradoxical situation. If the configuration is very close to the boundary of the paradoxical region (the case of $\theta_1=21$ deg), the duration for the stop of the relative tangential motion is about $t=0.13$ s. Once the configuration of the system enters into the paradoxical region, the duration for the tangential motion of the contact point changing from slip to stick will be less than 0.01 s (as shown for the case of $\theta_1=25$ deg), a short time scale that can be connected with an impact process. The above experimental phenomena well agree with the mechanism that the Painlevé paradox is due to the coupling between friction and the configuration of the system. This further confirms that the dynamical behavior of the system in the Painlevé paradox could be described by a shock.

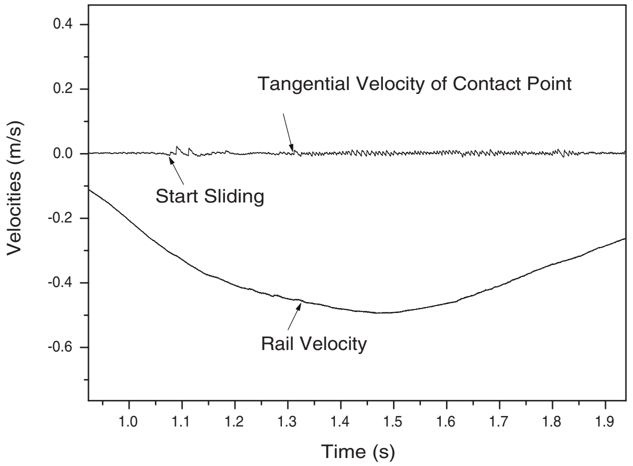

Fig. 8 The tangential velocity of the tip with $H=0.3775$ m and $\theta_1=-15$ deg

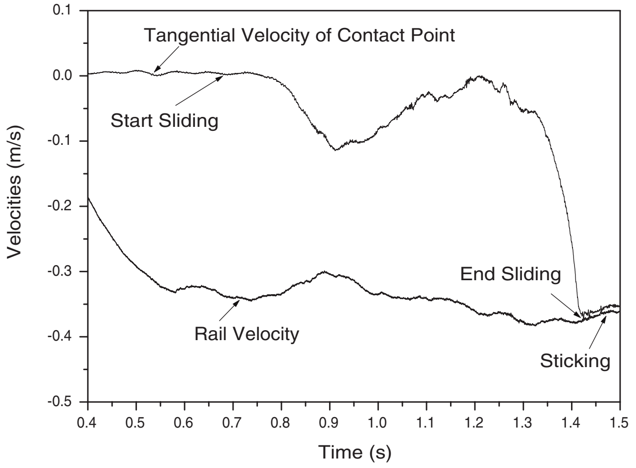

Fig. 10 The tangential velocity of the tip with $H=0.3775$ m and $\theta_1=15$ deg

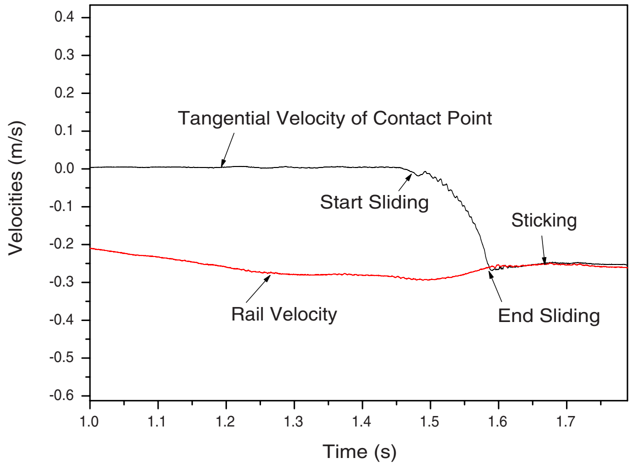

Fig. 11 The tangential velocity of the tip with $H=0.3775$ m and $\theta_1=21$ deg

If the initial configuration is far away from the singular region,

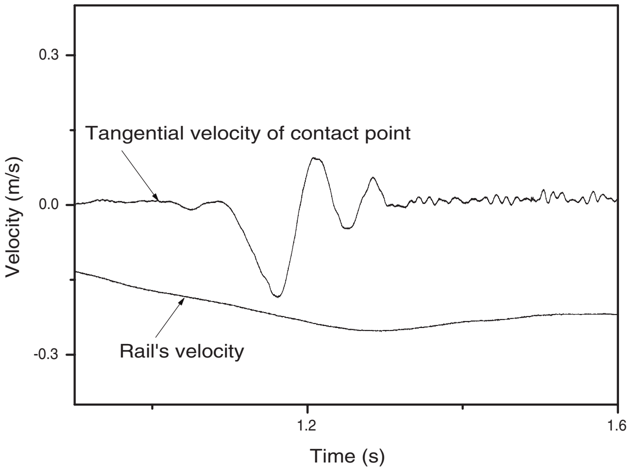

Fig. 12 The tangential velocity of the tip without the Painlevé paradox (H=0.25 m and θ_1=69.4 deg)

as shown in Fig. 8 for the system with $\theta_1=-15$ deg and in Fig. 12 for the robotic system with height H=0.25 m, neither sticking phenomena nor the bouncing motion can be found in the robotic system.

In some cases, the stick-slip phenomenon is also found in our experiments. By setting the initial configuration of the system to H=0.314 m and θ_1=50 deg, Fig. 13 shows that the friction will bring the tip into a stick, and then make the slip resume. Such a process can be repeated to render the robotic system unstable on the contact surface.

5 Comparison Between Experimental and Numerical Results

The experimental results presented in the above section have confirmed that the Painlevé paradox does induce a tangential impact at the contact point, and then makes the robotic system behave in a more complex way, with slip phases, stick phases, flight without contact phases, as well as tangential and normal impacts with friction. In this section, we will use an event-driven algorithm to perform the numerical simulations.

First, we will carefully estimate the parameters used for the simulations. According to property of the collision between plastic and steel materials, the coefficient of the restitution can be set as e_p=0.1. A single pendulum system (shown in Fig. 14 is established to obtain its frequency f, and the value of the stiffness of the torsional spring k can be calculated by using the following expression:

$$k=\frac{1}{3}ml^2(2\pi f)^2-\frac{l}{2}mg \tag{22}$$

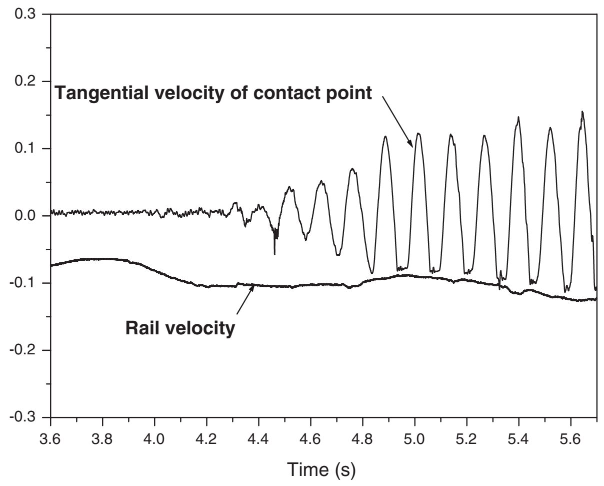

Fig. 13 The stick-slip phenomenon in the configuration (H=0.314 m and θ_1=50 deg)

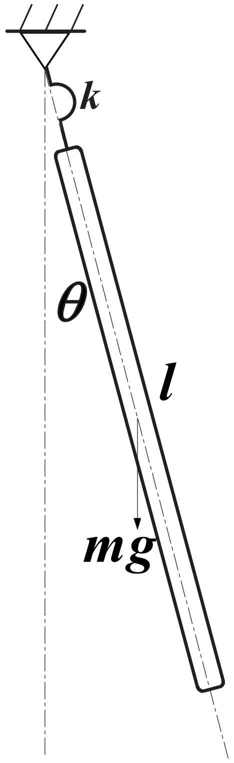

Fig. 14 A single pendulum composed by a link and a torsional spring

Based on f=4.6 Hz measured from experiments, we have k=1.3 N m/rad.

Since the damping coefficient c is difficult to obtain from the experiments, a fitting method is used for its estimation. By setting c with different values to perform the simulations, we choose the best one among the different values of c as the damping coefficient that can make the corresponding numerical simulation better coincide with the experimental results. According to the numerical experiments, we find that the change of c limited in the range of [0.003, 0.007] has little influence on the numerical results. So the damping coefficient is chosen as c=0.005 N ms/red for the following simulations.

Roughly speaking, the dynamical behaviors of the system are governed by Eqs. (4) and (5) with the variations of the contact forces, which depend on the mode of motion at the contact point. For instance, the contact forces can be set to zero for the flying mode, while in the case of preserved contact, the contact forces should be determined by using LCP's equations and Coulomb's friction law. If the paradoxical situations appear in the rigid body model, the simulation can be continued by setting Eq. (4) with new initial conditions that can be obtained from the tangential impact rule expressed in Eqs.(18) and (19). Similar process is also carried out for the collisions with friction [21], in which the changes of the velocities of the system are obtained by integrating the impulsive differential equations expressed in Eq.(12). Since there are no accumulations of events, event-driven schemes are well suited to the numerical integration of this nonsmooth system, see, e.g. Ref. [40].

Figure 15 presents the comparisons between the experimental and numerical results by setting the system to the initial configu-

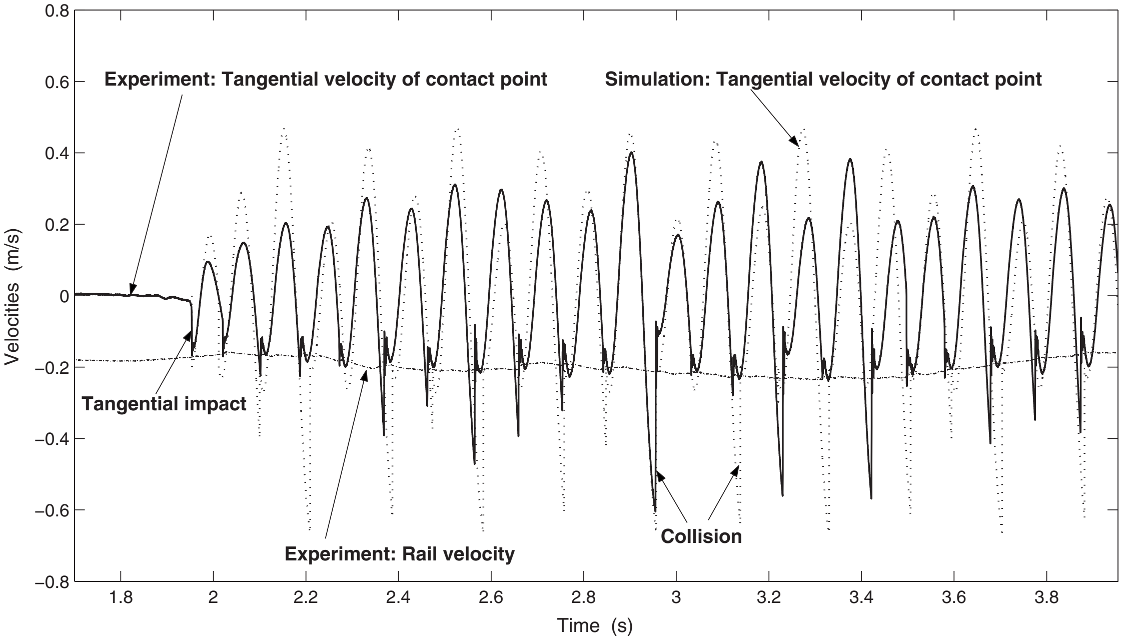

Fig. 15 Experimental and numerical results for the tangential speed ($H=0.3775$ m, $\theta_1=32$ deg, and $v_t=-0.2$ m/s)

ration of $H=0.3775$ m and $\theta_1=32$ deg. It is clear that the model used in simulation can well reproduce the qualitative behaviors of the system. The discrepancies appearing in Fig. 10 are partly due to the unmodeled effects existing in the experimental setup, such as the vibration of the sensitive papers, the clearances in the revolute joints, and the errors of the physical parameters. Other sources of discrepancies are the nonuniformity of the rail's speed in experiments, since it is assumed to be a constant in the numerical simulations.

Figure 16 shows the comparisons of the normal velocities between the experimental and numerical results. The vibration of the sensitive paper induced by the bouncing motion will much influence the accuracy of the measurements. Nevertheless, the qualitative behavior of the system can still be captured through the numerical simulations.

Keeping the system with the same height $H=0.3775$ m as in the previous case, we can change the initial configuration by adjusting the joint angle from $\theta_1=32$ deg to 30.5 deg. The results obtained from the simulation also agree well with the experimental results (shown in Fig. 17).

As mentioned in the above subsection, the phenomenon of stick-slip motion can be found in experiments even though there is no paradox appearing. By setting the initial configuration of the system with $H=0.314$ m and $\theta_1=55$ deg, Fig. 18 presents the curves corresponding to the tangential velocities of the contact point obtained from simulations and experiments, respectively. The numerical results indicate that the sticklip is a pure periodic

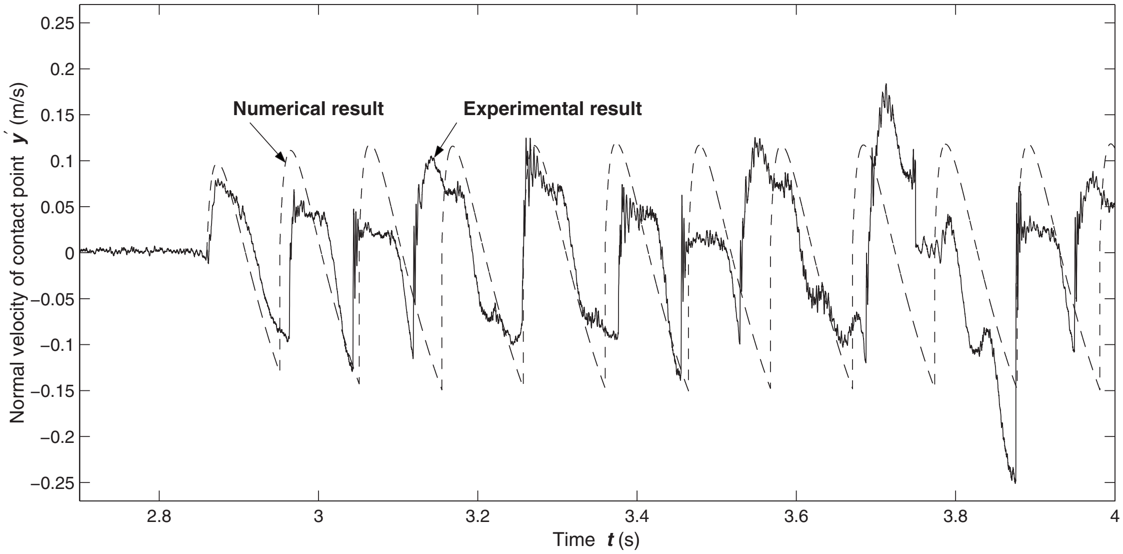

Fig. 16 Experimental and numerical results for the normal velocity ($H=0.3775$ m, $\theta_1=32$ deg, and $v_t=-0.24$ m/s)

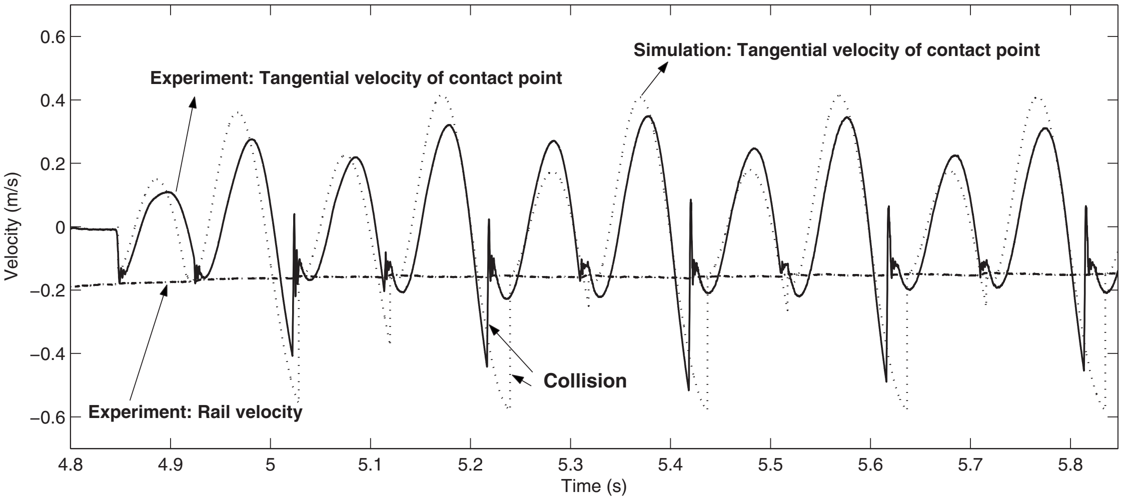

Fig. 17 The comparison of the tangential speed between experimental and numerical results ($H=0.3775$ m, $\theta_1=30.5$ deg, and $v_t=-0.2$ m/s)

motion when the rail speed takes a constant value, but this characteristic will be slightly destroyed due to the nonuniformity of the rail's motion.

Summarizing the comparisons between the numerical and experimental results presented above, we can conclude that the dynamical behaviors of the system can be well captured qualitatively by using the rigid body model. Even in the paradoxical situation, the simulations can be led by using the tangential impact rule to reinitialize the dynamical equations. The numerical results show that such a tangential impact induced by the Painlevé paradox can be well governed by the impact rule presented in Ref. [28].

6 Summary and Conclusion

This study mainly developed an experimental setup to demonstrate the phenomenon of the Painlevé paradox that appears in a robotic system coming into contact with a moving rail. According to the experimental results, we have verified that a shock is truly related to the problem of the Painlevé paradox, and takes a particular property that a tangential stick appears at the contact point.

Two kinds of instability phenomena for the robotic system are observed from the experiments. The first one is induced by the tangential impact, in which the robotic system will bounce or stick on the moving rail, depending on the value of the rail's speed. The other form of the instability is the stick-slip motion, which appears in the system does not involve the Painlevé paradox.

Based on the careful estimation of the physical parameters, an event-driven algorithm is used to perform numerical simulations. By setting the robotic system with paradoxical situations, comparisons between the numerical and experimental results are carried out and show good agreement. This illustrates that the rigid body model can well reproduce the complexly dynamical behaviors, and the Painlevé paradox can be overcome by using the tangential impact rule obtained from the Darboux–Keller' shock dynamics. The present work not only provides a basis for the

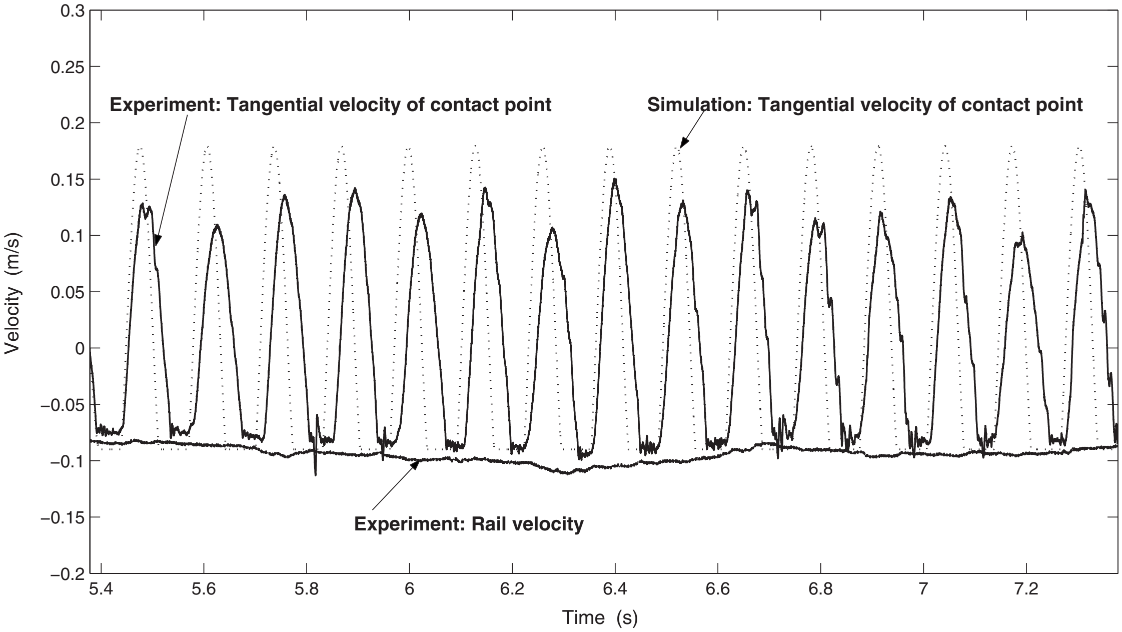

Fig. 18 Comparison between the experimental and numerical results for the stick-slip phenomena under the configuration taken as $H=0.314$ m and $\theta_1=55$ deg

theoretical results associated with the problem of the Painlevé paradox, but also may be useful for the design of feedback controllers in robotic systems.

Acknowledgment

We would like to express our sincere thanks to Dr. Bernard Brogliato for his valuable comments and the suggestions to this paper. We also appreciate the assistance from Dr. Zhili Sun, Jiyan Huo, and Ming Qiang to the work of experiment. This research was supported by the National Science Foundation of China (Grant Nos. 60334030, 10642001, and 10772002).

References

[1] Hurmuzlu, Y., Génot, F., and Brogliato, B., 2004, “Modeling, Stability and Control of Biped Robots A General Framework,” Automatica, **40**, pp. 1647–1664.
[2] Pfeiffer, F., and Glocker, C., 1996, *Multibody Dynamics With Unilateral Contacts*, Wiley, New York.
[3] Stronge, W. J., 2000, *Impact Mechanics*, Cambridge University Press, Cambridge.
[4] Brogliato, B., 2003, “Some Perspectives on the Analysis and Control of Complementarity Systems,” IEEE Trans. Autom. Control, **48**(6), pp. 918–935.
[5] Brogliato, B., 1999, *Nonsmooth Mechanics*, 2nd ed., Springer, London.
[6] Painlevé, P., 1895, “Sur les Lois du Ffrottement de Glissement,” C. R. Hebd. Seances Acad. Sci., **121**, pp. 112–115.
[7] Klein, F., 1909, “Zu Painlevés Kritik der Coulombschen Reibungsgesetze,” Zeit. Math. Physik, **58**, pp. 186–191.
[8] Lötstedt, P., 1981, “Coulomb Friction in Two-Dimensional Rigid-Body Systems,” Z. Angew. Math. Mech., **61**, pp. 605–615.
[9] Lötstedt, P., 1982, “Mechanical Systems of Rigid Bodies Subject to Unilateral Constraints,” SIAM J. Appl. Math., **42**, pp. 281–296.
[10] Erdmann, M., 1994, “On a Representation of Friction in Conguration Space,” Int. J. Robot. Res., **13**(3), pp. 240–271.
[11] Moreau, J. J., 1988, “Unilateral Contact and Dry Friction in Finite Freedom Dynamics,” *Nonsmooth Mechanics and Applications*, Springer-Verlag, Vienna, pp. 1–82.
[12] Wang, Y., and Mason, M. T., 1992, “Two-Dimensional Rigid-Body Collisions With Friction,” J. Appl. Mech., **59**, pp. 635–642.
[13] Baraff, D., 1991, “Coping With Friction for Non-Penetrating Rigid Body Simulation,” Comput. Graph., **25**(4), pp. 31–40.
[14] Payr, M., and Glocker, C., 2005, “Oblique Frictional Impact of a Bar, Analysis and Comparison of Different Impact Laws,” Nonlinear Dyn., **41**, pp. 361–383.
[15] Leine, R. I., Brogliato, B., and Nijmeijer, H., 2002, “Periodic Motion and Bifurcations Induced by the Painlevé Paradox,” Eur. J. Mech. A/Solids, **21**, pp. 869–896.
[16] Génot, F., and Brogliato, B., 1999, “New Results on Painlevé Paradoxes,” Eur. J. Mech. A/Solids, **18**, pp. 653–677.
[17] Ivanov, A. P., 1997, “The Problem of Constrainted Impact,” J. Appl. Math. Mech., **61**(3), pp. 341–253.
[18] Ivanov, A. P., 2003, “Singularities in the Dynamics of Systems With Non-Ideal Constraints,” J. Appl. Math. Mech., **67**, pp. 185–192.
[19] Brach, R. M., 1997, “Impact Coefficients and Tangential Impacts,” Trans. ASME, J. Appl. Mech., **64**, pp. 1014–1016.
[20] Zhao, Z., Chen, B., and Liu, C., 2004, “Impact Model Resolution on Painlevé’s Paradox,” Acta Mech. Sin., **20**(6), pp. 659–660.
[21] Zhao, Z., Liu, C., and Chen, B., 2006, “The Numerical Method for Three-Dimensional Impact With Friction of Multi-Rigid-Body System,” Sci. China, Ser. G, **49**(1), pp. 102–118.
[22] Peng, S., Kraus, P., Kumar, V., and Dupont, P., 2001, “Analysis of Rigid-Body Dynamic Models for Simulation of Systems With Frictional Contacts,” J. Appl. Mech., **68**, pp. 118–128.
[23] Grigoryan, S. S., 2001, “The Solution to the Painlevé Paradox for Dry Friction,” Dokl. Phys., **46**(7), pp. 499–503.
[24] Stewart, D. E., 2000, “Rigid-Body Dynamics With Friction and Impact,” SIAM Rev., **42**(1), pp. 3–39.
[25] Stewart, D. E., 1998, “Convergence of a Time-Stepping Scheme for Rigid-Body Dynamics and Resolution of Painleve’s Problem,” Arch. Ration. Mech. Anal., **145**, pp. 215–260.
[26] Wilms, E. V., and Cohen, H., 1997, “The Occurrence of Painlevé’s Paradox in the Motion of a Rotating Shaft,” J. Appl. Mech., **64**, pp. 1008–1010.
[27] Ibrahim, R. A., 1994, “Friction-Induced Vibration, Chatter, Sequeal and Chaos. Part ii, Dynamics and Modeling,” Appl. Mech. Rev., **47**(7), pp. 227–253.
[28] Liu, C., Zhao, Z., and Chen, B., 2007, “The Bouncing Motion Appearing in a Robotic System With Unilateral Constraint,” Nonlinear Dyn., **49**(1–2), pp. 217–232.
[29] Zhao, Z., Liu, C., and Chen, B., 2008, “The Painlevé Paradox Studied at a 3D Slender Rod,” Multibody Syst. Dyn., **19**(4), pp. 323–343.
[30] Anitescu, M., and Potra, F. A., 2002, “Time-Stepping Schemes for Stiff Multi-Rigid-Body Dynamics With Contact and Friction,” Int. J. Numer. Methods Eng., **55**(7), pp. 753–784.
[31] Anitescu, M., Potra, F. A., and Stewart, D., 1999, “Time-Stepping for Three-Dimensional Rigid-Body Dynamics,” Comput. Methods Appl. Mech. Eng., **177**, pp. 183–197.
[32] Kane, T. R., and Levinson, D. A., 1985, *Dynamics: Theory and Applications*, McGraw-Hill, New York.
[33] Stronge, W. J., 1994, “Swerve During Three-Dimensional Impact of Rough Rigid Bodies,” Trans. ASME, J. Appl. Mech., **61**, pp. 605–611.
[34] Keller, J. B., 1986, “Impact With Friction,” Trans. ASME, J. Appl. Mech., **53**, pp. 1–4.
[35] Bhatt, V., and Koechling, J., 1995, “Partitioning the Parameter Space According to Different Behaviors During Three-Dimensional Impacts,” Trans. ASME, J. Appl. Mech., **62**, pp. 740–746.
[36] Batlle, J. A., 1996, “Rough Balanced Collisions,” Trans. ASME, J. Appl. Mech., **63**, pp. 168–172.
[37] Darboux, G., 1880, “Etude Géométrique sur les Percussions et le Choc des Corps,” Bulletin des Sciences Mathématiques et Astronomiques, deuxième série, **4**, pp. 126–160.
[38] Moreau, J. J., 1963, “Les Liaisons Unilatérales rt le Principe de Gauss,” Acad. Sci., Paris, C. R., **256**, pp. 871–874.
[39] Moreau, J. J., 1971, *Mécanique Classique*, Masson, Paris, Tome II.
[40] Brogliato, B., ten Dam, A. A., Paoli, L., Génot, F., and Abadie, M., 2002, “Numerical Simulation of Finite Dimensional Multibody Nonsmooth Dynamical Systems,” Appl. Mech. Rev., **55**(2), pp. 107–150.

J. Girish
Professor
Department of Civil Engineering,
Bapatla Engineering College,
Bapatla 522101, India
e-mail: girish_iitkgp@yahoo.co.in

L. S. Ramachandra
Professor
Department of Civil Engineering,
IIT,
Kharagpur 721302, India
e-mail: lsr@civil.iitkgp.ernet.in

Stability and Vibration Behavior of Composite Cylindrical Shell Panels Under Axial Compression and Secondary Loads

The nonlinear static response and vibration behavior of cross-ply laminated cylindrical shell panels subjected to axial compression combined with other secondary loading are examined. The shell theory adopted in the present case is based on a higher-order shallow shell theory, includes geometric imperfection and von Kármán-type geometric nonlinearity. The solutions to the governing nonlinear partial differential equations are sought using the multiterm Galerkin technique. The nonlinear equilibrium paths through limit points and bifurcation points are traced using the Newton–Raphson method coupled with the Riks approach. The free vibration frequencies of post-buckled cylindrical panels about the static equilibrium state are reported by solving the associated linear eigenvalue problem. Results are presented for simply supported cross-ply laminated cylindrical shell panels, which illustrates the influence of initial geometric imperfection, temperature field, lateral pressure loads, and mechanical edge loads on the static response and vibration behavior of the shell panel. [DOI: 10.1115/1.2910772]

Keywords: shell panels, stability, limit points, Galerkin technique, axial compression

Introduction

The changes in the plate and shell panel vibration characteristics due to the interaction of thermal and mechanical loads influence panel dynamic response and flutter characteristics. The nonlinear equilibrium paths of shell panels are more complex compared to plates, as there are limit points on the equilibrium paths of shell panels. A great number of methods have been proposed to trace the snap-through and snap-back portion of equilibrium paths. Although the free vibration analyses of pre-buckled and post-buckled laminated plates and shell panels are important in the analysis and design of aerospace and spacecraft components, the work done in this area is relatively scarce.

Kapania and Yang [1] studied the buckling, post-buckling, and nonlinear vibrations of perfect and imperfect, isotropic, and laminated thin plates using finite element method. Subsequently, Kapania and Byun [2] studied the vibrations of imperfect laminated panels under arbitrary in-plane and out-of-plane loads. Yang and Han [3] studied the buckled plate vibrations and large amplitude vibrations using high-order triangular elements.

Lee and Lee [4] investigated the vibration behavior of thermally post-buckled anisotropic plates using finite element method. Illanko [5] studied the vibration and post-buckling of mechanically loaded rectangular plates using a multiterm Galerkin's method. Librescu et al. [6,7] presented results of an analytical study on the vibration behavior of flat and shallow curved panels subjected to temperature field and mechanical loads. Subsequently, Librescu and Lin [8] studied the effects of tangential edge constraints on the vibrational behavior of doubly curved shallow panels subjected to thermomechanical loading. In Refs. [6–8], the governing equations of the problem were solved using a one-term Galerkin approximation.

The research on the post-buckling of plates reported in the literature (see Refs. [9,10,5,11]) shows that the results obtained from the multiterm Galerkin method differ considerably from that obtained from the one-term solution. Shin et al. [12] examined the convergence of the series solution (Rayleigh–Ritz method) for the post-buckling analysis of isotropic and specially orthotropic graphite-epoxy plates. To the authors' knowledge, convergence of the post-buckling results for the case of laminated cylindrical shell panels using multiterm Galerkin method does not exist in the literature. Hence, the results presented here are believed to be useful for comparison in the future.

In the present investigation, analytical results are presented for the nonlinear stability and free vibration analysis of cross-ply laminated cylindrical shell panels subjected to mechanical edge loads in addition to preexisting nondestabilizing lateral pressure and uniform through-thickness temperature distribution, using a multiterm Galerkin method. The mechanical edge loads include uniaxial compressive loads and combinations of uniaxial compressive and transverse compressive or tensile loads. The present higher-order formulation is based on the displacement field proposed by Reddy and Liu [13], which accounts for parabolic distribution of the transverse shear strains through thickness of the shell and tangential stress-free boundary conditions on the boundary surfaces of the shell. The governing equations of shallow shell are established using Love's first-order geometric approximation and Reissner's shallow shell simplifications. The dynamic equations of motion are derived using Hamilton's principle. By neglecting the inertia terms, the static equations of equilibrium are obtained. The governing nonlinear partial differential equations expressed in terms of displacements are solved using a multiterm Galerkin method. The nonlinear equilibrium paths are traced using the Newton–Raphson method, in conjunction with the Riks [14] approach to overcome the limit points. The free vibration frequencies of a post-buckled cylindrical shell panel about a static equilibrium state are obtained by solving the linear eigenvalue problem.

Formulation

We consider a doubly curved shell on a rectangular planform of constant thickness h composed of a finite number of orthotropic

---

Contributed by the Applied Mechanics Division of ASME for publication in the JOURNAL OF APPLIED MECHANICS. Manuscript received November 30, 2006; final manuscript received February 3, 2008; published online May 13, 2008. Review conducted by Edmundo Corona.

layers of uniform thickness. The coordinate system is such that the surface coordinates (x,y) of the orthogonal coordinate system (x,y,z) are located on the middle surface of the laminate, and are coincident with the lines of principal curvature; the z coordinate is normal to the middle plane; R_x and R_y are the principal radii of curvature of the middle surface.

The present higher-order theory is based on a displacement field, in which the displacements of the middle surface are expanded as cubic functions of the thickness coordinate, and the transverse displacement is assumed to be constant through the thickness. The latter assumption is equivalent to neglecting stretching of normal to the middle surface of the shell. The additional dependent unknowns introduced with the quadratic and cubic powers of the thickness coordinate are evaluated in terms of the derivatives of the transverse displacement and the rotations of the normals at the middle surface. This displacement field leads to the parabolic distribution of the transverse shear stress (and zero transverse normal strain), and therefore no shear correction factors are required. The terms classical shell theory (CST) and first-order shear deformation theory (FSDT) are not described in the present formulation. However, the displacement fields appropriate to CST and FSDT can be easily obtained from the present displacement field. The details are not furnished for the sake of brevity.

The displacement fields used in the present study are (Reddy and Liu [13])

$$u = (1 + z/R_x)u^0 + z\varphi_1 + z^3(4/3h^2)[-\varphi_1 - w^0_{,x}]$$

$$v = (1 + z/R_y)v^0 + z\varphi_2 + z^3(4/3h^2)[-\varphi_2 - w^0_{,y}]$$

$$w = w^0 \tag{1}$$

Here, u, v, and w are displacement components, respectively, along the x, y, and z directions; u^0, v^0, w^0 are the displacements of a generic point on the midplane; and φ_1 and φ_2 are the rotations of the cross sections perpendicular to the x and y axes, respectively.

In the present theory, the governing equations of shallow shell are established using Love's first-order geometric approximation (neglecting z/R_x and z/R_y in comparison with unity) and Reissner's shallow shell simplifications (Kraus [15]), which are identical to Donnell's assumptions for cylindrical shells (i.e. (i) the transverse shearing force makes a negligible contribution to the equilibrium of forces in the circumferential direction and (ii) neglecting the tangential displacements and their derivatives for the midsurface changes in curvature and twist.) The above displacement fields can be rearranged as (Soldatos [16])

$$u = (1 + z/R_x)u^0 - zw^0_{,x} + f(z)\phi_1,$$

$$v = (1 + z/R_y)v^0 - zw^0_{,y} + f(z)\phi_2, \quad w = w^0 \tag{2}$$

where

$$\phi_1 = \varphi_1 + w^0_{,x}, \quad \phi_2 = \varphi_2 + w^0_{,y}, \quad f(z) = z[1 - (4/3)(z/h)^2]$$

The introduction of $f(z)$ in the displacement field reduces certain higher-order moment and transverse shear force resultants. These are due to the particular form of the proposed displacement field. It is apparent that the unknown functions ϕ_1 $(\varphi_1 + w^0_{,x})$ and ϕ_2 $(\varphi_2 + w^0_{,y})$ represent the action of transverse shear strains on the shell middle surface. This action, by means of the first partial derivatives of ϕ_1 and ϕ_2, gives rise to some additional changes of curvature, $\phi_{1,x}$ and $\phi_{2,y}$, and twist $(\phi_{2,x} + \phi_{1,y})$, of the shell middle surface.

The nonlinear strain-displacement relations at a distance z away from the midplane of a shallow shell can be written as

$$\varepsilon_x = \varepsilon^0_x - zw^0_{,xx} + f(z)\phi_{1,x}$$

$$\varepsilon_y = \varepsilon^0_y - zw^0_{,yy} + f(z)\phi_{2,y}$$

$$\varepsilon_{xy} = \varepsilon^0_{xy} - 2zw^0_{,xy} + f(z)\phi_{1,y} + f(z)\phi_{2,x}$$

$$\varepsilon_{xz} = u_{,z} + w_{,x} = f'(z)\phi_1$$

$$\varepsilon_{yz} = v_{,z} + w_{,y} = f'(z)\phi_2 \tag{3}$$

where ε^0_x, ε^0_y, and ε^0_{xy} are reference surface strains and are defined as

$$\varepsilon^0_x = u^0_{,x} + \frac{w^0}{R_x} + \frac{1}{2}(w^0_{,x})^2$$

$$\varepsilon^0_y = v^0_{,y} + \frac{w^0}{R_y} + \frac{1}{2}(w^0_{,y})^2$$

$$\varepsilon^0_{xy} = u^0_{,y} + v^0_{,x} + w^0_{,x}w^0_{,y}$$

For a slightly imperfect shell, let w^* denote a known small geometric imperfection, i.e., a small deviation of the shell middle surface from the midplane of a perfect shell. The unloaded imperfect shell is assumed to be stress-free. In the case of imperfect shell, w^0 is measured from the load-free imperfect middle surface. The geometric imperfection of a simply supported shell based on fundamental buckling mode of a geometrically perfect shell is assumed as

$$w^* = e \sin\frac{\pi x}{a} \sin\frac{\pi y}{b} \tag{4}$$

The coefficient e represents the amplitude of the initial imperfection. The initial strains due to the imperfection can be written as

$$\varepsilon^*_x = \tfrac{1}{2}(w^*_{,x})^2, \quad \varepsilon^*_y = \tfrac{1}{2}(w^*_{,y})^2, \quad \varepsilon^*_{xy} = w^*_{,x}w^*_{,y}$$

$$\varepsilon^*_{xz} = w^*_{,x}, \quad \varepsilon^*_{yz} = w^*_{,y} \tag{5}$$

The net strain component in the middle surface of the imperfect shell becomes (small angles of rotation $w^0_{,x}$ in the equations for an initially perfect shell are replaced by $(w^0 + w^*)_{,x}$)

$$\bar{\varepsilon}^0_x = u^0_{,x} + \frac{w^0}{R_x} + \frac{1}{2}[(w^0 + w^*)^2_{,x}] - \varepsilon^*_x = (\varepsilon^0_x + w^0_{,x}w^*_{,x})$$

$$\bar{\varepsilon}^0_y = v^0_{,y} + \frac{w^0}{R_y} + \frac{1}{2}[(w^0 + w^*)^2_{,y}] - \varepsilon^*_y = (\varepsilon^0_y + w^0_{,y}w^*_{,y})$$

$$\begin{aligned}\bar{\varepsilon}^0_{xy} &= u^0_{,y} + v^0_{,x} + [(w^0 + w^*)_{,x}(w^0 + w^*)_{,y}] - \varepsilon^*_{xy} \\ &= (\varepsilon^0_{xy} + w^0_{,x}w^*_{,y} + w^*_{,x}w^0_{,y})\end{aligned} \tag{6}$$

Introducing Eq. (6) into Eq. (3) (i.e., replacing ε^0_x, ε^0_y, and ε^0_{xy} with $\bar{\varepsilon}^0_x$, $\bar{\varepsilon}^0_y$ and $\bar{\varepsilon}^0_{xy}$), the strain components of the imperfect shell are written as

$$\varepsilon_x = \varepsilon^0_x + w^0_{,x}w^*_{,x} - zw^0_{,xx} + f(z)\phi_{1,x}$$

$$\varepsilon_y = \varepsilon^0_y + w^0_{,y}w^*_{,y} - zw^0_{,yy} + f(z)\phi_{2,y}$$

$$\varepsilon_{xy} = \varepsilon^0_{xy} + w^0_{,x}w^*_{,y} + w^*_{,x}w^0_{,y} - 2zw^0_{,xy} + f(z)\phi_{1,y} + f(z)\phi_{2,x}$$

$$\varepsilon_{xz} = u_{,z} + w_{,x} = f'(z)\phi_1$$

$$\varepsilon_{yz} = v_{,z} + w_{,y} = f'(z)\phi_2 \tag{7}$$

The stress strain relations for the kth lamina are given by

$$\begin{Bmatrix} \sigma_x \\ \sigma_y \\ \sigma_{yz} \\ \sigma_{xz} \\ \sigma_{xy} \end{Bmatrix}^{(k)} = \begin{bmatrix} Q_{11} & Q_{12} & 0 & 0 & 0 \\ Q_{12} & Q_{22} & 0 & 0 & 0 \\ 0 & 0 & Q_{44} & 0 & 0 \\ 0 & 0 & 0 & Q_{55} & 0 \\ 0 & 0 & 0 & 0 & Q_{66} \end{bmatrix}^{(k)} \begin{Bmatrix} \varepsilon_x - \alpha_1^{(k)}T \\ \varepsilon_y - \alpha_2^{(k)}T \\ \varepsilon_{yz} \\ \varepsilon_{xz} \\ \varepsilon_{xy} \end{Bmatrix} \tag{8}$$

where $Q_{ij}^{(k)}$ are the material constants of the kth lamina in the laminate coordinate system and $\alpha_1^{(k)}$ and $\alpha_2^{(k)}$ are the coefficients of linear thermal expansion for layer k in the laminate coordinates; T denotes temperature rise in the laminate.

The equations of motion appropriate to the displacement field (2) and constitutive equations (8) can be derived using Hamilton's principle. Neglecting both tangential and rotary inertia terms, the principle can be stated as

$$\int_0^t \left[\int_{-h/2}^{h/2} \left\{ \int_\Omega^{(k)} [\sigma_x \delta\varepsilon_x^{(k)} + \sigma_y \delta\varepsilon_y^{(k)} + \sigma_{xy}\delta\varepsilon_{xy}^{(k)} + \sigma_{xz}\delta\varepsilon_{xz}^{(k)} + \sigma_{yz}\delta\varepsilon_{yz}^{(k)}]dxdy \right\} dz \right] dt - \int_0^t \left[\int_\Omega q\,\delta w^0 dxdy \right] dt - \int_0^t \left[\delta \int_{-h/2}^{h/2} \left\{ \int_\Omega^{(k)} \rho (w_{,t})^2 dxdy \right\} dz \right] dt = 0 \tag{9}$$

The stress resultants can be defined as

$$\left(\begin{pmatrix} N_x \\ N_y \\ N_{xy} \end{pmatrix}, \begin{pmatrix} M_x \\ M_y \\ M_{xy} \end{pmatrix}, \begin{pmatrix} P_x \\ P_y \\ P_{xy} \end{pmatrix} \right) = \int_{-h/2}^{h/2} \begin{pmatrix} \sigma_x \\ \sigma_y \\ \sigma_{xy} \end{pmatrix} (1,z,f(z))dz \tag{10}$$

and

$$(V_{xz}, V_{yz}) = \int_{-h/2}^{h/2} (\sigma_{xz}, \sigma_{yz}) f'(z) dz \quad \text{where } f'(z) = \frac{d}{dz} f(z)$$

where $f'(z)=d/dzf(z)$ where N_x, N_y, and N_{xy}, and M_x, M_y, and M_{xy} are the force and moment resultants; P_x, P_y, and P_{xy} are additional moment resultants due to additional changes of curvature $\phi_{1,x}$, $\phi_{2,y}$, $(\phi_{2,x}+\phi_{1,y})$; V_{xz} and V_{yz} are transverse shear force resultants.

For uniform through-thickness temperature distribution, the thermal forces and moments are defined by

$$\begin{pmatrix} N_x^T & M_x^T & P_x^T \\ N_y^T & M_y^T & P_y^T \end{pmatrix} = \sum_{k=1}^{N} \int_{z_{k-1}}^{z_k} \begin{bmatrix} Q_{11} & Q_{12} \\ Q_{12} & Q_{22} \end{bmatrix} \begin{Bmatrix} \alpha_1 \\ \alpha_2 \end{Bmatrix} (1,z,f(z))T dz \tag{11}$$

The equations of motion of the shell derived from Hamilton's principle (9) can be written as (Soldatos [16])

$$N_{x,x} + N_{xy,y} = 0$$

$$N_{xy,x} + N_{y,y} = 0$$

$$M_{x,xx} + 2M_{xy,xy} + M_{y,yy} - (N_x/R_x) - (N_y/R_y) + N_x w_{,xx} + 2N_{xy} w_{,xy} + N_y, w_{,yy} + q = \rho h w_{,tt}^0$$

$$P_{x,x} + P_{xy,y} - V_{xz} = 0$$

$$P_{xy,x} + P_{y,y} - V_{yz} = 0 \tag{12}$$

where $(\ )_{,x}$ denotes partial differentiation with respect to x; q is the distributed transverse load; and ρ is the mass per unit area of the shell. Expressing the stress resultants in terms of displacements in Eq. (12), the governing equilibrium equations are obtained in displacement variables and are given in the Appendix.

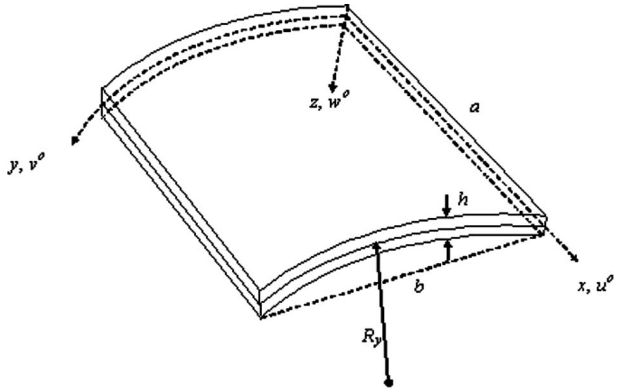

Fig. 1 Geometry of cylindrical shell panel

Solution Procedure

Nonlinear Static Response. Let a and b denote lengths of a cylindrical shell panel $(R_x=\infty, R_y=R)$ along x and y directions, respectively (see Fig. 1). It is assumed that the cylindrical shell considered is subjected to the following set of simply supported boundary conditions:

$$N_x = v^0 = w^0 = P_x = \phi_2 = M_x = 0 \quad \text{at } x = 0, a$$

$$u^0 = N_y = w^0 = \phi_1 = P_y = M_y = 0 \quad \text{at } y = 0, b \tag{13}$$

The displacement fields appropriate to simply supported boundary conditions are represented as

$$u = \sum_{m=1}^{i} \sum_{n=1}^{j} U_{mn} \cos\left(\frac{m\pi x}{a}\right) \sin\left(\frac{n\pi y}{b}\right),$$

$$\phi_1 = \sum_{m=1}^{i} \sum_{n=1}^{j} \alpha_{mn} \cos\left(\frac{m\pi x}{a}\right) \sin\left(\frac{n\pi y}{b}\right)$$

$$v = \sum_{m=1}^{i} \sum_{n=1}^{j} V_{mn} \sin\left(\frac{m\pi x}{a}\right) \cos\left(\frac{n\pi y}{b}\right),$$

$$\phi_2 = \sum_{m=1}^{i} \sum_{n=1}^{j} \beta_{mn} \sin\left(\frac{m\pi x}{a}\right) \cos\left(\frac{n\pi y}{b}\right)$$

$$w = \sum_{m=1}^{i} \sum_{n=1}^{j} W_{mn} \sin\left(\frac{m\pi x}{a}\right) \sin\left(\frac{n\pi y}{b}\right) \tag{14}$$

where i and j denote the number of modes/terms associated with x and y directions in the multiterm Galerkin's method. Applying Galerkin's procedure, one obtains a system of nonlinear algebraic equations in constant coefficients U_{mn}, V_{mn}, W_{mn}, α_{mn}, and β_{mn}. The critical buckling loads are obtained from the solution of the linear eigenvalue problem. Using the Newton–Raphson method in conjuction with the Riks approach, the system of nonlinear algebraic equations is solved for deflections. The nonlinear algebraic equations based on the multiterm Galerkin procedure are not presented for the sake of brevity.

Small Amplitude Vibration About a Static Equilibrium State. For the free vibration analysis about a static equilibrium state, the unknown modal amplitudes are assumed to be the sum of time-independent and time-dependent solutions, which may be written as

Table 1 Nondimensional center deflections of [0/90] cross-ply laminated cylindrical shells subjected to sinusoidal temperature distribution ($a/b=1$, $a/h=10$, $R_x=\infty$, $R_y=R$) $\bar{w}=(wh/\alpha_1 Tb^2)\times 10$

	Present		Khdeir et al. (1992)	
R/a	CST	HSDT	CST	HSDT
5	1.1280	1.1235	1.1280	1.1235
10	1.1447	1.1421	1.1447	1.1421
25	1.1494	1.1475		
50	1.1501	1.1482	1.1501	1.1482
75	1.1502	1.1484		
100	1.1503	1.1484		
Plate	1.1504	1.1485	1.1504	1.1485

Table 2 Critical buckling coefficients of cross-ply laminated cylindrical shells subjected to uniaxial compression ($a/b=1$, $R_x=\infty$, $R_y/a=10$) $N_x^*=N_{xcr}a^2/100h^3E_2$

	[0/90/0]			[0/90]		
a/h	CST	FSDT[a]	HSDT	CST	FSDT[a]	HSDT
5	0.2351	0.0768	0.0704	0.0954	0.0577	0.0609
10	0.2354	0.1519	0.1427	0.0957	0.0824	0.0838
20	0.2368	0.2078	0.2029	0.0971	0.0934	0.0938
30	0.2391	0.2252	0.2226	0.0995	0.0978	0.0980
40	0.2424	0.2344	0.2328	0.1028	0.1018	0.1020
50	0.2467	0.2414	0.2404	0.1070	0.1064	0.1065
75	0.2610	0.2589	0.2584	0.1215	0.1213	0.1212
100	0.2837	0.2804	0.2801	0.1416	0.1422	0.1415

[a] Shear correction factor=5/6.

$$\{w\}=\{w_s\}+\{w_t\} \tag{15}$$

where $\{w_s\}$ is the static deflection and $\{w_t\}$ is the dynamic deflection about a static equilibrium state. In the case of small amplitude vibration $\{w_t\}^2 \ll \{w_s\}$, hence-higher order time-dependent terms are neglected. Substituting the displacement field (Eq. (14)) into the governing partial differential equations (see the Appendix) and adopting Galerkin's technique, we obtain a set of ordinary differential equations. The equation of motion may be written as

$$([M]\{\ddot{w}_t\}+[K]+[N])\{w_t\}=0 \tag{16}$$

where $[M]$ is the mass matrix, $[K]$ is the linear elastic stiffness, and $[N]$ is the nonlinear stiffness due to large deformation. The nonlinear stiffness matrix $[N]$ is a function of only time-independent amplitude (large deformation). For the free vibration analysis at frequency ω, the following one-harmonic approximation is assumed to solve the ordinary differential equations (16):

$$\{w_t\}=\{\tilde{w}_t\}\sin \omega t \tag{17}$$

In the analysis, the tangential and rotary inertia terms are neglected and consequently the in-plane displacements become a function of $\sin^2 \omega t$. Now, condensing the equations of motion, the standard eigenvalue problem is obtained. By substituting the converged static deflection values obtained from the nonlinear static analysis, the free vibration frequencies are obtained by solving the linear eigenvalue problem.

Results and Discussion

Numerical results are presented for simply supported, cross-ply cylindrical shell panels ($R_x=\infty, R_y=R$). The following lamina material properties are used (Reddy and Liu [13]) in the analysis:

$$E_1=25E_2, \quad G_{12}=G_{13}=0.5E_2, \quad G_{23}=0.2E_2,$$

$$\nu_{12}=0.25, \quad \alpha_2/\alpha_1=3, \quad a/b=1$$

To validate the present formulation, the nondimensional center deflections of [0/90] antisymmetric cross-ply cylindrical shells subjected to sinusoidal temperature distributed load are compared in Table 1 with that of Khdeir et al. [17] for various radius-to-span ratios. It is observed that the results agree very well.

Table 2 presents the influence of shear deformation on the variation of dimensionless critical buckling loads (N_x^*) versus side-to-thickness ratio (a/h) for [0/90] and [0/90/0] cross-ply cylindrical shell panels subjected to in-plane uniform edge compression in the x direction. It can be seen that the CST overpredicts the buckling loads as compared to the FSDT and higher-order shear deformation theory (HSDT). The difference between the solutions predicted by FSDT and HSDT is not significant. Moreover, due to the coupling between bending and extension, the influence of shear deformation is less effective in the case of antisymmetric [0/90] cross-ply shell panel in comparison with symmetric cross-ply shell panel [0/90/0].

Figure 2 shows the post-buckled equilibrium paths of a three-layered [0/90/0] symmetric cross-ply cylindrical shell panel un-

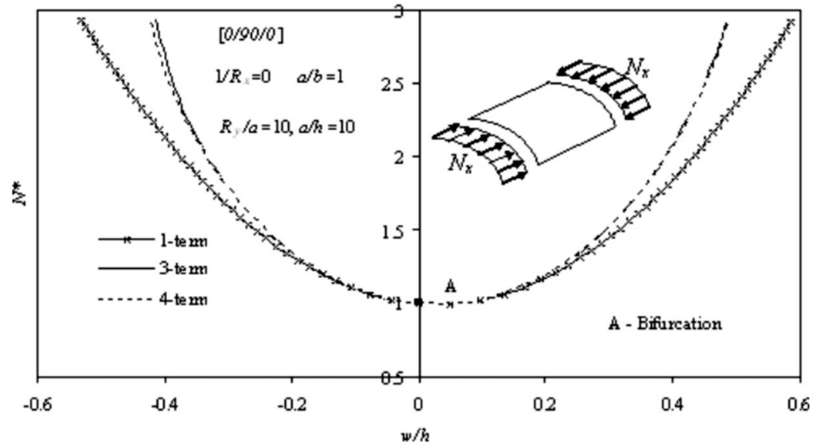

Fig. 2 Comparison of one-term, three-term and four-term solutions for the post-buckling behavior of a composite cylindrical shell panel [0/90/0] under uniaxial edge compression

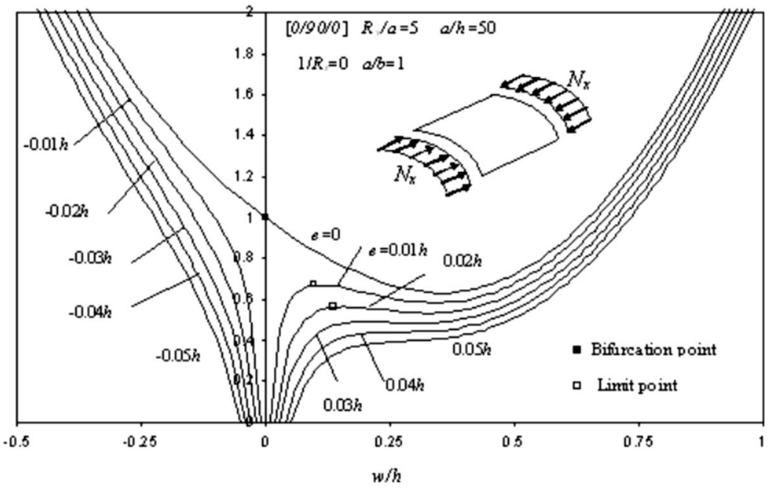

Fig. 3 The influence of initial geometric imperfections on the post-buckling behavior of composite cylindrical shell panel under uniaxial edge compression

der uniaxial edge compression. The nondimensional axial load ($N^*=N_x/N_{x\text{cr}}$) is shown in the figure against nondimensional out-of-plane displacement (w/h) at the center of the panel. The panels have a radius-to-span ratio $R_y/a=10$ and a length-to-thickness ratio $a/h=10$ and are square ($a/b=1$) in planform. The equilibrium paths are traced by taking one-term ($m=n=1$), three-term (($m=n=1$), ($m=1,n=3$), ($m=3,n=1$)), and four-term (($m=n=1$), ($m=1,n=3$), ($m=3,n=1$), ($m=n=3$)) in the displacement fields (see Eq. (14)). It can be seen that the three-term and four-term solutions compare well. However, the discrepancy between the one-term and three-term results is noticeable. At a load level $N^*=2$, the difference in the central deflections as calculated by considering one-term and three-term solutions is 12.11%, whereas at $N^*=3$, the difference is 22.45%, whereas the difference between three-term and four-term solutions is less than 1%. Thus, three terms are sufficient to obtain accurate results for the problem under consideration.

The post-buckled equilibrium paths for flat and curved panels are significantly different. Flat panels exhibit a stable-symmetric point of bifurcation, whereas curved panels exhibit an unstable-asymmetric point of bifurcation (Figs. 3, 4, 8, 10, and 12, 8, 10, and 12). In these figures, after the bifurcation point, for positive (inward) out-of-plane displacements, the load carrying capacity of the shell panels initially decreases due to decrease in curvature of the deformed panel. After flattening, the deformed surface begins to develop more curvature, which results in an increase of load. In the snap-through region, the panel changes its equilibrium configuration from unstable equilibrium path to stable equilibrium path. For the curves shown in Fig. 2, with a radius-to-span ratio $R_y/a=10$ and a length-to-thickness ratio $a/h=10$, the asymmetric post-buckling response is not visible. This is due to the fact that the intensity of the snap-through response of a shell panel depends on the radius-to-span and length-to-thickness ratios. However, the asymmetric point of bifurcation is clearly visible in Figs. 3 and 4, 8, 10, and 12.

The influence of initial geometric imperfections on the post-buckled equilibrium paths of $[0/90/0]$ symmetric cross-ply shell panel subjected to in-plane uniform edge compression (N_x) is shown in Fig. 3. The panels have a radius-to-span ratio (R_y/a) of 5 and length-to-thickness ratio (a/h) of 50 and are square in planform ($a=b$). Positive values of e correspond to the amplitude of imperfections that are toward the center of curvature of a point on a panel, and the value $e=0$ corresponds to a geometrically perfect panel. It can be seen that due to the presence of both positive and negative initial imperfections, bifurcation buckling does not take place. For initial positive (inward) imperfections (e) of $0.01h$ and

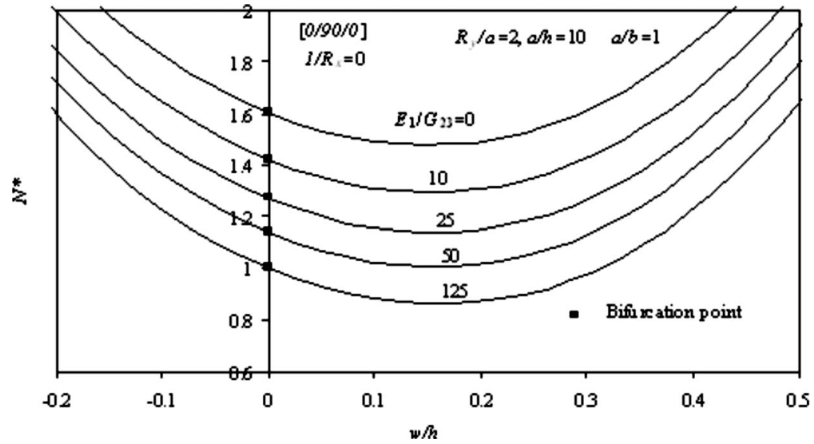

Fig. 4 The influence of shear deformation on the post-buckling behavior of composite cylindrical shell panel under uniaxial edge compression

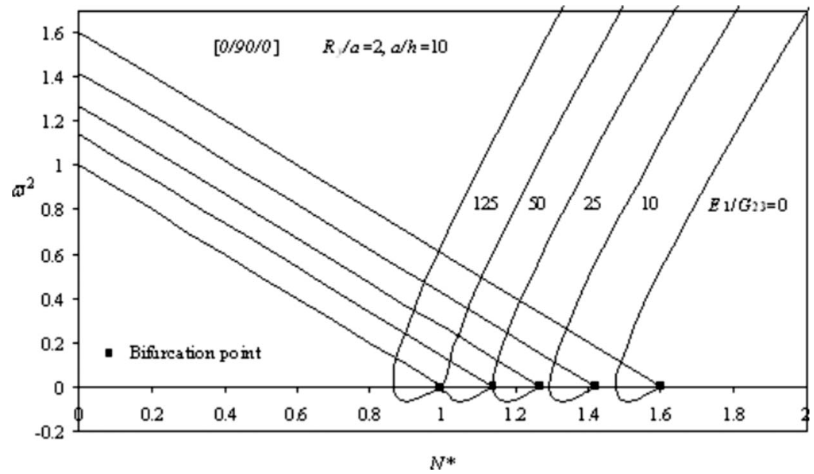

Fig. 5 The influence of shear deformation on the fundamental frequencies of composite cylindrical shell panel under uniaxial edge compression

0.02h, the equilibrium path shows limit point and snap-through behavior and for higher values of imperfection (0.03h–0.05h), the equilibrium paths do not show snap-through behavior. However, for the negative (outward) imperfections (−0.01h to −0.05h), the equilibrium paths show a hardening type behavior.

The effect of shear deformation on the post-buckling behavior of a three-layered [0/90/0] symmetric cross-ply shell panel ($R_y/a=2$, $a/h=10$) subjected to in-plane uniaxial compressive load is shown in Fig. 4. The curves are shown for various values of transverse-shear flexibility $E_1/G_{23}=0$, 10, 25, 50, and 125. The in-plane compressive loads shown in the figure are normalized with critical buckling load of a shell panel with $E_1/G_{23}=125$. The transverse-shear flexibility $E_1/G_{23}=0$ corresponds to a shell panel that has no transverse-shear flexibility (CST). It is evident from the figure that, as the value of E_1/G_{23} increases, the critical buckling load decreases and the post-buckled equilibrium paths are unsymmetrical with respect to bifurcation points. For positive (inward) displacements of the shell panel, the equilibrium paths show snap-through behavior, whereas for negative (outward) displacements of the shell panel, the equilibrium path follows stable equilibrium path.

Figure 5 shows the influence of transverse shear (E_1/G_{23}) on the fundamental frequencies of a symmetric cross-ply shell panel ($R_y/a=2$, $a/h=10$) subjected to uniaxial compressive edge load. The frequencies are normalized with the fundamental frequency of a shell panel with $E_1/G_{23}=125$. It can be seen that upon increasing the compressive load (N^*), the frequencies start decreasing and reaches zero value at critical buckling load. The bifurcation point shown on the abscissa corresponds to the buckling load of a static equilibrium path (see Fig. 4) and the imaginary frequencies below the abscissa correspond to unstable (snap-through behavior) equilibrium path of the shell. In the snap-through region, the shell changes its equilibrium configuration from unstable equilibrium path to stable equilibrium path. Therefore, on the stable equilibrium path, the fundamental frequencies increase with the increase of compressive load.

The influence of span-to-thickness ratio (a/h) on the nonlinear behavior of a symmetric cross-ply shell panel subjected to uniform lateral pressure (q^*) is shown in Fig. 6. It is observed that, with the increase of a/h (70, 80, and 90), the shell panel exhibits snap-through behavior. Figure 7 shows the fundamental frequencies, which correspond to the static equilibrium paths shown in Fig. 6. The fundamental frequencies shown in the figure are normalized with the natural frequency of the shell panel with $a/h=50$. It can be seen that the increase in a/h ratio decreases the fundamental frequencies. The imaginary frequencies shown in the figure below the abscissa for $a/h=70$, 80, and 90 correspond to the limit point instability behavior of the respective shell panels.

Figure 8 shows the post-buckled equilibrium paths of a symmetric cross-ply shell panel, for load interaction between the me-

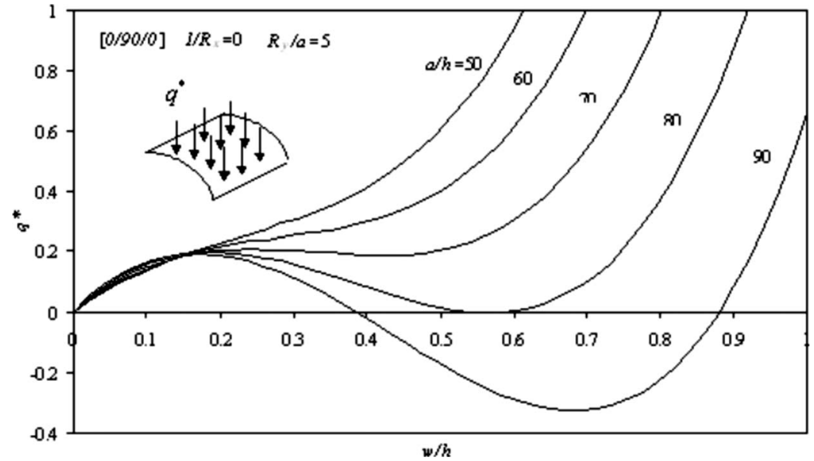

Fig. 6 The influence of span-to-thickness ratio on the nonlinear behavior of cross-ply cylindrical shell panel under uniform lateral pressure

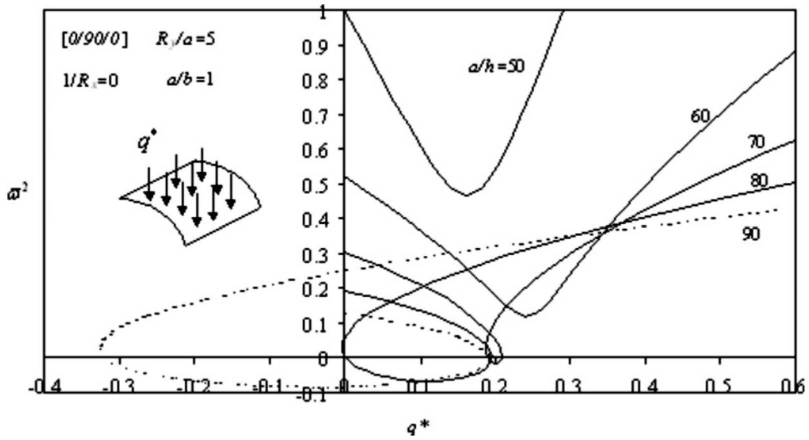

Fig. 7 The influence of span-to-thickness ratio on the fundamental frequencies of symmetric cross-ply cylindrical shell panel under uniform lateral pressure

chanical edge loads N_x and N_y. The load ratio N_0 (N_y/N_x) is the ratio of compressive (positive) or tensile (negative) edge load in the y direction $(\pm N_y)$ and compressive edge load in the x direction (N_x), respectively. For uniaxial edge compression $(N_0=0)$, the post-buckling path shows bifurcation buckling and snap-through behavior, whereas, for biaxial (N_0) edge loading bifurcation, buckling does not takes place. It can be seen that for negative load ratio $N_0=-0.02$, the equilibrium path shows the limit point and with the increase of load ratio $(N_0=-0.1,-0.2)$, the curves follow the stable equilibrium path. For positive load ratio $(N_0=0.02, 0.1, 0.2)$, the shell panel begins with negative displacements (outward) and the curves follow stable equilibrium paths.

The influence of biaxial mechanical edge load on the fundamental frequencies of a symmetric cross-ply shell panel $(R_y/a=5, a/h=50)$ is shown in Fig. 9. The bifurcation point shown on the abscissa $(N_0=0)$ corresponds to critical buckling load of a shell panel. For $N_0=-0.02$, the frequencies show a limit point on the abscissa, as the panel snaps through into another stable equilibrium configuration. In general, the fundamental frequency decreases with increase of load due to decrease in panel curvature of the deformed shell. After flattening, the deformed surface begins to develop more curvature, which results in increase of fundamental frequency.

Figure 10 shows the influence of uniform lateral pressure and biaxial edge load on the post-buckling behavior of symmetric cross-ply shell panel. In this study, the lateral pressure is kept constant, whereas the edge load is varied. It can be observed that the initial $(N^*=0)$ positive (inward) and negative (outward) deflections of the panel are due to positive and negative lateral pressures, respectively. For the case $q^*=0.2$, $N_0=0.2$, the results show that as soon as mechanical edge load is applied, the positive deflection decreases and with the increase of mechanical edge load the displacements transit to negative deflection. Whereas, for $q^*=0.2$, $N_0=-0.2$, the initial positive deflection increases monotonically with the increase of edge load, the shell panel shows a stiffening behavior. In the case of $q^*=-0.2$, $N_0=-0.2$, the initial negative deflection transit to positive deflection. However, for $q^*=-0.2$, $N_0=-0.1$, the shell panel exhibits a limit point instability response. For the case $q^*=-0.2$, $N_0=0.2$, the initial negative deflection increases monotonically with the increase of edge load.

The frequency results presented in Fig. 11 correspond to the static equilibrium paths shown in Fig. 10. The decrease in the fundamental frequency is due to flattening of deformed surface. After flattening, the deformed surface begins to develop curvature, as a result the fundamental frequency increases with the increase of bending stiffness. The bifurcation point shown in the figure corresponds to critical buckling load of a uniaxially compressed shell.

The influence of uniform through-thickness temperature distri-

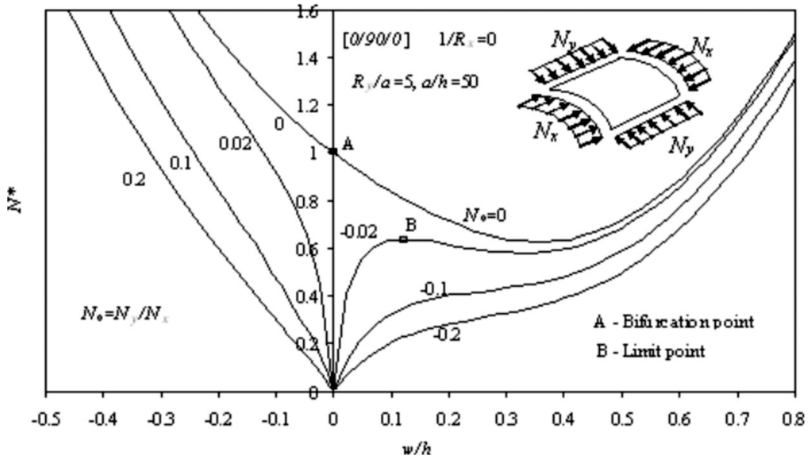

Fig. 8 The influence of biaxial edge load on the post-buckling behavior of symmetric cross-ply cylindrical shell panel

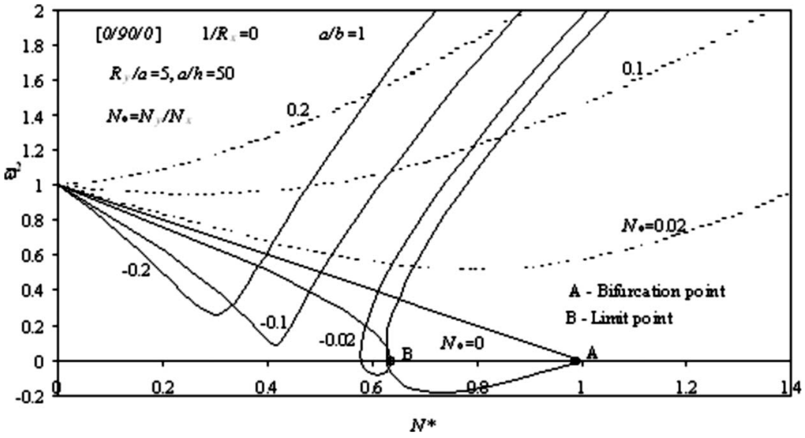

Fig. 9 The influence of biaxial edge load on the fundamental frequencies of cross-ply cylindrical shell panel

bution and biaxial edge load on post-buckling behavior of symmetric cross-ply shell panel is shown in Fig. 12. In this study, the temperature is kept constant, whereas the mechanical edge load is varied. In this figure, positive sign represents rise in the temperature and negative sign represents fall in the temperature. The initial ($N^*=0$) negative displacements and positive displacements correspond to the rise ($T^*=2.5$) and fall ($T^*=-2.5$) in the temperature, respectively. It can be seen that the initial rise or fall in the temperature acts as a load imperfection and hence bifurcation buckling does not take place. It is observed that for the case $T^*=2.5$, $N_0=-0.2$, the results show that as soon as mechanical edge

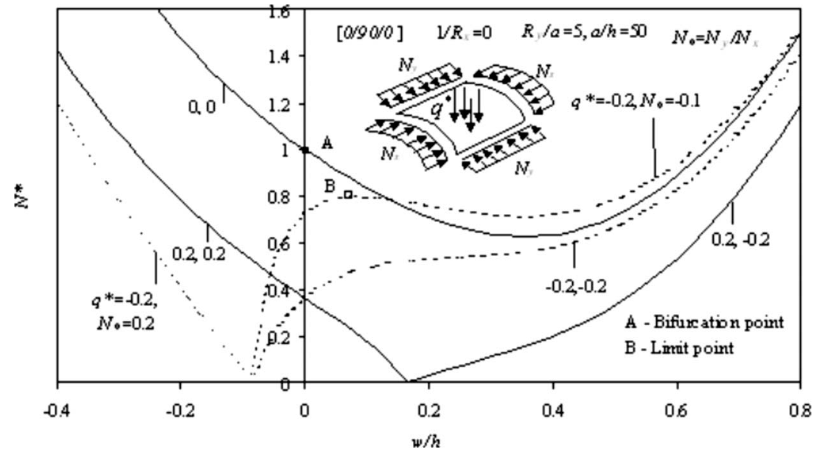

Fig. 10 The influence of uniform lateral pressure and bi axial edge load on post-buckling behavior of cross-ply cylindrical shell panel

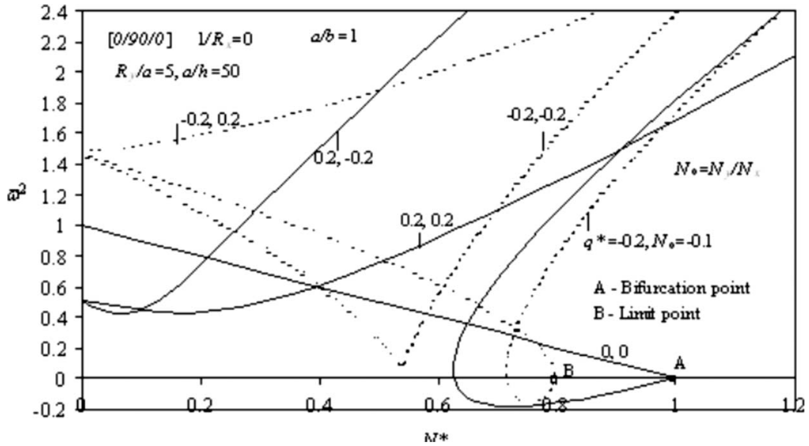

Fig. 11 The influence of uniform lateral pressure and biaxial edge load on fundamental frequencies of cross-ply cylindrical shell panel

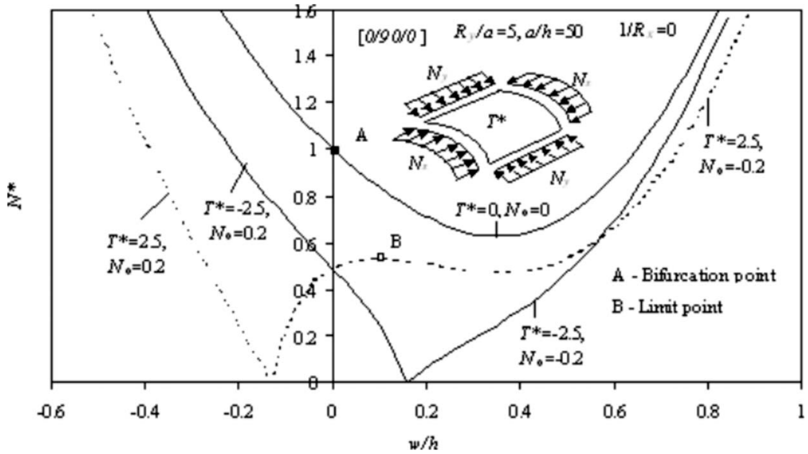

Fig. 12 The influence of uniform through-thickness temperature and biaxial edge load on post-buckling behavior of cross-ply cylindrical shell panel

load is applied, the negative deflection decreases and with the increase of mechanical edge load the displacements transit to positive deflection. These results also indicate limit point instability response of the shell panel. Whereas, for $T^*=2.5$, $N_0=0.2$, the initial negative deflection increases monotonically with the increase of edge load. In case of $T^*=-2.5$, $N_0=0.2$, the initial positive deflection transits to negative deflection. For the case $T^*=-2.5$, $N_0=-0.2$, the initial positive deflection increases monotonically with the increase of edge load. In general, the static response of the shell panel is sensitive to the sign of the lateral pressure and edge loading.

Figure 13 shows the fundamental frequencies, which correspond to the static equilibrium paths shown in Fig. 12. The fundamental frequencies are normalized with the natural frequency of the shell panel. It can be seen that for positive temperature, the curvature of the shell panel increases and results in high natural frequencies. Whereas, for negative temperature, the curvature of the shell panel decreases and results in low natural frequencies. With the increase of egde load (N^*), the fundamental frequencies of the shell decrease and exhibit limit point on the abscissa, ($T^*=2.5, N_0=-0.2$), which corresponds to the limit point instability of static equilibrium path. In general, the fundamental frequencies of the shell panel are sensitive to the sign of the temperature and edge loading.

Conclusions

The multiterm Galerkin method is used to obtain analytical solutions for the nonlinear static response and free vibration behavior of simply supported cross-ply laminated cylindrical shell panels, based on the higher-order transverse shear deformation theory. It is observed from results that the multiterm Galerkin method gives better results than the single-term solution. Numerical results of a parametric study of the nonlinear static response and vibration behavior of curved panels subjected to thermomechanical loads are presented. When the cylindrical panel is subjected to uniaxial compression in the x direction, the post-buckled equilibrium path is asymmetric about the bifurcation point and the panel is sensitive to the magnitude and direction of the initial geometric imperfections, lateral load, temperature field, and edge load in the y direction. It can be concluded that, by suitably adjusting the geometric parameters and loading conditions, beneficial results can be obtained. The analytical results reported in this paper using the multiterm Galerkin method serve as a basis for comparison and verification of results obtained from other numerical methods.

Nomenclature

The various notations and symbols used in the text or in the figures have been enlisted below for ease of reference. Symbols not

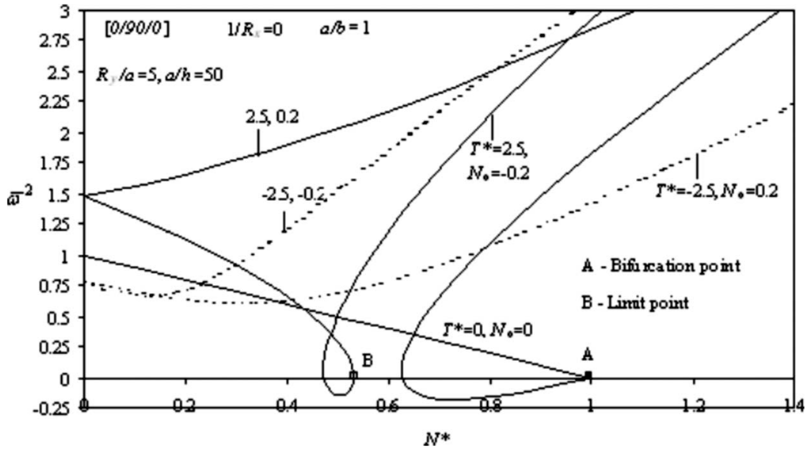

Fig. 13 The influence of uniform through-thickness temperature and biaxial edge load on fundamental frequencies of cross-ply cylindrical shell panel

contained in the list have been explained in the sections when they appear first.

E_1, E_2 = longitudinal and transverse Young's moduli, respectively
G_{12}, G_{13}, G_{23} = shear moduli
$N_{x\text{cr}}$ = critical buckling load of the shell
T = sinusoidal temperature distribution ($T_0 \sin(\pi x/a)\sin(\pi y/b)$)
a, b = planform dimension of the shell
h = thickness of the cylindrical shell panel
m, n = positive odd integers
a/h = span-to-thickness ratio
w/h = central displacement-to-thickness ratio
R_y/a = radius-to-span ratio
N^* = nondimensional uniaxial edge compression in the x direction ($N_x/N_{x\text{cr}}$)
q = uniform lateral pressure
q^* = nondimensional distributed load parameter $(qa^4/E_2h^4)10^2$
T^* = nondimensional temperature distribution $(TR\alpha_1/h)10^2$
ω_0 = natural frequency of the shell panel
$\bar{\omega}$ = nondimensional frequency (ω/ω_0)

Appendix: Governing Nonlinear Partial Differential Equations

$$\begin{aligned}&A_{11}u^0_{,xx}+A_{66}u^0_{,yy}+(A_{12}+A_{66})v^0_{,xy}+(A_{11}/R_x+A_{12}/R_y)w^0_{,x}-\{B_{11}w^0_{,xxx}+(B_{12}+2B_{66})w^0_{xyy}\}+(C_{11}\phi_{1,xx}+C_{66}\phi_{1,yy})+(C_{12}+C_{66})\phi_{2,xy}\\&\quad+\{A_{11}(w^0_{,xx}+w^*_{,xx})+A_{66}(w^0_{,yy}+w^*_{,yy})\}w^0_{,x}+(A_{11}w^0_{,xx}+A_{66}w^0_{,yy})w^*_{,x}+(A_{12}+A_{66})(w^0_{,y}w^0_{,xy}+w^0_{,y}w^*_{,xy}+w^*_{,y}w^0_{,xy})=0\end{aligned}\tag{A1}$$

$$\begin{aligned}&(A_{12}+A_{66})u^0_{,xy}+A_{66}v^0_{,xx}+A_{22}v^0_{,yy}+(A_{12}/R_x+A_{22}/R_y)w^0_{,y}-B_{22}w^0_{yyy}-(B_{12}+2B_{66})w^0_{xxy}+(C_{12}+C_{66})\phi_{1,xy}+(C_{22}\phi_{2,yy}+C66\phi_{1,xx})\\&\quad+\{A_{66}(w^0_{,xx}+w^*_{,xx})+A_{22}(w^0_{,yy}+w^*_{,yy})\}w^0_{,y}+(A_{66}w^0_{,xx}+A_{22}w^0_{,yy})w^*_{,y}+(A_{12}+A_{66})(w^0_{,x}w^0_{,xy}+w^0_{,x}w^*_{,xy}+w^*_{,x}w^0_{,xy})=0\end{aligned}\tag{A2}$$

$$\begin{aligned}&B_{11}u^0_{,xxx}+(B_{12}+2B_{66})u^0_{,xyy}+(B_{12}+2B_{66})v^0_{,xxy}+B_{22}v^0_{,yyy}+2(B_{11}/R_x+B_{12}/R_y)w^0_{,xx}+2(B_{12}/R_x+B_{22}/R_y)w^0_{,yy}+\{B_{11}w^0_{,xxx}+(B_{12}\\&\quad+2B_{66})w^0_{,xyy}\}w^0_{,x}+\{B_{22}w^0_{,yyy}+(B_{12}+2B_{66})w^0_{,xxy}\}w^0_{,y}+2B_{12}(w^0_{,xy})^2-2B_{12}w^0_{,xx}w^0_{,yy}-2B_{66}(w^0_{,xy})^2+2B_{66}w^0_{,xx}w^0_{,yy}+E_{11}\phi_{1,xxx}+(E_{12}\\&\quad+2E_{66})\phi_{1,xyy}+E_{22}\phi_{2,yyy}+(E_{12}+2E_{66})\phi_{2,xxy}-(C_{11}/R_x+C_{12}/R_y)\phi_{1,x}-(C_{12}/R_x+C_{22}/R_y)\phi_{2,y}+(C_{11}w^0_{,xx}+C_{12}w^0_{,yy})\phi_{1,x}\\&\quad+2C_{66}w^0_{,xy}\phi_{1,y}+(C_{12}w^0_{,xx}+C_{22}w^0_{,yy})\phi_{2,y}+2C_{66}w^0_{,xy}\phi_{2,x}-\{D_{11}w^0_{,xxxx}+2(D_{12}+2D_{66})w^0_{,xxyy}+D_{22}w^0_{,yyyy}\}+E_{11}\phi_{1,xxx}+(E_{12}\\&\quad+2E_{66})(\phi_{1,xyy}+\phi_{2,xxy})+E_{22}\phi_{2,yyy}-1/R_x[A_{11}\{u^0_{,x}+w^0/R_x+0.5(w^0_{,x})^2+w^0_{,x}w^*_{,x}\}+A_{12}\{v^0_{,y}+w^0/R_y+0.5(w^0_{,y})^2+w^0_{,y}w^*_{,y}\}]\\&\quad-1/R_y[A_{12}\{u^0_{,x}+w^0/R_x+0.5(w^0_{,x})^2+w^0_{,x}w^*_{,x}\}+A_{22}\{v^0_{,y}+w^0/R_y+0.5(w^0_{,y})^2+w^0_{,y}w^*_{,y}\}]+[\{A_{11}(u^0_{,x}+w^0/R_x+0.5(w^0_{,x})^2+w^0_{,x}w^*_{,x})\\&\quad+A_{12}(v^0_{,y}+w^0/R_y+0.5(w^0_{,y})^2+w^0_{,y}w^*_{,y})\}-N_x](w^0_{,xx}+w^*_{,xx})+[2\{A_{66}(u^0_{,y}+v^0_{,x}+w^0_{,x}w^0_{,y}+w^0_{,x}w^*_{,y}+w^*_{,x}w^0_{,y})-N_{xy}\}](w^0_{,xy}+w^*_{,xy})\\&\quad+[\{A_{12}(u^0_{,x}+w^0/R_x+0.5(w^0_{,x})^2+w^0_{,x}w^*_{,x})+A_{22}(v^0_{,y}+w^0/R_y+0.5(w^0_{,y})^2+w^0_{,y}w^*_{,y})\}-N_y](w^0_{,yy}+w^*_{,yy})=0\end{aligned}\tag{A3}$$

$$\begin{aligned}&(C_{11}u^0_{,xx}+C_{66}u^0_{,yy})+(C_{12}+C_{66})v^0_{,xy}+(C_{11}/R_x+C_{12}/R_y)w^0_{,x}+(C_{11}w^0_{,xx}+C_{66}w^0_{,yy})w^0_{,x}+(C_{12}+C_{66})w^0_{,y}w^0_{,xy}-E_{11}w^0_{,xxx}-(E_{12}+2E_{66})w^0_{,xyy}\\&\quad+F_{11}\phi_{1,xx}+F_{66}\phi_{1,yy}+(F_{12}+F_{66})\phi_{2,xy}-H_{55}\phi_1=0\end{aligned}\tag{A4}$$

$$\begin{aligned}&(C_{12}+C_{66})u^0_{,xy}+(C_{22}v^0_{,yy}+C_{66}v^0_{,xx})+(C_{12}/R_x+C_{22}/R_y)w^0_{,y}+(C_{12}+C_{66})w^0_{,x}w^0_{,xy}+(C_{22}w^0_{,yy}+C_{66}w^0_{,xx})w^0_{,y}-E_{22}w^0_{,yyy}-(E_{12}+2E_{66})w^0_{,xxy}\\&\quad+F_{66}\phi_{2,xx}+F_{22}\phi_{2,yy}+(F_{12}+F_{66})\phi_{1,xy}-H_{44}\phi_2=0\end{aligned}\tag{A5}$$

where

$$(A_{ij},B_{ij},D_{ij})=\int_{-h/2}^{h/2}Q_{ij}(1,z,z^2)dz,\quad (C_{ij},E_{ij},F_{ij})=\int_{-h/2}^{h/2}Q_{ij}(1,z,f(z))f(z)dz\quad \text{for } i,j=1,2,6,$$

$$(H_{ij})=\int_{-h/2}^{h/2}Q_{ij}(f'(z))f'(z)dz\quad \text{for } i,j=4,5$$

References

[1] Kapania, R. K., and Yang, T. Y., 1987, "Buckling, Postbuckling, and Nonlinear Vibrations of Imperfect Plates," AIAA J., **25**(10), pp. 1338–1347.
[2] Kapania, R. K., and Byun, C., 1992, "Vibrations of Imperfect Laminated Panels Under Complex Preloads," Int. J. Non-Linear Mech., **27**(1), pp. 51–62.
[3] Yang, T. Y., and Han, A. D., 1983, "Buckled Plate Vibrations and Large Amplitude Vibrations Using High-Order Triangular Elements," AIAA J., **21**(5), pp. 758–766.
[4] Lee, D. M., and Lee, I., 1997, "Vibration Behaviors of Thermally Postbuckled Anisotropic Plates Using First-Order Shear Deformable Plate Theory," Comput. Struct., **63**(3), pp. 371–378.
[5] Illanko, S., 2002, "Vibration and Post-Buckling of In-Plane Loaded Rectangular Plates Using a Multiterm Galerkin's Method," ASME J. Appl. Mech., **69**, pp. 589–592.
[6] Librescu, L., Lin, W., Nemeth, M. P., and Starnes,Jr. J. H., 1996, "Frequency-Load Interaction of Geometrically Imperfect Curved Panels Subject to Heating," AIAA J., **34**(1), pp. 166–177.
[7] Librescu, L., Lin, W., Nemeth, M. P., and Starnes, J. H., Jr., 1996, "Vibration of Geometrically Imperfect Panels Subjected to Thermal and Mechanical Loads," J. Spacecr. Rockets, **33**(2), pp. 285–291.
[8] Librescu, L., and Lin, W., 1997, "Vibration of Thermomechanically Loaded Flat and Curved Panels Taking Into Account Geometric Imperfections and Tangential Edge Restraints," Int. J. Solids Struct., **34**(17), pp. 2161–2181.
[9] Girish, J., and Ramachandra, L. S., 2005, "Thermal Postbuckled Vibrations of Symmetrically Laminated Composite Plates With Initial Geometric Imperfections," J. Sound Vib., **67**(4), pp. 453–460.
[10] Girish, J., and Ramachandra, L. S., 2005, "Postbuckling and Vibration Analy-

sis of Antisymmetric Angle-Ply Composite Plates," J. Therm. Stresses, **28**(11), pp. 1145–1159.
[11] Shi, Y., Lee, R. Y. Y., and Mei, C., 1999, "Thermal Postbuckling Analysis of Composite Plates Using the Finite Element Modal Coordinate Method," J. Therm. Stresses, **22**(6), pp. 595–614.
[12] Shin, D. K., Griffin, Jr. O. H., and Gürdal, Z., 1993, "Postbuckling Response of Laminated Plates Under Uniaxial Compression," Int. J. Non-Linear Mech., **28**(1), pp. 95–115.
[13] Reddy, J. N., and Liu, C. F., 1985, "A Higher-Order Shear Deformation Theory of Laminated Elastic Shells," Int. J. Eng. Sci., **23**(3), pp. 319–330.
[14] Riks, E., 1979, "An Incremental Approach to the Solution of Snapping and Buckling Problems," Int. J. Solids Struct., **15**, pp. 529–551.
[15] Kraus, H., 1967, *Thin Elastic Shells*, Wiley, New York.
[16] Soldatos, K. P., 1991, "A Refined Laminated Plate and Shell Theory With Applications," J. Sound Vib., **144**(1), pp. 109–129.
[17] Khdeir, A. A., Rajab, M. D., and Reddy, J. N., 1992, "Thermal Effects on the Response of Cross-Ply Laminated Shallow Shells," Int. J. Solids Struct., **29**, pp. 653–667.

M. Utsumi
Machine Element Department,
Technical Research Laboratory,
IHI Corporation,
1 Shinnakaharacho,
Isogo-ku, Yokohama,
Kanagawa Prefecture 235-8501, Japan

K. Ishida
Energy and Plant,
IHI Corporation,
1-1, Toyosu 3-chome,
Koto-ku,
Tokyo 135-8710, Japan

Vibration Analysis of a Floating Roof Taking Into Account the Nonlinearity of Sloshing

The vibration of a floating roof hydroelastically coupled with nonlinear sloshing is analyzed. Influences of the nonlinearity of sloshing on the magnitude of stresses arising in a floating roof are investigated. Numerical results show that (i) neglecting the nonlinearity of sloshing significantly underestimates the magnitude of the stresses, even when the nonlinear effect is small for the roof displacement; and (ii) the underestimation associated with the use of the linear approximation becomes more marked with the decrease in the liquid depth. The reasons for these results are explained based on the fact that in the nonlinear sloshing, the modal component with circumferential wave number 2 is excited. [DOI: 10.1115/1.2912739]

1 Introduction

Over the past few decades, extensive studies have been conducted in the area of sloshing [1,2]. There are a number of investigations concerned especially with hydroelastic vibrations caused by sloshing [3–11] and nonlinear response behaviors of the system [6–11]. One feature of conventional works is that they considered sloshing with a free liquid surface. Studies for the case in which a liquid surface is covered with a floating roof are relatively scarce. However, for large ground-supported liquid storage tanks, floating roofs are widely used to protect the internal liquid from atmosphere. The oscillatory motion of a floating roof coupled with the liquid sloshing is near resonance with low-frequency components of earthquake ground motions, and thus can lead to serious accidents such as flood, fire, and structural failure. Therefore, it is necessary to investigate the vibration of a floating roof subjected to sloshing. Examples of past works for this problem include calculation of the frequency response of a rigid floating roof [12], free [13] and forced [14] vibration analyses for an elastic floating roof [13,14], and experimental studies using actual earthquake ground motion records as the tank excitation [15]. In conventional studies, the linear approximation was applied to the formulation of the liquid motion, and thus influences of the nonlinearity of sloshing on the magnitude of stresses in an elastic floating roof have not been investigated. The purpose of this paper is to analyze the vibration of an elastic floating roof coupled with nonlinear sloshing. By comparing the solutions obtained by linear and nonlinear analyses, it is shown that neglecting the nonlinearity of sloshing results in underestimation of the magnitude of stresses in the floating roof. The physical reason for this result is discussed.

2 Analysis

2.1 Computational Model. The system to be considered is shown in Fig. 1. The floating roof consisting of deck, pontoon, and stiffeners is modeled as an axisymmetric elastic shell. In Fig. 1, a is the radius of the tank and h is the liquid depth. The detailed parameters for the floating roof geometry are given in the section for numerical examples. This analysis is performed under the assumption that the liquid motion is inviscid, incompressible, and irrotational and the wall and bottom of the tank are rigid. The nonlinearity of the boundary conditions at the interface between the liquid and the floating roof is considered. The static position of the interface is considered a plane expressed by $z=h$ and $0 \leqslant r \leqslant a$ in formulating the nonlinear boundary conditions, because the variation in the z coordinate of the static position is very small compared to the liquid depth and the difference between the radii of the tank wall and the floating roof is very small compared to the tank radius.

2.2 Variational Principle. In this paper, a system of governing equations is derived using a variational principle. Based on the fact that the Lagrangian density of the liquid is equal to the liquid pressure [16], the action of the liquid motion can be expressed as

$$\int_{t_1}^{t_2} L_f dt = \int_{t_1}^{t_2} \int\int\int_V p_l dV dt \tag{1}$$

where L_f is the Lagrangian of the liquid, V is the liquid domain, and p_l is the liquid pressure. By using the pressure equation for unsteady flow, the liquid pressure can be expressed in terms of the velocity potential ϕ, which describes the liquid motion relative to the moving tank as follows:

$$p_l = -\rho_f \left[\frac{\partial \phi}{\partial t} + g(z-h) + x\ddot{f}_x(t) + y\ddot{f}_y(t) + \frac{1}{2}(\nabla \phi)^2 + \dot{G}(t) \right] \tag{2}$$

where ρ_f is the liquid density, g is the gravitational acceleration, $G(t)$ is an arbitrary time-dependent function, and $\ddot{f}_x(t)$ and $\ddot{f}_y(t)$ are the earthquake acceleration inputs in the x and y directions, respectively.

We substitute Eq. (2) into Eq. (1) and calculate the variation of the functional. We must consider the variation for the liquid domain as well as for the liquid pressure because the liquid domain is variable due to the vertical displacement $\bar{u}$ of the floating roof. By following the detailed derivation explained in Ref. [17], we can obtain

$$\delta \int_{t_1}^{t_2} L_f dt = \int_{t_1}^{t_2} \left[\rho_f \int\int\int_V \nabla^2 \phi \delta\phi dV \right.$$
$$- \rho_f \int\int_W \nabla\, \phi \cdot \mathbf{N}_W \delta\phi dW$$
$$+ \rho_f \int\int_S \left\{ -\frac{\partial \bar{u}}{\partial t} \cos(\mathbf{N}_S, z) - \nabla \phi \cdot \mathbf{N}_S \right\} \delta\phi dS$$

Contributed by the Applied Mechanics Division of ASME for publication in the JOURNAL OF APPLIED MECHANICS. Manuscript received December 8, 2006; final manuscript received February 6, 2008; published online May 14, 2008. Review conducted by Arif Masud.

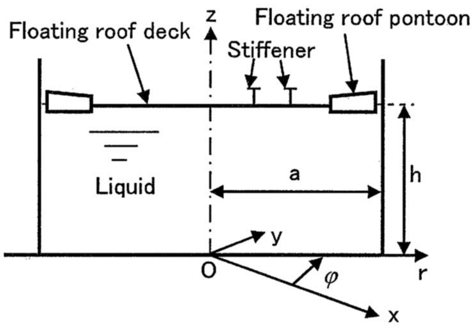

Fig. 1 Computational model

$$-\int\int_{S} p_l\delta\bar{u}\cos(\mathbf{N}_S,z)dS$$

$$-\rho_f\delta G\int\int_{S}\frac{\partial\bar{u}}{\partial t}\cos(\mathbf{N}_S,z)dS\Bigg]dt \qquad (3)$$

where W is the wall and bottom of the tank, S is the interface between the liquid and the floating roof; $\mathbf{N}_W$ and $\mathbf{N}_S$ are the outward unit normal vectors of these surfaces, and $\cos(a,b)$ is the cosine of the angle between a and b directions. Because the interface S is expressed by $f(r,\varphi,z,t)=z-\bar{u}(r,\varphi,t)=0$ and the position vector of S is given by $\mathbf{X}=\mathbf{e}_x r\cos\varphi+\mathbf{e}_y r\sin\varphi+\mathbf{e}_z[h-\bar{u}(r,\varphi,t)]$, the nonlinear expressions of the normal vector $\mathbf{N}_S$ and the surface element dS can be obtained as follows:

$$\mathbf{N}_S=\frac{\text{grad} f}{|\text{grad} f|}=\left[\mathbf{e}_r\frac{\partial\bar{u}}{\partial r}+\mathbf{e}_\varphi\frac{1}{r}\frac{\partial\bar{u}}{\partial\varphi}+\mathbf{e}_z\right]\left[\left(\frac{\partial\bar{u}}{\partial r}\right)^2+\left(\frac{1}{r}\frac{\partial\bar{u}}{\partial\varphi}\right)^2+1\right]^{-1/2} \qquad (4)$$

$$dS=\left|\frac{\partial\mathbf{X}}{\partial r}\times\frac{\partial\mathbf{X}}{\partial\varphi}\right|drd\varphi=\left[\left(\frac{\partial\bar{u}}{\partial r}\right)^2+\left(\frac{1}{r}\frac{\partial\bar{u}}{\partial\varphi}\right)^2+1\right]^{1/2}rdrd\varphi \qquad (5)$$

Next, the motion of the floating roof is formulated based on the finite element approach using the ring shell elements. Let $\bar{u}$, $\bar{v}$, and $\bar{w}$ be the displacement components in the $-z$, φ, and r directions, respectively. For these components, a nodal displacement vector is defined for a node i and is decomposed into two components with different circumferential variations:

$$\sum_{m=0}^{\infty}\left\{\begin{array}{c}\bar{u}_{m,i}\\ \bar{v}_{m,i}\\ \bar{w}_{m,i}\\ \left(\dfrac{\partial\bar{w}}{\partial s}\right)_{m,i}\end{array}\right\}=\sum_{m=0}^{\infty}\left\{\begin{array}{l}\bar{u}_{mx,i}\cos m\varphi+\bar{u}_{my,i}\sin m\varphi\\ \bar{v}_{mx,i}\sin m\varphi-\bar{v}_{my,i}\cos m\varphi\\ \bar{w}_{mx,i}\cos m\varphi+\bar{w}_{my,i}\sin m\varphi\\ \left(\dfrac{\partial\bar{w}}{\partial s}\right)_{mx,i}\cos m\varphi+\left(\dfrac{\partial\bar{w}}{\partial s}\right)_{my,i}\sin m\varphi\end{array}\right\} \qquad (6)$$

By calculating the kinetic and potential energies following the procedure of the finite element method (FEM), the variation of the action for the floating roof can be expressed as

$$\delta\int_{t_1}^{t_2}L_r dt=\delta\int_{t_1}^{t_2}\frac{1}{2}\sum_{m=0}^{\infty}[(\dot{\mathbf{X}}_{mx}^t\mathbf{M}_m\dot{\mathbf{X}}_{mx}-\mathbf{X}_{mx}^t\mathbf{K}_m\mathbf{X}_{mx})$$

$$+(\dot{\mathbf{X}}_{my}^t\mathbf{M}_m\dot{\mathbf{X}}_{my}-\mathbf{X}_{my}^t\mathbf{K}_m\mathbf{X}_{my})]dt$$

$$=\int_{t_1}^{t_2}\sum_{m=0}^{\infty}[-\delta\mathbf{X}_{mx}^t(\mathbf{M}_m\ddot{\mathbf{X}}_{mx}+\mathbf{K}_m\mathbf{X}_{mx})$$

$$-\delta\mathbf{X}_{my}^t(\mathbf{M}_m\ddot{\mathbf{X}}_{my}+\mathbf{K}_m\mathbf{X}_{my})]dt \qquad (7)$$

where $\mathbf{M}_m$ and $\mathbf{K}_m$ are the mass and stiffness matrices, and $\mathbf{X}_{mx}$ and $\mathbf{X}_{my}$ are the collections of $\{\bar{u}_{mx,i},\bar{v}_{mx,i},\bar{w}_{mx,i},(\partial\bar{w}/\partial s)_{mx,i}\}^t$ and $\{\bar{u}_{my,i},\bar{v}_{my,i},\bar{w}_{my,i},(\partial\bar{w}/\partial s)_{my,i}\}^t$, respectively. For both components, the mass and stiffness matrices $\mathbf{M}_m$ and $\mathbf{K}_m$ are common. Since the dimension of these matrices is very large, much computation time and cost are required to transform the equations of motion expressed in terms of the nodal displacements into modal equations. To solve this problem, the floating roof is decomposed into several components $c(c=1,2,3,\ldots)$, and their equations of motion

$$\mathbf{M}_{mc}\ddot{\mathbf{X}}_{mxc}+\mathbf{K}_{mc}\mathbf{X}_{mxc}=\mathbf{0} \qquad (8)$$

are expressed in the following form:

$$\begin{bmatrix}\mathbf{M}_{mc11}\mathbf{M}_{mc12}\\ \mathbf{M}_{mc21}\mathbf{M}_{mc22}\end{bmatrix}\begin{Bmatrix}\ddot{\mathbf{X}}_{mxc1}\\ \ddot{\mathbf{X}}_{mxc2}\end{Bmatrix}+\begin{bmatrix}\mathbf{K}_{mc11}\mathbf{K}_{mc12}\\ \mathbf{K}_{mc21}\mathbf{K}_{mc22}\end{bmatrix}\begin{Bmatrix}\mathbf{X}_{mxc1}\\ \mathbf{X}_{mxc2}\end{Bmatrix}=\begin{Bmatrix}\mathbf{0}\\ \mathbf{0}\end{Bmatrix} \qquad (9)$$

where $\mathbf{X}_{mxc1}$ is the collection of the displacements of the nodes that are not at the joints with the adjacent components while $\mathbf{X}_{mxc2}$ is the collection of the other nodal displacements. The eigenmodes of $\mathbf{X}_{mxc1}$ under the condition that $\mathbf{X}_{mxc2}$ is fixed to zero are determined by solving the eigenvalue problem

$$(-\omega^2\mathbf{M}_{mc11}+\mathbf{K}_{mc11})\mathbf{X}_{mxc1}=\mathbf{0} \qquad (10)$$

The static solution of $\mathbf{X}_{mxc1}$ for the case in which $\mathbf{X}_{mxc2}$ is arbitrarily given is obtained by neglecting the inertia term of Eq. (9) as follows:

$$\mathbf{K}_{mc11}\mathbf{X}_{mxc1}=-\mathbf{K}_{mc12}\mathbf{X}_{mxc2} \qquad (11)$$

Expressing $\mathbf{X}_{mxc1}$ by the sum of the linear combination of the eigenmodes and the static solution yields

$$\begin{Bmatrix}\mathbf{X}_{mxc1}\\ \mathbf{X}_{mxc2}\end{Bmatrix}=\begin{bmatrix}\mathbf{T}_{mc11} & -\mathbf{K}_{mc11}^{-1}\mathbf{K}_{mc12}\\ \mathbf{O} & \mathbf{I}\end{bmatrix}\begin{Bmatrix}\mathbf{q}_{mxc1}\\ \mathbf{X}_{mxc2}\end{Bmatrix} \qquad (12)$$

where $\mathbf{T}_{mc11}$ is the modal transformation matrix whose columns are the eigenvectors of the eigenvalue problem (10) and $\mathbf{q}_{mxc1}$ is the modal coordinates. The dimension of $\mathbf{q}_{mxc1}$ and $\mathbf{X}_{mxc2}$ can be made much smaller than the dimension of $\mathbf{X}_{mxc1}$. Therefore, the dimension of the numerical problem to be solved can be markedly reduced by the transformation (12). By defining

$$\mathbf{C}_{mc}=\begin{bmatrix}\mathbf{T}_{mc11} & -\mathbf{K}_{mc11}^{-1}\mathbf{K}_{mc12}\\ \mathbf{O} & \mathbf{I}\end{bmatrix},\quad \mathbf{X}'_{mxc}=\begin{Bmatrix}\mathbf{q}_{mxc1}\\ \mathbf{X}_{mxc2}\end{Bmatrix} \qquad (13)$$

Eq. (12) can be expressed as

$$\mathbf{X}_{mxc}=\mathbf{C}_{mc}\mathbf{X}'_{mxc} \qquad (14)$$

Repeating the foregoing procedures for each component $c(c=1,2,3,\ldots)$, the global form of Eq. (14) for the whole floating roof structure can be obtained as

$$\mathbf{X}_{mx}=\mathbf{C}_m\mathbf{X}'_{mx} \qquad (15)$$

Similarly, the corresponding equation $\mathbf{X}_{my}=\mathbf{C}_m\mathbf{X}'_{my}$ can be obtained for the displacement components with subscript y in Eq. (7). Substituting these equations into Eq. (7) yields

$$\delta\int_{t_1}^{t_2}L_r dt=\int_{t_1}^{t_2}\sum_{m=0}^{\infty}[-\delta\mathbf{X}_{mx}'^{t}(\mathbf{M}'_m\ddot{\mathbf{X}}'_{mx}+\mathbf{K}'_m\mathbf{X}'_{mx})$$

$$-\delta\mathbf{X}_{my}'^{t}(\mathbf{M}'_m\ddot{\mathbf{X}}'_{my}+\mathbf{K}'_m\mathbf{X}'_{my})]dt \qquad (16)$$

where

$$\mathbf{M}'_m=\mathbf{C}_m^t\mathbf{M}_m\mathbf{C}_m,\quad \mathbf{K}'_m=\mathbf{C}_m^t\mathbf{K}_m\mathbf{C}_m \qquad (17)$$

By summing Eqs. (3) and (16), using Eqs. (4) and (5) to express the normal vector and the surface element in terms of the circular cylindrical coordinates, and considering the virtual work done by the inertial force for each element of the floating roof, the required variational principle for the system can be obtained as

$$\begin{aligned}
&\rho_f \int\int\int_V \nabla^2\phi\delta\phi dV - \rho_f \int_0^{2\pi}\int_0^h \left.\frac{\partial\phi}{\partial r}\right|_{r=a} \delta\phi|_{r=a} a dz d\varphi + \rho_f \int_0^{2\pi}\int_0^a \left.\frac{\partial\phi}{\partial z}\right|_{z=0} \delta\phi|_{z=0} r dr d\varphi - \rho_f \\
&\quad\times \int_0^{2\pi}\int_0^a \left(\frac{\partial\bar{u}}{\partial t} + \left.\frac{\partial\phi}{\partial z}\right|_{z=h-\bar{u}} + \left.\frac{\partial\phi}{\partial r}\right|_{z=h-\bar{u}} \frac{\partial\bar{u}}{\partial r} + \frac{1}{r^2}\left.\frac{\partial\phi}{\partial\varphi}\right|_{z=h-\bar{u}} \frac{\partial\bar{u}}{\partial\varphi}\right) \delta\phi|_{z=h-\bar{u}} r dr d\varphi \\
&\quad+ \sum_{m=0}^{\infty} [-\delta\mathbf{X}_{mx}'^{t}(\mathbf{M}_m'\ddot{\mathbf{X}}_{mx}' + \mathbf{K}_m'\mathbf{X}_{mx}') - \delta\mathbf{X}_{my}'^{t}(\mathbf{M}_m'\ddot{\mathbf{X}}_{my}' + \mathbf{K}_m'\mathbf{X}_{my}')] + \rho_f \int_0^{2\pi}\int_0^a \left\{ \left.\frac{\partial\phi}{\partial t}\right|_{z=h-\bar{u}} - g\bar{u} + r\cos\varphi\ddot{f}_x(t) + r\sin\varphi\ddot{f}_y(t) \right.\\
&\quad\left.+ \frac{1}{2}\left[\left(\frac{\partial\phi}{\partial r}\right)^2 + \left(\frac{1}{r}\frac{\partial\phi}{\partial\varphi}\right)^2 + \left(\frac{\partial\phi}{\partial z}\right)^2\right]_{z=h-\bar{u}}\right\} \delta\bar{u} r dr d\varphi + \sum_{\text{elem}} \int_0^{2\pi}\int_{s_1}^{s_2} \rho_r h_r \{[-\ddot{f}_x(t)\cos\varphi - \ddot{f}_y(t)\sin\varphi]\delta\bar{w} \\
&\quad+ [\ddot{f}_x(t)\sin\varphi - \ddot{f}_y(t)\cos\varphi]\delta\bar{v}\} r ds d\varphi - \rho_f \delta G \int_0^{2\pi}\int_0^a \frac{\partial\bar{u}}{\partial t} r dr d\varphi = 0
\end{aligned} \tag{18}$$

Since the variations in the velocity potential, the floating roof displacement, and the arbitrary time-dependent function are arbitrary and independent of one another, we obtain the system of governing equations. The first term of Eq. (18) yields the Laplace equation corresponding to the condition of continuity in the liquid domain as follows:

$$\nabla^2\phi = 0 \tag{19}$$

The second and third terms of Eq. (18) give the boundary condition on the tank wall and bottom as follows:

$$\left.\frac{\partial\phi}{\partial r}\right|_{r=a} = 0, \qquad \left.\frac{\partial\phi}{\partial z}\right|_{z=0} = 0 \tag{20}$$

In a similar manner, the fourth term of Eq. (18) represents the condition that on the moving interface S, the normal velocity components of the fluid particle and the floating roof are equal to each other; the fifth to seventh terms of Eq. (18) lead to the equation of motion for the floating roof subjected to the liquid pressure; and the last term of Eq. (18) yields the volume constant condition. Since the volume constant condition can be derived from other kinematic conditions, the first to seventh terms of Eq. (18) constitute the system of governing equations for the hydroelastic system.

2.3 Nonlinear Differential Equations. The Galerkin method is applied to transform the variational principle into ordinary differential equations. The admissible function for the velocity potential can be determined by solving the Laplace equation (19) under the boundary condition (20) as follows:

$$\begin{aligned}
\phi(r,\varphi,z,t) = \sum_{m=0}^{\infty}\sum_{n=1}^{\infty} [\dot{A}_{mnx}(t)\cos m\varphi + \dot{A}_{mny}(t)\sin m\varphi] \\
\times J_m(\lambda_{mn} r)\frac{\cosh(\lambda_{mn} z)}{\cosh(\lambda_{mn} h)}
\end{aligned} \tag{21}$$

where A_{mnx} and A_{mny} are the generalized coordinates for the vibration modes that are symmetric and asymmetric for the x axis, respectively; J_m is the Bessel function of the first kind of order m; and λ_{mn} is the nth positive root of $J_m'(\lambda a) = 0$.

The nodal displacement vectors $\mathbf{X}_{mx}$ and $\mathbf{X}_{my}$ of the floating roof have a common eigenvector for each value of m. Hence, the kth components of $\mathbf{X}_{mx}$ and $\mathbf{X}_{my}$ can be expressed as

$$X_{mxk}(t) = \sum_{p=1}^{\infty} T_{mkp}E_{mpx}(t), \quad X_{myk}(t) = \sum_{p=1}^{\infty} T_{mkp}E_{mpy}(t) \tag{22}$$

where T_{mkp} is the kth component of the pth eigenvector while $E_{mpx}(t)$ and $E_{mpy}(t)$ are the modal coordinates. In terms of these modal coordinates, the floating roof displacement at an arbitrary position can be expressed, e.g., as

$$\bar{u}(r,\varphi,t) = \sum_{m=0}^{\infty}\sum_{p=1}^{\infty} [E_{mpx}(t)\cos m\varphi + E_{mpy}(t)\sin m\varphi]S_{mp}(r) \tag{23}$$

where $S_{mp}(r)$ is the pth modal function defined at the position of interest. This function can be determined through the interpolation of the nodal displacements expressed in the local coordinates and the transformation from the local coordinates to the global coordinates.

Substituting Eqs. (21)–(23) into the variational principle (18) and vanishing the coefficients of the variations δA_{mqx}, δA_{mqy}, δE_{mqx}, and δE_{mqy} lead to a system of nonlinear ordinary differential equations with respect to the generalized coordinates as follows:

$$\begin{aligned}
-\rho_f^{-1}\tilde{M}_{mq}(\ddot{E}_{mqx} + \Omega_{mq}^2 E_{mqx}) + \sum_{n=1}^{\infty} c_{mnq}^{(1)}\ddot{A}_{mnx} - \sum_{p=1}^{\infty} c_{mpq}^{(2)}E_{mpx} \\
+ \delta_{m1}c_{mq}^{(3)}\ddot{f}_x(t) + G_{mqx}^{(1)} = 0 \quad (\text{for } \delta E_{mqx}; m = 0,1,2)
\end{aligned} \tag{24}$$

$$\begin{aligned}
-\rho_f^{-1}\tilde{M}_{mq}(\ddot{E}_{mqy} + \Omega_{mq}^2 E_{mqy}) + \sum_{n=1}^{\infty} c_{mnq}^{(1)}\ddot{A}_{mny} - \sum_{p=1}^{\infty} c_{mpq}^{(2)}E_{mpy} \\
+ \delta_{m1}c_{mq}^{(3)}\ddot{f}_y(t) + G_{mqy}^{(1)} = 0 \quad (\text{for } \delta E_{mqy}; m = 1,2)
\end{aligned} \tag{25}$$

$$-\sum_{p=1}^{\infty} c_{mpq}^{(4)}\ddot{E}_{mpx} - c_{mq}^{(5)}\ddot{A}_{mqx} + G_{mqx}^{(2)} = 0 \quad (\text{for } \delta A_{mqx}; m = 0,1,2) \tag{26}$$

Table 1 Parameters of numerical example

Radius of tank a	41.7 m
Liquid depth h	20.3 m
Liquid density ρ_f	887 $\mathrm{kg/m^3}$
Radius of deck b_1	36.08 m
Position of compartments $b_2=b_3=b_4$	1.78 m
Height of pontoon H	0.918 m
Attachment position of pontoon to deck $H_1=H_2$	0.272 m
Slope $\tan^{-1}(dz/dr)$ of the deck	0.002 deg
Slope $\tan^{-1}(dz/dr)$ of the top of pontoon	4 deg
Slope $\tan^{-1}(dz/dr)$ of the bottom of pontoon	−0.002 deg
Thickness (deck)	0.0045 m
Thickness (pontoon except inner rim)	0.006 m
Thickness (inner rim of pontoon)	0.02 m
Radial coordinates of stiffeners	$5.5+6i$ m ($i=0-4$)
Height and breadth of stiffeners	0.2 m, 0.4 m
Thickness of stiffeners	0.0045 m
Density of floating roof	7850 $\mathrm{kg/m^3}$
Young's modulus of floating roof	2.1×10^{11} $\mathrm{N/m^2}$
Poisson's ratio of floating roof	0.3

$$-\sum_{p=1}^{\infty} c_{mpq}^{(4)}\ddot{E}_{mpy} - c_{mq}^{(5)}\ddot{A}_{mqy} + G_{mqy}^{(2)} = 0 \quad (\text{for } \delta A_{mqy}; m = 1,2) \tag{27}$$

where $\tilde{M}_{mq}$ and Ω_{mq} are the modal mass and the eigenfrequency of the floating roof uncoupled with the liquid motion, and δ_{m1} is Kronecker's delta. Constants $c_{mnq}^{(1)}$, etc., and lengthy nonlinear terms $G_{mqx}^{(1)}$, etc., are presented in Appendix A together with a brief explanation for the derivation of the nonlinear terms. By solving Eqs. (24)–(27), the response of the system can be determined.

3 Numerical Examples

Numerical calculation was conducted for the parameters presented in Table 1. The detailed geometry of the floating roof used for the numerical example is shown in Fig. 2. The damping term $\mu\phi|_{z=h}$ is added to the pressure term of Eq. (18) and the constant μ is determined as $\mu=2\zeta_{mn}\omega_{mn}$ [$\zeta_{mn}=0.01$, $\omega_{mn}^2=g\lambda_{mn}\tanh(\lambda_{mn}h)$] for each modal component of ϕ given by Eq. (21). Furthermore, for the radial displacement of the outer rim of the pontoon relative to the tank wall, the spring and damping support constants per unit area 86,000 $\mathrm{N/m^3}$ and 5000 $\mathrm{N\,s/m^3}$ were taken into account. The excitations were given as $\ddot{f}_x(t)=0.08\sin(\omega t)$ $(0\leqslant t\leqslant 6\pi/\omega)$, $\ddot{f}_x(t)=0$ $(6\pi/\omega<t)$, and $\ddot{f}_y(t)=0$ $(0\leqslant t)$, where $\omega=1.05\omega_{11}$. The responses at the circumferential coordinate $\varphi=0$ of the vertical displacement at the outer rim of the pontoon and the out-of-plane stresses σ_A, σ_B, and σ_C at Positions A, B, and C shown in Fig. 3 are presented in Fig. 4. These out-of-plane stresses just near the joint between the deck and the pontoon were found to attain high levels by searching the maximum magnitude of the in-plane and out-of-plane components of each stress component at all places over the floating roof. These out-of-plane stresses can be calculated by subtracting the stress values at $\zeta=-0.5h_r$ from those at $\zeta=0.5h_r$, where h_r is the thickness of the roof at the position of interest and ζ is the coordinate measured along the normal of the midplane of the shell. The positive direction of ζ is $-z$ on the deck and $+r$ on the inner rim of the pontoon.

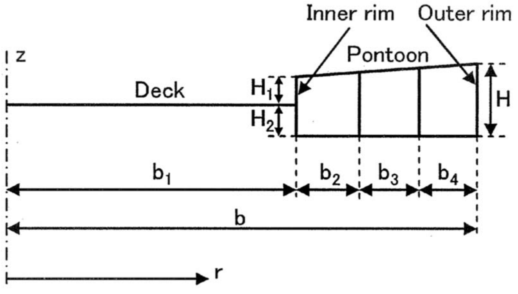

Fig. 2 Geometry of floating roof used for numerical example

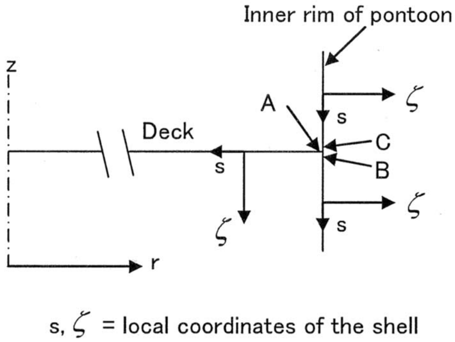

Fig. 3 Positions A, B, and C at which responses of out-of-plane stresses are computed.

In Fig. 4, the solutions obtained by the linear analysis are shown using thin lines for the sake of comparison. In the linear analysis, only the modal component with circumferential wave number 1 is excited because all the nonlinear terms in Eqs. (24)–(27) are neglected. It can be seen from Fig. 4 that although the nonlinear effect is weak for the displacement of the floating roof, underestimation of the response associated with the use of the linear approximation is marked for the stresses σ_B and σ_C. Thus, the nonlinear analysis is obligatory for avoiding the underestimation of these stresses.

Another important point is that these stresses are of the same order in magnitude as the stress shown in Fig. 4(*b*) although the inner rim of the pontoon is much thicker than the deck. Figure 5 shows the responses of the stresses σ_B and σ_C for the case where the thickness of the inner rim of the pontoon is reduced to 0.01 m, which is still larger than the thickness 0.0045 m of the deck. In this case, the response of the stress σ_A remains almost the same as in Fig. 4(*b*), so that the stresses σ_B and σ_C become considerably larger than the stress σ_A. It is recognized that many structural failure accidents were caused at the inner rim of the pontoon just near its joint with the deck, although the inner rim of the pontoon was made thicker than the other places of the floating roof. The results presented here are useful to explain the physical reason for these structural failure accidents.

Figure 6 shows circumferential variations of the stresses σ_B and σ_C, which exhibit the large nonlinear effect. It can be seen from Fig. 6 that for the nonlinear responses, the contribution of the modal component with circumferential wave number 2 is large. Therefore, the physical reason for the large nonlinear effect can be explained by a characteristic of this modal component. Figures 7–9 show the vertical displacement modes of the floating roof along the interface with the liquid for the circumferential wave number $m=0$, 1, and 2, respectively. For the modes with $m=0$ and 1, the radial lowest mode is a rigid-body displacement mode, and the elastic vibration of the inner rim of the pontoon (circular cylindrical shell) is described by the axisymmetric mode and the beam-bending-type mode, respectively. Because these modes exhibit low flexibility, the elastic vibration amplitude of the floating roof is large over the thin plate deck $(0<r<36.08\text{ m})$ and is

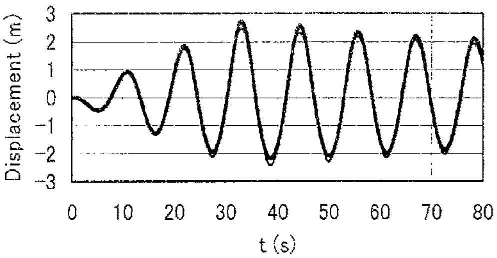

(a) Displacement $-\overline{u}$ in the $+z$ direction at the outer rim of the pontoon

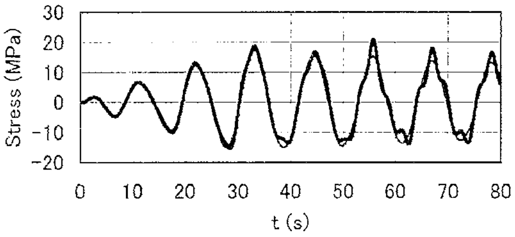

(b) Out-of-plane stress σ_A at the position A shown in Fig. 3

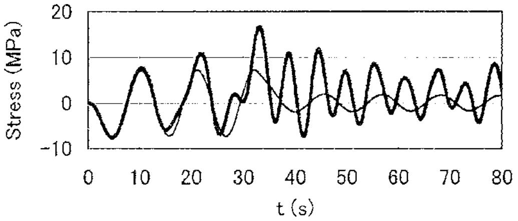

(c) Out-of-plane stress σ_B at the position B shown in Fig. 3

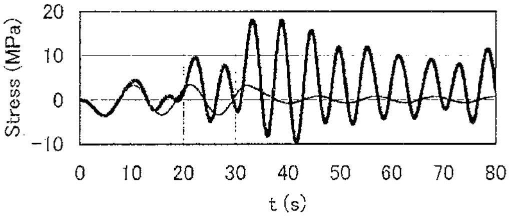

(d) Out-of-plane stress σ_C at the position C shown in Fig. 3

Fig. 4 Comparison between the linear and nonlinear responses (solid line, linear; bold line, nonlinear)

small at the pontoon for the radial higher modes. On the other hand, for the modes with $m=2$ shown in Fig. 9, the circular cylindrical shell oscillates in the flexible mode that renders the circular cross section of the shell elliptical. Hence, there exists a radial mode in which the oscillation of the pontoon is predominant to the vibration of the deck, although in many radial modes the amplitude of the displacement is large over the thin deck and is small at the pontoon. An example for this type of mode is the fifth radial mode in Fig. 9. This mode is referred to as the pontoon vibration mode in the subsequent discussion. The displacement of the pontoon in this pontoon vibration mode is shown in Fig. 10.

Except for the fifth radial mode in Fig. 9, the pontoon vibration mode was not found within the range of the radial 1st–12th modes for the circumferential wave number $m=0$, 1, and 2. The pontoon vibration mode with $m=2$ does not cause a large difference between the linear and nonlinear solutions for the roof displacement, because the rigid-body displacement mode with $m=1$ has the main contribution. However, for the stresses shown in Figs. 4(*c*) and 4(*d*), this rigid-body displacement mode does not have any contribution. Therefore, the pontoon vibration mode with $m=2$ makes the nonlinear solutions considerably larger than the linear responses. If the pontoon vibration mode is neglected in the non-

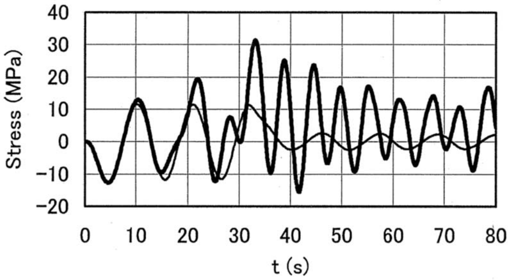

(a) Out-of-plane stress σ_B at the position B shown in Fig. 3

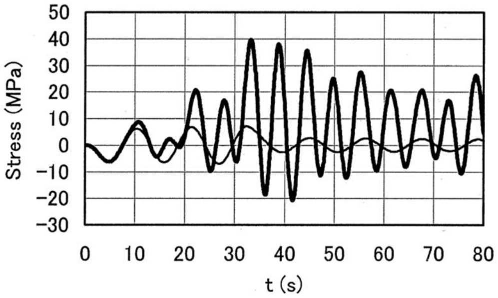

(b) Out-of-plane stress σ_C at the position C shown in Fig. 3

Fig. 5 Results for the case where the thickness of the inner rim of the pontoon is reduced to 0.01 m (solid line, linear; bold line, nonlinear)

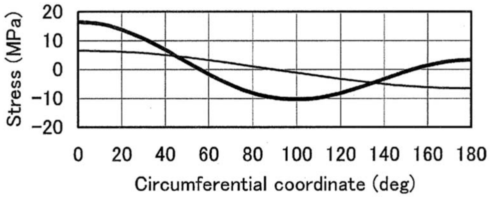

(a) Out-of-plane stress σ_B at the position B shown in Fig. 3

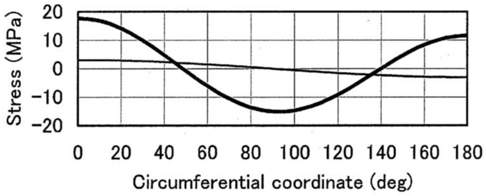

(b) Out-of-plane stress σ_C at the position C shown in Fig. 3

Fig. 6 Circumferential variations of the out-of-plane stresses shown in Figs. 4(*c*) and 4(*d*) at $t=33$ s (solid line, linear; bold line, nonlinear)

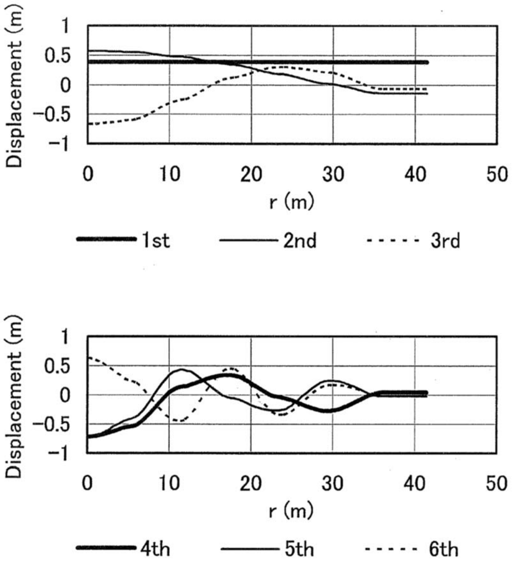

Fig. 7 Vertical displacement modes of the floating roof (circumferential wave number is 0)

linear analysis, the large difference between the linear and nonlinear solutions observed in Figs. 4(*c*) and 4(*d*) is not caused, as is illustrated in Fig. 11.

Figure 12 illustrates that the underestimation of the stress magnitude due to the linear analysis becomes more marked when the liquid depth decreases. The physical reason for this tendency is discussed in Appendix B. This result indicates that the stress magnitude estimation is important irrespective of the liquid-filling level in contrast to the analysis for the vertical displacement of the roof for avoiding flood accidents.

In Appendix C, an experimental validation is presented, which illustrates that the linear analysis results in underestimation of the response and that the nonlinear solution is in good agreement with the experimental result.

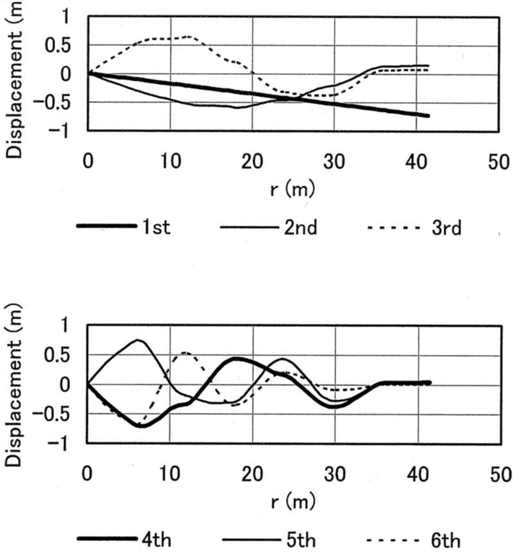

Fig. 8 Vertical displacement modes of the floating roof (circumferential wave number is 1)

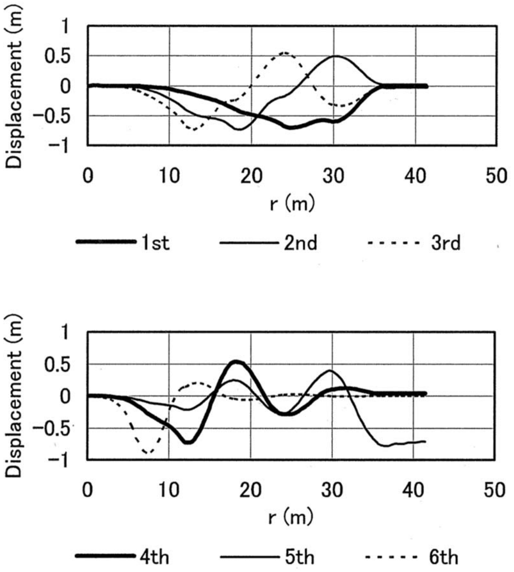

Fig. 9 Vertical displacement modes of the floating roof (circumferential wave number is 2)

4 Summary and Conclusions

A vibration analysis of a floating roof hydroelastically coupled with sloshing has been presented. The nonlinearity of sloshing was taken into consideration, thereby examining the effect of the nonlinearity on the magnitude of the stresses arising in the floating roof. It was shown that if the nonlinearity of the sloshing is neglected, the magnitude of the stresses is considerably underestimated, even when the nonlinear effect is very small for the displacement of the floating roof. The physical reason for this result was explained by the fact that the vibration modes of the floating roof with circumferential wave number 2, which are excited by the nonlinearity of the sloshing, may include an eigenmode in

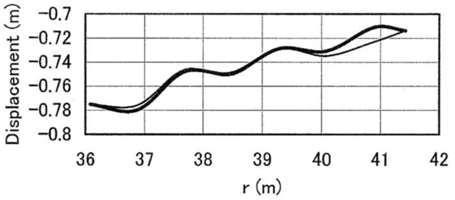

(a) Displacement in the z direction of the upper and lower surfaces of the pontoon (_____ , upper surface; _____ , lower surface)

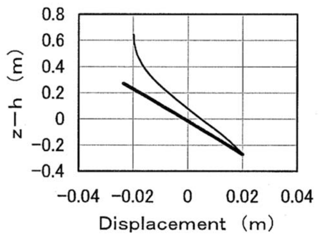

(b) Displacement in the r direction of the outer and inner rims of the pontoon (_____ , outer rim; _____ , inner rim)

Fig. 10 Displacement of the pontoon in the radial fifth mode with circumferential wave number 2

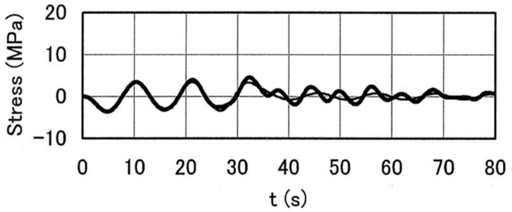

Fig. 11 Response of the out-of-plane stress σ_C at Position C shown in Fig. 3 (solid line, linear analysis; bold line, nonlinear analysis neglecting the radial fifth mode shown in Fig. 9)

which the oscillation of the pontoon is predominant to the vibration of the deck. Furthermore, the underestimation associated with the use of linear approximation becomes more marked with the decrease in the liquid depth. This is due to the fact that some of the excitation terms for the modal component with circumferential wave number 2 remain constant, while the other excitation terms reduce in magnitude with the decrease in the eigenfrequency of the sloshing.

Nomenclature

A_{mnx}, A_{mny} = generalized coordinates of velocity potential
a = radius of tank
E_{mpx}, E_{mpy} = generalized coordinates of floating roof displacement
$\ddot{f}_x(t), \ddot{f}_y(t)$ = earthquake acceleration in the x and y directions, respectively
g = gravitational acceleration
h = liquid depth
L_f, L_r = Lagrangian of liquid and floating roof, respectively
$\mathbf{N}_S$ = outward unit normal vector of the interface between liquid and floating roof
$\mathbf{N}_W$ = outward unit normal vector of the tank wall and bottom
p_l = liquid pressure
S = interface between liquid and floating roof
$\bar{u}, \bar{v}, \bar{w}$ = displacements of floating roof shell in the $-z$, φ, and r directions
V = liquid domain
W = tank wall and bottom
ρ_f = liquid density
ϕ = velocity potential describing liquid motion relative to the tank

Appendix A: Constants and Nonlinear Terms in Equations (24)–(27)

The constants in the linear terms of the differential equations (24)–(27) are as follows:

$$c_{mnq}^{(1)} = \int_0^a J_m(\lambda_{mn}r)S_{mq}(r)rdr, \quad c_{mpq}^{(2)} = g\int_0^a S_{mp}(r)S_{mq}(r)rdr$$

$$c_{mq}^{(3)} = \int_0^a r^2 S_{mq}(r)dr + \delta_{m1}\sum_{\text{emem}}\int_{s_1}^{s_2} \rho_r h_r(\bar{V}_{1q} - \bar{W}_{1q})rds \quad \text{(A1)}$$

$$c_{mpq}^{(4)} = \int_0^a S_{mp}(r)J_m(\lambda_{mq}r)rdr, \quad c_{mq}^{(5)} = \tanh(\lambda_{mq}h)\int_0^a J_m^2(\lambda_{mq}r)rdr$$

To derive the nonlinear terms, we first expand the time and spatial derivatives of the velocity potential given by Eq. (21) into the Tayler series with respect to $\bar{u}$, thereby expressing the integrands in the fourth and sixth terms of Eq. (18) in terms of algebraic nonlinear functions of the generalized coordinates. Through the circumferential integration, it is found that (i) nonlinear terms in the ordinary differential equations with respect to the generalized coordinates with circumferential wave number 1 include products of three generalized coordinates with circumferential wave number 1 and products of two generalized coordinates whose circumferential wave numbers are, respectively, 1 and 2, or 1 and 0; and that (ii) nonlinear terms in the ordinary differential equations with respect to the generalized coordinates with circumferential wave numbers 2 and 0 include products of two generalized coordinates with circumferential wave number 1. Through these considerations, the ordinary differential equations that are derived taking into account these products lead to the second-order approximation solution. Examples of the resulting nonlinear terms are presented below:

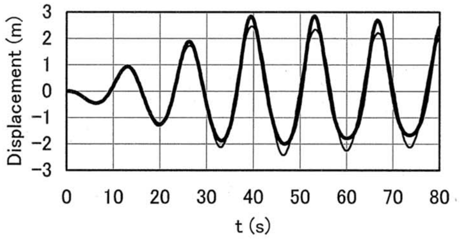

(a) Displacement $-\bar{u}$ in the $+z$ direction at the outer rim of the pontoon

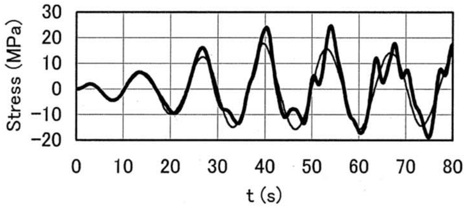

(b) Out-of-plane stress σ_A at the position A shown in Fig. 3

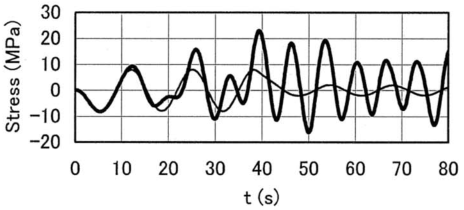

(c) Out-of-plane stress σ_B at the position B shown in Fig. 3

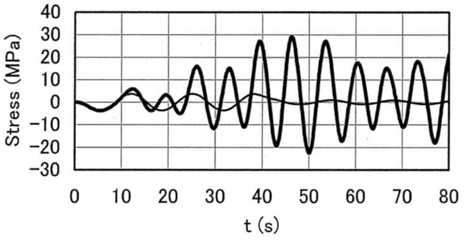

(d) Out-of-plane stress σ_C at the position C shown in Fig. 3

Fig. 12 Results for the case where the liquid depth is decreased to 12.3 m (solid line, linear; bold line, nonlinear)

$$
\begin{aligned}
G_{1qx}^{(1)} = \sum_{n=1}^{\infty}\sum_{l=1}^{\infty}\sum_{j=1}^{\infty} [\alpha_{nljq}^{(1)}(3\ddot{A}_{1nx}E_{1lx}E_{1jx} + \ddot{A}_{1nx}E_{1ly}E_{1jy} + \ddot{A}_{1ny}E_{1lx}E_{1jy} + \ddot{A}_{1ny}E_{1ly}E_{1jx}) + \alpha_{nljq}^{(2)}(3\dot{A}_{1nx}\dot{A}_{1lx}E_{1jx} + \dot{A}_{1ny}\dot{A}_{1ly}E_{1jx} + \dot{A}_{1nx}\dot{A}_{1ly}E_{1jy} \\
+ \dot{A}_{1ny}\dot{A}_{1lx}E_{1jy}) + \alpha_{nljq}^{(3)}(\dot{A}_{1nx}\dot{A}_{1lx}E_{1jx} + 3\dot{A}_{1ny}\dot{A}_{1ly}E_{1jx} - \dot{A}_{1nx}\dot{A}_{1ly}E_{1jy} - \dot{A}_{1ny}\dot{A}_{1lx}E_{1jy}) + \alpha_{nljq}^{(4)}(3\dot{A}_{1nx}\dot{A}_{1lx}E_{1jx} + \dot{A}_{1ny}\dot{A}_{1ly}E_{1jx} \\
+ \dot{A}_{1nx}\dot{A}_{1ly}E_{1jy} + \dot{A}_{1ny}\dot{A}_{1lx}E_{1jy})] + \sum_{n=1}^{\infty}\sum_{l=1}^{\infty} [\alpha_{nlq}^{(11)}(\ddot{A}_{1nx}E_{2lx} + \ddot{A}_{1ny}E_{2ly}) + \alpha_{nlq}^{(12)}(\ddot{A}_{2nx}E_{1lx} + \ddot{A}_{2ny}E_{1ly}) + \alpha_{nlq}^{(13)}\ddot{A}_{1nx}E_{0lx} + \alpha_{nlq}^{(14)}\ddot{A}_{0nx}E_{1lx} \\
+ (\alpha_{nlq}^{(15)} + \alpha_{nlq}^{(16)} + \alpha_{nlq}^{(17)})(\dot{A}_{1nx}\dot{A}_{2lx} + \dot{A}_{1ny}\dot{A}_{2ly}) + (\alpha_{nlq}^{(18)} + \alpha_{nlq}^{(19)})\dot{A}_{1nx}\dot{A}_{0lx}]
\end{aligned}
\tag{A2}
$$

$$
G_{2qx}^{(1)} = \sum_{n=1}^{\infty}\sum_{l=1}^{\infty} [\alpha_{nlq}^{(21)}(\ddot{A}_{1nx}E_{1lx} - \ddot{A}_{1ny}E_{1ly}) + (\alpha_{nlq}^{(23)} - \alpha_{nlq}^{(24)} + \alpha_{nlq}^{(25)})(\dot{A}_{1nx}\dot{A}_{1lx} - \dot{A}_{1ny}\dot{A}_{1ly})]
\tag{A3}
$$

$$
G_{0qx}^{(1)} = \sum_{n=1}^{\infty}\sum_{l=1}^{\infty} [\alpha_{nlq}^{(22)}(\ddot{A}_{1nx}E_{1lx} + \ddot{A}_{1ny}E_{1ly}) + (\alpha_{nlq}^{(26)} + \alpha_{nlq}^{(27)} + \alpha_{nlq}^{(28)})(\dot{A}_{1nx}\dot{A}_{1lx} + \dot{A}_{1ny}\dot{A}_{1ly})]
\tag{A4}
$$

$$
\begin{aligned}
G_{1qx}^{(2)} = \sum_{n=1}^{\infty}\sum_{l=1}^{\infty}\sum_{j=1}^{\infty} [\beta_{nljq}^{(1)}(-d/dt)(3\dot{A}_{1nx}E_{1lx}E_{1jx} + \dot{A}_{1nx}E_{1ly}E_{1jy} + \dot{A}_{1ny}E_{1lx}E_{1jy} + \dot{A}_{1ny}E_{1ly}E_{1jx}) + \beta_{nljq}^{(2)}(-d/dt)(\dot{A}_{1nx}E_{1lx}E_{1jx} - \dot{A}_{1nx}E_{1ly}E_{1jy} \\
- \dot{A}_{1ny}E_{1lx}E_{1jy} + 3\dot{A}_{1ny}E_{1ly}E_{1jx}) + \beta_{nljq}^{(3)}(-d/dt)(3\dot{E}_{1nx}E_{1lx}E_{1jx} + \dot{E}_{1nx}E_{1ly}E_{1jy} + \dot{E}_{1ny}E_{1lx}E_{1jy} + \dot{E}_{1ny}E_{1ly}E_{1jx})] \\
+ \sum_{n=1}^{\infty}\sum_{l=1}^{\infty} [(\beta_{nlq}^{(11)} + \beta_{nlq}^{(12)})(-d/dt)(\dot{A}_{1nx}E_{2lx} + \dot{A}_{1ny}E_{2ly}) + (\beta_{nlq}^{(13)} + \beta_{nlq}^{(14)})(-d/dt)(\dot{A}_{2nx}E_{1lx} + \dot{A}_{2ny}E_{1ly}) + \beta_{nlq}^{(15)}(-d/dt)(\dot{A}_{1nx}E_{0lx}) \\
+ \beta_{nlq}^{(16)}(-d/dt)(\dot{A}_{0nx}E_{1lx}) + \beta_{nlq}^{(17)}(-d/dt)(\dot{E}_{2nx}E_{1lx} + \dot{E}_{2ny}E_{1ly}) + \beta_{nlq}^{(18)}(-d/dt)(\dot{E}_{1nx}E_{2lx} + \dot{E}_{1ny}E_{2ly}) + \beta_{nlq}^{(19)}(-d/dt)(\dot{E}_{0nx}E_{1lx}) \\
+ \beta_{nlq}^{(20)}(-d/dt)(\dot{E}_{1nx}E_{0lx})]
\end{aligned}
\tag{A5}
$$

$$
\begin{aligned}
G_{2qx}^{(2)} = \sum_{n=1}^{\infty}\sum_{l=1}^{\infty} [(\beta_{nlq}^{(21)} - \beta_{nlq}^{(22)})(-d/dt)(\dot{A}_{1nx}E_{1lx} - \dot{A}_{1ny}E_{1ly}) \\
+ \beta_{nlq}^{(25)}(-d/dt)(\dot{E}_{1nx}E_{1lx} - \dot{E}_{1ny}E_{1ly})]
\end{aligned}
\tag{A6}
$$

$$
\begin{aligned}
G_{0qx}^{(2)} = \sum_{n=1}^{\infty}\sum_{l=1}^{\infty} [(\beta_{nlq}^{(23)} + \beta_{nlq}^{(24)})(-d/dt)(\dot{A}_{1nx}E_{1lx} + \dot{A}_{1ny}E_{1ly}) \\
+ \beta_{nlq}^{(26)}(-d/dt)(\dot{E}_{1nx}E_{1lx} + \dot{E}_{1ny}E_{1ly})]
\end{aligned}
\tag{A7}
$$

where $\alpha_{nljq}^{(1)}$, etc., are constants. Because these are lengthy, few examples are given below.

$$
\alpha_{nljq}^{(1)} = \int_0^a \frac{1}{8}\lambda_{1n}^2 J_{1n}S_{1l}S_{1j}S_{1q}rdr, \quad \alpha_{nljq}^{(2)} = -\int_0^a \frac{1}{4}\psi_{1l}J'_{1n}J'_{1l}S_{1j}S_{1q}rdr
$$

$$
\begin{aligned}
\beta_{nljq}^{(1)} = \int_0^a \Bigg[\left(\frac{1}{8}\lambda_{1n}^2\psi_{1n} + \frac{1}{4}\lambda_{1n}^2\psi_{1q} + \frac{1}{8}\psi_{1n}\lambda_{1q}^2\right)J_{1n}S_{1l}S_{1j}J_{1q} \\
- \frac{1}{4}\psi_{1n}J'_{1n}S_{1l}S'_{1j}J_{1q} - \frac{1}{4}\psi_{1q}J'_{1n}S'_{1l}S_{1j}J_{1q}\Bigg]rdr
\end{aligned}
\tag{A8}
$$

$$
\beta_{nljq}^{(2)} = -\int_0^a \frac{1}{4}(\psi_{1n} + \psi_{1q})\hat{J}_{1n}\hat{S}_{1l}S_{1j}J_{1q}rdr
$$

where the following symbols are introduced for concise description:

$$
J_{mn} = J_m(\lambda_{mn}r), \quad J'_{mn} = \frac{dJ_m(\lambda_{mn}r)}{dr}, \quad \hat{J}_{mn} = \frac{1}{r}J_m(\lambda_{mn}r)
\tag{A9}
$$

$$
S_{mn} = S_{mn}(r), \quad S'_{mn} = \frac{dS_{mn}(r)}{dr}, \quad \hat{S}_{mn} = \frac{1}{r}S_{mn}(r)
$$

$$
\psi_{mn} = \lambda_{mn}\tanh(\lambda_{mn}h)
\tag{A10}
$$

The operator $-d/dt$ in Eqs. (A5)–(A7) arises from integration by parts that transforms the stationary conditions for $\delta\dot{A}_{mqx}$ into those for δA_{mqx}.

Appendix B: The Reason Why the Nonlinear Effect is Accentuated With the Decrease in the Liquid Depth

To facilitate the discussion, let us consider the case in which the excitation in the y direction is not present and the generalized coordinates with suffix y are not excited. First, we obtain the first-order approximation solution. Since the mass of the floating roof is much smaller than the liquid mass, the first term of Eq. (24) can be neglected. Equations (24) and (26) for $m=1$ can be reduced to the following matrix equations by neglecting the third-order nonlinear functions:

$$
\mathbf{C}_1^{(1)}\ddot{\mathbf{A}}_1 - \mathbf{C}_1^{(2)}\mathbf{E}_1 + \mathbf{C}_1^{(3)}\ddot{f}_x(t) = 0
\tag{B1}
$$

$$
\mathbf{C}_1^{(4)}\ddot{\mathbf{E}}_1 + \mathbf{C}_1^{(5)}\ddot{\mathbf{A}}_1 = 0
\tag{B2}
$$

where the column vectors $\mathbf{A}_1$ and $\mathbf{E}_1$ are the collections of A_{1nx} and E_{1px}, respectively, while the matrices $\mathbf{C}_1^{(i)}$ are the collections of $c^{(i)}$ presented in Eq. (A1). Eliminating $\ddot{\mathbf{A}}_1$ from Eqs. (B1) and (B2) leads to

$$
\ddot{\mathbf{E}}_1 + \mathbf{M}_1^{-1}\mathbf{K}_1\mathbf{E}_1 = \mathbf{M}_1^{-1}\mathbf{C}_1^{(3)}\ddot{f}_x(t)
\tag{B3}
$$

where $\mathbf{M}_1 = \mathbf{C}_1^{(1)}(\mathbf{C}_1^{(5)})^{-1}\mathbf{C}_1^{(4)}$ and $\mathbf{K}_1 = \mathbf{C}_1^{(2)}$. Eigenvalues of $\mathbf{M}_1^{-1}\mathbf{K}_1$ for lower modes can be approximated by the eigenfrequencies $\omega_{1n}^2 = g\lambda_{1n}\tanh(\lambda_{1n}h)$ of the sloshing. From Eq. (A1), the coeffi-

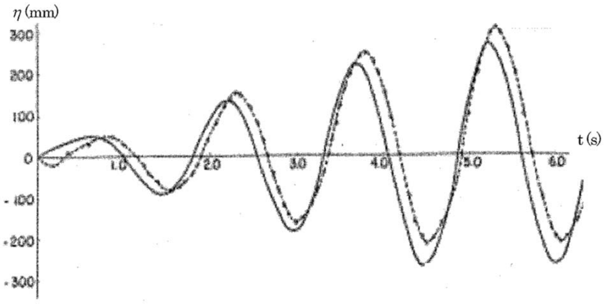

(a) Results cited from Ref. [18] (Fig. 3.6) (____, linear analysis; ......, experiment)

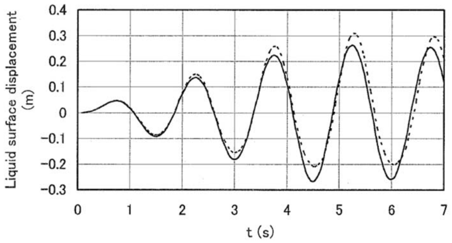

(b) Present analysis (____, linear; ......, nonlinear)

Fig. 13 The responses of liquid surface displacement (a=1 m, h=1.263 m; damping ratio 0.005; the tank is excited by the displacement $f_x(t)=0.2\sin\omega_{11}t$ where $\omega_{11}=[g\lambda_{11}\tanh(\lambda_{11}h)]^{1/2}$ and $0\leq t\leq 6\pi/\omega_{11}$)

cient $\mathbf{M}_1^{-1}\mathbf{C}_1^{(3)}$ of the excitation term is proportional to $\tanh(\lambda_{1n}h)$ included in $\mathbf{C}_1^{(5)}$. Therefore, dependence of the responses of the predominant lower modes to the excitation $\ddot{f}_x(t)=\sin\omega t$ on the liquid depth can be evaluated as

$$E_{1nx}\propto\tanh(\lambda_{1n}h)\sin\omega t/(\omega_{1n}^2-\omega^2) \tag{B4}$$

Because we consider the case in which the liquid depth normalized by the tank radius is decreased and the excitation frequency is near the resonance of the sloshing, the following relations hold:

$$\tanh(\lambda_{1n}h)\propto O(h),\quad \omega^2\propto O(h),\quad \mathbf{C}_1^{(5)}\propto O(h) \tag{B5}$$

Hence, from Eqs. (B2) and (B4), we obtain

$$E_{1nx}=\hat{E}_{1nx}\sin\omega t\propto O(h^0),\quad A_{1nx}=\hat{A}_{1nx}\sin\omega t\propto O(h^{-1}) \tag{B6}$$

For Eqs. (24) and (26) with m=2, the matrix equations similar to Eqs. (B1) and (B2) can be written as

$$\mathbf{C}_2^{(1)}\ddot{\mathbf{A}}_2-\mathbf{C}_2^{(2)}\mathbf{E}_2+\mathbf{G}_2^{(1)}=\mathbf{0} \tag{B7}$$

$$-\mathbf{C}_2^{(4)}\ddot{\mathbf{E}}_2-\mathbf{C}_2^{(5)}\ddot{\mathbf{A}}_2+\mathbf{G}_2^{(2)}=\mathbf{0} \tag{B8}$$

Eliminating $\ddot{\mathbf{A}}_0$ from Eqs. (B7) and (B8) yields

$$\ddot{\mathbf{E}}_2+\mathbf{M}_2^{-1}\mathbf{K}_2\mathbf{E}_2=\mathbf{M}_2^{-1}[\mathbf{G}_2^{(1)}+\mathbf{C}_2^{(1)}(\mathbf{C}_2^{(5)})^{-1}\mathbf{G}_2^{(2)}] \tag{B9}$$

where $\mathbf{M}_2=\mathbf{C}_2^{(1)}(\mathbf{C}_2^{(5)})^{-1}\mathbf{C}_2^{(4)}$ and $\mathbf{K}_2=\mathbf{C}_2^{(2)}$. For lower modes, the eigenvalues of $\mathbf{M}_2^{-1}\mathbf{K}_2$ nearly equal the eigenfrequencies $\omega_{2n}^2=g\lambda_{2n}\tanh(\lambda_{2n}h)$ and Eq. (B9) can be expressed as

$$\ddot{E}_{2qx}+\omega_{2q}^2E_{2qx}=\varepsilon_{2q}^{(1)}G_{2qx}^{(1)}+\varepsilon_{2q}^{(2)}G_{2qx}^{(2)} \tag{B10}$$

Because $\mathbf{C}_2^{(5)}$ depends on h through $\tanh(\lambda_{2n}h)$ (see Eq. (A1)), we see that

$$\varepsilon_{2q}^{(1)}\propto O(h),\quad \varepsilon_{2q}^{(2)}\propto O(h^0) \tag{B11}$$

The nonlinear functions on the right-hand side of Eq. (B10) can be calculated by substituting Eq. (B6) into Eqs. (A3) and (A6) as follow:

$$\begin{aligned}G_{2qx}^{(1)}=\sum_{n=1}^{\infty}\sum_{l=1}^{\infty}\Bigg[&\alpha_{nlq}^{(21)}\hat{A}_{1nx}\hat{E}_{1lx}\frac{1}{2}\omega^2(\cos 2\omega t-1)\\&+(\alpha_{nlq}^{(23)}-\alpha_{nlq}^{(24)}+\alpha_{nlq}^{(25)})\hat{A}_{1nx}\hat{A}_{1lx}\frac{1}{2}\omega^2(1+\cos 2\omega t)\Bigg]\end{aligned} \tag{B12}$$

$$\begin{aligned}G_{2qx}^{(2)}=\sum_{n=1}^{\infty}\sum_{l=1}^{\infty}[&(\beta_{nlq}^{(21)}-\beta_{nlq}^{(22)})\hat{A}_{1nx}\hat{E}_{1lx}(-\omega^2)\cos 2\omega t\\&-\beta_{nlq}^{(25)}\hat{E}_{1nx}\hat{E}_{1lx}\omega^2\cos 2\omega t]\end{aligned} \tag{B13}$$

Substituting Eqs. (B5) and (B6) into Eqs. (B12) and (B13) and using Eq. (B11) lead to the following order estimation of the right-hand side of Eq. (B10):

$$\begin{aligned}\varepsilon_{2q}^{(1)}G_{2qx}^{(1)}\propto\sum_{n=1}^{\infty}\sum_{l=1}^{\infty}[&\alpha_{nlq}^{(21)}O(h)(\cos 2\omega t-1)\\&+(\alpha_{nlq}^{(23)}-\alpha_{nlq}^{(24)}+\alpha_{nlq}^{(25)})O(h^0)(1+\cos 2\omega t)]\end{aligned} \tag{B14}$$

$$\varepsilon_{2q}^{(2)}G_{2qx}^{(2)}\propto\sum_{n=1}^{\infty}\sum_{l=1}^{\infty}[(\beta_{nlq}^{(21)}-\beta_{nlq}^{(22)})O(h^0)-\beta_{nlq}^{(25)}O(h)]\cos 2\omega t \tag{B15}$$

Here, some of the parameters depend on h through ψ_{mn} defined by Eq. (A10), e.g.,

$$\begin{aligned}&\alpha_{nlq}^{(21)}=-\int_0^a\frac{1}{2}\psi_{1n}J_{1n}S_{1l}S_{2q}rdr,\quad \alpha_{nlq}^{(23)}=\int_0^a\frac{1}{4}J_{1n}'J_{1l}'S_{2q}rdr\\&\alpha_{nlq}^{(24)}=\int_0^a\frac{1}{4}\hat{J}_{1n}\hat{J}_{1l}S_{2q}rdr\end{aligned} \tag{B16}$$

The dependence of these parameters on the liquid depth is as follows:

$$\begin{aligned}&\alpha_{nlq}^{(21)}\propto O(h),\quad \alpha_{nlq}^{(23)},\alpha_{nlq}^{(24)}\propto O(h^0),\quad \alpha_{nlq}^{(25)}\propto O(h^2)\\&\beta_{nlq}^{(21)},\beta_{nlq}^{(22)}\propto O(h^0),\quad \beta_{nlq}^{(25)}\propto O(h)\end{aligned} \tag{B17}$$

From Eqs. (B14) and (B15), Eq. (B10) can be expressed in the form $\ddot{E}_{2q}+\omega_{2q}^2E_{2q}=C_1+C_2\cos 2\omega t$. Its solution is $E_{2q}=C_1/\omega_{2q}^2+C_2\cos 2\omega t/(\omega_{2q}^2-4\omega^2)$, where the squared frequencies are $O(h)$ as can be seen from Eq. (B5). Therefore, the terms of the solution including $\alpha_{nlq}^{(23)},\alpha_{nlq}^{(24)}$, $\beta_{nlq}^{(21)}$, and $\beta_{nlq}^{(22)}$ become large with $O(h^{-1})$ and accentuate the nonlinear effect. Thus, it can be found that the accentuated nonlinear effect for the decreased liquid depth originates in the $O(h^0)$ terms in Eqs. (B14) and (B15) to be divided by the squared eigenfrequencies of the sloshing with the order of $O(h^1)$. By looking into the derivation of the nonlinear functions, it can be found that these terms come from the nonlinear terms $\partial\phi/\partial z|_{z=h-\bar{u}}$, $\partial\phi/\partial r|_{z=h-\bar{u}}\partial\bar{u}/\partial r$, $r^{-2}\partial\phi/\partial\varphi|_{z=h-\bar{u}}\partial\bar{u}/\partial\varphi$, $(\partial\phi/\partial r)^2|_{z=h-\bar{u}}$, and $r^{-2}(\partial\phi/\partial\varphi)^2|_{z=h-\bar{u}}$ in Eq. (18), not from the term $\partial\phi/\partial t$ or $(\partial\phi/\partial z)^2$ in the pressure equation.

Appendix C: Validation for the Comparison Between Linear and Nonlinear Analyses

For this validation, the response of a free liquid surface is calculated and is compared with experimental data that could be found in previous literature [18]. This response analysis can be conducted by altering the admissible function for the vertical displacement $\bar{u}$ of the floating roof to the liquid surface displacement η as follows

$$\eta(r,\varphi,t)=\sum_{m=0}^{\infty}\sum_{n=1}^{\infty}[E_{mnx}(t)\cos m\varphi+E_{mny}(t)\sin m\varphi]J_m(\lambda_{mn}r) \tag{C1}$$

The results are presented in Fig. 13. As can be seen from Fig. 13(*a*), the linear analysis results in underestimation of the response. The positive maximal and negative minimal values of the nonlinear solution shown in Fig. 13(*b*) are in good agreement with the experimental result presented in Fig. 13(*a*) although phase difference at the initial time is caused in the experiment.

References

[1] 1966, "The Dynamic Behavior of Liquids in Moving Containers," NASA SP-106, H. N. Abramson, ed.

[2] Ibrahim, R. A., Pilipchuk, V. N., and Ikeda, T., 2001, "Recent Advances in Liquid Sloshing Dynamics," Appl. Mech. Rev., **54**, 133–199.

[3] Kondo, H., 1989, "Seismic Response of a Reactor Vessel Subjected to Horizontal Excitation," Sloshing and Fluid Structure Vibration, ASME Pressure Vessel and Piping Conference, PVP-Vol. 157, 55–59.

[4] Fujita, K., 1981, "A Seismic Response Analysis of a Cylindrical Liquid Storage Tank Including the Effect of Sloshing," Bull. JSME, **24**, pp. 1634–1641.

[5] Bauer, H. F., 1987, "Coupled Frequencies of a Hydroelastic System Consisting of an Elastic Shell and Frictionless Liquid," J. Sound Vib., **113**, pp. 217–232.

[6] Bauer, H. F., Chang, S. S., and Wang, J. T. S., 1971, "Nonlinear Liquid Motion in a Longitudinally Excited Container With Elastic Bottom," AIAA J., **9**, 2333–2339.

[7] Ibrahim, R. I., and El-Sayad, M. A., 1999, "Simultaneous Parametric and Internal Resonances in Systems Involving Strong Nonlinearities," J. Sound Vib., **225**, pp. 857–885.

[8] Ikeda, T., and Nakagawa, N., 1997, "Nonlinear Vibrations of a Structure Caused by Water Sloshing in a Rectangular Tank," J. Sound Vib., **201**, pp. 23–41.

[9] Ikeda, T., and Nakagawa, N., 1995, "Nonlinear Vibrations of a Structure Caused by Water Sloshing in a Cylindrical Tank," Fluid Structure Interaction and Structure Mechanics, ASME PVP-Vol. 310, pp. 63–76.

[10] Peterson, L. D., Crawley, E. F., and Hansman, R. J., 1989, "Nonlinear Slosh Coupled to the Dynamics of a Spacecraft," AIAA J., **27**, 1230–1240.

[11] Utsumi, M., Kimura, K., and Sakata, M., 1987, "The Non-Stationary Random Vibration of an Elastic Circular Cylindrical Liquid Storage Tank in Simulated Earthquake Excitation (Straightforward Analysis of Tank Wall Deformation)," JSME Int. J., Ser. III, **30**, 467–475.

[12] Nakagawa, K., 1955, "On the Vibration of an Elevated Water Tank-II," Technol. Rep. Osaka Univ., **5**, pp. 317–336.

[13] Kondo, H., 1978, "Free Vibration Analysis for Vertical Motion of a Floating Roof," Trans. Jpn. Soc. Mech. Eng., **44**, 1214–1223.

[14] Sakai, F., Nishimura, M., and Ogawa, H., 1984, "Sloshing Behavior of Floating Roof Oil Storage Tanks," Comput. Struct., **19**, 183–192.

[15] Shimizu, S., Naito, K., and Koyama, Y., 1984, "A Study on Sloshing Behaviors of Floating Roof Oil Storage Tanks During Earthquake Excited by Three-Dimensional Dynamic Simulator," Ishikawajima-Harima Eng. Rev., **24**, 379–384.

[16] Seliger, R. L., and Whitham, G. B., 1968, "Variational Principles in Continuum Mechanics," Proc. R. Soc. London, Ser. A, **305**, 1–25.

[17] Utsumi, M., 1998, "Low-Gravity Propellant Slosh Analysis Using Spherical Coordinates," J. Fluids Struct., **12**, 57–83.

[18] Yamauchi, Y., Kamei, A., Zama, S., and Uchida, Y., 2006, "Seismic Design of Floating Roof of Oil Storage Tanks Under Liquid Sloshing," Sloshing and Fluid Structure Vibration, ASME Pressure Vessels and Piping Division Conference, PVP2006-ICPVT-11-93280.

Chuanxiang Zheng
Associate Professor
e-mail: zhengcx@21cn.com

Shaohui Lei

Institution of Chemical Process Machinery,
Zhejiang University,
Hangzhou 310027, P.R.C.

Optimal Winding Conditions of Flat Steel Ribbon Wound Pressure Vessels With Controllable Stresses

Stress analysis of flat steel ribbon wound pressure vessels (FSRWPVs) is very difficult because they have a special discrete structure and complex pretensions exit in the flat steel ribbons, which are wound around the inner shell layer by layer. An analytical multilayered model for stress analysis is presented in this paper, which involves the effect of prestress in every flat steel ribbon layer as well as in the inner shell. Based on this model, an optimal design method for FSRWPV is suggested, which can assure a reasonable stress level and distribution along the wall thickness during the operation. A practical example of a large FSRWPV is finally given for illustration.
[DOI: 10.1115/1.2912740]

Keywords: flat steel ribbon wound pressure vessel (FSRWPV), stress analysis, analytical model, optimal design

1 Introduction

There are more than 10,000 flat steel ribbon wound pressure vessels (FSRWPVs) used in the chemical industry all over the world, and none of them has been suffered from sudden burst since their first operation in 1970. This strongly implies the good safety of FSRWPV, which is, in fact, an outcome of its special discrete structure, as shown in Fig. 1. The design method and other related matters have been formed into Code Cases 2229 and 2269 in Divisions 1 and 2, Sec. VIII, ASME Code, in 1996 and 1997, respectively. The title of the code is “Design of Layered Vessel Using Flat Ribbon Wound Cylindrical Shells,” which serves an excellent guide to the practical design and manufacture [1–4].

Traditional high-pressure vessels are fabricated in a single-layered, thick-walled form, and hence no gaps or cracks are permitted in the wall. This makes the corresponding analysis simpler than that of FSRWPV, in which gaps can exist all over the cylindrical body. Furthermore, there is prestress in the steel ribbons, between which friction also exists. Currently, there are several theoretical models for stress analysis of FSRWPVs that have been employed for the purpose of design. One model that is well known to the area was built by Professor Zhu, who took consideration of the frictional forces as well as gaps between steel ribbons, but ignored the effect of prestress in steel ribbons [5]. The design based on Zhu’s model is conservative since the prestress is obviously beneficial to the load capacity of FSRWPV. However, to achieve a safe and also economic design, the effect of prestress in steel ribbons should be precisely evaluated. In fact, the prestress in steel ribbons is very important since it can change the stress distribution in FSRWPV by adjusting the value of prestress in every steel ribbon, and hence optimal design could be achieved [6–8]. This paper sets up an optimal design model by extending Zhu’s model to include the effect of prestress in the steel ribbons. Practical example is given to show the optimized stress distribution in FSRWPV.

2 Vessel Structure

The structure of FSRWPV has an inner cylindrical shell (at 1/4–1/6 of total thickness) and flat steel ribbon wound layers (see Fig. 1). Its ends are made up of single or multilayer convex covers. Its flat steel ribbons are wound in a spiral angle layer by layer. Every neighbor layers are wound in contrary angle. The wound angle is 15–30 deg. There is prestress in every flat steel ribbon. The prestress can be designed according to necessity. The outside of FSRWPV is a thin safeguard shell that can prevent FSRWPV from corroding, and where can also install leakage sensor for detecting leaking condition of inner shell.

3 Model of Stress Analysis

In order to guarantee the safety of FSRWPVs during operation, the following two requirements should generally be followed: (1) The stress distribution in the vessel wall should be uniform, without any stress concentration; (2) the stress in the inner shell should be low enough or even negative if possible. The second is essentially important because high stress level in the inner layer is generally very dangerous, especially when FSRWPV works with corrosive gases or fluids. The above two requirements can be readily satisfied under the concept of optimal design by properly adjusting prestress in the steel ribbons [9,10].

3.1 Final State of Stress. After steel ribbons are wound with prestress around the inner shell of FSRWPV, residual stresses are induced in the vessel. Hence, the final state of stress is the combination of the residual stress and the stress caused by the operating pressure. Introducing the stress vector $\boldsymbol{\sigma}=[\sigma_h,\sigma_r,\sigma_z]^T$, we have

$$\boldsymbol{\sigma}_{\text{final}}=\boldsymbol{\sigma}_{\text{pre}}+\boldsymbol{\sigma}_{\text{ope}} \tag{1}$$

where σ_h, σ_r, σ_z (MPa) are the hoop, radial, and axial stresses, respectively, and the subscripts “final,” “pre,” and “ope” denote the final, prestress, operating states, respectively.

The operating stresses can be readily calculated using Lamé formulas [11], and are fixed if the shape of vessel and the operating pressure P are determined. Thus, the adjustment of stress distribution in the vessel can only be realized by controlling $\boldsymbol{\sigma}_{\text{pre}}$, by altering either the prestress level or the winding angle of each steel ribbon. As the basic requirements of the design of FSRWPV

Contributed by the Applied Mechanics Division of ASME for publication in the Journal of Applied Mechanics. Manuscript received January 26, 2007; final manuscript received February 21, 2008; published online May 14, 2008. Review conducted by Jian Cao.

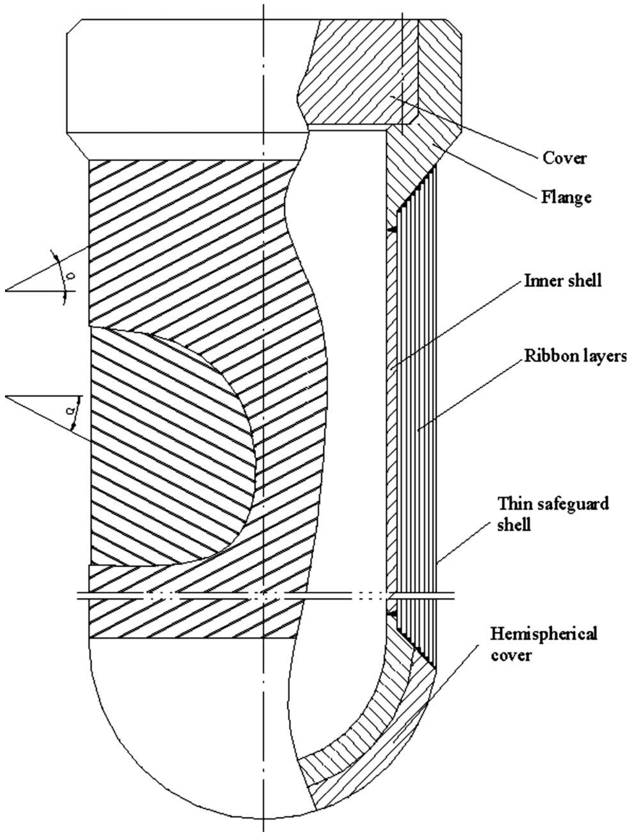

Fig. 1 Structure of a FSRWPV

as just mentioned, it is better that the hoop stress in the inner shell is zero or even negative, while the stress in the flat steel ribbon layers is uniform [12,13]. This kind of stress distribution is advantageous to prolonging the service lifetime of the vessel [14]. If the distribution of the final stresses $\boldsymbol{\sigma}$ is determined according to a particular design, the prestress $\boldsymbol{\sigma}_{\text{pre}}$ can then be calculated from Eq. (1).

3.2 Residual Stresses. The dimension of the cross section of FSRWPV with m layers of flat steel ribbons is shown in Fig. 2. Denote $\mathbf{F}$ as the vector consisting of pretensioning stresses in all steel ribbons:

$$\mathbf{F} = [F_1 \quad F_2 \quad \cdots \quad F_m] \tag{2}$$

where F_k is the pretensioning stress in the kth layer of steel ribbons, MPa.

As shown in Fig. 3, when the kth layer is wound, the pretensioning stress F_k not only yields longitudinal stress σ_{Fk} in the direction of ribbon but also causes radial stress σ_{rk} (or radial pressure P_{rk}) that acts on the finished part of vessel (i.e., the inner shell plus the prior wound $k-1$ layers of steel ribbons). The radial pressure vector $\mathbf{P}_r=[P_{r1},P_{r2},\cdots,P_{rm}]$ can be calculated according to

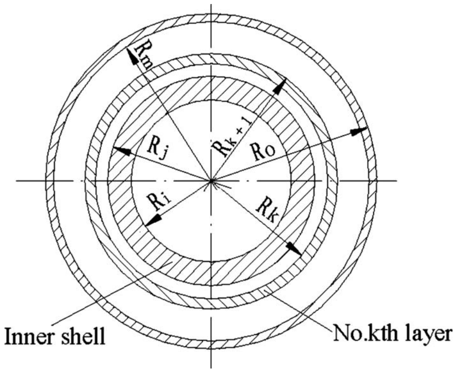

Fig. 2 Cross section of FSRWPV

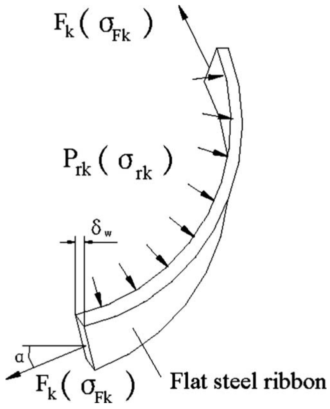

Fig. 3 Equilibrium of flat steel ribbon

$$\mathbf{P}_r = \delta_w \cos^2 \alpha \mathbf{F}\mathbf{R}^{-1} \tag{3}$$

where δ_w (mm) is the thickness of a single steel ribbon, and α (deg) is the winding angle, and

$$\mathbf{R} = \begin{bmatrix} R_1 & 0 & 0 & \cdots & 0 \\ 0 & R_2 & 0 & \cdots & 0 \\ 0 & 0 & R_3 & \cdots & 0 \\ \vdots & \vdots & \vdots & \ddots & \vdots \\ 0 & 0 & 0 & \cdots & R_m \end{bmatrix}$$

with R_k (mm) being the inner radius of the kth layer [15,16].

Regarding the above calculated radial pressure as the outer pressure acting on the pressure vessel, we can easily calculate the residual stresses with Lamé formulas, after all layers of FSRWPV are wounded, as follows:

$$\boldsymbol{\sigma}_{r,\text{pre}} = \mathbf{L}_r(\mathbf{P}_r)^T = \delta_w \cos^2 \alpha \mathbf{L}_r \mathbf{R}^{-1}\mathbf{F}^T \tag{4}$$

$$\boldsymbol{\sigma}_{h,\text{pre}} = \mathbf{M}\mathbf{F}^T + \mathbf{L}_h(\mathbf{P}_r)^T = (\mathbf{M} + \delta_w \cos^2 \alpha \mathbf{L}_h \mathbf{R}^{-1})\mathbf{F}^T \tag{5}$$

$$\boldsymbol{\sigma}_{z,\text{pre}} = \mathbf{L}_z(\mathbf{P}_z)^T \tag{6}$$

where $\boldsymbol{\sigma}_{r,\text{pre}}$, $\boldsymbol{\sigma}_{h,\text{pre}}$, and $\boldsymbol{\sigma}_{z,\text{pre}}$ are the radial, hoop, and axial prestress vectors caused by the pretensioning, respectively. In Eq. (4), $\mathbf{L}_r$ is the stress calculation matrix, an upper triangular matrix, with its element on the sth row and qth column $(q \geq s)$ given by

$$L_{r,sq} = -\frac{R_q^2}{R_q^2 - R_i^2}\left(1 - \frac{R_i^2}{R_s^2}\right) \tag{7}$$

where R_i is the inner radius of FSRWPV, see Fig. 2. Thus, $\mathbf{L}_r$ takes the following form:

$$
\mathbf{L}_r = -\begin{bmatrix}
1 & \frac{R_2^2}{R_2^2 - R_i^2}\left(1 - \frac{R_i^2}{R_1^2}\right) & \frac{R_3^2}{R_3^2 - R_i^2}\left(1 - \frac{R_i^2}{R_1^2}\right) & \cdots & \frac{R_m^2}{R_m^2 - R_i^2}\left(1 - \frac{R_i^2}{R_1^2}\right) \\
0 & 1 & \frac{R_3^2}{R_3^2 - R_i^2}\left(1 - \frac{R_i^2}{R_2^2}\right) & \cdots & \frac{R_m^2}{R_m^2 - R_i^2}\left(1 - \frac{R_i^2}{R_2^2}\right) \\
0 & 0 & 1 & \cdots & \frac{R_m^2}{R_m^2 - R_i^2}\left(1 - \frac{R_i^2}{R_3^2}\right) \\
\vdots & \vdots & \vdots & \ddots & \vdots \\
0 & 0 & 0 & \cdots & 1
\end{bmatrix} \tag{8}
$$

In Eq. (5), the matrix **M** is determined by the winding angle and is given by

$$
\mathbf{M} = \begin{bmatrix}
0 & 0 & 0 & \dots & 0 \\
\cos^2\alpha & 0 & 0 & \dots & 0 \\
0 & \cos^2\alpha & 0 & \dots & 0 \\
\vdots & \vdots & \vdots & \ddots & \vdots \\
0 & 0 & 0 & \dots & \cos^2\alpha
\end{bmatrix} \tag{9}
$$

and the upper triangular calculation matrix $\mathbf{L}_h$ is

$$
\mathbf{L}_h = -\begin{bmatrix}
\frac{2R_1^2}{R_1^2 - R_i^2} & \frac{2R_2^2}{R_2^2 - R_i^2} & \frac{2R_3^2}{R_3^2 - R_i^2} & \cdots & \frac{2R_m^2}{R_m^2 - R_i^2} \\
0 & \frac{R_2^2}{R_2^2 - R_i^2}\left(\mathrm{I} + \frac{R_i^2}{R_1^2}\right) & \frac{R_3^2}{R_3^2 - R_i^2}\left(1 + \frac{R_i^2}{R_1^2}\right) & \cdots & \frac{R_m^2}{R_m^2 - R_i^2}\left(1 + \frac{R_i^2}{R_1^2}\right) \\
0 & 0 & \frac{R_3^2}{R_3^2 - R_i^2}\left(1 + \frac{R_i^2}{R_2^2}\right) & \cdots & \frac{R_m^2}{R_m^2 - R_i^2}\left(1 + \frac{R_i^2}{R_2^2}\right) \\
\vdots & \vdots & \vdots & \ddots & \vdots \\
0 & 0 & 0 & \cdots & \frac{R_m^2}{R_m^2 - R_i^2}\left(1 + \frac{R_i^2}{R_{m-1}^2}\right)
\end{bmatrix} \tag{10}
$$

In Eq. (6), $\mathbf{P}_z = \sin^2\alpha\mathbf{F}$, and

$$
\mathbf{L}_z = \begin{bmatrix}
\frac{R_1^2}{R_1^2 - R_i^2} & \frac{R_2^2}{R_2^2 - R_i^2} & \frac{R_3^2}{R_3^2 - R_i^2} & \cdots & \frac{R_m^2}{R_m^2 - R_i^2} \\
0 & \frac{R_2^2}{R_2^2 - R_i^2} & \frac{R_3^2}{R_3^2 - R_i^2} & \cdots & \frac{R_m^2}{R_m^2 - R_i^2} \\
0 & 0 & \frac{R_3^2}{R_3^2 - R_i^2} & \cdots & \frac{R_m^2}{R_m^2 - R_i^2} \\
\vdots & \vdots & \vdots & \ddots & \vdots \\
0 & 0 & 0 & \cdots & \frac{R_m^2}{R_m^2 - R_i^2}
\end{bmatrix} \tag{11}
$$

3.3 Operating Stresses. FSRWPV can be regarded as integrated thick-walled pressure vessel, and hence Lamé formulas can again be employed for calculating stresses under the operating pressure. The radial stress vector is then determined by

$$
\boldsymbol{\sigma}_{r,\mathrm{ope}} = \mathbf{M}_r\mathbf{P}^T \tag{12}
$$

where **P** is the operating pressure vector and $\mathbf{M}_r$ is the corresponding radial stress calculation matrix as follows:

$$
\mathbf{M}_r = \begin{bmatrix}
\frac{R_i^2}{R_o^2 - R_i^2}\left(1 - \frac{R_o^2}{R_i^2}\right) & 0 & 0 & \cdots & 0 \\
0 & \frac{R_i^2}{R_o^2 - R_i^2}\left(1 - \frac{R_o^2}{R_1^2}\right) & 0 & \cdots & 0 \\
0 & 0 & \frac{R_i^2}{R_o^2 - R_i^2}\left(1 - \frac{R_o^2}{R_2^2}\right) & \cdots & 0 \\
\vdots & \vdots & \vdots & \ddots & \vdots \\
0 & 0 & 0 & \cdots & \frac{R_i^2}{R_o^2 - R_i^2}\left(1 - \frac{R_o^2}{R_{m-1}^2}\right)
\end{bmatrix} \tag{13}
$$

where R_o is the outer radius of FSRWPV, see Fig. 2.

In the same manner, we have

$$\boldsymbol{\sigma}_{h,\mathrm{ope}} = \mathbf{M}_h \mathbf{P}^T \tag{14}$$

where

$$\mathbf{M}_h = \begin{bmatrix} \frac{R_i^2}{R_o^2 - R_i^2}\left(1 + \frac{R_o^2}{R_i^2}\right) & 0 & 0 & \cdots & 0 \\ 0 & \frac{R_i^2}{R_o^2 - R_i^2}\left(1 + \frac{R_o^2}{R_1^2}\right) & 0 & \cdots & 0 \\ 0 & 0 & \frac{R_i^2}{R_o^2 - R_i^2}\left(1 + \frac{R_o^2}{R_2^2}\right) & \cdots & 0 \\ \vdots & \vdots & \vdots & \ddots & \vdots \\ 0 & 0 & 0 & \cdots & \frac{R_i^2}{R_o^2 - R_i^2}\left(1 + \frac{R_o^2}{R_{m-1}^2}\right) \end{bmatrix} \tag{15}$$

The axial stress vector is calculated from

$$\boldsymbol{\sigma}_{z,\mathrm{ope}} = \mathbf{M}_z \mathbf{P}^T \tag{16}$$

where

$$\mathbf{M}_z = \frac{R_i^2}{R_o^2 - R_i^2}\mathbf{I} \tag{17}$$

Here, **I** is an *m*th-order identity matrix.

3.4 Final Stress. The final stresses are calculated according to Eq. (1), i.e.,

$$\boldsymbol{\sigma}_{r,\mathrm{final}} = \boldsymbol{\sigma}_{r,\mathrm{pre}} + \boldsymbol{\sigma}_{r,\mathrm{ope}}$$

$$\boldsymbol{\sigma}_{h,\mathrm{final}} = \boldsymbol{\sigma}_{h,\mathrm{pre}} + \boldsymbol{\sigma}_{h,\mathrm{ope}}$$

$$\boldsymbol{\sigma}_{z,\mathrm{final}} = \boldsymbol{\sigma}_{z,\mathrm{pre}} + \boldsymbol{\sigma}_{z,\mathrm{ope}} \tag{18}$$

4 Controllable Stresses and Optimal Design of FSRWPV

It can be seen that $\boldsymbol{\sigma}_{\mathrm{pre}}$ depends on the pretensioning stress **F** and the winding angle α of flat steel ribbons, and $\boldsymbol{\sigma}_{\mathrm{ope}}$ is fixed if the operating pressure P is determined. Thus, the distribution of the final stresses in FSRWPV can only be adjusted by altering **F** and the winding angle α, however, in a rather simple way. If a particular distribution of final stresses in FSRWPV is desired, the corresponding **F** and α shall be determined from the following formula:

$$\boldsymbol{\sigma}_{\mathrm{pre}} = \boldsymbol{\sigma}_{\mathrm{final}} - \boldsymbol{\sigma}_{\mathrm{ope}} \tag{19}$$

The details for calculating the hoop, radial, and axial stresses are given in the following.

4.1 Hoop Stress. If we expect the final hoop stress is $\boldsymbol{\sigma}_{h,\mathrm{final}}$, the prestress due to the pretension is

$$\boldsymbol{\sigma}_{h,\mathrm{pre}} = \boldsymbol{\sigma}_{h,\mathrm{final}} - \boldsymbol{\sigma}_{h,\mathrm{ope}} \tag{20}$$

where $\boldsymbol{\sigma}_{h,\mathrm{ope}}$ is given in Eq. (14). Combining with Eq. (5) gives

$$(\delta_w \cos^2 \alpha \mathbf{L}_h \mathbf{R}^{-1} + \mathbf{M})\mathbf{F}^T = (\boldsymbol{\sigma}_{h,\mathrm{final}})^T - (\boldsymbol{\sigma}_{h,\mathrm{ope}})^T \tag{21}$$

from which **F** can be determined.

4.2 Axial Stress. The axial stress is related to the hoop stress and can be easily controlled through adjusting the winding angle α. If we want to arrive at $2\boldsymbol{\sigma}_{z,\mathrm{final}} = \zeta\boldsymbol{\sigma}_{h,\mathrm{final}}$, by continuously changing α and calculating $\Delta\boldsymbol{\sigma} = 2\boldsymbol{\sigma}_{z,\mathrm{final}} - \zeta\boldsymbol{\sigma}_{h,\mathrm{final}}$, we can compare $\Delta\boldsymbol{\sigma}$ to a small value $\boldsymbol{\varepsilon}$. If $\Delta\boldsymbol{\sigma} \leqslant \boldsymbol{\varepsilon}$, then the corresponding value of α is what we want. Here, ζ is the strength ratio between the two stresses, and is usually taken to be 1.0, meaning the strengths in the hoop direction and axial direction are equal for FSRWPV.

4.3 Radial Stress. Because the radial stress in FSRWPV is relatively small, it is not controlled in the present design method. Rather, it is determined from the other two stresses according to the equilibrium equations.

4.4 Optimal Design. From the above analysis, the flow chart

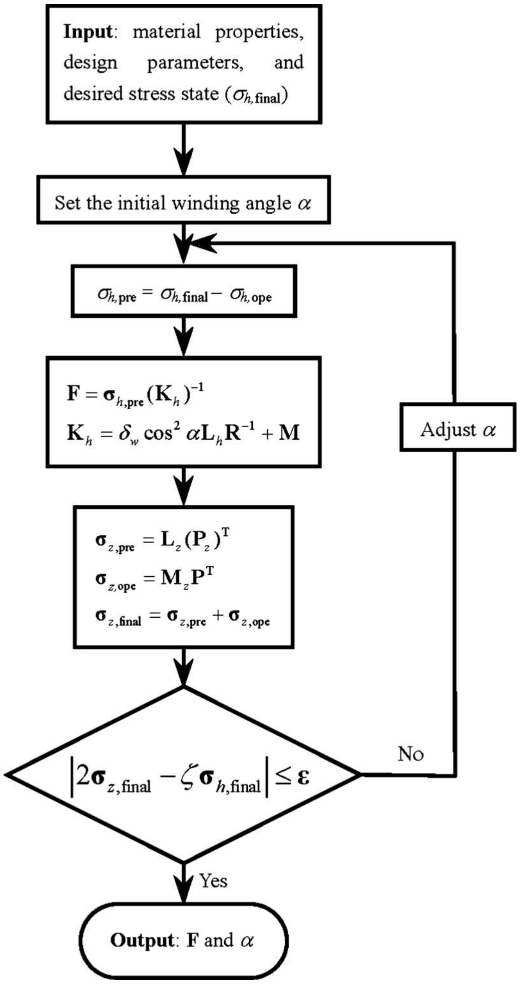

Fig. 4 Flow chart of optimal design

Table 1 Optimal results of pretension and the residual stresses in flat steel ribbon layers

Layer No. (k)	Inner shell	1	2	3	4	5	6	7	8	9	10	11	12
F_k		182.16	172.16	155.08	143.1	131.3	122.3	117.2	110.2	103.0	96.95	91.52	87.52
$\sigma_{h,\mathrm{pre}}$	−157.79	19.76	29.78	30.26	31.15	32.21	32.99	36.75	37.96	38.05	38.45	38.71	39.65
Layer No. (k)		13	14	15	16	17	18	19	20	21	22	23	24
F_k		85.89	80.89	78.20	77.20	75.26	71.26	69.77	68.77	66.77	65.77	64.88	64.88
$\sigma_{h,\mathrm{pre}}$		41.17	41.62	42.46	44.45	45.51	45.71	45.75	47.08	47.46	48.54	49.62	51.51

of optimal design is given in Fig. 4. In the practical design and manufacture, usually α can be chosen based on experience, and this can simplify the calculation. After several times of calculation, **F** and α can be determined, and a FSRWPV can be manufactured accordingly, which shall have an optimized stress distribution along the wall thickness.

5 Application

5.1 Parameters. A real FSRWPV has been designed and manufactured with 24 layers of flat steel ribbons according to the present approach. The parameters are given as follows: The operating pressure is 32 MPa; the inner diameter is 1000 mm; the thickness of the inner shell is 20 mm; the thickness and width of the flat steel ribbon are 3.8 mm and 8 mm, respectively; the material of the inner shell is 304(0Cr18Ni9) with the allowable stress $[\sigma]=137$ MPa; and the flat steel ribbon is made of 16MnR (SA516Gr70) with the allowable stress $[\sigma]=186.7$ MPa.

5.2 Stresses Optimal Analysis Result. As the design objects, the final stress shall be uniform in every flat steel ribbon layer and shall be zero in the inner shell when the vessel is in operation. In order to achieve this target, the flow chart in Fig. 4 is followed by letting $\varepsilon=1.0$ and the initial winding angle $\alpha=25$ deg. The strength ratio is also selected as $\zeta=0.95$, which indicates that the strength in the axial direction is a little stronger than that in the hoop direction. One optimal solution is eventually found with $\alpha=27.7$ deg and the pretensioning stresses $F_k(k=1,2,\cdots,24)$ (MPa) given in Table 1. The corresponding residual hoop stresses (MPa) are also listed in the table.

The FSRWPV manufactured according to above values of **F** and α has a uniform hoop stress distribution along the wall thickness in the flat steel ribbon layers at $\sigma_{h,\mathrm{final}}=181.1$ MPa and a zero hoop stress in the inner shell when it is operated under a pressure of 32 MPa. The corresponding axial stress can be found to be 172 MPa. The distributions of prestress-state, residual, and final hoop stresses are shown in Figs. 5–7, respectively.

It is clear that any stress distribution could be achieved by following the optimal design flow summarized in Fig. 4.

5.3 Application and Validation. Usually, the residual stresses in FSPWPV are obtained by measuring the axial and circumferential shrinkages after manufacture [4,5,17]. Here, this simple but proper method is also adopted. Before steel ribbons are wound, the interior perimeter and length of the inner shell are measured to be 1006.7 mm and 10143.5 mm, respectively. After all flat steel ribbons are wound, its axial length and interior perimeter become 10139.7 mm and 1004.3 mm, respectively. This means that the axial and circumferential shrinkages are 3.8 mm and 2.4 mm respectively. The axial residual stress and hoop residual stress can then be calculated to be 77.2 MPa and 156.4 MPa, respectively. It proves that the axial strength almost equals to the hoop strength at this winding angle under pretension **F**. Because the FSRWPV is a linear elastic body, and the axial stress is connected with the hoop stress through the winding angle α, the ratio of its axial strain to hoop strain must keep the same whenever under interior operating pressure or pretension **F**. In fact, when the FSRWPV is tested under hydraulic pressure of 32 MPa, the length of FSRWPV is 10143.3 mm. This proves that the axial stress in the inner shell of FSRWPV is still negative stress under the operating pressure, and the residual stress is approximately zero. Though we do not measure the interior perimeter in this practical FSRWPV, it matches the theoretical value very well [18], and therefore its hoop stress also approaches zero under the operating pressure. In conclusion, according to this optimal designing method that appropriately adjusts residual stress and keeps axial strength equal to hoop strength, the final stress distribution in FSRWPV can be even.

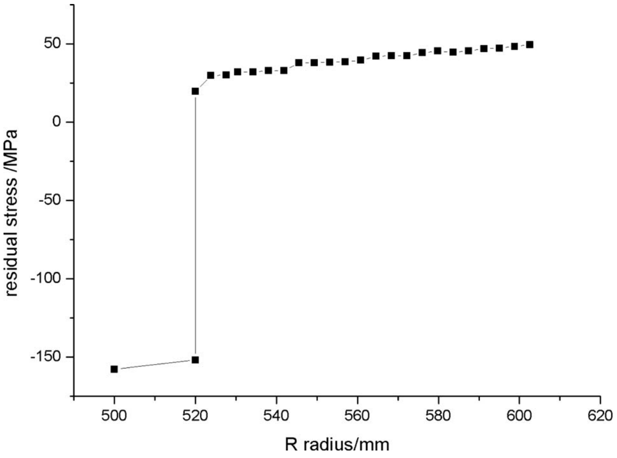

Fig. 5 Residual hoop stress

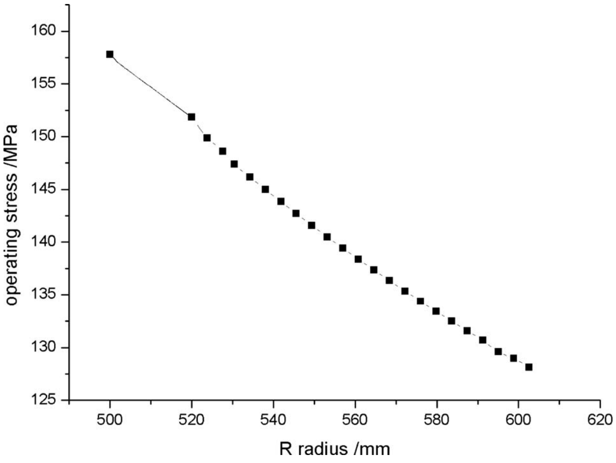

Fig. 6 Operating hoop stress

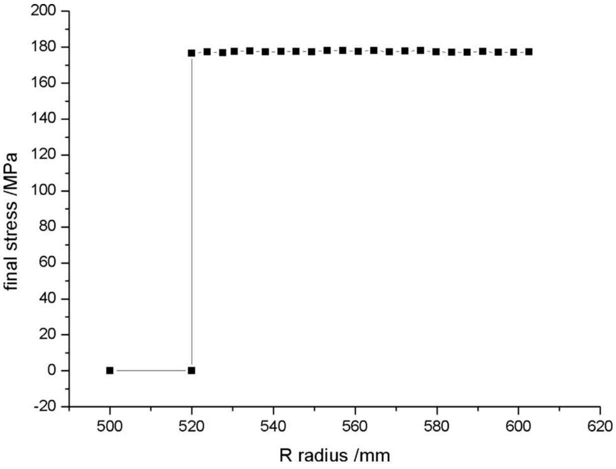

Fig. 7 Final hoop stress

6 Conclusion

The structure of FSRWPV has a discrete structure and pretension can be incorporated into the wounded steel ribbons in an arbitrary way. The well-known Zhu's model is further extended to a multilayered cylindrical vessel model, which involves the effect of prestress in the flat steel ribbon layers and in the inner cylindrical shell. Based on this analytical model, an optimal design method is presented, by which ideal stress distribution in FSRWPV in operation can be obtained through adjusting the pretensions in flat steel ribbons as well as the winding angle.

An example of a large FSRWPV, which is operating in high-pressure hydrogen gas storage station, was designed and manufactured according to the optimal approach, and finally was demonstrated in this paper.

Nomenclature

$\mathbf{F}$ = pretensioning stress vector of the flat steel ribbons, MPa
F_k = pretensioning stress of the kth flat steel ribbon, MPa
$\mathbf{I}$ = identity matrix
$\mathbf{L}_r$ = calculation matrix for radial stress in the prestress state
$\mathbf{L}_h$ = calculation matrix for hoop stress in the prestress state
$\mathbf{L}_z$ = calculation matrix for axial stress in the prestress state
$\mathbf{M}$ = matrix related to the winding angle of flat steel ribbon
$\mathbf{M}_r$ = calculation matrix for radial stress in operation
$\mathbf{M}_h$ = calculation matrix for hoop stress in operation
$\mathbf{M}_z$ = calculation matrix for axial stress in operation
$\mathbf{P}_z$ = axial pressure, MPa
$\mathbf{P}_r$ = radial pressure, MPa
R_i, R_j = inner and outer radii of the inner shell, mm
R_o = outer radius of FSRWPV, mm
R_k = inner radius of the kth layer of flat steel ribbon, $k=1,2,\ldots,m$, mm
α = winding angle of the flat steel ribbon, deg
δ_i = thickness of the inner shell, mm
δ_w = thickness of a single flat steel ribbon, mm
$\boldsymbol{\sigma}_h$, $\boldsymbol{\sigma}_r$, $\boldsymbol{\sigma}_z$ = hoop, radial, and axial stresses, MPa
σ_{rk} (P_{rk}) = stress acting on the finished part of vessel caused by F_k, MPa
σ_{Fk} = stress in the ribbon direction, MPa
$[\sigma]$ = allowable stress, MPa
ζ = strength ratio
ε = small controlling parameter in the optimal design

Subscripts

final = stress corresponding to the final state
pre = stress corresponding to the pretension
ope = stress corresponding to the operation

References

[1] Huang, P. S., 1993, "Prestress Analysis of Flat Steel Ribbon Wound Vessel," ASME J. Pressure Vessel Technol., **115**, pp. 305–308.

[2] ASME Boiler and Pressure Vessel Code, Section VII, Division 1 and 2, 1996, 1997, Code Cases 2229, 2269, "Design of Layered Vessels Using Flat Steel Ribbon Wound Cylindrical Shells."

[3] Shah, M., and Zhu, G. H., 2004, "Steel Composite Structural Pressure Vessel Technology: Future Development Analysis of Worldwide Important Pressure Vessel Technology," Process Saf. Prog., **23**(1), pp. 65–71.

[4] Zheng, C. X., 2006, "The Research of Reasonable Winding Angle of Ribbons of Flat Steel Ribbon Wound Pressure Vessel," J. Zhejiang Univ., Sci., **7**(3), pp. 438–442, in Chinese.

[5] Zhu, G. H., 1995, *Chinese Steel Ribbon Wound Pressure Vessel*, Machinery Industry Publishing, Beijing, China, in Chinese.

[6] Martikka, H., 2001, "Optimum Design of Industrial Vessels for Prescribed Loads to Obtain Customer Satisfying Material Selections and Dimensions," *Proceedings of the International Conference on Computer Aided Optimum Design of Structures*, OPTI, Vol. 7, pp. 63–72.

[7] Zheng, C. X., 2006, *Composite Material Pressure Vessels*, Chemical Industry, Beijing, China, in Chinese.

[8] Huang, P. S., Zhu, G. B., and Barron, R., 1993, "Prestress Analysis of Flat Steel Ribbon-Wound Vessel," ASME J. Pressure Vessel Technol., **115**(2), pp. 171–176.

[9] Urbaniec, K., 1988, *Optimal Design of Process Equipment*, Wiley, New York.

[10] Carroll, N., and McElhaney, M., 2003, "Optimization of a Rotationally Molded Pressure Vessel," *Proceedings of Annual Technical Conference-ANTEC*, Vol. 1, pp. 1246–1249.

[11] Wang, Z. W., 2005, *Pressure Vessel Design*, Chemical Industry, Beijing, China, in Chinese.

[12] Jahed, H., Farshi, B., and Karimi, M., 2006, "Optimum Autofrettage and Shrink-Fit Combination in Multi-Layer Cylinders," ASME J. Pressure Vessel Technol., **128**(2), pp. 196–200.

[13] Tierney, J., Andersen, S., Yarlagadda, S., Gillespie, J. W., Jr., Hyland, E., Crayon, D., Littlefield, A., Tzeng, J., and Burton, L., 2005, "Optimal Design of Cylindrical Steel/Composite Hybrid Structures for Gun Barrel Applications," *Proceedings of the International SAMPE Symposium and Exhibition (SAMPE 05: New Horizons for Materials and Processing Technologies)*, Vol. 50, pp. 3267–3281.

[14] Malinowski, M., and Magnucki, K., 2005, "Optimal Design of Sandwich Ribbed Flat Baffle Plates of a Circular Cylindrical Tank," Int. J. Pressure Vessels Piping, **82**(3), pp. 227–233.

[15] Rajan, K. M., 2002, "Experimental Studies on Bursting Pressure of Thin-Walled Flow Formed Pressure Vessels," J. Mater. Process. Technol., **125–126**, pp. 228–234.

[16] Huang, P. S., and Friedrich, C. R., 1994, "New Approach to Stress Analysis of Various Wound Vessels," ASME J. Pressure Vessel Technol., **116**(4), pp. 359–364.

[17] Zheng, J. Y., Zhu, G. H., 1992, "Experimental Research of Residual Stresses of Flat Steel Ribbon Wound Pressure Vessel," Petro-Chemical Equipment, **21**(1), pp. 6–8

[18] Yu, Z. H., 1999, "Strengthened Action of Frictional Force of FSRWPV," Modern Machinery, **2**, pp. 34–37.

Stability Analysis of an Inflatable Vacuum Chamber

Sean A. Barton
Department of Physics,
Florida State University,
Tallahassee, FL 32306

A lightweight "inflatable" tensioned-membrane-structure vacuum container is proposed and its stability is analyzed. The proposed structure consists of a pressurized lobed cylindrical "wall" surrounding a central evacuated space. Stability is analyzed by discretizing the system and diagonalizing the second derivative of the potential energy. The structure is found to be stable when the pressure in the wall is greater than a critical pressure. When membranes are nonelastic, the critical pressure is found to be greater than the pressure required for equilibrium by a factor of 4/3. When membranes have only finite stiffness, a first-order correction to the critical pressure is found. Preliminary experimental data show that a stable structure can be made in this way, and that the observed critical pressure is consistent with theory. It is also found that such structures can be designed to have net positive buoyancy in air. [DOI: 10.1115/1.2912742]

Introduction

A structurally stable vacuum container that is of minimal total mass for a given evacuated volume might have applications in airship design (buoyancy control) [1], aerospace (low aerodynamic drag magnetic levitation launch systems) [2], industry (large industrial vacuum chambers), transportation (supersonic maglev trains) [2], and solar energy production (solar chimney technology) [3]. Unfortunately, issues of structural stability are often overwhelming in the design of such a structure.

The history of lightweight vacuum containers is somewhat disconnected. Von Guericke created the first artificial vacuum around 1654 [4]. Traditional containers were thick heavy shells, the thickness being required to give sufficient stability to prevent buckling. In 1878, Tracy patented an "aircraft" that aimed to derive lift from the buoyancy of a vacuum enclosed in an unstable lightweight container [5]. In 1921, Armstrong patented another such craft that claimed to stabilize its vacuum volume in an, in fact, unstable inflated tensioned shell [6]. More recently, Michaelis and Forbes have discussed the basic forces required to achieve equilibrium (not stability) in a tensional vacuum vessel and have proposed the lightweight or weightless inflatable vacuum chamber [7]. Lennon and Pellegrino have discussed the stability of inflated structures [8]; however, a stability analysis of an inflated vacuum vessel (the purpose of the current work) has not been carried out.

In the current work, we propose an axially symmetric "cylindrical" structure composed of a "wall" surrounding a central evacuated volume. The wall consists of pressurized regions within a network of tensioned membranes. Rigorous stability analysis is carried out by (a) discretizing the degrees of freedom of the system, (b) forming the matrix, which represents the second derivative of the potential energy with respect to these degrees of freedom, and (c) diagonalizing the matrix to confirm positive definiteness and, hence, stability. The proposed structure is found to be stable when sufficiently pressurized. Judicious choice of membrane materials and pressurizing gas can lead to a structure that has over half of its total volume completely evacuated and net positive buoyancy in air.

Proposed Structure

The proposed structure is shown and described in Fig. 1 and the caption thereof. The inspiration for the present design is as follows. The radial members must exist to transmit the tension, which will prevent the inner membrane from imploding. One can see this by considering the mean stress tensor in the wall required to give equilibrium as indicated by the method of sections. The hydrostatic pressure of the gas contributes positively and equally to all three eigenvalues of the mean stress tensor, but the method of sections indicates (for any circular cylinder subjected to hydrostatic pressure from inside or outside) that the eigenvalues of the mean stress tensor in the wall must be in the approximate ratio of 2 to 1 to 0 in the circumferential, axial, and radial directions, respectively. Thus (in addition to the hydrostatic pressure), there must exist members under tension (the membranes) that contribute negatively to the eigenvalues corresponding to the radial and axial directions. Thus, one adds membranes in the plane of the axial and radial directions to carry these tensions. The lobes are then added to terminate these tensions. If the curvature of the lobes is decreased (compared to Fig. 1), the tension in the lobes is increased and somewhat redirected such that the eigenvalue of the mean stress tensor in the circumferential direction is reduced requiring additional pressure to maintain equilibrium. This is undesirable and thus the curvature in the lobes is kept at the maximum permitted by geometrical constraints. These radial members and lobes are sufficient to establish equilibrium; however, this geometry is highly unstable through what one might call the "accordion" effect, similar to the instability of the hypothetical inflated lobed column described in the introduction of Ref. [8]. Thus, the addition of the circumferential members is necessary to eliminate this instability.

Here, we briefly consider some practical points related to the fabrication and use of such a vacuum chamber. Likely, pressure will be supplied to a single compartment and inter-compartmental holes will allow pressure to distribute to all compartments. We note, for equilibrium, that the axial tension in each membrane is approximately one-half the tension in the perpendicular direction. We also note that the vacuum chamber will require additional structures to close and seal the ends. The ends of the chamber may be capped with a single membrane in the form of a concave hemisphere. It might also be capped with a complex network of membranes that extend the cylindrical wall into a convex hemispherical wall that closes the end. Where weight of the ends is of little concern, the end might be capped with a traditional compressive structure. We also note that the weight of the end structures as a fraction of the total weight is inversely proportional to the length and thus is negligible for long chambers. For chambers where the length to diameter ratio is small, the end structures may enhance

---

Contributed by the Applied Mechanics Division of ASME for publication in the Journal of Applied Mechanics. Manuscript received February 16, 2007; final manuscript received November 26, 2007; published online May 14, 2008. Review conducted by Edmundo Corona.

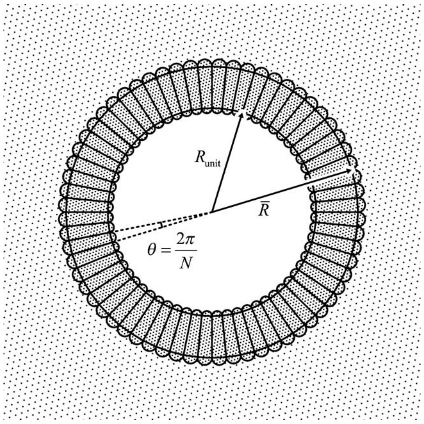

Fig. 1 General cross section of the proposed structure. The wall of the structure is composed of membranes under tension (solid lines) containing pressurized gas (heavily hatched area). The wall encloses the evacuated space at the center (unhatched area) isolating that space from the ambient pressure (lightly hatched area). R_{unit}, $\bar{R}$, and N are the inner radius, outer radius, and number of sections, respectively.

equilibrium and stability; in our analysis, however, we will consider the situation where the end structures are very far from the section under analysis.

Note About Units

Before analyzing the proposed structure, we first define our notational convention. Each physical quantity with appropriate units is represented by a barred symbol (i.e., $\bar{R}$); each corresponding "reduced" quantity (a dimensionless number which is the physical quantity divided by a reference value) is denoted by the unbarred symbol (i.e., R). Many of the equations that follow are more conveniently expressed in terms of these dimensionless quantities. The reference values for the physical parameters are indicated with a subscript "unit" (i.e., R_{unit}) and are given in Appendix A. For example, the reduced values of tension, potential energy, and outside radius are

$$T \equiv \frac{\bar{T}}{T_{\text{unit}}}, \quad U \equiv \frac{\bar{U}}{U_{\text{unit}}}, \quad R \equiv \frac{\bar{R}}{R_{\text{unit}}}$$

respectively. In the text, we will refer to the physical quantities and the reduced quantities interchangeably. For example, we will refer to both $\bar{U}$ and U as "potential energy," which meaning is intended will be clear from the context.

Modeling of the Proposed Structure

We wish to analyze the stability of the structure depicted in Fig. 1. The structure is axially symmetric and of uniform cross section, i.e., invariant under translations in the direction perpendicular to the plane of the drawing. We will analyze the most general form of this system having N sections ($N=64$ in Fig. 1) and having an outside tension hoop of vertex radius R (reduced), where the vertex radius of the inside tension hoop is taken to be the reference length R_{unit} ($R \equiv \bar{R}/R_{\text{unit}} \cong 1.4$ in Fig. 1). For structural considerations, the central vacuum will be assumed to be "complete" (absolute pressure of exactly 0 atm). The absolute pressure within the wall is P (where the reference pressure P_{unit} is the ambient pressure). (Recall $P \equiv \bar{P}/P_{\text{unit}}$.)

In order to analyze the equilibrium and stability of the system, we must write its potential energy U as a function of configuration or deformation. We characterize the configuration of the system by coordinates x_{ni} specifying the radial and circumferential displacements of the N inside vertices and the N outside vertices according to the convention established in Fig. 2. Note in Fig. 2 that the first subscript specifies which unit cell and that the second subscript specifies which degree of freedom within the unit cell. Thus, $x_{ni}=0$ characterizes the nominal, intended, or undeformed configuration, which corresponds to an extremum (local minimum, local maximum, or saddle point) in the total potential energy for any given value of P. One then writes U as a function of these x_{ni}. For equilibrium (or instantaneous balance of forces), one needs only to confirm that the first derivatives of U with respect to the x_{ni} are all zero. For stability, the second derivative of U with respect to any and all linear combinations of the x_{ni} must be nonnegative. Third- and higher-order derivatives are neglected in stability analysis as displacements are assumed to be small. For this reason, our representation of U need be valid only to second order about the nominal configuration.

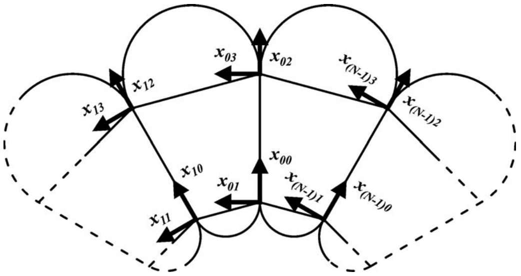

Fig. 2 Definition of the 4N degrees of freedom of the structure x_{ni}

In order to write an expression for U, we consider the forms of potential energy that the system possesses. The system has two types of potential energy, "solid-elastic" energy and "pressure-volume" energy. Each tensioned membrane has a solid-elastic energy of the form

$$\Delta U_{\text{membrane}} = T\Delta l + \frac{1}{2}K\Delta l^2 \tag{1}$$

where Δl is the change in length of the membrane relative to the equilibrium configuration, T is the pretensioning, and K is the elastic constant. This equation is valid only to second order in Δl and thus the representation of Δl need be valid only to second order in the x_{ni}. To achieve equilibrium, T will be different for different membranes and since the elastic constant of a membrane K depends on its length, thickness, and elastic modulus, K will also be different for different membranes.

Each volume under pressure has a pressure-volume energy of the form

$$\Delta U_{\text{gas}} = -\Delta p \Delta V \tag{2}$$

where Δp is the difference in pressure across the boundary defining the volume and ΔV is the change in volume relative to the equilibrium configuration. In order for this equation to be valid to second order in ΔV, one must make the simplifying assumption that the pressure P is constant during any change in volume. Thus, we assume the structure is connected to a large reservoir that maintains constant pressure. If this is not true, pressure can increase with a decrease in volume, thus enhancing stability. This assumption can lead to a false conclusion that the system is unstable but can never lead to a false conclusion that the system is stable. We call this a "failure-safe" assumption. As with Δl, the representation of ΔV must be valid to second order in the x_{ni}.

To simplify the form of U, we note that all pairs of circumferential nearest-neighbor vertices are connected by a curved membrane and a straight membrane that enclose a pseudosemicylindrical volume. The solid-elastic energy of these two membranes and the pressure-volume energy of the enclosed space are all determined only by the distance between the pair of vertices. Thus, there is no need to separately represent these energies in U as they

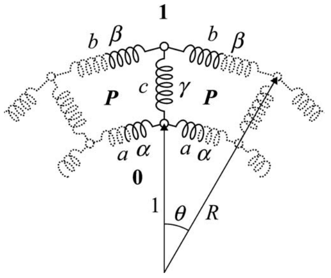

Fig. 3 One "unit cell" of the idealized model of the system showing the pretension *c*, the spring constant γ, the effective pretensions *a* and *b*, the effective spring constants α and β, and pressures in bold type

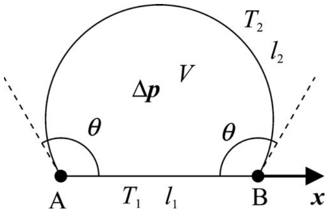

Fig. 4 Subsystem for illustrating the meaning of effective tension

can be absorbed into a single hypothetical "spring" with an "effective" pretensioning T and an effective elastic constant K (see a, α, b, and β defined in the caption of Fig. 3).

As an example of an effective tension, take the subsystem of Fig. 4 consisting of two nodes, two membranes, and the enclosed pressurized volume. (Here, in this example, the symbols θ and x are unrelated to previous uses of the same symbols.) We can write the potential energy of the subsystem as a power series in the horizontal displacement of Point B, x.

$$U = U_0 + xU_1 + \frac{1}{2}x^2U_2 + \frac{1}{3!}x^3U_3 + \dots \quad \text{where } U_1 = \frac{dl_1}{dx}T_1 + \frac{dl_2}{dx}T_2 - \frac{dV}{dx}\Delta p = T_1 + T_2 \cos\theta$$

We now identify U_1 as the effective tension between Point A and Point B and we see that it can be calculated from the membrane tensions (T_1 and T_2). (Note that if θ is greater than 90 deg and T_2 is sufficiently large compared to T_1 the effective tension U_1 can be negative.)

Again to simplify calculation, we assume that there is an infinitesimal clearance angle between the curved membranes so that we need not consider their interference with each other. If they were to interfere, stability would be enhanced as this is an additional constraint on the system. Again, this is a failure-safe assumption.

Stability Analysis

The Δl's and the ΔV's are written as polynomials in the x_{ni} retaining terms up to second order. These polynomials are inserted into the general forms of $\Delta U_{\text{membrane}}$ and ΔU_{gas} to give U, which we write as a power series in x_{ni},

$$U = U_0 - \sum_{ni} F_{ni}x_{ni} + \sum_{nimj} \frac{1}{2}K_{nimj}x_{ni}x_{mj} + \dots \tag{3}$$

where $U_0 \equiv U|_{x=0}$, $-F_{ni} \equiv \partial U/\partial x_{ni}|_{x=0}$, and $K_{nimj} \equiv \partial^2 U/\partial x_{ni}\partial x_{mj}|_{x=0}$ (necessarily symmetric). (Here the symbol K_{nimj} is unrelated to the previously used symbol K in Eq. (1).) In Eq. (3), K_{nimj} can be thought of as a "block" matrix [9] (p. 8) and F_{ni} and x_{ni} can be thought of as "block" vectors. We are able to find all of the elements of F_{ni} and K_{nimj} by considering the contributions to Eq. (3) from all of the hypothetical springs (1) and the pressurized volumes (2) of Fig. 4 (see Appendixes B and C for example contributions). Because the potential energy is relative, we are free to set $U_0=0$. For equilibrium (all $\ddot{x}_{ni}=0$), we require $F_{ni}=0$. It can be shown (see Appendix B and C) that $F_{n0}=SC-4\delta^2A-2\varepsilon P$, $F_{n2}=-SC-4\delta^2RB+2\varepsilon RQ$, and $F_{n1}=F_{n3}=0$ where (for notational convenience) we have defined $S\equiv R-1$, $C\equiv c/S$, $A\equiv a/2\delta$, $B\equiv b/2\delta R$, $Q\equiv P-1$, $D\equiv\cos(\theta/2)$, $\delta\equiv\sin(\theta/2)$, $E\equiv\cos(\theta/2)$, and $\varepsilon\equiv\sin(\theta/2)$ as in "Nomenclature" below. Notice that the A, B, and C terms originate from the membranes and the P and Q terms originate from the pressurized gas. These conditions lead to $A=(SC-2\varepsilon P)/4\delta^2$ and $B=-(SC+2\varepsilon RQ)/4\delta^2R$ but do not lead to a unique solution for A, B, and C. By the method of sections, we find that the tension in a membrane T, the radius of cylindrical curvature of the membrane r, and the pressure difference across the membrane Δp are related by $\Delta p\cdot r=T$. This determines the tension in the curved membranes of the outer and inner lobes. Then requiring that the tension in the tension hoops be non-negative, we find a constraint on the tension in the radial membranes,

$$\frac{2\delta P}{DS} \le C \le \frac{2\delta RQ}{DS} \tag{4}$$

and since the left hand side (LHS) of Eq. (4) must be less than the right hand side (RHS), we find

$$P \geqslant \frac{R}{R-1} \tag{5}$$

as shown by Michaelis and Forbes [7].

It can now be seen (given the spectrum of solutions for A, B, and C) that the system is statically indeterminate. The actual values of A, B, and C will (in practice) depend on the precise unstressed lengths of the membranes. Slight variations in these unstressed lengths will determine the distribution of forces (and C) when the load (pressure) is applied. The value of C may be difficult to control without very precise means of manufacture; however, we will assume that the structure can be fabricated with enough precision that C can be made to fall within the range required for equilibrium (4). In practice, one may test the structure through inflation to determine C. If C is found to lie outside the desired range, the inner or outer tension hoops may be lengthened or shortened to adjust C. One may note that the minimum value of C (4) corresponds to zero tension in the inner tension hoop, the maximum value of C (4) corresponds to zero tension in the outer tension hoop, and the minimum value of P (5) corresponds to zero tension in both the inner and outer tension hoops.

Note that, while it is true that the pretensioning in a membrane cannot be negative, no such restriction applies to an effective tension (as illustrated in the example of Fig. 3); for example, the effective tension b is often negative.

Returning to the stability analysis, we wish to explore only infinitesimal deformations about the equilibrium position and thus terms third order in x_{ni} are negligible compared to the second-order terms. Thus, we write simply $U=\sum_{nimj}\frac{1}{2}K_{nimj}x_{ni}x_{mj}$ or equivalently

$$U = \frac{1}{2}\sum_{nimj} x^*_{ni}K_{nimj}x_{mj} \tag{6}$$

(where the asterisk "*" denotes complex conjugate) as we are free to do because the x_{ni} are real. Recall that K_{nimj} is symmetric and real and thus Hermitian and therefore has orthogonal eigenvectors [9] (p. 268). For stability, K_{nimj} must be such that no real x_{ni} leads to a U that is less than zero. To determine if K_{nimj} is of such form, we wish to make unitary transformation to a new basis $\chi_{k\mu} = \sum_{k\mu ni}X_{k\mu ni}x_{ni}$, where

$$U=\frac{1}{2}\sum_{k\mu l\nu}\chi_{k\mu}^{*}\kappa_{k\mu l\nu}\chi_{l\nu} \tag{7}$$

such that $\kappa_{k\mu l\nu}=\delta_{kl}\delta_{\mu\nu}\kappa_{k\mu}=\Sigma_{nimj}X_{k\mu ni}K_{nimj}X_{mjl\nu}^{\dagger}$ the dagger denotes the Hermitian conjugate (e.g., $X_{mjl\nu}^{\dagger}=X_{l\nu mj}^{*}$), and δ_{kl} is the Kronecker delta symbol (i.e., the matrix elements of the identity matrix). Thus, we have made a unitary similarity transformation to the diagonal representation of K_{nimj}, where the $X_{k\mu ni}$ (which define the similarity transform) are the orthogonal eigenvectors of K_{nimj} with the eigenvalues $\kappa_{k\mu}$. The condition of stability is satisfied when the $\kappa_{k\mu}$ are non-negative. Thus, our problem reduces simply to confirming that K_{nimj} is positive semidefinite (or non-negative definite [9] (p. 7)).

Confirming that K_{nimj} is Positive Semidefinite

Beginning with K_{nimj}, we make unitary similarity transformations with the goal of eventually finding the diagonal representation of K_{nimj}. Because the system has rotational symmetry and couplings only between nearest-neighbor unit cells, we can write $K_{nimj}=\delta_{nm}G_{ij}+\delta_{(n+1)m}J_{ij}+\delta_{(n-1)m}J_{ij}^{\mathrm{T}}$, where G describes the couplings within a unit cell and J describes the couplings between neighboring unit cells. (Given the cylindrical symmetry, the Kronecker delta symbol is understood to function cyclically (e.g., $\delta_{0N}=1$).) With the intent to diagonalize K_{nimj} we note the symmetry $K_{nimj}=K_{(n+1)i(m+1)j}$ and thus K_{nimj} commutes with the operation of rotating the entire system by one unit cell, $\hat{\mathbf{\Phi}}$ (the matrix elements of which are $\hat{\Phi}_{nimj}\equiv\delta_{(n+1)m}\delta_{ij}$). Moreover, because matrices that commute can be simultaneously diagonalized, each eigenvector of K_{nimj} must completely lie within a subspace spanned by the degenerate eigenvectors of $\hat{\mathbf{\Phi}}$ characterized by a single eigenvalue. Thus if we transform to a basis of the eigenvectors of $\hat{\mathbf{\Phi}}$, K_{nimj} becomes block diagonal in blocks corresponding to the distinct eigenvalues of $\hat{\mathbf{\Phi}}$. We note that the eigenvectors of any translation operator are Fourier components. Thus, following a technique similar to that used in Ref. [10], we block diagonalize K_{nimj} with a Fourier transform V_{kn} to give

$$K'_{kilj}=\sum_{nm}V_{kn}K_{nimj}V_{ml}^{\dagger} \tag{8}$$

where $V_{kn}\equiv e^{-ikn\theta}/\sqrt{N}$. We find

$$K'_{kilj}=\sum_{nm}\frac{e^{i(lm-kn)\theta}}{N}(\delta_{nm}G_{ij}+\delta_{(n+1)m}J_{ij}+\delta_{(n-1)m}J_{ij}^{\mathrm{T}})=\delta_{kl}(G_{ij}$$
$$+e^{ik\theta}J_{ij}+e^{-ik\theta}J_{ij}^{\mathrm{T}})\equiv\delta_{kl}K'_{kij} \tag{9}$$

and thus the diagonal blocks of K'_{kilj} are

$$K'_{kij}=G_{ij}+e^{ik\theta}J_{ij}+e^{-ik\theta}J_{ij}^{\mathrm{T}} \tag{10}$$

We again realize that there must exist an additional transformation $W_{k\mu i}$ such that $\Sigma_{ij}W_{k\mu i}K'_{kij}W_{kj\nu}^{\dagger}=\delta_{\mu\nu}\kappa_{k\mu}$ (i.e., $W_{k\mu i}V_{kn}=X_{k\mu ni}$), where $W_{kj\nu}^{\dagger}=W_{k\nu j}^{*}$ and thus the $W_{k\mu i}$ are the eigenvectors of K'_{kij} with eigenvalues $\kappa_{k\mu}$. Thus, our problem further simplifies to confirming that each K'_{kij} has no negative eigenvalues. By considering all contributions to U, such as $\Delta U_{\mathrm{membrane}}$ (1) and ΔU_{gas} (2) (see Appendix B and C, respectively, for examples), one can determine the matrix elements of G_{ij} and J_{ij}. For example, G_{00} is the self-coupling elastic constant for any inside node moving in the radial direction. This takes major contributions from the elastic constant of the radial membrane γ and the effective tension in the inside tension hoop a. It can be shown that $G_{00}=\gamma+2D^2A+2\delta^2\alpha$, $G_{11}=C+2\delta^2A+2D^2\alpha$, $G_{22}=\gamma+2D^2B+2\delta^2\beta$, $G_{33}=C+2\delta^2B+2D^2\beta$, $G_{02}=G_{20}=-\gamma$, $G_{13}=G_{31}=-C$, and all other elements in G_{ij} equal zero, and that $J_{00}=-D^2A+\delta^2\alpha+\varepsilon P$, $J_{11}=\delta^2A-D^2\alpha+\varepsilon P$, $J_{22}=-D^2B+\delta^2\beta-\varepsilon Q$, $J_{33}=\delta^2B-D^2\beta-\varepsilon Q$, $J_{01}=-J_{10}=\varepsilon A+\varepsilon\alpha+EP$, $J_{23}=-J_{32}=\varepsilon B+\varepsilon\beta-EQ$, and all other elements in J_{ij} equal zero.

To aid in confirming the positive definiteness of each K'_{kij}, we will assume that all of the elastic constants (α, β, and γ) are large compared to the other variables (A, B, C, P, and Q). This approximation is often valid for inflatable structures because the effective elastic modulus (or Young's modulus) of an ideal diatomic gas is only 1.4 times its effective yield strength (or pressure). This is in contrast to solids, which often have elastic moduli several orders of magnitude larger than their yield strengths. Thus, compared to gases, solids are "stiff." The same approximation was made by Lennon and Pellegrino in their analysis [8]. We will call this the "stiff-solid" approximation. We will later reexamine this approximation to find a first-order correction. We know that α, β, and γ must give positive contributions to the eigenvalues as they represent springs with only positive spring constants. Thus, in the limit that they are large, the only possibility of finding a negative eigenvalue will be to look in the null space of the α, β, and γ terms.

Now neglecting A, B, C, P, and Q terms and considering only α, β, and γ terms in K'_{kij}, we have K''_{kij}. A simple analysis indicates that K''_{kij} has exactly one null vector (unnormalized)

$$\begin{bmatrix}-i\delta\sin\frac{k\theta}{2} & \varepsilon\cos\frac{k\theta}{2} & -i\delta\sin\frac{k\theta}{2} & \varepsilon\cos\frac{k\theta}{2}\end{bmatrix}$$

for each k except $k=0$. When $k=0$, one finds the two null vectors, [0 1 0 0] and [0 0 0 1].

Thus, we have found two potentially unstable modes for $k=0$ and one for every other k for a total of $N+1$ modes allowed within the stiff-solid approximation. The remaining $3N-1$ modes have eigenvalues going to positive infinity in the stiff-solid approximation and are thus stable and not of interest. We are interested only in the $N+1$ modes in which the elastic constants α, β, and γ do not contribute to the eigenvalue and thus the stability is governed by the pressure differences. It is in this $N+1$ dimensional space that we expect to find the $N+1$ noninfinite energy eigenmodes of the system. For $k=0$, which allows more than one mode, we must again diagonalize in that two-dimensional subspace to find the eigenmodes. We thus operate the K'_{kij} (including the A, B, C, P, and Q terms) onto these null eigenvectors of K''_{kij} to determine if their eigenvalues (considering all terms) are positive or negative. One need not normalize the vectors in order to simply determine the sign of the eigenvalue.

In the basis of the two $k=0$ modes allowed in the stiff-solid approximation, the matrix elements of K'_{kij} are

$$\begin{bmatrix}RC & -C\\ -C & R^{-1}C\end{bmatrix}$$

The determinant of this matrix is found to be zero and the trace is found to be positive indicating one zero eigenvalue and one positive eigenvalue. (The zero eigenvalue corresponds to overall rotation of the system.) We continue with the remaining $N-1$ values of k in search of the mode of greatest instability. By operating K'_{kij} on the remaining null eigenvectors of K''_{kij} (where k does not equal 0), we find that the sign of each eigenvalue is determined by the sign of

$$(\cos\theta-\cos k\theta)(CS^2\cos\theta-R\sin\theta-CS^2\cos k\theta+R\cos k\theta\sin\theta)$$

Note that when $k=1$ or $N-1$, we have an eigenvalue of zero independent of C, R, or θ. Linear combinations of these two modes correspond to overall translation of the system in directions perpendicular to the axis of the structure.

For $2\leqslant k\leqslant N-2$, note that the sign of each eigenvalue is determined by the sign of

$$\frac{CS^2}{R} - \frac{(1-\cos k\theta)\sin\theta}{\cos\theta - \cos k\theta}$$

Taking first and second derivatives of this with respect to k, it is quickly found that it is most negative when $k=2$ or $N-2$. So the greatest possibility of making the eigenvalue less than zero is for the modes $k=2$ and $k=N-2$. Hence, these are always the most unstable modes and thus they determine the overall stability of the system.

Note that the condition for overall stability of the system is thus

$$\frac{CS^2}{R} \geq \frac{(1-\cos 2\theta)\sin\theta}{\cos\theta - \cos 2\theta} \tag{11}$$

From this, it is seen that a maximum C enhances stability; thus, reducing tension in the outer tension hoop is desirable. However, in keeping with our failure-safe assumptions, we will assume that C takes its minimum value (4). This leads to an expression for stability in terms of pressure and radius,

$$P\frac{S}{R} \geq \frac{4\left(\cos\frac{1}{2}\theta\right)^4}{1+2\cos\theta} \tag{12}$$

The right side of Eq. (12) goes to $4/3$ in the small-θ limit (many sections or large N) and does not exceed $4/3$ for any reasonable N (larger than 3). Thus, the failure-safe requirement for overall stability of the entire system given the stiff-solid approximation is

$$P \geq \frac{4}{3}\frac{R}{R-1} \tag{13}$$

Note that the requirement for stability (13) compared to that of equilibrium (5) is to simply increase the absolute pressure by a factor of $4/3$.

One may be surprised that the result (13) is somewhat insensitive to the precise value of N. Recall, however, that some N dependence has been removed between Eqs. (12) and (13). For example, if we take Eq. (12) with $N=4$ ($\theta=\pi/2$), the factor of $4/3$ in Eq. (13) becomes unity. In this case, however, the external and internal lobes occupy a large fraction of the total volume of the system and thus $N=4$ is not practical. To minimize the total volume of the system while maximizing the evacuated volume, large values of N are of interest. In this limit, the RHS of Eq. (12) tends to $4/3$ and never exceeds $4/3$; thus Eq. (13) is a general result that is failure safe. In the large-N limit (given the stiff-solid approximation), the complete potential energy of the system can be approximated as the pressure-volume energy of a system of two coaxial thin-walled cylinders (of radii unity and R) constrained such that each point on the inner cylinder remains a fixed distance $S \equiv R-1$ from the point on the outer cylinder that corresponds when the cylinders take the nominal circular cross section. This pressure-volume energy would depend on the overall distortion of the cylinders, not on the roughness of the boundaries, which each cylinder defines. Thus, when N is large, the system can be approximated by a continuous system for which the prefactor is exactly $4/3$

Given a violation of the stability requirement (13), failure by the $k=2$ and $k=N-2$ modes may occur. It is instructive to discuss these failures in direct physical terms. A linear combination of these two modes is shown in Fig. 5. Note that the intended cylindrical form has distorted to give a pseudoelliptical cross section. Other linear combinations of the two failure modes give the same elliptical distortion but with the major axis of the ellipse differently oriented. From Fig. 5, one can see that the deformation is allowed because, while the wall structure is bending stiff, it is shear weak. The shear is concentrated at the quarter points approximately 45 deg from the major and minor axes of the ellipse. This shear weakness (in contrast to the bending stiffness) can be easily understood given the stiff-solid approximation. This approximation assumes that no elastic energy can be stored in the membranes and hence the length of every membrane is fixed. With no means of stretching any membrane, one can show that the only way to accommodate bending of the wall structure (without shear) is to eliminate the tension in either the outer or inner circumferential membranes such that they buckle. This leads to an increase in potential energy of the wall because the pressurized volume is then reduced. One can show that when the wall is bent by this mechanism, the increase in potential energy is proportional to the absolute value of the change in the wall's curvature; because the absolute value function has an infinite second derivative at its origin, this bending mode is "infinitely" stable (given the stiff-solid approximation). A similar consideration of the shearing mode illuminates the origin of the weakness. To accommodate shearing of the wall structure, there is no need to change the length of any membrane. Like the bending, the shearing causes a reduction in the pressurized volume, but one can show that this change in volume is proportional to the square of the change in curvature, in contrast to the bending mode where the change in volume is proportional to the absolute value of the change in curvature. Because the potential energy in this case has a finite second derivative, the shearing mode is much more active than the bending mode.

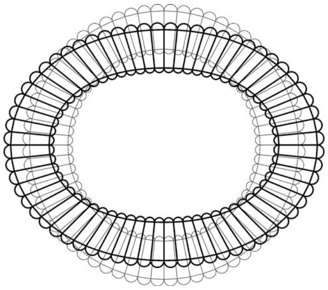

Fig. 5 Linear combination of $k=2$ mode and $k=N-2$ mode

Stability Without the Stiff-Solid Approximation

The analysis thus far depends on the stiff-solid approximation. Let us now reexamine that approximation. If one assumes that all solid components of a system have infinite stiffness (as the stiff-solid approximation assumes), then any continuous solid system is stable and there is no need to consider inflatable structures to enhance stability. However, experience shows that as the wall of a vacuum chamber becomes progressively thinner, the stiff-solid approximation at some point becomes inadequate. We will now show that the same is true of inflatable vacuum chambers, that Eq. (13) is inadequate when R is sufficiently small. To understand this, we must go back and find the critical P that makes K'_{2ij} positive semidefinite without assuming that α, β, and γ are large. To arrive at the smallest possible values for α, β, and γ (and thereby achieve a failure-safe result), we will assume that every membrane is only thick enough to just meet its strength requirement. (We continue to take C at its minimum value.) We further assume that membranes comprising the inner and outer tension hoops are of equal thickness and only of sufficient strength to withstand venting of the chamber. We also neglect the small contributions that the curved membranes make to the effective elastic constants α and β. Given the unitless number M, which is the elastic modulus divided by the tensile strength, these assumptions determine the elastic constant of every membrane. We insert these explicit forms of α, β, and γ into K'_{2ij}. We will still assume that θ is small (a failure-safe assumption) and thus expand each element of K'_{2ij} in a power series in θ keeping only the leading nonzero term. For every nonzero element, this is the term first order in θ. We then explicitly set the determinant to zero,

$$M^3\frac{3Q^2P(3PS-4R)S\theta^4}{R^2}+M^2\frac{-3QP(3P^2S^4+S^2R(3R-4)-P(3-18R+27R^2-22R^3+6R^4))\theta^4}{R^2S}+M\frac{-18QP^2(PS-R)S\theta^4}{R^2}+\frac{12P^3\theta^4}{RS}=0 \tag{14}$$

to find the critical P. (Note that the elastic constant of each membrane depends on its thickness, and the thickness chosen depends on the yield strength. Thus, Eq. (14) is not dependent on elastic modulus alone but on the ratio M.) If we take the limit that M is large by only considering the term third order in M, we find that this determinant equals zero when $P=P_0\equiv(4/3)R/(R-1)$ as expected (13). To find the first-order correction to P when M is not so large, we consider the third- and second-order terms. We expand this in a power series in $P-P_0\equiv\Delta P$ keeping only the zero- and first-order terms in ΔP. Then solving this for ΔP and looking at the term first order in M^{-1}, we find that

$$\frac{\Delta P}{P_0}\approx\frac{1}{M}\frac{R(11+3R+R^2+R^3)}{4(R-1)^2(R+3)} \tag{15}$$

which blows up as R goes to unity. In this limit we find

$$\frac{\Delta P}{P_0}\approx\frac{1}{(R-1)^2M} \tag{16}$$

For an example case where $R=1.4$ and $M=65$ (typical for carbon fiber), we find that $\Delta P/P_0\approx 15.2\%$ (15). A numerical solution of Eq. (14) in the same case gives $\Delta P/P_0=14.8\%$. In summary, by comparing ΔP with P_0 (16) we find that Eq. (13) is inadequate when R is close to or less than $1+M^{-1/2}$.

Preliminary Experimental Data

A model was constructed of polyester film bonded with acrylic adhesive having $R=2$ and $N=12$ (see Fig. 6). The pressure in the wall of the structure was raised above atmospheric pressure by 1.01 ± 0.10 psi (6.96 ± 0.69 kPa). Partial evacuation of the central volume was then begun. Stability was maintained until the central pressure reached 0.72 ± 0.10 psi (4.96 ± 0.69 kPa) below atmospheric pressure. At this point, the central volume began to decrease by means of the $k=2$ deformation, thus preventing further reduction in pressure even though pumping continued. Pressure in the wall of the structure was then raised to 2.0 psi (13.8 kPa) above atmospheric pressure; however, before another measurement could be made, an internal failure of the acrylic adhesive redistributed stresses to rupture the exterior film and hence the pressure was lost. The model was not repaired.

The current stability theory is not directly applicable to this experiment because the absolute pressure in the central space is not zero; however, note that Eqs. (1) and (2) are invariant under a global offset in the hydrostatic pressure. Thus, the current experiment can be analyzed by subtracting from all pressures, the pressure in the central space. Therefore, the one data point obtained has the same stability as $P\equiv\bar{P}/P_{\text{unit}}=(1.01\text{ psi}+0.72\text{ psi})/0.72\text{ psi}=2.40$. Given $N=12$ and $R=2$ and knowing the bounds on C (4), the theory predicts the critical P required for stability between 2.27 and 2.55 (11), which is consistent with this observation.

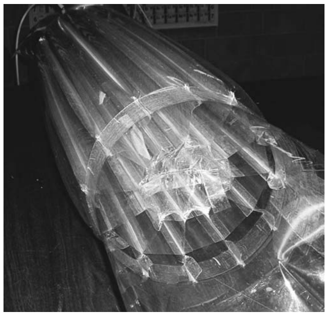

Fig. 6 Experimental model of the inflatable vacuum chamber

Application of Theory

To apply this theory to achieve a structure that is lighter than air, careful consideration is required. A simple analysis shows that inflatable vacuum chambers of a cylindrical form contain at least twice as many moles of pressurized gas as the moles of gas they displace [7]. Thus, pressurizing with air can never lead to a structure that is lighter-than-air. Additionally, one should note that, if a particular design is found to possess sufficient strength to transmit the required forces when evacuated, these forces can increase when the chamber is vented (especially in the tension hoops), leading to failure of the system unless P is simultaneously reduced. However, if pressurization is accomplished with helium, and membranes are constructed of advanced materials such as Kevlar- or carbon-fiber composites, calculations show that such a structure could be lighter-than-air with over half of its volume completely evacuated and still resist failure when vented. For example, if $R\approx1.4$ and the structure is constructed of 60% carbon fiber/40% polyester composite with a safety factor of unity and pressurized with helium, it will have a total mass about one-third the mass of air it displaces and (with sufficiently large N) over half of its total volume is completely evacuated.

If net positive buoyancy is not necessary, more basic materials and pressurized air could be used while still reducing the required amount of raw material by about two orders of magnitude compared to the conventional chamber designs.

Future Directions

Preliminary analysis suggests that the structure of Fig. 1 can be modified to further enhance stability and ease of fabrication. While all of the modified structures shown in Fig. 7 might have greater stability, the greatest stability is likely to be found in the structure of Fig. 7(*a*) or 7(*b*) The structure of Fig. 7(*c*), however, appears to be easiest to fabricate.

The logic behind the modification of Fig. 1 to arrive at Fig. 7(*a*) is that when the radial membranes are slightly diagonal, the shearing mode (the mode of failure) may be somewhat more stable. Because of this modification, the circumferential eigenvalue of the mean stress tensor in the wall may be additionally reduced and thus the pressure required for equilibrium might be slightly greater (which is of no consequence unless this is the mode of failure). Thus, setting the angle of the radial membranes slightly off the exact radial direction could reduce the critical pressure; however, an excessive angle could result in the pressure required for equilibrium becoming larger than the pressure required for stability. Thus, it appears that there is an optimal angle given a particular situation. Of course, the angle is related to N and R; however, given N and R, there still remains some freedom in the choice of this angle as one can have the membranes cross each other or reflect off of each other at one (or more) points intermediate their length as in Fig. 7(*b*).

The modification of Fig. 7(*a*) to arrive at Fig. 7(*c*) is simply to increase ease of fabrication. All members still serve the same purposes (lobes to terminate radial tensions and circumferential

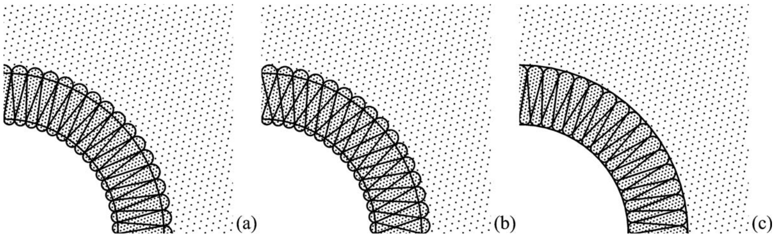

Fig. 7 Three possible modifications of the structure of Fig. 1

members to prevent the "accordion" effect), but the rearranged geometry now permits construction from three continuous membranes (a first membrane on the inner surface, a second membrane on the outer surface, and a third membrane meandering between the first and second). Stability may be somewhat reduced compared to the model of Fig. 7(*a*), but such reduction is likely to be minimal. Note that holes for equalization of pressure will exist in the first and second membranes and that only the third membrane (not directly exposed to the environment) constitutes the gas-tight seal.

Rigorous stability analysis of these structures appears to be more complex than that of the current model and has not yet been carried out.

Acknowledgment

The author would like to acknowledge D. Van Winkle, S. Safron, F. Flaherty, E. Manousakis, L. Van Dommelen, S. Bellenot, and J. Skofronick for useful discussions, I. Winger for introducing polyester film to the project and for recognizing the project's application to "solar chimney" [3], R. Fatema for assistance in building the first model to successfully contain partial vacuum, and MARTECH for logistical support. Additionally, the author would like to acknowledge the two anonymous reviewers who patiently worked through the manuscript to bring it into its present form.

Nomenclature

x_{ni} = displacement of the *i*th degree of freedom in the *n*th unit cell
c and γ = pretensioning T and elastic constant K of one radial membrane, respectively
a and α = effective pretensioning T and effective elastic constant K of one segment of the inside tension hoop, respectively
b and β = effective pretensioning T and effective elastic constant K of one segment of the outside tension hoop, respectively
P = absolute pressure in the pressurized regions
R = vertex radius of the outside tension hoop
U = potential energy of the system
N = multiplicity of the axial symmetry (the system has N-fold axial symmetry)

For notational convenience we define $S \equiv R-1$, $C \equiv c/S$, $A \equiv a/2\delta$, $B \equiv b/2\delta R$, $Q \equiv P-1$, $\theta \equiv 2\pi/N$, $D \equiv \cos(\theta/2)$, $\delta \equiv \sin(\theta/2)$, $E \equiv \cos(\theta/2) = (D^2-\delta^2)/2$, and $\varepsilon \equiv (\sin\theta)/2 = D\delta$.

Appendix A

The "reference" values discussed in section "Note About Units" above are given below. Here, Δz is the differential length considered in the axial dimension.

$$R_{\text{unit}} = x_{\text{unit}} = l_{\text{unit}} = \text{radius to inside nodes}$$

$$P_{\text{unit}} = \Delta p_{\text{unit}} = \text{ambient pressure}$$

$$T_{\text{unit}} = a_{\text{unit}} = b_{\text{unit}} = c_{\text{unit}} = R_{\text{unit}} P_{\text{unit}} \Delta z$$

$$K_{\text{unit}} = \alpha_{\text{unit}} = \beta_{\text{unit}} = \gamma_{\text{unit}} = P_{\text{unit}} \Delta z$$

$$U_{\text{unit}} = R_{\text{unit}}^2 P_{\text{unit}} \Delta z$$

Appendix B

As an example of Eq. (1), we calculate $\Delta U_{\text{membrane}}$ for the membrane in the outer tension hoop connecting the unit cells $n=5$ and $n=6$.

$$\Delta U_{\text{membrane}} = T\Delta l + \frac{1}{2}K\Delta l^2$$

$$T = b = 2\delta BR$$

$$K = \beta$$

$$\Delta l = l - l_0$$

$$l_0 = 2R\delta$$

$$l = \sqrt{\left(\begin{bmatrix} \delta \\ -D \\ \delta \\ D \end{bmatrix}^{\mathrm{T}} \begin{bmatrix} x_{52} \\ x_{53} \\ x_{62} \\ x_{63} \end{bmatrix} + 2R\delta \right)^2 + \left(\begin{bmatrix} D \\ \delta \\ -D \\ \delta \end{bmatrix}^{\mathrm{T}} \begin{bmatrix} x_{52} \\ x_{53} \\ x_{62} \\ x_{63} \end{bmatrix} \right)^2}$$

where the first and second terms in parentheses are the displacements parallel and perpendicular to the membrane, respectively. The square root is then evaluated to give

$$\Delta l = \begin{bmatrix} \delta \\ -D \\ \delta \\ D \end{bmatrix}^{\mathrm{T}} \begin{bmatrix} x_{52} \\ x_{53} \\ x_{62} \\ x_{63} \end{bmatrix} + \begin{bmatrix} x_{52} \\ x_{53} \\ x_{62} \\ x_{63} \end{bmatrix}^{\mathrm{T}} \frac{1}{4R\delta} \begin{bmatrix} D^2 & \varepsilon & -D^2 & \varepsilon \\ \varepsilon & \delta^2 & -\varepsilon & \delta^2 \\ -D^2 & -\varepsilon & D^2 & -\varepsilon \\ \varepsilon & \delta^2 & -\varepsilon & \delta^2 \end{bmatrix} \times \begin{bmatrix} x_{52} \\ x_{53} \\ x_{62} \\ x_{63} \end{bmatrix} + \cdots$$

where the ellipsis represents terms third order in the x_{ni}. We then insert these into Eq. (1) and find that $\Delta U_{\text{membrane}}$ is equal to

$$\begin{bmatrix} 2BR\delta^2 \\ -2BR\varepsilon \\ 2BR\delta^2 \\ 2BR\varepsilon \end{bmatrix}^{\mathrm{T}} \begin{bmatrix} x_{52} \\ x_{53} \\ x_{62} \\ x_{63} \end{bmatrix} + \frac{1}{2} \begin{bmatrix} x_{52} \\ x_{53} \\ x_{62} \\ x_{63} \end{bmatrix}^{\mathrm{T}}$$

$$\times \begin{bmatrix} BD^2+\beta\delta^2 & B\varepsilon-\beta\varepsilon & -BD^2+\beta\delta^2 & B\varepsilon+\beta\varepsilon \\ B\varepsilon-\beta\varepsilon & B\delta^2+\beta D^2 & -B\varepsilon-\beta\varepsilon & B\delta^2-\beta D^2 \\ -BD^2+\beta\delta^2 & -B\varepsilon-\beta\varepsilon & BD^2+\beta\delta^2 & -B\varepsilon+\beta\varepsilon \\ B\varepsilon+\beta\varepsilon & B\delta^2-\beta D^2 & -B\varepsilon+\beta\varepsilon & B\delta^2+\beta D^2 \end{bmatrix}$$

$$\times \begin{bmatrix} x_{52} \\ x_{53} \\ x_{62} \\ x_{63} \end{bmatrix} + \cdots$$

The elements of the first column vector contribute to F_{ni} and the elements of the matrix contribute to K_{nimj}. For example, the contribution to K_{5362} is $-B\varepsilon-\beta\varepsilon$.

Appendix C

As an example of Eq. (2), we calculate ΔU_{gas} for one sector of the volume inside the outer tension hoop. We take the triangular sector whose three vertices are the two nodes on the outer tension hoop in unit cells $n=7$ and $n=8$ and the center of the vacuum chamber.

$$\Delta U_{\mathrm{gas}} = -\Delta p \Delta V$$

$$\Delta p = P - 1 = Q$$

$$\Delta V = V - V_0$$

$$V_0 = \varepsilon R^2$$

$$V = \frac{1}{2} \det \begin{bmatrix} DR + Dx_{72} + \delta x_{73} & -\delta R - \delta x_{72} + Dx_{73} \\ DR + Dx_{82} - \delta x_{83} & \delta R + \delta x_{82} + Dx_{83} \end{bmatrix}$$

$$\Delta U_{\mathrm{gas}} = \begin{bmatrix} -\varepsilon QR \\ EQR \\ -\varepsilon QR \\ -EQR \end{bmatrix}^{\mathrm{T}} \begin{bmatrix} x_{72} \\ x_{73} \\ x_{82} \\ x_{83} \end{bmatrix} + \frac{1}{2} \begin{bmatrix} x_{72} \\ x_{73} \\ x_{82} \\ x_{83} \end{bmatrix}^{\mathrm{T}} Q \begin{bmatrix} 0 & 0 & -\varepsilon & -E \\ 0 & 0 & E & -\varepsilon \\ -\varepsilon & E & 0 & 0 \\ -E & -\varepsilon & 0 & 0 \end{bmatrix}$$

$$\times \begin{bmatrix} x_{72} \\ x_{73} \\ x_{82} \\ x_{83} \end{bmatrix}$$

Again, the elements of the first column vector contribute to F_{ni} and the elements of the matrix contribute to K_{nimj}. For example, the contribution to F_{73} is $-EQR$. (Note the sign reversal on F_{ni} in Eq. (3).)

References

[1] Mowforth, E., 1999, *Airship Technology*, Cambridge University Press, Cambridge, Chap. 14.

[2] Post, R. F., and Ryutov, D. D., 2000, "The Inductrack: A Simpler Approach to Magnetic Levitation," IEEE Trans. Appl. Supercond., **10**(1), pp. 901–904.

[3] dos S. Bernardes, M. A., Voß, A., and Weinrebe, G., 2003, "Thermal and Technical Analyses of Solar Chimneys," Sol. Energy, **75**, pp. 511–524.

[4] da C. Andrade, E. N., 1957, "The Early History of the Vacuum Pump," Endeavour, Jan., pp. 29–35.

[5] Tracy, J., 1878, "Improvement in Balloons," U.S. Patent No. 205,319.

[6] Armstrong, L. M., 1921, "Aircraft of the Lighter-Than-Air Type," U.S. Patent No. 1,390,745.

[7] Michaelis, M. M., and Forbes, A., 1994, "Vacuum Vessels in Tension," Vacuum, **45**(1), pp. 57–60.

[8] Lennon, B. A., and Pellegrino, S., 2000, "Stability of Lobed Inflatable Structures," Paper No. AIAA-2000-1728.

[9] Golub, G. H., 1983, *Matrix Computations*, The Johns Hopkins University Press, Baltimore.

[10] Ashcroft, N. W., and Mermin, N. D., 1976, *Solid State Physics*, Holt, Rinehart and Winston, New York, p. 439.

Evaluation of Planar Harmonic Impedance for Periodic Elastic Strips of Rectangular Cross Section by Plate Mode Expansion

Eugene J. Danicki
Polish Academy of Science,
21 Świętokrzyska Street,
Warsaw 00-049, Poland
e-mail: edanicki@ippt.gov.pl

A system of periodic elastic strips (each one considered as a piece of a plate) is characterized by a matrix relation between the Bloch series of displacement and traction at the bottom side of the system. Both these mechanical fields are involved in the boundary conditions at the contact plane between the strips and the substrate supporting a Rayleigh wave. The analysis exploits the mechanical field expansion over the plate modes, including complex modes; numerical results satisfy the energy conservation law satisfactorily. The derived planar harmonic Green's function provides an alternative tool for investigation of surface waves propagation under periodic elastic strips, with respect to pure numerical methods mostly applied in the surface acoustic wave devices literature. Perfect agreement of the presented theory with the experimentally verified perturbation model of thin strips is demonstrated. [DOI: 10.1115/1.2912931]

1 Introduction

In surface acoustic wave (SAW) electronic devices, thin metal strips distribute the electric potential on a piezoelectric substrate surface in order to generate SAWs on it (Fig. 1). The SAW generation efficiency has the highest value if the strip spacing (a period) equals half wavelength of SAW at given frequency [1]. At low frequencies, the strips are relatively thin (with respect to their width), and their mechanical interaction with the propagating SAWs can be evaluated by using the perturbation methods [2]. For higher frequencies, however, the strips must be much thicker in order to obtain sufficient electric conductivity. This makes the perturbation methods inadequate, and more advanced analysis must be applied accounting for the strip vibration. Pure numerical methods are frequently applied by engineers designing SAW devices (see Ref. [3], for instance).

In this paper, we develop a promising alternative method in which each strip is considered as a piece of a plate supporting an infinite system of modes. The modal wave fields are used for the mechanical field expansion between the bottom side of the strip contacting the substrate up to the upper free plane of the strip, assuming the side planes of the plate (i.e., the strip sides) to be stress free. This allows us to evaluate the traction at the strip system-substrate contact plane resulting from the known displacements at this plane; both wave fields being expanded in the spatial Bloch series, natural for a periodic system of strips. This is the strip impedance or the inverse of the planar harmonic Green's function for strips, sufficient for analysis of surface wave propagation on the substrate (which is characterized by the corresponding planar harmonic Green's function of elastic half-space [4]), covered by strips.

There are many papers in the existing literature [5–8] analyzing similar problems of a half-infinite plate with free or fixed end and free plate sides (a half-infinite, w-wide mechanical waveguide, which is free or fixed at the end or attached to a substrate). It was shown that the traction at the fixed end of the plate is singular, with intensity depending on the plate material and also on the material of the attached substrate [9–14]. In the analogous problem considered here, a displacement is assumed known (in the form of a truncated Bloch series) at the plate-substrate contact plane, and the resulting traction at this plane is searched, provided that the traction at the other plate cross section (the upper side of the strip) is traction free. It characterizes the strip mechanical property. The contacting body is not specified, however, because we seek the strip characterization only, to be applied in the analysis of different SAW devices made on different substrates.

The singular traction that arises at the strip corners causes slow decaying of the Bloch series expansion of the wave field. This is why we must include high number of complex modes in the analysis. The truncation of the Bloch series is justified by this physical argumentation that the influence of very high spatial harmonics on the propagating SAWs having a wave number within the first Brillouin zone (which is the typical case of SAW devices) is expected to be technically negligible. In this paper, the results are compared to the perturbation theory for thin strips, which theory, accounting for only the two lowest Bloch components of mechanical field, was proved to be quite accurate for thin strips, and also very convenient in the analysis of SAW devices [15,16]. Good agreement validates the above argumentation and the perturbation theory as well.

The paper is organized as follows. In the next section, modes in an elastic waveguide (an infinite plate of thickness w) are analyzed. In the following section, the mode scattering at a traction-free cross section of the waveguide is solved by using the ordinary boundary conditions ($T=0$ expressed in spectral representation by the Bloch series), instead of the frequently applied spatial variational ones [6–8] (the plate edge resonances [17] are not expected to appear in the considered short piece of a plate). This scattering matrix allows us to evaluate both the traction and the displacement fields at the other plate cross section corresponding to the bottom, substrate-contacting side of the strip, as dependent on the modal amplitudes. Their elimination yields what we seek: the dependence of the traction on the displacement, both expressed in Bloch series. Final sections present computational details and a proof that the analysis presented here primarily for thick strips is also suitable for thin strips as well, by the comparison with the perturbation model. Certain technical details of application of the presented analysis in the theory of SAW devices are discussed in conclusions.

Contributed by the Applied Mechanics Division of ASME for publication in the JOURNAL OF APPLIED MECHANICS. Manuscript received February 22, 2007; final manuscript received February 25, 2008; published online May 14, 2008. Review conducted by Professor Sridhar Krishnaswamy.

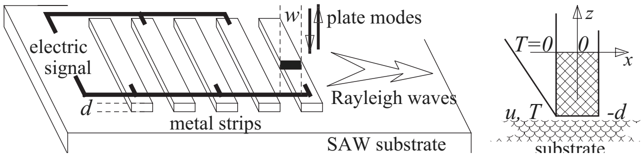

Fig. 1 An interdigital transducer comprising a number of periodic strips on a substrate. A piece of plate modeling the strip is shown at the right.

2 Plate Modes

The harmonic wave fields in isotropic solids characterized by mass density ρ and Lamé constants μ,λ are considered here, having the general form (the time-harmonic dependence of frequency ω is dropped in further equations; note the field independence of $y=x_2$):

$$e^{j\omega t}e^{-jqx}e^{-jpz}, \quad x=x_1, \quad z=x_3$$

$$q_{l,t}=\sqrt{k_{l,t}^2-p^2}=-j\sqrt{p^2-k_{l,t}^2}$$

$$k_l=\omega[\rho/(\lambda+2\mu)]^{1/2}, \quad k_t=\omega(\rho/\mu)^{1/2} \tag{1}$$

Both the wave fields of longitudinal wave having wave number k_l and shear wave (wave number k_t) contribute to the displacement field u_i, $i=1,3$ and the resulting stress T_{ij}, $j=1,3$, which can be evaluated from the constitutive equations of the solid. By noticing that the longitudinal wave displacement vector is parallel to the wave vector $\mathbf{u}_l \| \mathbf{k}_l=(p,q_l)$ and that of shear wave is perpendicular to its wave vector $\mathbf{u}_t \perp \mathbf{k}_t=(p,q_t)$, we obtain [18]

$$[u_i]=\mathbf{u}_q\begin{bmatrix} e^{-jq_lx}F_l \\ e^{-jq_tx}F_t \end{bmatrix}, \quad \mathbf{u}_q=\frac{1}{\omega\sqrt{\rho\omega}}\begin{bmatrix} q_l & p \\ p & -q_t \end{bmatrix} \tag{2}$$

$$[T_{1i}]=\bar{\mathbf{T}}_q\begin{bmatrix} e^{-jq_lx}F_l \\ e^{-jq_tx}F_t \end{bmatrix}, \quad \bar{\mathbf{T}}_q=-j\frac{\mu/\omega}{\sqrt{\rho\omega}}\begin{bmatrix} q_t^2-k_t^2 & 2pq_t \\ 2pq_l^2 & k_t^2-2q_t^2 \end{bmatrix} \tag{3}$$

where $F_{l,t}$ are certain amplitudes of the considered waves, longitudinal and shear, respectively [18]. The spectral variables p and $q_{l,t}$ are wave numbers characterizing the plate modes propagation (or decaying) in the z and x-directions, respectively; both can have complex values. In the applied notations, the index q turns our attention that both $+q_{l,t}$ and $-q_{l,t}$ can be included in the wave field (this requires simultaneous replacement of their signs in both the matrices and the corresponding exponential functions in the above equations).

The boundary-value problem is considered for the plate having traction-free surfaces $x=\pm w/2$. By applying these two values of x, the system of four homogeneous equations results for unknown $F_{l,t}^{\pm}$:

$$[T_{1i}](x)=\bar{\mathbf{T}}_{+q}\,\mathrm{diag}\begin{Bmatrix} e^{-jq_l(w/2+x)} \\ e^{-jq_t(w/2+x)} \end{Bmatrix}\begin{bmatrix} F_l^+ \\ F_t^+ \end{bmatrix}+\bar{\mathbf{T}}_{-q}\,\mathrm{diag}\begin{Bmatrix} e^{-jq_l(w/2-x)} \\ e^{-jq_t(w/2-x)} \end{Bmatrix} \times\begin{bmatrix} F_l^- \\ F_t^- \end{bmatrix}=0 \tag{4}$$

($w/2$ is included in the exponential functions to avoid their large values for higher modes, provided that the values of $q_{l,t}$ are chosen with negative imaginary part; the same will be applied in the expression for displacements). They have a nontrivial solution if the determinant of the system matrix $\mathbf{D}$ vanishes, which is the condition for the plate mode wave number p_m. An infinite system of eigenvalue-eigenvector pairs results as follows:

$$\{p_m,\mathbf{F}^{(m)}\}, \quad \mathbf{F}=[F_l^+;F_t^+;F_l^-;F_t^-] \tag{5}$$

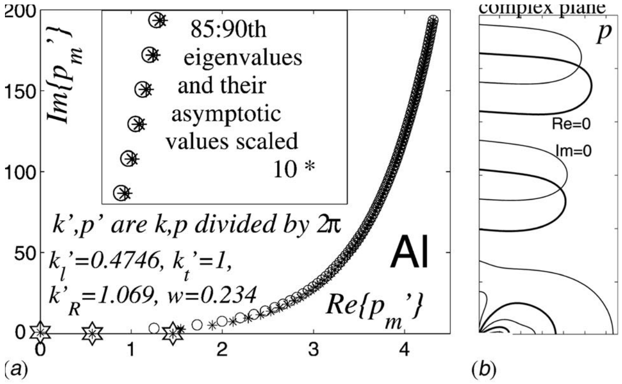

Fig. 2 (*a* Distribution of the modal wave numbers on the complex *p*-plane and their asymptotic approximation (circles). (*b*) Zero lines of real and imaginary parts of det{D} on the *p*-plane (thick and thin lines, respectively); p_m reside at their intersections.

$$p_m=\frac{1}{w}\left[\ln(2\pi m)+j\pi\left(m+\frac{1}{2}\right)\right]$$

$$\mathbf{F}^{(m)}=\frac{1}{2}\left[1;-j\cos(\pi m);\left(\cos\frac{\pi}{2}m-\sin\frac{\pi}{2}m\right);\right. \left. j\left(\cos\frac{\pi}{2}m+\sin\frac{\pi}{2}m\right)\right], \quad m\to\infty \tag{6}$$

The last two equations present the asymptotic values [5] for large modal number m, as it can be easily numerically checked (see Fig. 2). Note that $-p_m$ as well as $\pm p_m^*$ are also correct eigenvalues; the associated eigenvectors can be evaluated as the null space of the matrix of Eq. (4) (applied with $x=\pm w/2$) for given p.

There are two sets of modes: Those carrying the wave power toward $x\to\infty$ (or vanishing there), which will be denoted as $+m$ modes, and others propagating in opposite directions, denoted as $-m$ modes. Their wave numbers are $p_{\pm m}=\pm p_m$ and $\mathbf{F}^{(\pm m)}$, respectively. The following mode arrangement (counted by m) is applied for further convenience:

$$[p_m]=[p_r,\ldots,-p_I,-p_1,p_1^*,-p_2,p_2^*,\ldots]$$

where p_r are positive real, p_I is positive imaginary, and p_i, $i=1,2,\ldots$ are complex valued wave numbers with positive imaginary parts. All these modes satisfy the radiation conditions at $z\to\infty$ (except for backward real modes not discussed here; see comments in Ref. [8]).

At the plate cross section $z=0$, the modal wave field (the modal indices are omitted below; note that $q_{l,t}$ also depend on p_m)

$$[u_i](x)=\mathbf{u}_{+q}\,\mathrm{diag}\begin{Bmatrix} e^{-jq_l(w/2+x)} \\ e^{-jq_t(w/2+x)} \end{Bmatrix}\begin{bmatrix} F_l^+ \\ F_t^+ \end{bmatrix}+\mathbf{u}_{-q}\,\mathrm{diag}\begin{Bmatrix} e^{-jq_l(w/2-x)} \\ e^{-jq_t(w/2-x)} \end{Bmatrix} \times\begin{bmatrix} F_l^- \\ F_t^- \end{bmatrix} \tag{7}$$

$$[T_{3i}](x)=\mathbf{t}_{+q}\,\mathrm{diag}\begin{Bmatrix} e^{-jq_l(w/2+x)} \\ e^{-jq_t(w/2+x)} \end{Bmatrix}\begin{bmatrix} F_l^+ \\ F_t^+ \end{bmatrix}+\mathbf{t}_{-q}\,\mathrm{diag}\begin{Bmatrix} e^{-jq_l(w/2-x)} \\ e^{-jq_t(w/2-x)} \end{Bmatrix} \times\begin{bmatrix} F_l^- \\ F_t^- \end{bmatrix} \tag{8}$$

where $\mathbf{t}_q$ is evaluated from constitutive equations like in Eq. (3),

$$\mathbf{t}_q = -j\frac{\mu/\omega}{\sqrt{\rho\omega}}\begin{bmatrix} 2pq_l & k_t^2-2q_t^2 \\ k_t^2-2q_l^2 & -2pq_t \end{bmatrix} \tag{9}$$

can be conveniently represented by the Fourier series in the domain $x \in (-w/2, w/2)$:

$$f(x) = \sum_n f_n e^{-jnWx}, \quad f_n = \int_{-w/2}^{w/2} f(x)e^{jnWx}dx/w \tag{10}$$

$W=2\pi/w$. Making the corresponding easy integration over x yields the following matrices $\mathbf{c}_n^{\pm}$, which replace the diagonal matrices in Eqs. (7) and (8):

$$\mathbf{c}_n^{\pm} = \pm j(-1)^n \begin{bmatrix} \dfrac{1-\exp(-jq_lw)}{2\pi n \mp q_lw} & 0 \\ 0 & \dfrac{1-\exp(-jq_tw)}{2\pi n \mp q_tw} \end{bmatrix} \tag{11}$$

for $\pm m$ modes and nth Bloch series component: $\exp(-jnWx), W=2\pi/w$.

By multiplying the corresponding matrices, Eq. (7) transforms into (in MATLAB notations)

$$[u_i]_n = \underbrace{\mathbf{u}_{+q}\mathbf{c}_n^{+}[F_l^{+};F_t^{+}]}_{\mathbf{U}_n^{+}} + \underbrace{\mathbf{u}_{-q}\mathbf{c}_n^{-}[F_l^{-};F_t^{-}]}_{\mathbf{U}_n^{-}}$$

and similarly for $[T_{3i}]$, Eq. (8), where $\mathbf{T}_n^{\pm}=\mathbf{t}_{\pm q}\mathbf{c}_n^{\pm}[F_l^{\pm};F_t^{\pm}]$ (modal indices dropped). The Fourier expansion of the wave field in the plate is the superposition of all the modal fields:

$$\begin{pmatrix} u_i \\ T_{3i} \end{pmatrix}(x) = \sum_{n,m}\begin{pmatrix} \mathbf{U}_n^{(\pm m)} \\ \mathbf{T}_n^{(\pm m)} \end{pmatrix} a_{\pm m}e^{-jnWx}e^{\mp jp_mz} \tag{12}$$

where $a_{\pm m}$ are arbitrary amplitudes of modes propagating (or vanishing) toward $z \to \pm\infty$, respectively, and $\mathbf{U}_n^{\pm}$ and $\mathbf{T}_n^{\pm}$ are the two-component Bragg cells describing harmonics ($\pm m$ Bragg orders) of both components of displacement $[u_i]$ and stress $[T_{3i}]$, $i=1,3$.

This field representation is convenient for checking whether the numerically evaluated modes satisfy the energy conservation law. The complex (evanescent) modes having complex p_m cannot carry real power along the plate, that is, along the axis z; hence, the real part of $j\omega u_i^*T_{3i}/2$ integrated over the plate thickness $w=2\pi/W$ should be zero if p_m is complex. Performing easy integration yields the complex power of the mode:

$$P_m = j\omega w(\mathbf{U}^m)^*\mathbf{T}^m/2 \tag{13}$$

(asterisk means the Hermitian matrix conjugation; $\mathbf{U}^m$ and $\mathbf{T}^m$ are column vectors including all Bloch components enumerated by n), because none of the products of different Bloch orders contributes to the modal power:

$$\int_{-w/2}^{w/2} \exp\{j(n_1-n_2)Wx\}dx = 0, \quad n_1 \neq n_2$$

3 Scattering at the Free End of Half-Infinite Plate

Now, the fundamental scattering problem can be solved for the half-infinite plate having stress-free end at $z=0$. Let the $+m$ mode (either truly propagating and having real p_m or complex) propagate from $z=-\infty$ toward $z=0$, inducing stress $T_{3i}^{(m)}$ there, which must be nullified by the reflected modes a_{-l} to obtain

$$[T_{3i}] = \sum_{-l,n}(\mathbf{T}_n^{(m)}a_{+m} + \mathbf{T}_n^{(-l)}a_{-l})e^{-jnWx} = 0 \tag{14}$$

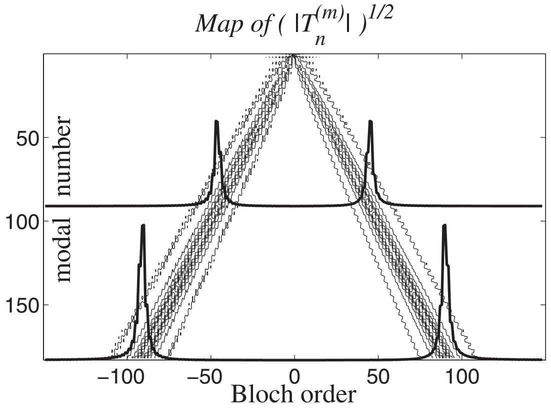

Fig. 3 A contour map of the matrix |T|—its characteristic V-like shape (shown upside down) indicates a localized spectrum dependence on the modal number; the spectra of 183rd and 91st modes are drawn in thick lines. Thin frame shows the truncated spectrum.

$$[a_{-m}] = \mathbf{S}[a_{+m}], \quad \mathbf{S} = -[\mathbf{T}_n^{(-l)}]\backslash[\mathbf{T}_n^{(+m)}] \tag{15}$$

where $\mathbf{S}$ is the scattering matrix. In order to effectively evaluate it, we need to truncate the Fourier and modal expansion in Eq. (12). For m spanning up to M (it is important not to miss any modes below M), there are M “plus” modes. In order to have division of the square matrices $\mathbf{T}_n^{(\pm m)}$ defining $\mathbf{S}$, it is required that the Fourier series include $N=M/2$ harmonics for each T_{3i}, $i=1,3$, which N is preferred to be an odd number in order to obtain spectrum in symmetric domain $-N'/2 \leqslant n \leqslant N'/2$. Hence, $M=2N=4N'+2$ is the required number of modes for the applied truncated spectrum resulting in both square matrices: $[\mathbf{T}_n^{(\pm m)}]$.

This kind of truncation is possible due to the specific asymptotic property of $q_{l,t}$ for large $p_{\pm m}$, Eq. (6). Indeed, careful inspection of Eq. (11), where $q_{l,t} \to \pm mW/2$ for large $|m|$, shows that Mth mode mostly contributes to $(\pm M/2)$th harmonics, which should be the last accounted for in the truncated square matrix. Figure 3 presents example spatial spectra of $[\mathbf{T}_n^{(m)}]$ and the map of the matrix $[\mathbf{T}_n^{(m)}]$ with n spanning over somewhat wider domain with respect to the above-discussed limits in order to present the matrix truncation marked by the square frame. The evaluated scattering matrix $\mathbf{S}$ must satisfy the energy conservation law for the real propagating modes. This feature can be used for verification of the computed results (doing this, however, one needs to pay attention that $\mathbf{F}^{(m)}$, as evaluated by MATLAB, satisfy $\mathbf{F}^*\mathbf{F}=1$; another normalization is required to conveniently obtain $P_m=|a_m|^2/2$).

4 Piece of Plate as a Model of Strip

By combining the incident and reflected modal wave fields at the cross section $z=-d$, the displacements and stress result at the bottom strip side. The following problem can now be formulated: Find a set of incident ($+m$) modes to obtain given displacement field at $z=-d$, then evaluate the resulting traction there. This will be the traction yielded by the d-long piece of the plate excited by the known displacements at its bottom end (at $z=-d$) and having the other end traction free (at $z=0$). This is exactly what is needed for description of mechanical properties of the strip contacting a substrate and interacting with SAW propagating on it. Represented by the Fourier series, the wave fields at $z=-d$ are $[\mathbf{u}_n]$ and $[\mathbf{t}_n]$, where n is the harmonics number (Bloch order) and $\mathbf{u}_n$, $\mathbf{t}_n$ are Bloch cells of $[u_i]\exp(-jnKx)$ and $[T_{3i}]\exp(-jnKx)$, $i=1,3$, respectively.

By noticing that the incident mode amplitude a_{+m} at $z=-d$ changes into $a_{+m}\exp(-jp_md)$ at $z=0$ and that the reflected modes at $z=0$ change their amplitude similarly at $z=-d$ (the corresponding exponential function is again $\exp(-jp_m d)$ because $p_{-m}=-p_m$), the above described solution for the wave field at $z=-d$ takes the form

$$\mathbf{u} = [\mathbf{U}^+ + \mathbf{U}^- \mathbf{E}]\mathbf{a}^+, \quad \mathbf{t} = [\mathbf{T}^+ + \mathbf{T}^- \mathbf{E}]\mathbf{a}^+$$

$$\mathbf{E} = \mathrm{diag}\{\exp(-jp_m d)\}\mathbf{S}\,\mathrm{diag}\{\exp(-jp_m d)\} \qquad (16)$$

as represented by Fourier series, where the square matrices are $\mathbf{U}^{\pm}=[\mathbf{U}_n^{(\pm m)}]$ and $\mathbf{T}^{\pm}=[\mathbf{T}_n^{(\pm m)}]$. The amplitudes $\mathbf{a}^+=[a_m]$ are evaluated to obtain given $\mathbf{u}$. This yields the traction $\mathbf{t}$ dependent on $\mathbf{u}$, both in the spectral representations:

$$\mathbf{t} = \mathbf{h}\mathbf{u}, \quad \mathbf{h} = (\mathbf{T}^+ + \mathbf{T}^- \mathbf{E})/(\mathbf{U}^+ + \mathbf{U}^- \mathbf{E}) \qquad (17)$$

where $\mathbf{h}$ is the strip impedance or the inverse of the w-based spectral representation of the Green's function of an elastic strip of width w and thickness d. (Strictly, the Green's function expresses displacement by traction, $\mathbf{u}=\mathbf{h}^{-1}\mathbf{t}$, and the acoustic impedance expresses traction by displacement velocity; hence, it is $(j\omega)^{-1}\mathbf{h}$.) Careful inspection of the matrix $\mathbf{h}$ proves that the real part of its diagonal must vanish in order to satisfy the energy conservation law: $\mathrm{Re}\{j\omega \mathbf{u}^* \mathbf{t}\} \sim \mathrm{Re}\{j\omega\, \mathrm{diag}(\mathbf{h})\}=0$. Moreover, due to the symmetry of positive and negative harmonics, the 2×2 matrices $[h_{ij}]$ of Bloch cells of $\mathbf{h}$ describing the relations between harmonics of stress T_{3i} and displacement u_j (i.e., of given Bloch order n,m) possess this symmetry (superscript T means matrix transposition):

$$[\mathbf{h}_{n,m}] = [\mathbf{h}_{-n,-m}]^T, \quad \mathbf{h}_{nm} = [h_{ij}] \qquad (18)$$

which symmetry can be exploited for improving the computed values of $\mathbf{h}$.

5 Periodic Strips

Although the above characterization of the strip mechanical properties is sufficient, it is not convenient for application in the analysis of SAW propagation under Λ-periodic strips, where the surface wave field is represented in a Λ-based Bloch series like ($K=2\pi/\Lambda$):

$$[u_i] = \sum_k \mathbf{U}_k e^{-jkKx} e^{-jrx}, \quad r \in (0,K) \qquad (19)$$

for the surface displacements, and similarly for the surface traction ($\mathbf{T}_k$).

To obtain the required transformation of the harmonic Green's function $\mathbf{h}$ into the Λ-representation, we first notice that the surface traction vanishes between strips, while traction and displacements are equal on both sides of the contact area of strips and the substrate. The corresponding transformations are as follows:

$$\mathbf{u}_n = \int_{-w/2}^{w/2} e^{jnWx} \sum_k \mathbf{U}_k e^{-j(r+kK)x} dx/w$$

$$\mathbf{T}_k = \int_{-w/2}^{w/2} e^{j(r+kK)x} \sum_n \mathbf{t}_n e^{-jnWx} dx/\Lambda \qquad (20)$$

where $\mathbf{u}_n$, $\mathbf{t}_n$ are in w-representation, Eq. (17), and $\mathbf{U}_k$, $\mathbf{T}_k$ are in the searched Λ-representation. The above substituted into Eq. (17) results in

$$\mathbf{T} = \mathbf{H}\mathbf{U}, \quad \mathbf{H} = \frac{w}{\Lambda}\mathbf{C}^T \mathbf{h}\mathbf{C}$$

$$\mathbf{C} = [\mathbf{C}_{nk}], \quad \mathbf{C}_{nk} = \begin{bmatrix} 1 & 0 \\ 0 & 1 \end{bmatrix} \frac{\sin \pi(n - r/W - kK/W)}{\pi(n - r/W - kK/W)} \qquad (21)$$

The matrix form of $\mathbf{C}_{nk}$ results from the applied structure of $\mathbf{U}$ and $\mathbf{T}$, alternately comprising harmonics of u_1, u_3 and T_{31}, T_{33}, respectively.

The matrix $\mathbf{H}^{-1}$ is called the planar harmonic Green's function for periodic strips. Note that only the last transformation, Eq. (20), depends on r, which is the searched SAW wave number accounting for the strip interaction with the substrate. To verify the evaluation of $\mathbf{H}$, one may apply the energy conservation law that requires that the power P delivered to a lossless strip must vanish. Due to the earlier discussed property of the Fourier series representation of both $\mathbf{U}$ and $\mathbf{T}$, we obtain that

$$P \sim \mathrm{Im}\{\mathrm{diag}(\mathbf{H})\} = 0 \qquad (22)$$

The applied spectrum truncation may result in certain departure from the above condition.

6 Numerical Details

In the numerical example presented in the next section, we applied $k_{l,t}/(2\pi)=0.541$ and 1, respectively (aluminum strips), w equal to a quarter of the Rayleigh wavelength $2\pi/k_R$, and $\Lambda=2w$, $r=K/2=k_R$, which are typical cases of SAW devices working at their fundamental frequency (with two strips per SAW period).

There are two propagating modes having positive real p_a, p_b: one below, and the other above the cutoff wave number of bulk waves k_t, existing in such a plate. There is also one positive imaginary p_I. Another 90 computed complex p_i in the first quadrant of the complex p plane are shown in Fig. 2 (asterisks). Appended by $\pm p_i^*$ and $-p_i$, they yield a set of 366 wave numbers, which were arranged in the following data array:

$$[\underbrace{p_a; p_b; -p_I; \cdots; -p_m; p_m^*; \cdots; -p_M;}_{\text{`+' modes}}$$
$$\underbrace{-p_a; -p_b; p_I; \cdots; p_m; -p_m^*; \cdots; p_M}_{\text{`−' modes}}]$$

The corresponding eigenvectors $\mathbf{F}^{(m)}$ were calculated next by repeating the null-vector evaluation of the matrix $\mathbf{D}$ at given p_m. The "rule of thumb" for choosing M is that the highest complex mode accounted for should sufficiently decay over the distance d, that is, by applying Eq. (5): $\exp(-\pi M d/w) \ll 1$. The applied value of M in the computation of Figs. 2 and 3 resulted in the matrix condition numbers about 8.E2 and 3.E4, in evaluation of $\mathbf{S}$ and $\mathbf{H}$, respectively.

Evaluation of all eigenvalues p_m, $m \leqslant M$ is crucial for the above matrix conditioning. Happily, rather simple geometry of zero lines of real and imaginary parts of $\det\{\mathbf{D}\}$ on the complex plane p, see the example presented in Fig. 2(*b*), helps much in the numerical evaluation of a complete set of all p_m for $m \leqslant M$. See Ref. [5] for further detailed discussion.

7 Perturbation Theory Verified

The perturbation theory [2] models thin periodic strips by a sinusoidal corrugation of the substrate surface. It yields the following dependence of the resulting traction on the surface displacements (both at a certain midplane) for two lowest harmonics accounted for, 0th and −1st, having wave numbers r and $r-K$, respectively:

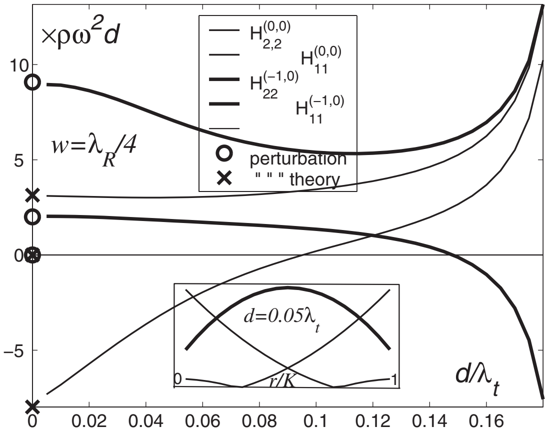

Fig. 4 Dependence of the diagonal elements of the lowest Bloch cells of H on strip thickness *d* (there is a resonance at $d\approx 0.19\lambda_t$). Inset: The dependence of H on *r* nicely compares to the perturbation theory prediction.

$$\begin{bmatrix} T_{31} \\ T_{33} \end{bmatrix}_0 = \frac{d}{2}\begin{bmatrix} \rho\omega^2 - 4\dfrac{r^2}{k_t^2}\left(1-\dfrac{k_l^2}{k_t^2}\right) & 0 \\ 0 & \rho\omega^2 \end{bmatrix}\begin{bmatrix} u_1 \\ u_3 \end{bmatrix}_0 + \frac{d}{\pi}\begin{bmatrix} \rho\omega^2 + 4\dfrac{r(K-r)}{k_t^2}\left(1-\dfrac{k_l^2}{k_t^2}\right) & 0 \\ 0 & \rho\omega^2 \end{bmatrix}\begin{bmatrix} u_1 \\ u_3 \end{bmatrix}_{-1} \tag{23}$$

and similarly for $[T_{3i}]_{-1}$ with substitutions $r\leftrightarrow K-r$, and in subscripts: $0\leftrightarrow -1$. The above two matrices correspond to the following Bloch cells: $\mathbf{H}_{0,0}$, $\mathbf{H}_{0,-1}$ (in Fig. 4, Bloch orders are shown in superscripts for convenience; subscripts represent the Bloch cell matrix components).

For the case of Bragg reflection, $r=K/2$, the dependence of the diagonal matrix elements on d is shown in Fig. 4, starting from d as low as $0.001\lambda_t$ (this value is perhaps too small for the applied truncated system of modes); the results of Eq. (23) are presented at $d=0$ for comparison (the perturbation theory yields zero off-diagonal elements, while they are nonzero, although small, in the computed matrices $\mathbf{H}_{i,j}$). The agreement for the most important diagonal matrix elements appears to be very satisfactory. It is also interesting that the dependence of the above matrix elements on r compares well to perturbation results (inset). This verifies both the developed here and the perturbation theories.

8 Conclusions

Consider the simplest application of the above strip model in the analysis of surface wave propagation in the substrate with corrugated surface. Periodic groove grating [19] can be, otherwise, considered as periodic strips made of the substrate material. The planar harmonic Green's function of an elastic substrate (a half-space) is in notation of [18]

$$\mathbf{U} = \mathbf{G}\mathbf{T}$$

$$\mathbf{G} = \frac{j}{\mu \mathrm{R}}\begin{bmatrix} q_l k_t^2 & -p(q_t^2 - p^2 - 2q_l q_t) \\ p(q_t^2 - p^2 - 2q_l q_t) & q_t k_t^2 \end{bmatrix} \tag{24}$$

where the Rayleigh determinant $\mathrm{R}=(k_t^2-2p^2)^2+4p^2 q_l q_t$ and $\mathbf{U}$, $\mathbf{T}$ describe the displacement and traction on the substrate surface $z=0$. By taking the evaluated $\mathbf{H}$ for periodic strips, one may formulate the boundary-value problem for SAW propagation in the system as follows:

$$\mathbf{U} = \tilde{\mathbf{G}}\mathbf{H}\mathbf{U} \tag{25}$$

where $\tilde{\mathbf{G}}$ is the set of $\mathbf{G}$ evaluated at $p=r+nK$, corresponding to the spectral distribution applied in $\mathbf{H}$. Similar boundary-value problems may be formulated for piezoelectric substrate, the fundamental one for the theory of interdigital transducers [1].

This shows the value of the above presented theoretical results in modeling of periodic strips. Analogous problems find interest in geophysics [5] and qualitative nondestructive testing [19]. It can also be applied in developing the theory old SAW comb transducers, either having separately excited strips [20] or excited by incident bulk waves [21]. The analysis may also be of certain value for designing micromechanical systems, where some elements can be considered as joined, forklike systems of three strips. The boundary conditions at their junction would be correspondingly formulated in spectral domain (in Bloch series). Naturally, properties of all the above devices can be computed by using the available numerical software. The novel approach, however, may contribute to physical understanding of the involved wave phenomena of vibrating acoustic systems that is very important in optimization of complicated constructions.

The presented analysis provides the required generalization [22] of the earlier theory of SAW devices for applications at higher frequencies where thicker strips are necessary in order to minimize their electric resistivity.

Acknowledgment

This work was supported by the State Committee for Scientific Research under Grant No. N-N 501-0072-33.

References

[1] Danicki, E., 1992, "Generation and Bragg Reflection of Surface Acoustic Waves in Nearly Periodic System of Elastic Metal Strips on Piezoelectric Half-Space," J. Acoust. Soc. Am., **93**, pp. 116–131.
[2] Danicki, E., 1984, "Perturbation Theory of Surface Acoustic Wave Reflection from a Periodic Structure With Arbitrary Angle of Incidence," Arch. Mech., **36**, pp. 623–638.
[3] Biriukov, S. V., Martin, G., and Polevoi, V. G., 1995, "Derivation of COM Equations Using the Surface Impedance Method," IEEE Trans. Ultrason. Ferroelectr. Freq. Control, **UFFC-42**, pp. 602–611.
[4] Danicki, E. J., 1998, "An Approximation to the Planar Harmonic Green's Function at Branch Points in Wave-Number Domain," J. Acoust. Soc. Am., **104**, pp. 651–663.
[5] Besserer, H., and Malishevsky, P. S., 2004, "Mode Series Expansions at Vertical Boundaries in Elastic Waveguides," Wave Motion, **39**, pp. 41–59.
[6] Karunasena, W., Liew, K. M., and Kitipornchai, S., 1995, "Reflection of Plate Waves at Fixed Edge of a Composite Plate," J. Acoust. Soc. Am., **98**, pp. 644–651.
[7] Torvik, P. J., 1971, "The Elastic Strip With Prescribed End Displacements," ASME J. Appl. Mech., **38**, pp. 929–936.
[8] Torvik, P. J., 1967, "Reflection of Wave Trains in Semi-Infinite Plates," J. Acoust. Soc. Am., **41**, pp. 346–353.
[9] Gregory, R. D., and Gladwel, I., 1983, "The Reflection of a Symmetric Rayleigh-Lamb Wave at the Fixed or Free Edge of a Plate," J. Elast., **13**, pp. 185–206.
[10] Gregory, R. D., and Gladwell, I., 1982, "The Cantilever Beam Under Tension, Bending Or Flexure at Infinity," J. Elast., **12**, pp. 317–343.
[11] Dempsey, J. P., and Sinclair, G. B., 1979, "On the Stress Singularities in the Plane Elasticity of the Composite Wedge," J. Elast., **9**, pp. 373–391.
[12] Williams, M. I., 1952, "Stress Singularities Resulting From Various Boundary Conditions in Angular Corners of Plates in Extension," ASME J. Appl. Mech., **19**, pp. 526–528.
[13] Bogy, D. B., 1971, "Two Edge-Bonded Elastic Wedges of Different Materials and Wedge Angles Under Surface Traction," ASME J. Appl. Mech., **38**, pp. 377–386.
[14] Gregory, R. D., 1979, "Green's Function, Bi-Linear Forms, and Completeness of the Eigenfunctions for the Elastostatic Strip and Wedge," J. Elast., **9**, pp. 283–309.
[15] Danicki, E. J., Hickernell, F. S., and Mateescu, I., 2005, "Closed-Form Solution for SPUDTS," IEEE Freq. Contr. Symp. Proc., **1**, pp. 152–155.
[16] Danicki, E. J., 2003, "Surface Acoustic Wave Diffraction in Spectral Theory of Interdigital Transducers," J. Acoust. Soc. Am., **114**, pp. 813–820.
[17] Pagneux, V., 2006, "Revisiting the Edge Resonance for Lamb Waves in a Semi-Infinite Plate," J. Acoust. Soc. Am., **120**, pp. 647-656.
[18] Danicki, E. J., 1999, "Resonant Phenomena in Bulk-Wave Scattering by In-Plane Periodic Cracks," J. Acoust. Soc. Am., **105**, pp. 84-92.
[19] Kundu, T., Banerjee, S., and Jata, K. V., 2006, "An Experimental Investigation

of Guided Vawe Propagation in Corrugated Plates Showing Stop Bands and Pass Bands," J. Acoust. Soc. Am., **120**, pp. 1217–1226.

[20] Quarry, M. J., and Rose, J. L., 1997, "Multimode Guided Wave Inspection of Piping Using Comb Transducers," Mater. Eval., **45**, pp. 504–508.

[21] Danicki, E. J., 2002, "Scattering by Periodic Cracks and the Theory of Comb Transducers," Wave Motion, **35**, pp. 355–370.

[22] Danicki, E. J., 2007, "Spectral Theory of Interdigital Transducers," http://www.ippt.gov.pl/~edanicki/danickibook.pdf.

Modeling of Hydraulic Pipeline Transients Accompanied With Cavitation and Gas Bubbles Using Parallel Genetic Algorithms

Songjing Li[1]
e-mail: lisongjing@hit.edu.cn

Chifu Yang

Dan Jiang

Department of Fluid Control and Automation,
Harbin Institute of Technology,
Harbin 150001, P.R.C.

Mathematical models of pressure transients accompanied with cavitation and gas bubbles are studied in this paper to describe the flow behavior in a hydraulic pipeline. The reasonable prediction for pressure transients in a low pressure hydraulic pipeline largely depends on several unknown parameters involved in the mathematical models, including the initial gas bubble volumes in hydraulic oils, gas releasing and resolving time constants. In order to identify the parameters in the mathematical models and to shorten the computation time of the identification, a new method—parallel genetic algorithm (PGA)—is applied in this paper. Based on the least-square errors between the experimental data and simulation results, the fitness function of parallel genetic algorithms is programed and implemented. The global optimal parameters for hydraulic pipeline pressure transient models are obtained. The computation time of parallel genetic algorithms is much shorter than that of serial genetic algorithms. By using PGAs, the executing time is 20 h. However, it takes about 204 h by using GAs. Simulation results with identified parameters obtained by parallel genetic algorithms agree well with the experimental data. The comparison between simulation results and the experimental data indicates that parallel genetic algorithms are feasible and efficient to estimate the unknown parameters in hydraulic pipeline transient models accompanied with cavitation and gas bubbles. [DOI: 10.1115/1.2912934]

Keywords: pressure transients, cavitation, gas bubbles, parallel genetic algorithms, parameter identification

1 Introduction

Pressure transients accompanied with cavitation and gas bubbles inside low pressure hydraulic pipelines, such as the suction line of a hydraulic pump and the return line of a hydraulic system, are often generated due to the sudden standstill of hydraulic pumps or closure of valves on the pipeline where the working pressure is near to the atmospheric pressure. The presence of cavitation and gas bubbles not only badly influences the performance of hydraulic pumps and systems, but also affects the pressure transient behavior in hydraulic pipelines. Consequently, the prediction for pressure transients accompanied with cavitation and gas bubbles in low pressure hydraulic pipelines is more difficult than that in high pressure hydraulic pipelines. The reasonable prediction of pressure transients accompanied with cavitation and gas bubbles in low pressure hydraulic pipelines is of critical importance for the analysis and design of hydraulic pumps and other components, although it is more difficult and complex than that without cavitation and gas bubbles [1–3]. A rather complete overview of the transient vaporous cavitation has been given by Bergant et al. [4].

In the past few years, the majority of research has focused on models of pressure transients occurring in high pressure pipelines [5]. Although these models have attained a good level of accuracy, the development of a mathematical model for flow behaviors in low pressure pipelines accompanied with cavitation and gas bubbles has proved to be more difficult. From the previous investigations [6,7], one problem at present is that there is no agreement yet on the gas releasing and resolving time constants and the correct assumption for initial gas bubble volumes that should be used in the calculation. In order to numerically simulate pressure transients accompanied with cavitation and gas bubbles in low pressure hydraulic pipelines, it is necessary to develop appropriate pressure transient models. In this paper, a technique—parallel genetic algorithms—is presented to identify the involved unknown parameters in the fluid transient models, for the pressure transient prediction accompanied with cavitation and gas bubbles.

Parallel genetic algorithms (PGAs) are similar to the sequential genetic algorithms (GAs) [8]. They are based on the natural evolutionary principle. However, PGA can be used to improve the quality of solutions and to reduce the computing time [9]. Alba and Troya [10] proposed six different models of PGA. James et al. [11] investigated the performance of the same global PGA on two popular parallel architectures to investigate the interaction of parallel platform choice and GA design. Kirley and Li [12] presented and implemented PGA on a hypercube parallel computer. Li and Cho [13] implemented PGA on PCs based on Linux clusters with message passing interface (MPI) libraries in C++. Sena et al. [14] designed and implemented PGA on PCs based on Linux clusters with parallel virtual machine (PVM) libraries. MPI or PVM functions are, in fact, the standard nowadays, but they are complicated and require lots of coding and fine tuning. In addition, hypercube parallel computers are expensive and Linux system is complex and not widespread in engineering application areas. Instead, in this paper, MATLAB distribute computing toolbox (DCT) and MATLAB GA toolbox are chosen to implement the parameter identification in Windows XP system by PGA, which are actualized in several computers. PGA can reduce the executing time significantly compared with GA running on a single computer. Hence,

---

[1] Corresponding author.

Contributed by the Applied Mechanics Division of ASME for publication in the JOURNAL OF APPLIED MECHANICS. Manuscript received February 26, 2007; final manuscript received March 27, 2008; published online May 14, 2008. Review conducted by Nesreen Ghaddar.

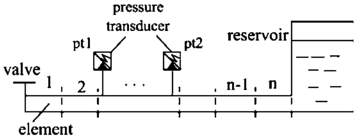

Fig. 1 Studied pipeline

parameter identification is carried out in this paper by means of PGA whose fitness function is the sum of the least-square errors between the experimental and simulation results. The PGAs are applied to perform a global search and obtain the optimal parameters for pressure transient models.

2 Problem Description

The fluid transient problem in a horizontal hydraulic pipeline is studied in this paper. The horizontal hydraulic pipeline with a reservoir at one end and a valve at the other end is shown in Fig. 1. The parameters of the pipeline are shown in Table 1. The reservoir supplies a constant upstream pressure. If there is a steady flow flowing to the valve side from the reservoir side inside the pipeline, after the valve is suddenly shut off, there will be a fluid transient in the form of pressure pulsations propagating along the pipeline. If the pressure inside the pipeline falls below the atmospheric pressure or even reaches the vapor pressure of the hydraulic oil, gas bubbles and cavitation will occur inside the fluid.

Suppose that the initial flow inside the pipeline is one-dimensional single-phase unsteady compressible flow. If outside forces and heat exchanging are ignored, the mathematical models for the fluid transients in the low pressure hydraulic pipeline can be described as

$$\frac{1}{C_0^2}\frac{\partial p}{\partial t}+\frac{\rho}{\pi r_0^2}\frac{\partial q}{\partial x}=0 \tag{1}$$

$$\frac{\rho}{\pi r_0^2}\frac{\partial q}{\partial t}+\frac{\partial p}{\partial x}+F(q)+\rho g\sin\theta_0=0 \tag{2}$$

$$C_0=\sqrt{\frac{B_{\text{eff}}}{\rho}} \tag{3}$$

$$F(q)=F_0+\frac{1}{2}\sum_{i=1}^{k}Y_i \tag{4}$$

where $\frac{1}{2}\Sigma_{i=1}^{k}Y_i$ was given in Ref. [15] and $F_0=8\rho\mu q/\pi r_0^4$. If the pipeline is horizontal, the gravity term can be neglected. If the elasticity of pipe wall is taken into account, the effective bulk modulus of gas-liquid mixture B_{eff} in the pipeline can be expressed as

$$\frac{1}{B_{\text{eff}}}=\frac{1}{B_{\text{pipe}}}+\frac{1}{B_{\text{liquid}}}+\frac{V_{\text{gas}}}{V_0}\left(\frac{1}{B_{\text{gas}}}-\frac{1}{B_{\text{liquid}}}\right) \tag{5}$$

In this paper, both B_{liquid} and B_{gas} are taken as constants in order to simplify the simulation. Formula (5) shows that the cavitation and gas bubbles influence the fluid transients by influencing the effective bulk modulus of the gas-liquid mixture. Hence, it is important to take the volume of cavitation and gas bubbles into account in the fluid transient models.

We assume the following.

(1) Cavitation starts to grow when the pressure reaches below or equals to the vapor pressure (near zero). On the contrary, cavitation disappears.
(2) Pressure equals to the vapor pressure at vaporous conditions.
(3) Volume of gas bubbles increases when the pressure goes below the saturation pressure (assumed atmospheric pressure in this paper). On the contrary, the volume of gas bubbles decreases.

The volume of cavitation and gas bubbles can be calculated from the following formulas:

$$V_{\text{gas}}=V_{\text{gasb}}+V_{\text{cav}} \tag{6}$$

$$\frac{dV_{\text{gas}}}{dt}=q_{\text{out}}-q_{\text{in}},\quad p\le p_{\text{vapor}}$$

$$V_{\text{cav}}=0,\quad p>p_{\text{vapor}} \tag{7}$$

$$V_{\text{gasb}}=V_{\text{ingas}}+v_e-v \tag{8}$$

$$\frac{dv}{dt}=\frac{v_\infty-v}{\tau},\quad \tau=\begin{cases}\tau_{\text{out}}, & p\le p_e\\ \tau_{\text{in}}, & p>p_e\end{cases} \tag{9}$$

$$v_e=S\cdot V_0 \tag{10}$$

where S is 0.1 for hydraulic oils and 0.02 for water at room temperature and atmospheric pressure [16]. Moreover, from Henry's law for dissolved gas in liquid, it can be written as

$$v_\infty=v_e\frac{p}{p_e} \tag{11}$$

Formulas (8) and (9) show that not only the initial gas volume but also the gas releasing time constant and the gas resolving time constant will influence the gas bubble volumes inside the oils at a certain time during the transients.

In order to investigate the influence of initial gas bubble volumes on the fluid transients, simulations are carried out on the assumption of initial gas bubble volumes being 0.1%, 1%, and 3% of the oil volume, respectively. The gas releasing time constant and the gas resolving time constant are 5 s and 10 s in all the simulations, respectively. The predicted pressure pulsations inside the pipeline are shown in Fig. 2. An upwind/central finite difference method is used to calculate the pipeline transients after the pipeline is divided into n number of elements in length, as shown in Fig. 1. Simulation results when the element number is 20, 40, or 80 are given in Fig. 10 in Appendix B. It can be seen that the predicted pressure pulsations are almost consistent with each other at the first three pressure peaks when the element number is 20, 40, and 80. Hence, for those problems that only the first three pressure peaks are concerned, 20 elements are enough. If the fourth pressure peaks are considered, the pressure pulsations are consistent when the element number is 40 and 80. Therefore, for the problem that four pressure peaks are concerned in this paper, 40 elements are enough. The simulation results in Fig. 2 show the pressure pulsations at the eighth element.

Figure 2 shows that the predicted pressure transients change largely with the initial gas bubble volumes inside the pipeline. The

Table 1 Parameters of the pipeline

Parameters	Value
Bulk modulus of hydraulic oil B_{liquid}, Pa	1.9E009
Bulk modulus of gas B_{gas}, Pa	3E007
Kinetic viscosity of hydraulic oil μ, mm^2/s	44
Density of hydraulic oil at 25°C ρ, kg/m^3	875
Reservoir pressure p_0, Pa	1.025E005
Initial flow rate q, m^3/s	8.49$E-$005
Pipeline diameter d, m	0.0102
Length of pipeline L, m	3.856
Wall thickness of pipeline h, m	0.0015
Modulus of elasticity of pipe wall material E, Pa	105.6E009

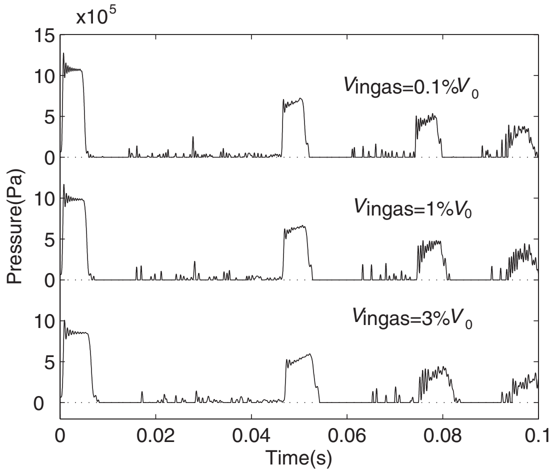

Fig. 2 Pressure pulsations with different initial volumes of gas bubbles

oscillations on the top of the first pressure peak are the numerical oscillations. The larger the element number is, the less the numerical oscillations. However, the oscillations can hardly be removed entirely.

The initial gas volume V_{ingas} can also be estimated from the Joukowsky equation

$$C_0 = \frac{A\Delta p}{\rho \Delta q} \tag{12}$$

If the gas content ratio α is $\alpha = V_{\mathrm{gas}}/V_0$, the density of gas-oil mixture ρ can be expressed as

$$\rho = \alpha\rho_{\mathrm{gas}} + (1-\alpha)\rho_{\mathrm{liquid}} \tag{13}$$

By combining Eqs. (3), (12), and (13), the initial gas volume V_{ingas} can be estimated.

Similarly, being a function of pressure and time, the gas releasing and resolving rates are unknown for the fluid transient models. When the pressure in a hydraulic pipe goes down, gas absorbed in hydraulic oils tends to come out in the form of gas bubbles in the oil. The volume of gas bubbles will increase. Moreover, when the pressure rises up, gas bubbles will go back to the solution. The volume of gas bubbles will decrease. From experience and previously published study [17], it is accepted that the gas resolving time constant and gas releasing time constant influence the pressure pulsations in hydraulic pipelines significantly. In order to investigate the influence of time constants on the pipeline transients, simulations are carried out using the three groups of parameters in Table 2. The three groups of gas releasing and resolving time constants were published in Ref. [18]. The initial gas bubble volume was estimated from the Joukowsky equation. The predicted pressure pulsations are shown in Fig. 3 and compared with experimental data, which will be introduced in the later part of this paper.

Figure 3 shows that gas releasing time constant and gas resolving time constant have significant effects on the pressure transients in hydraulic pipelines accompanied with cavitation and gas bubbles, especially on the durations between pressure peaks. In order to develop an accurate mathematical model of the pipeline pressure transients, the gas releasing time constant and gas resolving time constant are the vital identification parameters.

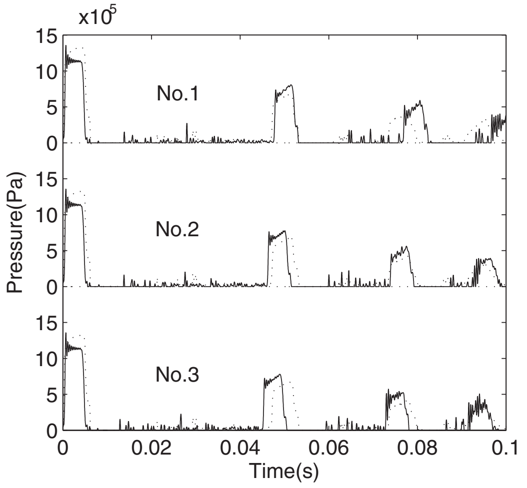

Fig. 3 Pressure pulsations with different time constants of gas releasing and resolving (see Table 2)

3 Parallel Genetic Algorithms

PGAs are parallel stochastic optimization methods for solving constrained and unconstrained optimization problems based on biological evolution theories. In PGA, there is always a selection-crossover-mutation cycle the same as in serial GAs. Parameter identification problems for pressure transient modeling accompanied with cavitation and gas bubbles involve computationally expensive fitness functions. For each generation of GAs, the fitness function must be evaluated on the local computer serially. It may take several days to get a result. The bottleneck is the serial calculation of the individual fitness value in GAs and the number of individual fitness calculations. Usually, for better accuracy, the GAs should be terminated after enough number of generations and each population should have enough individuals. As the calculating time of the fitness function is higher than the communication time between the master processor and the slave processors, it is necessary to distribute the fitness evaluations across processors and compute them in parallel.

3.1 Identified Parameters. From the introduction in Sec. 2, the unknown parameters for the fluid transient modeling accompanied with cavitation and gas bubbles are the gas releasing time constant and the gas resolving time constant. As the simulation and experimental errors exist, the initial gas volume estimated from Eq. (12) may not be accurate. In this paper, the initial gas volume is taken as a parameter that needs to be identified too.

3.2 Encoding. PGAs work with encoded parameters rather than parameters themselves. In order to optimize parameters in pressure transient models, parameters need to be encoded separately as binary strings. The parameters are a set of real numbers and later they are encoded as bit strings and concatenated to form chromosomes. The length of a chromosome depends on the re-

Table 2 Simulation parameters with different gas releasing and resolving time constants

Group No.	Gas releasing time τ_{out}, s	Gas resolving time τ_{in}, s	Initial volume of gas bubbles V_{ingas}, m^3	Volume of element V_0, m^3
1	0.43	4.44	3.938442E−009	7.876884E−006
2	5.13	8.86	3.938442E−009	7.876884E−006
3	65	557	3.938442E−009	7.876884E−006

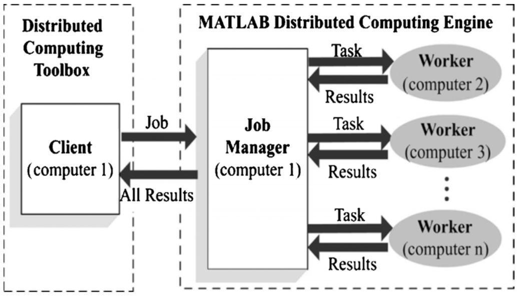

Fig. 4 Basic cluster computing configuration

quired precision. As each parameter is encoded to B binary bits and the number of identified parameters is 3, the total length of a chromosome is $3B$ bits and the solution space is 2^{3B}. In order to avoid being negative, the optimal range is defined from zero to infinitely large.

3.3 Fitness Function. A fitness function is used to compute the fitness of each chromosome and therefore plays a very important role in PGA. Traditionally, the value of fitness function is a positive value. A fitness value should represent how good a chromosome is for the given problem. The strings with better fitness value are more likely to be selected for reproduction in the following generation.

In order to find the optimal values of the parameters, the fitness function is minimized in the form of a sum of the least-squared errors between the experimental data and predicted pressure pulsations. As both of the pressure peaks and the time duration between them are concerned, the fitness function is constructed by evaluating both the difference between the predicted and tested pressure peaks and the difference between the predicted and tested durations between the peaks. It can be described as

$$\min \phi = k_1 \sqrt{\sum_t \left[(y(t)-y_0(t))^T (y(t)-y_0(t))\right]} + k_2 \sum_i \left|t^{(i)}_{p_{\max}} - t^{(i)}_{0p_{\max}}\right|, \quad i=2,3,4 \tag{14}$$

where ϕ is the fitness function, $y(t)$ is the predicted pressure results, $y_0(t)$ is the experimental pressure data, $t_{0p_{\max}}$ is the time duration between the tested pressure peaks, $t_{p_{\max}}$ is the time duration between the predicted pressure peaks, and k_1 and k_2 are weighting factors.

3.4 Parallel Computing Using MATLAB. By using the Windows OS and local network, the DCT and MATLAB distributed computing engine (MDCE) are used to implement the simultaneous computation of the fitness functions on a cluster of computers by PGA. DCT and MDCE can facilitate the coordination and execution of independent operations simultaneously on a cluster of computers in order to speed up the execution of time consuming jobs. All the originally complete large-scale jobs are broken down into segments. The segments are also called tasks. The DCT defines the job as the computation of the fitness function on a cluster of computers. Each computer is a worker where the user's MATLAB program runs. The MDCE performs the job execution by evaluating each of its tasks and returning the results to the client. The job manager is the part of the engine that coordinates the execution of jobs and the evaluation of their tasks. It distributes the tasks for evaluation to all workers, as shown in Fig. 4.

The job manager can be run on any computer through the network. It runs jobs in the order in which they are submitted, unless a job in its queue is promoted, demoted, canceled, or destroyed. A MDCE setup usually includes many workers that can execute all tasks simultaneously. The MDCE Daemon makes it possible for these processors to communicate with each other on different computers. Each worker is given a task from the running job by the job manager to execute the task and return the results to the job manager. Thereafter, another task is given. The job manager then returns the results of all the tasks in the job to a client session (client session is a computer). It is generally not important which worker executes which specific task. After the fitness functions of all individuals in a population are computed completely, the algorithm program returns to serial GAs to execute.

4 PGA Implementation

PGAs can be implemented without changing the GA codes in WINDOWS/MATLAB. Only the distributed computing environment needs to be set up and a function has to be used to distribute all the tasks across the worker computers.

4.1 Simulation Model. The prediction of pipeline transients is carried out based on the MATLAB SIMULINK platform because it can be easily linked with the predictions of other hydraulic components, which are usually in a MATLAB SIMULINK environment as well. In the SIMULINK program, the flow rate and pressure variables are created as vectors. As the finite difference method is used for the simulation, the pipeline is divided into n elements with equal length. The vectors of flow and pressure inside the pipeline can be described as

$$q=[q_1\ q_2\ \cdots\ q_n]^T, \quad p=[p_1\ p_2\ \cdots\ p_n]^T$$

The partial differential terms in the time domain $\partial/\partial t$ in Eqs. (1) and (2) can be easily calculated using a standard integral block in SIMULINK. The partial differential terms in the spatial domain $\partial/\partial x$ in Eqs. (1) and (2) can be constructed by using the selector block in SIMULINK. The selector block in MATLAB/SIMULINK is used to select or reorder the specified elements from an input vector or matrix.

For example, by using the selector block, the first $n-1$ elements in the flowrate vector can be selected. If the boundary condition (the flow rate at the valve side $q_0=0$ after the sudden closure of the valve) is specified and this together with the other $n-1$ elements forms a new flow rate vector $q'=[q_0\ q_1 \cdots q_{n-1}]^T$, dq/dx can be described as

$$\frac{dq}{dx} = \frac{(q-q')}{dx} = \frac{[q_1\ q_2\ \cdots\ q_n]^T - [q_0\ q_1\ \cdots\ q_{n-1}]^T}{dx} = \frac{\begin{bmatrix} q_1-q_0 \\ q_2-q_1 \\ \vdots \\ q_n-q_{n-1} \end{bmatrix}}{dx} = \frac{\begin{bmatrix} \Delta q_1 \\ \Delta q_2 \\ \vdots \\ \Delta q_n \end{bmatrix}}{dx} \tag{15}$$

From the pressure vector $p=[p_1\ p_2 \cdots p_n]^T$, the last $n-1$ elements are selected. The boundary condition (the pressure at the reservoir side $p_0=1.0257\times 10^5$ Pa) is taken as the last element and this together with the other $n-1$ elements forms a new n-dimensional pressure vector $p'=[p_2 \ldots p_n p_0]^T$. So that dp/dx can be described as

$$\frac{dp}{dx} = \frac{(p'-p)}{dx} = \frac{[p_2\ \cdots\ p_n\ p_0]^T - [p_1\ p_2\ \cdots\ p_n]^T}{dx} = \frac{\begin{bmatrix} p_2-p_1 \\ p_3-p_2 \\ \vdots \\ p_n-p_{n-1} \\ p_0-p_n \end{bmatrix}}{dx} = \frac{\begin{bmatrix} \Delta p_1 \\ \Delta p_2 \\ \vdots \\ \Delta p_{n-1} \\ \Delta p_n \end{bmatrix}}{dx} \tag{16}$$

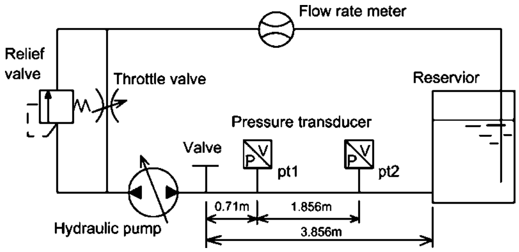

Fig. 5 Test rig for pressure pulsation

The SIMULINK block diagram for dq/dx and dp/dx can be described by MATLAB/SIMULINK blocks, as introduced in Ref. [5].

The whole simulation model, which is used to identify the initial gas bubble volume, gas releasing time constant and gas resolving time constant by PGA, can be described by a SIMULINK block diagram. When the pressure and flow rate of each element are decided, the gas bubble volumes V_{gasb} can be calculated using Eqs. (8)–(11) and the cavitation volume can be calculated using Eq. (7). Similarly, the effective bulk modulus B_{eff} can be calculated using Eq. (5) and the acoustic velocity C_0 in oils can be calculated from Eq. (3).

4.2 Programming and Realization of the Algorithms. The PGA is implemented based on the distributing parallel computing environment. The parallel computing environment is based on a local network with four PCs.

In order to guarantee the communication between computers, the "cmd" command should be inputted and run in Windows OS RUN. Then, in the directory of MATLAB, commands should run in the MS-DOS system to install and setup parallel computing soft environment MDCE on the job manager and worker computers.

The fitness function for pressure transient models defines the variables in SIMULINK models and requires the calling of the models. Based on the least-square errors between predicted and experimental pressure peaks, as well as the difference of time durations, the fitness function is evaluated by calling the simulation and experimental curves from SIMULINK models. In the parallel computing, the "assignin" function should be used to define the global variables and send the variable values to the SIMULINK models to actualize the data share and transmission between m-files and SIMULINK models when programming the fitness function.

By using the MATLAB DCT, MATLAB GA, and directed search toolbox, the PGAs for the pressure transient parameter identifications can be implemented. The "ga" function is selected to execute genetic algorithms. The "FileDependencies" function of DCT is used to copy the MATLAB files and SIMULINK models from the client session to worker computers and then executes them on the workers. The "distributionpopulation" function is used to distribute the population of points into a cell array. The "dfeval" function is applied to implement the simultaneous computation of the fitness function on the worker computers. The "gaoptimset" function is selected to setup PGA parameters and the population size (20 in this paper) of a generation. The number of generations is set to be 50 in this paper. The selection method is "roulette elite" and the number is 2. The crossover fraction is 0.8 and the migration fraction is 0.2. The "tic" and "toc" functions are used to note the overall executing time of the PGAs.

5 Optimized Results

Parameter identifications are carried out by using the experimental data to select the reasonable parameter values in the simulation models. The experimental data were obtained from the pipeline test rig for pressure pulsations, as shown in Fig. 5. The test rig consists of a pump driven by an electric motor, a on-off valve, a reservoir, a relief valve, a throttle valve, the pipeline, two pressure transducers, a temperature meter, and a flow rate meter. The on-off valve is used to create the pressure pulsations inside the pipeline. The reservoir at one end of the pipeline provides a constant upstream pressure. The relief valve guards the safety of the system. The throttle valve is used to heat the oil to a certain temperature. Usually, it is fully opened. The rotating speed of the electric motor can be adjusted, so that the flow rate of the pump is variable. Two piezoelectric pressure transducers for the dynamic pressure measurement were fitted on the pipe and used to directly record the pressure pulsations with 0.1 ms sample time. The dynamic response of the piezoelectric transducer is 200 kHz. Some construction parameters of the test rig, as well as the information of hydraulic oils, are the same as the simulation parameters in Table 1. All the other parameters are labeled in Fig. 5. After an experiment is performed, a large number of gas bubbles may be accumulated in the reservoir. Then, the initial gas volume for the next experiment will be changed and the reproducibility of the experiment will be influenced. In order to avoid the influence of a previous experiment, enough long time should be waited until the same experiment is repeated. Sometimes, overnight resting of the test rig is necessary. Pressure pulsations measured by the first pressure transducer in three repeat experiments are shown in Fig. 11 in Appendix C.

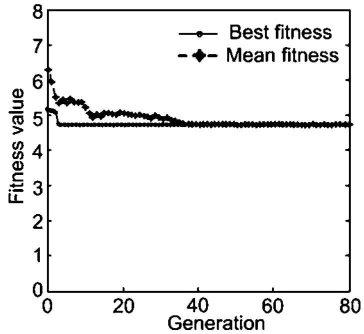

Fig. 6 Fitness value with generation

Hence, two sets (pt1 and pt2) of data from the same experiment were obtained by the two transducers. One is used for the model parameter identification by PGA. The other is used to validate the accuracy of pressure transient models with optimized parameters. Swapping the roles of the two transducers will not change the results of the identification. In the procedure of PGA, experimental data were taken from the first pressure transducer close to the valve. As the "Spline" function in MATLAB software is effective for removing noise, it is used to denoise the experimental data in the MATLAB program before the PGA runs.

For the optimization procedure, the PGA is set up on a population of chromosomes made up of three genes, which are the parameters of initial gas bubble volume V_{ingas}, gas releasing time constant τ_{out}, and gas resolving time constant τ_{in}, respectively. Figure 6 presents the average fitness value and the optimal fitness value during the identification. It shows that the algorithm is well convergent and the average fitness value achieves the best value. The results of parameter identifications are reported in Table 3. The initial gas volume V_{ingas} (almost 0.05% V_0) estimated from

Table 3 Results of parameter identifications

Parameters	Value
Gas releasing time constant τ_{out}, s	11.35
Gas resolving time constant τ_{in}, s	23.61
Identified initial volume of gas bubbles V_{ingas}, m^3	$4.019562E-009$
Estimated initial volume of gas bubbles V_{ingas}, m^3	$3.938442E-009$
The volume of element V_0, m^3	$7.876884E-006$

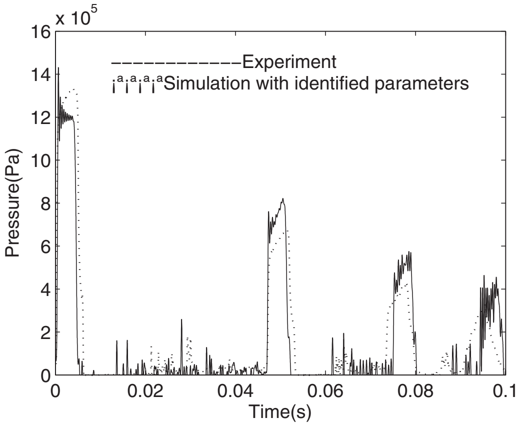

Fig. 7 Comparison of simulation and experimental pressure pulsations from the first transducer

formulas (3), (5), and (11) is also shown in the table. It can be seen that the identified gas releasing time constant τ_{out} and the gas resolving time constants τ_{in} are close to the experimental values for the heavy lubricating oil (11.7 s for evolution and 32.7 s for solution) given in Ref. [18]. The table also shows that the identified initial gas volume nearly agrees with the estimated initial gas volume.

The pressure pulsations predicted by using the mathematical models with the identified parameters are shown in Fig. 7 and compared with the experimental data from the first pressure transducer.

The comparison between the simulation and experimental results in Fig. 7 shows that the pressure transient model with identified parameters handles the simulation of pressure transients, especially the first four peaks and the time duration between the peaks, with a better accuracy compared with the models using parameters in Table 2 given by Ref. [18]. See Fig. 3.

In order to verify the practicability of the model with identified parameters, the other set of experimental data from the second transducer is compared with the simulation results of the model with the same identified parameters, as shown in Fig. 8.

Good agreement between the two curves is seen in Fig. 8. Comparison of the results in Figs. 7 and 8 demonstrates that optimization using the PGA method presented in this paper is capable of estimating unknown parameters in the pressure transient models accompanied with cavitation and gas bubbles inside low pressure hydraulic pipelines.

To prove the PGA performance, the PGA programs with different numbers of workers and the serial GA programe are executed to identify the unknown parameters in the pressure transient models. The executing times of different programs are shown in Table 4.

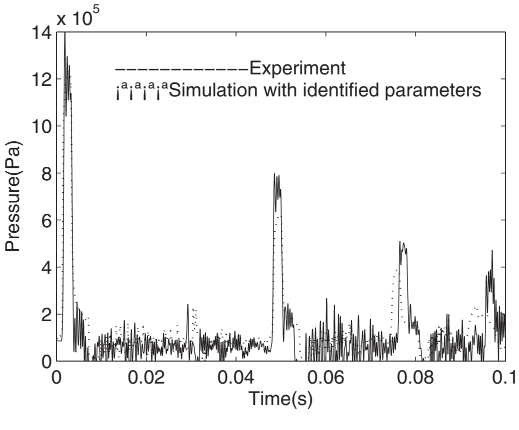

Fig. 8 Comparison of simulation and experimental pressure pulsations from the second transducer

Table 4 Executing time of PGA and GAs

Algorithms	No. of computers	No. of workers	Executing time t_e, h
GAs	1	0	204
PGA	2	1	207
PGA	3	2	39
PGA	4	3	20

Table 4 shows that the executing time using GAs is about 204 h, which is about 9 days. By using PGA with three workers, the executing time is shortened to be 20 h, which is about 0.8 day only. The comparison of executing times indicates that the executing time of PGA with two or three workers is much shorter than that of GAs. However, the computing time of PGA with one worker is a little longer than that of GAs. This is probably because of the communication time wasted by the PGA. The executing time shows that the PGA with more than one worker can shorten the parameter-identification time for pressure transient models accompanied with cavitation and gas bubbles significantly.

6 Conclusions

In order to predict the fluid transients accompanied with cavitation and gas bubbles inside hydraulic pipelines, the parameter identification for the transient process modeling is completed using PGAs. Based on the Windows OS and a local network, PGAs are executed on a cluster of computers. By applying PGA, the global optimal parameters for the gas releasing time constant and the gas resolving time constant in the pipeline transient models are identified. The comparison of executing time when PGA and GAs are executed for the parameter identifications shows that PGA with more than two workers can save computing time significantly. The comparison of simulation and experimental pressure data shows that PGA is able to identify efficiently, not only the gas releasing and resolving time constants, but also other parameters necessary for the low pressure hydraulic pipeline transient models.

However, it should be kept in mind that the proposed procedure for parameter identification is sensitive to many things. The estimation of the unknown parameters depends on the validity and accuracy of the mathematical models and the applied numerical methods, as well as the accuracy of the experiments. Further work still needs to be done to see if the identified time constants are universal for all kinds of hydraulic oils under all kinds of conditions.

Acknowledgment

The authors would like to give their acknowledgement to Professor Kevin A. Edge in the University of Bath in the UK for his supervision on some parts of the work in this paper.

Nomenclature

A = flow area of pipeline, m^2
B_{eff} = effective bulk modulus of gas and liquid mixture, Pa
B_{gas} = bulk modulus of gas, Pa
B_{liquid} = bulk modulus of oil in the pipeline, Pa
B_{pipe} = bulk modulus of pipe wall, Pa
C_0 = acoustic velocity inside the fluid, m/s
E = modulus of elasticity of pipe wall material, Pa
F_0 = steady state friction term, N
$F(q)$ = friction term, N
g = acceleration because of gravity, m/s^2
h = thickness of pipe wall, m

n = number of elements
p = pressure of an element, Pa
p_e = saturation pressure (atmospheric pressure) of hydraulic oil, Pa
p_{vapor} = vapor pressure of hydraulic oil, Pa
q = flow rate of an element, m^3/s
q_{in} = flow rate coming into each element, m^3/s
q_{out} = flow rate going out of each element, m^3/s
r_0 = inner pipeline radius, m
r_1 = outer pipeline radius, m
S = solubility constant of hydraulic oil
t = time variable, s
V_0 = volume of each element, m^3
V_{gas} = volume of gas bubbles and cavitation during fluid transients, m^3
V_{liquid} = volume of liquid, m^3
V_{cav} = volume of cavitation, m^3
V_{gasb} = volume of gas bubbles, m^3
V_{ingas} = initial gas volume, m^3
V_{pipe} = volume of pipe interior, m^3
x = spatial variable, m
α = gas content ratio
μ = kinetic viscosity of fluid, m^2/s
ρ = density of gas and oil mixture, kg/m^3
ρ_{liquid} = density of oil, kg/m^3
ρ_{gas} = density of gas, kg/m^3
θ_0 = inclination of pipe, rad
v_e = volume of gas resolved in oil at initial state, m^3
v = transient volume of gas resolved in oil before equilibrium is achieved, m^3
v_∞ = volume of gas resolved at pressure p when equilibrium is achieved, m^3
τ = gas releasing time constant or gas resolving time constant, s
τ_{out} = gas releasing time constant, s
τ_{in} = gas resolving time constant, s
Δp = pressure rise after valve closure
Δq = initial flow rate of pipeline

Appendix A: Derivation of Equation (4)

Initially, the total volume of an element V_0 can be written as

$$V_0 = V_{\text{liquid}} + V_{\text{gas}} \tag{A1}$$

where V_{liquid} and V_{gas} are initial volumes of the liquid and gas, respectively, and $V_0 = V_{\text{pipe}}$. As shown in Fig. 9, when there is a pressure increase Δp in the pipeline, there will be a decrease in the initial volume of

$$\Delta V_0 = -\Delta V_{\text{gas}} - \Delta V_{\text{liquid}} + \Delta V_{\text{pipe}} \tag{A2}$$

where the subscripts gas, liquid, and pipe refer to the gas, liquid, and pipe wall, respectively. The effective or total bulk modulus B_{eff} can be defined by

$$\frac{1}{B_{\text{eff}}} = \frac{\Delta V_0}{V_0 \Delta p} \tag{A3}$$

Combining Eqs. (A1) and (A2) yields

$$\frac{1}{B_{\text{eff}}} = \frac{V_{\text{gas}}}{V_0}\left(-\frac{\Delta V_{\text{gas}}}{V_{\text{gas}}\Delta p}\right) + \frac{V_{\text{liquid}}}{V_0}\left(-\frac{\Delta V_{\text{liquid}}}{V_{\text{liquid}}\Delta p}\right) + \left(\frac{\Delta V_{\text{pipe}}}{V_0 \Delta p}\right) \tag{A4}$$

The bulk modulus of a liquid can be expressed as

$$B_{\text{liquid}} = -\frac{V_{\text{liquid}}\Delta p}{\Delta V_{\text{liquid}}} \tag{A5}$$

The bulk modulus of a gas may be defined by

$$B_{\text{gas}} = -\frac{V_{\text{gas}}\Delta p}{\Delta V_{\text{gas}}} \tag{A6}$$

The quantity

$$B_{\text{pipe}} = \frac{V_0 \Delta p}{\Delta V_{\text{pipe}}} \tag{A7}$$

may be defined as the bulk modulus of the pipe wall with respect to the total volume. Substituting (A5)–(A7) into (A4) gives the final result. Therefore,

$$\frac{1}{B_{\text{eff}}} = \frac{V_{\text{gas}}}{V_0}\left(\frac{1}{B_{\text{gas}}}\right) + \frac{V_{\text{liquid}}}{V_0}\left(\frac{1}{B_{\text{liquid}}}\right) + \frac{1}{B_{\text{pipe}}} \tag{A8}$$

This is a general equation, which gives the equivalent bulk modulus for a liquid-gas mixture in a flexible pipeline. Solving Eq. (A1) for V_0 and substituting $V_{\text{liquid}} = V_0 - V_{\text{gas}}$ into Eq. (A8) give

$$\frac{1}{B_{\text{eff}}} = \frac{1}{B_{\text{pipe}}} + \frac{1}{B_{\text{liquid}}} + \frac{V_{\text{gas}}}{V_0}\left(\frac{1}{B_{\text{gas}}} - \frac{1}{B_{\text{liquid}}}\right) \tag{A9}$$

For a thin-walled metal pipeline, such that $r_0 \approx r_1$, the bulk modulus of pipe wall can be approximated to

$$B_{\text{pipe}} = \frac{hE}{2r_0} \tag{A10}$$

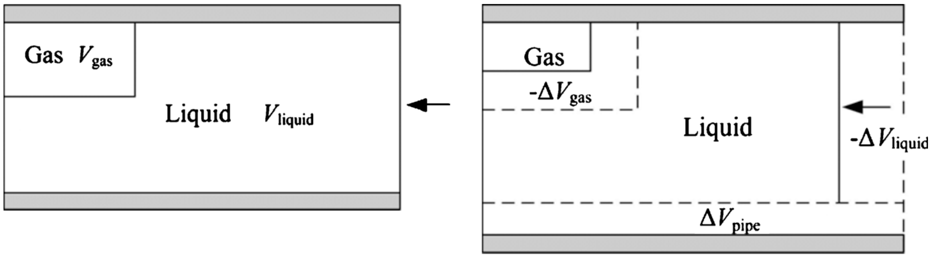

(*a*) (*b*)

Fig. 9 Pipeline filled with gas-liquid mixture: (*a*) initial situation and (*b*) under compression

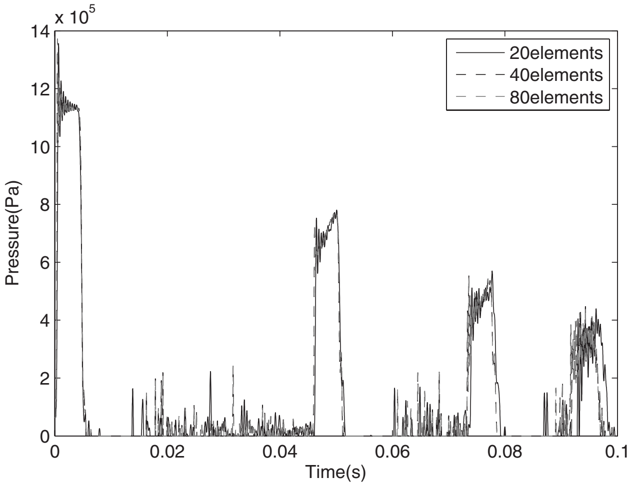

Fig. 10 Predicted pressure pulsations when the element number is 20, 40, and 80, respectively ($V_{\mathrm{ingas}}=0.1\% V_0$)

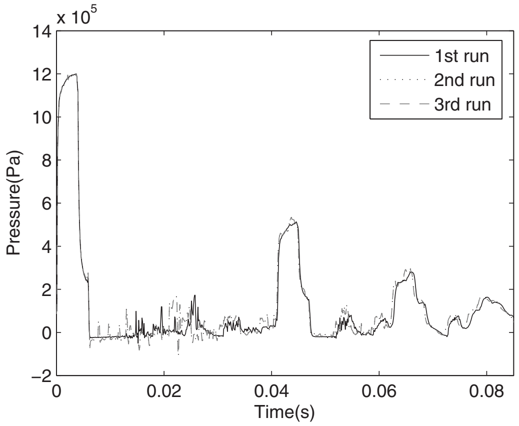

Fig. 11 Tested pressure pulsations in three repeated experiments

Appendix B: Predicted Pressure Pulsations When the Element Number is 20, 40, and 80

Please see Fig. 10 for tested pressure pulsations.

Appendix C: Tested Pressure Pulsations in Three Repeated Experiments

Please see Fig. 11 for predicted pressure pulsations.

References

[1] Shu, J. J., Burrows, C. R., and Edge, K. A., 1997, "Pressure Pulsation in Reciprocating Pump Piping Systems Part 1: Modeling," Proc. Inst. Mech. Eng., Part I., **211**, pp. 229–237.

[2] Shu, J. J., 2003, "Modeling Vaporous Cavitation on Fluid Transients," Int. J. Pressure Vessels Piping, **80**, pp. 187–195.

[3] Bergant, A., and Simpson, R. S., 1999, "Pipeline Column Separation Flow Regimes," J. Hydraul. Eng., **125**(11), pp. 835–848.

[4] Bergant, A., Simpson, A., and Tijsseling, A., 2006, "Water Hammer With Column Separation: A Historical Review," J. Fluids Struct., **22**, pp. 135–171.

[5] Li, S. J., Edge, K. A., and Bao, W., 2005, "Simulation of Hydraulic Pipeline Pressure Transients Using Matlab Simulink," in Proceedings of the Sixth International Conference on Fluid Power Transmission and Control (ISFP'2005), Hangzhou, China, pp. 468–471.

[6] Wylie, E. B., Streeter, V. L., and Suo, L. S., 1993, *Fluid Transients in Systems*, Prentice-Hall, Englewood Cliffs, N.J.

[7] Zielke, W., Perko, H. D., and Keller, A., 1989, "Gas Release in Transient Pipe Flow," in Proceedings of the Sixth International Conference on Pressure Surges, BHRA, Cambridge, UK, pp. 3–13.

[8] Holland, J. H., 1992, *Adaptation in Natural and Artificial Systems*, MIT, Cambridge, MA.

[9] Solar, M., Parada, V., and Urrutia, R., 2002, "A. Parallel Genetic Algorithm to Solve the Set-Covering Problem," Comput. Oper. Res., **29**(9), pp. 1221–1235.

[10] Alba, E., and Troya, J. M., 2001, "Analyzing Synchronous and Asynchronous Parallel Distributed Genetic Algorithms," FGCS, Future Gener. Comput. Syst., **17**(4), pp. 451–465.

[11] James, T. L., Barkhi, R., and Johnson, J. D., 2006, "Platform Impact on Performance of Parallel Genetic Algorithms: Design and Implementation Considerations," Eng. Applic. Artif. Intell., **19**(8), pp. 843–856.

[12] Kirley, M., and Li, X. D., 2002, "The Effects of Varying Population Density in a Fine-Grained Parallel Genetic Algorithm," in Proceedings of the 2002 IEEE Congress on Evolutionary Computation, Honolulu, HI, Vol. 2, pp. 1709–1714.

[13] Li, Y. M., and Cho, Y. Y., 2006, "Parallel Genetic Algorithm for SPICE Model Parameter Extraction," in 20th IEEE International Parallel and Distributed Processing Symposium, Rhodes Island, Greece, Paper No. IPDPS1639609.

[14] Sena, G. A., Megherbi, D., and Isern, G., 2001, "Implementation of a Parallel Genetic Algorithm on a Cluster of Workstations: Traveling Salesman Problem, A Case Study," Adv. Perform. Mater, **17**(4), pp. 477–488.

[15] Kagawa, T., Lee, I. Y., Kitagawa, A., and Takenaka, T., 1983, "High Speed and Accurate Computing Method of Frequency-Dependent Friction in Laminar Pipe Flow for Characteristic Method," Trans. JSME, Ser. B., **49**(447), pp. 2638–2644.

[16] Lee, I. Y., Kitagawa, A., and Takenaka, T., 1985, "On the Transient Behaviour of Oil Flow Under Negative Pressure," Bull. JSME, **28**(240), pp. 1097–1104.

[17] Wiggert, D. C., and Sundquist, M. J., 1979, "The Effect of Gaseous Cavitation on Fluid Transients," J. Fluids Eng., **101**, pp. 79–86.

[18] Schweitzer, P. H., and Szebehely, V. G., 1950, "Gas Evolution in Liquids and Cavitation," J. Appl. Phys., **21**(12), pp. 1218–1224.

Davresh Hasanyan[1]
Zhanming Qin[2]
Liviu Librescu[3]

Department of Engineering Science
and Mechanics,
Virginia Polytechnic Institute
and State University,
Blacksburg, VA 24061-0219

Elastic Stress and Magnetic Field Concentration Near the Vertex of a Soft-Ferromagnetic 2D Compound Wedge

The problem of elastic stress and magnetic field concentration near the vertex of a compound wedge is modeled and investigated. The wedge is made of two isotropic dielectric soft-ferromagnetic materials and is immersed in a static magnetic field. The technique of eigenfunction series expansion is applied on the components of the elastic displacement field and the induced magnetic potentials near the vertex. It is shown that in this region, the magnetic susceptibility and the applied magnetic field have a strong influence on the elastic stress and magnetic field concentration. The results are instrumental toward actively controlling the stress concentration intensity via the applied magnetic field. [DOI: 10.1115/1.2912937]

1 Introduction

The recent years have witnessed the development of a new concept, namely, that of multifunctional materials/structures (see, e.g., Refs. [1] and [2]). A great deal of research activity associated with this concept have been conducted. It is especially targeted to provide broader capabilities to the next generation of aeronautical/aerospace vehicles and spacecraft. One underlying idea of this concept is to exploit multiphysical and/or multiscale properties of materials or structures in such a way that besides its major designated functionality, the same structural component should accomplish at least one more function. One example of such a design is a load carrying smart structure that can conduct nondestructive crack diagnosis or health monitoring by itself. This can lead to truly integrated structures, being able to perform multiple structural, as well as electromagnetic and electromechanical functions. To implement this concept in various contexts, e.g., in aerospace vehicles and nuclear reactor constructions, a better understanding of static and dynamic behaviors of the deformable structures subjected to simultaneous action of multiphysical fields becomes imperative. These physical fields may consist of mechanical, thermal, electrical, and magnetic ones.

One critically important area, which needs such an improvement in understanding, is the stress concentration behavior of elastic compound wedges subject to multiphysical fields. We note here that with the absence of physical field(s), the stress concentration in the vicinity of an elastic wedge's vertex has been extensively investigated. For example, in an early paper by Williams [3], the stress singularities in angular corners of plates subjected to extension in their own plane were investigated, and in Ref. [4], Dempsey and Sinclair investigated the concentration behavior at the vertex of a bi-material wedge, while in a recent paper [5] by Lin and Sung, the stress concentration intensity at the verticies of compound wedges composed of orthotropic materials was examined. With the presence of thermal field, Hwu and Lee [6] showed that the stress concentration intensities are influenced by the heat conduction coefficients. Under the influence of electric field, Fil'shtinskii and Matvienko [7] examined the singularities of the coupled electroelastic fields near the vertex of a piezoceramic wedge. In the present paper, a wedge made of magnetosoft ferromagnetic materials and immersed in a stationary magnetic field is considered. The governing equations and surface conditions are obtained by using the theory of magnetosoft ferromagnetic media (see, e.g., Ref. [8]). Solutions are constructed for the formulated boundary problem. All the components of the magnetoelastic stress and the perturbed magnetic field near the vertex are analyzed via the use of eigenfunction series expansions, which leads to a set of ordinary differential equations. The unknown coefficients associated with singularities depend on the boundary and continuity conditions, and the characteristics of stresses and the magnetic disturbance near the vertex can be predicted by locating the critical fixed point of a highly nonlinear equation.

As will be demonstrated in the sequel of this paper, accounting for the magnetic susceptibility (or permeability) and incorporating the external magnetic field can completely change the overall characteristics of the state of stresses in the vicinity of the vertex of a soft-ferromagnetic wedge. This fact makes it possible to control the stress concentration near the vertex of compound wedges by applying an external magnetic field.

2 Modeling of the Problem

Consider the plane-strain problem of an inhomogeneous compound wedge made of two isotropic dielectric magnetosoft ferromagnetic materials, which are perfectly bonded together, with each constituent body featuring different magnetoelastic properties. The materials are assumed elastically deformable and only the long-range magnetic forces defined by Pao and Yeh [8] are considered. As a result, magnetostriction through constitutive equations is omitted (see also Ref. [9]).

In order to investigate the state of stresses and the magnetic field near the vertex of the wedge (denoted as P, see Fig. 1), a cylindrical coordinate system (z,r,θ) is adopted so that the origin of the polar coordinate system (r,θ) is located at point P. The angle θ is measured counterclockwise from the bonding line and the wedge is immersed in an external stationary magnetic field, while the medium surrounding the wedge is assumed to be vacuum. In a general case, the external magnetic field $\mathbf{H}_0^{(e)} = H_\theta \mathbf{e}_\theta + H_r \mathbf{e}_r$ is produced by such magnetic sources as electrical

---

[1] Present address: Institute of Mechanics, National Academy of Sciences of Armenia, Yerevan, Republic of Armenia, 0019.

[2] Present address: School of Aerospace, Xi'an Jiaotong University, Xi'an, P. R. China, 710049.

[3] Deceased on April 16, 2007 for saving lives of students in his class during the campus tragedy at Virginia Tech, Blacksburg.

Contributed by the Applied Mechanics Division of ASME for publication in the JOURNAL OF APPLIED MECHANICS. Manuscript received May 1, 2007; final manuscript received December 27, 2007; published online May 14, 2008. Review conducted by Zhigang Suo.

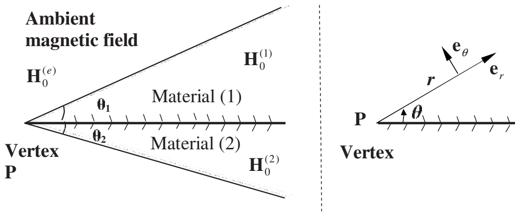

Fig. 1 Geometry (left) and the coordinates (right) of a compound wedge. In the left, $\mathbf{H}_0^{(1)}$ and $\mathbf{H}_0^{(2)}$ denote the static magnetic fields in Materials (1) and (2), respectively.

current or other magnetized materials, with the magnetic field components H_θ and H_r being given. Since we focus our investigation area in the vicinity of the wedge's vertex, we assume that $H_r=0$. As a result, $\mathbf{H}_0^{(e)}=H_\theta^{(e)}\mathbf{e}_\theta$, with $H_\theta^{(e)}$ being positive in the direction of $\mathbf{e}_\theta$ (see Fig. 1).

Apart from the undisturbed equilibrium configuration reached by the wedge under the influence of the external magnetic field, we denote by $u_r^{(i)}$, $u_\theta^{(i)}$ $(i=1,2)$ the components of the disturbed displacement vector $\mathbf{U}^{(i)}$ near the vertex P of the wedge in directions r and θ, while $\varphi^{(i)}$ is the disturbed magnetic potential induced within the wedge. For the problem being considered herein, the stresses within the ith constituent body can be represented as

$$\sigma_{\theta\theta}^{(i)}=2G^{(i)}\frac{[1-\nu^{(i)}]\varepsilon_{\theta\theta}^{(i)}+\nu^{(i)}\varepsilon_{rr}^{(i)}}{1-2\nu^{(i)}},\quad \sigma_{rr}^{(i)}=2G^{(i)}\frac{[1-\nu^{(i)}]\varepsilon_{rr}^{(i)}+\nu^{(i)}\varepsilon_{\theta\theta}^{(i)}}{1-2\nu^{(i)}} \tag{1a}$$

$$\sigma_{r\theta}^{(i)}=2G^{(i)}\varepsilon_{r\theta}^{(i)},\quad \sigma_{zz}^{(i)}=\frac{2G^{(i)}}{1-2\nu^{(i)}}[\varepsilon_{rr}^{(i)}+\varepsilon_{\theta\theta}^{(i)}] \tag{1b}$$

in which the superscript (i) denotes the quantities associated with the ith constituent body, $G^{(i)}$ and $\nu^{(i)}$ are the shear modulus and Poisson's ratio, respectively; $\sigma_{\theta\theta}$, σ_{rr}, $\sigma_{r\theta}$, and σ_{zz} are the elastic stress components in plane strain state, while $\varepsilon_{\theta\theta}$, ε_{rr}, and $\varepsilon_{r\theta}$ are the strain components.

In terms of the displacement components $u_r^{(i)}$ and $u_\theta^{(i)}$, the strain components in Eqs. (1a) and (1b) can be expressed as

$$\varepsilon_{\theta\theta}^{(i)}=\frac{1}{r}\frac{\partial u_\theta^{(i)}}{\partial\theta}+\frac{u_r^{(i)}}{r},\quad \varepsilon_{rr}^{(i)}=\frac{\partial u_r^{(i)}}{\partial r} \tag{2a}$$

$$2\varepsilon_{r\theta}^{(i)}=\frac{1}{r}\frac{\partial u_r^{(i)}}{\partial\theta}-\frac{u_\theta^{(i)}}{r}+\frac{\partial u_\theta^{(i)}}{\partial r} \tag{2b}$$

Denote the domain occupied by the ith constituent body by Ω_i $(i=1,2)$, then based on the equations of magnetoelasticity of dielectric magnetosoft ferromagnetic media, see Refs. [8,9] one obtains the following system of equations:

Equations in Ω_i:

$$\left[\nabla^2 u_r^{(i)}-\frac{u_r^{(i)}}{r^2}-\frac{2}{r^2}\frac{\partial u_\theta^{(i)}}{\partial\theta}\right]+k_i\frac{\partial}{\partial r}\left[\frac{\partial u_r^{(i)}}{\partial r}+\frac{u_r^{(i)}}{r}+\frac{1}{r}\frac{\partial u_\theta^{(i)}}{\partial\theta}\right] \\ \underline{+\beta^{(i)}H_\theta^{(i)}\left[\frac{1}{r}\frac{\partial^2\varphi^{(i)}}{\partial r\partial\theta}-\frac{1}{r^2}\frac{\partial^2\varphi^{(i)}}{\partial\theta^2}\right]}=0 \tag{3a}$$

$$\left[\nabla^2 u_\theta^{(i)}-\frac{u_\theta}{r^2}+\frac{2}{r^2}\frac{\partial u_r^{(i)}}{\partial\theta}\right]+k_i\frac{1}{r}\frac{\partial}{\partial\theta}\left[\frac{\partial u_r^{(i)}}{\partial r}+\frac{u_r^{(i)}}{r}+\frac{1}{r}\frac{\partial u_\theta^{(i)}}{\partial\theta}\right] \\ \underline{+\beta^{(i)}H_\theta^{(i)}\left[\frac{1}{r^2}\frac{\partial^2\varphi^{(i)}}{\partial\theta^2}+\frac{1}{r}\frac{\partial\varphi^{(i)}}{\partial r}\right]}=0 \tag{3b}$$

$$\nabla^2\varphi^{(i)}=0 \tag{3c}$$

where $\nabla^2\equiv\partial^2/\partial r^2+1/r\cdot\partial/\partial r+1/r^2\cdot\partial^2/\partial\theta^2$ is the 2D Laplace operator in the polar coordinate system; $k_i\equiv 1/(1-2\nu^{(i)})$; $\beta^{(i)}\equiv 2\mu_0\chi^{(i)}/G^{(i)}$, in which, $\chi^{(i)}$ is the magnetic susceptibility; while $H_\theta^{(i)}$ denotes the circumferential component of the static magnetic field. The underlined terms in Eqs. (3a) and (3b) are associated with the linearized radial and circumferential components of the body force due to magnetization, respectively [10],

$$\mathbf{f}^{(i)}=\mu_0\chi^{(i)}[\mathbf{H}_0^{(i)}\cdot\nabla]\nabla\varphi^{(i)} \tag{4}$$

in which μ_0 is the magnetic permeability of vacuum.

The induced magnetic field outside the wedge is governed by the equation

$$\nabla^2\varphi^{(e)}=0 \tag{5}$$

in which $\varphi^{(e)}$ is the disturbed magnetic potential induced outside of the wedge. In the sequel, the superscript (e) denotes the quantities associated with the vacuum.

The boundary conditions on the surfaces $\theta=\theta_1$ and $\theta=\theta_2$ can be expressed as

$$t_{r\theta}^{(i)}+t_{r\theta}^{m(i)}=t_{r\theta}^{m(e)} \tag{6a}$$

$$t_{\theta\theta}^{(i)}+t_{\theta\theta}^{m(i)}=t_{\theta\theta}^{m(e)} \tag{6b}$$

$$\varphi^{(i)}-\varphi^{(e)}+\frac{\chi^{(i)}}{\mu_r^{(i)}}H_\theta^{(e)}u_\theta^{(i)}=0 \tag{6c}$$

$$\mu_r^{(i)}\frac{\partial\varphi^{(i)}}{\partial\theta}-\frac{\partial\varphi^{(e)}}{\partial\theta}=0 \tag{6d}$$

where $t_{r\theta}^{(i)}$ and $t_{\theta\theta}^{(i)}$ are the components of the elastic stress; $t_{r\theta}^{m(i)}$, $t_{\theta\theta}^{m(i)}$, $t_{r\theta}^{m(e)}$, and $t_{\theta\theta}^{m(e)}$ are the components of the Maxwell stress tensor within the wedge and the vacuum, respectively; while $\mu_r^{(i)}$ is the relative permeability. It is noted that the conditions (6a) and (6b) state the fact that the surfaces $\theta=\theta_1$ and $\theta=\theta_2$ are free of total stresses, i.e., of those resulting from the superposition of the mechanical and the magnetic stresses; while Eqs. (6c) and (6d) define the jump conditions of the induced magnetic fields $\varphi^{(i)}$ and $\varphi^{(e)}$. Worthy of further noting is that condition (6c) is based on the conservation of circulation of the induced magnetic field enclosing the wedge, which is physically justified by the fact that the wedge is dielectric and no electric charge is generated on the wedge.

The continuity conditions of the displacements and stresses on the interface $\theta=0$ can be expressed as

$$\mathbf{U}^{(1)}=\mathbf{U}^{(2)} \tag{7a}$$

$$t_{r\theta}^{(1)}+t_{r\theta}^{m(1)}=t_{r\theta}^{(2)}+t_{r\theta}^{m(2)} \tag{7b}$$

$$t_{\theta\theta}^{(1)}+t_{\theta\theta}^{m(1)}=t_{\theta\theta}^{(2)}+t_{\theta\theta}^{m(2)} \tag{7c}$$

$$\varphi^{(1)}-\varphi^{(2)}+\left[\frac{\chi^{(1)}}{\mu_r^{(1)}}-\frac{\chi^{(2)}}{\mu_r^{(2)}}\right]H_\theta^{(e)}u_\theta^{(1)}=0 \tag{7d}$$

$$\mu_r^{(1)}\frac{\partial\varphi^{(1)}}{\partial\theta}-\mu_r^{(2)}\frac{\partial\varphi^{(2)}}{\partial\theta}=0 \tag{7e}$$

By superposing the stress components $t_{r\theta}^{(i)}$, $t_{\theta\theta}^{(i)}$, $t_{r\theta}^{m(i)}$, $t_{\theta\theta}^{m(i)}$, $t_{r\theta}^{m(e)}$, and $t_{\theta\theta}^{m(e)}$ on the undisturbed elastic and Maxwell stresses, the wedge reaches a new equilibrium state. These quantities due to the disturbance can be represented as follows:

$$t_{r\theta}^{(i)}=\sigma_{r\theta}^{(i)}+\mu_0\chi^{(i)}H_\theta^{(i)}h_r^{(i)} \tag{8a}$$

$$t_{\theta\theta}^{(i)}=\sigma_{\theta\theta}^{(i)}+2\mu_0\chi^{(i)}H_\theta^{(i)}h_\theta^{(i)} \tag{8b}$$

$$t_{r\theta}^{m(i)} = \mu_0 \mu_r^{(i)} H_\theta^{(i)} h_r^{(i)} \tag{8c}$$

$$t_{\theta\theta}^{m(i)} = \mu_0 [2\mu_r^{(i)} - 1] H_\theta^{(i)} h_\theta^{(i)} \tag{8d}$$

$$t_{r\theta}^{m(e)} = \mu_0 H_\theta^{(e)} h_r^{(e)} \tag{8e}$$

$$t_{\theta\theta}^{m(e)} = \mu_0 H_\theta^{(e)} h_\theta^{(e)} \tag{8f}$$

$$\mathbf{h}^{(i)} \equiv \nabla \varphi^{(i)} \tag{8g}$$

$$\mathbf{h}^{(e)} \equiv \nabla \varphi^{(e)} \tag{8h}$$

In Eqs. (8*a*) and (8*b*), $\sigma_{r\theta}^{(i)}$ and $\sigma_{\theta\theta}^{(i)}$ are defined by Eqs. (1*a*) and (1*b*).

It is further noted that the continuity conditions on the surfaces $\theta = \theta_1$ and $\theta = \theta_2$ require that

$$H_\theta^{(i)} = \frac{1}{\mu_r^{(i)}} H_\theta^{(e)} \tag{9}$$

3 Solution of the Problem

The displacement field and magnetic potential in each of the constituent body Ω_i $(i=1,2)$, as well as the magnetic potential in the external domain are found by assuming the following representation (see Refs. [11–13]):

$$[u_r^{(i)}, u_\theta^{(i)}, \varphi^{(i)}, \varphi^{(e)}] = r^\alpha [\bar{u}_r^{(i)}(\theta), \bar{u}_\theta^{(i)}(\theta), H_\theta^{(e)} \bar{\varphi}^{(i)}(\theta), H_\theta^{(e)} \bar{\varphi}^{(e)}(\theta)] \tag{10}$$

where $\bar{u}_r^{(i)}(\theta)$, $\bar{u}_\theta^{(i)}(\theta)$, $\bar{\varphi}^{(i)}(\theta)$, and $\bar{\varphi}^{(e)}(\theta)$ are unknown functions; and α is a parameter which quantifies the concentration intensity in the vicinity of the wedge vertex and will be determined later.

Substituting expressions in Eq. (10) into Eqs. (3*a*)–(3*c*), (4), and (5), a set of ordinary differential equations is obtained. Following the solution steps of eigenfunction expansion technique, the following solution form of $\bar{u}_r^{(i)}(\theta)$, $\bar{u}_\theta^{(i)}(\theta)$, $\bar{\varphi}^{(i)}(\theta)$, and $\bar{\varphi}^{(e)}(\theta)$ is adopted:

$$[\bar{u}_r^{(i)}(\theta), \bar{u}_\theta^{(i)}(\theta), \bar{\varphi}^{(i)}(\theta), \bar{\varphi}^{(e)}(\theta)] = \exp[\lambda\theta][\tilde{u}_r^{(i)}, \tilde{u}_\theta^{(i)}, \tilde{\varphi}^{(i)}, \tilde{\varphi}^{(e)}] \tag{11}$$

in which the quantities overheaded by tilde are parameters independent of r and θ.

The eigenvalues associated with $\bar{\varphi}^{(i)}$ and $\bar{\varphi}^{(e)}$ are $\pm j\alpha$, with j being defined as $\sqrt{-1}$, while the eigenvalues associated with the other basic unknowns are $\pm j(\alpha+1)$, $\pm j(\alpha-1)$. As a result, the solutions of $\bar{\varphi}^{(i)}$ and $\bar{\varphi}^{(e)}$ can be represented as

$$\bar{\varphi}^{(i)}(\theta) = E_i \sin(\alpha\theta) + F_i \cos(\alpha\theta) \tag{12a}$$

$$\bar{\varphi}^{(e)}(\theta) = E_e \sin(\alpha\theta) + F_e \cos(\alpha\theta) \tag{12b}$$

where the coefficients E_i, F_i, E_e, and F_e are unknown constants, which are to be determined by imposing the boundary and continuity conditions (6*a*)–(6*d*) and (7*a*)–(7*e*).

Corresponding to the eigenvalues $\lambda = \pm j\alpha$, part of the solution of $\bar{u}_r^{(i)}$ and $\bar{u}_r^{(i)}$ due to the presence of $\bar{\varphi}^{(i)}$ written in the form of Eq. (12*a*) is

$$\bar{u}_{r1}^{(i)}(\theta) = -\gamma_i E_i \cos(\alpha\theta) + \gamma_i F_i \sin(\alpha\theta) \tag{13a}$$

$$\bar{u}_{\theta 1}^{(i)}(\theta) = \gamma_{1i} E_i \sin(\alpha\theta) + \gamma_{1i} F_i \sin(\alpha\theta) \tag{13b}$$

where the coefficients γ_i and γ_{1i} are defined as

$$\gamma_i \equiv -\frac{2\mu_0 \chi^{(i)} (H_\theta^{(e)})^2}{G^{(i)}} \frac{\alpha(\alpha-1)(k_i\alpha + 2\alpha + 1)}{(k_i+1)(1-4\alpha^2)} \tag{14a}$$

$$\gamma_{1i} \equiv -\frac{2\mu_0 \chi^{(i)} (H_\theta^{(e)})^2}{G^{(i)}} \frac{\alpha(\alpha-1)(k_i\alpha + 2\alpha + k_i + 1)}{(k_i+1)(1-4\alpha^2)} \tag{14b}$$

Similarly, corresponding to the eigenvalues $\lambda = \pm j(\alpha+1)$ and $\lambda = \pm j(\alpha-1)$, the solutions of $\bar{u}_r^{(i)}$ can be written in the form

$$\bar{u}_{r2}^{(i)}(\theta) = A_i \sin[(\alpha-1)\theta] + B_i \cos[(\alpha-1)\theta] + C_i \sin[(\alpha+1)\theta] + D_i \cos[(\alpha+1)\theta] \tag{15}$$

in which the coefficients A_i, B_i, C_i, and D_i have to be determined by the boundary and continuity conditions (6*a*)–(6*d*) and (7*a*)–(7*e*). The corresponding solution form of $\bar{u}_\theta^{(i)}$ is obtained as

$$\bar{u}_{\theta 2}^{(i)}(\theta) = \gamma_{2i} A_i \cos[(\alpha-1)\theta] - \gamma_{2i} B_i \sin[(\alpha-1)\theta] + C_i \cos[(\alpha+1)\theta] - D_i \sin[(\alpha+1)\theta] \tag{16}$$

in which

$$\gamma_{2i} \equiv \frac{k_i\alpha + k_i + 2}{k_i\alpha - k_i - 2} \tag{17}$$

In summary, the total solutions of $\bar{u}_r^{(i)}$ and $\bar{u}_\theta^{(i)}$ can be in represented in the following form:

$$\bar{u}_r^{(i)}(\theta) = A_i \sin[(\alpha-1)\theta] + B_i \cos[(\alpha-1)\theta] + C_i \sin[(\alpha+1)\theta] + D_i \cos[(\alpha+1)\theta] - \gamma_i E_i \cos(\alpha\theta) + \gamma_i F_i \sin(\alpha\theta) \tag{18a}$$

$$\bar{u}_\theta^{(i)}(\theta) = \gamma_{2i} A_i \cos[(\alpha-1)\theta] - \gamma_{2i} B_i \sin[(\alpha-1)\theta] + C_i \cos[(\alpha+1)\theta] - D_i \sin[(\alpha+1)\theta] + \gamma_{1i} E_i \sin(\alpha\theta) + \gamma_{1i} F_i \cos(\alpha\theta) \tag{18b}$$

Substituting Eqs. (18*a*), (18*b*), (12*a*), and (12*b*) into the boundary and continuity conditions (6*a*)–(6*d*) and (7*a*)–(7*e*), the following homogeneous system of linear algebraic equations with respect to the unknown constants A_i, B_i, C_i, D_i, E_i, F_i, E_e, and F_e is obtained:

$$\underbrace{\begin{bmatrix} \mathbb{Z}_{11} & \mathbb{Z}_{12} \\ \mathbb{Z}_{21} & \mathbb{Z}_{22} \end{bmatrix}_{14\times 14}}_{\mathbb{Z}} \begin{Bmatrix} \mathbf{Y}^{(el)} \\ \mathbf{Y}^{(mg)} \end{Bmatrix}_{14\times 1} = \mathbf{0} \tag{19}$$

in which the entries of the submatrices $\mathbb{Z}_{ij}$ $((i,j) = \overline{1,2})$ are defined in the Appendix, while the vectors $\mathbf{Y}^{(el)}$ and $\mathbf{Y}^{(mg)}$ are defined as

$$\mathbf{Y}^{(el)} \equiv [A_1, B_1, C_1, D_1, A_2, B_2, C_2, D_2]^T \tag{20a}$$

$$\mathbf{Y}^{(mg)} \equiv [E_{s1}, F_{s1}, E_{s2}, F_{s2}, E_e, F_e]^T \tag{20b}$$

It is noted that in Eq. (20*b*), due to the wide variation of permeability of soft-ferromagnetic materials (see, e.g., Refs. [14,15]), for the purpose of rescaling, E_{si} and F_{si} are used to replace $[\chi^{(i)}+1]E_i$ and $[\chi^{(i)}+1]F_i$, respectively.

The condition of existence of nontrivial solution of this algebraic system (19), i.e., $\det[\mathbb{Z}] = 0$, determines the unknown parameter α, which leads to the following transcendental equation:

$$\mathcal{F}(\alpha, \hat{B}_0^2, \theta_1, \theta_2, \mu_r^{(1)}, \mu_r^{(2)}, G^{(1)}/G^{(2)}, \nu^{(1)}, \nu^{(2)}) = 0 \tag{21}$$

where the nondimensional magnetic field intensity parameter $\hat{B}_0 \equiv H_\theta^{(e)} \sqrt{\mu_0 / G^{(2)}}$, $\mathcal{F}$ is an operator whose expression is very complicated and lengthy and is omitted here.

As a special case, in the absence of the external magnetic field, i.e., $\hat{B}_0 = 0$, the submatrix $\mathbb{Z}_{12}$ in Eq. (19) reduces to zero. As a result, Eq. (21) splits into two independent transcendental equations

$$\det(\mathbb{Z}_{11}) = 0 \tag{22a}$$

or

$$\det(\mathbb{Z}_{22}) = 0 \tag{22b}$$

While Eq. (22*a*) has been obtained by Chobanyan [12] to investigate the characteristics of elastic stress near the vertex of a

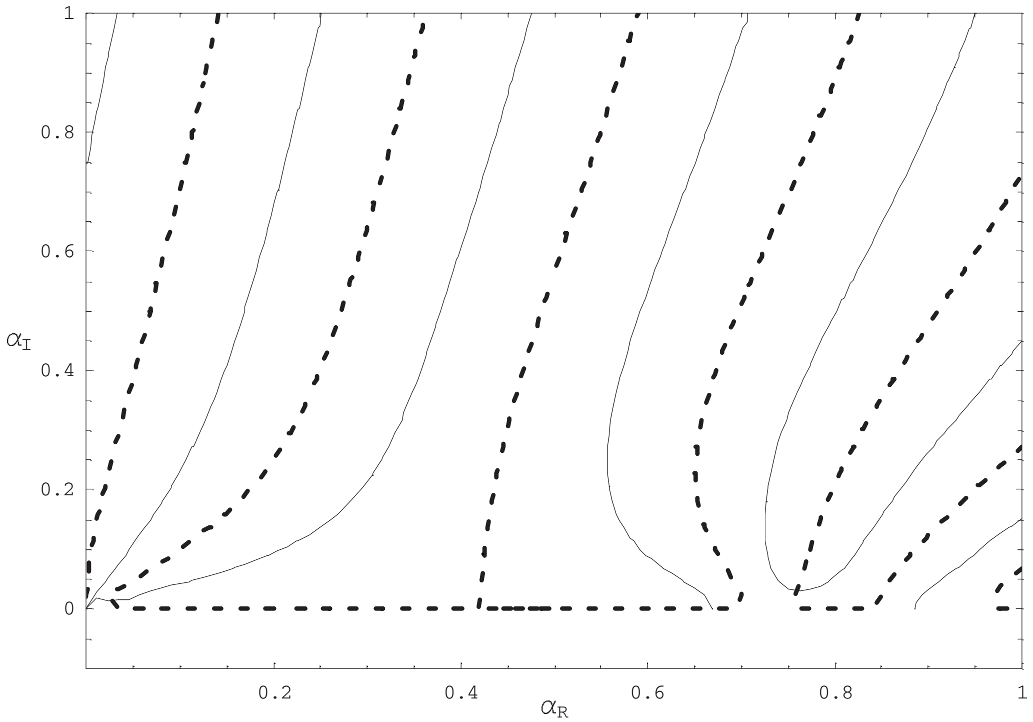

Fig. 2 Zero-value contour plot of the function $\mathcal{F}(\cdots)$ in Eq. (21) in the range ($\alpha_R \in (0,1]$, $\alpha_I \in [0,1]$). $(\nu^{(1)},\nu^{(2)})=(0.32,0.28)$, $(\chi^{(1)},\chi^{(2)})=(10,10^4)$, $G^{(1)}/G^{(2)}=16$, $(\theta_1,\theta_2)=(7\pi/12,-5\pi/12)$, $\hat{B}_0=0.1$. The solid line is the solution of α, which fulfills $\mathrm{Re}[\mathcal{F}]=0$; while the dotted line is the solution of α, which fulfills $\mathrm{Im}[\mathcal{F}]=0$. The final solutions of α are the crossed points of these two types of lines.

compound body, Eq. (22*b*) has been obtained by Mittra and Li [13] to study the behavior of the magnetic field on the top of a piecewise homogeneous ferromagnetic wedge. From Eqs. (10), (1), and (8*a*)–(8*h*), it is readily seen that all components of the elastic stress and disturbed magnetic fields near the vertex of the wedge take the following form:

$$r^{\alpha_R-1}R(\alpha_I,r,\theta) \tag{23}$$

where $\alpha_R \equiv \mathrm{Re}(\alpha)$, $\alpha_I \equiv \mathrm{Im}(\alpha)$, and $R(r,\theta,\alpha_I)$ is bounded in amplitude and in general does not vanish when $r \rightarrow 0$.

From Eq. (23), it can be seen that the characteristics of the state of elastic stress and disturbed magnetic fields near the vertex of the wedge are determined by α_R. If $\alpha_R > 1$, we have a no-concentration state. If $\alpha_R < 1$, then the elastic stress and disturbed magnetic fields increase without bound at the vertex, implying that strong concentration occurs. It is recalled that due to the finiteness of the induced strain energy and of the induced magnetic potentials, see, e.g., Refs. [12,13], $\alpha_R > 0$. Consequently, we will consider in the sequel the solutions of $\alpha_R \in (0,1]$.

4 Numerical Issues, Results, and Discussion

Equation (21) is highly nonlinear with respect to α and the operation of direct differentiation of the function $\mathcal{F}(\cdots)$ in the left side with respect to α is by no means a trivial task. To locally search for a solution of α of Eq. (21), the secant method, which circumvents the direct differentiation, is employed. The details of the numerical procedure can be found in, e.g., Ref. [16]. In order to search for other nontrivial solutions of α of Eq. (21), the plot of contours, functionality of which is provided by MATHEMATICA® [17], of the expression of the left side is employed. Figure 2 shows the zero-value contour plot of the function $\mathcal{F}(\cdots)$ in the range $\alpha_R \in (0,1]$, $\alpha_I \in [0,1]$. The associated parameters are given in the figure caption.

Depending on the mechanical and magnetic properties, as well as on the geometry of the wedge, the presence of the applied magnetic field can have a significant influence on the eigenvalues of α. In Table 1, two wedges with different geometries are investigated and in both cases, although the increase of the amplitude of the magnetic field $\hat{B}_0$ has a negligible influence on the eigenvalue of α, which is initially (in the sense that $\hat{B}_0=0$) a measure of the intensity of the elastic stress concentration, it dramatically changes the eigenvalue of α associated with the most severe singularity (denoted by α_{ms}). In another two cases as shown in Table 2, besides the significant increase of the eigenvalue of α_{ms}, the increase of $\hat{B}_0$ also significantly increases the eigenvalue of α, which initially measures the intensity of the elastic stress concentration.

Table 1 Dependence of the eigenvalues α upon $\hat{B}_0$ in the case that $\nu^{(1)}=0.32$, $\nu^{(2)}=0.28$, $\mu_r^{(1)}=10^4$, and $G^{(1)}/G^{(2)}=16$

	$\theta_1=5\pi/6,\ \theta_2=-\pi/6$		$\theta_1=17\pi/24,\ \theta_2=-7\pi/24$	
$\hat{B}_0^2$	α[a]	α_{ms}[b] of the wedge	α[a]	α_{ms}[b] of the wedge
0	0.614	0.614	0.746	0.746
0.001	0.614	0.148	0.747	0.117
0.002	0.614	0.212	0.747	0.165
0.004	0.614	0.348	0.746	0.238
0.006	0.614	$0.397-0.106j$	0.746	0.302
0.008	0.613	$0.415+0.146j$	0.745	0.354
0.010	0.613	0.402	0.744	0.367

[a] Eigenvalue initially (in the sense that $\hat{B}_0=0$) measures the elastic stress concentration.

[b] α_{ms} denotes the eigenvalue having the smallest real part α_R, which, by Eq. (23), characterizes the most severe singularity.

Table 2 Dependence of the eigenvalues α upon $\hat{B}_0$ in the case that $\nu^{(1)}=0.32$, $\nu^{(2)}=0.28$, $\mu_r^{(1)}=10$, $\mu_r^{(2)}=10^4$, and $G^{(1)}/G^{(2)}=16$

	$\theta_1=5\pi/8,\ \theta_2=-3\pi/8$		$\theta_1=\pi/2,\ \theta_2=-\pi/2$	
$\hat{B}_0^2$	α^{a}	$\alpha_{\mathrm{ms}}{}^{\mathrm{b}}$ of the wedge	α^{a}	$\alpha_{\mathrm{ms}}{}^{\mathrm{b}}$ of the wedge
0	0.784	0.784	0.762	0.762
0.001	0.802	0.093	0.774	0.066
0.002	0.815	0.131	0.786	0.092
0.004	0.831	0.183	0.809	0.127
0.006	0.838	0.223	0.831	0.153
0.008	0.843	0.254	0.851	0.172
0.010	0.845	0.277	0.870	0.188

[a] Eigenvalue initially (in the sense that $\hat{B}_0=0$) measures the elastic stress concentration.
[b] α_{ms} denotes the eigenvalue having the smallest real part α_R, which, by Eq. (23), characterizes the most severe singularity.

Table 4 Influence of the magnetic susceptibilities ($\chi^{(1)}$, $\chi^{(2)}$) on the eigenvalues α in the case that $\nu^{(1)}=0.3$, $\nu^{(2)}=0.3$, $G^{(1)}/G^{(2)}=1$, $\theta_1=5\pi/6$, and $\theta_1=-\pi/6$

	$\chi^{(1)}=10^5,\ \chi^{(2)}=10^3$		$\chi^{(1)}=1,\ \chi^{(2)}=10^5$	
$\hat{B}_0$	α^{a}	$\alpha_{\mathrm{ms}}{}^{\mathrm{b}}$ of the wedge	α^{a}	$\alpha_{\mathrm{ms}}{}^{\mathrm{b}}$ of the wedge
0	1.0	1.0	$0.777+0.114j$	$0.777+0.114j$
0.02	1.0	0.026	$0.777+0.114j$	0.020
0.04	1.0	0.051	$0.778+0.113j$	0.040
0.06	1.0	0.076	$0.778+0.111j$	0.060
0.08	1.0	0.100	$0.778+0.109j$	0.079
0.1	1.0	0.125	$0.779+0.106j$	0.099

[a] Eigenvalue initially (in the sense that $\hat{B}_0=0$) measures the elastic stress concentration.
[b] α_{ms} denotes the eigenvalue having the smallest real part α_R, which, by Eq. (23), characterizes the most severe singularity.

Table 3 traces the changes of all eigenvalues initially in the range $\alpha_R \in (0,1)$. It is remarkable to note that in this case the following are observed.

(a) Initially, there are three roots of α in the range $\alpha_R \in (0,1)$. However, with the presence of the applied magnetic field, an additional eigenvalue appears (shown in the second column), which also characterizes the most severe singularity:

(b) To some eigenvalues, e.g., in Columns 2 and 5, the increase of the magnetic field $\hat{B}_0$ brings in an *increase* of α_R of these eigenvalues; while to some other eigenvalue, e.g., in Column 4, the increase of the magnetic field $\hat{B}_0$ brings in a *decrease* of α_R.

(c) Some eigenvalues, which initially involve the singularity of the wedge, can be transformed to nonsingular type by the applied magnetic field, as shown in Column 5. This implies that the applied magnetic field may be beneficially explored to actively remove stress concentration.

Table 4 shows the significant influence of the magnetic susceptibilities of the compound wedge on the eigenvalues of α initially in the range $\alpha_R \in (0,1]$. The elastic properties of the two constituent materials are the same. In this case, the eigenvalues, which initially measure the intensity of the elastic stress concentration, are dramatically changed by the magnetic susceptibilities.

5 Conclusions

The elastic stress and magnetic field concentration of soft-ferromagnetic 2D compound wedges immersed in a static magnetic field are investigated. The major conclusions are as follows.

- The presence of the applied magnetic field can effectively change the eigenvalues of α; it can even bring in new eigenvalue(s). These eigenvalues quantify the concentration intensity in the vicinity of the wedge vertex. As a result, the presence of the applied magnetic field can dramatically change the concentration behavior near the wedge vertex.
- The magnetic susceptibility also has a strong influence on the eigenvalues of α.

Table 3 Roots of α within the range $\alpha_R \le 1$ versus the change of the applied magnetic field amplitude. $\nu^{(1)}=0.32$, $\nu^{(2)}=0.28$, $\mu_r^{(1)}=10$, $\mu_r^{(2)}=10^4$, $G^{(1)}/G^{(2)}=16$, $\theta_1=3\pi/4$, and $\theta_2=-\pi/4$.

$\hat{B}_0^2$	Roots of α in the range $\alpha_R \in (0,1]$			
0	...	0.694	0.92	0.966
0.001	0.128	0.695	0.869	$0.983+0.107j$
0.002	0.183	0.695	0.855	$0.990+0.165j$
0.004	0.270	0.696	0.839	$0.990+0.162j$
0.006	0.377	0.696	0.829	$0.994+0.182j$
0.008	0.400	0.695	0.822	$0.997+0.197j$
0.01	0.398	0.694	0.815	$1.001+0.209j$

Appendix: Definitions of Matrix Entries in Equation (19)

$$\mathbb{Z}_{11} \equiv \begin{bmatrix} 0 & 1 & 0 & 1 & 0 & -1 & 0 & -1 \\ Z_{21}^{(1)} & 0 & 1 & 0 & Z_{21}^{(2)} & 0 & -1 & 0 \\ Z_{31}^{(1)} & 0 & 1 & 0 & Z_{31}^{(2)} & 0 & Z_{33}^{(2)} & 0 \\ 0 & Z_{42}^{(1)} & 0 & 1 & 0 & Z_{42}^{(2)} & 0 & Z_{44}^{(2)} \\ W_{11}^{(1)} & W_{12}^{(1)} & W_{13}^{(1)} & W_{14}^{(1)} & 0 & 0 & 0 & 0 \\ W_{21}^{(1)} & W_{22}^{(1)} & W_{23}^{(1)} & W_{24}^{(1)} & 0 & 0 & 0 & 0 \\ 0 & 0 & 0 & 0 & W_{11}^{(2)} & W_{12}^{(2)} & W_{13}^{(2)} & W_{14}^{(2)} \\ 0 & 0 & 0 & 0 & W_{21}^{(2)} & W_{22}^{(2)} & W_{23}^{(2)} & W_{24}^{(2)} \end{bmatrix}_{8\times 8}$$

$$\mathbb{Z}_{12} \equiv \begin{bmatrix} Z_{15}^{(1)} & 0 & Z_{15}^{(2)} & 0 & 0 & 0 \\ 0 & Z_{26}^{(1)} & 0 & Z_{26}^{(2)} & 0 & 0 \\ 0 & Z_{36}^{(1)} & 0 & Z_{36}^{(2)} & 0 & 0 \\ Z_{45}^{(1)} & 0 & Z_{45}^{(2)} & 0 & 0 & 0 \\ W_{15}^{(1)} & W_{16}^{(1)} & 0 & 0 & W_{1E}^{(1)} & W_{1F}^{(1)} \\ W_{25}^{(1)} & W_{26}^{(1)} & 0 & 0 & W_{2E}^{(1)} & W_{2F}^{(1)} \\ 0 & 0 & W_{15}^{(2)} & W_{16}^{(2)} & W_{1E}^{(2)} & W_{1F}^{(2)} \\ 0 & 0 & W_{25}^{(2)} & W_{26}^{(2)} & W_{2E}^{(2)} & W_{2F}^{(2)} \end{bmatrix}_{8\times 6}$$

$$\mathbb{Z}_{21} = \begin{bmatrix} 0 & 0 & 0 & 0 & 0 & 0 & 0 & 0 \\ Z_{61}^{(1)} & 0 & Z_{63}^{(1)} & 0 & 0 & 0 & 0 & 0 \\ W_{31}^{(1)} & W_{32}^{(1)} & W_{33}^{(1)} & W_{34}^{(1)} & 0 & 0 & 0 & 0 \\ 0 & 0 & 0 & 0 & W_{31}^{(2)} & W_{32}^{(2)} & W_{33}^{(2)} & W_{34}^{(2)} \\ 0 & 0 & 0 & 0 & 0 & 0 & 0 & 0 \\ 0 & 0 & 0 & 0 & 0 & 0 & 0 & 0 \end{bmatrix}_{6\times 8}$$

$$\mathbb{Z}_{22} \equiv \begin{bmatrix} 1 & 0 & -1 & 0 & 0 & 0 \\ 0 & Z_{66}^{(1)} & 0 & -1 & 0 & 0 \\ W_{35}^{(1)} & W_{36}^{(1)} & 0 & 0 & W_{3E}^{(1)} & W_{3F}^{(1)} \\ 0 & 0 & W_{35}^{(2)} & W_{36}^{(2)} & W_{3E}^{(2)} & W_{3F}^{(2)} \\ W_{45}^{(1)} & W_{46}^{(1)} & 0 & 0 & W_{4E}^{(1)} & W_{4F}^{(1)} \\ 0 & 0 & W_{45}^{(2)} & W_{46}^{(2)} & W_{4E}^{(2)} & W_{4F}^{(2)} \end{bmatrix}_{6\times 6}$$

In these matrices,

$$Z_{15}^{(i)} \equiv (-1)^{i+1} G_{ri} \hat{B}_0^2 \mathcal{R}_7^{(i)}$$

where

$$G_{ri} \equiv \frac{G^{(i)}}{G^{(2)}}$$

and

$$\mathcal{R}_7^{(i)} \equiv \frac{2\chi^{(i)}}{\chi^{(i)}+1} \frac{\alpha(\alpha-1)(k_i\alpha+2\alpha+1)}{(k_i+1)(1-4\alpha^2)}$$

$$Z_{21}^{(i)} \equiv (-1)^{i+1}\mathcal{R}_5^{(i)}, \quad Z_{26}^{(i)} \equiv (-1)^{i} G_{ri}\hat{B}_0^2 \mathcal{R}_8^{(i)}$$

where

$$\mathcal{R}_5^{(i)} \equiv \frac{k_i\alpha+k_i+2}{k_i\alpha-k_i-2}$$

and

$$\mathcal{R}_8^{(i)} \equiv \frac{2\chi^{(i)}}{\chi^{(i)}+1} \frac{\alpha(\alpha-1)(k_i\alpha+2\alpha+k_i+1)}{(k_i+1)(1-4\alpha^2)}$$

$$Z_{31}^{(i)} \equiv \mathcal{R}_1^{(i)}, \quad Z_{36}^{(1)} \equiv G_{r1}\hat{B}_0^2 \mathcal{R}_2^{(1)}, \quad Z_{31}^{(2)} \equiv -G_{r1}\mathcal{R}_1^{(2)}$$

$$Z_{33}^{(2)} \equiv -G_{r1} \quad Z_{36}^{(2)} \equiv -G_{r1}\hat{B}_0^2 \mathcal{R}_2^{(2)}$$

where

$$\mathcal{R}_1^{(i)} \equiv \frac{k_t(\alpha-1)}{k_i\alpha-k_i-2}$$

and

$$\mathcal{R}_2^{(i)} \equiv \frac{\chi^{(i)}+1/2}{[\chi^{(i)}+1]^2} - \frac{\chi^{(i)}}{\chi^{(i)}+1} \frac{(\alpha-1)[2\alpha^2(k_i+2)-(k_i+1)]}{(k_i+1)(1-4\alpha^2)}$$

$$Z_{42}^{(i)} \equiv \mathcal{R}_3^{(1)}, \quad Z_{45}^{(1)} \equiv G_{r1}\hat{B}_0^2 \mathcal{R}_4^{(1)}, \quad Z_{42}^{(2)} \equiv -G_{r1}\mathcal{R}_3^{(2)}$$

$$Z_{44}^{(2)} \equiv -G_{r1} \quad Z_{45}^{(2)} \equiv -G_{r1}\hat{B}_0^2 \mathcal{R}_4^{(2)}$$

where

$$\mathcal{R}_3^{(i)} \equiv \frac{k_i(\alpha+1)}{k_i\alpha-k_i-2}$$

and

$$\mathcal{R}_4^{(i)} \equiv \frac{\chi^{(i)}}{\chi^{(i)}+1} \frac{(\alpha-1)[(k_i+1)^2+(4+k_i+k_i^2)\alpha^2]}{(k_i+1)(1-4\alpha^2)} - \frac{4\chi^{(i)}+1}{2[\chi^{(i)}+1]^2}$$

$$Z_{61}^{(1)} \equiv \left[1-\frac{\mu_r^{(2)}}{\mu_r^{(1)}}\right]\mathcal{R}_5^{(1)}, \quad Z_{63}^{(1)} \equiv \left[1-\frac{\mu_r^{(2)}}{\mu_r^{(1)}}\right]$$

$$Z_{66}^{(1)} \equiv \frac{\mu_r^{(2)}}{\mu_r^{(1)}}\left\{1-\left[\frac{1}{\mu_r^{(2)}}-\frac{1}{\mu_r^{(1)}}\right] \times G_{r1}\hat{B}_0^2 \frac{2\chi^{(1)}\alpha(\alpha-1)(k_1\alpha+2\alpha+k_1+1)}{(k_1+1)(1-4\alpha^2)}\right\}$$

$$W_{11}^{(i)} \equiv \mathcal{R}_1^{(i)}\cos[(\alpha-1)\theta_i], \quad W_{12}^{(i)} \equiv -\mathcal{R}_1^{(i)}\sin[(\alpha-1)\theta_i]$$

$$W_{13}^{(i)} \equiv \cos[(\alpha+1)\theta_i], \quad W_{14}^{(i)} \equiv -\sin[(\alpha+1)\theta_i]$$

$$W_{15}^{(i)} \equiv G_{ri}\hat{B}_0^2[\mathcal{R}_2^{(i)}\sin(\alpha\theta_i)], \quad W_{16}^{(i)} \equiv G_{ri}\hat{B}_0^2[\mathcal{R}_2^{(i)}\cos(\alpha\theta_i)]$$

$$W_{1E}^{(i)} \equiv -\tfrac{1}{2}G_{ri}\hat{B}_0^2\sin(\alpha\theta_i), \quad W_{1F}^{(i)} \equiv -\tfrac{1}{2}G_{ri}\hat{B}_0^2\cos(\alpha\theta_i)$$

$$W_{21}^{(i)} \equiv \mathcal{R}_3^{(i)}\sin[(\alpha-1)\theta_i], \quad W_{22}^{(i)} \equiv \mathcal{R}_3^{(i)}\cos[(\alpha-1)\theta_i]$$

$$W_{23}^{(i)} \equiv \sin[(\alpha+1)\theta_i], \quad W_{24}^{(i)} \equiv \cos[(\alpha+1)\theta_i]$$

$$W_{25}^{(i)} \equiv G_{ri}\hat{B}_0^2[\mathcal{R}_4^{(i)}\cos(\alpha\theta_i)], \quad W_{26}^{(i)} \equiv -G_{ri}\hat{B}_0^2[\mathcal{R}_4^{(i)}\sin(\alpha\theta_i)]$$

$$W_{2E}^{(i)} \equiv \tfrac{1}{2}G_{ri}\hat{B}_0^2\cos(\alpha\theta_i), \quad W_{2F}^{(i)} \equiv -\tfrac{1}{2}G_{ri}\hat{B}_0^2\sin(\alpha\theta_i)$$

$$W_{31}^{(i)} \equiv \frac{\chi^{(i)}}{\chi^{(i)}+1}\mathcal{R}_5^{(i)}\cos[(\alpha-1)\theta_i]$$

$$W_{32}^{(i)} \equiv -\frac{\chi^{(i)}}{\chi^{(i)}+1}\mathcal{R}_5^{(i)}\sin[(\alpha-1)\theta_i]$$

$$W_{33}^{(i)} \equiv \frac{\chi^{(i)}}{\chi^{(i)}+1}\cos[(\alpha-1)\theta_i], \quad W_{34}^{(i)} \equiv -\frac{\chi^{(i)}}{\chi^{(i)}+1}\sin[(\alpha-1)\theta_i]$$

$$W_{35}^{(i)} \equiv \mathcal{R}_6^{(i)}\sin(\alpha\theta_i), \quad W_{36}^{(i)} \equiv \mathcal{R}_6^{(i)}\cos(\alpha\theta_i)$$

$$W_{3E}^{(i)} \equiv -\sin(\alpha\theta_i), \quad W_{1F}^{(i)} \equiv -\cos(\alpha\theta_i)$$

in which $\mathcal{R}_6^{(i)}$ is defined by

$$\mathcal{R}_6^{(i)} \equiv \frac{1}{\chi^{(i)}+1} - 2\left[\frac{\chi^{(i)}}{\chi^{(i)}+1}\right]^2 \frac{\alpha(\alpha-1)(k_i\alpha+2\alpha+k_i+1)}{(k_i+1)(1-4\alpha^2)} G_{ri}\hat{B}_0^2$$

$$W_{45}^{(i)} \equiv \cos(\alpha\theta_i), \quad W_{46}^{(i)} \equiv -\sin(\alpha\theta_i)$$

$$W_{4E}^{(i)} \equiv -\cos(\alpha\theta_i), \quad W_{4F}^{(i)} \equiv \sin(\alpha\theta_i)$$

References

[1] Barnett, D. M., Rawal, S., and Rummel, K., 2001, “Multifunctional Structures for Advanced Spacecraft,” J. Spacecr. Rockets, **38**(2), pp. 226–230.

[2] Noor, A. K., 2000, “Structures Technology for Future Aerospace Systems,” *Progress in Astronautics and Aeronautics*, American Institute of Aeronautics and Astronautics, Inc., Reston, VA, Vol. 188, Chap. 1, pp. 18–20.

[3] Williams, M. L., 1952, “Stress Singularities Resulting From Various Boundary Conditions in Angular Corners of Plates in Extension,” ASME J. Appl. Mech., **19**, pp. 526–528.

[4] Dempsey, J. P., and Sinclair, G. B., 1981, “On the Singular Behavior at the Vertex of a Bimaterial Wedge,” J. Elast., **11**(3), pp. 317–327.

[5] Lin, Y. Y., and Sung, J. G., 1998, “Stress Singularities at the Apex of a Dissimilar Anisotropic Wedge,” ASME J. Appl. Mech., **65**, pp. 454–463.

[6] Hwu, C., and Lee, W. J., 2004, “Thermal Effect on the Singular Behavior of Multibonded Anisotropic Wedges,” J. Therm. Stresses, **27**, pp. 111–136.

[7] Fil’shtinskii, L. A., and Matvienko, T. S., 1999, “Singularities of Physical Fields at the Apex of a Piezoceramic Wedge (Plane Strain),” Int. Appl. Mech., **35**(3), pp. 301–304; 1999, Prikl. Mekh., **35**(3), pp. 89–92.

[8] Pao, Y. W., and Yeh, C. S., 1973, “A Linear Theory for Soft Ferromagnetic Elastic Solids,” Int. J. Eng. Sci., **11**, pp. 415–436.

[9] Shindo, Y., 1978, “The Linear Magnetoelastic Problem for Soft Ferromagnetic Elastic Solid With a Finite Crack,” ASME J. Appl. Mech., **44**, pp. 47–51.

[10] Oates, G. C., 1974, “Vector analysis,” *Handbook of Applied Mathematics*, C. E. Pearson, ed., Van Nostrand Reinhold, New York, Chap. 3.

[11] Zadoyan, M., 1992, *Spatial Problems of the Plasticity Theory*, Nauka, Moscow, in Russian.

[12] Chobanyan, K. S., 1987, *Contact Stresses in Composite Bodies*, Printing House of Academy of Science of Armenia, Yerevan, in Russian.

[13] Mittra, R., and Li, S. W., 1971, *Analytical Techniques in the Theory of Guided Waves*, Macmillan, New York, pp. 4–11.

[14] Bozorth, R. M., 1953, *Ferromagnetism*, Van Nostrand, New York, Chaps. 1 and 3.

[15] Moon, F. C., 1984, *Magneto-Solid Mechanics*, Wiley-Interscience, New York, pp. 423–425.

[16] Lin, T., 2002, *Numerical Methods*, Class Notes, Fall Semester, Virginia Polytechnic Institute and State University, Department of Mathematics, Blacksburg, VA, pp. 176–179.

[17] MATHEMATICA®6, Wolfram Research, Inc.

An Adaptive Meshless Method for Analyzing Large Mechanical Deformation and Contacts

Qiang Li

Kok-Meng Lee[1]
e-mail: kokmeng.lee@me.gatech.edu

The G. W. Woodruff School of Mechanical Engineering,
Georgia Institute of Technology,
801 Ferst Drive,
Atlanta, GA 30332-0405

Design for manufacturing of equipment (that handles deformable objects) and disposable medical devices (such as medical needles, optic fibers, and catheters for inserting into the human body) involves solving mechanical contact problems. Unlike rigid component manufacturing, which has been relatively well established, the handling of deformable bodies remains a challenging research. This paper offers an adaptive meshless method (MLM) for solving mechanical contact problems, which automatically insert additional nodes into large error regions identified in terms of mechanical stresses. This adaptive MLM employs a sliding line algorithm with penalty method to handle contact constraints. The method does not rely on small displacement assumptions; thus, it can solve nonlinear contact problems with large deformation. We validate the method by comparing results against those computed by using a commercial FEM software and analytical solution for two different situations, namely, large deformation and contact. Four practical applications are illustrated: large deflection of a compliant finger, mechanical contact, snap-fit assembly, and surgical needle insertion. [DOI: 10.1115/1.2912938]

Keywords: deformable contact, adaptive meshless method, finite element, sliding line, partition unity

1 Introduction

Mechanical deformable contacts are common problems in automated handling of food products [1], tooling, fixturing, and compliant grasping [2], robotic assembly of snap fits [3], and design for manufacturing of medical/biomedical devices [4]. Accurate solutions to mechanical contact problems involving large deformation are essential to help optimize designs and improve the performance of these systems. However, analytical solutions to contact problems are limited because of their highly nonlinear nature. With few exceptions, acceptable solutions to deformable contact problems are often numerically solved. Among these methods, finite element method (FEM) has been most popular due to its generality and its ability to handle complicated geometry.

After decades of development, commercial FEM software has been widely available to solve many engineering contact problems [5,6]. The accuracy of FEM results, however, significantly depends on the quality of the mesh. For contact problems, the mesh density must be maintained at a sufficiently high level around the contact region to reasonably obtain accurate results. However, additional elements in noncontact regions do not generally help improve the overall accuracy. Thus, the mesh density should not be uniformly high as they would simply slow down the computational speed; clearly, an appropriately designed mesh is very important for a FEM analysis so that accurate results can be efficiently obtained. This is especially true for solving contact problems where a large number of iterations are often needed for the highly nonlinear solution to converge. However, for contact problems involving large deformation, it is very difficult to construct a good initial mesh even with the help from an experience FEM analyst because the contact region in such a problem cannot be accurately located before the computation begins. Thus, it is desired to have a method that can automatically identify large error regions and can systematically increase the nodal density in those regions to improve the overall accuracy with minimum or no human involvement. Previous researches have developed adaptive FEM algorithms [7–12] to solve this problem. Although FEM meshes provide the generality to handle complicated geometries, appropriate mesh structures are often difficult to create or modified especially for applications where meshes must be automatically reconstructed during the computational process. Considerable research effort must be devoted to develop an adaptive mesh generation and deletion algorithm [12] in order to simulate dynamic contact/impact problems. Existing mesh generation programs for FEM, in general, have difficulties to simultaneously meet the demands of both accuracy and computational efficiency in computation due to the stringent shape requirement of FEM elements; additional manual modification of the meshes is often employed (see, for examples, an assumed strain approach [13], superelement technique [14] for frictionless contact problems of isotropic elastic materials, and mortar-FEM [15] for surface to surface contacts).

Recently, meshless methods (MLMs) (which inherit many advantages of FEM and yet need no explicit mesh structure to discretize geometry) have been gaining attention [16–18]. ML methods have been built on the same theoretical framework of FEM. The construction of the basis function for MLM, however, does not rely on the mesh structure. This significantly reduces the difficulties of developing an automatic algorithm to increase node density, and makes MLM a very attractive alternative to FEM for solving engineering problems where automatic remeshing is needed. Recently, research efforts have been seen in solving two technical problems related to adaptive MLM. The first problem is to estimate computational error in MLM. Methods such as residual technique in Ref. [19] and recovery technique in Ref. [20] are effective, but they are often mathematically difficult to derive and relatively complicated to apply in practice. The second problem is the development of a nodal insertion algorithm for reconstructing the integration cells after the nodes are inserted. Most existing adaptive MLMs use a background cell technique, which demands a significant amount of computation time particularly when the nodal distribution becomes irregular. Methods (such as

---

[1] Corresponding author.

Contributed by the Applied Mechanics Division of ASME for publication in the JOURNAL OF APPLIED MECHANICS. Manuscript received May 10, 2007; final manuscript received March 28, 2008; published online May 14, 2008. Review conducted by Sanjay Govindjee.

quadtree technique) have been proposed to improve the efficiency of the reconstruction process [21,22]. However, the addition of the computational load cannot be totally eliminated. In Ref. [23], a stabilized conforming nodal integration technique has been proposed to avoid the need for constructing background cells. This method has some successful applications in adaptive computation, for example, Ref. [24], but its extension to three dimensional computations remains a challenge. In this paper, we develop an adaptive MLM for solving nonlinear problems of mechanical contact involving large deformation.

The remainder of this paper offers the following.

1. We present a general formulation for solving large-deformation mechanical contact problems, and the numerical method for solving for the solutions using MLM. This formulation, which applies the sliding line algorithm [25] along with the penalty method [6] for handling contact constraints, does not rely on small (or linear) displacement assumptions commonly made in formulating mechanical contacts. Thus, the solution method presented here is rather general and can be used to solve nonlinear contact problems with large deformation.
2. We have developed an adaptive MLM for solving nonlinear mechanical problems with emphases on contact problems. In FEM, the posteriori error estimation technique [26,27], which has been based on results obtained by different-order polynomial basis functions, is easy to use and popular in practice. However, the basis function in MLM is, in general, not a polynomial; the posteriori error estimation technique developed for FEM cannot be directly applied to MLM. We present here a modified error estimation (built on two different support sizes of a basis function) to identify regions of large computational errors for automatic node insertion. We derive the error estimation based on mechanical stresses since large displacement due to rigid body motion does not necessarily result in mechanical stresses. In addition, we use the partition unity integration technique [28] to avoid the reconstruction of integration cells during the adaptive process.
3. Four examples are given to illustrate the automatic node inserting procedure of the adaptive MLM algorithm and its effectiveness in simulating large mechanical deformation and/or contact. As will be shown, unlike FEM where excessively large deformation could cause severe element distortion and consequently break down the simulation, the adaptive MLM algorithm is able to construct basis functions without using mesh structure.
4. The adaptive MLM algorithm for solving mechanical contact problems has been validated by comparing the MLM computed results against the analytical solution whenever possible, and those simulated using ANSYS (a commercial finite element analysis package).

2 Formulation of Mechanical Contact and Deformation

Mechanical contact problems are formulated for solving with meshless methods in weak form. Contact is then modeled as a constraint imposed onto the weak-form formulation.

2.1 Formulation of Mechanical Contact. Consider two bodies Ω_A and Ω_B bound by boundaries Γ_A and Γ_B, respectively, as shown in Fig. 1, where X is the original undeformed coordinate of a particle, and $\mathbf{x}_A(X,t)$ and $\mathbf{x}_B(X,t)$ represent the deformed coordinate of an arbitrary particle on the Bodies A and on B at time t, respectively. Physically, contact can be interpreted as a constraint imposed on continuum mechanics implying that the two bodies cannot penetrate into each other:

$$\Omega_A \cap \Omega_B = 0 \tag{1}$$

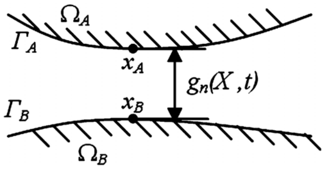

Fig. 1 Illustration of contact between two bodies

Defining the contact condition. Although the contact constraint (1) can be easily understood, it is inconvenient to numerically handle as computational methods require a discretized form. Thus, we formulate the contact problem as a displacement constraint posed on discretized nodes. The distance between two particles on Γ_A and Γ_B can be expressed as a gap function $g_n(X,t)$, which obeys the following rules:

$$g_n(X,t)\begin{cases} >0 & \text{when two points are not in contact} \\ =0 & \text{when two points are at contact} \\ <0 & \text{penetration occurs} \end{cases} \tag{2}$$

The first two conditions in Eq. (2) state that the distance between the two points at the same contact should be zero when the two bodies are in contact or greater than zero when they depart. The last condition in Eq. (2) is physically invalid since the two bodies cannot move into each other. However, small penetration is numerically necessary such as in penalty methods. In formulating the contact problem, the penalty method assumes that the normal component of the contact force τ_{cn} is proportional to g_n:

$$\tau_{cn} = \begin{cases} 0, & g_n \geqslant 0 \\ k_n g_n, & g_n < 0 \end{cases} \tag{3}$$

where the penalty proportionality k_n is a very large number. This approximation approaches ideal contact as $k_n \to \infty$. Since g_n is negative when there is a contact, the force vector $\tau_{cn}\mathbf{n}$ points outward at the boundary of the contact object.

Effect of friction. Once the contact force in the normal direction is known, the tangential component of the contact force (or the friction force) τ_{ct} can be obtained by the classic Coulomb friction law in Eq. (4): stick occurs if

$$0 < |\tau_{ct}| \leqslant -\mu\tau_{cn}$$

slip occurs if

$$|\tau_{ct}| = -\mu\tau_{cn} \tag{4}$$

where μ is the friction coefficient. Since there is a need to quantitatively determine the current state of contact (either "stick" or "slip"), we introduce another gap function g_t to depict the distance that the contact point slips for two adjacent time steps. With g_t, τ_{ct} can be computed as follows:

$$\tau_{ct} = \begin{cases} k_t g_t, & \mu\tau_{cn} \geqslant |k_t g_t| \quad \text{(stick)} \\ \mu\tau_{cn}\,\mathrm{sgn}(g_t), & \mu\tau_{cn} < |k_t g_t| \quad \text{(slip)} \end{cases} \tag{5}$$

where k_t is the tangential penalty parameter. As in the treatment for the normal contact force in Eq. (2), the first condition in Eq. (5) does not exactly satisfy Coulomb law since for the stick situation, $g_t \equiv 0$; as a result, τ_{ct} must be zero as well. However, the friction force can be approximately obtained if we allow for a small slipping distance, and as k_t increases Eq. (5) approaches the ideal Coulomb law. Unlike τ_{cn}, which is always negative, when there is a contact, the sign of τ_{ct} can be positive or negative depending on the direction of the slip.

Discretization of contact for numerical solutions. In the discretized domain, the two contact bodies are referred here as the slave and master. The assignment of master and slave is arbitrary and exchangeable. The coordinates of the discrete nodes are defined in Fig. 2, where $\mathbf{x}_s$ and $\mathbf{x}_c$ are the slave node and the contact

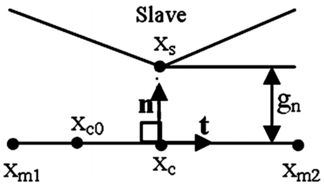

Fig. 2 Contact gap function between two discretized bodies

point on the master segment, respectively, $\mathbf{x}_{m1}$ and $\mathbf{x}_{m2}$ are the two adjacent master nodes, and $\mathbf{x}_{c0}$ is the contact point of the last computational step. In Fig. 2, $\mathbf{n}$ and $\mathbf{t}$ are, respectively, the unit normal and tangential vectors at $\mathbf{x}_c$. The vector $\mathbf{t}$ can be computed from the master nodes

$$\mathbf{t}=(\mathbf{x}_{m2}-\mathbf{x}_{m1})/\ell \quad \text{where } \ell=\|\mathbf{x}_{m2}-\mathbf{x}_{m1}\| \tag{6}$$

and $\mathbf{n}$ can then be obtained from the orthogonality $\mathbf{n}=\mathbf{e}_z\times\mathbf{t}$, where $\mathbf{e}_z$ is a unit vector along the z axis.

The normal gap function g_n, which is defined as the distance from the slave node to the master segment, can be computed as follows:

$$g_n=(\mathbf{x}_s-\mathbf{x}_{m1})\cdot\mathbf{n} \tag{7}$$

Similarly, the tangential gap function g_t, which is the distance between $\mathbf{x}_c$ and $\mathbf{x}_{co}$, can be computed as

$$g_t=(\mathbf{x}_c-\mathbf{x}_{c0})\cdot\mathbf{t} \tag{8}$$

2.2 Formulation of Large Deformation Mechanics. For static or quasistatic problems involving large deformation, the three governing equations are given by Ref. [29],

$$\sum_{j=1}^{3}\frac{\partial P_{ji}}{\partial X_j}+\rho_0 b_{0i}=0 \quad (i=1,2,3) \tag{9}$$

where ρ_0 and b_0 are the density and body force of the original undeformed state, and P_{ji} is the element of the first Piola–Kirchhoff (PK) stress tensor $\mathbf{P}$. For linear, small displacement problems, the Cauchy stress $\boldsymbol{\sigma}$ is used in place of $\mathbf{P}$. To solve Eq. (9) for the displacement function u as an independent variable, the asymmetric stress tensor $\mathbf{P}$ is transformed to the symmetric second PK stress tensor $\mathbf{S}$ by

$$P_{ji}=\sum_{r=1}^{3}S_{ir}\frac{\partial x_r}{\partial X_j} \tag{10}$$

where S_{ir} is the element of $\mathbf{S}\in R^{3\times 3}$ (that is related to the displacement u through a material constitutive model). In this paper, general Hooke's law is used:

$$S_{ir}=\sum_{k=1}^{3}\sum_{l=1}^{3}C_{irkl}(\varepsilon_{kl}+\bar{\varepsilon}_{kl}) \tag{11}$$

where C_{irkl} is the element of the material compliant tensor $\mathbf{C}$ (a material property), and $\varepsilon_{kl}+\bar{\varepsilon}_{kl}$ are the terms in the element of the Green's strain tensor given by

$$\varepsilon_{kl}=\frac{1}{2}\left(\frac{\partial u_k}{\partial X_l}+\frac{\partial u_l}{\partial X_k}\right) \tag{12a}$$

and

$$\bar{\varepsilon}_{kl}=\sum_{m=1}^{3}\frac{\partial u_m}{\partial X_k}\frac{\partial u_m}{\partial X_l} \tag{12b}$$

For linear small displacement problems, the higher order terms in the Green's strain tensor can be ignored or $\bar{\varepsilon}_{kl}\approx 0$; the Green's strain tensor reduces to Cauchy strain ε_{kl}.

To complete the formulation so that the solution to Eq. (9) is physically relevant, we consider two types of boundary conditions (BCs) for a continuum body; the Dirichlet and Neumann BCs correspond to the displacement $\bar{u}_i$ and traction $\bar{t}_i$ (or force per unit area) BCs respectively:

$$u_i=\bar{u}_i \quad (i=1,2,3) \quad \text{on } \Gamma_u \tag{13}$$

$$\sum_{j=1}^{3}P_{ij}n_j=\bar{t}_i \quad (i=1,2,3) \quad \text{on } \Gamma_t \tag{14}$$

where $\mathbf{n}$ is the normal vector of the boundary.

2.3 Weak-Form Formulation of Contact Mechanics. The basic MLM approximation form for an unknown displacement function $u(\mathbf{X})$ is

$$u(\mathbf{X})=\mathbf{x}-\mathbf{X}=\sum_{i=1}^{n}\Psi_i(\mathbf{X})u_i \tag{15}$$

where u_i is the nodal control value associated with the ith node, and $\Psi(\mathbf{X})$ is a ML basis function that can be constructed, for example, by using reproducing kernel method [30]. If the ML basis function at the ith node is an interpolating function, u_i is the displacement at this node $u_i=u(\mathbf{X}_i)$. Otherwise, $u_i\neq u(\mathbf{X}_i)$.

The large deformation problem is numerically formulated in weak form. For this, we multiply both sides of Eq. (9) by the ML basis functions, and integrate the resulting equation by parts, which leads to the following governing equation in weak form:

$$\int_{\Omega_0}\sum_{j=1}^{3}\left(\frac{\partial\Psi_k}{\partial X_j}P_{ji}\right)d\Omega_0-\int_{\Omega_0}\Psi_k\rho_0 b_i\,d\Omega_0-\int_{\Gamma_0}\Psi_k\bar{t}_i\,d\Gamma_0=0 \tag{16}$$

Note that Ψ_k is the basis function at the kth node.

We formulate the contact problem by using the penalty method as follows:

$$\delta W_i=\delta W_e+\delta G_p \tag{17}$$

where W_i and W_e are the virtual internal and external works without contact constraint, G_p is the virtual work contributed by the contact force τ_{cn} and τ_{ct}, and

$$G_p=\int_{\Gamma_c}\tau_{cn}g_n+\tau_{ct}g_t\,d\Gamma \tag{18}$$

The variations of W_i and W_e are given by

$$\delta W_i=\int_{\Omega_0}\frac{\partial\Psi_I}{\partial X_j}P_{ji}\delta\mathbf{x}_I\,d\Omega_0 \tag{19}$$

and

$$\delta W_e=\int_{\Omega_0}\Psi_I\rho_0 b_i\delta\mathbf{x}_I\,d\Omega_0+\int_{\Gamma_0}\Psi_I\bar{t}_i\delta\mathbf{x}_I\,d\Gamma_0 \tag{20}$$

By incorporating the assumptions (3) and (5) in the penalty method, the variation of G_p becomes

$$\delta G_P=\int_{\Gamma_c}\tau_{cn}\delta g_n+\tau_{ct}\delta g_t\,d\Gamma \tag{21}$$

where the variation of the gap functions can be derived from Eqs. (7) and (8):

$$\delta g_n=[\mathbf{n},\ -(1-\alpha)\mathbf{n},\ -\alpha\mathbf{n}]^T\cdot\delta\mathbf{x}_w \quad \text{and}$$

$$\delta g_t=\frac{\ell}{\ell_o}\left[\mathbf{t},\ -\frac{g_n}{\ell}\mathbf{n}-(1-\alpha)\mathbf{t},\ \frac{g_n}{\ell}\mathbf{n}-\alpha\mathbf{t}\right]^T\cdot\delta\mathbf{x}_w$$

where $\delta\mathbf{x}_w=[\delta\mathbf{x}_s,\delta\mathbf{x}_{m1},\delta\mathbf{x}_{m2}]^T$, $\alpha=(\mathbf{x}_s-\mathbf{x}_{m1})\cdot\mathbf{t}/\ell$, and ℓ and ℓ_o

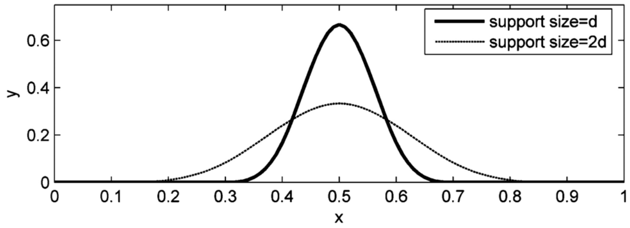

Fig. 3 RKP basis function with two different support sizes

are the current and previous distances defined in Eq. (6).

In summary, the governing equation in weak form can be obtained by substituting Eqs. (18)–(20) into Eq. (16). As shown in Eq. (10), (11), (12*a*), and (12*b*), the first PK stress tensor **P** is a nonlinear function of displacement *u*. Thus, for large deformation, the discretized governing equations in weak form are a set of nonlinear system equations, the solution of which can be obtained by applying the Newton method. The natural (or Neumann) boundary conditions are applied in the process when the governing equations are converted to weak form. The essential (or Dirichlet) boundary conditions are applied before solving the linearized sets of weak-form governing equations. To impose contact constraints by using the penalty method, the penalty parameters must be properly chosen. If the penalty parameters are too small, the contact penetration will be too large. On the other hand, if the penalty parameters are too large, the tangent matrix will be ill condition. In our implementation, the penalty parameters are chosen to be relatively small for the initial computation. Once the initial computation is complete, the contact penetration will be checked. If the contact penetration is not smaller than the preset threshold, the penalty parameter will be increased and the computation will continue.

3 Adaptive MLM for Computation Mechanics

A simple way to improve the accuracy of the numerical approximation is to uniformly increase the nodal density in the whole computational domain. This method, however, is inefficient if large errors only occur in certain regions. A more effective way is to estimate the error distribution and accordingly insert additional nodes, or more specifically, into the large error regions.

3.1 Error Estimation. We introduce an error estimation technique for the adaptive ML computation based on two different support sizes:

$$\tilde{e}(\mathbf{x}) = \sum_{i=1}^{n} \Psi_{i,d}(\mathbf{x})\Phi_{i,d} - \sum_{i=1}^{n} \Psi_{i,2d}(\mathbf{x})\Phi_{i,2d} \tag{22}$$

where $\tilde{e}(\mathbf{x})$ is the estimated error, $\Psi_{i,d}$ and $\Psi_{i,2d}$ denote the basis functions at the *i*th node with a support size *d* and 2*d*, respectively, $\Phi_{i,d}$ is the solution solved in the previous computation step, and $\Phi_{i,2d}$ is the fitted result by using the basis function with a support size of 2*d*. The rationale for Eq. (22) can be explained with the aid of Fig. 3, which compares two different support sizes of a RPK basis function. In general, the larger the support size, the smoother is the basis function, and more difficult to approximate a function with an abrupt change in the solution. Thus, regions of large errors can be characterized by comparing the approximation solutions solved using the two different basis functions. As will be shown later in Example 1, numerical experiments have confirmed this finding.

3.2 Adaptive Node Insertion. Once the errors are estimated from Eq. (22), locations of large errors are identified as follows:

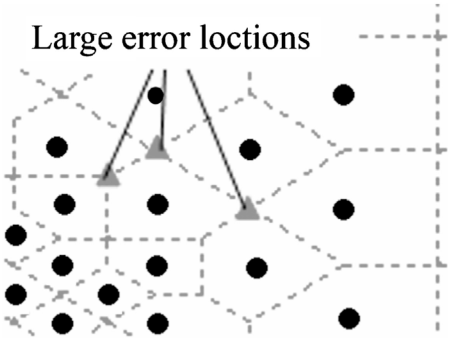

Fig. 4 Voronoi plot with three large error point

$$\forall \mathbf{x}_a : |\tilde{e}(\mathbf{x}_a)| > e_p \tag{23}$$

where x_a is the test location and e_p is a specified error threshold. Additional nodes can be inserted into the computational domain by using the Voronoi plot [31] technique that constructs one Voronoi cell for each node. As shown in Fig. 4, a Voronoi cell is a polygon containing all the points closest to the node that it surrounds. The error at the vertices of each Voronoi cell is computed from Eq. (22). If the error satisfies criterion (23), a new node is created at that point, as illustrated in Fig. 4. The three triangles at the corners of a Voronoi cell are example regions of large numerical errors. The support size of the inserted node is calculated by using Eq. (24) as the maximum distance from the node to its surrounding nodes whose Voronoi cell is adjacent to this node:

$$r_i = a_p \max(\|\mathbf{x}_j - \mathbf{x}_i\|) \tag{24}$$

where r_i is the support radius for the *i*th node, $\mathbf{x}_i$ and $\mathbf{x}_j$ are the coordinates of the *i*th and *j*th nodes, respectively. The Voronoi cell of the *j*th node is adjacent to the Voronoi cell of the *i*th node. In Eq. (24), a_p is a constant coefficient normally taken a value between 1 and 3. For the newly inserted node, the choice of the support radius of the basis function is a trade-off between two considerations: It must be sufficiently large to cover enough nodes for constructing the ML basis function but kept small to localize the effect of the newly inserted nodes. Additionally, computational load increases as the support radius increases.

3.3 Partition Unity Integration. When using partition unity integration, a new integration cell is automatically created once a new node is inserted as illustrated in Fig. 5, and thus this numerical integration scheme is very suitable for adaptive computation. Most of the basis functions (including the RKP method [30]) used in MLM have the partition unity property:

$$\sum_{i=1}^{n} \Psi_i(\mathbf{x}) = 1 \tag{25}$$

with which the integration for an arbitrary function $f(\mathbf{x})$ in the computational domain can be computed by using as follows:

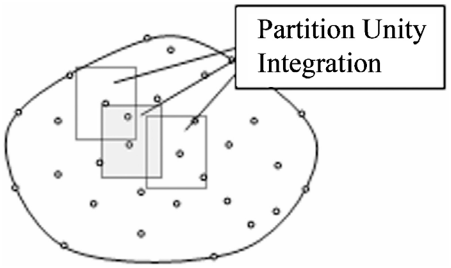

Fig. 5 Partition unity integration cells

$$\int_{\Omega} f(\mathbf{x})d\mathbf{x} = \int_{\Omega} f(\mathbf{x})\sum_{i=1}^{n}\Psi_i(\mathbf{x})dx = \sum_{i=1}^{n}\int_{\Omega} f(\mathbf{x})\Psi_i(\mathbf{x})dx \quad (26)$$

where Ω is the computational domain. To exclude points outside the computational domain, Eq. (26) is written such that the integration is within the support domain S_i of ith basis function:

$$\sum_{i=1}^{n}\int_{\Omega} f(\mathbf{x})\Psi_i(\mathbf{x})dx = \sum_{i=1}^{n}\int_{S_i} f(\mathbf{x})P(\mathbf{x})\Psi_i(\mathbf{x})dx \quad \text{where}$$

$$P(\mathbf{x}) = \begin{cases} 1 & \text{when } \mathbf{x} \in \Omega \\ 0 & \text{when } \mathbf{x} \notin \Omega \end{cases} \quad (27)$$

The global integration for the whole computational domain is divided into n subintegration domains and performed upon the support domain of n basis functions. Because the support domain of the basis functions, in general, has a regular shape, the conventional numerical integration scheme such as Gaussian quadrature can be easily applied.

3.4 Nodal Insertion for Computation Mechanics. In Sec. 3.1, the weak-form formulation is based on displacements, which may simply be a result of a rigid body motion and do not necessarily induce stresses or strains in the mechanical body. For error estimation in solving mechanical problems, the stress or strain is a more appropriate quantitative variable.

The mechanical stress is a nine-component tensor $\boldsymbol{\sigma}_{ij}$ (or S_{ij} in the case of large deformation), which in matrix form can be represented as a 3×3 symmetric matrix. The three principal stress components, which are usually used as criteria to determine material failure, are the eigenvalues of the stress matrix. They are coordinate independent and can be utilized to locate the region of high stresses. The overall magnitude of the stress T_{in} can be written as

$$T_{\text{in}} = \sum_{i=1}^{3}\lambda_i^2 \quad (28)$$

where λ_i is the eigenvalue of the stress matrix. As shown in the Appendix, T_{in} is computed from

$$T_{\text{in}} = \left[\sum_{i=1}^{3}\boldsymbol{\sigma}_{ii}\right]^2 + 2\sum_{i=1}^{3}\sum_{j=1}^{3}\kappa_{ij}(\boldsymbol{\sigma}_{ij}^2 - \sigma_{ii}\sigma_{jj}) \quad \text{where}$$

$$\kappa_{ij} = \begin{cases} 1 & \text{when } i \neq j \\ 0 & \text{when } i = j \end{cases} \quad (29)$$

The error estimation for inserting additional nodes in solving mechanical problems can be executed as follows:

1. determine an appropriate support size for the ML basis function
2. compute the displacement field $u(\mathbf{X})$ with the original basis function
3. fit the displacement result by using the basis function but a larger support size
4. compute the stress field $\sigma(x)$ from the linear or nonlinear strain (12*a*) and (12*b*) by using the original and the new displacements
5. compute T_{in} for the original and the new results
6. estimate the error as the difference between two stress magnitudes.

Example 1: Adaptive MLM for computation mechanics. To illustrate the error estimation and node insertion in the adaptive MLM computation, we consider a 2D finger with one of its ends clamped and a vertical shear force P applied at the other free end. Since exact solutions for large deformation are not available for comparison, FEM is chosen here as a basis for illustration. We compare MLM results against those computed by using ANSYS, for which condensed 288 second-order elements (937 nodes) are used to ensure the accuracy of the FEM results. The analysis is done with "large deformation static" option in ANSYS. Figure 6 shows the parameters that characterize the undeformed finger and a typical deformed shape of the FEM-meshed finger. The material properties (Young's modulus E and the Poisson's ratio μ) and geometry of the beam are given in Table 1.

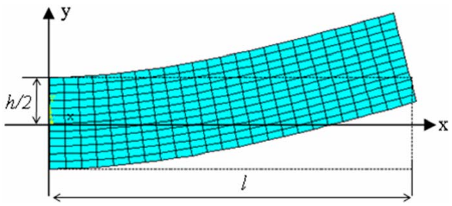

Fig. 6 FEM mesh and its deformed result (ANSYS)

The initial uniform distribution of 7×4 nodes is used for the MLM computation. In each adaptive computation, only the Voronoi cells inside the boundary are kept, and the infinite Voronoi cells are cut off by the boundary. In addition, potential new nodes inside the boundary are checked by using a boundary mesh to ensure that there are no invalid nodes being added. After three adaptive computations, the total number of nodes increases to 99. The difference in the y-displacements between the adaptive MLM and the FEM solution was computed for each of the iterations. Figures 7 and 8 illustrate the computed results. In Fig. 7, error$=100\%\times(y_{\text{MLM}}-y_{\text{FEM}})/y_{\text{FEM}}$; large % errors are primarily located near $x=0$ where the beam is clamped. Figure 8 shows a snapshot of the node distributions after two adaptive computations, where "●" and "×" denote the original and adaptive inserted nodes respectively. As expected, new nodes, are automatically inserted to the regions near the clamped end of the beam. This implies that the adaptive algorithm correctly identifies the large error regions, then accordingly inserts new nodes to those regions, and effectively reduces the computational errors.

Table 1 Parameters for Example 1

l (m)	h (m)	E (MPa)	μ	P (kN)
48	12	30	0.0001	1

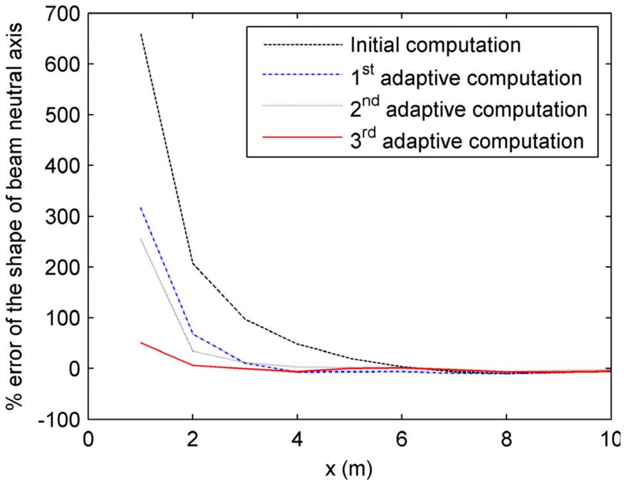

Fig. 7 Percentage error of MLM for four consecutive adaptive computations

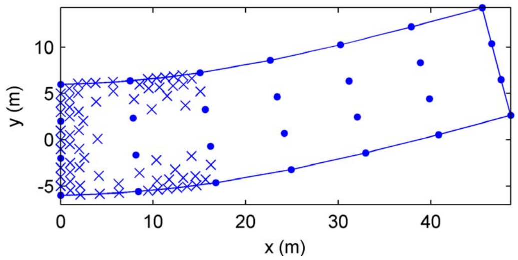

Fig. 8 MLM nodes after the final adaptive computation

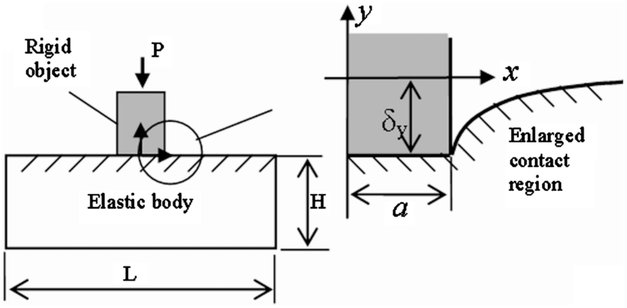

Fig. 9 Rigid punch contacts with elastic foundation

4 Adaptive MLM for Mechanical Contact Simulation

We illustrate here three mechanical contact examples. The first example, where analytical solution is available, is to validate the adaptive MLM and contact algorithm. We also compare the results against the solution obtained from ANSYS. The second example investigates the effect of friction for a snap-fit mechanism. The third example shows the potential of MLM in medical surgery applications. Since the focus here is to illustrate the adaptive MLM for solving contact problems, only 2D example problems are considered, where a surface mesh is used to formulate and compute the contact.

Table 2 Geometry parameters of Example 2

L (m)	H (m)	A (m)	δ_y
0.08	0.04	0.0025	0.0001

Example 2: Contact between rigid and elastic objects. Figure 9 schematically shows a classic two-body contact problem, where a small rigid object (which may be a rigid punch or robotic finger) is normally driven into an elastic body. Both objects are infinite in the z-axis. The structure is symmetric with respect to the y-axis; thus, only half of the geometry on the positive x-axis is solved. The closed form analytical solution describing the displacement along the y-direction for the frictionless case can be found in Ref. [32].

$$u_y(x) = \delta_y - \begin{cases} 0 & \text{when } x \leqslant a \\ \dfrac{2(1-\nu^2)P}{\pi E} \ln\left[\dfrac{x}{a} + \sqrt{\dfrac{x^2}{a^2} - 1}\right] & \text{when } x > a \end{cases} \tag{30}$$

where u_y is the displacement in the y direction, P is the force applied on rigid punch, a is the half-width of rigid punch, and d_y is the distance that the rigid object moves into the elastic body.

To demonstrate the effectiveness of the adaptive method, no special node refinement is made around the contact region and the computation starts with a uniform distribution of 11×11 nodes. Specific values used in the simulation are given in Table 2. After three successive computations, the total number of nodes increases from its initial 121 nodes to 194. Figures 10(*a*) and 10(*b*) show the Voronoi diagrams of the initial and second node distributions. The final node distribution is shown in Fig. 10(*c*). As illustrated in Fig. 10, the adaptive algorithm effectively identifies the contact region and automatically inserts additional nodes around the contact region. The MLM and FEM results are compared against the analytical solutions in Fig. 11, where FEM uses a total of 544 nodes with special refinement around the contact area.

As shown in Fig. 11, the final MLM result greatly improves after three adaptive computations from the initial calculation. Both FEM and MLM agree very well in final results but are slightly higher than the analytical solution. The discrepancy is somewhat expected because the analytical solution assumes that the elastic body has an infinite depth in the x-direction while the numerical solutions base on a finite dimension.

Example 3: Contact of a snap fit. Snap fits are commonly used for locking, attachment, or part assembly. In practical application, sharp edges are often used in the snap fit mechanism to provide a

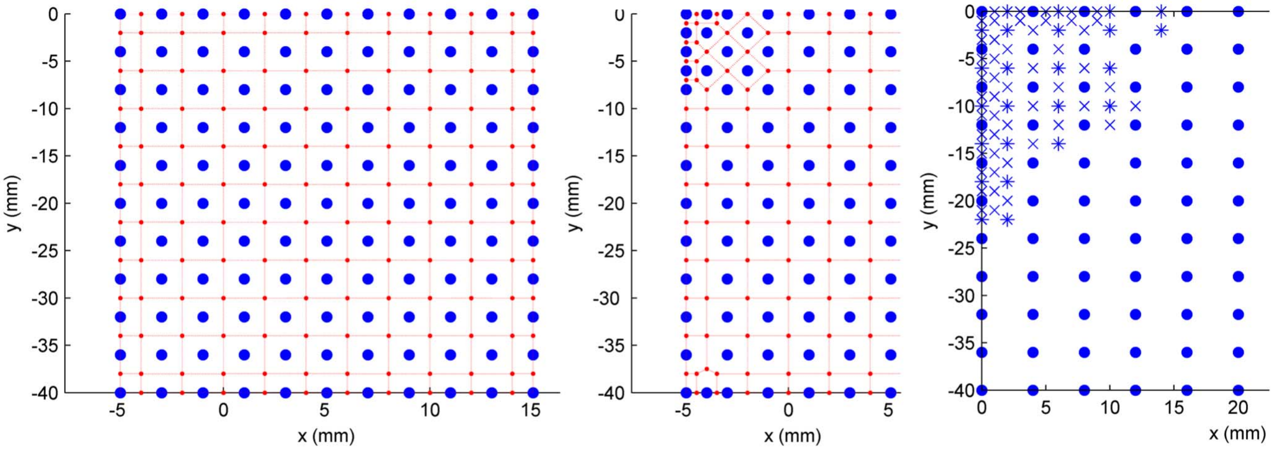

a) Initial Voronoi diagram
(• node; ?vertexes of a Voronoi cell)

b) 2nd Voronoi diagram

c) Final node distribution

Fig. 10 Adaptive node insertion

positive retention. In addition, a snap-fit must have a large retention force but a small insertion force. Since these forces are the result of the contact between components of a snap fit, contact analyses are very important for designing a snap-fit mechanism. We demonstrate here the use of MLM for analyzing contact forces of a snap fit, and compare the results against those computed by ANSYS.

A typical snap-fit geometry is shown in Fig. 12. Without loss of generality, the retention block (that is assumed to be undeformable) horizontally moves from right to left (x_c is not fixed in this case). The cantilever hook is clamped at the left end and deflected upon contact; the geometry and material parameters of the cantilever hook along with the options used for ANSYS and MLM are given in Table 3.

Figure 13 compares the contact forces computed by using MLM against those obtained by using ANSYS for both frictionless ($\mu=0$) and frictional ($\mu=0.2$) contacts. The MLM and FEM closely agree with each other up to the location where the edge of the retention block passes the tip of the jaw, beyond which ANSYS computation breaks down due to the large distortion of elements. Large stresses build up when the corner (x_c, y_c) reaches the tip of the jaw; as a result, FEM has excess element distortion around the corners and leads to divergence. More elements and finer load steps do not improve the result. Unlike FEM, MLM is free from mesh distortion and predicts the contact forces throughout the snap fitting process. It is interesting to note that the contact force in the y direction only slightly increases with friction, but the contact force in the x direction significantly increases. This result suggests that the cantilever-hook surface should be smooth in order to reduce the insertion force of a snap fit.

In this example, we assume that the assembly process is relatively slow and can be quasistatically analyzed. The adaptive MLM can be extended to solve dynamic problems, the implementation of which is tedious but straightforward. As in the static problem, additional nodes can be added to the contact location. However, for sliding, the added nodes in the previous contact location are removed once the contact moves to a new location; the removal of these nodes helps improve the efficiency. Thus, for solving the dynamic problem, the adaptive MLM requires tracking the added nodes in each time step, checking if the contact moves to the new location in the new time step, and if so removing the added nodes in the previous time step.

Example 4: Contact simulation of needle insertion. Flexible medical devices (such as needles and catheters for inserting into

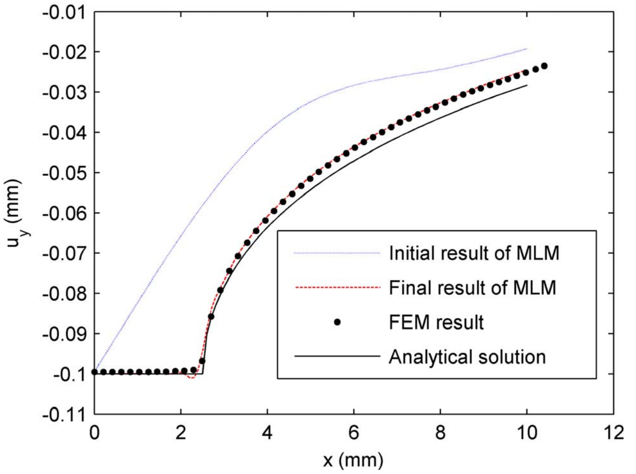

Fig. 11 Comparison between MLM, FEM, and analytical result

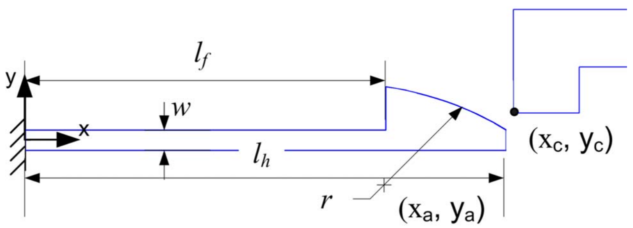

Fig. 12 Geometry of a snap-fit mechanism

Table 3 Simulation parameters of snap-fit mechanism

Parameters	Values	Numerical 2D model
Young's modulus (Pa)	2.62*E*9	Plane stress (thickness of 10 mm)
Poisson's ratio	0.4	ANSYS with 3282 nodes
Thickness w (mm)	3.2	Element type: Plane2,
l_f (mm)	57	Contact175, Target169
l_h (mm)	76	MLM
Radius r (mm)	50	Number of nodes: 169 (initial)
x_a, y_a (mm)	49.9, −41.0	180−200 (after two adaptive
y_c (mm)	2.6	computations)

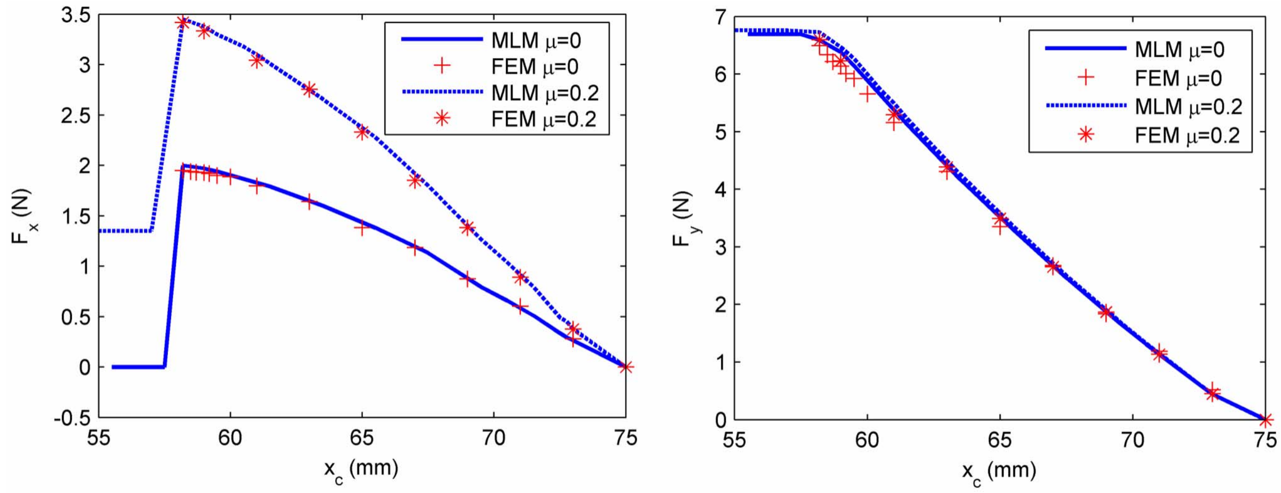

a) x direction force b) y direction force

Fig. 13 Contact forces

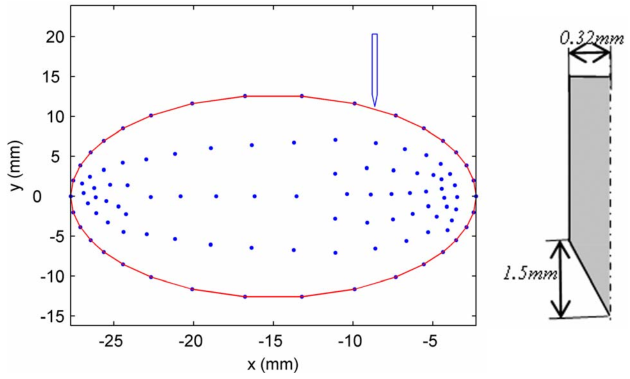

Fig. 14 Initial geometry and node distribution (deformable body: Young's modulus $E=1\times10^6$ Pa; Poisson's ratio $\mu=0.4$)

Table 4 Contact force

Location of needle tip(mm)	9.99	9.74	9.49	9.24
Contact force (N)	24.2	31.1	36.5	42.6

human or animal bodies to perform different procedures) are notoriously difficult to model as the devices and/or the targets are highly deformable. Design for manufacturing of these devices has been relied on empirical techniques. This example illustrates an application of MLM as an attractive means for analyzing a design.

Subcutaneous insertion of needles is one of the most common procedures employed in modern clinical practice. Applications of these procedures include the biopsy of deep-seated, prostate brachytherapy, and neurosurgical probe insertion, which are usually without visual feedback from below the skin's surface. Maximum force and stresses generally occur at the contact point before the needle penetrates the surface. As demonstrated in this example, the adaptive MLM can computationally provide efficient detailed information at the contact region between the surgery tool and tissues for applications in the medical surgery simulation. Specifically, we simulate here a needle contacting an elliptical elastic body. The material properties and initial geometry of the deformable body, along with the initial node distribution of the MLM, are shown in Fig. 14. No special refinement has been made around the contact region for initial node distribution. The needle vertically moves downward from its initial position. The contact at the tip of the needle is computed for four locations starting from the location at 9.99 mm and then increasing at an interval of 0.25 mm.

At the initial or first contact position, four adaptive computations are performed. The converged results for the initial node distribution and the three subsequent adaptive computations are shown in Figs. 15(*a*)–15(*d*). Figure 15(*a*) shows that computation with a small number of initial nodes cannot reveal the detailed deformation at the contact location. With more nodes used around the contact region, a small shape change can be seen at that location from Fig. 15(*d*). The corresponding contact forces of the four computations at the initial position are shown in Fig. 15(*e*). The convergence can be observed from the fact that the difference between the contact forces from two computations becomes smaller as the adaptive procedure proceeds.

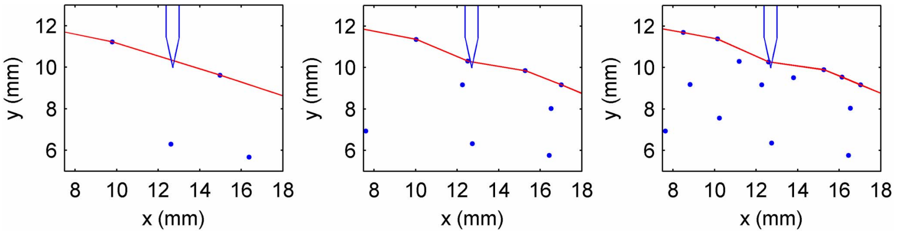

(a) Initial (b) After 1st computation (c)After 2nd computation

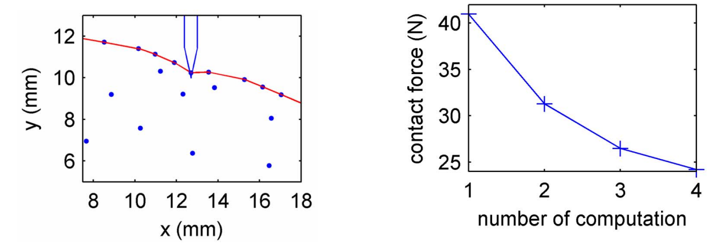

(d) After 3rd adaptive computation (e) Contact force

Fig. 15 Result after each adaptive computation at the first position

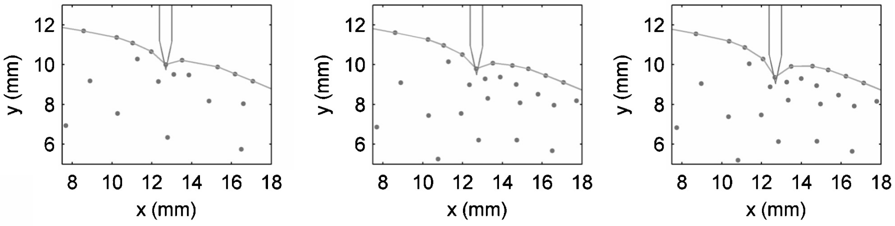

(a) 2nd position (b) 3rd position (c) 4th position

Fig. 16 Results of MLM simulation

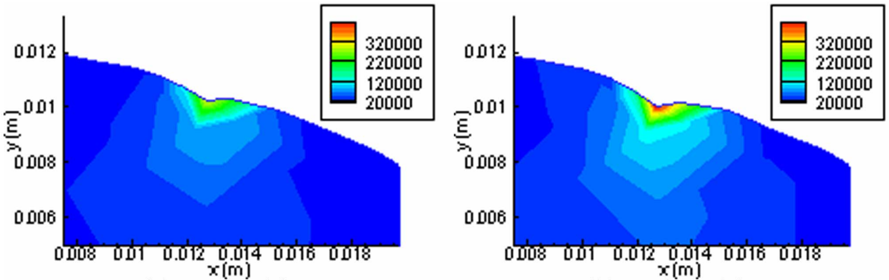

(a) 1st position (b) 2nd position

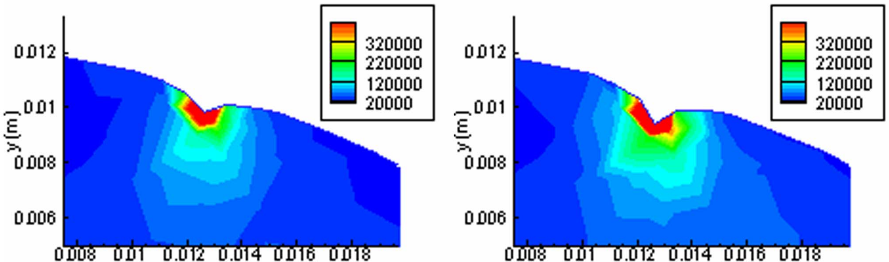

(c) 3rd position (d) 4th position

Fig. 17 Equivalent stress distribution (N/m^2)

By inheriting the nodes added from the first position, three additional adaptive computations are performed at the second position. No significant improvement was observed between these computations, indicating that the node density is sufficiently large. The deformed geometry and the node distributions at the other three positions (9.24×10^{-3}) are plotted in Figs. 16(*a*)–16(*c*). The final results of the contact force at the four locations are listed in Table 4. The contact force increases as the needle moves downward.

Figures 17(*a*)–17(*d*) show the equivalent stress distribution around the contact region for each of the needle positions. As expected, the magnitude of stress increases as the needle moves from Position 1 to Position 4, and its maximum occurs at the contact location. The stress information, which serves as the criterion for material failure in the theory of fracture mechanics, provides a means to judge when the penetration happens.

5 Conclusions

An adaptive MLM method for solving large deformation and mechanical contact problems has been presented. This method, utilizing sliding line and penalty methods for handling contact constraint, has been validated for two different situations; namely, large deformation and contact. Four practical examples have been illustrated. Simulation results show that the adaptive MLM algorithm can effectively identify regions of large computational errors, progressively add nodes accordingly. As demonstrated by using intermediate results, the overall error is reduced as the adaptive procedure proceeds. These illustrative examples also demonstrate that the adaptive MLM has potentials in automated handing of deformable bodies (such as food products) as well as the manufacture of compliant devices (such as medical needles, optic fibers, and catheters) for inserting into the human body.

The adaptive MLM presented in this paper is applicable to other problems, which may have different boundary conditions (for example, mechanical contact between two deformable objects); additional examples can be found in Ref. [33]. For a 2D contact problem, the adaptive MLM can be effectively formulated with a surface mesh. For 3D problems with extremely large deformation, a 3D surface or volume mesh may be employed; this will be considered in the future research.

Acknowledgment

This project is jointly funded by Georgia Agriculture Technology Research Program and the US Poultry and Eggs Association.

Appendix

The stress matrix is symmetric and can thus be written as

$$\begin{bmatrix} \boldsymbol{\sigma}_{11} & \boldsymbol{\sigma}_{12} & \boldsymbol{\sigma}_{13} \\ \boldsymbol{\sigma}_{12} & \boldsymbol{\sigma}_{22} & \boldsymbol{\sigma}_{23} \\ \boldsymbol{\sigma}_{13} & \boldsymbol{\sigma}_{23} & \boldsymbol{\sigma}_{33} \end{bmatrix} \tag{A1}$$

The stress matrix has real eigenvalues $(\lambda_1, \lambda_2, \lambda_3)$, which can be solved from its characteristic equation

$$\begin{vmatrix} \boldsymbol{\sigma}_{11} - \lambda & \boldsymbol{\sigma}_{12} & \boldsymbol{\sigma}_{13} \\ \boldsymbol{\sigma}_{12} & \boldsymbol{\sigma}_{22} - \lambda & \boldsymbol{\sigma}_{23} \\ \boldsymbol{\sigma}_{13} & \boldsymbol{\sigma}_{23} & \boldsymbol{\sigma}_{33} - \lambda \end{vmatrix} = 0 \tag{A2}$$

which leads to

$$\lambda_1 + \lambda_2 + \lambda_3 = \boldsymbol{\sigma}_{11} + \boldsymbol{\sigma}_{22} + \boldsymbol{\sigma}_{33} = \sum_{i=1}^{3} \boldsymbol{\sigma}_{ii} \tag{A3}$$

and

$$\lambda_1\lambda_2 + \lambda_2\lambda_3 + \lambda_3\lambda_1 = \sum_{i=1}^{3} \sum_{j=1}^{3} \kappa_{ij}(\boldsymbol{\sigma}_{ij}^2 - \boldsymbol{\sigma}_{ii}\boldsymbol{\sigma}_{jj}) \tag{A4}$$

Since

$$T_{in} = \sum_{i=1}^{3} \lambda_i^2 = (\lambda_1 + \lambda_2 + \lambda_3)^2 - 2(\lambda_1\lambda_2 + \lambda_2\lambda_3 + \lambda_3\lambda_1) \tag{A5}$$

with Eqs. (A3) and (A4), we have

$$T_{in} = \left[\sum_{i=1}^{3} \boldsymbol{\sigma}_{ii} \right]^2 + 2 \sum_{i=1}^{3} \sum_{j=1}^{3} \kappa_{ij} (\boldsymbol{\sigma}_{ij}{}^2 - \boldsymbol{\sigma}_{ii} \boldsymbol{\sigma}_{jj}) \tag{A6}$$

References

[1] Lee, K. M., Joni, J., and Yin, X., 2001, "Compliant Grasping Force Modeling for Handling of Live Objects," *ICRA2001*, Seoul, South Korea, pp. 1059–1064.

[2] Xiong, C.-H., Wang, M. Y., Tang, Y., and Xiong, Y.-L., 2005, "Compliant Grasping With Passive Forces," J. Rob. Syst., **22**, pp. 271–285.

[3] Lan, C.-C., and Lee, K.-M., "An Analytical Method for Design of Compliant Grippers With Macro/Micro Manipulation and Assembly Applications," *AIM2005*, Monterey, CA, pp. 1023–1028.

[4] Okamura, A. M., Simone, C., and O'Leary, M. D., 2004, "Force Modeling For Needle Insertion Into Soft Tissue," IEEE Trans. Biomed. Eng., **51**, pp. 1707–1716.

[5] Simo, J. C., and Laursen, T. A., 1992, "An Augmented Lagrangian Treatment Of Contact Problems Involving Friction," Comput. Struct., **42**, pp. 97–116.

[6] Wriggers, P., Vu Van, T., and Stein, E., 1990, "Finite Element Formulation of Large Deformation Impact-contact Problems With Friction," Comput. Struct., **37**, pp. 319–331.

[7] Wriggers, P., Scherf, P., and Carstensen, C., 1995, "An Adaptive Finite Element Model for Frictionless Contact Problems," Z. Angew. Math. Mech., **75**, pp. 37–40.

[8] Adelaide, L., Jourdan, F., and Bohatier, C., 2003, "Frictional Contact Solver and Mesh Adaptation in Space-Time Finite Element Method," Eur. J. Mech. A/Solids, **22**, pp. 633–647.

[9] Rieger, A., and Wriggers, P., 2001, "Adaptive Methods for Frictionless Contact Problems," Comput. Struct., **79**, pp. 2197–2208.

[10] Hu, G., and Wriggers, P., 2002, "On the Adaptive Finite Element Method Of Steady-state Rolling Contact for Hyperelasticity in Finite Deformations," Comput. Methods Appl. Mech. Eng., **191**, pp. 1333–1348.

[11] Wriggers, P., and Scherf, O., 1998, "Adaptive Finite Element Techniques for Frictional Contact Problems Involving Large Elastic Strains," Comput. Methods Appl. Mech. Eng., **151**, pp. 593–603.

[12] Bessette, G. C., Becker, E. B., Taylor, L. M., and Littlefield, D. L., 2003, "Modeling of Impact Problems Using an h-Adaptive, Explicit Lagrangian Finite Element Method in Three Dimensions," Comput. Methods Appl. Mech. Eng., **192**, pp. 1649–1679.

[13] Flores, F. G., 2006, "A Two-Dimensional Linear Assumed Strain Triangular Element for Finite Deformation Analysis," ASME J. Appl. Mech., **73**(6), pp. 970–976.

[14] Pedersen, P., 2006, "A Direct Analysis of Elastic Contact Using Super Elements," Comput. Mech., **37**(3), pp. 221–231.

[15] Yang, B., and Laursen, T. A., 2006, "A Contact Searching Algorithm Including Bounding Volume Trees Applied to Finite Sliding Mortar Formulations," Comput. Mech., **41**(2), pp. 189–205.

[16] Belytschko, T., Krongauz, Y., Organ, D., Fleming, M., and Krysl, P., 1996, "Meshless Methods: An Overview and Recent Developments," Comput. Methods Appl. Mech. Eng., **139**, pp. 3–47.

[17] Babuska, I., and Melenk, J. M., 1997, "The Partition of Unity Method," Int. J. Numer. Methods Eng., **40**, pp. 727–758.

[18] Duarte, C. A., and Oden, J. T., 1996, "h-p Adaptive Method Using Clouds," Comput. Methods Appl. Mech. Eng., **139**, pp. 237–262.

[19] Park, S.-H., Kwon, K.-C., and Youn, S.-K., 2003, "A Posteriori Error Estimates and an Adaptive Scheme of Least-Squares Meshfree Method," Int. J. Numer. Methods Eng., **58**, pp. 1213–1250.

[20] Rossi, R., and Alves, M. K., 2005, "An h-Adaptive Modified Element-Free Galerkin Method," Eur. J. Mech. A/Solids, **24**, pp. 782–799.

[21] Rabczuk, T., and Belytschko, T., 2005, "Adaptivity for Structured Meshfree Particle Methods in 2D And 3D," Int. J. Numer. Methods Eng., **63**, pp. 1559–1582.

[22] Tabarraei, A., and Sukumar, N., 2005, "Adaptive Computations on Conforming Quadtree Meshes," Finite Elem. Anal. Design, **41**, pp. 686–702.

[23] Chen, J.-S., Wu, C.-T., Yoon, S., and You, Y., 2001, "Stabilized Conforming Nodal Integration for Galerkin Mesh-free Methods," Int. J. Numer. Methods Eng., **50**, pp. 435–466.

[24] You, Y., Chen, J. S., and Lu, H., 2003, "Filters, Reproducing Kernel, and Adaptive Meshfree Method," Comput. Mech., **31**, pp. 316–326.

[25] Hallquist, J. O., 1978, "A Numerical Treatment of Sliding Interfaces and Impact," *Computational Techniques for Interface Problems*, ASME, New York, pp. 117–133.

[26] Zienkiewicz, O. C., and Zhu, J. Z., 1992, "Superconvergent Patch Recovery and A Posteriori Error Estimates. Part Error Estimates And Adaptivity," Int. J. Numer. Methods Eng., **33**, pp. 1365–1382.

[27] Zienkiewicz, O. C., and Zhu, J. Z., 1992, "Superconvergent Patch Recovery and A Posteriori Error Estimates. Part The Recovery Technique," Int. J. Numer. Methods Eng., **33**, pp. 1331–1364.

[28] Ferro Carpinteri, A. G., and Ventura, G., 2002, "The Partition of Unity Quadrature in Meshless Methods," Int. J. Numer. Methods Eng., **54**, pp. 987–1006.

[29] Malvern, L. E., 1969, *Introduction to the Mechanics Of A Continuous Medium*, Prentice-Hall, Englewood Cliffs, N.J..

[30] Liu, W. K., Jun, S., and Zhang, Y. F., 1995, "Reproducing Kernel Particle Methods," Int. J. Numer. Methods Fluids, **20**, pp. 1081–1106.

[31] Barber, C. B., Dobkin, D. P., and Huhdanpaa, H., 1996, "The Quickhull Algorithm for Convex Hulls," ACM Trans. Math. Softw., **22**, pp. 469–483.

[32] Johnson, K. L., 1985, *Contact Mechanics*, Cambridge University Press, Cambridge.

[33] Li, Q., 2007, "Effects of Adaptive Discretization on Numerical Computation Using Meshless Method With Live-Object Handling Applications," Ph.D. thesis, Georgia Institute of Technology, Atlanta.

The Dynamic Compressive Response of Open-Cell Foam Impregnated With a Newtonian Fluid

M. A. Dawson
e-mail: dawson@mit.edu

G. H. McKinley

Department of Mechanical Engineering,
Massachusetts Institute of Technology,
Cambridge, MA 02139

L. J. Gibson
Department of Materials Science
and Engineering,
Massachusetts Institute of Technology,
Cambridge, MA 02139

This analysis considers the flow of a highly viscous Newtonian fluid in a reticulated, elastomeric foam undergoing dynamic compression. A comprehensive model for the additional contribution of viscous Newtonian flow to the dynamic response of a reticulated, fluid-filled, elastomeric foam under dynamic loading is developed. For highly viscous Newtonian fluids, the flow in the reticulated foam is assumed to be dominated by viscous forces for nearly all achievable strain rates; Darcy's law is assumed to govern the flow. The model is applicable for strains up to the densified strain for all grades of low-density, open-cell, elastomeric foam. Low-density, reticulated foam is known to deform linear elastically and uniformly up to the elastic buckling strain. For strains greater than the elastic buckling strain but less than the densified strain, the foam exhibits bimodal behavior with both linear-elastic and densified regimes. The model presented in this analysis is applicable for all strains up to the densified strain. In the bimodal regime, the model is developed by formulating a boundary value problem for the appropriate Laplace problem that is obtained directly from Darcy's law. The resulting analytical model is more tractable than previous models. The model is compared with experimental results for the stress-strain response of low-density polyurethane foam filled with glycerol under dynamic compression. The model describes the data for foam grades varying from 70 ppi to 90 ppi and strain rates varying from 2.5×10^{-3} to 10^{1} s^{-1} well. The full model can also be well approximated by a simpler model, based on the lubrication approximation, which is applicable to analyses where the dimension of the foam in the direction of fluid flow (radial) is much greater than the dimension of the foam in the direction of loading (axial). The boundary value model is found to rapidly converge to the lubrication model in the limit of increasing aspect ratio given by the ratio of the radius R, to the height h, of the foam specimen with negligible error for aspect ratios greater than $R/h \sim 4$. [DOI: 10.1115/1.2912940]

Keywords: boundary value problem, fluid-structure interaction, foam, lubrication approximation, porous media

1 Introduction

Over the past century, much of the research in developing armor has focused on providing protection against ballistics. This research has culminated in highly advanced armor for defending against projectiles [1]; however, existing armor is inefficient at protecting against the enormous pressure gradients generated by explosive devices. These blast waves can cause severe damage to the human body as well as vehicles and structures. Recently, a novel reactive armor design to mitigate the effects of blast waves has been explored [2]. This design incorporates open-cell (reticulated) foams filled with shear thickening, non-Newtonian liquids into existing composite armor. Open-cell foams filled with non-Newtonian liquids have the potential to absorb energy and impede shock waves, which decrease the resulting pressure gradient experienced by underlying media (e.g., tissue). As a first step in modeling this nonlinear phenomenon, we analyze the flow of a Newtonian fluid through an open-cell, elastomeric foam. The flow of fluids through open-cell foams has been investigated extensively for a variety of engineering applications, but characterizing the contribution of the fluid to energy absorption under dynamic loading is still a critical area of research. Previous research has resulted in the development of complex models to describe the contribution of Newtonian fluids in an open-cell foam under impact loading. Hilyard [3] provided one of the first and only in-depth analytical and experimental analyses of the contribution of fluid flow to the impact behavior of open-cell foams, developing a third order, nonlinear equation of motion. Rehkopf, et al. [4], Mills and Lyn [5], and Schraad and Harlow [6] all developed finite difference and finite volume techniques to analyze the contribution of the fluid flow in an open-cell foam under dynamic loading. However, the inherent complexity of these models has limited their use.

In this paper, we develop a tractable but comprehensive analytical model for the additional contribution of viscous Newtonian flow to the stress-strain response of low-density, reticulated, fluid-filled, elastomeric foams under dynamic loading. Elastomeric foams deform in a linear-elastic manner, primarily by cell wall bending at strains below the elastic buckling strain. At strains between the elastic buckling strain and the densified strain, local bands of cells collapse, so that the foam has both a linear-elastic regime and a densified regime. As the overall strain increases, the densified regime expands at the expense of the linear-elastic regime [7]. We consider a model, which governs both the single regime and the bimodal regime of the fluid-filled foam. The prob-

---

Contributed by the Applied Mechanics Division of ASME for publication in the JOURNAL OF APPLIED MECHANICS. Manuscript received May 18, 2007; final manuscript received February 14, 2008; published online May 14, 2008. Review conducted by Nesreen Ghaddar.

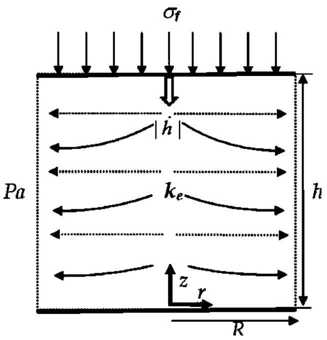

Fig. 1 One-regime model of fluid-filled cylindrical foam with strain less than the elastic buckling strain, $\varepsilon < \varepsilon^*_{\mathrm{el}}$. Velocity of fluid (solid arrow). Relative velocity of fluid with respect to the velocity of foam (dotted arrow).

lem considers the axial compression of a cylindrical specimen of low-density, elastomeric foam filled with a highly viscous Newtonian fluid between a fixed plate and a moving plate (Figs. 1 and 2). Based on the low values of the characteristic Reynolds number in the pores, the flow of viscous Newtonian fluids in porous media is dominated by viscous forces for nearly all achievable strain rates; therefore, Darcy's law is assumed to govern the flow. Darcy's law is selected instead of the slightly more complicated Brinkman–Darcy model, which incorporates both a viscous contribution and an additional term, attributed primarily to the inertial forces dominant in the high Reynold's number regime (Dawson et al. [7]). For the more complex bimodal regime problem, Darcy's law is used to formulate a boundary value problem with Laplace's equation as the governing differential equation. The solution to Laplace's equation in cylindrical coordinates for the pressure distribution in the fluid is formulated in terms of an infinite series of Bessel functions. The solution rapidly converges within the first few terms and is readily evaluated numerically. The pressure distribution is used to find a model for the contribution of the fluid to the stress-strain response of the fluid-filled foam.

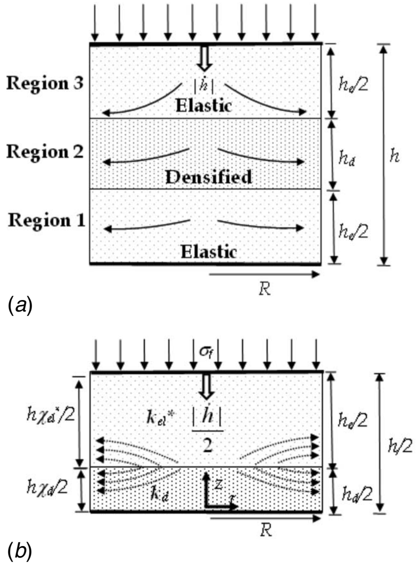

Fig. 2 (*a*) Bimodal regime model of fluid-filled cylindrical foam compressed beyond elastic buckling strain, $\varepsilon^*_{\mathrm{el}} < \varepsilon < \varepsilon_d$. Velocity of fluid. (solid arrow) (*b*). Top symmetric half of bimodal regime model of fluid-filled cylindrical foam compressed beyond elastic buckling strain, $\varepsilon^*_{\mathrm{el}} < \varepsilon < \varepsilon_d$, in the reference frame of the densified regime. Relative velocity of fluid with respect to the velocity of foam (dotted arrow).

The model is analytically tractable and applicable for strains up to the densified strain for all grades of low-density, flexible, open-cell foam. We also develop a more simple model based on the lubrication approximation to approximate the more comprehensive boundary value model in the limit where the characteristic dimension in the direction of fluid flow (radial) is assumed to be much greater than that in the direction of loading (axial). The rapid convergence of the boundary value model toward the lubrication, as the aspect ratio is increased, is discussed. The model is also compared with experimental results of the stress-strain response of low-density polyurethane foam filled with glycerol under dynamic loading. The model gives a good description of the experimental results for foam grades varying from 70 ppi to 90 ppi and for strain rates varying from 2.5×10^{-3} to 10^1 s^{-1}. The model in this paper is not compared to previous models found in literature because comparable models with the ability to characterize the stress response necessitate extensive computational effort and would require dedicating a large portion of the paper to simply review the models and their applicability.

2 Literature Review

2.1 Stress-Strain Response of Foam. Gibson and Ashby [8] previously developed a model for the compressive stress-strain response of reticulated foam, neglecting any contribution of a viscous fluid. The governing equations are given by [8]

$$\sigma^* = \varepsilon E^*, \quad 0 < \varepsilon < \varepsilon^*_{\mathrm{el}} \tag{1}$$

$$\sigma^* = \sigma^*_{\mathrm{el}}, \quad \varepsilon^*_{\mathrm{el}} < \varepsilon < \varepsilon_D\left(1 - \frac{1}{D}\right) + \varepsilon^*_{\mathrm{el}} \tag{2}$$

$$\sigma^* = \frac{\sigma^*_{\mathrm{el}}}{D}\left(\frac{\varepsilon_D}{\varepsilon_D - \varepsilon}\right)^m, \quad \varepsilon > \varepsilon_D\left(1 - \frac{1}{D}\right) + \varepsilon^*_{\mathrm{el}} \tag{3}$$

where $\sigma^\star$ is the average, uniform stress response of the foam or the axial compressive force divided by the cross-sectional area of the foam, $E^\star$ is the effective modulus of the foam, ε is the strain, taken to be positive in compression and given by the compression deformation of the foam over the initial height of the foam, $\varepsilon^*_{\mathrm{el}}$ is the elastic buckling strain, σ^*_{el} is the elastic buckling stress, and m and D are constants associated with the microstructure of the foam. For polyurethane foams, Gibson and Ashby [8] gave the constant m as unity. The fully densified strain ε_D is the strain at which point the cells have collapsed sufficiently that opposing cell walls touch and further deformation compresses the cell wall material itself. The densified strain is given by

$$\varepsilon_D = 1 - 1.4\left(\frac{\rho^*_0}{\rho_s}\right) \tag{4}$$

where ρ^*_0 is the initial density of the foam at zero strain, and ρ_s is the density of the solid from which the foam is made. The constant D is given by

$$D = \frac{\varepsilon_D}{\varepsilon_D - \varepsilon^*_p} \tag{5}$$

where the strain ε^*_p corresponds to the strain at which the stress at the end of the plateau region begins to exceed the elastic buckling stress.

2.2 Microstructural Behavior of Foam Under Deformation. We utilize the model for the microstructural behavior of low-density, reticulated foam under compressive strain presented by Dawson et al. [7]. The cells of the foam under compressive strain remain elastic up to the linear-elastic buckling strain (Fig. 1). As the foam is compressed beyond the elastic buckling strain, cells buckle and collapse without laterally expanding so that Poisson's ratio in this regime is approximately zero. These collapsed regions generate local bands of large deformation in which the average diameter of the cells is reduced substantially. The strain of the collapsed cells in these densified bands is assumed to be uniform and given by the densified strain ε_d, while the cells outside the densified bands remain in the linear elastic regime, at strains given by the elastic buckling strain (Fig. 2). Therefore, for strains less than the elastic buckling strain, the entire specimen is assumed to be uniform and completely within the linear-elastic regime, which results in a single regime problem. For strains greater than the elastic buckling strain but less than the densified strain, the foam is assumed to be a two-regime problem with both a linear-elastic region and a densified region (Fig. 2). Dawson et al. [7] used visual imaging to establish the value of the densified strain $\varepsilon_d=0.6$, for low-density, reticulated polyurethane foam. It is important to distinguish the densified strain ε_d from the fully densified strain ε_D given by Eq. (4), where the former effectively represents the onset of the densification regime, and the latter effectively represents the end of the densification regime.

At any given strain, the volume fractions of the cells remaining in the linear-elastic regime χ^*_{el} and the densified regime χ_d are given by [7]

$$\chi^*_{\text{el}}=\frac{(\varepsilon_d-\varepsilon)(1+\varepsilon^*_{\text{el}})}{(1+\varepsilon)(\varepsilon_d-\varepsilon^*_{\text{el}})} \tag{6}$$

$$\chi_d=\frac{(\varepsilon-\varepsilon^*_{\text{el}})(1+\varepsilon_d)}{(1+\varepsilon)(\varepsilon_d-\varepsilon^*_{\text{el}})} \tag{7}$$

After the densified strain is exceeded, cells begin to densify further, and this model is no longer applicable. Based on this model, Dawson et al. developed equations for the local permeability of open-cell foams in the linear-elastic regime, k_e, at the elastic buckling strain, k^*_{el}, and at the densified strain, k_d, which are given by [7]

$$k_e=Ad_0^2(1-\varepsilon)\left(1-\frac{\rho^*_0}{\rho_s}\frac{1}{(1-\varepsilon)}\right)^3 \quad \text{for } 0\le\varepsilon\le\varepsilon^*_{\text{el}} \tag{8}$$

$$k^*_{\text{el}}=Ad_0^2(1-\varepsilon^*_{\text{el}})\left(1-\frac{\rho^*_0}{\rho_s}\frac{1}{(1-\varepsilon^*_{\text{el}})}\right)^3 \quad \text{for } \varepsilon=\varepsilon^*_{\text{el}} \tag{9}$$

$$k_d=Ad_0^2(1-\varepsilon_d)^{2a}\left(1-\frac{\rho^*_0}{\rho_s}\frac{1}{(1-\varepsilon_d)}\right)^3 \quad \text{for } \varepsilon=\varepsilon_d \tag{10}$$

where d_0 is the average pore diameter at zero strain, and A is an empirical constant given by Brace [9] as 0.025 for a porous microstructure consisting of tubes with circular cross sections. The material properties of the foam, ρ^*_0, ρ_s, and d_0, are readily available and typically specified by the manufacturer. Dawson et al. [7] also found that these models are independent of the fluid flow direction with respect to the compression direction of the foam.

2.3 Flow in Porous Media. The flow of highly viscous Newtonian fluids in low-density, open-cell foam with small cell sizes (typically less than 500 μm) is dominated by viscous forces for nearly all achievable strain rates. Therefore, the model presented in this paper only considers flows in which the viscous effects dominate the inertial effects. The Reynolds number Re, a measure of the inertial forces to the viscous forces, can be used to determine where this model is applicable. A characteristic pore Reynolds number based on the average diameter of a pore, d, and average velocity through that pore, v, is given by

$$\text{Re}=\frac{\rho v d}{\mu} \tag{11}$$

where ρ is the density of the fluid and μ is the viscosity of the fluid. Based on an analytical study, Comiti et al. [10] proposed a transition from the viscous dominated regime to the inertial dominated regime at a critical pore Reynolds number of $\text{Re}^*=0.83$ for flow through low-density, porous media. This corresponds well with the experimental findings of Gent and Rusch [11] for flow through reticulated foam, Tek [12] for flow through porous rock, and Dybbs and Edwards [13] for flow through fixed beds of spheres and cylinders. Therefore, the model presented in this analysis is taken to be applicable for $\text{Re}\ll 1$ when viscous forces dominate. Based on a transition number of $\text{Re}\approx 1$, the maximum strain rate for which this analysis accurately models the flow of a highly viscous fluid in an open-cell foam can be determined. The experimental results presented below consist of a dynamic compression glycerol-filled, reticulated foam with an approximate radius and average cell diameter of 12.7 mm and 235 μm, respectively. At 23°C, the density and viscosity of glycerol are taken to be $\rho=1260\ \text{kg/m}^3$ and $\mu=1.1$ Pa s, respectively. The maximum strain rate for which the flow will remain in the viscous regime is found to be approximately 600 s^{-1}. The maximum strain rate of the foam specimens in the experiments presented is 10 s^{-1}, which thus lies well within the viscous dominated regime.

3 Analysis

3.1 Fluid Contribution to the Stress-Strain Response. A comprehensive model for the contribution of the fluid to the stress-strain response of fluid-filled, elastomeric foam under dynamic compression can be developed by extending the model presented by Dawson et al. [7]. We consider the case of axial compression of a cylindrical foam specimen where the lower plate is fixed and the upper plate is moving with the magnitude of the velocity given by $|\dot{h}|$, or the time rate of change of the height of the foam specimen, as shown in Figs. 1 and 2(*a*). The initial height and radius of the specimen are taken to be h_0 and R. As the foam undergoes compression, the radius of the specimen remains unchanged while the current height is given as $h(t)$. This analysis considers both the response at strains less than the elastic buckling strain and the response at strains greater than the elastic buckling strain but less than the densified strain. For strains less than the elastic buckling strain, the entire specimen is assumed to be uniform and completely within the linear-elastic regime, which results in a single regime problem (Fig. 1). For strains greater than the elastic buckling strain but less than the densified strain, the foam is assumed to coexist in two states with both a linear-elastic regime and a densified regime (Figs. 2(*a*) and 2(*b*)).

3.2 Single Regime Model $\boldsymbol{\varepsilon<\varepsilon^*_{\text{el}}}$. We first consider the single regime problem with strain less than the elastic buckling strain. As the upper plate compresses the foam, the foam is assumed to deform uniformly. The relative velocity of the fluid with respect to the foam in the compression direction (z-direction) is taken to be zero throughout the foam. Any nonzero relative velocity in the z-direction would require flow up a pressure gradient in the radial direction, which violates Darcy's law. Therefore, neglecting gravitational effects, the pressure gradient throughout the foam in the z-direction is taken to be zero. Thus, the radial velocity of the fluid in the linear-elastic regime V_e is uniform in the z-direction and given as (after Gibson and Ashby [8])

$$V_e=\frac{-\dot{h}r}{2h\Phi}, \quad 0\le\varepsilon\le\varepsilon^*_{\text{el}} \tag{12}$$

where Φ is the porosity of the foam, r is the radial distance, and h is the current height of the foam specimen, given by $h(t)=h_0(1-\varepsilon)$. According to Darcy's law, the gradient of the pressure across the specimen $\partial P/\partial r$ for viscous Newtonian flow in the r-direction is given as [14]

$$\frac{\partial P}{\partial r} = \frac{-\mu V_e}{k_e}, \quad 0 \leq \varepsilon \leq \varepsilon^*_{\mathrm{el}} \tag{13}$$

where μ is the dynamic viscosity of the fluid and the linear-elastic permeability k_e is taken to be isotropic. Combining Eqs. (12) and (13) and integrating give

$$P^* = \frac{\mu \dot{h}}{4\Phi h k_e}(r^2 - R^2), \quad 0 \leq \varepsilon \leq \varepsilon^*_{\mathrm{el}} \tag{14}$$

where P^* is the local pressure minus the atmospheric pressure at the free surface of the foam. Neglecting inertial effects, a force balance can be used to find an equivalent average uniform stress distribution σ_f applied by the fluid to the top compression plate by integrating the pressure field over the radius giving

$$\sigma_f \pi R^2 = \int_0^R P^*|_h 2\pi r dr, \quad 0 \leq \varepsilon \leq \varepsilon^*_{\mathrm{el}} \tag{15a}$$

$$\sigma_f = \frac{-\mu \dot{h} R^2}{8\Phi h k_e}, \quad 0 \leq \varepsilon \leq \varepsilon^*_{\mathrm{el}} \tag{15b}$$

3.3 Bimodal Regime Model $\varepsilon^*_{\mathrm{el}} < \varepsilon < \varepsilon_d$. For strains beyond the elastic buckling strain but less than the densified strain, the cells of the foam are assumed to be either at the elastic buckling strain or at the densified strain, corresponding to the bimodal regime model previously discussed. The resulting pressure distribution in both regimes is more complex than in the single regime problem and can be solved by means of coupling two boundary value problems. In formulating the boundary conditions for this problem, a model for the behavior of the foam must be developed. Under axial compression, densified bands are commonly observed to initiate in the center of the sample. Our model assumes that the densified regime initiates in the center of the foam and symmetrically propagates toward the plates through the elastic buckling of one layer of foam (of roughly one cell thickness) at a time, as shown in Fig. 2(a). The foam in the elastic regime below the densified regime (Region 1) is stationary while the foam in the elastic regime above the densified regime (Region 3) is moving downward with the upper plate at velocity $|\dot{h}|$, as shown in Fig. 2(a). Therefore, the densified regime (Region 2) is moving downward at velocity $\frac{1}{2}|\dot{h}|$. In the reference frame of the densified regime of the foam, the problem can be viewed as a completely symmetric problem with the elastic regimes (Regions 1 and 3) of the foam moving toward the densified regime, in opposite directions, at a speed of $\frac{1}{2}|\dot{h}|$. Since there is no flow across the center of the densified regime by symmetry, we analyze only the top half of the foam in the reference frame of the densified regime, as shown in Fig. 2(b). The problem is analyzed as two one-regime models with local reference heights $\frac{1}{2}h_e$ and $\frac{1}{2}h_d$ for the elastic and densified regimes, respectively, given as (Fig. 2)

$$h_e = \chi^*_{\mathrm{el}} h \tag{16}$$

$$h_d = \chi_d h \tag{17}$$

The boundary conditions at the foam-plate interfaces are no flux conditions since the relative velocity of the fluid with respect to the foam is zero. Therefore, according to Darcy's law, the corresponding pressure gradients in the z-direction are zero at both foam-plate interfaces. Boundary conditions applied at the interface between the two regimes are given. The pressure field is taken to be continuous between the two regimes with a discontinuity in the pressure gradient, corresponding to the change in the permeability. In addition, a mass flux corresponding to the fluid exiting the layer undergoing elastic buckling enters both the linear-elastic and the densified regimes at the interface between the two regimes. Since the surface area between the layer undergoing elastic buckling and the linear-elastic and densified regimes is much greater than the surface area of the buckling layer at the free surface of the foam, we assume all of the fluid exiting the layer undergoing elastic buckling flows vertically into either the elastic or the densified regimes and neglect the radial flow in the buckling layer out of the foam. The boundary conditions for the two-regime problem are given as

$$P^*_d = P^*_e = 0 \quad \text{on} \quad r = R \tag{18a}$$

$$\frac{\partial P^*_d}{\partial z} = 0 \quad \text{on} \quad z = 0 \tag{18b}$$

$$\frac{\partial P^*_e}{\partial z} = 0 \quad \text{on} \quad z = \tfrac{1}{2}h \tag{18c}$$

$$\frac{\partial P^*_d}{\partial z} = \frac{-(1-\alpha)\mu\dot{h}}{2k_d} \quad \text{on} \quad z = \tfrac{1}{2}h_d \tag{18d}$$

$$\frac{\partial P^*_e}{\partial z} = \frac{\alpha\mu\dot{h}}{2k^*_{\mathrm{el}}} \quad \text{on} \quad z = \tfrac{1}{2}h_d \tag{18e}$$

$$P^*_d = P^*_e \quad \text{on} \quad z = \tfrac{1}{2}h_d \tag{18f}$$

where α, determined below, is a constant representing the fraction of the flux into the linear-elastic regime, P^*_e is the pressure in the linear-elastic regime, and P^*_d is the pressure in the densified regime.

As before, Darcy's law is assumed to govern the flow of a viscous Newtonian fluid throughout each regime of the foam and is given as [14]

$$\nabla P^* = \frac{-\mu V}{k} \tag{19}$$

where V is the relative velocity of the fluid with respect to the foam, and k is the local permeability, which is assumed to be isotropic. Taking the gradient of both sides of Eq. (19), applying continuity for an incompressible Newtonian fluid, and considering there is no variation in the velocity of the foam within each region give Laplace's equation

$$\nabla^2 P^* = \frac{\partial^2 P^*}{\partial r^2} + \frac{1}{r}\frac{\partial P^*}{\partial r} + \frac{1}{r^2}\frac{\partial^2 P^*}{\partial \theta^2} + \frac{\partial^2 P^*}{\partial z^2} = \frac{-\mu \nabla \cdot V}{k} = 0 \tag{20}$$

A well known method of solving Laplace's equation in cylindrical coordinates is separation of variables. We assume the pressure is not a function of the circumferential direction (θ-direction) and propose a solution in the form

$$P^* = R(r)Z(z) \tag{21}$$

Substituting Eq. (21) into Eq. (20) and dividing through by $R(r)Z(z)$ give

$$\frac{1}{R(r)}\frac{\partial^2 R(r)}{\partial r^2} + \frac{1}{rR(r)}\frac{\partial R(r)}{\partial r} + \frac{1}{Z(z)}\frac{\partial^2 Z(z)}{\partial z^2} = 0 \tag{22}$$

Since the first two terms are functions of r only and the last term is a function of z only, Eq. (22) can be broken up into the following two equations:

$$\frac{1}{Z(z)}\frac{d^2 Z(z)}{dz^2} = -\eta \tag{23}$$

$$\frac{1}{R(r)}\frac{d^2R(r)}{dr^2}+\frac{1}{rR(r)}\frac{dR(r)}{dr}=\eta \tag{24}$$

where η is a constant. Equation (23) is a standard second order differential equation, which is readily solved. Equation (24) is one form of Bessel's equation and solutions can be expressed in terms of Bessel functions. Combining these solutions, the solution to Laplace's equation for the pressure distribution in either regime of the foam is given as

$$P_i^* = \sum_{n=1}^{\infty} (A_{ni}e^{k_n z}+B_{ni}e^{-k_n z})J_0(k_n r) \tag{25}$$

where the index i represents either the elastic regime or the densified regime with indices e and d, respectively, A_{ni}, B_{ni}, and k_n are constants, and J_0 is a zero order Bessel function of the first kind.

Applying both the Neumann and Dirichlet boundary conditions in Eqs. (18*a*)–(18*f*) to the solution to Laplace's equation given in Eq. (25), the pressure distribution throughout the foam can be determined. It is recognized that each term in Eq. (25) will satisfy the free surface boundary condition given by Eq. (18*a*) if

$$J_0(k_n R)=0 \tag{26}$$

Equation (26) therefore gives the values of k_n, corresponding to the zeros of the zero order Bessel function. The values can be determined from a table of Bessel functions. Typically, these solutions converge very quickly, so we assume that only the first five terms of the infinite series are necessary for most values of h/R. The corresponding values of k_n are given as

$$k_1=\frac{2.405}{R}, \quad k_2=\frac{5.520}{R}, \quad k_3=\frac{8.645}{R}, \quad k_4=\frac{11.792}{R}, \tag{27}$$

$$k_5=\frac{14.931}{R}$$

To solve for the unknowns A_{ni} and B_{ni}, the following orthogonality principle of zero order Bessel functions is utilized:

$$\int_0^R rJ_0(k_n r)J_0(k_m r)dr=0 \quad \text{for } n\neq m \tag{28}$$

where $J_0(k_n r)$ is orthogonal to $J_0(k_m r)$. Applying the boundary conditions given by Eqs. (18*b*)–(18*e*) to Eq. (25), multiplying each side by r times a zero order Bessel function, and integrating allow for each coefficients A_{ni} and B_{ni} to be determined by the following set of equations:

$$(A_{nd}k_n - B_{nd}k_n)\int_0^R rJ_0^2(k_n r)dr=0 \tag{29}$$

$$(A_{ne}k_n e^{(1/2)k_n h} - B_{ne}k_n e^{-(1/2)k_n h})\int_0^R rJ_0^2(k_n r)dr=0 \tag{30}$$

$$(A_{nd}k_n e^{(1/2)k_n h_d} - B_{nd}k_n e^{-(1/2)k_n h_d})\int_0^R rJ_0^2(k_n r)dr$$

$$=\frac{-(1-\alpha)\mu\dot{h}}{2k_d}\int_0^R rJ_0(k_n r)dr \tag{31}$$

$$(A_{ne}k_n e^{(1/2)k_n h_d} - B_{ne}k_n e^{-(1/2)k_n h_d})\int_0^R rJ_0^2(k_n r)dr$$

$$=\frac{\alpha\mu\dot{h}}{2k_{\text{el}}^*}\int_0^R rJ_0(k_n r)dr \tag{32}$$

Solving Eqs. (29)–(32) gives the coefficients A_{ni} and B_{ni} as

$$A_{nd}=\frac{-(1-\alpha)\mu\dot{h}RJ_1(k_nR)}{2k_d(k_nR)^2\sinh\left(\frac{1}{2}k_nh_d\right)[J_0^2(k_nR)+J_1^2(k_nR)]} \tag{33}$$

$$A_{ne}=\frac{\alpha\mu\dot{h}RJ_1(k_nR)}{k_{\text{el}}^*(k_nR)^2(1-e^{k_nh_e})[J_0^2(k_nR)+J_1^2(k_nR)]} \tag{34}$$

$$B_{nd}=\frac{-(1-\alpha)\mu\dot{h}RJ_1(k_nR)}{2k_d(k_nR)^2\sinh\left(\frac{1}{2}k_nh_d\right)[J_0^2(k_nR)+J_1^2(k_nR)]} \tag{35}$$

$$B_{ne}=\frac{\alpha\mu\dot{h}RJ_1(k_nR)e^{k_nh_e}}{k_{\text{el}}^*(k_nR)^2(1-e^{k_nh_e})[J_0^2(k_nR)+J_1^2(k_nR)]} \tag{36}$$

where $J_1(k_nR)$ is a first order Bessel function. Substituting Eqs. (33)–(36) into Eq. (25) and applying Eq. (26) give the adjusted pressure distribution in both the densified regime and the elastic regime as

$$P_d^*=\sum_{n=1}^{\infty}\frac{-(1-\alpha)\mu\dot{h}R\cosh(k_nz)J_0(k_nr)}{k_d(k_nR)^2\sinh\left(\frac{1}{2}k_nh_d\right)J_1(k_nR)}, \tag{37}$$

$$\varepsilon_{\text{el}}^*\leqslant\varepsilon\leqslant\varepsilon_d, \quad 0\leqslant z\leqslant\tfrac{1}{2}h_d$$

$$P_e^*=\sum_{n=1}^{\infty}\frac{\alpha\mu\dot{h}R(e^{k_n(z-(1/2)h_d)}+e^{k_n(h_e-z+(1/2)h_d)})J_0(k_nr)}{k_{\text{el}}^*(k_nR)^2(1-e^{k_nh_e})J_1(k_nR)}, \tag{38}$$

$$\varepsilon_{\text{el}}^*\leqslant\varepsilon\leqslant\varepsilon_d, \quad \tfrac{1}{2}h_d\leqslant z\leqslant\tfrac{1}{2}h$$

Applying the remaining boundary condition in Eq. (18*f*), the constant α can be determined numerically. Since the terms of the pressure distribution given in Eqs. (37) and Eq. (38) decay rapidly, a good approximation to α can be given using only the first term in the series

$$\alpha=\frac{k_{\text{el}}^*\tanh\left(\frac{1}{2}k_1h_e\right)}{k_{\text{el}}^*\tanh\left(\frac{1}{2}k_1h_e\right)+k_d\tanh\left(\frac{1}{2}k_1h_d\right)} \tag{39}$$

The fraction of the flux into the linear-elastic regime α, as a function of strain, is given in Fig. 3. A force balance can be used to find an equivalent uniform stress distribution σ_f, applied to the top compression plate by integrating the pressure field in the elastic regime at $z=\frac{1}{2}h$ over the radius as follows:

$$\sigma_f\pi R^2=\int_0^R P_e^*|_{h/2}2\pi r dr, \quad \varepsilon_{\text{el}}^*\leqslant\varepsilon\leqslant\varepsilon_d \tag{40a}$$

$$\sigma_f\pi R^2=\left(\sum_{n=1}^{\infty}\frac{2\pi\alpha\mu\dot{h}R(2e^{k_n((1/2)h_e)})}{k_{\text{el}}^*(k_nR)^2(1-e^{k_nh_e})J_1(k_nR)}\right)\left(\int_0^R rJ_0(k_nr)dr\right), \tag{40b}$$

$$\varepsilon_{\text{el}}^*\leqslant\varepsilon\leqslant\varepsilon_d$$

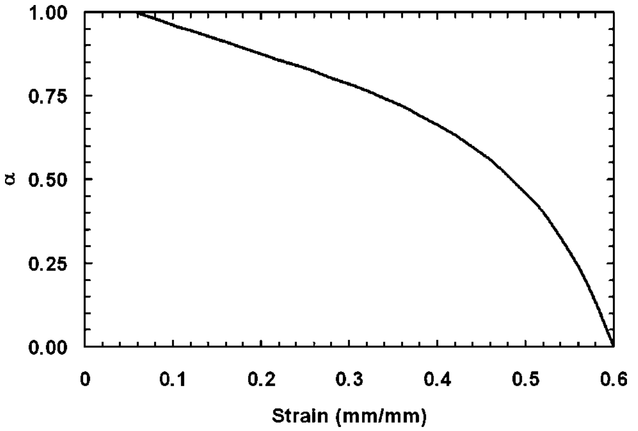

Fig. 3 The fraction of the flux into the linear-elastic regime (α) as a function of strain in the bimodal model

$$\sigma_f R^2 = \sum_{n=1}^{\infty} \left(\frac{4\alpha\mu\dot{h}R}{k_{\mathrm{el}}^{*}(k_nR)^2(e^{-k_n((1/2)h_e)} - e^{k_n((1/2)h_e)})J_1(k_nR)} \right) \times \left(\frac{R^2 J_1(k_nR)}{(k_nR)} \right), \quad \varepsilon_{\mathrm{el}}^{*} \leqslant \varepsilon \leqslant \varepsilon_d \tag{40c}$$

$$\sigma_f = \frac{-2\alpha\mu\dot{h}R}{k_{\mathrm{el}}^{*}} \sum_{n=1}^{\infty} \frac{1}{(k_nR)^3 \sinh\left(\frac{1}{2}k_nh_e\right)}, \quad \varepsilon_{\mathrm{el}}^{*} \leqslant \varepsilon \leqslant \varepsilon_d \tag{40d}$$

Equation (40*d*) is taken to be the contribution of the fluid to the stress-strain response of foam filled with a Newtonian fluid under dynamic compression in the two-regime model. The dependence of the response given by Eq. (40*d*) on strain is built in through the terms α and h_e, which are functions of the volume fraction of the cells remaining in the linear-elastic and densified regimes, and therefore, are functions of the strain.

3.4 Effect of Tortuous and Anisotropic Foam Microstructure. A discrepancy is typically found between analytical models for flow through porous media and experimental measurements. Models are often adjusted by an empirical constant, which accounts for the tortuous shape of the foam microstructure [15]. Similarly, empirical constants are also used to account for the tortuous microstructure of foam in studies of heat transfer through porous media. Glicksman [16] determined an efficiency factor of 2/3 accounted for the effective loss in the thermal conductivity of porous media. Furthermore, it is known that the permeability of low-density, open-cell foam is slightly anisotropic, which may also lead to deviations of the model presented in this analysis from experimental data. The combination of these effects necessitates the addition of empirical constant C to the model. Therefore, we propose that the stress contribution of a Newtonian fluid to the response of a fluid-filled foam under dynamic loading is given by

$$\sigma_f = \frac{-C\mu\dot{h}R^2}{8\Phi h k_e}, \quad 0 \leqslant \varepsilon \leqslant \varepsilon_{\mathrm{el}}^{*} \tag{41}$$

$$\sigma_f = \frac{-2C\alpha\mu\dot{h}R}{k_{\mathrm{el}}^{*}} \sum_{n=1}^{\infty} \frac{1}{(k_nR)^3 \sinh\left(\frac{1}{2}k_nh_e\right)}, \quad \varepsilon_{\mathrm{el}}^{*} \leqslant \varepsilon \leqslant \varepsilon_d \tag{42}$$

where C is a single constant to be determined by regression from experiments.

3.5 Squeezing Flow Between Parallel Plates. We now proceed to develop a more tractable model for the dynamic response of fluid-filled foam, which can be used to approximate the boundary value model in the lubrication limit where the aspect ratio of the foam is much greater than unity. We first consider a model for squeezing flow between two parallel plates in the absence of an open-cell foam where the lower plate is fixed and the upper plate is moving similar to Fig. 1. The flow is assumed to be incompressible and locally fully developed with no variation in the circumferential direction (θ-direction). The gravitational effects are assumed to be negligible. Since the flow is assumed to be dominated by viscous forces, inertial effects can also be neglected. The following velocity profiles are assumed:

$$V_r = V_r(r,z), \quad V_z = V_z(z), \quad V_\theta = 0 \tag{43}$$

where V_r, V_z, and V_θ are the velocity components in the radial (r), axial (z), and circumferential (θ) directions, respectively. Coupling the equation of continuity with the full Navier–Stokes equations of motion, this problem is readily solved. The equation of continuity and the Navier–Stokes equations of motion in the radial and axial directions reduce to

$$\frac{1}{r}\frac{\partial(rV_r)}{\partial r} + \frac{\partial V_z}{\partial z} = 0 \tag{44}$$

$$\mu\left(\frac{\partial}{\partial r}\frac{1}{r}\frac{\partial}{\partial r}(rV_r) + \frac{\partial^2 V_r}{\partial z^2} \right) - \frac{\partial P}{\partial r} = 0 \quad (r\text{-direction}) \tag{45}$$

$$\mu\left(\frac{1}{r}\frac{\partial}{\partial r}r\frac{\partial V_z}{\partial r} + \frac{\partial^2 V_z}{\partial z^2} \right) - \frac{\partial P}{\partial z} = 0 \quad (z\text{-direction}) \tag{46}$$

where P is the local pressure within the fluid. To solve Eqs. (44)–(46), we initially impose a lubrication approximation in which the square of the ratio of the characteristic dimension in the radial flow direction (R) to that in the axial compression direction (h) is assumed to be much greater than unity, $(R/h)^2 \gg 1$. The resulting equations of motion are given as

$$\mu\left(\frac{\partial^2 V_r}{\partial z^2} \right) - \frac{\partial P}{\partial r} = 0 \quad (r\text{-direction}) \tag{47}$$

$$\frac{\partial P}{\partial z} = 0 \quad (z\text{-direction}) \tag{48}$$

The corresponding boundary conditions are

$$V_r|_{z=h} = 0, \qquad \left.\frac{\partial V_r}{\partial z}\right|_{z=h/2} = 0, \qquad V_z|_{z=0} = 0, \qquad V_z|_{z=h} = \dot{h}, \tag{49}$$

$$P|_{r=R} = P_a$$

where R is the radius of the plates, h is given as the current distance between the bottom plate and the top plate, P_a is the atmospheric pressure on the free surface, and the magnitude of the velocity of the top plate is given by $|\dot{h}|$, where $\dot{h}$ is the time rate of change of the distance between the two plates. Solving Eqs. (47) and (48) gives the pressure profile as

$$P - P_a = \frac{3\mu\dot{h}}{h^3}(r^2 - R^2) \tag{50}$$

The pressure distribution is found to be independent of the z- and θ-directions. We propose that the pressure field given by Eq. (50) for squeezing, viscous flow is similar to the pressure field for squeezing flow in a low-density foam. Therefore, in the lubrication limit, the pressure field for an incompressible, viscous Newtonian flow through a low-density foam is assumed to be independent of the z- and θ-directions.

3.6 Stress-Strain Response in the Lubrication Limit. The model of viscous squeezing flow between two parallel plates described above does not accurately describe the flow field for axial compression of a low-density, reticulated foam filled with a Newtonian fluid because of the nonlinear behavior of the foam under deformation; however, we assume that the pressure field of the parallel plate model is representative of that found in a lubrication model of a fluid-filled foam, such that the pressure field is independent of the z- and θ-directions.

Using this assumption, we extend the model presented by Dawson et al. [7] for reticulated foam under compressive strain. We consider the case of axial compression of a cylindrical foam specimen where the characteristic radius is much greater than the characteristic height. The initial radius and height of the specimen are taken to be R and h_0. As the foam undergoes compression, the radius of the specimen remains unchanged while the instantaneous height is given as $h(t)$. Compression occurs between two plates where the lower plate is assumed to be fixed and the magnitude of the velocity of the upper plate is $|\dot{h}|$, where $\dot{h}$ is the time rate of change of the height of the foam, as shown in Figs. 1 and 2. This analysis considers both the response at strains less than the elastic buckling strain and the response at strains greater than the elastic buckling strain but less than the densified strain. We first consider the single regime problem with strain less than the elastic buckling strain. Following the same methodology as used in Eqs. (12)–(14), the average radial velocity of the fluid, V_e, and the local pressure, P, in the elastic regime can be determined. As before, neglecting inertial effects, a force balance can be used to find an equivalent uniform stress distribution σ_f, applied to the top compression plate by integrating the pressure field given in Eq. (14) over the radius giving

$$\sigma_f = \frac{-\mu \dot{h} R^2}{8\Phi h k_e}, \quad 0 \le \varepsilon \le \varepsilon^*_{\mathrm{el}} \tag{51}$$

For strains beyond the elastic buckling strain but less than the densified strain, the model is taken to be a two-regime model, as shown in Fig. 2. Based on the previous assumptions regarding no axial variations in the pressure field, the pressure drop from the any radius r to the outer radius R is assumed to be the same in both the elastic region and the densified region. Coupling this relation between the pressure drops in each region with Eq. (13) gives

$$\frac{V_e}{k^*_{\mathrm{el}}} = \frac{V_d}{k_d}, \quad \varepsilon^*_{\mathrm{el}} \le \varepsilon \le \varepsilon_d \tag{52}$$

where V_d is the velocity of the fluid at any radius r in the densified region. Using Eq. (52), mass conservation about a cylindrical volume at any given r gives

$$V_e = \frac{-\dot{h} k^*_{\mathrm{el}} r}{2h\Phi(\chi^*_{\mathrm{el}} k^*_{\mathrm{el}} + \chi_d k_d)}, \quad \varepsilon^*_{\mathrm{el}} \le \varepsilon \le \varepsilon_d \tag{53}$$

Coupling Darcy's law with Eq. (53) gives the pressure gradient across the specimen $\partial P/\partial r$ for viscous Newtonian flow [14] as follows:

$$\frac{\partial P}{\partial r} = \frac{\mu \dot{h} r}{2h\Phi(\chi^*_{\mathrm{el}} k^*_{\mathrm{el}} + \chi_d k_d)}, \quad \varepsilon^*_{\mathrm{el}} \le \varepsilon \le \varepsilon_d \tag{54}$$

Integrating Eq. (54) and applying the atmospheric pressure boundary condition at the free surface give

$$P - P_a = \frac{\mu \dot{h}}{4h\Phi(\chi^*_{\mathrm{el}} k^*_{\mathrm{el}} + \chi_d k_d)}(r^2 - R^2), \quad \varepsilon^*_{\mathrm{el}} \le \varepsilon \le \varepsilon_d \tag{55}$$

As before, neglecting inertial effects, a force balance can be used to find an equivalent uniform stress distribution σ_f, applied to the top compression plate by integrating the pressure field over the radius giving

$$\sigma_f \pi R^2 = \int_0^R (P - P_a)|_h 2\pi r dr, \quad \varepsilon^*_{\mathrm{el}} \le \varepsilon \le \varepsilon_d \tag{56a}$$

$$\sigma_f = \frac{-\mu \dot{h} R^2}{8h\Phi(\chi^*_{\mathrm{el}} k^*_{\mathrm{el}} + \chi_d k_d)}, \quad \varepsilon^*_{\mathrm{el}} \le \varepsilon \le \varepsilon_d \tag{56b}$$

Table 1 Table of coefficients for the bimodal model as a function of the aspect ratio of the foam and for the lubrication model, corresponding to Eqs. (57) and (58).

R/h	C_1 (ε=0.05)	C_1 (ε=0.30)	C_1 (ε=0.60)
$\frac{1}{2}$	0.031	0.111	0.827
1	0.057	0.127	0.501
2	0.069	0.132	0.404
4	0.072	0.133	0.378
8	0.073	0.133	0.371
16	0.074	0.133	0.369
32	0.074	0.133	0.368
Lubrication	0.076	0.137	0.380

3.7 Convergence of the Boundary Value Model to the Lubrication Model. In this analysis, we consider the convergence of the boundary value model to the lubrication model in the limit of large R/h. A parametric study is used to compare the model given by Eqs. (41) and (42) for varying ratios of R/h to the lubrication model given by Eqs. (51), (56a), and (56b). The models can be readily compared if each model is rewritten in the following form:

$$\sigma_f = -C_1\left(\frac{\mu \dot{h} R^2}{h k_e}\right), \quad 0 \le \varepsilon \le \varepsilon^*_{\mathrm{el}} \tag{57}$$

$$\sigma_f = -C_1\left(\frac{\mu \dot{h} R^2}{h k^*_{\mathrm{el}}}\right), \quad \varepsilon^*_{\mathrm{el}} \le \varepsilon \le \varepsilon_d \tag{58}$$

where C_1 is the dimensionless coefficient corresponding to the numerically evaluated portion of each model, including the empirically derived coefficient C, which will be determined in Sec. 4. For strains less than the elastic buckling strain, the coefficient C_1 for the model presented in this paper is independent of the aspect ratio of the specimen. Therefore, for strains less than the elastic buckling strain, the model presented in this analysis is identical to that presented in the lubrication analysis for all aspect ratios of the foam, so there is no difference in the coefficients C_1, for the lubrication and boundary value models in this regime. However, for strains less than the densified strain but greater than the elastic buckling strain, the coefficient C_1 for the model presented in this paper is a function of the aspect ratio of the foam and the strain while that for the lubrication model is only a function of strain. Therefore, the convergence of this bimodal model toward the lubrication model with increasing aspect ratio is presented for three different strains in Table 1. To determine the coefficient C_1 for both the bimodal model presented in this analysis and the lubrication model, the necessary parameters are numerically evaluated based on the data presented in this analysis. The permeability of the foam at the densified strain is taken to be 20% of that of the foam at the elastic buckling strain, k_d=0.20k^*_{el}, the elastic buckling strain is taken to be $\varepsilon^*_{\mathrm{el}}$=0.05, the densified strain is taken to be ε_d=0.60, and the porosity is taken to be Φ=0.97 (after Dawson et al. [7]).

4 Experiments

4.1 Materials. Specimens of open-cell, flexible, polyester-based polyurethane foams (New Dimension Industries, Moonachie, NJ), with nominal cell diameters of 175 μm, 210 μm, and

235 μm based on manufacturers' specifications (corresponding to grades of 90 ppi, 80 ppi, and 70 ppi, respectively, were used in the tests. The densities of the foams ranged from $0.0318\ \mathrm{g/cm^3}$ to $0.0322\ \mathrm{g/cm^3}$. Based on the manufacturer's value of the density of the solid polyurethane ($\rho_s = 1.078\ \mathrm{g/cm^3}$) the relative density of the foams was taken to be $\rho_0^*/\rho_s \cong 0.03$. Using Eq. (4), the corresponding fully densified strain is determined to be $\varepsilon_D = 0.958$. The foam was cut into uniform cylindrical specimens with diameter and height, $D = 25.4$ mm and $h = 12.8$ mm, respectively. The dimensions of each sample were measured using a digital caliper accurate to within 0.01 mm. The Newtonian fluid used in these experiments is glycerol where the density and viscosity are measured to be $\rho = 1260\ \mathrm{kg/m^3}$ and $\mu = 1.1$ Pa/s at 23°C.

4.2 Experimental Procedure. Prior to testing, each sample was saturated with glycerol. Since the viscosity of glycerol is a strong function of temperature, it was heated to 40°C before saturation to aid in the saturation process. Samples were compressed by machine, submerged in glycerol, and uncompressed at 1 mm/s. Hager and Craig [17] demonstrated that the indentation force deflection loss (a measure of the load bearing capability of flexible polyurethane foam) of polyurethane foam compressed to 0.75 strain for a short duration of time is almost completely recoverable. Therefore, a compressive strain of 0.75 was selected for saturating the sample to minimize the microstructural damage caused by the filling process. After saturation, the fluid-filled foam was brought to a steady temperature of 23°C and allowed to recover. Based on the data for the recovery of low-density polyurethane foam after 0.75 compression presented by Hager and Craig [17], a recovery time of 2 h was selected.

The compressive stress-strain response of each glycerol-filled specimen was measured with the rise direction of the foam parallel to the direction of loading, from 0 to 0.60 strain over a range of strain rates from $\dot{\varepsilon} = 2.5 \times 10^{-3}\ \mathrm{s^{-1}}$ to $10^1\ \mathrm{s^{-1}}$. For strain rates of $\dot{\varepsilon} = 1\ \mathrm{s^{-1}}$ or less, a texture analyzer (TA XT Plus, Stable Microsystems, Hamilton, MA) was used at a constant strain rate; for strain rates greater than $\dot{\varepsilon} = 1\ \mathrm{s^{-1}}$, an Instron testing machine (Instron Model 1321, Instron Corp., Canton, MA) was used at constant velocity. During testing, the temperature was maintained at 23.0 ± 0.1°C to ensure that the glycerol retains a constant viscosity. Since the flow is assumed to be instantaneously fully developed, the model presented in this paper is applicable to both constant velocity and constant strain rate loading.

4.3 Experimental Results. A typical plot of the stress-strain response of the 90 ppi foam filled with glycerol loaded at a constant strain rate of $\dot{\varepsilon} = 0.01\ \mathrm{s^{-1}}$ is shown in Fig. 4. This strain rate is assumed to most accurately represent quasistatic loading where the loading is slow enough that the fluid is not expected to significantly contribute to the response of the specimen yet fast enough that viscoelastic effects in the foam are negligible. Using Fig. 4, the parameters and constants governing the response of the foam structure, given by Eqs. (1)–(5), can be determined. A detailed discussion of the microstructural behavior of open-cell foam under compressive loading in the direction of the rise direction of the foam is given by Gong and Kyriakides [18]. They discussed the complex local and global buckling behavior of low-density, open-cell foam. We consider a simplified model for the elastic buckling strain $\varepsilon_{\mathrm{el}}^*$, taken to be the average value of the strain at which the behavior of the foam begins to deviate from the linear-elastic regime and the strain corresponding to the peak stress prior to the plateau region, as shown in Fig. 4. The elastic buckling stress σ_{el}^* is taken to be the stress at the elastic buckling strain $\varepsilon_{\mathrm{el}}^*$. As previously discussed, ε_p^* corresponds to the strain at which the stress at the end of the plateau region is equal to the elastic buckling stress, as shown in Fig. 4. The values for the elastic buckling strain $\varepsilon_{\mathrm{el}}^*$, the strain at which the stress at the end of the plateau stress is equal to the elastic buckling stress, and the corresponding constant are provided for grades of 70 ppi, 80 ppi, and 90 ppi foams in Table 2. The final unknown parameter in the model for the response of the foam structure given by Eqs. (1)–(5) is the effective modulus. The effective modulus of the foam is found to depend strongly on the strain rate due to viscoelastic effects in the quasistatic loading regime and microinertial effects and localization phenomenon in the high rate loading regime. The effective modulus used in Eq. (1) for each grade of foam is found to be well approximated by $E^* = X \ln(\dot{\varepsilon}/\dot{\varepsilon}_0) + Y$ over the strain rates presented in this analysis where $\dot{\varepsilon}$ is taken to be $\dot{\varepsilon} = 1\ \mathrm{s^{-1}}$ and the constants X and Y are provided in Table 2. The elastic buckling strains correspond well with previous literature on low-density foams [8]. To plot the fluid model, the permeabilities at the elastic buckling strain and at the densified strain are required. These values are obtained using the equations for the local permeability and the corresponding intrinsic permeability at zero strain k_0. It has been observed that large strain compression causes microstructural damage to low-density foam, altering the permeability at zero strain [19]. Therefore, the permeability at zero strain for each specimen was measured after the specimens were subjected to the compressive filling technique used for saturating the foam with glycerol. The permeability was measured using the technique given by Dawson et al. [7]. Table 3 provides the measured permeability at zero strain and the corresponding permeabilities utilized in modeling the stress-strain response.

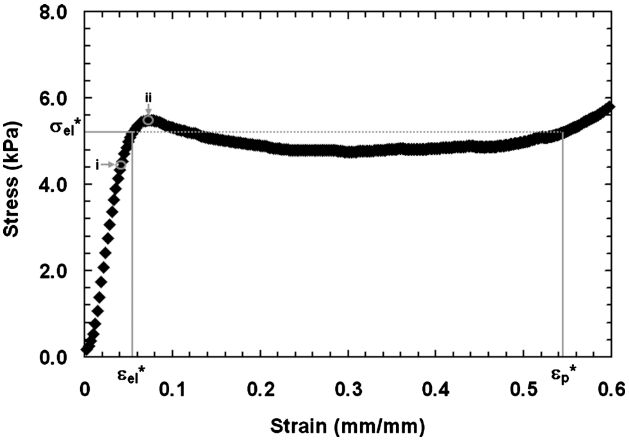

Fig. 4 Stress-strain response of the 90 ppi foam under a quasistatic load rate of $\dot{\varepsilon} = 1 \times 10^{-2}\ \mathrm{s^{-1}}$. (i) Strain corresponding to deviation from linear-elastic regime. (ii) Strain corresponding to peak stress before the plateau region.

A typical plot of the stress-strain response for the 70 ppi foam filled with glycerol loaded at a constant strain rate of $\dot{\varepsilon} = 1.0\ \mathrm{s^{-1}}$ is given in Fig. 5. The actual response of the fluid-filled foam is plotted along with the model for the total contribution to the stress-strain response, which results from the combination of the solid contribution given by Eqs. (1)–(3) and the fluid contribution given by Eqs. (41) and (42). The solid and fluid contributions are also given separately to demonstrate their relative contributions.

To fit the constant C given in Eqs. (41) and (42), a measure of

Table 2 Static parameters and constants. The elastic buckling strain $\varepsilon_{\mathrm{el}}^*$, the strain at which the stress begins to exceed the plateau stress ε_p^*, and the constants X, Y, and D (Eq. (5))

Foam grade (ppi)	$\varepsilon_{\mathrm{el}}^*$	ε_p^*	X (Pa)	Y (Pa)	D
70	0.058	0.55	$1.07E+04$	$1.35E+05$	2.3
80	0.049	0.54	$1.28E+04$	$1.70E+05$	2.3
90	0.057	0.55	$1.09E+04$	$1.42E+05$	2.3

Table 3 Permeability data for precompressed foam. The permeability at zero strain k_0, for each grade of foam, is given after being subjected to the saturation process. The permeabilities at the elastic buckling strain and densified strain are determined using the equations supplied in Eqs. (8)–(10)

Foam grade (ppi)	k_0 $(1\times10^{-9}\ \mathrm{m}^2)$	k^*_{el} $(1\times10^{-9}\ \mathrm{m}^2)$	k_d $(1\times10^{-9}\ \mathrm{m}^2)$
70	5.82	5.45	1.28
80	5.21	4.93	1.04
90	4.68	4.39	0.85

the goodness of fit is established. The measure for the goodness of fit R^2 is taken to be the sum of the squares of the difference between the experimental values and the average experimental value divided by the sum of the squares of the difference between the experimental values and the predicted values. This measure of the goodness of fit was maximized, over the sample of experimental data discussed in the following sections, to establish the empirical constant.

In Fig. 6, we show the stress response of the 70 ppi foam filled with glycerol at $\varepsilon=0.60$ strain, corresponding to an aspect ratio of 2.5, plotted against the strain rate. Each data point is the average of three experiments with error bars corresponding to 1 standard deviation. The error bars for most data points are not apparent since they are smaller than the size of the data points. The fluid and solid contributions of the stress, given by Eqs. (2), (3), and (42), respectively, are plotted separately showing their relative contributions. In Fig. 7, we show the stress at $\varepsilon=0.30$ strain and $\varepsilon=0.60$ strain, corresponding to aspect ratios of 1.4 and 2.5, respectively, for all three grades of reticulated foam filled with glycerol plotted against the strain rate. Each data point is again the average of three experiments with error bars corresponding to 1 standard deviation. The total contribution to the stress-strain response, which results from the combination of the solid contribution given by Eqs. (2) and (3) and the fluid contribution given by Eq. (42), is also shown in Fig. 7.

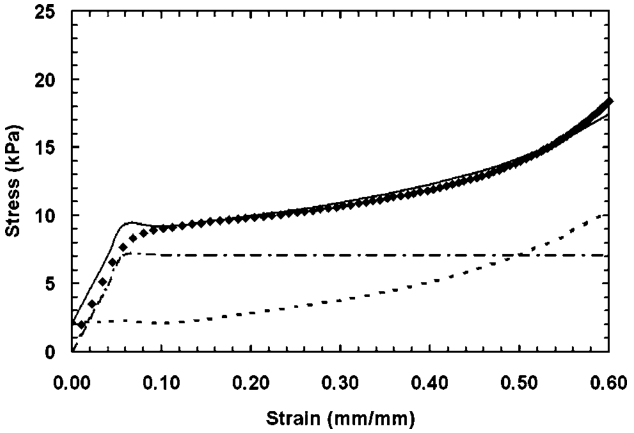

Fig. 5 Stress plotted against strain for 70 ppi foam. Experimental data (◆). Contribution to the stress response of fluid model given by Eqs. (41) and (42) (---), the solid model given by Eqs. (1) and (3) (–·–), and the total model (—).

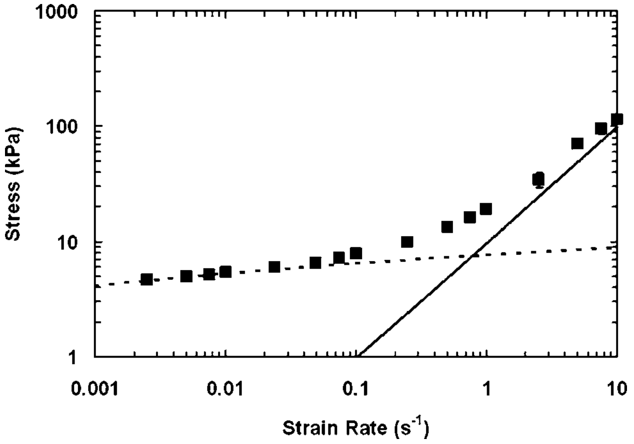

Fig. 6 Stress plotted against strain rate for 70 ppi foam at $\varepsilon=0.60$. Experimental data (■), the contribution to the stress response of fluid model given by Eqs. (41) and (42) (—) and solid model given by Eqs. (1) and (3) (---).

All of the data used to generate the plots in Fig. 7 are used to determine the empirical constant C. Using each data point along the 0.3 and 0.6 strain curves, which consist of the average of three experimental points, for all three foam grades, the empirical constant is determined to be $C=0.59$. Based on the data in Fig. 7, the R^2 values for each grade of foam at both $\varepsilon=0.30$ and $\varepsilon=0.60$ are given in Table 4; it is clear that the model describes the data well up to the densified strain for a range of foam grades and strain rates, as shown in Fig. 7. The empirical constant C, which primarily accounts for the tortuous and anisotropic microstructure of the foam, is independent of all of the parameters considered in this analysis. Figure 7 supports this initial assumption, demonstrating that C is independent of the cell size of low-density foam, the aspect ratio of the foam, the strain imposed on the foam, and the strain rate applied to the foam. Additional experimental studies, not presented here, that vary the aspect ratio of the foam also support this proposal. Using $C=0.59$, the model given by Eq. (42) accurately describes the data for fluid-filled foam samples over several orders of magnitude of strain rate with an aspect ratio of approximately 10 at $\varepsilon=0.60$.

5 Discussion

A boundary value model for the contribution of viscous Newtonian fluid flow to the stress-strain response of a fluid-filled foam under dynamic compression is given by Eqs. (41) and (42). The model governing viscous flow in the bimodal regime of the foam is given in the form of an infinite series of Bessel functions. As expected, this solution converges rapidly with an increasing number of terms, such that the boundary value model is readily evaluated numerically with only the first few terms. Based on the permeability studies of Dawson et al. [7], the models presented in this analysis are taken to be applicable for all grades of low-density foam and independent of whether the orientation of the rise direction of the foam is perpendicular or parallel to the direction of fluid flow. As previously discussed, the models in this analysis assume that the flow is dominated by viscous forces, which is shown to be the case for nearly all achievable strain rates. The boundary value model further assumes an instantaneous change in the velocity field of the foam at the elastic buckling strain $\varepsilon^*_{\mathrm{el}}$, which is the strain at which the model transitions from the single regime to the bimodal regime. The transition behavior between these two regimes is neglected, which results in a small discontinuity in the stress response of the boundary value model. However, as the aspect ratio of the foam R/h is increased, the effect of the assumed velocity field of the foam becomes negligible, and the boundary value model rapidly approaches a continuous solution. In addition, with increasing R/h, the bimodal model becomes independent of the location of the densified bands of the foam.

The boundary value model presented in this analysis is found to describe the experimental results presented in this paper for foam grades varying from 70 ppi to 90 ppi and strain rates varying from $\dot{\varepsilon}=2.5\times10^{-3}\ \mathrm{s}^{-1}$ to $10^1\ \mathrm{s}^{-1}$ well. All of the strain rates in these experiments satisfy the viscous flow requirements of the

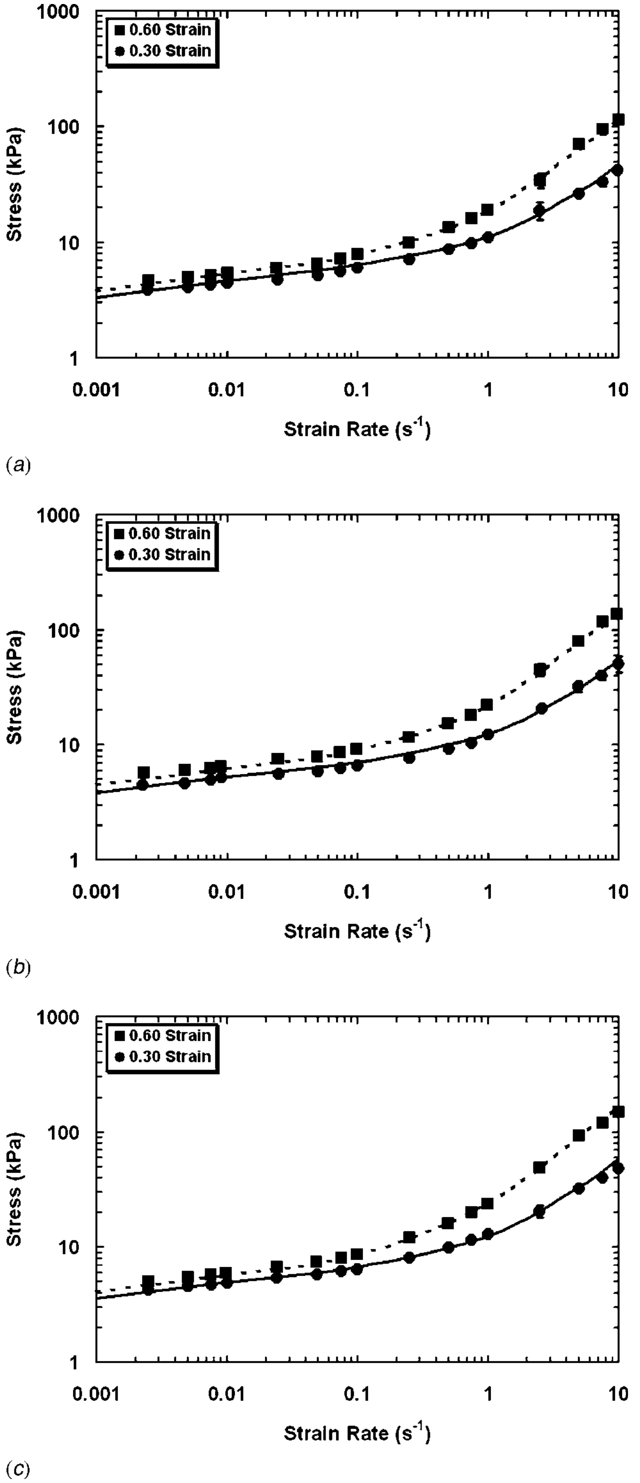

Fig. 7 (*a*) **Stress plotted against strain rate for 70 ppi foam. Experimental data at 0.60 strain (■), and 0.30 strain (●), respectively. Model given by combining Eqs. (2) and (3) with Eq. (42) at $\varepsilon=0.30$ (—) and $\varepsilon=0.60$ (---).** (*b*) **Stress plotted against strain rate for 80 ppi foam. Experimental data at 0.60 strain (■), and 0.30 strain (●), respectively. Model given by combining Eqs. (2) and (3) with Eq. (42) at $\varepsilon=0.30$ (—) and $\varepsilon=0.60$ (---).** (*c*) **Stress plotted against strain rate for 90 ppi foam. Experimental data at 0.60 strain (■), and 0.30 strain (●), respectively. Model given by combining Eqs. (2) and (3) with Eq. (42) at $\varepsilon=0.30$ (—) and $\varepsilon=0.60$ (---).**

Table 4 The measure for the goodness of fit of the boundary value model at 0.30 and 0.60 strains for each grade of foam

Foam grade (ppi)	R^2	
	0.30 strain	0.60 strain
70	0.97	0.99
80	0.99	0.99
90	0.95	0.99

models with $\mathrm{Re}<1$. The maximum Reynolds number in the experiments was found to be $\mathrm{Re}=0.017$, which corresponds to strain rate of $\dot{\varepsilon}=10\ \mathrm{s}^{-1}$ in a 70 ppi foam with an average cell diameter of 235 μm.

Figure 5 shows the individual contributions of both the solid model and the boundary value fluid model to the model of the total stress-strain response of the 70 ppi fluid-filled foam. The total model fits the data well over the entire range of interest, slightly overestimating the response at low strains. The previously discussed discontinuity in the models near the buckling strain is evident but shown to be negligible. Furthermore, Figs. 6 and 7 demonstrate that the boundary value model is representative of the actual response of the fluid-filled foam at both $\varepsilon=0.30$ and $\varepsilon=0.60$ for a range of foam grades and strain rates. The standard deviations of nearly all of the data are observed to be very small, on the order of the size of the data point. Overall, the goodness of fit measure given in Table 4 demonstrates that the boundary value model fits the data well for all grades of foam at both $\varepsilon=0.30$ and $\varepsilon=0.60$ for the range of strain rates considered. The boundary value model also fits the data well over all strains less than the densified strain, but the strains of $\varepsilon=0.30$ and $\varepsilon=0.60$ were selected as representative strains. The empirical constant $C=0.59$ primarily accounts for the tortuous and anisotropic microstructure of the foam and is found to be similar to the efficiency factor of 2/3 found by Glicksman [16] in his study of the thermal conductivity of porous media. Furthermore, the empirical constant is proposed to be independent of all of the parameters considered in this analysis. Figure 7 supports this proposal demonstrating that C is independent of the cell size of low-density foam, the aspect ratio of the foam, the strain of the foam, and the strain rate of the foam.

While the boundary value model is readily evaluated and compared with experimental results, extending it to a more advanced study of dynamic loading of non-Newtonian fluid-filled foam is challenging. However, this model is useful in validating the applicability of the more tractable lubrication model, which assumes the radius of the foam is much greater than the height of the foam. The boundary value model is found to converge rapidly to within 5% of the lubrication model for aspect ratios greater than 4 ($R/h>4$). The small discrepancy between the coefficient for the lubrication model and that for the boundary value model may be attributed to the fact that the lubrication model assumes a uniform radial flow, neglects pressure gradients in the z-direction, and neglects the flow in the z-direction; whereas the boundary value model does not make these assumptions.

Table 1 demonstrates that as R/h is increased, the numerical coefficients at $\varepsilon=0.05$ and $\varepsilon=0.30$ strain increase asymptotically while the coefficient at $\varepsilon=0.60$ strain decreases asymptotically. At any given strain, the coefficient C_1 is governed primarily by the following two factors: the aspect ratio of the foam sample and the distance between the collapsing band and the compression plate. For all strains as R/h is decreased, the dependence of the stress, given by Eq. (58), on R/h also decreases. In the limit of very small R/h, the stress contribution of the fluid becomes completely independent of R/h.

At $\varepsilon=0.60$ strain, the stress is independent of the distance between the collapsing band and the compression plate $(1/2h_e)$ since the collapsing band is effectively always at the interface between the compression plate and the foam. Therefore, it is expected that as R/h decreases, the coefficient C_1 would increase proportionally, such that the stress is independent of R/h in the limit of very small R/h. However, at 0.05 and 0.30 strains, the distance between the collapsing band and the compression plate $(1/2h_e)$ is also an important factor, which strongly influences the coefficient C_1. As R/h is decreased, the relative distance between the fluid in the collapsing band and the compression plate $(1/2h_e)$ to that of the fluid in the collapsing band and the free surface $(\sim R)$ increases; therefore, it is expected that the overall stress on the compression plate would decrease. For lower strains, this effect is more pronounced since the band is effectively farther from the compression plate, explaining the phenomenon observed in Table 1.

In the limit that $R/h \gg 1$, the effect of the distance between the collapsing bands and the compression plate is found to be inconsequential for all strains, and the stress becomes independent of the vertical location of the collapsing bands. Table 1 demonstrates that the model presented in this analysis becomes approximately independent of the aspect ratio of the foam for $R/h > 4$. As expected, this indicates that the lubrication model provides a good approximation to the flow for a large range of R/h values. Overall, the convergence of the more comprehensive boundary value model toward the lubrication model strongly supports the lubrication analysis. This is an important finding since the lubrication model is readily extended to more complex analyses, such as the study of the stress-strain response and energy absorption capabilities of a foam filled with a rate-dependent non-Newtonian fluid under dynamic loading.

6 Conclusion

In this paper, a comprehensive boundary value model for the contribution of viscous Newtonian fluid flow to the stress-strain response of a fluid-filled, elastomeric foam under dynamic compression is presented. Experimental results strongly support this model for a variety of foam grades over several orders of magnitude of strain rate. A simple explicit analytic solution based on a lubrication approximation is also presented. The robust boundary value model is found to converge rapidly toward the lubrication model as the aspect ratio of the foam is increased. This validation of the lubrication model is important since it is more readily extended to more complex analyses, such as the dynamic response of foam filled with a non-Newtonian fluid. Furthermore, using a lubrication model, both the Newtonian and non-Newtonian models can be extended to determine the energy absorption capabilities of a fluid-filled foam under dynamic loading, which is critical to the development of composite armor capable of absorbing energy and impeding shock waves.

Acknowledgment

This paper benefited from the insightful assistance provided by Professor Chiang Mei of the Department of Civil and Environmental Engineering, Massachusetts Institute of Technology. This research was performed while on appointment as a National Defense Science and Engineering Graduate Fellow administered by the American Society for Engineering Education (ASEE). This material is based upon work supported by the National Science Foundation under Grant No. 0408259.

Appendix

The velocity profiles in the absence of foam for the analysis in Sec. 3.5 are given as

$$V_r(r,z) = \frac{3\dot{H}r}{H}\left(\left(\frac{z}{H}\right)^2 - \frac{z}{H}\right) \tag{A1}$$

$$V_z(r,z) = 6\dot{H}\left(\frac{1}{2}\left(\frac{z}{H}\right)^2 - \frac{1}{3}\left(\frac{z}{H}\right)^3\right) \tag{A2}$$

References

[1] Cheeseman, B., and Bogetti, T., 2003, "Ballistic Impact Into Fabric and Compliant Composite Laminates," Compos. Struct., **61**, pp. 161–173.

[2] Bettin, G., and McKinley, G. H., 2005, "High Deformation Rate Behavior of Polymeric Foams Filled With Concentrated Silica Suspensions," The Society of Rheology 77th Annual Meeting.

[3] Hilyard, N. C., 1971, "Observations on the Impact Behaviour of Polyurethane Foams; II. The Effect of Fluid Flow," J. Cell. Plast., **7**, pp. 84–90.

[4] Rehkopf, J., Brodland, G., and McNeice, G., 1996, "Experimentally Separating Fluid and Matrix Contributions to Polymeric Foam Behavior," Exp. Mech., **36**, pp. 1–6.

[5] Mills, N., and Lyn, G., 2002, "Modeling Air Flow in Impacted Polyurethane Foam," Cell. Polym., **21**, pp. 343–365.

[6] Schraad, M., and Harlow, F., 2006, "A Multi-Field Approach to Modeling the Dynamic Response of Cellular Materials," Int. J. Mech. Sci., **48**, pp. 85–106.

[7] Dawson, M., Germaine, J., and Gibson, L., 2007, "Permeability of Open-Cell Foams Under Compressive Strain," Int. J. Solids Struct., **44**, pp. 5133–5145.

[8] Gibson, L. J., and Ashby, M. F., 1997, *Cellular Solids—Structures and Properties*, 2nd ed., Cambridge University Press, Cambridge.

[9] Brace, W., 1977, "Permeability From Resistivity and Pore Shape," J. Geophys. Res., **82**, pp. 3343–3349.

[10] Comiti, J., Sabiri, N., and Montillet, A., 2000, "Experimental Characterization of Flow Regimes in Various Porous Media—III: Limit of Darcy's or Creeping Flow Regime for Newtonian and Purely Viscous Non-Newtonian Fluids," Chem. Eng. Sci., **55**, pp. 3057–3061.

[11] Gent, A., and Rusch, K., 1966, "Permeability of Open-Cell Foamed Materials," J. Cell. Plast., **2**, pp. 46–51.

[12] Tek, M., 1957, "Development of a Generalized Darcy Equation," J. Pet. Technol., **9**(6), pp 45–47.

[13] Dybbs, A., and Edwards, R. V., 1984, "A New Look at Porous Media Fluid Mechanics—Darcy to Turbulent," *Fundamentals of Transport Phenomna in Porous Media*, J. Bear and Y. Corapcioglu, eds., Martinus Nishoff, Dordrecht, pp. 199–256.

[14] Darcy, H., 1856, *Les Fontaines Publiques de la Ville de Dijon*, Dalmont, Paris.

[15] Comiti, J., and Renaud, M., 1988, "A New Model for Determining Mean Structure Parameters of Fixed Beds From Pressure Drop Measurements: Applications to Beds Packed With Parallelpipedal Particles," Chem. Eng. Sci., **44**, pp. 1539–1545.

[16] Glicksman, L., 1994, *Heat Transfer in Foams—Low Density Cellular Plastics*, N. C. Hilyard and A. Cunningham, eds., Chapman and Hall, London.

[17] Hager, S. L., and Craig, T. A., 1992, "Fatigue Testing of High Performance Flexible Polyurethane Foam," J. Cell. Plast., **28**, pp. 285–303.

[18] Gong, L., and Kyriakides, S., 2005, "Compressive Response of Open Cell Foams Part II: Initiation and Evolution of Crushing," Int. J. Solids Struct., **42**, pp. 1381–1399.

[19] Hilyard, N., and Collier, P., 1987, "A Structural Model Air Flow in Flexible PUR Foams," Chem. Eng. Sci., **6**, pp. 9–26.

Ratko Pavlović[1]
e-mail: ratko@masfak.ni.ac.yu
e-mail: ratpav@yahoo.com

Predrag Rajković

Ivan Pavlović

Mechanical Engineering Faculty,
A. Medvedeva 14,
18000 Niš, Serbia

Almost Sure Stability of a Moving Elastic Band

In this paper, the stochastic stability problem of a moving elastic band subjected to action in-plane acting forces is investigated. Each force consists of a constant part and a time-dependent zero mean stochastic function. By using the direct Liapunov functional method, almost sure asymptotic stability conditions are obtained as the function of stochastic process variance, damping coefficient, and geometric and physical parameters of the band. Numerical calculations are performed for infinite mode and compared with known results. Almost sure stability regions are shown for infinite and first mode the two-dimensional density probability function, and for higher modes when the edge load Gaussian or harmonic process is known. [DOI: 10.1115/1.2839905]

Keywords: random loading, Liapunov functional, almost sure stability, Gaussian and harmonic process

1 Introduction

A study of the dynamical behavior of continuous moving bands is of practical importance in the design of band saws, conveyer systems, tape recorders, belt drives, etc. As Soler [1] pointed out, the presence of in-plane loads couples the lateral and torsional motions in the system differential equations and in the boundary conditions.

Wang [2] investigated the dynamic stability of the coupled transverse and longitudinal motions of high speed axially moving bands. A nonlinear model with end curvatures is developed and analyzed.

Torsional oscillations and stability conditions of moving bands subjected to harmonic tension fluctuation are studied by Ariaratnam and Asokanthan [3]. Later, the same authors [4] investigated flexural instabilities in moving band under random tension fluctuation. Explicit stability conditions based on the mean square amplitudes are established by employing a stochastic averaging procedure.

The dynamic stability of a coupled lateral and torsional motions of the moving elastic band subjected to random parametric excitations is investigated by Kozin and Milstead [5]. Galerkin's method is used to reduce the equations of motions in *n*th mode, which leads to restrictive results because in each equation three terms disappear.

Uniform stochastic stability of a moving elastic band under time- and space-dependent loadings is studied by Tylikowski [6].

In this paper, we study the almost sure asymptotic stability of a moving band subjected to zero mean in-plane loading by means Liapunov functional method. Stability regions are compared with ones obtained by Kozin and Milstead [5].

2 Problem Formulation

We will start from the Kozin-Milstead [5] nondimensional equations of motion (Eqs. 10(a) and 10(b)), which can be written as

$$\frac{\partial^2 u}{\partial t^2}+2\beta\left(\frac{\partial u}{\partial t}+\mu\frac{\partial u}{\partial x}\right)+2\mu\frac{\partial^2 u}{\partial t\partial x}+\gamma^2\frac{\partial^4 u}{\partial x^4}+[(\mu^2-\lambda^2)-g(t)]\frac{\partial^2 u}{\partial x^2}+(f_o+f(t))\frac{\partial}{\partial x}\left(x\frac{\partial\varphi}{\partial x}\right)=0 \tag{1}$$

$$\frac{\partial^2 \varphi}{\partial t^2}+2\beta\left(\frac{\partial \varphi}{\partial t}+\mu\frac{\partial \varphi}{\partial x}\right)+2\mu\frac{\partial^2 \varphi}{\partial t\partial x}+\gamma^2\frac{\partial^4 \varphi}{\partial x^4}+[(\mu^2-1)-g(t)]\frac{\partial^2 \varphi}{\partial x^2}+(f_o+f(t))\frac{\partial}{\partial x}\left(x\frac{\partial u}{\partial x}\right)=0 \tag{2}$$

with quantities,

$$\beta=\frac{\bar{\beta}L}{2\rho bC_T},\quad \mu=\frac{C}{C_T},\quad \lambda^2=\frac{T_o}{\rho bhC_T^2}=\frac{C_L^2}{C_T^2},\quad C_L^2=\frac{T_o}{\rho bh}$$

$$g(t)=\frac{T(t)}{\rho bhC_T^2}=\lambda^2\frac{T(t)}{T_o},\quad f_o=\frac{P_o}{\rho bhC_T^2}\frac{L}{h}=\lambda^2\frac{P_o}{T_o}\frac{L}{h},$$

$$f(t)=\frac{P(t)}{\rho bhC_T^2}\frac{L}{h}=\lambda^2\frac{P(t)}{T_o}\frac{L}{h} \tag{3}$$

$$\gamma^2=\frac{E}{12\rho(1-\nu^2)C_T^2}\left(\frac{b}{L}\right)^2,\quad C_T^2=\frac{4Gb^2}{\rho h^2}\left(1+\frac{T_oh}{4Gb^3}\right)=C_L^2+\frac{4Gb^2}{\rho h^2}$$

where u, φ are dimensionless lateral displacement and rotation of band about x axis, $\bar{\beta}$ the damping coefficient, ρ the band mass density, b, h, L the band thickness, band width, and length between supports, respectively, C the band axial velocity, E, G Young and shear modulus, ν Poison ratio, T_o, $T(t)$ the constant and time-dependent tension in the band, and P_o, $P(t)$ the constant and time-dependent edge load at the support. The time varying forces $T(t)$ and $P(t)$ are assumed to be zero mean stochastic processes.

The band is assumed to be simply supported and boundary conditions are

$$\left.\begin{matrix}x=0\\x=1\end{matrix}\right\}\quad u(t,x)=\varphi(t,x)=\frac{\partial^2 u}{\partial x^2}(t,x)=\frac{\partial^2\varphi}{\partial x^2}(t,x)=0 \tag{4}$$

The purpose of the present paper is the investigation of almost sure asymptotic stability of the moving band subjected to stochastic time-dependent loads. To estimate perturbated solutions, it is necessary to introduce a measure of distance $\|\cdot\|$ of solutions of

---

[1] Corresponding author.

Contributed by the Applied Mechanics Division for publication in the JOURNAL OF APPLIED MECHANICS. Manuscript received March 7, 2007; final manuscript received November 20, 2007; published online May 14, 2008. Review conducted by Igor Mezic.

Eqs. (1) and (2) with nontrivial initial conditions and the trivial one. Following Kozin [7], the equilibrium state of Eqs. (1) and (2) is said to be almost sure stochastically stable, if

$$P\{\lim_{t\to\infty}\|\mathbf{w}(.,t)\|=0\}=1 \tag{5}$$

where $\mathbf{w}=\mathrm{col}(u,\varphi)$, matrix column.

3 Stability Analyses

Applying the Liapunov method, we can construct the functional as is shown in Ref. [8]. Thus, let us write Eqs. (1) and (2) in the formal form $\mathfrak{L}\mathbf{w}=0$, where $\mathbf{w}=\mathrm{col}(u,\varphi)$, and introduce the linear $\mathfrak{R}$ operator, which is a formal derivative of the operator $\mathfrak{L}$ with respect to $\partial/\partial t$.

Integrating the scalar product of the vectors $\mathfrak{L}\mathbf{w}\ \mathfrak{R}\mathbf{w}$ on rectangular $C=[x:0\leqslant x\leqslant 1]\times[\tau:0\leqslant\tau\leqslant t]$ with respect to Eqs. (1) and (2), it is clear

$$\int_0^1\int_0^t \mathfrak{L}\mathbf{w}\ \mathfrak{R}\mathbf{w}\ dz d\tau=0 \tag{6}$$

After applying partial integration to Eq. (6), the sum of two integrals may be obtained. In the first, integration is only on the spatial domain, and it is chosen to be the Liapunov functional:

$$\begin{aligned}\mathbf{V}=\int_0^1\Bigg\{&\left(\nu+\beta u+\mu\frac{\partial u}{\partial x}\right)^2+\left(\beta u+\mu\frac{\partial u}{\partial x}\right)^2+\left(\omega+\beta\varphi+\mu\frac{\partial\varphi}{\partial x}\right)^2\\&+\left(\beta\varphi+\mu\frac{\partial\varphi}{\partial x}\right)^2+\gamma^2\left[\left(\frac{\partial^2u}{\partial x^2}\right)^2+\left(\frac{\partial^2\varphi}{\partial x^2}\right)^2\right]+(\lambda^2-\mu^2)\left(\frac{\partial u}{\partial x}\right)^2\\&+(1-\mu^2)\left(\frac{\partial\varphi}{\partial x}\right)^2\Bigg\}dx\end{aligned} \tag{7}$$

where $\nu=\partial u/\partial t$, $\omega=\partial\varphi/\partial t$.

Since it is evident

$$\mathbf{V}|_0^t-\int_0^t\frac{d\mathbf{V}}{dt}dt=0 \tag{8}$$

then the second integral in Eq. (6) is a time derivative of the functional (7) along with Eqs. (1) and (2):

$$\begin{aligned}\frac{d\mathbf{V}}{dt}=-2\int_0^1\Bigg\{&\nu\left(\beta\nu+\mu\frac{\partial\nu}{\partial x}\right)+2\beta\mu\frac{\partial u}{\partial x}\left(\nu+\beta u+\mu\frac{\partial u}{\partial x}\right)\\&+\gamma^2\frac{\partial^4u}{\partial x^4}\left(\beta u+\mu\frac{\partial u}{\partial x}\right)+(\mu^2-\lambda^2)\frac{\partial^2u}{\partial x^2}\left(\beta u+\mu\frac{\partial u}{\partial x}\right)\\&-g(t)\frac{\partial^2u}{\partial x^2}\left(\nu+\beta u+\mu\frac{\partial u}{\partial x}\right)+(f_o+f(t))\frac{\partial}{\partial x}\left(x\frac{\partial\varphi}{\partial x}\right)\Bigg(\nu+\beta u\\&+\mu\frac{\partial u}{\partial x}\Bigg)+\omega\left(\beta\omega+\mu\frac{\partial\omega}{\partial x}\right)+2\beta\mu\frac{\partial\varphi}{\partial x}\left(\omega+\beta\varphi+\mu\frac{\partial\varphi}{\partial x}\right)\\&+\gamma^2\frac{\partial^4\varphi}{\partial x^4}\left(\beta\varphi+\mu\frac{\partial\varphi}{\partial x}\right)+(\mu^2-1)\frac{\partial^2\varphi}{\partial x^2}\left(\beta\varphi+\mu\frac{\partial\varphi}{\partial x}\right)\\&-g(t)\frac{\partial^2\varphi}{\partial x^2}\left(\omega+\beta\varphi+\mu\frac{\partial\varphi}{\partial x}\right)+(f_o+f(t))\frac{\partial}{\partial x}\left(x\frac{\partial u}{\partial x}\right)\Bigg(\omega+\beta\varphi\\&+\mu\frac{\partial\varphi}{\partial x}\Bigg)\Bigg\}dx\end{aligned} \tag{9}$$

Functional $\mathbf{V}$ will be a Liapunov functional if it is a positive definite that will be fulfilled if $\lambda>\mu$ and $\mu<1$. From relations (3), it is evident that $\lambda<1$, so we have $\mu<\lambda<1$. This condition can be extended by using well known Steklov's inequality:

$$\int_0^1\left[\left(\frac{\partial^2u}{\partial x^2}\right)^2+\left(\frac{\partial^2\varphi}{\partial x^2}\right)^2\right]dx\geq\pi^2\int_0^1\left[\left(\frac{\partial u}{\partial x}\right)^2+\left(\frac{\partial\varphi}{\partial x}\right)^2\right]dx \tag{10}$$

and positive definite conditions become:

$$\gamma^2\pi^2+\lambda^2-\mu^2>0 \tag{11a}$$

$$\gamma^2\pi^2+1-\mu^2>0 \tag{11b}$$

4 Almost-Sure Stability

Let a scalar function $\varsigma(t)$ be defined as

$$\frac{1}{\mathbf{V}}\frac{d\mathbf{V}}{dt}\leq\varsigma(t) \tag{12}$$

As a maximum point, which is a particular case of the stationary point, we may write

$$\delta(\dot{\mathbf{V}}-\varsigma\mathbf{V})=0 \tag{13}$$

which can be written in the form

$$\int_0^1\{L_1\delta\nu+L_2\delta\omega+L_3\delta u+L_4\delta\varphi\}dx=0 \tag{14}$$

where

$$\begin{aligned}L_1&=(\varsigma+2\beta)\nu+\varsigma\left(\beta u+\mu\frac{\partial u}{\partial x}\right)+2\beta\mu\frac{\partial u}{\partial x}-g(t)\frac{\partial^2u}{\partial x^2}\\&\quad+(f_o+f(t))\frac{\partial}{\partial x}\left(x\frac{\partial\varphi}{\partial x}\right)\\L_2&=(\varsigma+2\beta)\omega+\varsigma\left(\beta\varphi+\mu\frac{\partial\varphi}{\partial x}\right)+2\beta\mu\frac{\partial\varphi}{\partial x}-g(t)\frac{\partial^2\varphi}{\partial x^2}\\&\quad+(f_o+f(t))\frac{\partial}{\partial x}\left(x\frac{\partial u}{\partial x}\right)\\L_3&=\varsigma\beta(\nu+2\beta u)+(\varsigma+2\beta)\Bigg[\gamma^2\frac{\partial^4u}{\partial x^4}+(\mu^2-\lambda^2)\frac{\partial^2u}{\partial x^2}-\mu\Bigg(\frac{\partial\nu}{\partial x}\\&\quad+2\mu\frac{\partial^2u}{\partial x^2}\Bigg)\Bigg]-g(t)\left(\frac{\partial^2\nu}{\partial x^2}+2\beta\frac{\partial^2u}{\partial x^2}\right)+(f_o+f(t))\Bigg\{\beta\frac{\partial}{\partial x}\left(x\frac{\partial\varphi}{\partial x}\right)\\&\quad-\mu\left(2\frac{\partial^2\varphi}{\partial x^2}+x\frac{\partial^3\varphi}{\partial x^3}\right)+\frac{\partial}{\partial x}\left[x\left(\frac{\partial\omega}{\partial x}+\beta\frac{\partial\varphi}{\partial x}+\mu\frac{\partial^2\varphi}{\partial x^2}\right)\right]\Bigg\}\\L_4&=\varsigma\beta(\omega+2\beta\varphi)+(\varsigma+2\beta)\Bigg[\gamma^2\frac{\partial^4\varphi}{\partial x^4}+(\mu^2-1)\frac{\partial^2\varphi}{\partial x^2}-\mu\Bigg(\frac{\partial\omega}{\partial x}\\&\quad+2\mu\frac{\partial^2\varphi}{\partial x^2}\Bigg)\Bigg]-g(t)\left(\frac{\partial^2\omega}{\partial x^2}+2\beta\frac{\partial^2\varphi}{\partial x^2}\right)+(f_o+f(t))\Bigg\{\beta\frac{\partial}{\partial x}\left(x\frac{\partial u}{\partial x}\right)\\&\quad-\mu\left(2\frac{\partial^2u}{\partial x^2}+x\frac{\partial^3u}{\partial x^3}\right)+\frac{\partial}{\partial x}\left[x\left(\frac{\partial\nu}{\partial x}+\beta\frac{\partial u}{\partial x}+\mu\frac{\partial^2u}{\partial x^2}\right)\right]\Bigg\}\end{aligned} \tag{15}$$

By putting $L_1=L_2=0$, we can eliminate ν and ω from L_3 and L_4. Then they have the form

$$\begin{aligned}L_5=&\ \zeta\beta^2(\zeta+4\beta)u-[4\beta^2g(t)+2(f_o+f(t))^2+\lambda^2(\zeta+2\beta)^2]\frac{\partial^2u}{\partial x^2}\\&-4(f_o+f(t))^2x\frac{\partial^3u}{\partial x^3}+[\gamma^2(\zeta+2\beta)^2-g^2(t)-(f_o+f(t))^2x^2]\frac{\partial^4u}{\partial x^4}\\&+4\beta^2(f_o+f(t))\frac{\partial}{\partial x}\left(x\frac{\partial\varphi}{\partial x}\right)+2g(t)(f_o+f(t))\frac{\partial^2}{\partial x^2}\left(x\frac{\partial^2\varphi}{\partial x^2}\right)\end{aligned}$$

$$L_6 = \zeta\beta^2(\zeta+4\beta)\varphi - [4\beta^2 g(t) + 2(f_o+f(t))^2 - (\zeta+2\beta)^2]\frac{\partial^2\varphi}{\partial x^2}$$
$$- 4(f_o+f(t))^2 x\frac{\partial^3\varphi}{\partial x^3} + [\gamma^2(\zeta+2\beta)^2 - g^2(t) - (f_o+f(t))^2x^2]\frac{\partial^4\varphi}{\partial x^4}$$
$$+ 4\beta^2(f_o+f(t))\frac{\partial}{\partial x}\left(x\frac{\partial u}{\partial x}\right) + 2g(t)(f_o+f(t))\frac{\partial^2}{\partial x^2}\left(x\frac{\partial^2 u}{\partial x^2}\right) \qquad (16)$$

According to the boundary condition (10), we shall choose the trial functions in the form

$$u(x,t) = \sum_{n=1}^{\infty} U_n(t)\sin\alpha_n x$$
$$\varphi(x,t) = \sum_{n=1}^{\infty} \Phi_n(t)\sin\alpha_n x \qquad (17)$$

where $\alpha_n = n\pi$, n is a natural number. By using Galerkin's method, from Eq. (16), we obtain an infinite system of algebraic equations, which has a nontrivial solution if its determinant is equal to zero, and one can find unknown function ς. Unfortunately, even in the case $n=1,2$, as is proposed by Ariaratnam and Asokanthan [3], we get an eighth order algebraic equation for ς. So, we are enforced to follow the Kozin-Milstead [5] procedure, and by taking only the single (nth) mode from Eq. (16):

$$\lfloor(\zeta+2\beta)^2k_{on} - k_{1n}(t)\rfloor U_n - k_{2n}(t)\Phi_n = 0$$
$$- k_{2n}(t)U_n + \lfloor(\zeta+2\beta)^2(k_{on}+k_{3n}) - k_{1n}(t)\rfloor\Phi_n = 0 \qquad (18)$$

where

$$k_{on} = \alpha_n^2(\gamma^2\alpha_n^2 + \lambda^2) + \beta^2,$$
$$k_{1n}(t) = (2\beta^2 - \alpha_n^2 g(t))^2 + \frac{1}{6}\alpha_n^2(2\alpha_n^2 - 3)(f_o+f(t))^2 \qquad (19)$$
$$k_{2n}(t) = \alpha_n^2(2\beta^2 - \alpha_n^2 g(t))(f_o+f(t)), k_{3n} = (1-\lambda^2)\alpha_n^2$$

Hence, from Eq. (18),

$$\varsigma_n(t) = \sqrt{\frac{k_{1n}(t)(2k_{on}+k_{3n}) + \sqrt{k_{3n}^2k_{1n}^2(t) + 4k_{on}k_{2n}^2(t)(k_{on}+k_{3n})}}{2k_{on}(k_{on}+k_{3n})}}$$
$$- 2\beta \qquad (20)$$

By solving the differential inequality (12), and estimation of the functional, we can conclude that the trivial solution of Eqs. (1) and (2), when the processes $g(t)$ and $f(t)$ are ergodic and stationary, is almost sure asymptotically stable if

$$E\{\zeta_n(t)\} < 0 \qquad (21)$$

where E denotes the operator of the mathematical expectation.

5 Numerical Results and Discussion

From Eqs. (19)–(21), it may be seen that almost sure stability condition is independent of band velocity, which is given throw parameter μ. It is also noticed in Ref. [5], but based on numerical results, while for band velocities exceeding torsional wave propagation ($\mu > 1$), explanation is insufficiently clear.

For $\mu < 1$, ($C < C_T$), relation (11b) is satisfied, and parameters λ, μ have to obey to relation (11a). If $\mu > 1$, ($C > C_T$), then $\mu^2 - 1$ must be less than $\gamma^2\pi^2$, and parameter $1-\gamma^2\pi^2 < \lambda^2 < 1$. We choose parameters λ and μ from the region under the solid straight line shown in Fig. 1.

First, we consider infinite mode ($n \to \infty$), and by using Schwartz inequality we get stability regions, which are compared with Kozin-Milstead [5] results. Second, both results are improved when we know the probability density function for the processes. Finally, we analyze cases when n is a finite number, especially the first mode ($n=1$).

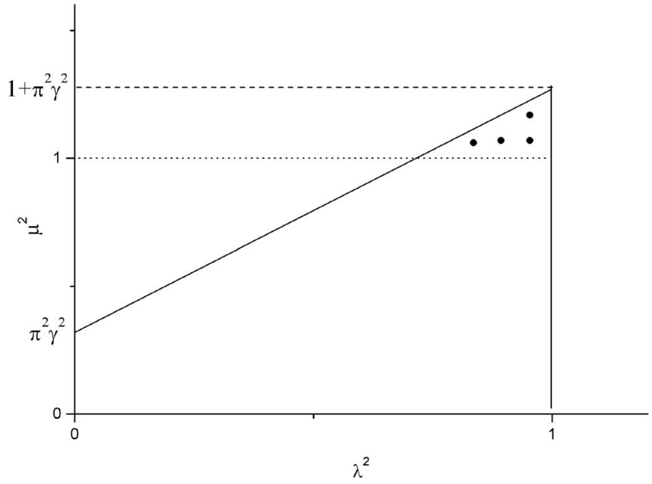

Fig. 1 Choosing moving band parameters

By putting in Eq. (21) that n tends to infinity, it takes the form

$$E\left\{\sqrt{g^2(t) + g(t)(f_o+f(\ t))) + \frac{1}{3}(f_o+f(\ t)))^2}\right\} - 2\beta\gamma < 0 \qquad (22)$$

and by applying Schwartz inequality, with respect to relations (3), we get

$$\left(\frac{T_o}{h}\right)^2\sigma^2(T/T_o) + \left(\frac{T_o}{h}\right)^2\frac{L}{h}r_o\sigma(T/T_o)\sigma(P/T_o)$$
$$+ \frac{1}{3}\left(\frac{T_o}{h}\right)^2\left(\frac{L}{h}\right)^2\sigma^2(P/T_o) - \frac{\bar{\beta}^2E}{12\rho(1-\nu^2)}\left(\frac{L}{h}\right)^2\left(\frac{b}{L}\right)^2 < 0 \qquad (23)$$

where r_o is the correlation coefficient between processes $T(t)$ and $P(t)$ and $\sigma(T/T_o)$, are $\sigma(P/T_o)$ are their variances.

Relation (23) gives us the possibility to show almost sure-stability regions. As we see, it represents simple quadratic function with respect to process variances, as well as geometric and physical parameters of the band. In Fig. 2, with stability regions

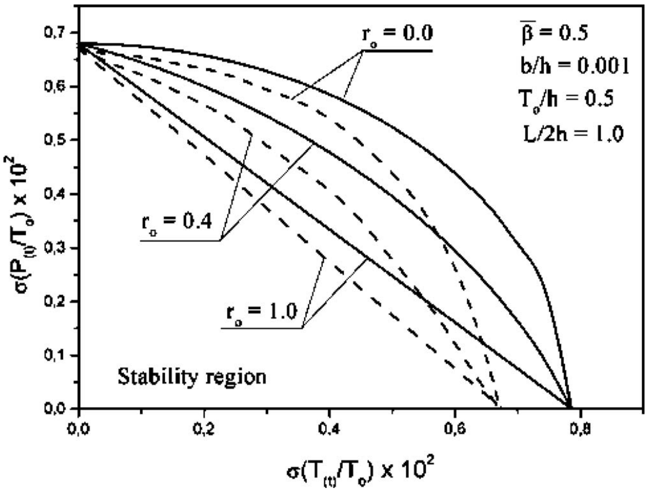

Fig. 2 Moving elastic band–infinite mode $\sigma(P/T_o)$ versus $\sigma(T/T_o)$: (—) after relation (23); (---) Ref. [5]

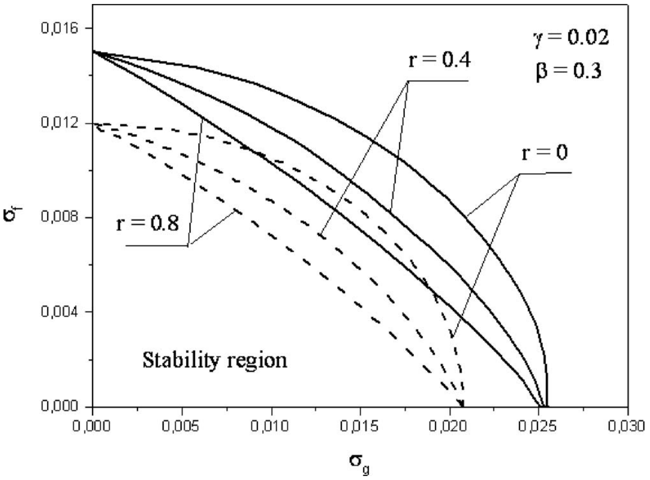

Fig. 3 Moving elastic band–infinite mode σ_f versus σ_g: (—) two-dimensional probability density function (23); (---) Schwartz inequality

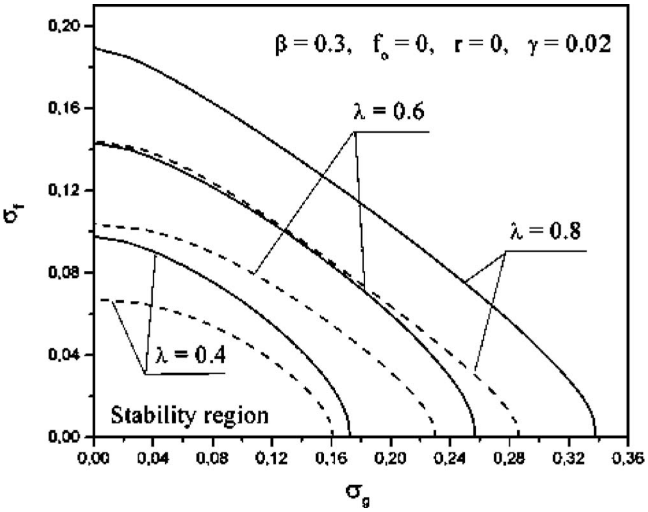

Fig. 4 Moving elastic band–first mode σ_f versus σ_g: (—) two-dimensional probability density function (23); (---) Schwartz inequality

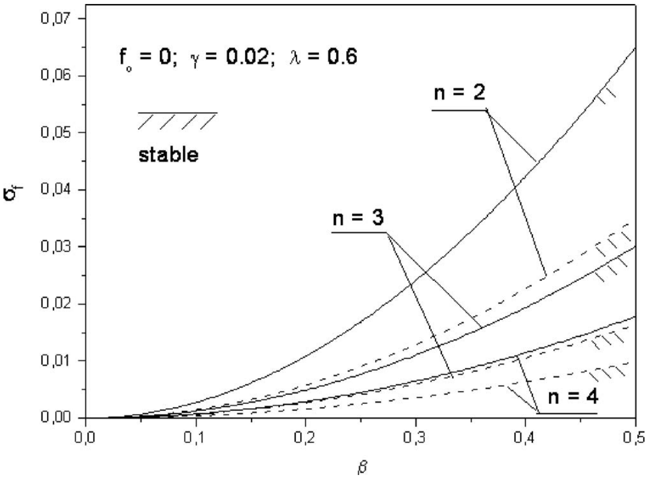

Fig. 5 Moving elastic band–second, third, and fourth modes σ_f versus damping coefficient β

obtained by relation (23) are given by a solid line, and with dashed line results obtained in Ref. [5]. It is evident that relation (23) gives significally larger stability regions. Due to its simplicity, we can obtain completely identical Figs. 7 and 8 in Ref. [5].

Our next intention is focused relation (22) on processes $g(t)$ and $f(t)$ have normal distribution. Two-dimensional probability density function is given by the Gaussian form:

$$p(g,f) = \frac{1}{2\pi\sigma_g\sigma_f\sqrt{1-r^2}}\exp\left[-\frac{1}{2(1-r^2)}\left(\frac{g^2}{\sigma_g^2} - 2r\frac{gf}{\sigma_g\sigma_f} + \frac{f^2}{\sigma_f^2}\right)\right] \tag{24}$$

where σ_g, σ_f are variances, and r is the correlation coefficient. Numerical calculation is performed by using Gauss-Hermite quadratures, as is shown in Ref. [9].

In Fig. 3, stability regions as functions of correlation coefficient are given by solid line, and for comparison, stability regions obtained by Schwartz inequality with a dashed line. It may be seen that our numerical difficulties related to solving an algebraic-integral equation are awarded by great enlarging stability regions.

Calculating of almost sure-stability regions for finite modes are performed by using relations (20) and (21). In Fig. 4, stability regions are given for the first mode ($n=1$) and various values of parameter λ. It is evident that by increasing the tensile force in the band, the stability region increases. As in upper case, knowing the two-dimensional probability density function enlarged almost sure-stability regions.

For higher modes ($n=2,3,4$), the stability regions are calculated when $g(t)=0$ (there is no fluctuation in the tensile force) and are shown as a function of variance σ_f and damping coefficient β in Fig. 5. The boundaries of the almost sure stability for Gaussian process are given by a solid line, and for harmonic one by dashed line. From Figs. 3–5, it has been seen that for the Gaussian process with increasing mode number, stability regions decrease to limit value, which can be read on the ordinate axis in Fig. 3. Numerical calculation for the harmonic process is performed by using Gauss–Chebyshev quadrature, as is shown in Ref. [10].

6 Conclusions

Almost sure-stability problem of a moving elastic band, where coupling of lateral and torsional motions is caused by in-plane acting forces, is investigated. Stability conditions are obtained by the direct Liapunov functional method, and the choice of parameters λ and μ is based on the positive definite condition of the Liapunov functional. By using the Schwartz inequality for the infinite mode the Kozin-Milstead [5], results are improved, and the almost sure-stability condition is reduced when solving the simple quadratic inequation, while stability regions are significally larger. Also, it is shown that if we know the two-dimensional probability function our results can be improved for all modes.

Stability region in plane of process variances is given as a function of correlation coefficient for infinite mode, and as functions of parameter λ for first mode. In the case when edge load process possesses Gaussian or harmonic distribution, stability regions are given for second, third, and fourth modes.

Acknowledgment

This work was supported by Ministry of Science and Environmental protection of the Republic of Serbia, through the Project No. 144023.

References

[1] Solar, A. I., 1968, “Vibrations and Stability of a Moving Band,” J. Franklin Inst., **286**(4), pp. 295–307.
[2] Wang, K. W., 1991, “Dynamic Stability Analysis of High Speed Axially Moving Bands With End Curvatures,” ASME J. Vibr. Acoust., **113**, pp. 62–68.
[3] Ariaratnam, S. T., and Asokanthan, S. F., 1988, “Torsional Oscillations in

Moving Bands," ASME J. Vib., Acoust., Stress, Reliab. Des., **110**, pp. 350–355.

[4] Ariaratnam, S. T., and Asokanthan, S. F., 1993, "Instabilities in Moving Bands Under Random Tension Fluctuation," J. Sound Vib., **167**(3), pp. 421–432.

[5] Kozin, F., and Milstead, R. M., 1979, "The Stability of a Moving Elastic Strip Subjected to Random Parametric Excitation," Trans. ASME, J. Appl. Mech., **46**, pp. 404–410.

[6] Tylikowski, A., 1988, "Stochastic Stability of a Moving Band Under Time and Space-Dependent Loading," *Proceedings of the XIII Symposium on Vibration: in Physics and Systems*, Poznan-Blazejevko, pp. 261–262.

[7] Kozin, F., 1972, *Stability of Linear Stochastic Systems*, Lecture Notes in Mathematics No. 294, Springer-Verlag, New York, pp. 186–229.

[8] Pavlović, R., Kozić, P., Rajković, P., and Pavlovic, I., 2007, "Dynamic Stability of a Thin-Walled Beam Subjected to Axial Loads and End Moments," J. Sound Vib., **301**, pp. 690–700.

[9] Pavlović, R., Kozić, P., and Rajković, P., 2005, "Influence of Randomly Varying Damping Coefficient on the Dynamic Stability of Continuous Systems," Eur. J. Mech. A/Solids, **24**, pp. 81–87.

[10] Pavlović, R., Kozić, P., and Rajković, P., 2001, "Influence of Transverse Shear on Stochastic Instability of Viscoelastic Beam," Int. J. Solids Struct., **38**, pp. 6829–6837.

Jumps Across an Outgoing Spherical Shock Wave Front

Yukio Sano
38-10 Shibatani-Cho,
Takatsuki,
Osaka 569-1025, Japan

Tomokazu Sano
Graduate School of Engineering,
Osaka University,
Suita,
Osaka 565-0871, Japan

The shock jump conditions have been used since Rankine published in 1870 and Hugoniot in 1889. However, these conditions, in which the geometrical effect is never included, may not be correctly applied to material responses caused by a spherical wave front. Here, a geometrical effect on jumps in radial particle velocity and radial stress across an outgoing spherical wave front is examined. Two types of jump equations are derived from the conservation laws of mass and momentum. The first equations of Rankine–Hugoniot (RH) type show that the geometrical effect may be neglected at distances of movement of the rear of the wave front that are more than ten times as long as the effective wave front thickness. Furthermore, using four conditions required to satisfy the RH jump conditions, which are contained in the RH type equations, a method is developed to judge the applicability of the RH jump conditions to the jumps. The second type equations for spherical wave fronts of general form are obtained by expressing a volumetric strain wave ε *in the wave front by more general wave forms. In the neighborhood of the center of the wave front, for* $\varepsilon < 0.09$*, radial particle velocity in the jump in any materials is inversely proportional to the square of a dimensionless distance from the center to the rear, and for* $\varepsilon < 0.04$*, radial stress in the jump in some viscous fluids and solids is inversely proportional to the distance. In conclusion, an outgoing spherical wave front attenuates greatly near the center due to the geometrical effect as well as rarefaction waves overtaking from behind, while the geometrical effect is negligible at the specified positions that are distant from the center.* [DOI: 10.1115/1.2912942]

1 Introduction

Rankine [1] published his dissertation on a plane shock wave in 1870. Hugoniot's work [2] was published posthumously in 1889. The discontinuous shock jump equations they proposed have become known as the Rankine–Hugoniot (RH) jump conditions. Davison [3] showed that the RH jump conditions were applicable to the jumps across a steady plane wave of finite rise time.

In plate impact experiments, several authors [4–7] observed unsteady wave fronts decreasing in their amplitudes and increasing in their thicknesses with propagation due to the smearing effect that is more predominant over the steepening effect. Sano [8] derived the equations of two different types for jumps across an unsteady plane wave front, and qualitatively examined the effect of unsteadiness on the jumps. The first equations of RH type for the wave front of finite rise time, which rear moved with a constant velocity, showed that the jump in particle velocity depended on the strain rate, and the jump in stress further on the strain acceleration. The second type equations are the jump equations for plane wave fronts (of infinitesimal rise time) of general form that are obtained by expressing a strain wave in the wave front by more general wave forms. These equations showed that both jumps implicitly depended further on the change in the strain wave form with time. Sano and Miyamoto [9] evaluated the influences of the unsteadiness and the time variation in the velocity of the rear of the wave front on both jumps using the strain wave parameters that were determined by Sano [10] on the basis of shock experiment data for a lithium fluoride (LiF) single crystal [5] and for sandstone [6]. The influence of the unsteadiness was considerably large for both materials. On the other hand, the influence of the time variation in the velocity was slight for the LiF single crystal because of the thin wave front thickness, and was appreciable for sandstone because of the much larger thickness.

Grady [11] developed a method that allowed analysis of attenuating experimental wave profiles of arbitrary shape in spherically symmetric flow. The method was applied to radial stress and particle velocity data for spherically divergent wave propagation in Westerly granite. The resulting relations among pressure, volume, and deviatoric stress are consistent with other available data on Westerly granite. This fact indicates that jumps in radial particle velocity and stress across explosion-induced spherical wave fronts in condensed matters such as liquids, solids, and porous materials are influenced by curvature of the wave front. This implies that if the jump equations for a plane wave front [1,2,8,9] are applied to calculations of the jumps across a spherical wave front, in general, the jumps would be inaccurately predicted. However, the jump equations for a spherical wave front are complicated and difficult to use. Therefore, it is important to find out conditions under which it is reasonable to ignore the geometric effects due to curvature of the wave front.

In the study reported here, equations of RH type for jumps in radial particle velocity and radial stress across an outgoing spherical wave front of finite rise time are first derived, and then reduced to equations that are appropriate only at distances of movement of the rear of the wave front that are much longer than the wave front thickness. For a strain wave of linear form in the wave front, the distances at which the effect of curvature can be neglected are specified. Furthermore, a method is presented to judge whether the RH jump conditions are applicable to the jumps at those distances. Next, jump equations for spherical wave fronts of general form are derived, and then reduced to equations where curvature is separated from the other factors that influence the jumps, although the reduced equations are not applicable to large amounts of volumetric strain. Using the reduced equations, the effect of curvature is examined near the center of the wave front.

2 Jump Equations of RH Type

2.1 Equations. Figure 1(*a*) schematically shows a propagation of a volumetric strain wave $\varepsilon(r,t)$ in an outgoing spherical wave front in the r direction, where r is the Lagrangian position and t is time. An initial spherical wave front at time 0 has a range

---

Contributed by the Applied Mechanics Division of ASME for publication in the Journal of Applied Mechanics. Manuscript received May 19, 2007; final manuscript received October 27, 2007; published online May 14, 2008. Review conducted by Horacio D. Espinosa.

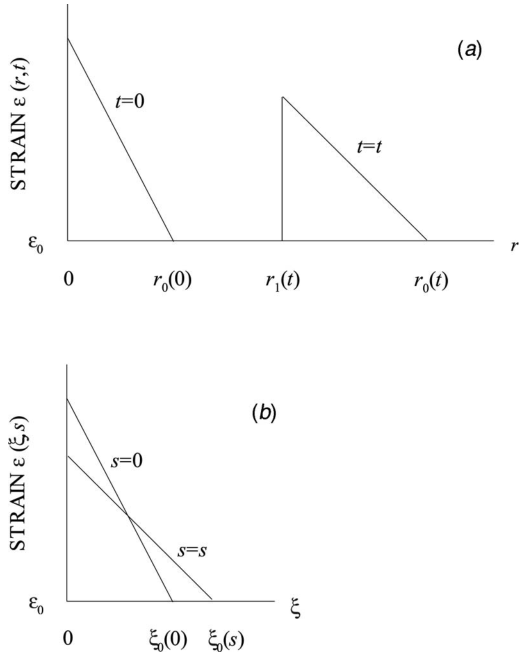

Fig. 1 Schematic diagrams of (*a*) an initial strain wave $\varepsilon(r,0)$ with a range $0\leqslant r\leqslant r_0(0)$ at time 0 and a strain wave $\varepsilon(r,t)$ with a range $r_1(t)\leqslant r\leqslant r_0(t)$ at time *t* in an inertial coordinate system (r,t); and (*b*) an initial strain wave $\varepsilon(\xi,0)$ with a range $0\leqslant\xi\leqslant\xi_0(0)$ at $s=0$ and a strain wave $\varepsilon(\xi,s)$ with a range $0\leqslant\xi\leqslant\xi_0(s)$ at $s=s$ in a moving coordinate system (ξ,s), where *s* $[\equiv r_1(t)]$ is the distance of movement of the rear of an outgoing spherical wave front from $t=0$ to $t=t$. The initial volumetric strain ε_0 is assumed to be constant along *r*.

$r_1(0)\leqslant r\leqslant r_0(0)$ where $r_1(0)=0$, where subscripts 0 and 1 refer to the leading edge and the rear of the wave front, respectively. Position $r=0$ is the position where the wave front is created, that is, the center of the wave front. The leading edge reaches position $r_0(t)$ at *t*, and the rear is at position $r_1(t)=\int_0^t c dt$, where $c(t)$ (>0) is the velocity of the rear. Note that the time variation $c(t)$ can be determined arbitrarily. The wave front thus has a range $r_1(t)\leqslant r\leqslant r_0(t)$ at *t*. In this range, the equations of conservation of mass and momentum are expressed [11–13] by

$$r^2\frac{\partial\varepsilon}{\partial t}+\frac{\partial(R^2u)}{\partial r}=0 \tag{1}$$

$$\rho_0\frac{\partial}{\partial t}\left\{\left(\frac{r}{R}\right)^2u\right\}+\frac{\partial\sigma}{\partial r}=-2\rho_0\frac{r^2}{R^3}\left(u^2+\frac{\sigma-\sigma_\theta}{\rho}\right) \tag{2}$$

where $R(r,t)$ is the Eulerian position expressed by $R=r+\int u dt$, $u(r,t)$ is the radial particle velocity, $\sigma(r,t)$ is the radial stress, $\sigma_\theta(r,t)$ is the circumferential stress, $\rho(r,t)$ is the material density, and ρ_0 is the initial density.

A coordinate system (ξ,s) moving at $c(t)$ with the rear of the wave front is introduced [14] as

$$\xi=r-s \tag{3a}$$

$$s=\int_0^t c(t)dt \tag{3b}$$

where s $[\equiv r_1(t)]$ is the distance of movement of the rear. Figure 1(*b*) schematically shows the strain wave $\varepsilon(\xi,0)$ in the initial wave front, and the strain wave $\varepsilon(\xi,s)$ in the wave front whose leading edge is at position $\xi_0(s)$ and whose rear is at position 0, where $\xi_0(s)=r_0(t)-s$. Note that $\xi_0(s)$ is the wave front thickness. In Secs. 2 and 3, symbols r_0, r_1, and ξ_0 denote $r_0(t)$, $r_1(t)$, and $\xi_0(s)$, respectively. Variables depending on ξ and s are related to the variables depending on r and t as follows:

$$R(\xi,s)\equiv R(r,t),\quad u(\xi,s)\equiv u(r,t),\quad \varepsilon(\xi,s)\equiv\varepsilon(r,t)$$

$$\sigma(\xi,s)\equiv\sigma(r,t),\quad \sigma_\theta(\xi,s)\equiv\sigma_\theta(r,t),\quad \rho(\xi,s)\equiv\rho(r,t)$$

Using $\partial/\partial t=-c(t)(\partial/\partial\xi-\partial/\partial s)$ and $\partial/\partial r=\partial/\partial\xi$, which are obtained from Eqs. (3*a*) and (3*b*), Eqs. (1) and (2) are transformed into

$$\frac{\partial(R^2u)}{\partial\xi}=c(t)\left\{\frac{\partial(r^2\varepsilon)}{\partial\xi}-\frac{\partial(r^2\varepsilon)}{\partial s}\right\}$$

$$\frac{\partial\sigma}{\partial\xi}=\rho_0c(t)\left[\frac{\partial}{\partial\xi}\left\{\left(\frac{r}{R}\right)^2u\right\}-\frac{\partial}{\partial s}\left\{\left(\frac{r}{R}\right)^2u\right\}\right]-2\rho_0\frac{r^2}{R^3}\left(u^2+\frac{\sigma-\sigma_\theta}{\rho}\right)$$

The equations above are integrated from ξ to ξ_0 to become

$$u(\xi,s)=c\left\{\left(\frac{r}{R}\right)^2\varepsilon-\left(\frac{r_0}{R}\right)^2\varepsilon_0+\frac{1}{R^2}\int_\xi^{\xi_0}r^2\frac{\partial\varepsilon}{\partial s}d\xi\right\}+\left(\frac{r_0}{R}\right)^2u_0 \tag{4}$$

$$\begin{aligned}\sigma(\xi,s)=\rho_0c^2&\left[\left(\frac{r}{R}\right)^2\left\{\left(\frac{r}{R}\right)^2\varepsilon-\left(\frac{r_0}{R}\right)^2\varepsilon_0+\frac{1}{R^2}\int_\xi^{\xi_0}r^2\frac{\partial\varepsilon}{\partial s}d\xi\right\}+\int_\xi^{\xi_0}\frac{\partial}{\partial s}\left\{\left(\frac{r}{R}\right)^4\varepsilon\right\}d\xi+\int_\xi^{\xi_0}\frac{\partial}{\partial s}\left\{\frac{r^2}{R^4}\int_\xi^{\xi_0}r^2\frac{\partial\varepsilon}{\partial s}d\xi\right\}d\xi\right]\\&+\rho_0c_t\left[\int_\xi^{\xi_0}\left(\frac{r}{R}\right)^4\varepsilon d\xi+\int_\xi^{\xi_0}\left\{\frac{r^2}{R^4}\int_\xi^{\xi_0}r^2\frac{\partial\varepsilon}{\partial s}d\xi\right\}d\xi\right]+2\rho_0\int_\xi^{\xi_0}\frac{r^2}{R^3}\left(u^2+\frac{\sigma-\sigma_\theta}{\rho}\right)d\xi+\rho_0c\left\{\left(\frac{r_0}{R}\right)^2\left(\frac{r}{R}\right)^2-1\right\}u_0\\&+\rho_0c\int_\xi^{\xi_0}\frac{\partial}{\partial s}\left\{\left(\frac{r_0}{R}\right)^2\left(\frac{r}{R}\right)^2(u_0-c\varepsilon_0)\right\}d\xi+\sigma_0\end{aligned} \tag{5}$$

where $c_t\equiv \mathrm{d}c/\mathrm{d}t$. At $\xi=0$, Eq. (4) is a jump equation for radial particle velocity

$$u_1-u_0=c\left\{\left(\frac{r_1}{R_1}\right)^2\varepsilon_1-\left(\frac{r_0}{R_1}\right)^2\varepsilon_0+\int_0^{\xi_0}\left(\frac{r}{R_1}\right)^2\frac{\partial\varepsilon}{\partial s}d\xi\right\}+\left\{\left(\frac{r_0}{R_1}\right)^2-1\right\}u_0 \tag{6}$$

where $\varepsilon_1\equiv\varepsilon_1(s)\equiv\varepsilon(0,s)$, $u_1\equiv u_1(s)\equiv u(0,s)$, and $R_1\equiv R_1(s)\equiv R(0,s)=R(r_1,t)\equiv R_1(t)=r_1+\int\tilde{u}(r_1,t)dt$. At $\xi=0$, Eq. (5) is a jump equation for radial stress

$$\sigma_1-\sigma_0=\rho_0c^2\left[\left(\frac{r_1}{R_1}\right)^2\left\{\left(\frac{r_1}{R_1}\right)^2\varepsilon_1-\left(\frac{r_0}{R_1}\right)^2\varepsilon_0+\int_0^{\xi_0}\left(\frac{r}{R_1}\right)^2\frac{\partial\varepsilon}{\partial s}d\xi\right\}+\int_0^{\xi_0}\frac{\partial}{\partial s}\left\{\left(\frac{r}{R}\right)^4\varepsilon\right\}d\xi+\int_0^{\xi_0}\frac{\partial}{\partial s}\left\{\frac{r^2}{R^4}\int_\xi^{\xi_0}r^2\frac{\partial\varepsilon}{\partial s}d\xi\right\}d\xi\right]$$
$$+\rho_0c_t\left[\int_0^{\xi_0}\left(\frac{r}{R}\right)^4\varepsilon d\xi+\int_0^{\xi_0}\left\{\frac{r^2}{R^4}\int_\xi^{\xi_0}r^2\frac{\partial\varepsilon}{\partial s}d\xi\right\}d\xi\right]+2\rho_0\int_0^{\xi_0}\frac{r^2}{R^3}\left(u^2+\frac{\sigma-\sigma_\theta}{\rho}\right)d\xi+c\rho_0\left\{\left(\frac{r_0}{R_1}\right)^2\left(\frac{r_1}{R_1}\right)^2-1\right\}u_0$$
$$+c\rho_0\int_0^{\xi_0}\frac{\partial}{\partial s}\left\{\left(\frac{r_0}{R}\right)^2\left(\frac{r}{R}\right)^2(u_0-c\varepsilon_0)\right\}d\xi \tag{7}$$

where $\sigma_1\equiv\sigma_1(s)\equiv\sigma(0,s)$. The radial particle velocity in the jump (the jump (u_1-u_0)) depends on the product of the strain rates and the positions r in the wave front, that is, the combined strain rates and curvatures. The radial stress in the jump (the jump $(\sigma_1-\sigma_0)$) depends further on the product of the strain accelerations and the positions, that is, on the combined strain accelerations and curvatures. Equations (6) and (7) are called jump equations of RH type for an outgoing spherical wave front. In the limit $r\to\infty$, where $r_1/R_1\to 1$, $r_0/R_1\to 1$, $r/R_1\to 1$, $r/R\to 1$, and $r_0/R\to 1$, they reduce to the RH type jump equations for an unsteady plane wave front [9].

2.2 Approximations. For an outgoing spherical wave front that is passing through a position r (or ξ), equation $R(\xi,s)=r+[\bar{u}(\xi)/\bar{c}(\xi)](r_0-r)$ is obtained by substituting $\Delta t=(r_0-r)/\bar{c}(\xi)$ into $R=r+\bar{u}(\xi)\Delta t$, where $\bar{c}(\xi)$ is the mean velocity of the leading edge of the wave front between positions r and r_0, and $\bar{u}(\xi)$ is the mean particle velocity at ξ over Δt. The value of $\bar{u}(\xi)/\bar{c}(\xi)$ approximates to that of the volumetric strain at ξ. The error δ of approximation $R\cong r$ at r in the range $r_1\leqslant r\leqslant r_0$ is between $\delta=0$ at $r=r_0$ and $\delta=\delta_1$ at $r=r_1$, that is, $0\leqslant\delta\leqslant\delta_1$, where $\delta_1=1-r_1/R_1$. The error δ_1 is expressed by $\delta_1=(\bar{u}/\bar{c})\ \xi_0/[s+(\bar{u}/\bar{c})\xi_0]$, where $\bar{c}\equiv\bar{c}(0)$ and $\bar{u}\equiv\bar{u}(0)$. The value of δ_1 changes from $\delta_1=1$ at $s=0$ to $\delta_1=0$ at $s\to\infty$. For example, at $s=10\xi_0$, δ_1 is given by $\delta_1=(\bar{u}/\bar{c})/[10+(\bar{u}/\bar{c})]\cong\varepsilon_1/10$, indicating that the error δ_1 is only about 1% for volumetric strain of 10%. If $R\cong r$ and $R_1\cong s$, then Eqs. (6) and (7) reduce to

$$u_1-u_0\cong c\left\{(\varepsilon_1-\varepsilon_0)+\int_0^{\xi_0}\left(\frac{r}{s}\right)^2\frac{\partial\varepsilon}{\partial s}d\xi\right\} \tag{8}$$

$$\sigma_1-\sigma_0\cong\rho_0c^2\left[(\varepsilon_1-\varepsilon_0)+\int_0^{\xi_0}\left\{\left(\frac{r}{s}\right)^2+1\right\}\frac{\partial\varepsilon}{\partial s}d\xi\right.$$
$$\left.+\int_0^{\xi_0}\frac{\partial}{\partial s}\left\{\frac{1}{r^2}\int_\xi^{\xi_0}r^2\frac{\partial\varepsilon}{\partial s}d\xi\right\}d\xi\right]$$
$$+\rho_0c_t\left[\int_0^{\xi_0}\varepsilon d\xi+\int_0^{\xi_0}\left\{\frac{1}{r^2}\int_\xi^{\xi_0}r^2\frac{\partial\varepsilon}{\partial s}d\xi\right\}d\xi\right]$$
$$+2\rho_0\int_0^{\xi_0}\frac{1}{r}\left(u^2+\frac{\sigma-\sigma_\theta}{\rho}\right)d\xi \tag{9}$$

where the values $\varepsilon_0=0$ and $u_0=0$ are assumed, and $(\varepsilon_1-\varepsilon_0)$ is the amplitude of the strain wave at s.

The third term on the right side of Eq. (9) may be able to be neglected in a situation where the effect of the curvatures in the wave front is small. This fact is demonstrated here. Using $u\leqslant c\varepsilon$ and $\sigma\leqslant\rho_0cu$, where the values $\varepsilon_0=0$, $u_0=0$, and $\sigma_0=0$ are assumed, as well as $\sigma-\sigma_\theta<\sigma$ and $\varepsilon=1-\rho_0/\rho$, the third term is expressed as

$$2\rho_0\int_0^{\xi_0}\frac{1}{r}\left(u^2+\frac{\sigma-\sigma_\theta}{\rho}\right)d\xi<2\rho_0c\int_0^{\xi_0}\frac{u}{r}d\xi \tag{10}$$

By integrating the right side of Eq. (10) after assuming $u=u_1(1-\xi/\xi_0)$, and then using $u_1\leqslant c\varepsilon_1$ in the resulting inequality,

$$2\rho_0\int_0^{\xi_0}\frac{1}{r}\left(u^2+\frac{\sigma-\sigma_\theta}{\rho}\right)d\xi<2\rho_0c^2(\varepsilon_1-\varepsilon_0)$$
$$\times\left[\left(1+\frac{s}{\xi_0}\right)\log\left(1+\frac{\xi_0}{s}\right)-1\right] \tag{11}$$

For $s\geqslant 10\xi_0$, the values of coefficient $2[(1+s/\xi_0)\log(1+\xi_0/s)-1]$ are smaller than a value of 10^{-1}. Therefore, the third term can be eliminated at the distances s where $s\geqslant 10\xi_0$.

2.3 Geometrical Effects. Values of the geometrical factor ξ_0/s where the effect of the curvatures in the wave front on the jumps is negligible are now specified. For the sake of simplicity, the following linear strain wave is assumed:

$$\varepsilon-\varepsilon_0=\delta\left(1-\frac{\xi}{\xi_0}\right) \tag{12}$$

where $\xi_0[\equiv\xi_0(s)]$ is the effective wave front thickness [15] and $\delta(s)$ $[\equiv\varepsilon_1(s)-\varepsilon_0]$ is the amplitude of the strain wave, where s represents the effective distance of movement of the rear of the wave front. The initial amplitude is expressed by $\delta(0)=\varepsilon_1(0)-\varepsilon_0$. The symbol δ denotes $\delta(s)$ below. The jump equations for the radial particle velocity and stress waves corresponding to the linear strain wave are obtained by substituting Eq. (12) into Eqs. (8) and (9) as follows:

$$u_1-u_0=c(\varepsilon_1-\varepsilon_0)\left[1+\frac{1}{2}\frac{\delta'}{\delta}\xi_0g_1+\frac{1}{2}\xi_0'g_2\right] \tag{13}$$

$$\sigma_1-\sigma_0=\rho_0c^2(\varepsilon_1-\varepsilon_0)\left[1+\frac{\delta'}{\delta}\xi_0g_{31}+\xi_0'g_{41}\right.$$
$$\left.+\frac{1}{\delta}\int_0^{\xi_0}\frac{\partial}{\partial s}\left\{\frac{1}{r^2}\int_\xi^{\xi_0}r^2\frac{\partial\varepsilon}{\partial s}d\xi\right\}d\xi\right]+\rho_0c^2(\varepsilon_1-\varepsilon_0)\left(\frac{\xi_0c_t}{c^2}\right)$$
$$\times\left[\frac{1}{2}+\frac{1}{6}\frac{\delta'}{\delta}\xi_0g_5+\frac{1}{3}\xi_0'g_6\right] \tag{14}$$

where the dashes on the variables refer to the differentiation with respect to s, and where the last term in the brackets of the first term on the right side of Eq. (14) is expressed by

Table 1 Values of g_1, g_2,…, and g_8, which are functions of the geometrical factor ξ_0/s, at $\xi_0/s=1$, 10^{-1}, 10^{-2}, and 10^{-3}

ξ_0/s	g_1	g_2	g_3	g_4	g_5	g_6	g_7	g_8
1	1.83	2.83	1.33	1.67	1.50	1.75	1.75	2.50
10^{-1}	1.07	1.14	1.03	1.07	1.05	1.08	1.08	1.15
10^{-2}	1.01	1.01	1.00	1.01	1.01	1.01	1.01	1.02
10^{-3}	1.00	1.00	1.00	1.00	1.00	1.00	1.00	1.00

$$\frac{1}{\delta}\int_0^{\xi_0}\frac{\partial}{\partial s}\{\ \}d\xi=\frac{\delta'}{\delta}\xi_0 g_{32}+\xi_0' g_{42}+\frac{1}{6}\frac{\delta''}{\delta}\xi_0^2 g_5+\frac{2}{3}\frac{\delta'}{\delta}\xi_0\xi_0' g_6$$

$$+\frac{1}{3}\xi_0''\xi_0 g_7+\frac{1}{3}\xi_0'^2 g_8$$

Here $g_1, g_2, \ldots$, and g_8 are expressed by

$$g_1=[(\xi_0/s)^2+4(\xi_0/s)+6]/6, \quad g_2=[3(\xi_0/s)^2+8(\xi_0/s)+6]/6$$

$$g_3=g_{31}+g_{32}=(\xi_0/s+3)/3, \quad g_4=g_{41}+g_{42}=(2\xi_0/s+3)/3$$

$$g_5=(\xi_0/s+2)/2, \quad g_6=g_7=(3\xi_0/s+4)/4, \quad g_8=(3\xi_0/s+2)/2$$

The jump (u_1-u_0) depends on g_1 and g_2, which are functions of ξ_0/s, as well as the rates δ' and ξ_0'. The jump $(\sigma_1-\sigma_0)$ depends on $g_3, g_4, \ldots, g_8$, which are also functions of ξ_0/s, the rates δ' and ξ_0', and the accelerations δ'' and ξ_0''. Values of the functions $g_1, g_2, \ldots, g_8$ at $\xi_0/s=1$, 10^{-1}, 10^{-2}, and 10^{-3} are listed in Table 1.

Substitutions of Eq. (12) into Eqs. (8) and (9) where $s\rightarrow\infty$ and hence $r\rightarrow s$, that is, into the jump equations for an unsteady plane wave front [15], yield

$$u_1-u_0=c(\varepsilon_1-\varepsilon_0)\left(1+\frac{1}{2}\frac{\delta'}{\delta}\xi_0+\frac{1}{2}\xi_0'\right) \tag{15}$$

$$\sigma_1-\sigma_0=\rho_0c^2(\varepsilon_1-\varepsilon_0)\left(1+\frac{\delta'}{\delta}\xi_0+\xi_0'+\frac{1}{6}\frac{\delta''}{\delta}\xi_0^2+\frac{2}{3}\frac{\delta'}{\delta}\xi_0'\xi_0+\frac{1}{3}\xi_0''\xi_0\right.$$
$$\left.+\frac{1}{3}\xi_0'^2\right)+\rho_0c^2(\varepsilon_1-\varepsilon_0)\left(\frac{\xi_0c_t}{c^2}\right)\left(\frac{1}{2}+\frac{1}{6}\frac{\delta'}{\delta}\xi_0+\frac{1}{3}\xi_0'\right) \tag{16}$$

The geometrical effect on the jump (u_1-u_0) is assessed by comparing Eq. (13) with Eq. (15). The value of g_1 decreases monotonically up to a value of 1 as the value of the geometrical factor ξ_0/s decreases. The same is true of the value of g_2. This result indicates that the geometrical factor intensifies the influence of other factors such as δ' and ξ_0' on the jump (u_1-u_0), and that as the rear of the wave front proceeds, the influence decreases. On the other hand, to assess the geometrical effect on the jump $(\sigma_1-\sigma_0)$, Eqs. (14) and (16) are compared. The values of $g_3, g_4, \ldots, g_8$ decrease up to a value of 1 linearly with a decrease in the value of ξ_0/s, indicating that the same is true of the influence on the jump $(\sigma_1-\sigma_0)$. At $\xi_0/s=1/10$, all the values of $g_1, g_2, \ldots, g_8$ are near a value of 1. Therefore, the effect of the curvatures on the jumps (u_1-u_0) and $(\sigma_1-\sigma_0)$ may be neglected at the distances s where $s\geqslant 10\xi_0$.

Sano and Miyamoto [9] obtained values of dimensionless quantity $\beta[\equiv\xi_0c_t/c^2]$ in Eq. (16) for two materials using data that were measured at their impact surfaces in plate impact experiments. The values are −0.004 ($\xi_0=0.32\times10^{-3}$ m, $c=7000$ m/s, and $c_t=-0.6\times10^9$ m/s^2) for the LiF single crystal, and −0.1 ($\xi_0=6.4\times10^{-3}$ m, $c=4000$ m/s, and $c_t=-0.25\times10^9$ m/s^2) for sandstone. The values of ξ_0 were calculated here from $\xi_0=cT$ using $T=0.045$ μs for the crystal and $T=1.6$ μs for sandstone, where T is the rise time measured at the impact surface.

The assumed linear strain wave form (Eq. (12)) may hardly manifest in reality. Therefore, note that this case provides valuable insight into the curvature effects but most likely will never correspond to any actual spherical shock accurately. It is expected that the factor ξ_0/s where the curvature effects are negligible will be evaluated for spherical wave fronts of more general wave forms.

2.4 Jump Equations for Arbitrarily Short Rise Time. For the wave fronts of thicknesses ξ_0, where $\xi_0<l$ (l is a positive number that is arbitrarily low), that is, for the wave fronts of arbitrarily short rise times, Eqs. (8) and (9) hold exactly because $R\rightarrow r$. The values of ε, u, σ, σ_θ, and $\partial\varepsilon/\partial s$ that are included in Eqs. (8) and (9) are finite. This means that as the value of ξ_0 is small, all the values of the terms of integration from 0 to ξ_0 in these equations become small, and that Eqs. (6) and (7) as well as Eqs. (8) and (9) reduce to

$$u_1-u_0=c(\varepsilon_1-\varepsilon_0)$$

$$\sigma_1-\sigma_0=\rho_0c^2(\varepsilon_1-\varepsilon_0)$$

the equations above are the same as the RH jump conditions for a plane wave front [8,9]. For any small value of ξ_0, which is expressed by $\xi_0=\xi_0^*f(s)$ (ξ_0^* is a positive number that is arbitrarily low, and the values of f and f' are finite), a finite value of $\partial\varepsilon/\partial s$ is illustrated by equation $\partial\varepsilon/\partial s=[\delta(\xi_0'/\xi_0)-\delta'](\xi/\xi_0)+\delta'$, which is obtained by substituting Eq. (12) into $\partial\varepsilon/\partial s$.

3 Applicability of the RH Jump Conditions

Shock wave front of finite rise time is formed by the balance struck between the wave front steepening effect by the nonlinear mechanical properties and the smearing effect by the energy dissipation such as strain rate effect. In plate impact experiments, several authors measured particle velocity-time or stress-time histories at several positions in a solid or in a porous material (see, for example, Refs. [4–7]). As the position is distant from the impact surface, the particle velocity profile rises slowly up to its peak. This fact indicates that the smearing effect is more predominant over the steepening effect at the more distant position, and that the thickness of the particle velocity wave increases with propagation. In addition, the fact that the measured value of the peak is lower at the more distant position, which is caused by the strain rate and the strain acceleration as well as rarefaction waves overtaking from behind, indicates that the amplitude of the particle velocity wave decreases with propagation. The same is true of the stress wave in the shock wave front. As clarified in Sec. 2.3, the geometrical factor intensifies the influence of other factors on the jumps (u_1-u_0) and $(\sigma_1-\sigma_0)$. Therefore, the behaviors similar to those of the wave thickness and amplitude that were observed in plate impact experiments would be observed during propagation of an outgoing spherical wave front. Applicability of the RH jump conditions to the jumps across an outgoing spherical wave front of finite rise time is discussed immediately below.

Equations (13) and (15) indicate that if $\xi_0'\ll 1$ and $|\delta'/\delta|\xi_0\ll 1$, then the RH jump relation $u_1-u_0=c(\varepsilon_1-\varepsilon_0)$ holds. As is found from Eq. (14) or Eq. (16), further if $|\xi_0''|\xi_0\ll 1$ and $|\delta''/\delta|\xi_0^2\ll 1$, then the RH jump relation $\sigma_1-\sigma_0=\rho_0c^2(\varepsilon_1-\varepsilon_0)$ holds. Whether two conditions $\xi_0'\ll 1$ and $|\xi_0''|\xi_0\ll 1$ hold for $s\geqslant 10\xi_0$ is first examined for the thickness ξ_0 that is expressed by a reasonable relation given below. Next, for the strain amplitude δ that is ex-

Table 2 Values of $\Delta\zeta/\zeta(0)$, α, $\Delta\xi_0/\xi_0$, and ξ_0' at $s=10\xi_0$ for $b=20$ and some values of α_0 in the region of $\alpha_0 \leqslant 10$

α_0	$\Delta\zeta/\zeta(0)$	$\alpha \times 10^2$	$\Delta\xi_0/\xi_0(0)$	$\xi_0' \times 10^2$
0	10	0	0	0
2	21.4	4.84	1.03	2.39
4	39.1	6.77	2.65	2.34
6	59.4	7.56	4.49	1.94
8	80.5	7.96	6.41	1.61
10	102	8.20	8.36	1.36

Table 4 Values of $(s/\xi_0)^n$, $|\dot{\delta}/\delta|s$, $(\ddot{\delta}/\delta)s^2$, and $\delta/\delta_0(0)$ at $s=10\xi_0$ for some values of n in the region of $n \leqslant 1.1$

n	$(s/\xi_0)^n$	$\lvert\delta'/\delta\rvert s$	$(\delta''/\delta)s^2$	$\delta/\delta(0)$
0	1	0	0	0.5
0.2	1.58	0.12	0.13	0.39
0.4	2.51	0.29	0.34	0.29
0.6	3.98	0.48	0.65	0.20
0.8	6.31	0.69	1.09	0.14
1.0	10	0.91	1.65	0.09
1.1	12.6	1.02	1.98	0.07

pressed by a reasonable relation given below, the severity between the other two conditions $|\delta'/\delta|\xi_0 \ll 1$ and $|\delta''/\delta|\xi_0^2 \ll 1$ is compared at $s=10\xi_0$. Finally, a condition is presented to be applied to judge whether strain data measured at positions s in the region of $s \geqslant 10\xi_0$ satisfy the severe condition.

Increments $\Delta r_0 = r_0(t) - r_0(0)$, $\Delta\xi_0 = \xi_0 - \xi_0(0)$, and $\Delta r_1 = r_1(t) - r_1(0) = r_1(t)$ $[\equiv s]$ are introduced, and a notation where $\zeta(t) \equiv r_0(t)$ and $\zeta(0) \equiv r_0(0) \equiv \xi_0(0)$ is used, so that $\Delta\zeta[\equiv \Delta r_0]$ is expressed by $\Delta\zeta = s + \Delta\xi_0$. Furthermore, a ratio of two rates $\alpha = [\Delta\xi_0/\xi_0(0)]/[\Delta\zeta/\zeta(0)]$ or $\alpha = y/x$ $[y \equiv \Delta\xi_0/\xi_0(0)$ and $x \equiv \Delta\zeta/\zeta(0)]$, which represents the degree of increase in the wave front thickness with propagation, is introduced. Here, y is the rate of increase from 0 to t in the effective wave front thickness, and x is that in the effective propagation distance. The distance s is expressed by $s = (1-\alpha)\Delta\zeta$. The rate y should satisfy the following two conditions. (1) The rate y increases monotonically with an increase in the rate x. (2) The rate approaches to a value as the rate x becomes large. Condition (1) is self-evident. Condition (2) is based on the fact that as a spherical wave front proceeds, it approaches to a steady plane wave front [3]. For $s/\xi_0 \geqslant 10$, a relation $y = \alpha_0 x/(x+b)$ that satisfies both conditions, or $\xi_0 = \xi_0(0)[\alpha_0 x/(x+b)+1]$, where α_0 is a value of y at $x \to \infty$, and b is a constant, is adopted. The relation for y yields a relation $\alpha = \alpha_0/(x+b)$, which has a reasonable property that the value of α decreases monotonically up to $\alpha=0$ with an increase in the rate x. A quadratic equation $x^2 - ax - bs/\xi_0 = 0$, where $a = (1+\alpha_0)(s/\xi_0) + \alpha_0 - b$, is obtained from three relations $\alpha = \alpha_0/(x+b)$, $s = (1-\alpha)\Delta\zeta$, and $\xi_0 = \zeta(0)(1+\alpha x)$. Transformation of the quadratic equation yields $s/\xi_0 = [x^2 + (b-\alpha_0)x]/[(1+\alpha_0)x + b]$, which relates s/ξ_0 to x. The rate x is related to s/ξ_0 by a solution $x = (1/2)[a + (a^2 + 4bs/\xi_0)^{1/2}]$ of the quadratic equation.

The following relation is derived by substituting the above equation for y into $\xi_0' \equiv \xi_0(0)\mathrm{d}y/\mathrm{d}s$

$$\xi_0' = b\alpha_0/[(x+b)\{x+b(1-\alpha)\}]$$

The value of ξ_0' decreases with an increase in the distance s. Values of $\Delta\zeta/\zeta(0)$, α, $\Delta\xi_0/\xi_0(0)$, and ξ_0' at $s=10\xi_0$ are listed in Table 2 for $b=20$ and some values of α_0 in the region of $\alpha_0 \leqslant 10$, and in Table 3 for $\alpha_0=6$ and some values of b in the region of $b \leqslant 50$. As the value of b increases, the value of $\Delta\xi_0/\xi_0(0)$ decreases, and the value of ξ_0' increases. For any values of α_0 and b examined here, the values of ξ_0' are smaller than a value of 10^{-1}, and therefore the condition $\xi_0' \ll 1$ is satisfied for $s \geqslant 10\xi_0$. Next, the following relation is obtained by substituting the above equation for ξ_0' into $\xi_0 \mathrm{d}\xi_0'/\mathrm{d}s$.

$$|\xi_0''|\xi_0 = 2\xi_0'(\xi_0/s)(1-\alpha)x(x+b)/[\,x+b(1-\alpha)\}]^2$$

Since $(1-\alpha)x(x+b)/[\,x+b(1-\alpha)\}]^2 \cong 1$, inequalities $|\xi_0''|\xi_0 < \xi_0'$, and therefore $|\xi_0''|\xi_0 \ll 1$ hold for $s \geqslant 10\xi_0$.

Table 3 Values of $\Delta\zeta/\zeta(0)$, α, $\Delta\xi_0/\xi_0$, and ξ_0' at $s=10\xi_0$ for $\alpha_0=6$ and some values of b in the region of $b \leqslant 50$

b	$\Delta\zeta/\zeta(0)$	$\alpha \times 10^2$	$\Delta\xi_0/\xi_0(0)$	$\xi_0' \times 10^2$
10	67.5	7.74	5.23	1.01
20	59.4	7.56	4.49	1.94
30	51.8	7.34	3.80	2.77
40	44.9	7.07	3.17	3.44
50	38.9	6.75	2.62	3.95

For $s \geqslant 10\xi_0$, if $|\delta'/\delta|s < 1$, then $|\delta'/\delta|\xi_0 < 10^{-1}$, while if $|\delta''/\delta|s^2 < 10$, then $|\delta''/\delta|\xi_0^2 < 10^{-1}$. The severity between the two conditions $|\delta'/\delta|s < 1$ and $|\delta''/\delta|s^2 < 10$ is compared at $s=10\xi_0$ by estimating values of $|\delta'/\delta|s$ and $|\delta''/\delta|s^2$. A relation $\delta = \delta(0)/(z+1)$, where $z \equiv (s/\xi_0)^n$, is adopted as $\delta(s/\xi_0)$. This relation for δ has a feature that for a fixed value of s/ξ_0, the amount of attenuation of the amplitude $[\delta(0)-\delta]$ is larger for the larger value of n. Note that δ is a function of s/ξ_0. Differentiation of δ with respect to s yields

$$|\delta'/\delta|s = [nz/(z+1)][1-\xi_0'(s/\xi_0)]$$

Table 2 shows $\xi_0'(s/\xi_0) \ll 1$, so that $|\delta'/\delta|s \cong nz/(z+1)$. By further differentiating,

$$(\delta''/\delta)s^2 \cong nz/(z+1) + n^2 z(z-1)/(z+1)^2$$

For some values of n in the region of $n \leqslant 1.1$, values of $(s/\xi_0)^n$, $|\delta'/\delta|s$, $(\delta''/\delta)s^2$, and $\delta/\delta(0)$ at $s=10\xi_0$ are listed in Table 4. For $n < 1.1$, it is found that $|\delta'/\delta|\xi_0 < 10^{-1}$ and $|\delta''/\delta|\xi_0^2 < 10^{-1}$. At any given values of n, the condition $|\delta'/\delta|s < 1$ is more severe than the condition $|\delta''/\delta|s^2 < 10$, because $(10 - |\delta''/\delta|s^2) > (1 - |\delta'/\delta|s)$. For some values of n in the region of $n \leqslant 1.1$, and at $s/\xi_0 = 10$, 15, 20, 25, and 30, values of ratio $\delta/\delta(10)$, which is expressed by $\delta/\delta(10) = (10^n+1)/(z+1)$, are listed in Table 5. At any given values of s/ξ_0, the amount of attenuation $[\delta(10)-\delta]$ is larger for the larger value of n.

To judge whether strain data measured at positions s in the region of $s \geqslant 10\xi_0$ satisfy the condition $|\delta'/\delta|s < 1$, a critical amplitude ratio $\delta_m(s/\xi_0)/\delta_m(10)$ is introduced. The ratio is expressed by

Table 5 Values of ratios $\delta/\delta(10)$ at $s/\xi_0=10$, 15, 20, 25, and 30 for some values of n in the region of $n \leqslant 1.1$

	s/ξ_0				
n	10	15	20	25	30
0.2	1	0.948	0.912	0.887	0.866
0.4	1	0.888	0.814	0.758	0.716
0.6	1	0.816	0.706	0.632	0.572
0.8	1	0.752	0.609	0.517	0.451
1.0	1	0.688	0.524	0.422	0.355
1.1	1	0.658	0.485	0.383	0.315

Table 6 Values of s/ξ_0 and $\delta_m/\delta_m(10)$ evaluated in the case of $\xi_0'(s/\xi_0)\ll 1$ for some given values of m in the region of $1.0<m<1.1$

m	s/ξ_0	$\delta_m/\delta_m(10)$
1.01	95.5	0.111
1.02	46.3	0.225
1.03	30.1	0.341
1.04	22.1	0.460
1.05	17.3	0.582
1.06	14.2	0.706
1.07	12.0	0.834
1.08	10.4	0.965

$$\delta_m/\delta_m(10) = (10^m + 1)/[(s/\xi_0)^m + 1]$$

where m (>1) is a number that satisfies $|\delta'/\delta|s=[nz/(z+1)][1-\xi_0'(s/\xi_0)]$; where $|\delta'/\delta|s=1$, that is, $[mz/(z+1)](1-\xi_0' s/\xi_0)=1$ where $z\equiv(s/\xi_0)^m$. A critical curve $\delta_m/\delta_m(10)-s/\xi_0$ can be drawn by first evaluating s/ξ_0 for given values of m from $s/\xi_0=\exp[-(1/m)\log\{m(1-\xi_0' s/\xi_0)-1\}]$ applying an iteration method, and then $\delta_m/\delta_m(10)$ using values of $(s/\xi_0)^m$. For some given values of m in the region of $1.0<m<1.1$, values of s/ξ_0 and $\delta_m/\delta_m(10)$ evaluated in the case of $\xi_0'(s/\xi_0)\ll 1$ are listed in Table 6.

Two differential inequalities $d(|\delta'/\delta|s)/dn>0$ for $s/\xi_0\geqslant 1$ and $d\delta/dn<0$ for $s/\xi_0>10$ are demonstrated. The first inequality indicates that the value of $|\delta'/\delta|s$ increases with an increase in the value of n, and therefore that $|\delta'/\delta|s<1$ for $n<m$. The second indicates that the value of δ decreases with an increase in the value of n, and therefore that δ_m has a minimum for $n<m$. For a measured value of s/ξ_0 in the region of $s/\xi_0>10$, if a measured value of $\delta/\delta(10)$ is larger than the calculated value of $\delta_m/\delta_m(10)$, then the condition $|\delta'/\delta|s<1$ is satisfied. Thus, for the amplitudes that follow $\delta=\delta(10)(10^n+1)/(z+1)$, if $\delta/\delta(10)>\delta_m/\delta_m(10)$, then the RH jump conditions hold approximately at positions s where the measurements were carried out. For strain data measured at positions s in a region of $s/\xi_0\geqslant k$, where $k\geqslant 1$, the judgment can be performed in the same manner as mentioned above by using a value of k instead of a value of 10. This method of judgment is also applicable to strain data measured in plate impact experiments.

4 Jump Equations for Spherical Waves of General Form

4.1 Equations. Figure 2(a) schematically shows strain waves in outgoing spherical wave fronts $\varepsilon(r,t)$ at time t_1 when the leading edge of the wave front, which is at position 0 at time 0, has arrived at a fixed position r_1, at time t when it proceeds to position $r_0(t)$, and at time T when it further proceeds to $r_0(T)$, at which point the rear of the wave front is at r_1. It is found from $r_0(t_1)\equiv r_1(T)\equiv r_1$ that as position r_1 is distant from the center of the wave front, the times t_1 and T increase. At t in $t_1<t\leqslant T$, the wave front has a range $r_1\leqslant r\leqslant r_0(t)$. Equations (1) and (2) are integrated from r to r_0 to become

$$u-\left(\frac{r_0}{R}\right)^2 u_0=\frac{1}{R^2}\int_r^{r_0} r^2\frac{\partial\varepsilon}{\partial t}dr \tag{17}$$

$$\sigma-\sigma_0=\rho_0\int_r^{r_0}\left(\frac{r}{R}\right)^2\frac{\partial u}{\partial t}dr+2\int_r^{r_0}\frac{\rho_0}{\rho}\frac{r^2}{R^3}(\sigma-\sigma_\theta)dr \tag{18}$$

where u and σ denote $u(r,t)$ and $\sigma(r,t)$, respectively.

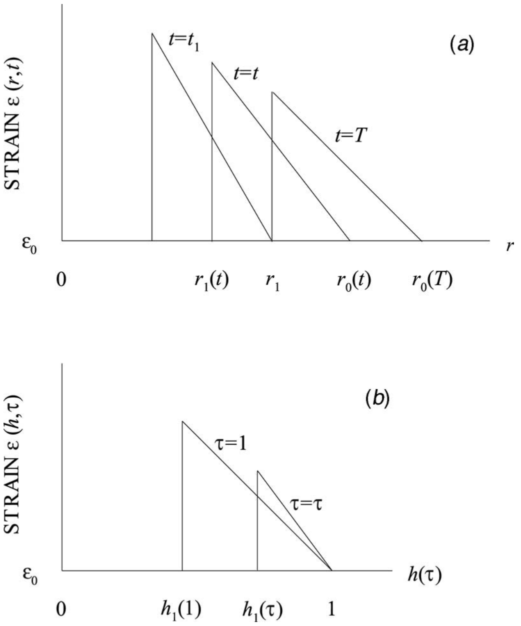

Fig. 2 Schematic diagrams of (a) strain waves in outgoing spherical wave fronts $\varepsilon(r,t)$ at three times t_1, t, and T from t_1 to T when the wave front is passing through a fixed position r_1; and (b) strain waves $\varepsilon(h,\tau)$ at $\tau=\tau$ and $\tau=1$, where τ is the dimensionless time expressed by $\tau=t/T$, and h is the dimensionless position expressed by $h=r/\zeta(\tau)$, where $\zeta(\tau)$ is the position of the leading edge of the wave front at τ. Three positions $r_0(t_1)$, $r_1(T)$, and r_1 are identical, that is, $r_0(t_1)\equiv r_1(T)\equiv r_1$.

A dimensionless time $\tau=t/T$ and a dimensionless position $h(\tau)=r/\zeta(\tau)$ are introduced here. Because the leading edge is at position 0 at time 0, $\zeta(\tau)$ is expressed by $\zeta(\tau)\equiv r_0(t)=\int_0^t c(t)dt$ or $\zeta(\tau)=T\int_0^\tau c(\tau)d\tau$, where $c(t)$ or $c(\tau)$ is the leading edge velocity. The strain waves $\varepsilon(h,\tau)$ at $\tau=\tau$ and at $\tau=1$ are shown schematically in Fig. 2(b). The wave front has a dimensionless range $h_1(\tau)\leqslant h(\tau)\leqslant 1$ at τ in $\tau_1<\tau\leqslant 1$, where $\tau_1=t_1/T$ and $h_1(\tau)=r_1/\zeta(\tau)$. The symbol h denotes $h(\tau)$ below. As the wave front thickness is thin, the value of τ_1 approaches to a value of 1. It follows from $t_1<T$ that $\tau_1<1$, and from $\zeta(\tau_1)\equiv r_0(t_1)=r_1$ that $h_1(\tau_1)=1$. The value of $h_1(\tau)$ decreases from a value of 1 at $\tau=\tau_1$ to a value of $h_1(1)$ at $\tau=1$, that is, $h_1(1)\leqslant h_1(\tau)\leqslant 1$. The dimensionless position $h_1(1)$ is expressed by $h_1(1)=1/[1+\xi_0(1)/r_1]$, where $\xi_0(1)$ is the wave front thickness at $\tau=1$. Asay et al. [5] observed near the impact surface in the plate impact experiment that as the position r_1 is distant from the surface, the thickness $\xi_0(1)$ increases, with the increment in $\xi_0(1)$ that is much less than that in r_1. Therefore, it is found that as the position r_1 is distant from the center of the wave front $r_1=0$, the position $h_1(1)$ is also distant from the center $h_1(1)=0$. Variables depending on h and τ are also identical to the variables depending on r and t. For example, $\varepsilon(h,\tau)\equiv\varepsilon(r,t)$.

A strain wave in a spherical wave front $\varepsilon(h,\tau)$ is expressed by a power series with respect to h up to the nth-order ($n\geqslant 1$) term

$$\varepsilon-\varepsilon_0=\sum_{i=0}^{n} f_i(\tau)h^i \tag{19}$$

where $[\varepsilon(h_1,\tau)-\varepsilon_0]$ is the amplitude of the stain wave at τ. Note that the power series is the approximation assumed for a wide class of wave forms. The equation for the radial particle velocity wave corresponding to the strain wave is obtained by substituting Eq. (19) into Eq. (17) as follows:

$$u-u_0=T^{-1}\left(\frac{r_0}{R}\right)^2\left[\sum_{i=0}^{n}\left\{\frac{1}{i+3}(\dot f_i\zeta-if_i\dot\zeta)(1-h^{i+3})\right\}\right.$$
$$\left.+\frac{1}{3}r_0\dot\varepsilon_0(1-h^3)\right]+\left\{\left(\frac{r_0}{R}\right)^2-1\right\}u_0 \tag{20}$$

where u and ζ denote $u(h,\tau)$ and $\zeta(\tau)$, respectively, and the dots on the variables refer to the differentiation with respect to τ. Here, r_0/R is expressed by $r_0/R=\{h+\bar u(r,\tau)/\bar c(\tau)\}^{-1}$, where $\bar c=(1/\tau)\int_0^\tau c(\tau)d\tau$ and $\bar u=(1/\tau)\int_{\tau_r}^\tau u(r,\tau)d\tau$, where τ_r is the dimensionless time that the leading edge has reached position r. Here, $[u(h_1,\tau)-u_0]$ is the amplitude of the particle velocity wave at τ. The particle velocity $u(h,\tau)$ depends on a combination of the strain and strain rate (f_i and $\dot f_i$), the position and velocity of the leading edge (ζ and $\dot\zeta$), and position h. The equation for the radial stress wave corresponding to the strain wave is obtained by substituting Eq. (20) into Eq. (18) as follows:

$$\sigma-\sigma_0=T^{-2}\rho_0\int_h^1\left(\frac{r_0}{R}\right)^2\left(\frac{r}{R}\right)^2\left(2\left(\frac{\dot r_0}{r_0}-\frac{\dot R}{R}\right)\left[\sum_{t=0}^{n}\left\{\frac{1}{i+3}\zeta(\dot f_i\zeta-if_i\dot\zeta)(1-h^{i+3})\right\}+\frac{1}{3}r_0^2\dot\varepsilon_0(1-h^3)\right]\right.$$
$$+\sum_{i=0}^{n}\left[\frac{1}{i+3}\zeta\{\ddot f_i\zeta+(1-i)\dot f_i\dot\zeta-if_i\ddot\zeta\}(1-h^{i+3})\right]+\sum_{i=0}^{n}\{\dot\zeta(\dot f_i\zeta-if_i\dot\zeta)h^{i+3}\}$$
$$\left.+r_0\left\{\frac{1}{3}(r_0\ddot\varepsilon_0+\dot r_0\dot\varepsilon_0)(1-h^3)+\dot r_0\dot\varepsilon_0h^3\right\}+\mathrm{Tr}_0\left(2\frac{\dot r_0}{r_0}u_0-2\frac{\dot R}{R}u_0+\dot u_0\right)\right)dh+2\int_h^1\frac{\rho_0}{\rho}\frac{r_0}{R}\left(\frac{r}{R}\right)^2(\sigma-\sigma_\theta)dh \tag{21}$$

where σ denotes $\sigma(h,\tau)$, and $r/R=h(h+\bar u/\bar c)^{-1}$, $\dot r_0/r_0=(c/\bar c)\tau^{-1}$, and $\dot R/R=(u/\bar c)(h+\bar u/\bar c)^{-1}\tau^{-1}$. Here, $[\sigma(h_1,\tau)-\sigma_0]$ is the amplitude of the stress wave at τ. The stress $\sigma(h,\tau)$ depends on a combination of the strain, strain rate, and strain acceleration (f_i, $\dot f_i$, and $\ddot f_i$), the position, velocity, and acceleration of the leading edge (ζ, $\dot\zeta$, and $\ddot\zeta$), and position h.

The position, the velocity, and the acceleration $\zeta(\tau)$, $\dot\zeta(\tau)$, and $\ddot\zeta(\tau)$ are expressed by

$$\zeta=\bar cT\tau,\quad \dot\zeta=cT,\quad \ddot\zeta=\dot cT$$

At $\tau=1$ at $h=h_1(1)$, Eqs. (20) and (21) are jump equations

$$u_1-u_0=\frac{c}{\{h_1(1)+\bar u/\bar c\}^2}\left[\sum_{i=0}^{n}\left\{\frac{1}{i+3}(\dot f_i(\bar c/c)-if_i)(1-h_1(1)^{i+3})\right\}\right] \tag{22}$$

where $f_i\equiv f_i(1)$, $c\equiv c(1)$, $\bar c\equiv\bar c(1)=\int_0^1c(\tau)d\tau$, and $\bar u\equiv\bar u(r_1,1)=\int_{\tau_1}^1u(r_1,\tau)d\tau$, and

$$\sigma_1-\sigma_0=\rho_0c^2\int_{h_1(1)}^1\frac{h^2}{(h+\bar u/\bar c)^4}\left[2\left(1-\frac{u/c}{h+\bar u/\bar c}\right)\sum_{t=0}^{n}\frac{1}{i+3}\{\dot f_i(\bar c/c)\right.$$
$$-if_i\}(1-h^{i+3})+\sum_{i=0}^{n}\frac{1}{i+3}(\bar c/c)\{\ddot f_i(\bar c/c)+(1-i)\dot f_i$$
$$\left.-if_i(\dot c/c)\}(1-h^{i+3})+\sum_{i=0}^{n}\{\dot f_i(\bar c/c)-if_i\}h^{i+3}\right]dh$$
$$+2\int_{h_1(1)}^1\frac{\rho_0}{\rho}\frac{h^2}{(h+\bar u/\bar c)^3}\{\sigma(h,1)-\sigma_\theta(h,1)\}dh \tag{23}$$

where the values $\varepsilon_0=0$ and $u_0=0$ are assumed. For finite values of $f_i(1)$, $\dot f_i(1)$, and $\ddot f_i(1)$, the amounts of both jumps are finite. Equations (22) and (23) are called jump equations for an outgoing spherical wave front of general form.

4.2 Geometrical Effect. The jumps are examined at $h_1(1)$ in the region of $u(r,\tau)/c(\tau)\ll h_1(1)\ll 1$, where r is in $r_1\leqslant r\leqslant r_0(1)$ and τ is in $\tau_1\ll\tau\leqslant 1$. The position of the rear of the wave front r_1 is expressed by $r_1=[h_1(1)/\{1-h_1(1)\}]\xi_0(1)$. The equation for r_1 indicates that $r_1\ll\xi_0(1)$ for $h_1(1)\ll 1$, that is, the position r_1 is near the center of the wave front. In addition, it is found from $\bar u(r_1,1)/\bar c(1)\cong(1-\tau_1)u(r_1,1)/c(1)$ that $\bar u(r_1,1)/\bar c(1)\ll h_1(1)$ for $u(r_1,1)/c(1)\ll h_1(1)$. Therefore, for $u(r_1,1)/c(1)\ll h_1(1)$, Eq. (22) is reduced to an equation in which $h_1(1)$ is separated from f_i and $\dot f_i$ as follows:

$$u_1-u_0\cong ch_1(1)^{-2}\sum_{i=0}^{n}\frac{1}{i+3}\{\dot f_i(\bar c/c)-if_i\} \tag{24}$$

As an example, inequalities $m[u(r_1,1)/c(1)]\leqslant h_1(1)\leqslant 1/m$, where $m\geqslant 5$, are given to the region of $h_1(1)$ where Eq. (24) holds. In this case, $u(r_1,1)/c(1)<0.04$ is obtained for $m=5$. For $m=5$ and $u/c=0.02$, the value of $h_1(1)$ increases from $h_1(1)=0.1$ to $h_1(1)=0.2$ in the region of $0.02\ll h_1(1)\ll 1$. Since the wave front thickness $\xi_0(1)$ does not vary greatly as described in Sec. 4.1, the value $h_1(1)=0.1$ is transformed to the value $(r_1)_1=(1/9)\xi_0(1)$, and the value $h_1(1)=0.2$ to the value $(r_1)_2=0.25\xi_0(1)$, indicating that two positions $(r_1)_1$ and $(r_1)_2$ are close. Distance $0.14\xi_0(1)$ between the two positions of the leading edges $[(r_1)_1+\xi_0(1)]$ and $[(r_1)_2+\xi_0(1)]$ is very short. While the leading edge moves for such a short distance, the value of $\bar c(1)/c(1)$ is nearly constant, so that $\Sigma[\{\dot f_i(\bar c/c)-if_i\}/(i+3)]\cong\Sigma[\{\dot f_i-if_i\}/(i+3)]$ holds in Eq. (24). During such a short propagation time, if the strain wave in the wave front attenuates only slightly, then the value of $\Sigma[\{\dot f_i-if_i\}/(i+3)]$ is nearly constant, because neither values of $f_i(1)$ and $\dot f_i(1)$ vary greatly. In the region of $0.1\leqslant h_1(1)\leqslant 0.2$, even for the strain wave that attenuates only slightly, the amount of the jump (u_1-u_0) is reduced approximately proportionally to $h_1(1)^{-2}$.

For $u(r,1)/c(1)\ll h_1(1)$, approximations $(h+\bar u/\bar c)\cong h$ and $(u/c)/(h+\bar u/\bar c)\cong 0$ hold in the region of $h_1(1)\leqslant h\leqslant 1$. Under these approximations, Eq. (23) is integrated to reduce to

Table 7 Values of f at $h_1(1)=0.1$, 0.15, and 0.2 for some values of n

	$h_1=(0.1)$		
n	0.1	0.15	0.2
0	1	1.24	1.40
0.4	1	1.13	1.20
0.8	1	1.01	0.99
1.2	1	0.88	0.79
1.6	1	0.77	0.63

$$\sigma_1-\sigma_0 \cong \rho_0 c^2 h_1(1)^{-1}\left(\sum_{i=0}^{n} a_i(1)\left[1-h_1(1)-\frac{1}{i+2}h_1(1)\right.\right.$$
$$\left.\times\{1-h_1(1)^{i+2}\}\right]+h_1(1)\sum_{i=0}^{n}\frac{1}{i+2}\{\dot{f}_i(\bar{c}/c)-if_i\}$$
$$\left.\times\{1-h_1(1)^{i+2}\}+2h_1(1)\int_{h_1(1)}^{1}\frac{1}{\rho c^2}\frac{\sigma-\sigma_\theta}{h}dh\right) \tag{25}$$

where

$$a_i(1)=\frac{1}{i+3}[\ddot{f}_i(\bar{c}/c)^2+(3-i)\dot{f}_i(\bar{c}/c)-if_i\{2+(\bar{c}/c)(\dot{c}/c)\}]$$

Because $h_1(1) \ll 1$, Eq. (25) has a simple form where $h_1(1)$ separates from f_i, $\dot{f}_i$, and $\ddot{f}_i$ as follows:

$$\sigma_1-\sigma_0 \cong \rho_0 c^2 h_1(1)^{-1}\left[A(1)+2h_1(1)\int_{h_1(1)}^{1}\frac{1}{\rho c^2}\frac{\sigma-\sigma_\theta}{h}dh\right] \tag{26}$$

where $A(1)=\Sigma a_i(1)$ and $c \equiv c(1)$. As explained above, $A(1) \cong \text{const}$ for the strain wave that attenuates only slightly.

In the region of $0.1 \leqslant h_1(1) \leqslant 0.2$, the dependence of the second term in brackets on the right side of Eq. (26) on $h_1(1)$ is examined by expressing this term by $B(1)f[h_1(1)]$, where variable f has $f=1$ at $h_1(1)=0.1$, and $B(1)$ represents $B(\tau)$ at $\tau=1$. As a result, Eq. (26) is expressed by

$$\sigma_1-\sigma_0 \cong \rho_0 c^2 A(1) h_1(1)^{-1}\left[1+\frac{B(1)}{A(1)}f\right]$$

If the value of $(\sigma-\sigma_\theta)/\rho$ varies greatly with propagation, then the value of $B(1)$ also varies. Regardless of such a variation of the value of $B(1)$, if $B(1) \ll A(1)$, then the second term in brackets on the right side of the above equation can be neglected. This indicates that even for the strain wave that attenuates only slightly, the amount of the jump $(\sigma_1-\sigma_0)$ is reduced approximately proportionally to $h_1(1)^{-1}$. If $B(1) \cong A(1)$ and furthermore the value of f decreases or does not increase greatly with an increase in the value of $h_1(1)$, then even for the strain wave that attenuates only slightly, the amount of the jump $(\sigma_1-\sigma_0)$ is reduced greatly. As an example, for some viscous fluids and solids, which may have a mechanical property that follows a monotone decreasing function of $h(1)$, $(\sigma-\sigma_\theta)/\rho=(1/2)c^2Bh(1)^{-n}$, where $B=B(1)/[(0.1^{1-n}-0.1)/n]$, the variable $f=[h_1(1)^{1-n}-h_1(1)]/(0.1^{1-n}-0.1)$ is evaluated in a region of $h_1(1) \leqslant h(1) \leqslant 1$. The values of f are listed in Table 7 for some values of n. For the values of n examined, the function f does not increase greatly with an increase in the value of $h_1(1)$.

In a region of $m(u/c) \leqslant h_1(1) \leqslant (1/m)^{1/2}$ where $m \geqslant 5$, Eq. (24) is also an approximate equation for Eq. (22). In this case, Eq. (24) has a lower precision of approximation with respect to $h_1(1)$. Because $h_1(1)^2 \ll 1$ in this region of $h_1(1)$, an approximate equation for Eq. (25) is

$$\sigma_1-\sigma_0 \cong \rho_0 c^2\left[h_1(1)^{-1}\left\{A(1)+2h_1(1)\int_{h_1(1)}^{1}\frac{1}{\rho c^2}\frac{\sigma-\sigma_\theta}{h}dh\right\}\right.$$
$$\left.+C(1)\right] \tag{27}$$

where

$$C(1)=\sum_{i=0}^{n}\frac{1}{i+2}[\dot{f}_i(\bar{c}/c)-if_i-a_i(1)]-A(1)$$

For $m=5$, inequalities $5(u/c) \leqslant h_1(1) \leqslant 0.45$ and $u/c < 0.09$ hold.

5 Conclusions

The Rankine–Hugoniot (RH) type equations were derived for the jumps in radial particle velocity and stress across an outgoing spherical wave front of finite rise time. For a linear volumetric strain wave ε, it was shown that the effect of the curvatures in the wave front might be neglected at distances of movement of the rear of the wave front s that were more than ten times as long as the effective wave front thickness ξ_0. Furthermore, a method was developed to judge the applicability of the RH jump conditions to the jumps at these distances. If the values of strain amplitude ratio $\delta(s/\xi_0)/\delta(10)$ measured are larger than the calculated value of the critical ratio $\delta_m(s/\xi_0)/\delta_m(10)$, the RH jump conditions are applicable. For strain data measured at positions s in a region of $s/\xi_0 \geqslant k$ $(k \geqslant 1)$, the judgment can also be performed in the same manner. This method of judgment is also applicable to strain data measured in plate impact experiments. The jump equations for spherical wave fronts of general form were also derived. For $\varepsilon < 0.09$, these equations showed that the particle velocity and stress in the jumps were greatly reduced near the center of the wave front by the effect of the curvatures.

References

[1] Rankine, W. J. M., 1870, "On the Thermodynamic Theory of Waves of Finite Longitudinal Disturbance," Trans. R. Soc. London, **160**, pp. 277–288.

[2] Hugoniot, H., 1889, "Sur la Propagation du Movement dans les Corps," J. Ec. Polytech. (Paris), **58**, pp. 1–125.

[3] Davison, L., 1971, "Shock-Wave Structure in Porous Solids," J. Appl. Phys., **42**, pp. 5503–5512.

[4] Gupta, Y. M., 1972, "Stress Relaxation in Shock Loaded Lithium Fluoride Single Crystals," Ph.D. thesis, Washington State University.

[5] Asay, J. R., Fowles, G. R., Durall, G. E., Miles, M. H., and Tinder, R. F., 1972, "Effects of Point Defects on Elastic Precursor Decay in LiF," J. Appl. Phys., **43**, pp. 2132–2145.

[6] Seaman, L., 1974, "Lagrangian Analysis for Multiple Stress or Velocity Gages in Attenuating Waves," J. Appl. Phys., **45**, pp. 4303–4314.

[7] Walsh, J. M., Rice, M. H., McQueen, R. G., and Yarger, F. L., 1957, "Shock-Wave Compressions of Twenty-Seven Materials. Equations of State of Metals," Phys. Rev., **108**, 196–216.

[8] Sano, Y., 1997, "Shock Jump Equations for Unsteady Wave Fronts," J. Appl. Phys., **82**, pp. 5382–5390.

[9] Sano, Y., and Miyamoto, I., 1998, "Shock Jump Equations for Unsteady Wave Fronts of Finite Rise Time," J. Appl. Phys., **84**, pp. 6606–6613.

[10] Sano, Y., 1999, "Precursor Decay Anomaly in Single-Crystal Lithium Fluoride," J. Appl. Phys., **85**, 7616–7625.

[11] Grady, D. E., 1973, "Experimental Analysis of Spherical Wave Propagation," J. Geophys. Res., **78**, pp. 1299–1307.

[12] Fowles, G. R., 1970, "Conservation Relations for Spherical and Cylindrical Stress Waves," J. Appl. Phys., **41**, pp. 2740–2741.

[13] Ranga Rao, M. P., 1986, "Spherical Shocks in Solids," *Shock Waves in Condensed Matter-1985*, Y. M. Gupta, ed., Elsevier, New York, pp. 681–685.

[14] Sano, Y., and Miyamoto, I., 2000, "Generalized Smooth and Weak-Discontinuous Unsteady Waves," J. Math. Phys., **41**, pp. 6233–6247.

[15] Sano, T., and Sano, Y., 2001, "Equilibrium Thermodynamic Theory Explicitly Including Heat Transport for Evaluation of Temperature Distributions in Steady Plane-Wave Fronts," J. Appl. Phys., **90**, pp. 5576–5584.

Experimental Data Have to Decide Which of the Nonprobabilistic Uncertainty Descriptions—Convex Modeling or Interval Analysis—to Utilize

Xiaojun Wang[1]
Institute of Solid Mechanics,
Beijing University of Aeronautics and Astronautics,
Beijing, 100083, P.R.C.
e-mail: xjwang@buaa.edu.cn

Isaac Elishakoff
Department of Mechanical Engineering,
Florida Atlantic University,
Boca Raton, FL 33431-0991
e-mail: elishako@fau.edu

Zhiping Qiu
Institute of Solid Mechanics,
Beijing University of Aeronautics and Astronautics,
Beijing, 100083, P.R.C.
e-mail: zpqiu@buaa.edu.cn

This study shows that the type of the analytical treatment that should be adopted for nonprobabilistic analysis of uncertainty depends on the available experimental data. The main idea is based on the consideration that the maximum structural response predicted by the preferred theory ought to be minimal, and the minimum structural response predicted by the preferred theory ought to be maximal, to constitute a lower overestimation. Prior to the analysis, the existing data ought to be enclosed by the minimum-volume hyper-rectangle V_1 that contains all experimental data. The experimental data also have to be enclosed by the minimum-volume ellipsoid V_2. If V_1 is smaller than V_2 and the response calculated based on it $R(V_1)$ is smaller than $R(V_2)$, then one has to prefer interval analysis. However, if V_1 is in excess of V_2 and $R(V_1)$ is greater than $R(V_2)$, then the analyst ought to utilize convex modeling. If V_1 equals V_2 or these two quantities are in close vicinity, then two approaches can be utilized with nearly equal validity. Some numerical examples are given to illustrate the efficacy of the proposed methodology. [DOI: 10.1115/1.2912988]

Keywords: uncertainty description, convex modeling, interval analysis, ellipsoid, hyper-rectangle

1 Introduction

Probabilistic approaches are used by numerous analysts for the safety assessment of structures whose parameters or loadings on them are modeled as uncertain variables or functions. In recent decades, some alternatives of it have been suggested. Fuzzy-sets based approaches gain much popularity. There are many discussions on philosophical implications of each of these approaches. Whereas the probabilistic methodology requires the knowledge of probability densities, the fuzzy-sets based approaches demand the knowledge of membership functions. More recently, yet another alternative is embraced by the investigators, that is, not based on any specified measure, either probabilistic or fuzzy, of uncertain variables. It presupposes the knowledge only of bounds of uncertain quantities. These are then called as unknown-but-bounded or uncertain-but-bounded variables. This analysis is both old and new. It is chronologically old but new by its revived use. Apparently, the first work on the response of a single-degree-of-freedom system under uncertain-but-bounded excitation was written by Bulgakov [1] in 1946. He especially mentioned that the task is to calculate the upper bounds of structural response "under unfavorable circumstances," when the "disturbing action $y_p(t)(p=1,2,\ldots,r)$ satisfies the condition $|y_p(t)|\leq l_p$ (l_p constant) but are otherwise arbitrary one-valued continuous functions of the time t possessing as many derivatives as necessary." This problem was dubbed by Bulgakov [1] as the "problem of accumulation of disturbances" (see also his other paper [2], in 1940, which considers a special case).

There is considerable literature in the Russian language on the Bulgakov problem. Independently, in late 1960s, Schweppe [3] developed an analogous thinking based on ellipsoidal modeling, representing the uncertain variables as belonging to an ellipsoid.

Recently, some researchers in uncertain mechanics develop interval analysis, whereas others follow convex modeling [4–12]. The question arises if these analyses are specifically interrelated, should one perform both analyses, or one of them is preferable? This work tries to elucidate the possible reply to this question. Some researchers performed a comparison of results derived by both methods. Elishakoff et al. [13] derived a minimum-volume ellipsoid that encloses the minimum-volume parallelepiped for buckling analysis. Elishakoff et al. [14] studied the buckling of elastic column on nonlinear elastic foundation by interval analysis, whereas Qiu et al. [15] dealt with the same problem via convex modeling. Qiu and Wang [16] specially distinguished between these two nonprobabilistic set-theoretical models.

Although convex modeling and interval analysis have been extensively used, in practice, which of the nonprobabilistic uncertain descriptions, convex modeling or interval analysis, should be preferred? In this study, this problem will be answered. The experimental data are shown to be of the cardinal influence on which of these methods ought to be given a preference.

Consider the case that due to high cost of the measurements, the experimental points are too scant to determine their statistical information on uncertain parameters: If we choose nonprobabilistic set-theoretical convex methods, convex modeling or interval analysis, for uncertain modeling, then the precondition is to seek or determine the suitable set containing the limited experimental points. In fact, there is more than one set to be able to enclose the limited experimental points. However, too big set will produce overconservative bounds on the structural responses. Of course, it is impossible for us to know the real bounds on uncertain param-

---

[1] Corresponding author.

Contributed by the Applied Mechanics Division of ASME for publication in the JOURNAL OF APPLIED MECHANICS. Manuscript received June 28, 2007; final manuscript received March 4, 2008; published online May 16, 2008. Review conducted by Martin Ostoja-Starzewski.

eters based on the limited experimental points. The enclosing set with minimal volume property may be a better selection, which will produce lower overestimation on the bounds of the structural responses. We can only act on what we know.

2 Description of the Method by Zhu, Elishakoff, and Starnes

In this section, the description of the method by Zhu et al. [17], in which the smallest hyper-rectangle and the smallest ellipsoid containing the given experimental data are determined, is stated in brief.

Suppose that there are m uncertain parameters $a_i (i = 1,2,\ldots,m)$ describing either the structural properties or the excitation. These parameters constitute an m-dimensional parameter space, namely, $\mathbf{a}=(a_1,a_2,\ldots,a_m)$. Suppose that we have limited information on these parameters, represented by M experimental points, $\mathbf{a}^{(r)}(r=1,2,\ldots,M)$ in this m-dimensional space. Convex modeling assumes that all these experimental points belong to an ellipsoid

$$(\mathbf{a}-\mathbf{a}_0)^T\mathbf{W}(\mathbf{a}-\mathbf{a}_0) \leqslant 1 \tag{1}$$

where $\mathbf{a}_0$ is the state vector of the central point of the ellipsoid and $\mathbf{W}$ is the weight matrix. Interval analysis assumes that all experimental points belong to a hyper-rectangle.

By using transformation matrix $\mathbf{T}_m(\theta_1,\theta_2,\ldots,\theta_{m-1})$ given in Ref. [17], the above M points in the rotated coordinate system will have their new coordinates denoted by $\mathbf{b}^{(r)}(r=1,2,\ldots,M)$. To obtain the smallest ellipsoid, let us first examine an m-dimensional box of the form

$$|\mathbf{b}-\mathbf{b}_0| \leqslant \mathbf{d} \tag{2}$$

which contains all M points. The vector of semiaxes $d = (d_1,d_2,\ldots,d_m)^T$ and the vector of central points $\mathbf{b}_0 = (b_{10},b_{20},\ldots,b_{m0})^T$ of the "box" in the rotated coordinate system are given by

$$\begin{aligned} d_k &= \frac{1}{2}(\max_r(b_k^{(r)}) - \min_r(b_k^{(r)})) \\ b_{k0} &= \frac{1}{2}(\max_r(b_k^{(r)}) + \min_r(b_k^{(r)})) \end{aligned} \qquad (r=1,2,\ldots,M; k=1,2,\ldots,m) \tag{3}$$

We now enclose this box by an ellipsoid

$$\sum_{k=1}^{m} \frac{(b_k - b_{k0})^2}{g_k^2} \leqslant 1 \tag{4}$$

where g_k are the semiaxes of the ellipsoid. There are infinite number of ellipsoids that contain the box given in Eq. (2). Clearly, the best choice is the one with minimum volume. The volume of an m-dimensional ellipsoid is given by

$$V_e = C_m \prod_{k=1}^{m} g_k \tag{5}$$

where C_m is a constant.

From the monograph by Elishakoff et al. [13] and paper by Qiu [18], corresponding to the smallest ellipsoid, the semiaxes of the smallest ellipsoid should be

$$g_i = \sqrt{m} d_i \quad (i=1,2,\ldots,m) \tag{6}$$

Thus, once the size of the box (Eq. (2)) is known, the semiaxes of the minimum-volume ellipsoid enclosing the box of the experimental data are readily determined by utilizing Eq. (6). If there are no experimental points at the corner of the box, the size of such an ellipsoid may further be reduced until one of the experimental points reaches the surface of the ellipsoid. The semiaxes of the ellipsoid in this case may be replaced by ηg_k, where the factor is determined from the condition

$$\eta = \sqrt{\max_r \sum_{k=1}^{m} \frac{(b_k^{(r)} - b_{k0})^2}{g_k^2}} \leqslant 1 \quad (r=1,2,\ldots,M) \tag{7}$$

If there are some experimental points in the corner of the multidimensional box, the factor η equals unity. The ellipsoid (4) can be written in the form

$$(\mathbf{b}-\mathbf{b}_0)^T\mathbf{D}(\mathbf{b}-\mathbf{b}_0) \leqslant 1 \tag{8}$$

in which $\mathbf{b}_0$ is the vector of central points whose components are given by Eq. (3) and $\mathbf{D}$ is a diagonal matrix

$$\mathbf{D} = \mathrm{diag}((\eta g_1)^{-2},(\eta g_2)^{-2},\ldots,(\eta g_m)^{-2}) \tag{9}$$

The volume of the ellipsoid now reads

$$V_e = C_m \eta^m \prod_{k=1}^{m} g_k \tag{10}$$

which is a function of a set of parameters $\theta_k(k=1,2,\ldots,m-1)$. Therefore, the best ellipsoid among these ellipsoids is the one which contains all given points and possesses the minimum volume, i.e.,

$$V_e = \min_{\theta_1,\theta_2,\ldots,\theta_{m-1}} \{V_e(\theta_1,\theta_2,\ldots,\theta_{m-1})\} \tag{11}$$

A possible approach to determine this ellipsoid is to search among all possible cases by increasing $\theta_k(k=1,2,\ldots,m-1)$ from 0 to $\pi/2$ in sufficiently small increments $\Delta\theta_k$ and to compare the volumes of so obtained ellipsoids. Once one finds the ellipsoid with minimum volume in one direction, say, $\theta_{k0}(k=1,2,\ldots,m-1)$, the ellipsoid can be transformed back into the original coordinate system by applying the transformation matrix $\mathbf{T}_m$. Hence, the vector $\mathbf{a}_0$ of the central point and the weight matrix $\mathbf{W}$ in Eq. (1) become

$$\mathbf{a}_0 = \mathbf{T}_m^T\mathbf{b}_0, \quad \mathbf{W} = \mathbf{T}_m^T\mathbf{D}\mathbf{T}_m \tag{12}$$

where $\mathbf{T}_m=\mathbf{T}_m(\theta_{10},\theta_{20},\ldots,\theta_{m0})$. So, Eq. (12) constitutes the smallest ellipsoid containing all experimental points. The box corresponding to the smallest ellipsoid is the smallest hyper-rectangle.

3 Convex Modeling and Interval Analysis for the Structural Response

For convenience, in this section, convex modeling method and interval analysis method for the static response analysis of structures with uncertain parameters are reformulated (see Ref. [18]). In fact, the presented concept in this study can also be applied to other linear elastic structural mechanics problem with uncertainty, such as the natural frequency analysis, the dynamic response analysis, etc.

The matrix equation of static equilibrium in the finite element method can be written as

$$\mathbf{K}(\mathbf{a})\mathbf{u}(\mathbf{a}) = \mathbf{f}(\mathbf{a}) \tag{13}$$

where $\mathbf{K}=(k_{ij})$ is the $n \times n$-dimensional stiffness matrix, $\mathbf{u}=(u_i)$ is the n-dimensional nodal displacement vector, $\mathbf{f}=(f_i)$ is the n-dimensional external load vector, and $\mathbf{a}=(a_1,a_2,\ldots,a_m)^T$ is the structural parameters, such as the physical, material, and geometric properties in structures.

Consider a realistic situation in which not enough information is available on the structural parameters to justify an assumption on their probabilistic characteristics. It is assumed that by using the method of Zhu et al. [17], the derived smallest ellipsoid and the derived smallest hyper-rectangle on the structural parameters can be obtained as, respectively,

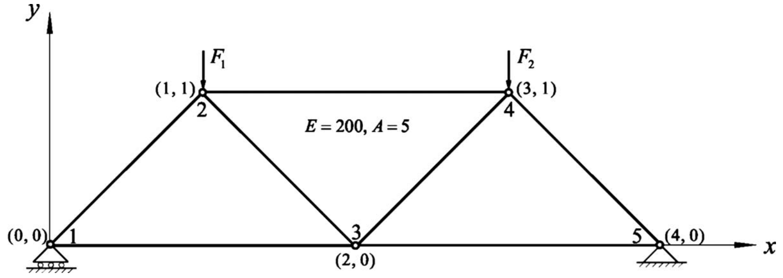

Fig. 1 A seven bar planar truss structure

$$Z(\mathbf{W},\theta) = \{\mathbf{a}:\mathbf{a} \in R^m, (\mathbf{a}-\mathbf{a}_0)^T\mathbf{W}(\mathbf{a}-\mathbf{a}_0) \leqslant \theta^2\} \tag{14}$$

and

$$\underline{\mathbf{a}} \leqslant \mathbf{a} \leqslant \bar{\mathbf{a}} \quad \text{or } \mathbf{a}_0 - \Delta\mathbf{a} \leqslant \mathbf{a} \leqslant \mathbf{a}_0 + \Delta\mathbf{a} \tag{15}$$

where $\mathbf{a}_0=(a_{i0}) \in R^m$ is the nominal value vector of the structural parameter vector $\mathbf{a}$, $\mathbf{W}$ is a positive definite matrix and is called the weight matrix, θ is a positive constant and is called the radius of the ellipsoid, $\underline{\mathbf{a}}$ and $\bar{\mathbf{a}}$ are the lower bound and upper bound of the hyper-rectangle, and $\Delta\mathbf{a}$ is the radius of the hyper-rectangle.

The structural parameter of a value slightly different from this nominal value can be denoted as

$$\mathbf{a} = \mathbf{a}_0 + \delta\mathbf{a} \quad \text{or } \mathbf{a}_i = \mathbf{a}_{i0} + \delta a_i, \quad i = 1,2,\ldots,m \tag{16}$$

where $\delta\mathbf{a}=(\delta a_i) \in R^m$ is a small quantity.

By Taylor's series expansion, the static displacement of the structure with uncertain parameter vector $\mathbf{a}=\mathbf{a}_0+\delta\mathbf{a}$, to first order in $\delta\mathbf{a}$, is

$$u_i(\mathbf{a}) = u_i(\mathbf{a}_0 + \delta\mathbf{a}) = u_i(\mathbf{a}_0) + \sum_{j=1}^{m} \frac{\partial u_i(\mathbf{a}_0)}{\partial a_j}\delta a_j, \quad i = 1,2,\ldots,n \tag{17}$$

For convenience of notation, let us define

$$\boldsymbol{\varphi}^T = \left(\frac{\partial u_i(\mathbf{a}_0)}{\partial a_1}, \frac{\partial u_i(\mathbf{a}_0)}{\partial a_2}, \ldots, \frac{\partial u_i(\mathbf{a}_0)}{\partial a_m}\right) = \left(\frac{\partial u_{i0}}{\partial a_1}, \frac{\partial u_{i0}}{\partial a_2}, \ldots, \frac{\partial u_{i0}}{\partial a_m}\right) \tag{18}$$

By combination of Eqs. (17) and (14), the most and least favorable response for convex modeling method can be obtained as (see Ref. [14])

$$\underline{\mathbf{u}}_C = \mathbf{u}_0 - \theta\sqrt{\boldsymbol{\varphi}^T\mathbf{W}^{-1}\boldsymbol{\varphi}} \quad \text{and } \bar{\mathbf{u}}_C = \mathbf{u}_0 + \theta\sqrt{\boldsymbol{\varphi}^T\mathbf{W}^{-1}\boldsymbol{\varphi}} \tag{19}$$

By combination of Eqs. (17) and (15), the most and least favorable responses for interval analysis method can be obtained as (see Ref. [18])

$$\underline{u}_{iI} = u_{i0} - \sum_{j=1}^{m}\left|\frac{\partial u_{i0}}{\partial a_j}\right|\Delta a_j \quad \text{and } \bar{u}_{iI} = u_{i0} + \sum_{j=1}^{m}\left|\frac{\partial u_{i0}}{\partial a_j}\right|\Delta a_j \tag{20}$$

Thus, in the case that the smallest intervals or hyper-rectangle containing uncertain parameters are known, interval analysis method can be adopted to obtain the most and least favorable responses. In the case that the smallest ellipsoid containing uncertain parameters are known, convex modeling method can be adopted to obtain the most and least favorable responses.

So, a question will arise. Which method is better? In other words, which method will give the tighter bounds on the structural responses? In the following, a 7-bar planar truss structure and a 60-bar space truss structure are used to reply to this quest.

4 Seven-Bar Planar Truss Structure

Let us consider a seven-bar planar truss structure with linear elastic properties depicted in Fig. 1. Here, $A=5$ is the cross-sectional area, $E=200$ is Young's modulus, F_1 is an external load at Node No. 2, and F_2 is an external load applied at Node No. 4. The parameters of the truss are given as dimensionless numbers, since the physical values are not relevant to our analysis.

This truss is the same as adopted by Skalna [19] but here the loads F_1 and F_2 are considered to be uncertain, and the other properties of the truss, such as A and E, are deterministic. Namely, the truss members have deterministic stiffness.

In the following, several sets of hypothesized data for uncertain parameters will be given. By using the method of Zhu et al. [17], the smallest ellipse and rectangle can be derived. Based on the derived ellipse and rectangle, the most and least favorable responses of the structure can be calculated by convex modeling method and interval analysis method, respectively.

We will discuss this problem in the following two cases: One is that the principal axes of the derived ellipse and rectangle are parallel to the global coordinate system; the other is that the principal axes of the derived ellipse and rectangle are not parallel to the global coordinate system.

4.1 Principal Axes of the Derived Ellipse and Rectangle are Parallel to the Global Coordinate System

Case I. Consider a set of hypothesized data for uncertain parameters as shown in Fig. 2, and they are listed in Table 1. Here, these hypothesized data are randomly generated in order to proceed to the numerical simulations, but in practice, the samples for uncertain parameters can be generally obtained by the experiments.

The smallest rectangle obtained from the set of data by using the method of Zhu et al. [17] is

$$F_1^I = [0.80, 1.20], \quad F_2^I = [0.90, 1.10] \tag{21}$$

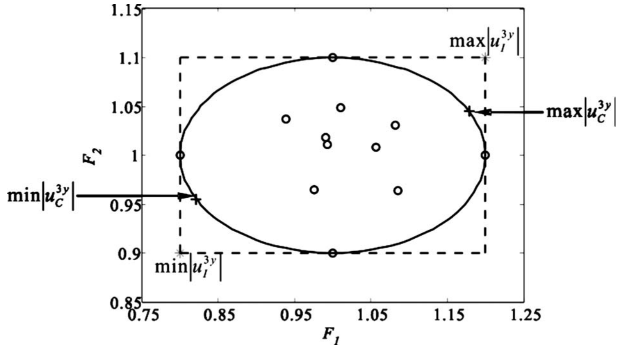

Fig. 2 Rectangle and ellipse containing the data on uncertain parameters F_1 and F_2

Table 1 The values of uncertain parameter F_1 and F_2

k	1	2	3	4	5	6	7	8	9	10	11	12
F_1	0.991	1.082	1.085	0.938	0.976	0.993	1.011	1.056	0.800	1.200	1.000	1.000
F_2	1.018	1.031	0.964	1.037	0.965	1.011	1.048	1.008	1.000	1.000	0.900	1.100

Based on Eq. (21), we conclude that the central values of F_1 and F_2 are, respectively,

$$F_{1c} = (0.80 + 1.20)/2 = 1.0, \quad F_{2c} = (0.90 + 1.10)/2 = 1.0 \tag{22}$$

and the values of radii F_1 and F_2 are, respectively,

$$\Delta F_1 = (1.20 - 0.80)/2 = 0.2, \quad \Delta F_2 = (1.10 - 0.90)/2 = 0.1 \tag{23}$$

Thus, one can analyze the system as subjected to an interval load vector with nominal values (1.0, 1.0) and scatter of (20%, 10%).

On the other hand, the smallest ellipse can be obtained from the set of data by using the method of Zhu et al. [17]. The optimal rotation angle θ_{10} obtained is 0 deg, so the transformation matrix $\mathbf{T}_2$ is

$$\mathbf{T}_2 = \begin{bmatrix} 1 & 0 \\ 0 & 1 \end{bmatrix} \tag{24}$$

In the case of $\theta_{10}=0$ deg, the vector of semiaxes and the vector of central point of the box in the optimal rotated coordinate system are, respectively, $d=(d_1,d_2)^T=(0.2,0.1)^T$ and $\mathbf{b}_0=(b_{10},b_{20})^T=(1.0,1.0)^T$. The semiaxes of the smallest ellipsoid are $g_1=\sqrt{2}d_1=0.2828$ and $g_2=\sqrt{2}d_2=0.1414$. The diagonal matrix $\mathbf{D}$ is

$$\mathbf{D} = \operatorname{diag}((\eta g_1)^{-2},(\eta g_2)^{-2}) = \operatorname{diag}(25,100) \tag{25}$$

where $\eta=\sqrt{2}/2$. Thus, we can get

$$\mathbf{a}_0 = \mathbf{T}_2^T\mathbf{b}_0 = (1.0,1.0)^T, \quad \mathbf{W} = \mathbf{T}_2^T\mathbf{D}\mathbf{T}_2 = \begin{bmatrix} 25 & 0 \\ 0 & 100 \end{bmatrix} \tag{26}$$

It can be seen from Fig. 2 that the derived rectangle contains the derived ellipse based on the hypothesized data listed in Table 1.

We can find that the higher-order derivatives of static responses of the seven-bar planar truss structure with respect to uncertain parameters are all zeros. Thus, Eq. (17) based on the first-order Taylor series for this example will be linear and exact, i.e.,

$$\begin{aligned} \mathbf{u}_i(F_1,F_2) &= \mathbf{u}_i(F_{1c} + \delta F_1, F_{2c} + \delta F_2) \\ &= \mathbf{u}_i(F_{1c},F_{2c}) + \frac{\partial \mathbf{u}_i(F_c)}{\partial F_1}\delta F_1 + \frac{\partial \mathbf{u}_i(F_c)}{\partial F_2}\delta F_2, \\ & i = 1,2,\ldots,n \end{aligned} \tag{27}$$

This is the reason why only the external loads are taken as the uncertain parameters in this study.

Taking the derivative of both sides of Eq. (13) yields

$$\frac{\partial \mathbf{K}}{\partial F_j}\mathbf{u} + \mathbf{K}\frac{\partial \mathbf{u}}{\partial F_j} = \frac{\partial \mathbf{f}}{\partial F_j}, \quad j = 1,2 \tag{28}$$

Due to the vanishing of $\partial K/\partial F_j$ for this problem, the sensitivity derivative of the structural response with respect to uncertain parameters becomes

$$\frac{\partial \mathbf{u}}{\partial F_j} = \mathbf{K}^{-1}\frac{\partial \mathbf{f}}{\partial F_j}, \quad j = 1,2 \tag{29}$$

Substitution of Eqs. (22), (23), and (29) into Eq. (20) yields the most and least favorable responses in the y-direction of Node 3 of the seven-bar planar truss structure obtained from interval analysis method as follows:

$$\min|u_I^{3y}| = 0.005803, \quad \max|u_I^{3y}| = 0.007852 \tag{30}$$

Substitution of Eqs. (26) and (29) into Eq. (19) provides us with the most and least favorable responses in the y-direction of Node 3 of the seven-bar planar truss structure obtained from convex modeling method as follows:

$$\min|u_C^{3y}| = 0.006064, \quad \max|u_C^{3y}| = 0.007591 \tag{31}$$

The "*" points on the derived rectangle in Fig. 2 are the most and least favorable points for interval analysis method. The "+" points on the derived ellipse in Fig. 2 are the most and least favorable points for convex modeling method. The two markers * and + have the same meaning in sequel figures.

Thus, it can be seen from Eqs. (30) and (31) that interval analysis method gives tighter bounds of responses than convex modeling method in the case of data points listed in Table 1.

Case II. Consider another set of hypothesized data for uncertain parameters as shown in Fig. 3, and they are listed in Table 2.

The smallest rectangle obtained from the set of data by using the method of Zhu et al. [17] is

$$F_1^I = [0.90,1.10], \quad F_2^I = [0.95,1.05] \tag{32}$$

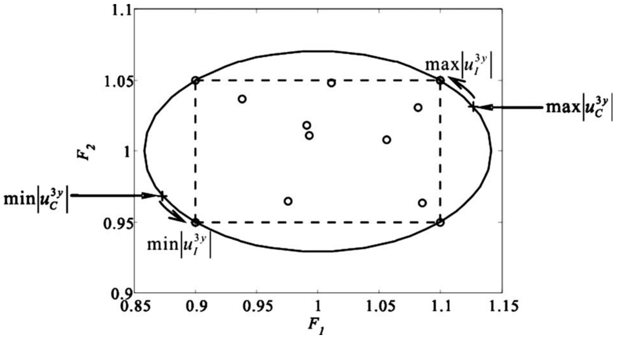

Fig. 3 Rectangle and ellipse containing the data on uncertain parameters F_1 and F_2

Table 2 The values of uncertain parameter F_1 and F_2

k	1	2	3	4	5	6	7	8	9	10	11	12
F_1	0.991	1.082	1.085	0.938	0.976	0.993	1.011	1.056	0.900	1.100	1.100	0.900
F_2	1.018	1.031	0.964	1.037	0.965	1.011	1.048	1.008	0.950	0.950	1.050	1.050

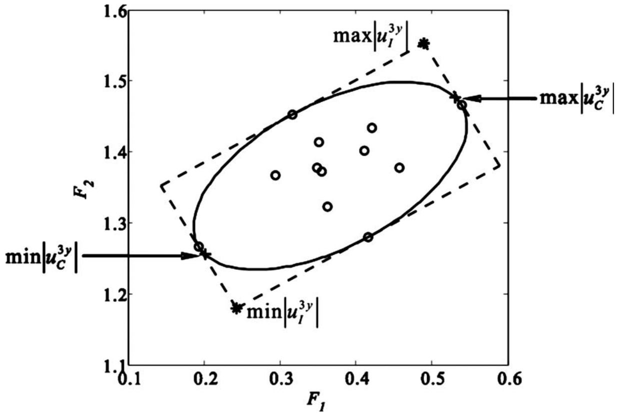

Fig. 4 Rectangle and ellipse containing the data on uncertain parameters F_1 and F_2

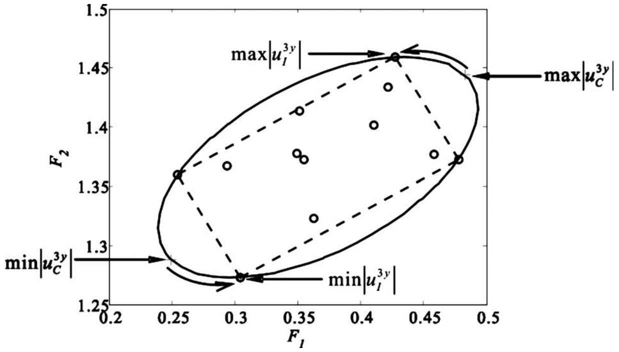

Fig. 5 Rectangle and ellipse containing the data on uncertain parameters F_1 and F_2

Based on Eq. (32), we conclude that the central values and the values of radii of F_1 and F_2 are, respectively,

$$F_{1c} = 1.0, \quad F_{2c} = 1.0, \quad \text{and } \Delta F_1 = 0.1, \quad \Delta F_2 = 0.05 \tag{33}$$

Thus, one can analyze the system as subjected to an interval load vector with nominal values (1, 1) and scatter of (10%, 5%).

On the other hand, the smallest ellipse can be obtained from the set of data by using the method of Zhu et al. [17]. The optimal rotation angle θ_{10} obtained is 0 deg. Similar to Eqs. (24)–(26), the vector $\mathbf{a}_0$ of the central point and the weight matrix $\mathbf{W}$ can be obtained as

$$\mathbf{a}_0 = \mathbf{T}_2^T\mathbf{b}_0 = (1.0, 1.0)^T, \quad \mathbf{W} = \mathbf{T}_2^T\mathbf{D}\mathbf{T}_2 = \begin{bmatrix} 50 & 0 \\ 0 & 200 \end{bmatrix} \tag{34}$$

It can be seen from Fig. 3 that the derived ellipse contains the derived rectangle based on the hypothesized data listed in Table 2.

By substituting Eqs. (33) and (29) into Eq. (20) and substituting Eqs. (34) and (29) into Eq. (19), the most and least favorable responses in the y-direction of Node 3 of the seven-bar planar truss structure can be, respectively, obtained from the interval analysis method and convex modeling method as follows:

$$\min|u_I^{3y}| = 0.006316, \quad \max|u_I^{3y}| = 0.007340 \tag{35}$$

and

$$\min|u_C^{3y}| = 0.006288, \quad \max|u_C^{3y}| = 0.007367 \tag{36}$$

Thus, it can be seen from Eqs. (35) and (36) that convex modeling method gives tighter bounds of responses than interval analysis method in the case of data points listed in Table 2.

Under this circumstance, an interesting phenomenon can be seen. For convex modeling method, the extreme value points on the ellipse in Fig. 3 may be different based on different structural parameters. Namely, the locations of the extreme value points of convex modeling method will change by changing the structural parameters. In certain particular case, the extreme value points of convex modeling method and interval analysis method will coincide.

4.2 Principal Axes of the Derived Ellipse and Rectangle are *not* Parallel to the Global Coordinate System

Case I. Consider a set of hypothesized data for uncertain parameters as shown in Fig. 4, and they are listed in Table 3.

The smallest rectangle obtained from the set of data by using the method of Zhu et al. [17] is shown in Fig. 4. The smallest ellipse can be obtained from the set of data by using the method of Zhu et al. [17]. The optimal rotation angle θ_{10} obtained is 30 deg. Similarly, the vector $\mathbf{a}_0$ of the central point and the weight matrix $\mathbf{W}$ can be obtained as

$$\mathbf{a}_0 = \mathbf{T}_2^T\mathbf{b}_0 = (0.366, 1.366)^T, \quad \mathbf{W} = \mathbf{T}_2^T\mathbf{D}\mathbf{T}_2 = \begin{bmatrix} 43.75 & -32.48 \\ -32.48 & 81.25 \end{bmatrix} \tag{37}$$

As mentioned above, Eq. (17) based on the first-order Taylor series will be exact and linear for this example. Due to the convexity of the derived smallest rectangle, the most and least favorable responses in the y-direction of Node 3 of the seven bar planar truss structure for interval analysis method will reach on the four vertiees of the smallest rectangle. By calculating and comparing the four responses, the most and least favorable responses or the minimum and maximum values of them are, respectively,

$$\min|u_I^{3y}| = 0.004855, \quad \max|u_I^{3y}| = 0.006970 \tag{38}$$

By substituting Eqs. (37) and (29) into Eq. (19), we obtain the most and least favorable responses in the y-direction of Node 3 of the seven-bar planar truss structure obtained from convex modeling method as follows:

$$\min|u_C^{3y}| = 0.004972, \quad \max|u_C^{3y}| = 0.006854 \tag{39}$$

Table 3 The values of uncertain parameter F_1 and F_2

k	1	2	3	4	5	6	7	8	9	10	11	12
F_1	0.349	0.422	0.458	0.294	0.362	0.355	0.351	0.411	0.193	0.539	0.416	0.316
F_2	1.377	1.434	1.377	1.367	1.323	1.372	1.413	1.401	1.266	1.466	1.279	1.453

Table 4 The values of uncertain parameter F_1 and F_2

k	1	2	3	4	5	6	7	8	9	10	11	12
F_1	0.349	0.422	0.458	0.294	0.362	0.355	0.351	0.411	0.304	0.478	0.428	0.254
F_2	1.377	1.434	1.377	1.367	1.323	1.372	1.413	1.401	1.273	1.373	1.459	1.359

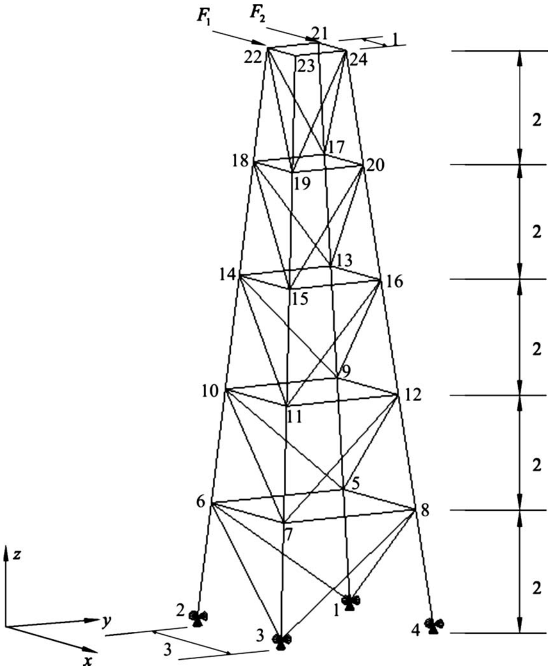

Fig. 6 A 60-bar space truss structure

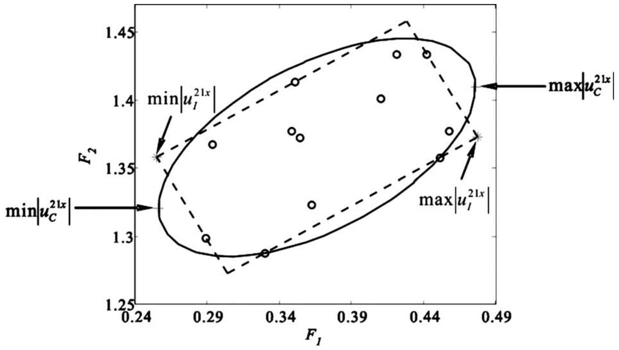

Fig. 7 Rectangle and ellipse containing the data on uncertain parameters F_1 and F_2

Thus, it can be seen from Eqs. (38) and (39) that interval analysis method gives tighter bounds of responses than convex modeling method in the case of data points listed in Table 3.

Case II. Consider another set of hypothesized data for uncertain parameters as shown in Fig. 5, and they are listed in Table 4.

The smallest rectangle obtained from the set of data by using the method of Zhu et al. [17] is shown in Fig. 5. The smallest ellipse can be obtained from the set of data by using the method of Zhu et al. [17]. The optimal rotation angle θ_{10} obtained is 30 deg. Similarly, the vector $\mathbf{a}_0$ of the central point and the weight matrix $\mathbf{W}$ can be obtained as

$$\mathbf{a}_0 = \mathbf{T}_2^T\mathbf{b}_0 = (0.366, 1.366)^T, \quad \mathbf{W} = \mathbf{T}_2^T\mathbf{D}\mathbf{T}_2 = \begin{bmatrix} 87.50 & -64.95 \\ -64.95 & 162.50 \end{bmatrix} \tag{40}$$

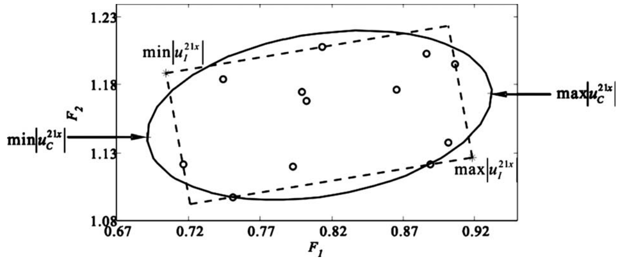

Fig. 8 Rectangle and ellipse containing the data on uncertain parameters F_1 and F_2

In perfect analogy with Eq. (38), the most and least favorable responses in the *y*-direction of Node 3 of the seven-bar planar truss structure for interval analysis method can be obtained as follows:

$$\min|u_I^{3y}| = 0.005384, \quad \max|u_I^{3y}| = 0.006441 \tag{41}$$

We substitute Eqs. (40) and (29) into Eq. (19) to get the most and least favorable responses in the *y*-direction of Node 3 of the seven-bar planar truss structure obtained from convex modeling method as follows:

$$\min|u_C^{3y}| = 0.005247, \quad \max|u_C^{3y}| = 0.006578 \tag{42}$$

Thus, it can be seen from Eqs. (41) and (42) that convex modeling method gives tighter bounds of responses than interval analysis method in the case of data points listed in Table 4. Although only the displacement responses in the *y*-direction of Node 3 of the seven-bar planar truss structure are compared, the analysis will not qualitatively change if a different aspect of response of the truss structure were used to carry out the comparisons of convex modeling with interval analysis due to the linear elastic properties.

We can find from the above analysis that the choice for two methods, convex modeling or interval analysis, is decided by the distribution of sample data points on uncertain parameters.

5 Sixty-Bar Space Truss Structure

Consider a 60-bar space truss structure with linear elastic properties subject to two *x*-directional loads, as shown in Fig. 6. The external loads F_1 and F_2, respectively, act on Node Nos. 21 and 22. Young's moduli of the bars are $E_i = 2.1 \times 10^{11} (i = 1, 2 \ldots, 60)$. The cross-sectional areas of the bars are $A_i = 1.0 \times 10^{-3} (i = 1, 2, \ldots, 60)$.

Suppose that the external loads F_1 and F_2 are still considered to be uncertain, and the other properties of the truss, such as *A* and *E*, are deterministic. Namely, the truss members have deterministic stiffness.

In the previous section, the case that there exists the inclusion relation between the derived ellipse and rectangle is studied. In this section, we will consider the noninclusion relation between them.

Case I. Consider a set of hypothesized data for uncertain parameters as shown in Fig. 7, and they are listed in Table 5.

The smallest rectangle obtained from the set of data by using the method of Zhu et al. [17] is shown in Fig. 7. The smallest ellipse can be obtained from the set of data by using the method of

Table 5 The values of uncertain parameter F_1 and F_2

k	1	2	3	4	5	6	7	8	9	10	11	12
F_1	0.349	0.422	0.458	0.294	0.362	0.355	0.351	0.411	0.330	0.452	0.443	0.289
F_2	1.377	1.434	1.377	1.367	1.323	1.372	1.413	1.401	1.288	1.358	1.433	1.299

Table 6 The values of uncertain parameter F_1 and F_2

k	1	2	3	4	5	6	7	8	9	10	11	12
F_1	0.7991	0.887	0.901	0.744	0.793	0.803	0.813	0.865	0.751	0.889	0.906	0.716
F_2	1.175	1.203	1.138	1.184	1.119	1.168	1.208	1.176	1.097	1.121	1.196	1.121

Zhu et al. [17]. The optimal rotation angle θ_{10} obtained is 30 deg. Similarly, the vector $\mathbf{a}_0$ of the central point and the weight matrix $\mathbf{W}$ can be obtained as

$$\mathbf{a}_0 = \mathbf{T}_2^T\mathbf{b}_0 = (0.3664,,1.3653)^T, \qquad (43)$$
$$\mathbf{W} = \mathbf{T}_2^T\mathbf{D}\mathbf{T}_2 = \begin{bmatrix} 119.71 & -91.10 \\ -91.10 & 224.91 \end{bmatrix}$$

Similar to Eqs. (38) and (41), the most and least favorable responses in the x-direction of Node 21 of the 60-bar space truss structure for interval analysis method can be obtained as follows:

$$\min|u_I^{21x}| = 1.6491 \times 10^{-7}, \quad \max|u_I^{21x}| = 3.0862 \times 10^{-7} \qquad (44)$$

Substitution of Eqs. (43) and (29) into Eq. (19) yields the most and least favorable responses in the x-direction of Node 21 of the 60-bar space truss structure obtained from convex modeling method as follows:

$$\min|u_C^{21x}| = 1.6575 \times 10^{-7}, \quad \max|u_C^{21x}| = 3.0777 \times 10^{-7} \qquad (45)$$

Thus, it can be seen from Eqs. (44) and (45) that convex modeling method gives tighter bounds of responses than interval analysis method in the case of data points listed in Table 5.

Case II. Consider another set of hypothesized data for uncertain parameters as shown in Fig. 8, and they are listed in Table 6.

The smallest rectangle obtained from the set of data by using the method of Zhu et al. [17] is shown in Fig. 8. The smallest ellipse is obtained from the set of data by using the method of Zhu et al. [17]. The optimal rotation angle θ_{10} obtained is 10 deg. Similarly, the vector $\mathbf{a}_0$ of the central point and the weight matrix $\mathbf{W}$ can be obtained as

$$\mathbf{a}_0 = \mathbf{T}_2^T\mathbf{b}_0 = (0.8113,1.1576)^T, \qquad (46)$$
$$\mathbf{W} = \mathbf{T}_2^T\mathbf{D}\mathbf{T}_2 = \begin{bmatrix} 73.46 & -35.98 \\ -35.98 & 271.17 \end{bmatrix}$$

Similar to Eq. (38), the most and least favorable responses in the x-direction of Node 21 of the 60-bar space truss structure for interval analysis method can be obtained as follows:

$$\min|u_I^{21x}| = 4.5511 \times 10^{-7}, \quad \max|u_I^{21x}| = 5.9339 \times 10^{-7} \qquad (47)$$

Substitution of Eqs. (46) and (29) into Eq. (19) results in the most and least favorable responses in the x-direction of Node 21 of the 60-bar space truss structure obtained from convex modeling method as follows:

$$\min|u_C^{21x}| = 4.4628 \times 10^{-7}, \quad \max|u_C^{21x}| = 6.0222 \times 10^{-7} \qquad (48)$$

Thus, it can be seen from Eqs. (47) and (48) that interval analysis method gives tighter bounds of responses than convex modeling method in the case of data points listed in Table 6.

From the analysis of this section, we can still find that the sample data points decide which of the nonprobabilistic uncertainty descriptions, convex modeling or interval analysis, to be preferred.

6 Conclusion

In this study, through numerical examples, convex modeling and interval analysis are extensively compared based on the same experimental points. Some explanations are given for the problem that which of the nonprobabilistic uncertainty descriptions, convex modeling or interval analysis, ought to be utilize. Given the experimental points, the smallest hyper-rectangle and the smallest ellipsoid containing them can be obtained. From these numerical examples, it can be concluded that (1) if V_1 is smaller than V_2, then one has to prefer interval analysis; (2) if V_1 is in excess of V_2, then the analyst ought to utilize convex modeling; and (3) if V_1 equals V_2 or these two quantities are in close vicinity, then two approaches can be utilized with nearly equal validity. Therefore, the type of the analytical treatment that should be adopted for nonprobabilistic analysis of uncertainty depends on the available experimental data.

Of course, the purpose of the paper is not to replace the probabilistic approach by the nonprobabilistic set-theoretic convex methods. The latter is a possible alternative or a supplementary way of the uncertainty analysis when scarce data are available to justify the probabilistic analysis. We conclude that the type of the analysis of uncertainty depends on the type and amount of available information.

Acknowledgment

X.W and Z.Q thank the National Outstanding Youth Science Foundation of the P.R. China (No. 10425208) and 111 Project (No. B07009) for support. I.E. expresses his grateful thanks to Beihang University for their kind and warm hospitality during his stay as a visiting Professor during months of April and May, 2007. He also appreciates the partial financial support by ONR, the J. M. Rubin Foundation of the Florida Atlantic University, Florida-Israel Institute, and the College of Judea and Samaria where he served as a Visiting Professor of Civil Engineering during May–August 2007.

References

[1] Bulgakov, B. V., 1946, "On the Accumulation of Disturbances in Linear Oscillatory Systems With Constant Coefficients," Proceedings of the USSR Academy of Sciences, **51**(5), pp. 343–345.

[2] Bulgakov, B. V., 1940, "Fehleranhaeufung Bei Kreiselapparaten," Ing.-Arch., **11**, pp. 461–469.

[3] Schweppe, F. C., 1968, "Recunsive State Estimation, Unknown but Bounded Errors and System Inputs," IEEE Trans. Autom. Control, **AC-13**, pp. 22–28.

[4] Ben-Haim, Y., and Elishakoff, I., 1990, *Convex Models of Uncertainty in Applied Mechanics*, Elsevier, Amsterdam.

[5] Rao, S. S., and Berke, L., 1997, "Analysis of Uncertain Structural System Using Interval Analysis," AIAA J., **35**, pp. 727–735.

[6] Lombardi, M., 1998, "Optimization of Uncertain Structures Using Non-Probabilistic Models," Comput. Struct., **67**(1–3), pp. 99–103.

[7] Pantelides, C. P., and Ganzerli, S., 1998, "Design of Trusses Under Uncertain Loads Using Convex Models," J. Struct. Eng., **124**(3), pp. 318–329.

[8] Ganzerli, S., and Pantelides, C. P., 1999, "Load and Resistance Convex Models for Optimum Design," Struct. Optim., **17**, pp. 259–268.

[9] Mullen, R. L., and Muhanna, R. L., 1999, "Bounds of Structural Response for all Possible Loading Combinations," J. Struct. Eng., **125**(1), pp. 98–106.

[10] Manson, G., 2005, "Calculating Frequency Response Functions for Uncertain Systems Using Complex Affine Analysis," J. Sound Vib., **288**, pp. 487–521.

[11] McWilliam, S., 2001, "Anti-Optimization of Uncertain Structures Using Interval Analysis," Comput. Struct., **79**, pp. 421–430.

[12] Moens, D., and Vandepitte, D., 2007, "Interval Sensitivity Theory and its Application to Frequency Response Envelope Analysis Of Uncertain Structures," Comput. Methods Appl. Mech. Eng., **196**, pp. 2486–2496.

[13] Elishakoff, I., Li, Y. W., and Starnes, Jr., J. H., 2001, *Non-Classical Problems*

in the Theory of Elastic Stability, Cambridge University Press, Cambridge.

[14] Elishakoff, I., Cai, G. Q., and Starnes, Jr., J. H., 1994, "Non-Linear Buckling of a Column With Initial Imperfection via Stochastic and Non-Stochastic Convex Models," Int. J. Non-Linear Mech., **29**(1), pp. 71–82.

[15] Qiu, Z. P., Ma, L. H., and Wang, X. J., 2006, "Ellipsoidal-Bound Convex Model for the Non-Linear Buckling of a Column With Uncertain Initial Imperfection," Int. J. Non-Linear Mech., **41**, pp. 919–925.

[16] Qiu, Z. P., and Wang, X. J., 2003, "Comparison of Dynamic Response of Structures With Uncertain-But-Bounded Parameters Using Non-Probabilistic Interval Analysis Method and Probabilistic Approach," Int. J. Solids Struct., **40**(20), pp. 5423–5439.

[17] Zhu, L. P., Elishakoff, I., and Strarnes, Jr., J. H., 1996, "Derivation of Multi-Dimensional Ellipsoidal Convex Model for Experimental Data," Math. Comput. Modell., **24**(2), pp. 103–114.

[18] Qiu, Z. P., 2003, "Comparison of Static Response of Structures Using Convex Models and Interval Analysis Method," Int. J. Numer. Methods Eng., **56**(12), pp. 1735–1753.

[19] Skalna, I., 2003, "Methods for Solving Systems of Linear Equations of Structure Mechanics With Interval Parameters," Comp. Assist. Mech. Eng. Sc., **10**, pp. 281–293.

Q. H. Fang

Y. W. Liu[1]
e-mail: liuyouw8294@sina.com

College of Mechanics and Aerospace,
Hunan University,
Changsha, 410082, P.R.C.

P. H. Wen
Department of Engineering, Queen Mary,
University of London,
London, El 4NS, U.K.

Screw Dislocations in a Three-Phase Composite Cylinder Model With Interface Stress

A three-phase composite cylinder model is utilized to study the interaction between screw dislocations and nanoscale inclusions. The stress boundary condition at the interface between nanoscale inclusion and the matrix is modified by incorporating surface/interface stress. The explicit solution to this problem is derived by means of the complex variable method. The explicit expressions of image forces exerted on screw dislocations are obtained. The mobility and the equilibrium positions of the dislocation near one of the inclusions are discussed. The results show that, compared to the classical solution (without interface stress), more equilibrium positions of the screw dislocation may be available when the dislocation is close to the nanoscale inclusion due to consider interface stress. Also, the mobility of the dislocation in the matrix will become more complex than the classical case. [DOI: 10.1115/1.2913041]

1 Introduction

Dislocation mobility plays a critical role in analyzing the physical and mechanical behavior of many materials, and this mobility is dependent on the internal forces acting on the dislocations [1]. The interaction of dislocations with inclusions embedded in the matrix is an important topic in studying the mechanical behavior of the materials. This is mainly due to the fact that internal forces acting on the dislocations can be significantly influenced by the presence of all kinds of inclusions. In view of its importance, this problem has received much attention for the past several decades (see, for example, Refs. [2–12] and references cited therein).

In general, bonding condition at the interface is one of the important factors that control the stress fields in studying the interaction between dislocations and inclusions. It is well known that the surface/interface of inclusions is a special region of very small thickness. Atoms at the surface/interface experience a different local environment than atoms in the interior of an inclusion, and the equilibrium position and energy of those atoms will, in general, be different from those of the atoms in the interior. Since the equilibrium lattice spacing in the surface/interface is different from that in the bulk, surface/interface stress appears. For a nanoscale inclusion, with a large ratio of the surface/interface region to the inclusion, the surface/interface plays a very important role, and there is thus a need to consider the contribution of the surface/interface stress [13]. A generic and mathematical exposition for elastic isotropic solids with the surface/interface energy (surface/interface stress) has been presented by Gurtin and his co-workers [14,15]. In their work, a surface/interface region is approximated as a vanishing thickness adhering to the bulk solid without slipping. The equilibrium and constitutive equations of the bulk solid are the same as those in the classical elasticity, while the surface has its own elastic constants and is characterized by an additional constitutive law. By utilizing this interface model (this model is the so-called interface stress model), great effort has been recently made to understand some unusual phenomena related to the interface stress in nanocomposites [16–22].

Most work mentioned above [2–12] on the dislocation was concerned with an isolated inclusion. It is noted that most of materials for applications are multiphase systems. Furthermore, for two-phase materials, when the inclusion phase has finite concentration, dislocation interacts not only with the nearest inclusion but also with the surrounding ones. However, to thoroughly probe the stress and strain fields based on all details of microstructure would be prohibitive. Fortunately, there is a reasonably simplified model to reflect the mean effect of these interactions. This model is the so-called three-phase model introduced by Christenson and Lo [23]. For a two-dimensional case, this model consists of three concentric regions: the inner circular region representing the inclusion phase, the intermediate annular region representing the matrix phase, and the infinitely extended outer region representing composite phase (or effective medium). In addition, the double inclusion model had been proposed by Tanaka and Mori [24] for considering the effect of the multiple inclusions.

Based on the three-phase composite cylinder model, Luo and Chen [25] derived the stress field due to an edge dislocation located in the intermediate matrix phase. Later, Xiao and Chen [26] investigated the interaction between a screw dislocation and surrounding circular inclusions with the above mentioned three-phase composite cylinder model. In these papers [25,26], all interfaces are assumed to be perfectly bonded (displacement and stress continuities are assumed to exist at interfaces). In addition, Wang and Shen [27] obtained an exact solution for the problem of an edge dislocation in a three-phase composite cylinder model with a sliding interface. In their work [27], the inclusion phase and the matrix phase circumferentially form homogeneous sliding interface and the edge dislocation is located in the matrix phase.

In the current paper, a three-phase composite cylinder model is utilized to study the interaction between screw dislocations and surrounding circular nanoscale inclusions. The screw dislocations are assumed to be located in the matrix phase. The boundary condition at the interface between the nanoscale inclusion and the matrix is modified by incorporating surface/interface stress [14]. The explicit complete expressions of elastic fields for one dislocation and two dislocations are derived. The corresponding image forces acting on the dislocations are also given. In particular, the motion and equilibrium positions of a single screw dislocation near one of the inclusions are presented by numerical calculations.

2 Model and Basic Equations

The schematic diagram of the three-phase composite cylinder model is shown in Fig. 1. The model consists of three concentric regions: the inner circular region representing the nanoscale inclu-

---

[1] Corresponding author.

Contributed by the Applied Mechanics Division of ASME for publication in the Journal of Applied Mechanics. Manuscript received July 13, 2007; final manuscript received December 25, 2007; published online May 16, 2008. Review conducted by Zhigang Suo.

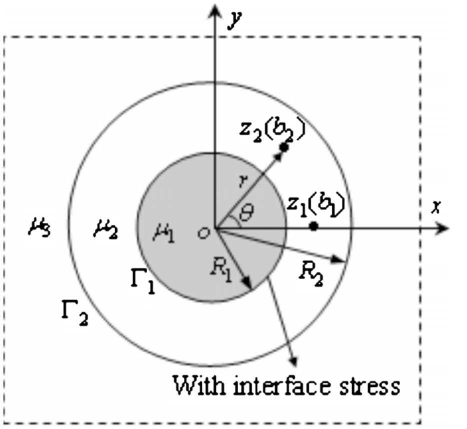

Fig. 1 Schematic diagram of screw dislocations in the three-phase composite cylinder model

sion phase with shear modulus μ_1, the intermediate annular region representing the matrix phase with shear modulus μ_2, and the infinitely extended outer region representing composite phase (effective medium) with shear modulus μ_3. The nanoscale inclusion is straight and infinitely extended in a direction perpendicular to the xy-plane. The symbols R_1 and R_2 are the inner and outer radii of the intermediate annular region (the matrix phase). Several parallel screw dislocations, which are assumed to be straight and infinite along the direction perpendicular to the xy-plane and suffer a finite discontinuity in the displacement across the slip plane, are located at arbitrary points in the matrix phase.

In the three-phase composite cylinder model scheme, the interface stress is additionally considered at the interface Γ_1 between the nanoscale inclusion and the matrix. According to Gurtin and Murdoch [14], the elastic field within the bulk solid is described by the differential equations of classical elasticity, while the interface Γ_1 has its own elastic constants and is characterized by an additional constitutive law. Under the assumption that the interface Γ_1 region adheres to the bulk solid without slipping and the body forces vanish, the equilibrium and constitutive equations for isotropic case have been given by Sharma et al. [16]. The conventional stress and displacement continuity conditions are assumed to prevail at the interface Γ_2 between the matrix and the effective medium.

For the current problem, the boundary conditions on the interfaces can be summarized as [16,28]

$$w_1(t) - w_2(t) = 0, \quad \tau_{rz1}(t) - \tau_{rz2}(t) = \frac{1}{R_1}\frac{\partial \tau^0_{\theta z}(t)}{\partial \theta}, \quad |t| = R_1 \quad (1)$$

$$w_2(t) - w_3(t) = 0, \quad \tau_{rz2}(t) - \tau_{rz3}(t) = 0, \quad |t| = R_2 \quad (2)$$

where w refers to antiplane displacement, and τ_{rz} and $\tau_{\theta z}$ are stress components in polar coordinates r and θ. The superscript "0" denotes the interface region and the subscripts 1, 2, and 3 refer to the inclusion, the matrix, and effective medium regions, respectively. The symbol t denotes the points on the circular arc interfaces. In addition, the constitutive equation for the interface $\Gamma_1(|t|=R_1)$ is given as [28]

$$\tau^0_{\theta z}(t) = 2(\mu^0 - \tau^0)\varepsilon^0_{\theta z}(t), \quad |t| = R_1 \quad (3)$$

where $\tau^0_{\theta z}$ and $\varepsilon^0_{\theta z}$ denote interfacial stress and strain, μ^0 is the interfacial elastic constant, and τ^0 is the residual interface tension. According to the work of Gurtin and Murdoch [14], the dimension of the elastic constant μ^0 is N/m. For a coherent interface, the interfacial strain $\varepsilon^0_{\theta z}$ is equal to the associated tangential strain in the abutting bulk materials. With semicoherent or incoherent interfaces, additional measures of the interfacial strain are required. In the following, we will study the case for a coherent interface.

Referring to the work of Muskhelishvili [29], in the bulk solid, the antiplane displacement w, and shear stresses τ_{rz} and $\tau_{\theta z}$ can be written in terms of an analytical function $f(z)$ of the complex variable $z=x+iy$ as follows:

$$w = [f(z) + \overline{f(z)}]/2 \quad (4)$$

$$\tau_{rz} - i\tau_{\theta z} = \mu f'(z)e^{i\theta} \quad (5)$$

where μ is the shear modulus of the isotropic material, the overbar represents the complex conjugate, and the prime denotes the derivative with respect to the argument z.

From Eq. (3), the second equation in Eq. (1), and the constitutive equation of the matrix $\tau_{\theta z2}=2\mu_2\varepsilon_{\theta z2}$, the stress boundary condition on the interface Γ_1 can be given as

$$\tau_{rz1}(t) - \tau_{rz2}(t) = \frac{(\mu^0 - \tau^0)}{R_1\mu_2}\frac{\partial \tau_{\theta z2}(t)}{\partial \theta}, \quad |t| = R_1 \quad (6)$$

where μ_2 is the shear modulus of the matrix.

The task now is to determine the complex potentials $f_1(z)$, $f_2(z)$, and $f_3(z)$ in the inclusion, the matrix, and effective medium regions, respectively, under the boundary conditions described by Eqs. (1), (2), and (6).

3 Solutions

First, consider a single screw dislocation with Burgers vector b_1 located at the point $z_1(z_1=x_1+iy_1)$ in the matrix. The complex potential in the matrix region can be taken in the form [3]

$$f_2(z) = \frac{b_1}{2\pi i}\ln(z - z_0) + f_{20}(z), \quad R_1 < |z| < R_2 \quad (7)$$

where function $f_{20}(z)$ is holomorphic in the region $R_1<|z|<R_2$. By neglecting the constant terms denoting the rigid body displacement, the analytical function $f_{20}(z)$ in the annular region can be expressed as a Laurent series in the form

$$f_{20}(z) = \sum_{k=0}^{\infty} c_k z^{-(k+1)} + \sum_{k=0}^{\infty} d_k z^{k+1}, \quad R_1 < |z| < R_2 \quad (8)$$

For the convenience of analysis, the following new analytical functions are introduced in the corresponding regions according to the Schwarz symmetry principle.

$$F_2(z) = zf_2'(z) = \frac{b_1}{2\pi i}\frac{z}{z - z_0} + G_N(z) + G_P(z), \quad R_1 < |z| < R_2 \quad (9)$$

$$F_{2*}(z) = \overline{F_2}(R_1^2/z) = \frac{b_1}{2\pi i}\left(\frac{z}{z - z^*} - 1\right) + \bar{G}_N(R_1^2/z) + \bar{G}_P(R_1^2/z), \quad R_1^2/R_2 < |z| < R_1 \quad (10)$$

$$F_{2**}(z) = \overline{F_2}(R_2^2/z) = \frac{b_1}{2\pi i}\frac{z}{z - z^{**}} + \bar{G}_N(R_2^2/z) + \bar{G}_P(R_2^2/z) \quad R_2 < |z| < R_2^2/R_1 \quad (11)$$

where $z^*=R_1^2/\overline{z_1}$, $z^{**}=R_2^2/\overline{z_1}$, $G_N(z)=-\Sigma_{k=0}^{\infty}(k+1)c_k z^{-(k+1)}$, and $G_P(z)=\Sigma_{k=0}^{\infty}(k+1)d_k z^{(k+1)}$.

According to the equilibrium condition of the interface Γ_2 between the matrix and the effective medium, the analytical function $F_3(z)$ in the effective medium regions is given by

$$F_3(z) = zf_3'(z) = \frac{b_1}{2\pi i} + F_{30}(z), \quad |z| > R_2 \quad (12)$$

where $F_{30}(z)$ is an analytical function in the effective medium region and $F_{30}(\infty)=\mathrm{O}(z^{-2})$.

With a view of Eq. (12), it is seen that

$$F_{3*}(z)=\overline{F_3}(R_2^2/z)=-\frac{b_1}{2\pi i}+F_{3*0}(z),\quad |z|<R_2 \tag{13}$$

Obviously, $F_1(z)=zf_1'(z)$ is holomorphic in the region $|z|<R_1$ for no existing singularities, and $F_{1*}(z)=\overline{F_1}(R_1^2/z)$ is holomorphic in the region $|z|>R_1$.

With the aid of Eqs. (4) and (5), the displacement and stress boundary conditions in Eq. (1) can be written as

$$[F_1(t)+F_{2*}(t)]^+=[F_2(t)+F_{1*}(t)]^-,\quad |t|=R_1 \tag{14}$$

$$\begin{aligned}&[\mu_1F_1(t)-\mu_2F_{2*}(t)-F_{2*}'(t)(\mu^0-\tau^0)/R_1]^+\\&=[\mu_2F_2(t)-\mu_1F_{1*}(t)-F_2'(t)(\mu^0-\tau^0)/R_1]^-,\quad |t|=R_1\end{aligned} \tag{15}$$

where the superscripts + and − denote the boundary values of a physical quantity as z approaches the interface.

By noting Eqs. (9) and (10) and according to the generalized Liouville theorem [29], Eqs. (14) and (15) lead to

$$h(z)=\begin{cases}F_1(z)+F_{2*}(z), & R_1^2/R_2<|z|<R_1\\ F_2(z)+F_{1*}(z), & R_1<|z|<R_2\end{cases} \tag{16}$$

$$g(z)=\begin{cases}\mu_1F_1(z)-\mu_2F_{2*}(z)-F_{2*}'(z)(\mu^0-\tau^0)/R_1, & R_1^2/R_2<|z|<R_1\\ \mu_2F_2(z)-\mu_1F_{1*}(z)-F_2'(z)(\mu^0-\tau^0)/R_1, & R_1<|z|<R_2\end{cases} \tag{17}$$

with

$$h(z)=\frac{b_1}{2\pi i}\left(\frac{z}{z-z_1}+\frac{z}{z-z^*}-1\right)+G_P(z)+\bar{G}_P(R_1^2/z) \tag{18}$$

$$\begin{aligned}g(z)=&\frac{\mu_2b_1}{2\pi i}\left(\frac{z}{z-z_0}-\frac{z}{z-z^*}+1\right)-\frac{b_1}{2\pi i}\frac{(\mu^0-\tau^0)}{R_1}\left[\frac{z}{z-z_1}\right.\\&\left.-\frac{z^2}{(z-z_1)^2}+\frac{z}{z-z^*}-\frac{z^2}{(z-z^*)^2}\right]+\mu_2[G_P(z)-\bar{G}_P(R_1^2/z)]\\&-\frac{(\mu^0-\tau^0)}{R_1}[zG_P'(z)+z\bar{G}_P'(R_1^2/z)]\end{aligned} \tag{19}$$

It is found from Eqs. (16) and (17) that

$$\begin{aligned}F_2(z)=&\frac{b_1}{2\pi i}\frac{z}{z-z_1}+\frac{\mu_1-\mu_2}{\mu_1+\mu_2}\frac{b_1}{2\pi i}\left(\frac{z}{z-z^*}-1\right)\\&+\frac{b_1}{2\pi i}\frac{(\mu^0-\tau^0)/R_1}{\mu_1+\mu_2}\frac{zz^*}{(z-z^*)^2}+G_P(z)+\frac{\mu_1-\mu_2}{\mu_1+\mu_2}\bar{G}_P(R_1^2/z)\\&+\frac{(\mu^0-\tau^0)}{R}[zG_N'(z)-z\bar{G}_P'(R_1^2/z)],\quad R_1<|z|<R_2\end{aligned} \tag{20}$$

The displacement and stress boundary conditions in Eq. (2) can be expressed as

$$[F_3(t)+F_{2**}(t)]^+=[F_2(t)+F_{3*}(t)]^-,\quad |t|=R_2 \tag{21}$$

$$[\mu_3F_3(t)-\mu_2F_{2**}(t)]^+=[\mu_2F_2(t)-\mu_3F_{3*}(t)]^-,\quad |t|=R_2 \tag{22}$$

Similarly, following Muskhelishvili [29] and considering Eqs. (9) and (11)–(13), the solutions of Eqs. (21) and (22) are explicitly derived as

$$T(z)=\begin{cases}F_2(z)+F_{3*}(z), & R_1<|z|<R_2\\ F_3(z)+F_{2**}(z), & R_2<|z|<R_2^2/R_1\end{cases} \tag{23}$$

$$\Omega(z)=\begin{cases}\mu_2F_2(z)-\mu_3F_{3*}(z), & R_1<|z|<R_2\\ \mu_3F_3(z)-\mu_2F_{2**}(z), & R_2<|z|<R_2^2/R_1\end{cases} \tag{24}$$

with

$$T(z)=\frac{b_1}{2\pi i}\left(\frac{z}{z-z_1}+\frac{z}{z-z^{**}}-1\right)+G_N(z)+\bar{G}_N(R_2^2/z) \tag{25}$$

$$\Omega(z)=\frac{\mu_2b_1}{2\pi i}\left(\frac{z}{z-z_1}+\frac{z}{z-z^{**}}+\frac{\mu_3}{\mu_2}\right)+\mu_2G_N(z)-\mu_2\bar{G}_N(R_2^2/z) \tag{26}$$

From Eqs. (23) and (24), we obtain the analytical function $F_2(z)$,

$$\begin{aligned}F_2(z)=&\frac{b_1}{2\pi i}\frac{z}{z-z_1}+\frac{\mu_3-\mu_2}{\mu_3+\mu_2}\frac{b_1}{2\pi i}\frac{z}{z-z^{**}}+G_N(z)\\&+\frac{\mu_3-\mu_2}{\mu_3+\mu_2}\bar{G}_N(R_2^2/z),\quad R_1<|z|<R_2\end{aligned} \tag{27}$$

In order to simultaneously satisfy all of the boundary conditions on the interfaces Γ_1 and Γ, the analytical function $F_2(z)$ expressed by Eqs. (20) and (27) must be compatible to each other [26]. Physically, the compatibility conditions $F_2(z)$ mean that the stress field and displacement field in the intermediate matrix ($R_1<|z|<R_2$) are unique. From Eqs. (20) and (27) as well as Eq. (9), we obtain the following equation to determine the unknown coefficients c_k and d_k.

$$\begin{aligned}&\frac{b_1}{2\pi i}\frac{\mu_2-\mu_3}{\mu_3+\mu_2}\sum_{k=0}^{\infty}\left(\frac{z}{z^{**}}\right)^{k+1}-\sum_{k=0}^{\infty}(1+k)c_kz^{-(1+k)}\\&+\frac{\mu_2-\mu_3}{\mu_3+\mu_2}\sum_{k=0}^{\infty}(1+k)\bar{c}_kR_2^{-2(1+k)}z^{(1+k)}\\&=\frac{b_1}{2\pi i}\frac{\mu_1-\mu_2}{\mu_1+\mu_2}\sum_{k=0}^{\infty}\left(\frac{z^*}{z}\right)^{k+1}+\sum_{k=0}^{\infty}(1+k)d_kz^{(1+k)}\\&+\frac{\mu_1-\mu_2}{\mu_1+\mu_2}\sum_{k=0}^{\infty}(1+k)\bar{d}_kR_1^{2(1+k)}z^{-(1+k)}+\frac{b_1}{2\pi i}\frac{(\mu^0-\tau^0)/R_1}{\mu_1+\mu_2}\\&\times\sum_{k=0}^{\infty}(1+k)\left(\frac{z^*}{z}\right)^{k+1}+\frac{(\mu^0-\tau^0)/R_1}{\mu_1+\mu_2}\left[\sum_{k=0}^{\infty}(1+k)^2c_kz^{-(1+k)}\right.\\&\left.+\sum_{k=0}^{\infty}(1+k)^2\bar{d}_kR_1^{2(1+k)}z^{-(1+k)}\right]\end{aligned} \tag{28}$$

Comparison of the coefficient of the same power terms yields

$$c_k=\frac{b_1}{2\pi i}\frac{\mu_2-\mu_1-(1+k)(\mu^0-\tau^0)/R_1}{1+k}\frac{(\mu_2+\mu_3)(R_1^2R_2^2/\bar{z}_1)^{(k+1)}+(\mu_3-\mu_2)R_1^{2(1+k)}z_1^{(k+1)}}{M} \tag{29}$$

$$d_k = \frac{b_1}{2\pi i}\frac{\mu_2 - \mu_3}{1+k}\frac{[\mu_1 + \mu_2 + (1+k)(\mu^0 - \tau^0)/R_1]\bar{z}_1^{(k+1)} + [\mu_1 - \mu_2 + (1+k)(\mu^0 - \tau^0)/R_1](R_1^2/z_1)^{(k+1)}}{M} \tag{30}$$

where $M=(\mu_3-\mu_2)[\mu_2-\mu_1-(1+k)(\mu^0-\tau^0)/R_1]R_1^{2(k+1)}+(\mu_2+\mu_3)[\mu_2+\mu_1+(1+k)(\mu^0-\tau^0)/R_1]R_2^{2(k+1)}$.

By substituting Eqs. (29) and (30) into Eq. (9), we obtain the solution of the analytical function $F_2(z)$,

$$F_2(z) = \frac{b_1}{2\pi i}\frac{z}{z-z_1} - \sum_{k=0}^{\infty}(k+1)c_k z^{-(k+1)} + \sum_{k=0}^{\infty}(k+1)d_k z^{(k+1)} \tag{31}$$

The solutions of the analytical functions $F_1(z)$ and $F_3(z)$ can be determined by Eqs. (16) and (17) as well as Eqs. (23) and (24).

Finally, by considering the relations $f_j(z)=\int[F_j(z)/z]dz$ $(j=1,2,3)$, the complete solutions of stress and displacement fields for the current problem can be obtained by means of Eqs. (4) and (5). Here, the explicit expressions of complex potentials $f_1(z)$, $f_2(z)$, and $f_3(z)$ are given as follows:

$$\begin{aligned} f_1(z) &= \frac{b_1}{2\pi i}\frac{2\mu_2}{\mu_1+\mu_2}\ln(z-z_1) + \frac{2\mu_2}{\mu_1+\mu_2}\sum_{k=0}^{\infty} d_k z^{(k+1)} \\ &\quad - \frac{b_1}{2\pi i}\frac{(\mu^0-\tau^0)}{R_1(\mu_1+\mu_2)}\left[2\ln(z-z_1) + \frac{z_1}{z-z_1}\right] \\ &\quad - \frac{(\mu^0-\tau^0)}{R_1(\mu_1+\mu_2)}\left[\sum_{k=0}^{\infty}(k+1)d_k z^{(k+1)} \right. \\ &\quad \left. - \sum_{k=0}^{\infty}\frac{1}{k+3}\bar{c}_k R_1^{-2(k+2)} z^{(k+3)}\right] \end{aligned} \tag{32}$$

$$f_2(z) = \frac{b_1}{2\pi i}\ln(z-z_1) + \sum_{k=0}^{\infty} c_k z^{-(k+1)} + \sum_{k=0}^{\infty} d_k z^{(k+1)} \tag{33}$$

$$f_3(z) = \frac{b_1}{2\pi i}\frac{2\mu_2}{\mu_3+\mu_2}\ln(z-z_1) + \frac{b_1}{2\pi i}\frac{\mu_3-\mu_2}{\mu_3+\mu_2} + \frac{2\mu_2}{\mu_3+\mu_2}\sum_{k=0}^{\infty} c_k z^{-(k+1)} \tag{34}$$

It is worth noting that from Eqs. (32)–(34), when the interface stresses vanish $(\mu^0=\tau^0=0)$, the solutions of complex potentials $f_j(z)$ are in agreement with the results of Xiao and Chen [26]. Here, we omit details for saving space. In addition, if we take $\mu_3=0$, the new solutions can be obtained for the two-phase cylinder model, which consists of a cylindrical nanoscale inclusion and a matrix with finite thickness.

4 Image Forces on Screw Dislocations

The image forces exerted on dislocations will be calculated in this section, which may play an important role in understanding the mobility and so-called trapping mechanism of the dislocations. According to the Peach–Koehler formula, the image force acting on a screw dislocation at the point z_1 can be obtained [11]

$$f_x - if_y = ib_1[\hat{\tau}_{xz2}(z_1) - i\hat{\tau}_{yz2}(z_1)] \tag{35}$$

where f_x and f_y are the force components in the x-axis and y-axis directions, respectively, and $\tau_{xz2}(z_1)$ and $\tau_{yz2}(z_1)$ denote the perturbation stress components at the dislocation point, which can be derived by subtracting those attributions to the dislocation in the corresponding infinite homogeneous medium from the current obtained stresses, then taking the limit as z approaches z_1. Referring to the work of Lee [30], the explicit expression of the image force acting on the screw dislocation for the present problem can be written as

$$\begin{aligned} f_x - if_y &= \frac{\mu_2 b_1^2(\mu_2-\mu_3)}{2\pi}\sum_{k=0}^{\infty}\frac{[\mu_1 + \mu_2 + (1+k)(\mu^0 - \tau^0)/R_1]\bar{z}_1^{(k+1)} + [\mu_1 - \mu_2 + (1+k)(\mu^0 - \tau^0)/R_1](R_1^2/z_1)^{(k+1)}}{z_1^{-k}M} \\ &\quad - \frac{\mu_2 b_1^2}{2\pi}\sum_{k=0}^{\infty}\frac{[\mu_2 - \mu_1 - (1+k)(\mu^0 - \tau^0)/R_1][(\mu_2+\mu_3)(R_1^2R_2^2/\bar{z}_1)^{(k+1)} + (\mu_3-\mu_2)R_1^{2(1+k)}z_1^{(k+1)}]}{z_1^{(k+2)}M} \end{aligned} \tag{36}$$

where $M=(\mu_3-\mu_2)[\mu_2-\mu_1-(1+k)(\mu^0-\tau^0)/R_1]R_1^{2(k+1)}+(\mu_2+\mu_3)[\mu_2+\mu_1+(1+k)(\mu^0-\tau^0)/R_1]R_2^{2(k+1)}$.

If we take $\mu_3=0$, the new solution of the image force acting on the dislocation is derived for the problem of a screw dislocation in the two-phase cylinder model, which consists of a cylindrical nanoscale inclusion and a matrix with finite thickness.

$$\begin{aligned} f_x - if_y &= \frac{\mu_2 b_1^2}{2\pi}\sum_{k=0}^{\infty}\frac{[\mu_1 + \mu_2 + (1+k)(\mu^0 - \tau^0)/R_1]\bar{z}_1^{(k+1)} + [\mu_1 - \mu_2 + (1+k)(\mu^0 - \tau^0)/R_1](R_1^2/z_1)^{(k+1)}}{z_1^{-k}m} \\ &\quad - \frac{\mu_2 b_1^2}{2\pi}\sum_{k=0}^{\infty}\frac{[\mu_2 - \mu_1 - (1+k)(\mu^0 - \tau^0)/R_1][(R_1^2R_2^2/\bar{z}_1)^{(k+1)} - R_1^{2(1+k)}z_1^{(k+1)}]}{z_1^{(k+2)}m} \end{aligned} \tag{37}$$

where $m=[\mu_2+\mu_1+(1+k)(\mu^0-\tau^0)/R_1]R_2^{2(k+1)}-[\mu_2-\mu_1-(1+k)\times(\mu^0-\tau^0)/R_1]R_1^{2(k+1)}$.

The image forces for the problem of multiple parallel screw dislocations located at arbitrary points in the matrix phase can be derived by the superposition method. Consider the case that two parallel screw dislocations with Burgers vectors b_1 and b_2 are located in points z_1 and z_2, respectively. The total image force on the dislocation z_1 is the summation of Eq. (35) and the image force exerted on the dislocation z_1 produced by the dislocation z_2. The result is

$$\begin{aligned} f_x - if_y = {} & \frac{\mu_2 b_1^2(\mu_2-\mu_3)}{2\pi}\sum_{k=0}^{\infty}\frac{[\mu_1+\mu_2+(1+k)(\mu^0-\tau^0)/R_1]\bar{z}_1^{(k+1)}+[\mu_1-\mu_2+(1+k)(\mu^0-\tau^0)/R_1](R_1^2/z_1)^{(k+1)}}{z_1^{-k}M} \\ & -\frac{\mu_2 b_1^2}{2\pi}\sum_{k=0}^{\infty}\frac{[\mu_2-\mu_1-(1+k)(\mu^0-\tau^0)/R_1][(\mu_2+\mu_3)(R_1^2R_2^2/\bar{z}_1)^{(k+1)}+(\mu_3-\mu_2)R_1^{2(1+k)}z_1^{(k+1)}]}{z_1^{(k+2)}M}+\frac{\mu_2 b_1 b_2}{2\pi(z_1-z_2)} \\ & +\frac{\mu_2 b_1 b_2(\mu_2-\mu_3)}{2\pi}\sum_{k=0}^{\infty}\frac{[\mu_1+\mu_2+(1+k)(\mu^0-\tau^0)/R_1]\bar{z}_2^{(k+1)}+[\mu_1-\mu_2+(1+k)(\mu^0-\tau^0)/R_1](R_1^2/z_2)^{(k+1)}}{z_1^{-k}M} \\ & -\frac{\mu_2 b_1 b_2}{2\pi}\sum_{k=0}^{\infty}\frac{[\mu_2-\mu_1-(1+k)(\mu^0-\tau^0)/R_1][(\mu_2+\mu_3)(R_1^2R_2^2/\bar{z}_2)^{(k+1)}+(\mu_3-\mu_2)R_1^{2(1+k)}z_2^{(k+1)}]}{z_1^{(k+2)}M} \end{aligned} \tag{38}$$

5 Numerical Examples and Discussion

Having the expressions of the image forces given in Eqs. (36)–(38), the influence of various parameters (the material elastic dissimilarity, the interface stress, and the location of the screw dislocation) upon image force acting on the screw dislocation can be evaluated in detail. The effect of the material mismatch and the dislocation location has been considered by Xiao and Chen [26]; thus, we will mainly focus on the impact of the interface stress on image force as the dislocation near the inclusion.

In this section, we utilize Eq. (36) to illustrate the influence of the interface stress upon the image force exerted on the dislocation when a single screw dislocation is located in the matrix. Without a loss of generality, we suppose that the screw dislocation lies at the point x_1 on the x-axis ($R_1<x_1<R_2$ is a real number) and the residual interface tension vanishes ($\tau^0=0$). In this case, $f_y=0$ and the component of the normalized image force along the x-axis direction is defined as $f_{x0}=2\pi R_1 f_x/\mu_2 b_1^2$. For the description of the interface, one needs the elastic constant μ^0. Unfortunately, it is unavailable in the literature. Miller and Shenoy [13] have computed the free surface for aluminum and silicon by the embedded atom method (EAM), and indicated that the surface properties can be either positive or negative, depending on the crystallographic orientation. Although the interface and free surface are not strictly the same, they have similar physical nature (free surface can be as some special interface) [19]. Since we cannot obtain datum of the interface constant μ^0, as a makeshift, in this paper, we assume that the absolute value of the interface constant is nearly the value of the surface constant. In addition, we define the relative shear modulus $\alpha=\mu_1/\mu_2$ and $\beta=\mu_3/\mu_2$, the intrinsic length $\gamma=\mu^0/\mu_2$, the relative location of the dislocation $\delta=x_1/R_1$, and the relative volume fraction of nanowires $\lambda=R_2/R_1$. According to the results in Ref. 13, the absolute value of the intrinsic length $\gamma=\mu^0/\mu_2$ is nearly 0.1 nm.

In Figs. 2 and 3, we illustrate the variation of the values of f_{x0} with respect to the parameter δ for the selected material constants and the intrinsic length γ ($\lambda=2$ and $R_1=15$ nm). It is observed from Figs. 2 and 3 that, if the distance of the screw dislocation with nanoscale inclusion is biggish, the screw dislocation will be attracted to the effective medium (composite phase) when the effective medium is softer than the matrix ($\mu_3<\mu_2$). The magnitude of the attractive force will be higher when the dislocation is closer to the interface between the matrix and the effective medium. On

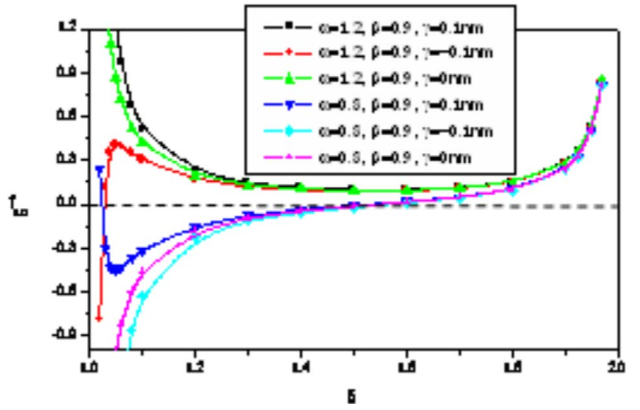

Fig. 2 Normalized force f_{x0} versus δ for $\beta=0.9$, λ=2, and $R_1=15$ nm

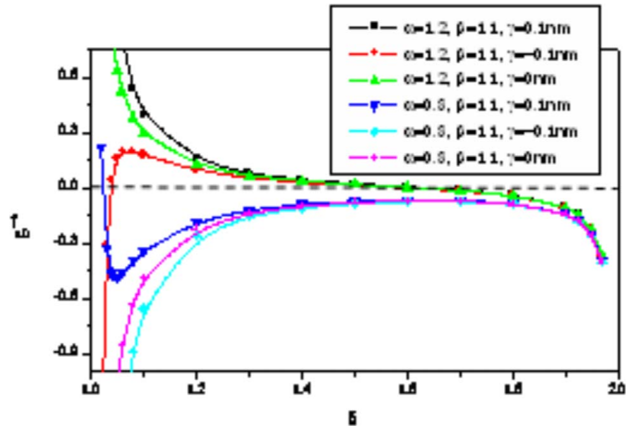

Fig. 3 Normalized force f_{x0} versus δ for $\beta=1.1$, λ=2, and $R_1=15$ nm

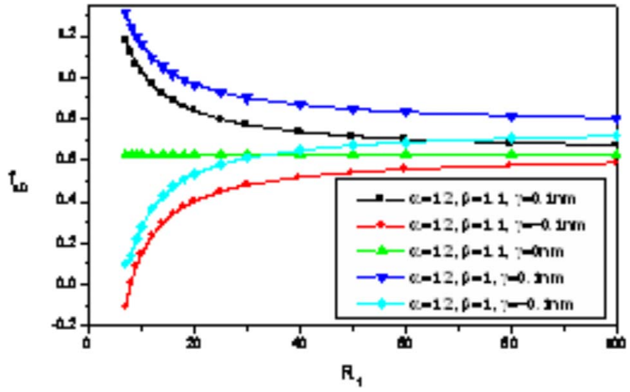

Fig. 4 Normalized force f_{x0} versus R_1 for $\lambda=2$ and $\delta=1.05$

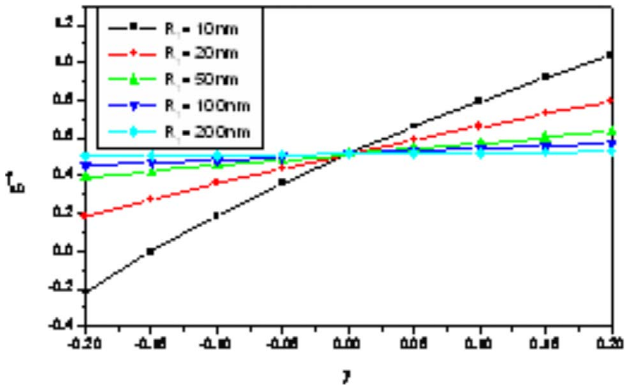

Fig. 5 Normalized force f_{x0} versus γ for $\lambda=2$, $\delta=1.06$, $\alpha=1.2$, and $\beta=1.1$

the other hand, the effective medium will repel the screw dislocation when the effective medium is stiffer than the matrix ($\mu_3 > \mu_2$).

It is seen from Fig. 2 that, when the inclusion is stiffer than the matrix ($\mu_1 > \mu_2$) and the effective medium is softer than the matrix ($\mu_3 < \mu_2$), there is not an equilibrium point for the screw dislocation in the matrix if the interface stress vanishes ($\gamma=0$), and there exists an unstable equilibrium point as the dislocation near the inclusion if the negative interface stress is considered ($\gamma=-0.1$ nm). Additionally, when the inclusion and the effective medium are all softer than the matrix ($\mu_1 < \mu_2$ and $\mu_3 < \mu_2$), there is an unstable equilibrium point in the matrix if the interface stress vanishes ($\gamma=0$), and there are two equilibrium points in the matrix as the dislocation near the inclusion if the positive interface stress is considered ($\gamma=0.1$ nm). The point that is closer to inclusion is stable and another point is unstable. The result indicates that a new stable equilibrium position for the screw dislocation near the inclusion is discovered due to consideration of the interface stress, which has never been observed in previous studies. Figure 3 indicates that, when the inclusion and the effective medium are all stiffer than the matrix ($\mu_1 > \mu_2$ and $\mu_3 > \mu_2$), there is a stable equilibrium point if the interface stress vanishes ($\gamma=0$), and there are two equilibrium points for the dislocation in the matrix if the negative interface stress is considered ($\gamma=-0.1$ nm). The point that is closer to inclusion is unstable and another point is stable. The result shows that a new unstable equilibrium position for the screw dislocation near the inclusion can exist by considering the interface stress. In addition, when the inclusion is softer than the matrix ($\mu_1 < \mu_2$) and the effective medium is stiffer than the matrix ($\mu_3 > \mu_2$), no equilibrium point is available if the interface stress vanishes ($\gamma=0$) and a stable equilibrium point for the dislocation in the matrix is available if the positive interface stress is considered ($\gamma=0.1$ nm). Compared to the classical solution ($\gamma=0$), we can obtain that more equilibrium positions of the dislocation may be available when the dislocation is near the nanoscale inclusion with interface stress. On the other hand, the mobility of the dislocation in the matrix will become more complex than the classical case.

The variation of the normalized image force f_{x0} versus the radius R_1 is depicted in Fig. 4 with the selected material constants and the intrinsic length γ for $\lambda=2$ and $\delta=1.05$. It can be seen that the positive value of γ causes the interface to repel the screw dislocation while the negative value of γ causes the interface to attract the dislocation. An additional repulsive force or attractive force will act on the screw dislocation by considering the interface stress, which causes the total image force to increase or decrease. This is a physical phenomenon unpredicted by the classical elasticity without considering the effect of the interface stress. The additional force acting on the dislocation increases with the decrease in the inclusion radius, and the size dependence becomes significant when the radius of the inclusion is very small. It is also found that the magnitude of the image force exerted on the screw dislocation produced by multiplying inclusion ($\beta=\mu_3/\mu_2=1.1$) is smaller than that produced by a single inclusion ($\beta=1$). The normalized image force f_{x0} as a function of γ with different values of R_1 is shown in Fig. 5 for $\alpha=1.2$, $\beta=1.1$, $\delta=1.06$, and $\lambda=2$. It is seen that the larger the absolute value of the intrinsic length λ or the smaller the radius of the inclusion R_1, the larger the effect of the interface stress upon the image force. An interesting result is that, when the radius of the inclusion is near 10 nm, the stiff inclusion first repels the screw dislocation, and then attracts it with the increment of the negative value of γ. Furthermore, the point where the dislocation is located is an equilibrium position of the screw dislocation when the value of γ reaches a certain value.

In Fig. 6, the normalized image force f_{x0} is plotted versus $\lambda=R_2/R_1$ with the selected material constants and the intrinsic length γ for $R_1=15$ nm and $\delta=1.05$. From Fig. 6, we found that, when the value of $\lambda=R_2/R_1$ continuously increases, the solution given by this model is slowly close to that derived from the two-phase model. Nevertheless, the repulsive force acting on the dislocation due to the presence of the stiff inclusion will decrease with the increment of the number of inclusions. The result shows that, when the dislocation approaches the inclusion, the total value of the repulsive force will become smaller by considering the effect of the surrounding inclusions. It is of theoretical interest to examine the influence of the elastic property of the effective medium. In Fig. 7, we illustrate the f_{x0} versus $\beta=\mu_3/\mu_2$ with different values of δ for $R_1=15$ nm, $\lambda=2$, $\gamma=0.1$ nm, and $\alpha=1.5$. It is shown that, when the rigidity of the effective medium is low, the

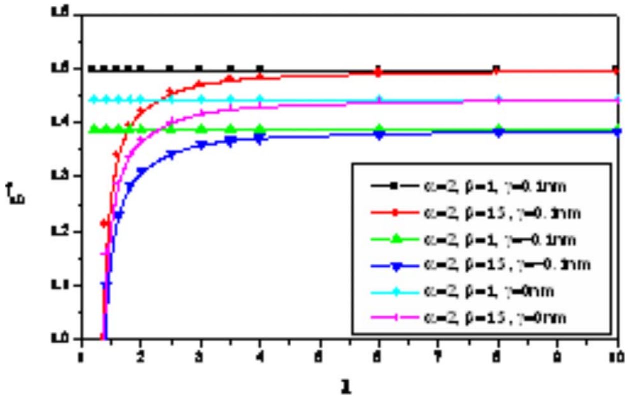

Fig. 6 Normalized force f_{x0} versus λ for $R_1=15$ nm, and $\delta=1.05$

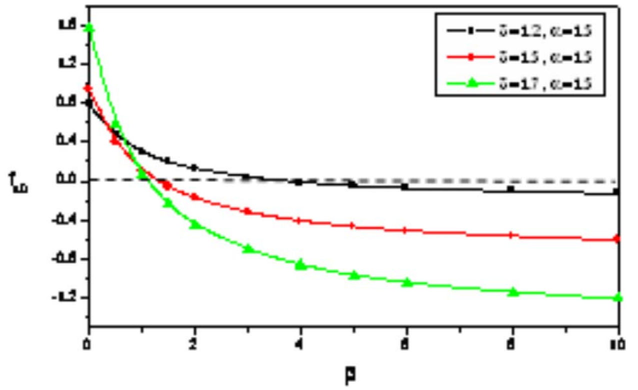

Fig. 7 Normalized force f_{x0} versus β for $R_1=15$ nm, $\lambda=2$, and $\gamma=0.1$ nm

dislocation tends to be repelled by the stiff inclusion; when the rigidity of the effective medium becomes hard, the dislocation will be repelled by the effective medium. There exists a critical value of β to alter the direction of the image force. The critical value of β will increase with the decrease in the distance between the dislocation and the inclusion.

In the following, we will illustrate the effect of the closer parallel screw dislocations. Consider the case that two parallel screw dislocations with Burgers vectors b_1 and b_2 are located in points $z_1(z_1=x_1)$ and $z_2=(z_2=re^{i\theta})$, respectively. The relative location of the dislocation z_2 relative to the nanoscale inclusion is defined as $\varepsilon=r/R_1$. The normalized image force f_{x0} with different values of b_2 as a function of δ is depicted in Fig. 8 for $\theta=20$ deg ($R_1=15$ nm, $\alpha=1.2$, $\beta=1.1$, $\varepsilon=1.8$, $\lambda=2$, and $\gamma=-0.1$ nm). It can be seen that, when δ goes up to a certain value, the direction of the image force acting on the screw dislocation z_1 produced by the dislocation z_2 can be changed for cases of both $b_2=b_1$ and $b_2=-b_1$. The unstable equilibrium point of the dislocation z_1 near the inclusion may be disappeared due to the effect of the nearby screw dislocation z_2. However, for the case of $b_2=b_1$, a new stable equilibrium point of the dislocation z_1 near the effective medium may be produced, and there also exist two equilibrium points when the dislocation z_1 approaches the inclusion from the interface between the matrix and the effective medium. On the other hand, for the case of $b_2=-b_1$, there is only one equilibrium point of the dislocation z_1 in the middle region of the matrix, and no equilibrium point is available when the dislocation is closer to the interface between the matrix and the effective medium. The normalized image force f_{x0} with different values of b_2 as a function of θ is depicted in Fig. 9 for $\delta=1.2$ ($R_1=15$ nm, $\alpha=1.2$, $\beta=1.1$, $\varepsilon=1.8$, $\lambda=2$, and $\gamma=-0.1$ nm). Figure 9 shows that the direction of the total image force exerted on the dislocation z_1 will be altered when the absolute value of the angle θ reaches a certain value for cases of both $b_2=b_1$ and $b_2=-b_1$. Furthermore, the point z_1 in the matrix is an equilibrium point of the screw dislocation along the x-axis direction. The effect of the dislocation z_2 on the image force acting on the dislocation z_1 is very obvious when two screw dislocations are all located on the x-axis. In addition, the effect of the dislocation z_2 will vanish when the absolute value of the angle θ goes up to the same critical value for cases of both $b_2=b_1$ and $b_2=-b_1$.

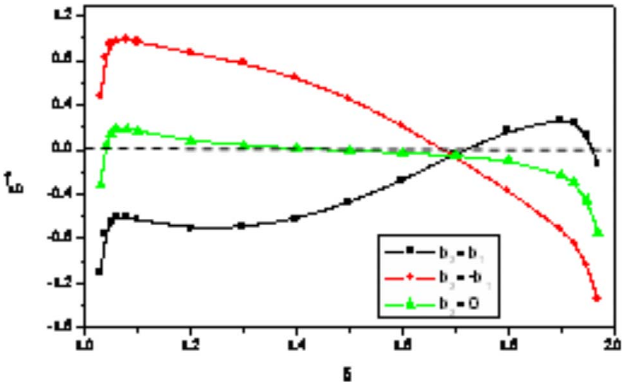

Fig. 8 Normalized force f_{x0} as a function of δ for $\theta=20$ deg ($R_1=15$ nm, $\alpha=1.2$, $\beta=1.1$, $\varepsilon=1.8$, $\lambda=2$, and $\gamma=-0.1$ nm)

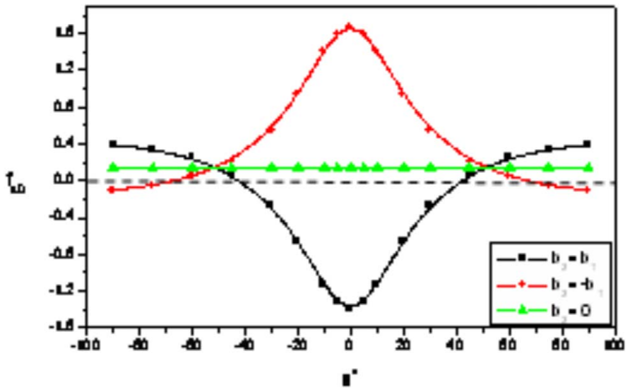

Fig. 9 Normalized force f_{x0} as a function of θ for $\delta=1.2$ ($R_1=15$ nm, $\alpha=1.2$, $\beta=1.1$, $\varepsilon=1.8$, $\lambda=2$, and $\gamma=-0.1$ nm)

6 Conclusions

The interaction between screw dislocations and multiple nanoscale inclusions with interface stresses is investigated by using a three-phase composite cylinder model. The explicit expressions of stress and displacement fields and image forces on the dislocations for the current problem are derived by means of the complex variable method. The image force and the equilibrium position of a single screw dislocation near one of the inclusions are presented by numerical calculations and discussed in detail. Some conclusions are summarized as follows. (1) When the inclusion and the effective medium are all softer than the matrix ($\mu_1<\mu_2$ and $\mu_3<\mu_2$) and the positive interface stress is considered, a new stable equilibrium position for the screw dislocation in the matrix is discovered. When the inclusion and the effective medium are all stiffer than the matrix ($\mu_1>\mu_2$ and $\mu_3>\mu_2$) and the negative interface stress is considered, a new unstable equilibrium position can exist. Furthermore, under certain conditions, there always exists a new stable or unstable equilibrium position of the dislocation near the nanoscale inclusion for different material combinations, which has never been observed in previous studies (without considering the interface stress). (2) The additional force exerted on the screw dislocation produced by considering the interface stress increases with the decrease in radius of the nanoscale inclusion, and the size dependence becomes significant when the radius is very small. (3) The magnitude of the so-called repulsive/attractive force acting on the screw dislocation produced by multiple nanoscale inclusions (three-phase model) is always smaller than that produced by a single inclusion (two-phase model). (4) The equilibrium positions of the appointed screw dislocation are strongly influenced by other parallel screw dislocations.

Acknowledgment

The authors would like to deeply appreciate the support by the National Natural Science Foundation of China (10472030).

References

[1] Hirth, J. P., and Lothe, J., 1982, *Theory of Dislocations*, McGraw-Hill, New York.

[2] Dundurs, J., and Mura, T., 1964, "Interaction Between an Edge Dislocation and a Circular Inclusion," J. Mech. Phys. Solids, **12**, pp. 177–189.

[3] Smith, E., 1968, "The Interaction Between Dislocations and Inhomogeneities-I," Int. J. Eng. Sci., **6**, pp. 129–143.

[4] Stagni, L., and Lizzio, R., 1983, "Shape Effects in the Interaction Between an Edge Dislocation and an Elliptic Inhomogeneity," Appl. Phys. A: Solids Surf., **30**, pp. 217–221.

[5] Warren, W. E., 1983, "The Edge Dislocation Inside an Elliptical Inclusion," Mech. Mater., **2**, pp. 319–330.

[6] Stagni, L., 1993, "Edge Dislocation Near an Elliptic Inhomogeneity With Either an Adhering or a Slipping Interface: A Comparative Study," Philos. Mag. A, **68**, pp. 49–57.

[7] Qaissaunee, M. T., and Santare, M. H., 1995, "Edge Dislocation Interaction With an Elliptical Inclusion Surrounding by an Interfacial Zone," Q. J. Mech. Appl. Math., **48**, pp. 465–482.

[8] Xiao, Z. M., and Chen, B. J., 2000, "A Screw Dislocation Interacting With a Coated Fiber," Mech. Mater., **32**, pp. 485–494.

[9] Xiao, Z. M., and Chen, B. J., 2001, "On the Interaction Between an Edge Dislocation and a Coated Inclusion," Int. J. Solids Struct., **38**, pp. 2533–2548.

[10] Fang, Q. H., Liu, Y. W., and Jiang, C. P., 2003, "Edge Dislocation Interacting With an Interfacial Crack Along a Circular Inhomogeneity," Int. J. Solids Struct., **40**, pp. 5781–5797.

[11] Shi, J., and Li, Z., 2006, "An Approximate Solution of the Interaction Between an Edge Dislocation and Inclusion of Arbitrary Shape," Mech. Res. Commun., **33**, pp. 804–810.

[12] Wang, X., and Sudak, L. J., 2006, "Interaction of a Screw Dislocation With an Arbitrary Shaped Elastic Inhomogeneity," ASME J. Appl. Mech., **73**, pp. 206–211.

[13] Miller, R. E., and Shenoy, V. B., 2000, "Size-Dependent Elastic Properties of Nanosized Structural Elements," Nanotechnology, **11**, pp. 139–147.

[14] Gurtin, M. E., and Murdoch, A. I., 1975, "A Continuum Theory of Elastic Material Surfaces," Arch. Ration. Mech. Anal., **57**, pp. 291–323.

[15] Gurtin, M. E., Weissmuller, J., and Larche, F., 1998, "A General Theory Curved Deformation Interfaces in Solids at Equilibrium," Philos. Mag. A, **78**, pp. 1093–1109.

[16] Sharma, P., Ganti, S., and Bhate, N., 2003, "Effect of Surfaces on the Size-Dependent Elastic State of Nano-Inhomogeneities," Appl. Phys. Lett., **82**, pp. 535–537.

[17] Sharma, P., and Ganti, S., 2004, "Size-Dependent Eshelby's Tensor for Embedded Nano-Inclusions Incorporating Surface/Interface Energies," ASME J. Appl. Mech., **71**, pp. 663–671.

[18] Duan, H. L., Wang, J., Huang, Z. P., and Karihaloo, B. L., 2005, "Size-Dependent Effective Elastic Constants of Solids Containing Nano-Inhomogeneities With Interface Stress," J. Mech. Phys. Solids, **53**, pp. 1574–1596.

[19] Lim, C. W., Li, Z. R., and He, L. H., 2006, "Size Dependent, Non-Uniform Elastic Field Inside a Nanoscale Spherical Inclusion Due to Interface Stress," Int. J. Solids Struct., **43**, pp. 5055–5065.

[20] Chen, T., and Dvorak, G. J., 2006, "Fibrous Nanocomposites With Interface Stress: Hill's and Levin's Connections for Effective Moduli," Appl. Phys. Lett., **88**, p. 211912.

[21] Tian, L., and Rajapakse, R. K. N. D., 2007, "Analytical Solution for Size-Dependent Elastic Field of a Nanoscale Circular Inhomogeneity," ASME J. Appl. Mech., **74**, pp. 568–574.

[22] Sharma, P., and Wheeler, L. T., 2007, "Size-Dependent Elastic State of Ellipsoidal Nano-Inclusions Incorporating Surface/Interface Tension," ASME J. Appl. Mech., **74**, pp. 447–454.

[23] Christensen, R. M., and Lo, K. H., 1979, "Solutions for Effective Shear Properties in Three Phase Sphere and Cylinder Models," J. Mech. Phys. Solids, **27**, pp. 315–330.

[24] Tanaka, K., and Mori, T., 1972, "Note on Volume Integrals of the Elastic Field Around an Ellipsoidal Inclusion," J. Elast., **2**, pp. 199–200.

[25] Luo, H. A., and Chen, Y., 1991, "An Edge Dislocation in a Three-Phase Composite Cylinder Model," ASME J. Appl. Mech., **58**, pp. 75–86.

[26] Xiao, Z. M., and Chen, B. J., 2000, "A Screw Dislocation Interacting With Inclusions in Fiber-Reinforced Composites," Acta Mech., **155**, pp. 203–214.

[27] Wang, X., and Shen, Y. P., 2002, "An Edge Dislocation in a Three-Phase Composites Cylinder Model With a Sliding Interface," ASME J. Appl. Mech., **69**, pp. 527–538.

[28] Povstenko, Z. Y., 1993, "Theoretical Investigation of Phenomena Caused by Heterogeneous Surface Tension in Solids," J. Mech. Phys. Solids, **41**, pp. 1499–1514.

[29] Muskhelishvili, N. L., 1975, *Some Basic Problems of Mathematical Theory of Elasticity*, Noordhoff, Leyden.

[30] Lee, S., 1987, "The Image Force on the Screw Dislocation Around a Crack of Finite Size," Eng. Fract. Mech., **27**, pp. 539–545.

Post-buckling and Snap-Through Behavior of Inclined Slender Beams

Jian Zhao

Jianyuan Jia

School of Elec-mechanical Engineering,
Xidian University,
Xi'an, 710071, P.R.C.

Xiaoping He
Institute of Electronic Engineering,
China Academy of Engineering Physics,
Mianyang 621900, P.R.C.

Hongxi Wang
School of Elec-mechanical Engineering,
Xidian University,
Xi'an, 710071, P.R.C.

Based on the geometrical nonlinear theory of large deflection elastic beams, the governing differential equations of post-buckling behavior of clamped-clamped inclined beams subjected to combined forces are established. By using the implicit compatibility conditions to solve the nonlinear statically indeterminate problems of elastic beams, the strongly nonlinear equations formulated in terms of elliptic integrals are directly solved in the numerical sense. When the applied force exceeds the critical value, the numerical simulation shows that the inclined beam snaps to the other equilibrium position automatically. It is in the snap-through process that the accurate configurations of the post-buckling inclined beam with different angles are presented, and it is found that the nonlinear stiffness decreases as the midpoint displacement is increased according to our systematical analysis of the inward relations of different buckling modes. The numerical results are in good agreement with those obtained in the experiments.

[DOI: 10.1115/1.2870953]

Keywords: geometrical nonlinearity, snap through, nonlinear stiffness, post-buckling, large deflection

1 Introduction

In microelectromechanical system (MEMS) fields, a need arises in engineering practice to predict accurately the nonlinear response of slender post-buckling beams, especially the nonlinear transverse stiffness. The bistability of the post-buckling beams is excellent in reducing power consumption of microdevices or microsystems. However, the major difficulty in analyzing the post-buckling and snap-through response is the intractability of the geometric nonlinear control equations of large deflection beams. Enikov et al. [1] designed a V-shaped thermal microacturator with buckling beams. Yet, the precise computation model for the buckling beam based on the large deflection theory has not been built. Seide [2] discussed the accuracy of some numerical methods for column buckling. Mau [3] studied the stability of the post-buckling paths of columns with discrete spring supports. Though Fang and Wickert [4] studied the static deformation of micromachined beams under in-plane compressive stress, they could not trace the post-buckling paths by making use of the linearized governing differential equation. Wang [5] presented the complete post-buckling and large deformations of an elastica rod, one end fixed and one end pinned. Hartono [6,7] applied the elastica solution to describe the large displacement behavior of a column with lateral bracing at the midheight and obtained the post-buckling configurations of the deformed column under the axial loading. Coffin and Bloom [8] analyzed the post-buckling response of an elastic and hygrothermal beam fully restrained against axial expansion. Li and Zhou [9] studied the post-buckling behavior of a hinge-fixed beam under evenly distributed follower forces. The post-buckling analysis of the easily fabricated MEMS beams with both ends fixed is really important in the design of microstructures. To solve the post-buckling problems of small deformation beams, the predominant approach is to use a nonlinear finite element (FE) model, or to resort to a linear analytical model based on the small deflection theory, which agrees only with experiments in a relatively limited range of loadings. The apex displacement of the bent beam can only be reduced in nearly linear proportion to the vertical force in the design of microactuators [10,11], and the error is large compared with the experimental results. This lack of a simple and yet accurate tool for analyzing the post-buckling bent beams results in a poor initial "guess" of the desired geometry and multidesign iterations, thus being unable to provide an insight into the deformation problems. Therefore, the large deflection buckling theory is needed to solve the intractability of the geometric nonlinear control equations of the bent beam.

Aiming at designing a novel MEMS threshold acceleration switch with post-buckling beams, this paper studies the post-buckling behavior in the snap-through process of the large deflection inclined beam with both ends fixed, and establishes the nonlinear governing equations of the post-buckling beam under combined forces acting on the ending point. These ordinary nonlinear differential equations consist of the boundary-value conditions, in which six unknown functions are contained and the length of the deformed beam is considered as one of the unknown functions. By using the implicit compatibility conditions to express the nonlinear statically indeterminate problems of elastic beams, the strongly nonlinear equations formulated in terms of elliptic integrals are directly solved in the numerical sense. Through an incremental displacement method, we can obtain the equilibrium paths of the deformed beam in the snap-through process, and describe explicitly the nonlinear force-and-displacement relations of the central point of the bent-beam structure. For further applications of the nonlinear stiffness of the post-buckling beams, an electronic testing device is designed. The simulation results are in good agreement with those by experiments.

2 Governing Equations of Post-buckling Beams

2.1 Nonlinear Structure Supported by Inclined Beams. A typical bent-beam structure is shown in Figs. 1 and 2. The structure consists of one inertial mass supported by two inclined beams with length L, both ends fixed. The central mass is constrained to move vertically. When a vertical force F_v is applied on the central node, the constraint beam is subjected to the compression and lateral bending moments, thus resulting in the symmetric response

---

Contributed by the Applied Mechanics Division of ASME for publication in the Journal of Applied Mechanics. Manuscript received April 16, 2007; final manuscript received November 9, 2007; published online May 16, 2008. Review conducted by Edmundo Corona.

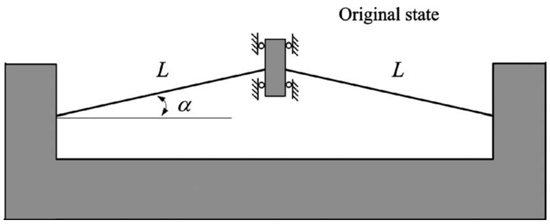

Fig. 1 Original state of the bent-beam structure

of the beam. When the vertical force F_v exceeds the critical buckling load, the inclined beam with initial angle α buckles, and then snaps to the next equilibrium state. During the whole snap-through process, the structural stiffness varies with the displacements of the central node. As we all know, the nonlinear stiffness of the inclined beam plays a crucial role in the action of the nonlinear system; therefore, it is of great importance to study the post-buckling behavior of the inclined beam, which experiences large deflections, and to show the equilibrium paths during the snap-through process.

2.2 Governing Equations of the Post-buckling Beam. Based on the symmetry of the structure, the left half span of the bent beam with reaction forces is analyzed, and the coordinate system used is shown in Fig. 3. When the right ending point of the beam moves vertically, the beam buckles and the configuration becomes asymmetric or symmetric depending on the number of inflection points along the deformed beam. The moment at the inflection point is zero. By using the geometric symmetry, a coordinate system is constructed accordingly. Let a Cartesian coordinate system (x,y) be located at the left fixed end, and s stands for the arclength. Then, we can get these geometrical relations of the right ending point (Eq. (1)) and the bending moment at any section along the beam (Eq. (2)) as follows:

$$y_m = \delta \cos \alpha, \quad x_m = L - u = L - \delta \sin \alpha \tag{1}$$

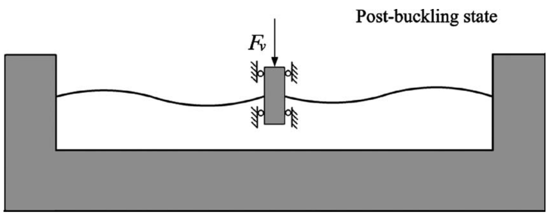

Fig. 2 Post-buckling state of the bent-beam structure

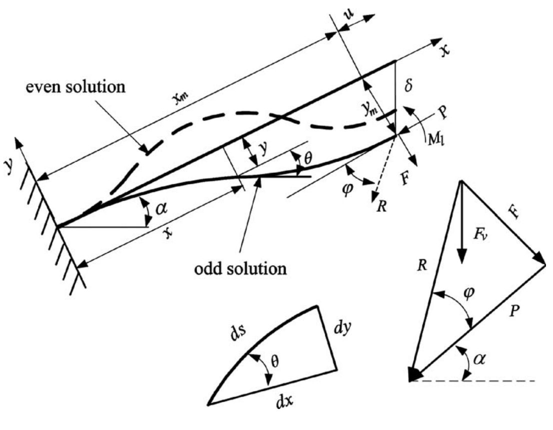

Fig. 3 Deformation of post-buckling beam under a combined load

$$M = -R((y+y_m)\cos\varphi + (x_m - x)\sin\varphi) + M_l \tag{2}$$

Here, δ, x_m, and y_m represent the vertical displacement, longitude deflection, and transverse deflection of the right ending point, respectively. φ is the angle of the elastic force R, θ the angle of any section along the buckled beam, and α the initial angle of the inclined beam. M_0 and M_l stand for the bending moments at the two ending points, respectively. P and F, which can be expressed as $P=R\cos\varphi$ and $F=R\sin\varphi$, are axial and transverse components of the elastic force R, respectively.

Then, from Euler–Bernoulli moment-curvature relationship

$$M = EI\frac{d\theta}{ds} \tag{3}$$

the governing equation of the post-buckling beam with both ends fixed is obtained from Eqs. (2) and (3),

$$\frac{d\theta}{ds} = \frac{-R[(y+y_m)\cos\varphi + (x_m - x)\sin\varphi] + M_l}{EI}$$

$$\frac{dy}{ds} = \sin\theta$$

$$\frac{dx}{ds} = \cos\theta \tag{4}$$

Upon the differentiation of s in Eq. (4), another expression of the governing equation can be obtained as

$$\frac{d^2\theta}{ds^2} = -\frac{R}{EI}(\cos\varphi\sin\theta - \sin\varphi\cos\theta) \tag{5}$$

By integrating θ, the relation between the moment and the elastic force can be derived from Eq. (5) as follows:

$$\frac{R}{EI}(\cos\varphi\cos\theta + \sin\varphi\sin\theta) + c = \frac{1}{2}\left(\frac{M}{EI}\right)^2 \tag{6}$$

where c is the integration constant.

At the inflection point of the deflected beam, where $\theta=\theta^*$, substituting $M=0$ in Eq. (6) results in

$$c = -\frac{R}{EI}\cos(\theta^* - \varphi) \tag{7}$$

The boundary conditions can be written as follows:

$$s=L, \quad \theta=0, \quad y=-y_m, \quad x=x_m$$

$$s=0, \quad \theta=0, \quad y=0, \quad x=0 \tag{8}$$

By applying the boundary conditions to Eq. (6), the relation between R and φ is found as follows:

$$c = \frac{1}{2}\left(\frac{M_l}{EI}\right)^2 - \frac{R\cos\varphi}{EI} = \frac{1}{2}\left(\frac{M_0}{EI}\right)^2 - \frac{R\cos\varphi}{EI} \tag{9}$$

Then, the moment at any section of the beam in different buckling modes is obtained by substituting Eq. (7) into Eq. (6),

$$M = \pm\left(\frac{R\cos(\theta-\varphi) - R\cos(\theta^*-\varphi)}{EI}\right)^{1/2} \tag{10}$$

where ± stands for the direction of the moment.

When the applied vertical force exceeds the critical buckling value, the inclined beam buckles and the second bifurcation of the post-buckling beam occurs. The phenomenon such as snap through, which includes the transition between the asymmetric and the symmetric buckling modes, can be described by the post-buckling analysis.

2.2.1 Asymmetric Mode (Odd Solution). Based on the deflection configuration, which has odd inflection points as shown in Fig. 2, and the concavo-convex relations of the curve, we can conclude that the directions of the moments at the two ending points of the beam are opposite. Therefore, the relation of the moments on the two ending points of the inclined beam can be obtained from Eq. (9),

$$M_0 = -M_l \tag{11}$$

The moment at the right ending point can be obtained from Eqs. (2) and (11),

$$M_l = \frac{R}{2}(y_m \cos \varphi + x_m \sin \varphi) \tag{12}$$

By substituting Eq. (7) into Eq. (9), the other expression of the moment at the right ending point can be deduced as

$$M_l^2 = 2REI[\cos \varphi - \cos(\theta^* - \varphi)] \tag{13}$$

Upon the substitution of Eq. (12) into Eq. (13), the following relation between θ^* and R can be obtained:

$$\cos(\theta^* - \varphi) = -\frac{R}{8EI}(y_m \cos \varphi + x_m \sin \varphi)^2 + \cos \varphi \tag{14}$$

2.2.2 Symmetric Mode (Even Solution). Based on the deflection configuration, which has even inflection points as shown in Fig. 2, and the symmetry of the beam configuration, we can learn that the moments at the two ending points are in the same direction. So, the moment relation between the two ending points can be deduced from Eq. (9)

$$M_0 = M_l \tag{15}$$

The direction angle φ of the elastic force R can be derived from Eq. (2),

$$\tan \varphi = \frac{F}{P} = -\frac{y_m}{x_m} \tag{16}$$

From Eq. (13), the moment at the right ending point can be written as

$$M_l = [2REI(\cos \varphi - \cos(\theta^* - \varphi))]^{1/2} \tag{17}$$

The condition (Eq. (8)) is self-explanatory and Eq. (1) indicates the fact that the right ending point of the beam can move only in the vertical direction, as shown in Fig. 2. With a given tip displacement δ (controlling parameter) and the three constraint conditions (Eqs. (1), (12), and (17)), the nonlinear differential equation (Eq. (4)) cannot be solved to determine the displacement variables (x,y) and the inclination θ. Therefore, another two constraint conditions are necessary to calculate the elastic force R and its direction angle φ to settle the strong nonlinear statically indeterminate problems.

3 Nonlinear Constraint Conditions of the Post-buckling Beam

3.1 Constraint Condition on the Beam Length. From Eq. (10), the moment-curvature equation of the buckled beam can be written as

$$\frac{d\theta}{ds} = \pm \left(\frac{R \cos(\theta - \varphi) - R \cos(\theta^* - \varphi)}{EI} \right)^{1/2} \tag{18}$$

where the symbol ± shows the curve direction of the statically indeterminate beam.

Here, set n as the number of the inflection points. When n is odd, the configuration becomes asymmetric; when n is even, the configuration becomes symmetric. The deflection curve can be divided into $2n$ parts by the inflection points and the peak points, and then the constraint condition on the beam length can be obtained by integrating the curved coordinate s in Eq. (18).

Upon substituting the following parameters,

$$\beta = \theta - \varphi, \quad \gamma = \theta^* - \varphi, \quad \sin \frac{\beta}{2} = \sin \frac{\gamma}{2} \sin \phi \tag{19}$$

into Eq. (18), we can get the expression for the beam length.

3.1.1 Asymmetric Modes (Odd Solution). When n is odd, the integration of Eq. (18) results in

$$\begin{aligned} L &= \sqrt{\frac{EI}{2R}} \sum_{k=1}^{2n} \int_{\theta^* \sin([(k-1)/2]\pi)}^{\theta^* \sin(k\pi/2)} \frac{\sin\left(\frac{k+2}{2}\pi\right) - \sin\left(\frac{k+1}{2}\pi\right)}{[\cos(\theta - \varphi) - \cos(\theta^* - \varphi)]^{1/2}} d\theta \\ &= -2n \sqrt{\frac{EI}{2R}} \int_0^{\theta^*} \frac{d\theta}{[\cos(\theta - \varphi) - \cos(\theta^* - \varphi)]^{1/2}} \end{aligned} \tag{20}$$

The constraint condition on the beam length is obtained by substituting Eq. (19) into Eq. (20),

$$L = -2n \sqrt{\frac{EI}{R}} \int_{\phi_0}^{\pi/2} \frac{d\phi}{\left(1 - \sin^2 \frac{\gamma}{2} \sin^2 \phi\right)^{1/2}} \tag{21}$$

When $\theta = 0$, from Eq. (19), an expression for Φ_0 can be deduced,

$$\sin \phi_0 = -\frac{\sin(\varphi/2)}{\sin(\gamma/2)} \tag{22}$$

3.1.2 Symmetric Mode (Even Solution). When n is even, the beam length can be calculated by the same method, which has been used in the asymmetric mode.

$$\begin{aligned} L &= \sqrt{\frac{EI}{2R}} \sum_{k=1}^{2n} \int_{\theta^* \sin([(k-1)/2]\pi)}^{\theta^* \sin(k\pi/2)} \frac{\sin\left(\frac{k+2}{2}\pi\right) - \sin\left(\frac{k+1}{2}\pi\right)}{[\cos(\theta - \varphi) - \cos(\theta^* - \varphi)]^{1/2}} d\theta \\ &= n \sqrt{\frac{EI}{R}} \int_0^{\gamma} \frac{d\beta}{\left(\sin^2 \frac{\gamma}{2} - \sin^2 \frac{\beta}{2}\right)^{1/2}} \\ &= 2n \sqrt{\frac{EI}{R}} \int_0^{\pi/2} \frac{d\phi}{\left(1 - \sin^2 \frac{\gamma}{2} \sin^2 \phi\right)^{1/2}} \end{aligned} \tag{23}$$

Therefore, by combining Eqs. (21) and (23), the general form of the constraint condition on the beam length can be obtained,

$$L = 2n(-1)^n \sqrt{\frac{EI}{R}} \int_{\phi_0}^{\pi/2} \frac{1}{\left(1 - \sin^2 \frac{\gamma}{2} \sin^2 \phi\right)^{1/2}} d\phi \tag{24}$$

Here, when n is even, Φ_0 is equal to zero; when n is odd, the value of Φ_0 can be determined by Eq. (22).

3.2 Constraint Condition on Displacement. From Eqs. (4) and (18), the displacement (x,y) at any section of the deformed beam can be obtained as follows:

$$x = \int_0^l \cos \theta ds$$

$$y = \int_0^l \sin \theta ds \tag{25}$$

By integrating the equations above, the longitude and transversal displacements (x_m, y_m) of the right ending point can be obtained as follows:

$$x_m = n(-1)^n \sqrt{\frac{2EI}{R}} \int_{\phi_0}^{\pi/2} \frac{\cos(\beta+\varphi)}{\left(1-\sin^2\frac{\gamma}{2}\sin^2\phi\right)^{1/2}} d\phi$$

$$y_m = n(-1)^n \sqrt{\frac{2EI}{R}} \int_{\phi_0}^{\pi/2} \frac{\sin(\beta+\varphi)}{\left(1-\sin^2\frac{\gamma}{2}\sin^2\phi\right)^{1/2}} d\phi \qquad (26)$$

Then, the relationship between the longitude and transverse displacements of the right ending point can be simplified as

$$x_m = n(-1)^n \left(\frac{2EI}{R}\right)^{1/2} [I_2 \cos\varphi - I_1 \sin\varphi]$$

$$y_m = n(-1)^n \left(\frac{2EI}{R}\right)^{1/2} [I_1 \cos\varphi + I_2 \sin\varphi] \qquad (27)$$

where

$$I_1 = 2\sqrt{2}\sin\frac{\gamma}{2}\int_{\phi_0}^{\pi/2} \sin\phi d\phi = 2\sqrt{2}\sin\frac{\gamma}{2}\cos\phi_0$$

$$\begin{aligned} I_2 &= \sqrt{2}\int_{\phi_0}^{\pi/2} \frac{2\cos^2\frac{\beta}{2}-1}{\left(1-\sin^2\frac{\gamma}{2}\sin^2\phi\right)^{1/2}} d\phi \\ &= 2\sqrt{2}\int_{\phi_0}^{\pi/2}\left(1-\sin^2\frac{\gamma}{2}\sin^2\phi\right)^{1/2} d\phi \\ &\quad - \sqrt{2}\int_{\phi_0}^{\pi/2} \frac{1}{\left(1-\sin^2\frac{\gamma}{2}\sin^2\phi\right)^{1/2}} d\phi \end{aligned}$$

When n is odd, the relation between φ and the displacements of the right ending point can be written from Eqs. (14), (19), and (27) as follows:

$$\tan\varphi = \frac{x_m}{y_m} \qquad (28)$$

The variables such as φ and R in Eq. (27) are unknowns; so, the displacement constraint relation of the right ending point can be obtained by solving Eq. (27),

$$x_m \cos\varphi - y_m \sin\varphi = 2n\sqrt{\frac{EI}{2R}} I_2 \qquad (29)$$

Then, the constraint equation for Eq. (4) can be explicitly found by substituting I_2 into Eq. (29),

$$\frac{1}{L}\int_{\phi_0}^{\pi/2} \frac{d\phi}{\left(1-\sin^2\frac{\gamma}{2}\sin^2\phi\right)^{1/2}} = \frac{2}{x_m\cos\varphi - y_m\sin\varphi + L}\int_{\phi_0}^{\pi/2}\left(1-\sin^2\frac{\gamma}{2}\sin^2\varphi\right)^{1/2} d\varphi \qquad (30)$$

The noncomplete elliptic integrals of the first kind can be expressed as the power series to simplify the nonlinear post-buckling governing equation (Eq. (4))

$$\begin{aligned} \int_0^{\pi/2} \frac{d\phi}{\left(1-\sin^2\frac{\gamma}{2}\sin^2\phi\right)^{1/2}} &= \frac{\pi}{2}\left\{1+\sum_{n=1}^{\infty}\left[\frac{(2n-1)!!}{(2n)!!}\right]^2\left(\sin^2\frac{\gamma}{2}\right)^n\right\} \\ &\quad \times \int_0^{\phi_0} \frac{d\phi}{\left(1-\sin^2\frac{\gamma}{2}\sin^2\phi\right)^{1/2}} \\ &= \phi_0 + \sum_{n=1}^{\infty}\frac{(2n-1)!!}{(2n)!!}\left(\sin^2\frac{\gamma}{2}\right)^n\int_0^{\phi_0}\sin^{2n}\phi d\phi \end{aligned} \qquad (31)$$

where

$$\int_0^{\phi_0}\sin^{2n}\phi d\phi = -\frac{(2n)!}{2^{2n}(n!)^2}\left[\cos\phi_0\sum_{k=0}^{n-1}\frac{2^{2k}(k!)^2\sin^{2k+1}\phi_0}{(2k+1)!} - \phi_0\right]$$

In other words, with a given displacement δ, the moment M_l can be obtained from Eqs. (12) and (17) and then, the elastic force R and its direction angle φ can be calculated by combining Eqs. (16), (24), (28), and (30). Finally, the strong nonlinear equation (Eq. (4)) can be solved numerically.

4 Analysis of Post-buckling Elastic Force

According to the minimal energy principle, the beam will find the path with the least energy such as the first and second buckling modes in the snap-through process. That is to say, there will be one or two inflection points along the deflection curve of the post-buckling beam under the combined forces.

Based on the geometric relations and force equilibrium relationship, the vertical elastic force F_v can be written as

$$F_v = R(\cos\varphi\sin\alpha + \sin\varphi\cos\alpha) \qquad (32)$$

where the elastic force can be expressed as $R = 2EI(I_1/L)^2$, which can be calculated from Eqs. (16), (19), (24), and (30). The transversal force F_v is a hidden function of the displacement of the right ending point δ.

When $\cos(\varphi)$ is less than $\cos(\theta^* - \varphi)$, the second bifurcation occurs, and then the buckled beam snaps from the symmetric mode to the asymmetric mode. The formula for calculating φ changes from Eq. (16) to Eq. (28), and the moment expression also changes from Eq. (17) to Eq. (12). Therefore, it is obvious that the snap-through characteristic of the post-buckling beam can be described by the relation between the elastic force and the vertical displacement.

5 Numerical Simulation and Experiments

Based on the theoretical derivation mentioned above, the structure parameters given below are used in simulating the post-buckling behavior of the inclined beam with both ends fixed.

By using the conditions expressed by Eqs. (12), (17), (16), (24), (28), and (30), and a given δ, the variables of M_l, R, and φ can be determined. Now, the modified numerical method of incremental displacement is adopted to solve the governing equation of the post-buckling beam. During the numerical simulation procedure, the variable n mentioned above is found to fulfill the nonlinear constraint conditions on the beam length (as in Eq. (24)). Then, with the inflection point number n, the nonlinear stiffness and the large deflection equilibrium paths during the post-buckling and snap-through process are presented in the following.

To validate the theoretic derivation and the further applications of post-buckling beams, an electronic testing device is designed as shown in Fig. 6, and a series of experiments is conducted to verify the nonlinear stiffness analytically calculated in this paper. As shown in Fig. 6, the post-buckling testing device consists of a

Table 1 Beam parameters

Parameters	Value
Length L	30 mm
Width b	1 mm
Thickness h	0.2 mm
Young's modulus E	160 GPa

displacement sensor, a force sensor, a supporting platform, and two output screens. The inclined Be-bronze beams are fixed on the post-buckling platform when the vertical force is applied to the fixed central point of the structure. When the central point moves vertically, the values of the central point displacement and the corresponding reaction force can be sensed and displayed on the two different screens, respectively. The parameters of the beam structure are identical to those in Table 1.

Figures 4 and 5 show the configurations of post-buckling beams with different initial angles α when the beam tip moves vertically under the applied forces. To facilitate the analytical process, it is necessary to point out that the beam tips shown in both Figs. 4 and 5 correspond to the fixed central point of the testing structure in Fig. 6. When the vertical force applied is zero or less than the critical buckling value, the beam stays in the original state. When the vertical force exceeds the critical buckling value, the beam experiences instability and produces two inflection points, as shown in Figs. 4 and 5. As the vertical displacement of the beam tip increases, the configuration of the beam becomes asymmetric; meanwhile, the inflection point number becomes odd correspondingly. These configurations of the post-buckling beams shown in Figs. 3 and 4 are almost the same as those obtained by the experiments.

Figures 7 and 8 show that the simulation results of nonlinear stiffness are in good agreement with those by experiments. In the oxy coordinate system in Figs. 7 and 8, the x axis is the vertical displacement of the beam tip (the central point of the structure) under the applied force. In Figs. 7 and 8, the origin of the x axis stands for the original position of the beam tip, as shown in Figs. 4 and 5. When the applied vertical force F_v exceeds the critical buckling value, the inclined beam will buckle under the compression load, and the elastic force F_v will decrease with the increas-

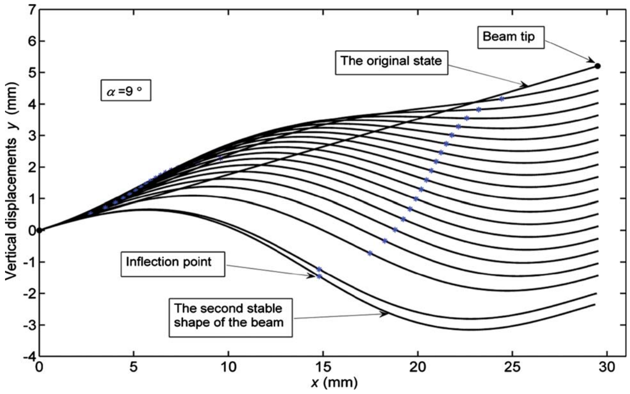

Fig. 4 Post-buckling configurations for α=9 deg

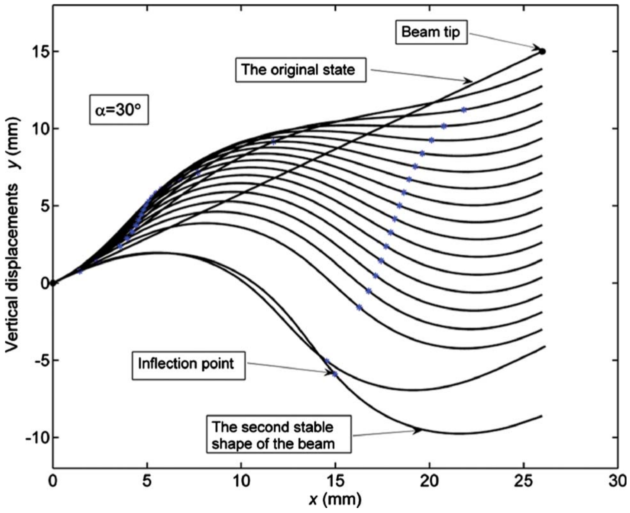

Fig. 5 Post-buckling configurations for α=30 deg

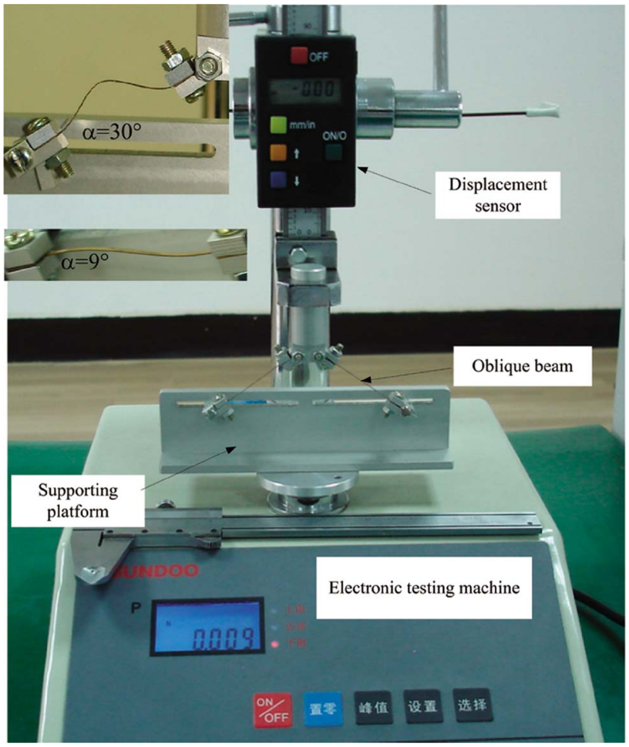

Fig. 6 Electronic testing device for post-buckling beams

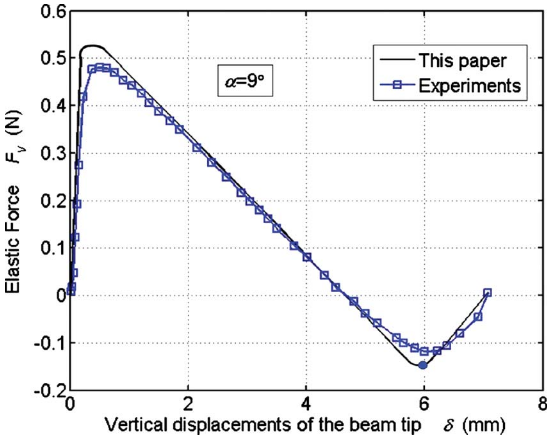

Fig. 7 Elastic force versus displacement for α=9 deg. The filled circle "●" stands for the position where the beam configuration changes from symmetric state to asymmetric state.

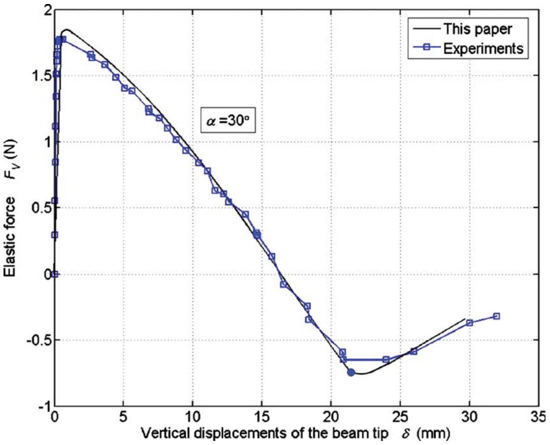

Fig. 8 Elastic force versus displacement for α=30 deg. The filled circle "●" stands for the position where the beam configuration changes from symmetric state to asymmetric state.

ing vertical displacement δ of the beam tip. The elastic force F_v keeps positive until the beam tip approaches a critical unstable position where the elastic force changes to zero. Then, the elastic force becomes negative as the displacement of the beam tip increases, which indicates that the beam will snap to the other stable position automatically. This nonlinear phenomenon of the post-buckling beam is consistent with the results obtained by experiments. The snap-through phenomenon is also depicted in Refs. [12,13]. By regulating the initial angle and dimensions of the post-buckling beams, different forcedisplacement curves can be obtained to fulfill practical applications. Therefore, the post-buckling nonlinear stiffness and the threshold characteristic of the bent beam can be utilized in designing different kinds of threshold accelerometers or other safe-arming systems.

In the special case shown in Fig. 9, when the initial angle equals 90 deg, the configurations obtained in this paper are consistent with the numerical results revealed in Ref. [7]. In Fig. 10, the variation of the axial force with the vertical displacement δ, which is consistent with the analytical results in Refs. [14,15], shows that the axial load increases with the displacement of the ending point δ. By a comparison of the results between the numerical simulation and the experiments, the analytical method for analyzing post-buckling beams proves feasible in this paper.

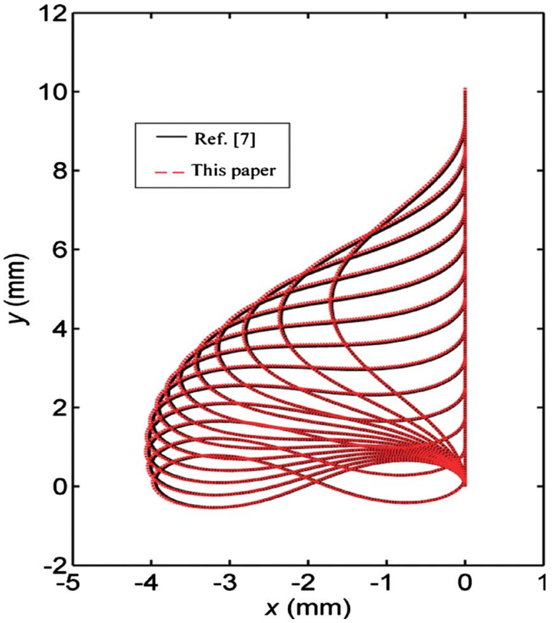

Fig. 9 Large deformation of the beam subjected to axial load for α=90 deg

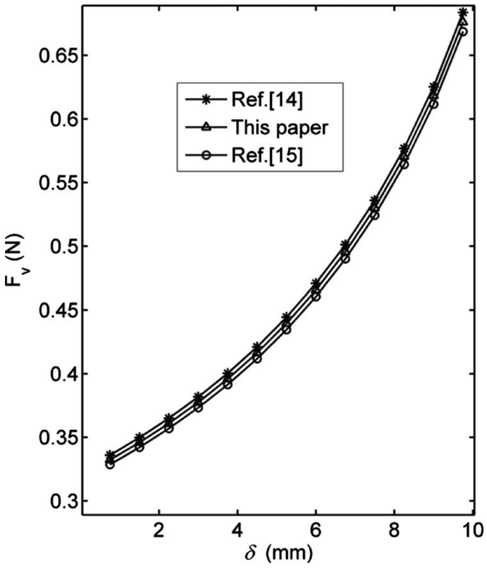

Fig. 10 Force-displacement curve for α=90 deg

6 Conclusion

In order to solve the post-buckling problem and analyze snap-through behavior of the inclined beam with both ends fixed, the governing differential equations of the post-buckling beam subjected to combined forces at the ending point are established. By using an incremental displacement numerical method, the post-buckling configurations of the large deflection beam at any initial inclination angle are presented, and the nonlinear stiffness of the post-buckling beam is obtained in the snap-through process. The numerical results are consistent with those by experiments. Some important conclusions are obtained to find application in optimal design of post-buckling structures.

Moreover, the postbuckled beam snaps from the double-inflection state to the single-inflection state only when the beam experiences large deflections. The high order mode configuration of the buckling beam does not appear in the snap-through process in the static experiments. In addition, the beam under a transversal force does not snap until the beam tip passes a certain unstable position. Furthermore, the critical buckling load increases with an increasing initial angle α, so does the critical displacement. Finally, the incremental displacement numerical method can be used to solve any nonlinear post-buckling problems of inclined beams with large deflection.

Acknowledgment

The authors wish to express their sincere thanks to the NSAF Joint Foundation of China (Grant No. 10476019).

Special gratitude is owed to the two anonymous referees, Ms. Li Wanli and Ms. Ren Lihua, whose comments and suggestions greatly helped us to improve the presentation and quality of the paper.

References

[1] Enikov, E. T., Kedar, S. S., and Lazarov, K. V., 2005, "Analytical Model for Analysis and Design of V-Shaped Thermal Microactuators," J. Microelectromech. Syst., **14**(4), pp. 788–798.
[2] Seide, P., 1975, "Accuracy of Some Numerical Methods for Column Buckling," J. Engrg. Mech. Div., **101**(5), pp. 549–560.

[3] Mau, S. T., 1989, “Buckling and Post-Buckling Analyses of Columns With Discrete Supports,” J. Eng. Mech., **115**(3), pp. 721–739.

[4] Fang, W., and Wickert, J. A., 1994, “Post-Buckling of Micromachined Beams,” J. Micromech. Microeng., **4**(3), pp. 182–187.

[5] Wang, C. Y., 1997, “Post-Buckling of a Clamped-Simply Supported Elastica,” Int. J. Non-Linear Mech., **32**(6), pp. 1115–1122.

[6] Hartono, W., 1997, “Elastic Nonlinear Behavior of Truss System Under Follower and Non-Follower Forces,” Comput. Struct., **63**(5), pp. 939–949.

[7] Hartono, W., 2001, “On the Post-Buckling Behavior of Elastic Fixed-End Column With Central Brace,” Z. Angew. Math. Mech., **81**(9), pp. 605–611.

[8] Coffin, D. W., and Bloom, F., 1999, “Elastica Solution for the Hygrothermal Buckling of a Beam,” Int. J. Non-Linear Mech., **34**(6), pp. 935–947.

[9] Li, S. R., and Zhou, Y. H., 2005, “Post-Buckling of a Hinged-Fixed Beam Under Uniformly Distributed Follower Forces,” Mech. Res. Commun., **32**(4), pp. 359–367.

[10] Gianchandani, Y. B., and Najafi, K., 1996, “Bent-Beam Strain Sensors,” J. Microelectromech. Syst., **5**(1), pp. 52–58.

[11] Que, L., Park, J. S., and Gianchandani, Y. B., 2001, “Bent-Beam Electrothermal Actuators-Part I: Single Beam and Cascaded Devices,” J. Microelectromech. Syst., **10**(2), pp. 247–253.

[12] Qiu, J., Lang, J. H., and Slocum, A. H., 2001, “A Centrally-Clamped Parallel-Beam Bistable MEMS Mechanism,” *14th IEEE International Conference on Micro Electro Mechanical System*, IEEE, Switzerland, pp. 353–356.

[13] Jasmina, C. T., and Andrei, S., 2004, “Dynamic Analysis of a Snap-Action Micromechanism,” *Conference on IEEE Sensors’04*, Vienna, Austria, pp. 1245–1248.

[14] Timoshenko, S. P., and Gere, J. M., 1988, *Theory of Elastic Stability*, 2nd ed., McGraw-Hill, New York, Chap. 2.

[15] Wang, L. M., and Fan, Q. S., 1996, “Study of Post Buckling Behaviour for the Phase to Phase Composite Spacer,” Journal of Tsinghua University (Science and Technology)., **36**(9), pp. 70–76.

A. Sahli
e-mail: sahli@univ-usto.dz

M. B. Guemmour

S. Kebdani

D. Boutchicha

O. Rahmani

Department of Mechanical Engineering,
Laboratory of Applied Mechanics,
LMA, University of Sciences and Technology,
B.P. 1505 Oran,
El Menaouer 31000, Algeria

Independent Meshing of Contact Surfaces in 3D Boundary Element Method Contact Analysis

This paper deals with the development of two new boundary element algorithms for solving 3D, frictional, and linear elastostatic contact problems. The main contribution of this research is that solving 3D boundary element models with nonconforming discretizations becomes possible for the first time by using the proposed algorithms. The new algorithms provide the contact constraint equations that will be added to the underdetermined linear system of equations. These algorithms are implemented in a new 3D boundary element code using C++ *and verified using several numerical examples. For the models studied, the results using the new boundary element algorithms match well with the finite element results and clearly demonstrate the feasibility of the new boundary element approach for 3D contact analysis.* [DOI: 10.1115/1.2912998]

Keywords: BEM, three-dimensional contact, nonconforming discretizations

Introduction

After Andersen [1] published the paper on the BEM for two-dimensional contact problem, many papers have followed [2–7]. The common characteristic in these papers is that they adopt a direct constraint technique with which contact constraints are directly imposed without using the penalty parameter or Lagrangian multiplier. Even though, there were research results using different approaches such as flexibility matrix method [8] or gap element method [9], it seems that the direct constraint approach is more suitable for boundary element methos (BEM) than for finite element method (FEM) because tractions are direct output of the BEM solution. The Lagrangian multiplier or the penalty parameter, which are the methods used to impose contact constraints in displacement based FEM, may not be beneficial for BEM, though it may be possible to use those approaches in BEM [10].

Like the FEM, the mathematical programming approach based on variational inequality form has also been used for the BEM, Kosoie et al. [11] Another interesting approach is to try to combine the advantages of FEM and BEM. Landenberger and El-Zafrany's work [9] adapted BEM for bodies and FEM for contact areas. On the contrary, Kosior et al. used FEM for bodies and BEM for contact areas.

Man's monograph [12] is a good starting point for the application of the BEM to contact problem even though it is only for two-dimensional problems. It also deals with the contact problems related to fracture mechanics. Dandekar and Conant's work [2] is also valuable in understanding the BEM contact program for solving 2D conformingly meshed problems.

For nonconforming discretization, Blazquez and Paris pioneered the initial work in their article [13] in 1992. Olukoko and Becker published similar work in 1993 [6]. Huesmann and Kuhn presented a similar work in 1994 [4]. Paris and Blazquez [14] suggested using linear discontinuous element for frictionless problem.

All the work mentioned above is only for two-dimensional problems and used the shape function approach. In 1998, Blazquez and Paris compared the approaches using shape functions and investigated the problems of this approach [15]. Blazquez et al. [16] proposed a new approach to remedy the problem arising from using the shape function approach. In 1992, Chen and Chen [17] proposed the transformation matrix method for two-dimensional contact problem with friction. They claim that the method is highly efficient. In 1998, Martin and Aliabadi [18] published a new approach for nonconforming mesh for two-dimensional contact problem. They utilized the fact that inside the element, which is a smooth surface, additional equation can be obtained by the singularity removal technique. In 1999, Iban et al. [19] proposed a new approach. They developed a variable shape function in which the center node of the quadratic line element can move. The moving center node will match to the node of the other body. By this method, the node-on-point situation become node-to-node situation.

For three-dimensional problems, Garrido et al. [20] did the first work for the frictional contact problem in 1994. Their formulation was based on an incremental form and used triangular constant element. Yamazaki et al. [10] published in 1994 a penalty parameter-based method using eight-node quadratic element. Segond and Tafreshi [7] used linear triangular element for frictionless problem in 1998. The advantage of Segond's work is that there exists analytical integration for linear triangular element. In 1998, Ghaderi-Panah and Fenner [21] published their work using quadratic element method for frictionless problems. Their formulation was based on the relatively simple contact condition of frictionless problem and used nine-node Lagrangian elements to model the contact region. Leahy and Becker's work [22] was based on localized contact variables. They used eight-node quadratic elements and aimed for frictional problem.

The above mentioned research (3D contact problems) is for elastostatic problems and needs a conforming mesh to solve the problems. If the current status of the BEM for contact problems is compared to that of the FEM, the lack of development of 3D BEM with nonconforming discretization is obvious.

As it happens in FEM, BEM for contact problems can be developed to solve nonlinear problems, such as plasticity, shape optimization, and crack problems [4,12,23–25].

In this paper, two new algorithms that adapt the boundary integral equation (BIE) approach to three-dimensional contact problems are developed because the BIE approach has some advantages over the other methods. This paper describes the contributions for solving nonconformingly discretized contact problems with a new three-dimensional BEM program. The new

---

Contributed by the Applied Mechanics Division of ASME for publication in the JOURNAL OF APPLIED MECHANICS. Manuscript received August 28, 2007; final manuscript received March 30, 2008; published online May 19, 2008. Review conducted by Subrata Mukherjee.

algorithms provide the contact constraint equations that will be added to the underdetermined linear system of equations.

The reasons for using nonconforming discretizations are as follows.

1. For problems that result in large deformation or large displacement, even an initially conformingly discretized mesh can become a nonconforming mesh as the load is applied.
2. For some problems, the geometry is so complex that it is impossible to conformingly discretize; otherwise a lot of effort is required to mesh. The conformity is questionable when a conforming mesh is used even for simple nonconforming geometry.
3. The analyst may want a quick and easy mesh because the accuracy of the result is relatively less important or the result with a nonconforming mesh is believed to be sufficiently accurate compared to the result with a conforming mesh.

Therefore, the ability to solve the contact problems with a nonconforming mesh is the first step to solve more advanced and realistic problems.

Development of the BEM for Contact Problems

The equations necessary to implement three-dimensional BEM for contact problems are given in this section. One of the purposes of this section is to explain the fundamental concept necessary to build three-dimensional BEM program for contact problems. Only the contents related to the direct constraint technique are described.

The BIE for three-dimensional linear elastostatics is [26–28]

$$C_{ij}u_j(P) + \int_\Gamma T_{ij}(P,Q)u_j(Q)dS(Q) = \int_\Gamma U_{ij}(P,Q)t_j(Q)dS(Q) \tag{1}$$

where $T_{ij}(P,Q)$ is the traction kernel function, and $U_{ij}(P,Q)$ is the displacement kernel function.

The term C_{ij} is generally a function of the geometry variation at the boundary point P. Provided that P is a smooth boundary point, that is, the outward normal vector to the boundary is continuous at P, then it can be shown that $C_{ij}=1/2\delta_{ij}$; P and Q are source and field point, respectively.

Because multiple bodies are involved in contact mechanics, the main issue in the contact BEM analysis is that the formation of the system matrix for each body is needed first. Then, the system matrix of each body will be combined to form the system matrix for the whole contact system. Incremental form combined with iterations is necessary to solve nonlinear contact problems using linearized system matrices.

First, a new total external force is represented as

$$F_j^m = F_j^{m-1} + \Delta F_j^m \tag{2}$$

where ΔF_j^m is the increment of the load at step m, with $m = 1, 2, \ldots,$ total number of load steps.

There are three cases of applying the load for contact problem. They are called the total loading scheme, pseudoincremental loading scheme, and fully incremental loading scheme. In Eq. (2), there are three possibilities for ΔF_j^m term—zero, fixed, or variable, which correspond to the three loading schemes.

For fully incremental loading scheme, the method to calculate the next increment of loading is necessary. Usually, the previous two loading steps are used to extrapolate and/or interpolate the next incremental load. Another issue that needs to be considered is how to decide the direction of tangential slip.

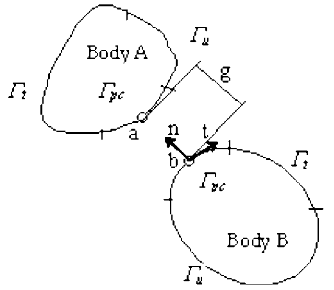

Fig. 1 Schematic diagram. Point *a* or *b* is either a node or a point on Body A or B

The traction and displacement corresponding to the increment of load (2) are

$$\begin{aligned} u_j^m &= u_j^{m-1} + \Delta u_j^m \\ t_j^m &= t_j^{m-1} + \Delta t_j^m \end{aligned} \tag{3}$$

When Eq. (3) is inserted into Eq. (1), we obtain the following BIE:

$$\begin{aligned} C_{ij}(u_j^{m-1} + \Delta u_j^m) &+ \int_\Gamma T_{ij}(P,Q)(u_j^{m-1}(Q) + \Delta u_j^m(Q))dS(Q) \\ &= \int_\Gamma U_{ij}(P,Q)(t_j^{m-1}(Q) + \Delta t_j^m(Q))dS(Q) \end{aligned} \tag{4}$$

At the $(m-1)$th step, the system is also in equilibrium condition as governed by Eq. (1). Therefore, Eq. (4) is reduced to the following incremental form:

$$C_{ij}\Delta u_j^m + \int_\Gamma T_{ij}(P,Q)\Delta u_j^m(Q)dS(Q) = \int_\Gamma U_{ij}(P,Q)\Delta t_j^m(Q)dS(Q) \tag{5}$$

In Eq. (5), the boundary for each body is divided as follows (Fig. 1):

$$\begin{aligned} \Gamma &= \Gamma_t + \Gamma_u + \Gamma_{pc} \\ \Gamma_{pc} &= \Gamma_{nc} + \Gamma_{rc} \\ \Gamma_{rc} &= \Gamma_{st} + \Gamma_{sl} \end{aligned} \tag{6}$$

First, the representation of Eq. (6) means that the boundary for each body (Γ) is divided into three types: the boundary where traction is given (Γ_t), the boundary where the displacement is given (Γ_u), and the assigned boundary where contact is possible to occur (Γ_{pc}).

The second representation of Eq. (6) means that the contact occurs at some part of assigned contact area. This fact requires that the first iteration loop at each load step should be used to distinguish the possible contact area (Γ_{pc}) as the region where contact occurs (Γ_{rc}) and the region where contact does not occur (Γ_{nc}).

The last representation of Eq. (6) means that there are two regions inside the contact area. The second iteration loop at each load step is therefore used to divide the contact area (Γ_{rc}) into two different regions—stick region (Γ_{st}) and slip region (Γ_{sl}).

Note that for possible contact region (Γ_{pc}), both displacement and traction are unknown variables. Therefore, the system matrix is underdetermined at the current step.

For each iteration, the contact status is checked to see if the compatibility or equilibrium is violated or not. After the contact mode is determined, the corresponding contact constraint equations are added to the underdetermined systems in the BEM. This iteration continues until the compatibility and equilibrium are satisfied. Then, the load step is increased and the procedure repeated.

As easily anticipated, the more the nodes are in the possible contact region, the slower the calculation because more iterations occur. However, in order to obtain reasonable results, some minimum number of elements should be employed in the contact region.

In the stick mode, the constraint equations are

$$\begin{gathered}
\Delta(t_{t1}^{a})^{m}-\Delta(t_{t1}^{b})^{m}=-[(t_{t1}^{a})^{m-1}-(t_{t1}^{b})^{m-1}]\\
\Delta(t_{t2}^{a})^{m}-\Delta(t_{t2}^{b})^{m}=-[(t_{t2}^{a})^{m-1}-(t_{t2}^{b})^{m-1}]\\
\Delta(t_{n}^{a})^{m}-\Delta(t_{n}^{b})^{m}=-[(t_{n}^{a})^{m-1}-(t_{n}^{b})^{m-1}]\\
\Delta(u_{t1}^{a})^{m}+\Delta(u_{t1}^{b})^{m}=0;\quad \Delta(u_{t2}^{a})^{m}+\Delta(u_{t2}^{b})^{m}=0,\\
\Delta(u_{n}^{a})^{m}+\Delta(u_{n}^{b})^{m}=g_{0}-[(u_{n}^{a})^{m-1}+(u_{n}^{b})^{m-1}]=g_{0}^{m}
\end{gathered}\tag{7}$$

where g is the distance between points a and b (Fig. 1). The subscripts n, t_1, t_2 mean normal direction and two tangential directions, respectively.

In the slip mode, the constraint equations are

$$\begin{gathered}
\Delta(t_{t1}^{a})^{m}-\Delta(t_{t1}^{b})^{m}=-[(t_{t1}^{a})^{m-1}-(t_{t1}^{b})^{m-1}],\\
\Delta(t_{t2}^{a})^{m}-\Delta(t_{t2}^{b})^{m}=-[(t_{t2}^{a})^{m-1}-(t_{t2}^{b})^{m-1}]\\
\Delta(t_{n}^{a})^{m}-\Delta(t_{n}^{b})^{m}=-[(t_{n}^{a})^{m-1}-(t_{n}^{b})^{m-1}],\\
\Delta(t_{t1}^{a})^{m}\pm\mu\Delta(t_{n}^{b})^{m}=-[(t_{t1}^{a})^{m-1}\pm\mu(t_{n}^{b})^{m-1}]\\
\Delta(t_{t2}^{a})^{m}\pm\mu\Delta(t_{n}^{b})^{m}=-[(t_{t2}^{a})^{m-1}\pm\mu(t_{n}^{b})^{m-1}],\\
\Delta(u_{n}^{a})^{m}+\Delta(u_{n}^{b})^{m}=g_{0}-[(u_{n}^{a})^{m-1}+(u_{n}^{b})^{m-1}]=g_{0}^{m}
\end{gathered}\tag{8}$$

In the separation mode, the constraint equations are

$$\begin{gathered}
\Delta(t_{t1}^{a})^{m}-\Delta(t_{t1}^{b})^{m}=-[(t_{t1}^{a})^{m-1}-(t_{t1}^{b})^{m-1}],\quad \Delta(t_{t2}^{a})^{m}-\Delta(t_{t2}^{b})^{m}\\
=-[(t_{t2}^{a})^{m-1}-(t_{t2}^{b})^{m-1}]\\
\Delta(t_{n}^{a})^{m}-\Delta(t_{n}^{b})^{m}=-[(t_{n}^{a})^{m-1}-(t_{n}^{b})^{m-1}],\quad \Delta(t_{t1}^{a})^{m}=-[(t_{t1}^{a})^{m-1}]\\
\Delta(t_{t2}^{a})^{m}=-[(t_{t2}^{a})^{m-1}],\quad \Delta(t_{n}^{a})^{m}=-[(t_{n}^{a})^{m-1}]
\end{gathered}\tag{9}$$

The equations used to check and change the contact status from separate to contact and vice versa are

$$(\Delta u_{n}^{a}+\Delta u_{n}^{b})^{m}\geq g_{0}^{m-1},\quad t_{n}^{m-1}+\Delta t_{n}^{m}<0\tag{10}$$

The equations used to check and change the contact status from slip to stick and vice versa are

$$|t_{t}^{m-1}+\Delta t_{t}^{m}|\geq|\mu(t_{n}^{m-1}+\Delta t_{n}^{m})|,\quad (t_{n}^{m-1}+\Delta t_{n}^{m})^{b}(\Delta u_{t}^{a}+\Delta u_{n}^{b})^{m}\leq 0\tag{11}$$

In the BIE approach, this idea is based on the observation that a boundary element is always a smooth curve (2D) or smooth surface (3D). Thus, the displacement and traction at any point b on a boundary element can be evaluated using the following boundary integral equations:

$$\begin{aligned}
\frac{1}{2}u_{i}^{b}+\sum_{m=1}^{M_B}\left\{\int_{\Gamma^m}T_{ij}(P=b,Q)u_{j}(Q)d\Gamma(Q)\right\}
&=\sum_{m=1}^{M_B}\left\{\int_{\Gamma^m}U_{ij}(P=b,Q)t_{j}(Q)d\Gamma(Q)\right\}
\end{aligned}\tag{12}$$

The boundary traction integral equation is obtained by differentiating Eq. (1) and applying the material constitutive relationships

$$\begin{aligned}
\frac{1}{2}t_{i}^{b}+E_{ijkl}n_{j}(b)\sum_{m=1}^{M_B}\left\{\int_{\Gamma^m}T_{kpl}(P=b,Q)u_{p}(Q)d\Gamma(Q)\right\}
&=E_{ijkl}n_{j}(b)\sum_{m=1}^{M_B}\left\{\int_{\Gamma^m}U_{kpl}(P=b,Q)t_{p}(Q)d\Gamma(Q)\right\}
\end{aligned}\tag{13}$$

where E_{ijkl} is Young's modulus tensor, $n_j(b)$ is the component of the outward unit normal to the boundary at the Point b, $P=b$ represents a point that is inside an element in the contact area. The factor $1/2$ multiplying the traction component t_i corresponds to the jump on the displacement derivatives and on the tractions due to the limiting process. This factor is the traction counterpart to the term C_{ij} appearing in the displacement integral equation.

$$U_{kpl}=\frac{\partial U_{kp}}{\partial x_{l}(b)},\quad T_{kpl}=\frac{\partial T_{kp}}{\partial x_{l}(b)},$$

M_B the total number of elements on Body B

The advantages of this approach are that the displacement and traction calculated from the above BIEs are more theoretically accurate and that the system is more stable compared to the shape function approach because the equations from this approach are global contrary to the equations from shape functions, which are local. The disadvantage is that, for each node in the contact region, numerical integration needs to be performed, so that the time to build the system matrix for each iteration is dramatically increased compared to the shape function approach.

BEM Approaches for 3D Contact Analysis

First Method. The main idea of the first new algorithm is that the BIE approach explained in previous section is extended to three-dimensional problems due to the advantages of the BIE approach. Even though it seems simple to extend the 2D idea to 3D, there are many technical difficulties to be overcome and these difficulties will be described in this section. Some of the difficulties are from the BEM itself (the singularities of kernels, especially traction kernel) and some of them are from the complications of programming for contact problem. These may be part of the reasons why there is no published work regarding 3D BEM for contact problem with nonconforming discretizations. The concept of the new approach is depicted in Fig. 2.

Dealing With Singular Integrals. The first difficulty to be overcome is the singularities of the integrand of Eqs. (12) and (13). This singularity occurs for each docking point when the integration on the element where the docking point is located is performed.

It was decided not to use Eq. (13) for evaluating the traction at the docking point in forming the system matrix, since the cost of computing the system matrix will become too high and the difficulties in dealing the singular integrals. Thus, for the surface of one of the bodies in contact (let it be called slave surface), shape function approach is used instead to form the system matrix. The BIE approach is employed to evaluate the displacement at the docking point. When the integration of the element on which a docking point (Fig. 2) resides is needed (i.e., integrations in Eq. (12)), transformation of the variable method is used to deal with the singular kernels. The variables will be changed as

$$\begin{gathered}
\xi=\sum_{c=1}^{3}\bar{N}_{c}(\bar{\xi},\bar{\eta})(\xi)_{c}\\
\eta=\sum_{c=1}^{3}\bar{N}_{c}(\bar{\xi},\bar{\eta})(\eta)_{c}
\end{gathered}\tag{14}$$

where

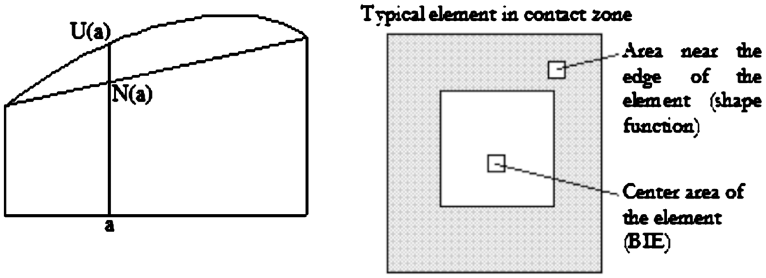

(a) Accuracy of variables from BIE: U(a) is an accurate value from the BIE equation and N(a) is an approximated value from the linear shape function.

(b) Concept of the first algorithm. if a docking point is inside the hatched area, the shape function approach is used. Otherwise the BIE approach is used. (☐) is a docking point

Fig. 2 Conceptual diagrams for the first algorithm

$$\bar{N}_1 = \frac{1}{4}(1+\bar{\xi})(1-\bar{\eta}), \quad \bar{N}_2 = \frac{1}{4}(1+\bar{\xi})(1+\bar{\eta}), \quad \bar{N}_3 = \frac{1}{2}(1-\bar{\xi}) \tag{15}$$

and

$$\bar{J} = \frac{\partial \xi}{\partial \bar{\xi}}\frac{\partial \eta}{\partial \bar{\eta}} - \frac{\partial \eta}{\partial \bar{\xi}}\frac{\partial \xi}{\partial \bar{\eta}} \tag{16}$$

Since the new Jacobian of Eq. (16) is of order $O(r)$, one order of the singularity is removed from the new integrand. Therefore, the displacement kernel becomes regular and traction kernel becomes weakly singular for Eq. (12).

The research about integrating strong singular kernel in 3D BEM can be found in Refs. [29–31]. In fact, the integration for the traction kernel in Eq. (12) for the element where the docking point is located exists in the Cauchy principal value sense. The methods mentioned in Refs. [29–31] have been developed for 3D BEM, so they are well suited for the current problem. The code for dealing with the strongly singular integrals is adapted from the work of Doblaire and Gracia [30].

After the integration is executed, Eq. (12) produces linear algebraic equations like

$$u_j^b = f(d_1, \ldots, d_i, \ldots, d_N) \tag{17}$$

where d_i is an unknown degree of freedom.

Dealing With Nearly Singular Integration. When the docking point is near the edge of an element, the integration on the neighboring element becomes nearly singular and it is difficult to integrate. Theoretically, we can use adaptive integration, where the element to be integrated is subdivided, or the line integral approach [32], where the integral is converted to line integrals to overcome this difficulty.

A different approach is employed in this research in order to increase the efficiency. The new approach is that if the distance between the docking point and the edge of the element is less than a predetermined value, the shape function approach is used. It is based on the observation that the error from using shape functions may be smaller when the docking point is near the edge of the element than the BIE approach. The decision of the critical distance by which whether the shape function approach or BIE approach will be used is a trade-off between accuracy and efficiency, and can be a further research topic. Factors such as mesh quality, integration scheme, and so on can play a role in the decision.

Second Method. The main idea of this approach is shown in Fig. 3. In this approach, Eq. (12) is used for the center point of each element, i.e., $(\xi, \eta) = (0, 0)$ and saved as

$$u_j^0 = f^0(d_1, \ldots, d_i, \ldots, d_N) \tag{18}$$

When the docking point of the element is determined, the equation for the displacement or traction is formulated using a new set of shape functions employing the value at the center point. The new shape functions are different from the element shape functions. They are used to generate constraint equations by algebraic operation and will not add computational overhead. Depending on the original shape functions used for integrating the BIE, the new shape functions to be used will be decided.

For Linear Element. The shape functions for linear triangular elements are used for this case. Then, for the docking point b, a new equation is produced as

$$u_j^b = N_1'(u_j)_1 + N_2'(u_j)_2 + N_3' u_j^0 = f'(d_1, \ldots, d_i, \ldots, d_N) \tag{19}$$

N_i' are the triangular shape functions: $N_1' = \xi$; $N_2' = \eta$; $N_3' = 1 - \xi - \eta$. The new equation is added to the system matrix with more manipulations such as coordinate transformation and imposing boundary conditions and contact constraints.

For Eight-Node Quadratic Element. The same procedure is necessary to produce the equations for docking point except that nine-node Lagrangian interpolation is used. We have

$$\begin{aligned} u_j^b = {} & N_1'(u_j)_1 + N_2'(u_j)_2 + N_3'(u_j)_3 + N_4'(u_j)_4 + N_5'(u_j)_5 + N_6'(u_j)_6 \\ & + N_7'(u_j)_7 + N_8'(u_j)_8 + N_9' u_j^0 = f'(d_1, \ldots, d_i, \ldots, d_N) \end{aligned} \tag{20}$$

where the nine-node shape functions are

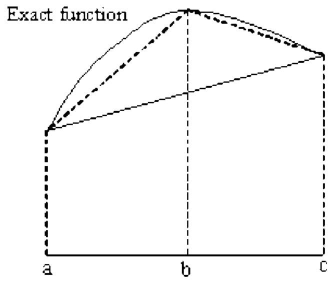

Fig. 3 The concept of second algorithm: Because one more value is known, new approximation (blue dashed line) is more accurate than original approximation (black solid line)

$$
\begin{gathered}
N'_1 = \frac{1}{4}\xi\eta(1-\xi)(1-\eta), \quad N'_2 = -\frac{1}{4}\xi\eta(1+\xi)(1-\eta) \\
N'_3 = \frac{1}{4}\xi\eta(1+\xi)(1+\eta) \\
N'_4 = -\frac{1}{4}\xi\eta(1-\xi)(1+\eta), \quad N'_5 = -\frac{1}{2}\eta(1-\xi^2)(1-\eta) \\
N'_6 = \frac{1}{2}\xi(1+\xi)(1-\eta^2) \\
N'_7 = \frac{1}{2}\eta(1-\xi^2)(1+\eta), \quad N'_8 = -\frac{1}{2}\xi(1-\xi)(1-\eta^2) \\
N'_9 = (1-\xi^2)(1-\eta^2)
\end{gathered}
\tag{21}
$$

Formation of System Matrix. Once all the necessary equations are obtained as described above, the next step is to form the system matrix. There are many ways to assemble the system matrix. Whatever partitioning is selected, the tracking of the locations of the columns should be carefully recorded. In this study, the system matrix is partitioned as

$$
\begin{bmatrix}
\mathbf{A}_{\mathrm{nc}} & 0 & \mathbf{A}_{\mathrm{c}}^{u} & 0 & \mathbf{A}_{\mathrm{c}}^{t} & 0 \\
0 & \mathbf{B}_{\mathrm{nc}} & 0 & \mathbf{B}_{\mathrm{c}}^{u} & 0 & \mathbf{B}_{\mathrm{c}}^{t} \\
0 & \mathbf{C}_{A}^{1} & \mathbf{C}_{A}^{2} & \mathbf{C}_{A}^{3} & 0 & \mathbf{C}_{A}^{4} \\
0 & 0 & 0 & 0 & \mathbf{C}_{B}^{1} & \mathbf{C}_{B}^{2}
\end{bmatrix}
\begin{Bmatrix}
d_A^{\mathrm{nc}} \\ d_B^{\mathrm{nc}} \\ d_A^{u} \\ d_B^{u} \\ d_A^{t} \\ d_B^{t}
\end{Bmatrix}
=
\begin{Bmatrix}
f_1 \\ f_2 \\ f_3 \\ f_4
\end{Bmatrix}
\tag{22}
$$

Subscripts A and B refer to Bodies A and B. Subscripts nc and c mean noncontact and contact regions. Subscripts u and t show the relationship to displacement and traction. Submatrices **A** and **B** are formulated from Bodies A and B, and **C** is formulated from contact constraints.

Because only part of the system matrix changes as the load changes, static condensation or other schemes can be employed to save the time in inverting the whole system matrix for each iteration. In addition, iterative solvers such as (generalized minimal residual) (GMRES) or (conjugate gradient) (CG) [33] can be more effectively utilized for this system than solving a fully populated system because this system is in some way banded, as shown in Eq. (22).

There are two loops. The first loop is to decide the appropriate load increment and the corresponding contact area by checking whether the control pair near the contact area edge for the previous load step is contacted or separated. The second loop is to divide the determined contact area as stick or slip zone. When the slip condition is imposed on the system, the direction of the tangential traction becomes opposite to the direction of the displacement for the frictionless problem.

Every time before imposing contact constraints in the system equation, a coordinate transformation is necessary because contact constraints are described using local coordinates. If only shape function approach is used for both bodies to satisfy the compatibility and equilibrium condition of the contact mode, then methods such as least squares or minimum potential are necessary to make sure that the traction is correctly transmitted.

Because there are many possible sources of numerical errors in the BEM, it is possible that the solution converges to wrong values. To prevent this, the implementation in this research adopted force convergence scheme. For every step of load increment, the global force equilibrium in the L_2 norm sense is checked for the two contact bodies.

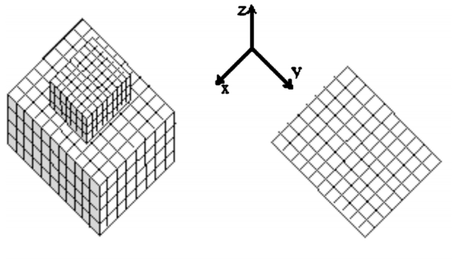

a) One mesh b) Contact elements

Fig. 4 Geometry and mesh for flat punch problem

Numerical Examples

To test the developed 3D BEM schemes for contact mechanics analysis, two examples are presented and the results are reported in this section. The example problems are three-dimensional problems with frictional contact.

It is not a straightforward task to investigate whether the solution for a contact problem is accurate enough or not. Solving three-dimensional contact problems is still a difficult problem. First, experimental measurement of contact pressure and especially tangential traction is not easy, if not impossible. In addition, because each specimen has variations at the microscale in surface characteristics, material properties, etc., experimental results can vary for each test specimen, which makes it difficult to compare experimental models with numerical ones.

Second, the analytical solutions for contact problems are often limited to simple cases. Proving the existence and uniqueness of the solution for a contact problem in the general setting is still not available [34]. These two limitations make it difficult to verify numerical methods including FEM and BEM for contact problems.

Though each algorithm can be implemented for both bilinear and quadratic elements, the first algorithm is implemented with bilinear elements and the second algorithm is implemented with quadratic elements. The reason is that the second algorithm can utilize nine-node Lagrangian shape functions when eight-node serendipity elements are used for the mesh.

Even though the mathematically rigorous verification is almost impossible and how the model for a specific problem behaves as parameters change is still not understood well. FEM has been utilized to solve the real world problems and has turned out to be very successful in most of the applications. In this context, the FEM solutions are used in this study for comparison because the proposed BEM algorithms are supposed to be equivalent to the FEM regarding the accuracy, if not better. The developed BEM code has been verified using several stress analysis (noncontact) problems before it is applied to solve the contact problems study; the entire bodies in contact are meshed in both FEM (ANSYS) and BEM cases. The mesh for the BEM model is the same as the surface nodes and elements in the corresponding FEM mesh. The results of the BEM incorporating the proposed algorithms are compared to the ANSYS FEM results, although one to one comparison has limitations because many parameters, such as values of the chosen penalty parameter (ANSYS only), are different and thus affect the FEM and BEM results.

Flat Punch Problem. This is a problem with conforming contact geometry, which is used first to test the developed BEM algorithm. The geometry and mesh of this example are shown in Fig. 4. The length, height, and width of the upper block are 1 m. The length, height, and width of the lower block are 2 m. Though the geometry is conforming, nonconforming mesh is used, as shown in Fig. 4. For testing purposes, the material properties used for this test case are Young's modulus $E=1.0\ \mathrm{N/m^2}$ and Poisson ratio $\nu=0.3$ for both contact bodies. A pressure of $0.1\ \mathrm{N/m^2}$ is applied for the upper surface of the punch (the upper block) and

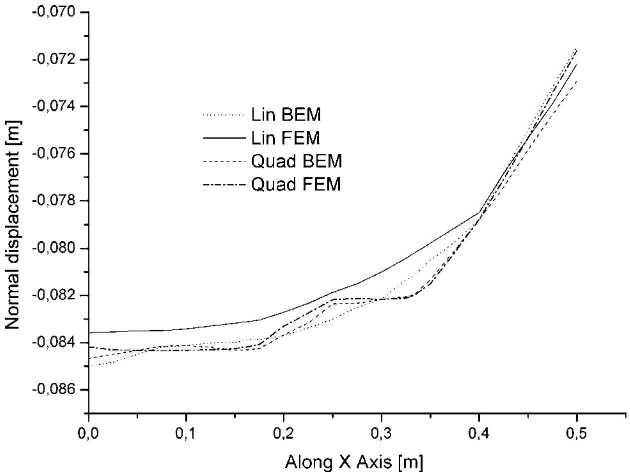

Fig. 5 Displacement in the direction normal to contact surface and along the *X* axis (block on block)

the lower surface of the foundation (the lower block) is constrained in all directions. Friction coefficient used in this example is 0.2.

For the BEM models, 1950 four-node linear elements and 702 eight-node quadratic elements are used. The analytical solution for a rigid punch on an infinite foundation has infinite stress values at the edges. At the sharp edge of the punch, tractions become very high as a singularity exists in the elastic solution. This singularity in stress can cause numerical instability if the punch is much harder than the foundation. The easy part of this example is that the nominal contact area is known a priori.

The results for the normal displacement, normal pressure, and tangential traction on the master surface along the positive *X* axis (from the center of the lower surface of the upper block to the edge of the lower surface) are summarized in Figs. 5–7. Note that the BEM results in all the cases are comparable with the FEM results in showing the correct trend. However, the BEM results exhibit some oscillations. The convergence from using linear elements to quadratic elements is not evident for BEM. These discrepancies may be due to the numerical difficulties in the nonlinear analysis and the singular behaviors of the solution for this problem. Further study on selecting the parameters and using finer meshes can be conducted.

Compared to the published results, although the numerical values are not the same, because of the differences in the geometries, material properties, and boundary conditions, the overall shapes of these plots show similar trends as in the results published in Ref. [22].

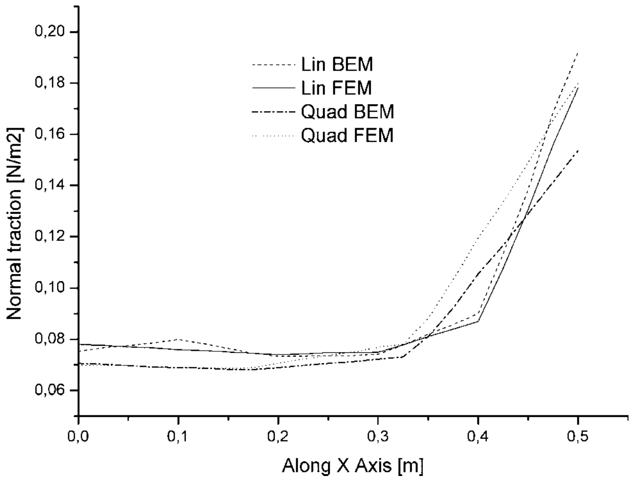

Fig. 6 Normal traction on contact surface (block on block)

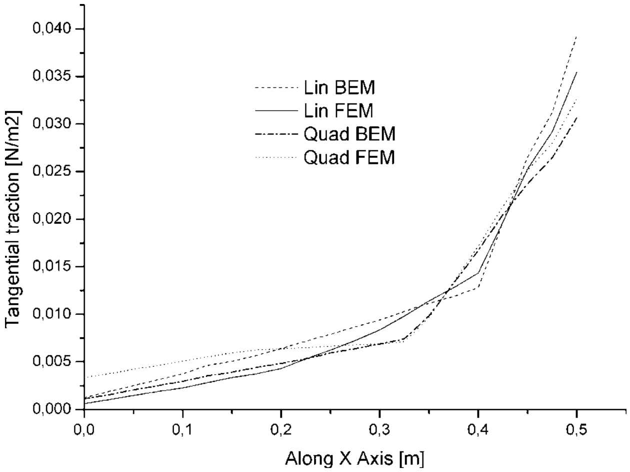

Fig. 7 Tangential traction on contact surface (block on block)

Cylinder on Block Problem. This example is one of the nonconforming contact problems. The geometry and one mesh for this example are shown in Fig. 8. The radius of the partial cylinder is 1 m, and the length along the axial direction is 1 m. The maximum height (*y*-direction) of the partial cylinder is 0.5 m. The block has the dimensions of 1 m, 0.5 m, and 1 m in the *X*, *Y*, and *Z* directions, respectively. The material properties used are the same as those used for the previous example. For testing, a pressure of 0.01 $\mathrm{N/m^2}$ is applied on the upper surface of the partial cylinder and the lower surface of foundation (lower block) is constrained in all directions. Friction coefficient used in this example is also 0.2.

For the BEM models, 2192 four-node linear elements and 2192 eight-node quadratic elements are used.

The results are summarized in Figs. 9 and 10. The *X* axis for the graphs starts from the center of the contact region and points to the direction, as shown in Fig. 8. In Fig. 9, the normal displacement is plotted, which shows good agreements regardless of the mesh density and the method used. The shape of the curve also looks very similar to the Hertz analytical result, which assumes an infinitely long rigid cylinder in contact with an elastic half space. The numerical results for the normal contact pressure are compared to the Hertz results in Fig. 10 and show good agreements (results are normalized by the Hertz solution with the half width of the contact area $a=0.14$ m and the maximum contact pressure $p0=0.0455\ \mathrm{N/m^2}$), even though Hertz solution is based on a *rigid* cylinder. When we consider the rigid cylinder assumption in Hertzian solution, the contact area may be larger for elastic cylinder on elastic foundation, as shown in Fig. 10, because the elastic cylinder becomes flattened as load increases. Note that the normal contact pressure changes in the *Z* direction for any fixed *X* coor-

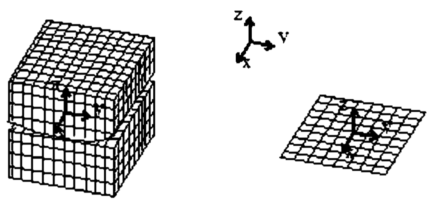

a) One mesh b) Contact elements

Fig. 8 Geometry and mesh of the second example

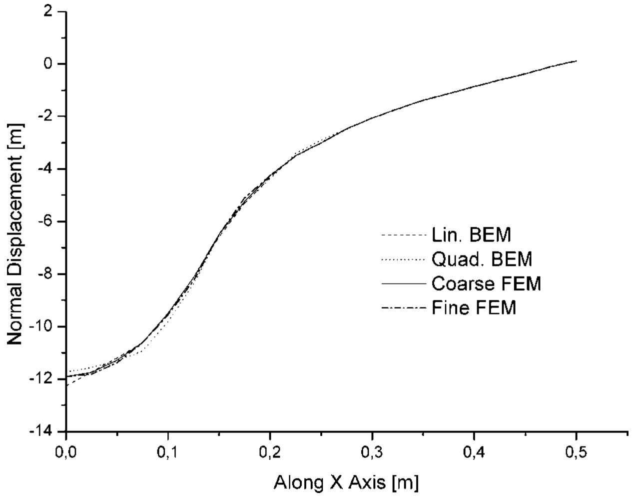

Fig. 9 Displacement in the direction normal to contact surface (cylinder on block)

dinate. For the Hertz solution, this phenomenon does not happen because the Hertz solution is for a plane strain half space.

Discussion

The results of the proposed BEM algorithms for the examples studied show reasonable agreement with the FEM results (with about 5–16% differences). The efficiency of the BEM, however, was not good for the given meshes, as expected. Considering that the current implementation has a lot of room for improving and that smaller number of BEM elements may have been sufficient to obtain results with similar accuracy, the efficiency difference may not be that large for real problems. In addition, total analysis time including preprocessing for building geometry and meshing can be much shorter with the BEM as compared to the FEM.

For both cases, FEM models using quadratic elements showed fluctuating results. Though the results of proposed BEM algorithms also show fluctuations for the examples, the fluctuation is less for the BEM. These fluctuations may be caused by numerical errors or instability and need to be further investigated.

The loads applied for the example problems are compression only. The reason why the tangential load is not applied is that the possibility of rigid-body motion exists. Because current implementation is for solving static problems only, inertia force that can resist the rigid-body motion is not incorporated in the program. In other words, because at initial increment the load is so small that the contact force may not be large enough to hold the body that does not have displacement constraints or, numerically, initial gap may exist, the system matrix becomes singular or nearly singular. To avoid this problem, initial penetration can be imposed or temporary damping elements can be used. However, the algorithms proposed in this research can play an essential role as a foundation for solving dynamic contact problems, friction induced vibration problems, and large deformation problems.

Though simple examples as compared to real industrial problems (such as the gear coupling problem) are used in this BEM research, the results show the applicability of the BEM for certain contact problems, such as problems with complex geometries or problems with cracks, for both of which the BEM has been proved much easier to use in the modeling.

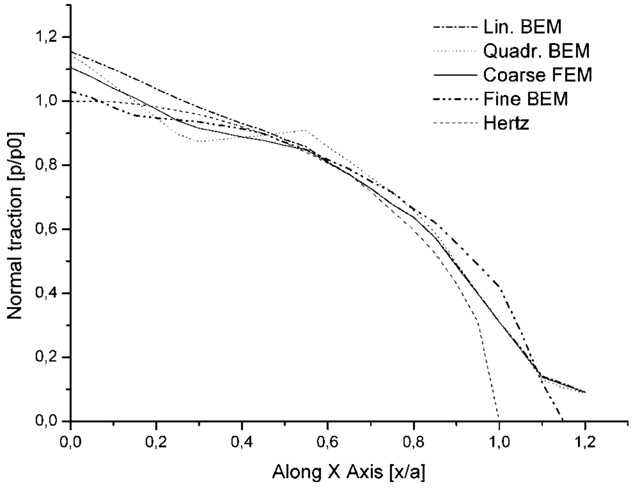

Fig. 10 Normal traction on contact surface (cylinder on block)

Conclusion

As the main contribution of this paper, two algorithms to solve the three-dimensional and frictional contact problem by the BEM with nonconforming discretizations are proposed and implemented in C++. A new approach to improve the efficiency of the 3D boundary element method by taking into account the zero boundary conditions is proposed for computing the system matrix. The formation time of the system matrix can be reduced by roughly 20–40%.

Acknowledgment

This work was supported by the “Ministry of higher education and scientific research” Project CNEPRU (J0301920060015).

References

[1] Andersson, T., and Allan-Persson, B. G., 1981, “The Boundary Element Method Applied to Two-Dimensonal Contact Problems With Friction,” *Third International Seminar on Recent Advances in Boundary Element Methods*, Springer, Irvine.
[2] Dandekar, B. W., and Conant, R. J., 1992, “Numerical Analysis of Elastic Contact Problems Using the Boundary Integral Equation Method. Part 1: Theory,” Int. J. Numer. Methods Eng., **33**, pp. 1513–1522.
[3] Hack, R. S., and Becker, A. A., 1999, “Frictional Contact Analysis Under Tangential Loading Using a Local Axes Boundary Element Formulation,” Int. J. Mech. Sci., **41**, pp. 419–436.
[4] Huesman, A., and Kuhn, G., 1995, “Automatic Load Incrementation Technique for Plane Elastoplastic Frictional Contact Problems Using Boundary Element Method,” Comput. Struct., **56**(5), pp. 733–744.
[5] Karami, G., 1993, “Boundary Element Analysis of Two-Dimensional Elastoplastic Contact Problems,” Int. J. Numer. Methods Eng., **36**, pp. 221–235.
[6] Olukoko, O. A., and Becker, A. A., 1993, “A New Boundary Element Approach for Contact Problems With Fricion,” Int. J. Numer. Methods Eng., **36**, pp. 2625–2642.
[7] Segond, D., and Tafreshi, A., 1998, “Stress Analysis of Three-Dimensional Contact Problems Using the Boundary Element Method,” Eng. Anal. Boundary Elem., **22**, pp. 199–214.
[8] Takahashi, S., and Brebbia, C. A., 1992, “A Boundary Element Flexibility Aproach for Solving Contact Problems With Friction,” Eng. Anal. Boundary Elem., **4**.
[9] Landenberger, A., and El-Zafrany A., 1999, “A Boundary Element Analysis of Elasic Contact Problems Using Gap Finite Elements,” Comput. Struct., **71**, pp. 651–661.
[10] Yamazaki, K., Sakamoto, J., and Takumi, S., 1994, “Penalty Method for Three-Dimensional Elastic Contact Problems by Boundary Element Method,” Comput. Struct., **52**(5), pp. 895–903.
[11] Kosior, F., Guyot, N., and Maurice, G., 1999, “Anaysis of Frictional Contact Problem using Boundary Element Method and Domain Decomposition Method,” Int. J. Numer. Methods Eng., **46**, pp. 65–82.
[12] Man, K. W., 1994, *Contact Mechanics Using Boundary Elements*, Computational Mechanics, Southampton.
[13] Blazquez, A. et al., 1992, “An Algorithm for Frictionless Contact Problems With Non-Conforming Discretiations Using BEM,” *Boundary Element XIV*, C. A. Brebbia, J. Dominguez, and F. Paris, eds., Computational Mechanics, Southampton, pp. 409–420.
[14] Paris, F., Blazquez, A., and Canas, J., 1995, “Contact Problems With Nonconforming Discretizations Using Boundary Element Method,” Comput. Struct., **57**(5), pp. 829–839.
[15] Blazquez, A., Paris, F., and Canas, J., 1998, “Interpretation of the Problems Found in Applying Contact Conditions in Node-to-Point Schemes With Boundary Element Non-Conforming Discretizations,” Eng. Anal. Boundary Elem., **21**, pp. 361–375.
[16] Blazquez, A., Paris, F., and Mantic, V., 1998, “BEM Solution of Two-

Dimensional Contact Problems by Weak Application of Contact Conditions With Non-Conforming Discretizations," Int. J. Solids Struct., **35**(24), pp. 3259–3278.

[17] Chen, W. H., and Chen, T. C., 1992, "Boundary Element Analysis for Contact Problems With Friction," Comput. Struct., **45**(3), pp. 431–438.

[18] Martin, D., and Aliabadi, M., 1998, "A BE Hyper-Singular Formulation for Contact Problems Using Non-Conforming Discretization," Comput. Struct., **69**, pp. 557–565.

[19] Iban, A. L., Garrido, J. A., and Prieto, I., 1999, "Contact Algorithm for Non-Linear Elastic Problems With Large Displacements and Friction Using the Boundary Element Method," Comput. Methods Appl. Mech. Eng., **178**, pp. 51–67.

[20] Garrido, J. A., Forces, A., and Paris, F., 1994, "An Incremental Procedure for Three-Dimensional Contact Problems With Friction," Comput. Struct., **50**, pp. 201–215.

[21] Ghaderi-Panah, A., and Fenner, R. T., 1998, "A General Boundary Element Method Approach to the Solution of Three-Dimensional Frictionless Contact Problems," Eng. Anal. Boundary Elem., **21**, pp. 305–316.

[22] Leahy, J. G., and Becker, A. A., 1999, "The Numerical Treatment of Local Variables in Three-Dimensional Frictional Contact Problems Using the Boundary Element Method," Comput. Struct., **71**, pp. 383–395.

[23] Abascal, R., 1995, "2D Transient Dynamic Friction Contact Problems. I. Numerical Analysis," Eng. Anal. Boundary Elem., **16**, pp. 227–233.

[24] Martin, D., and Aliabadi, M., 1998, "Boundary Element Analysis of Two-Dimensional Elastoplastic Contact Problems," Eng. Anal. Boundary Elem., **21**, pp. 349–360.

[25] Simunovic, S., and Saigal, S., 1995, "Contact Surface Optimization Using Boundary Element Method," Comput. Struct., **56**(5), pp. 745–750.

[26] Becker, A. A., 1992, *The Boundary Element Method in Engineering: A Complete Course*, McGraw-Hill, New York.

[27] Beer, G., 2001, *Programming the Boundary Element Method: An Introduction for Engineers*, Wiley, New York.

[28] Gao, X., and Davies, T. G., 2002, *Boundary Element Programming in Mechanics*, Cambridge University Press, Cambridge.

[29] Dominguez-Hernandez, J., Gracia, L., and Doblare, M., 1995, "A Non-Linear transformation Algorithm for the Integration of the Singular Kernels in 3D BEM for Elastostatics," Eng. Anal. Boundary Elem., **17**, pp. 27–32.

[30] Doblare, M., and Gracia, L., 1997, "On Non-linear Transformations for the Integration of Weakly-singular and Cauchy Principal Value Integrals," Int. J. Numer. Methods Eng., **40**, pp. 3325–3358.

[31] Guiggiani, M., and Gigante, A., 1990, "A General Algorithm for Multidimensional Cauchy Principal Value Integrals in the Boundary Element Method," ASME J. Appl. Mech., **57**, pp. 906–915.

[32] Liu, Y., 1998, "Analysis of Shell like Structures by the Boundary Element Method Based on 3-D Elasticity: Formulation and Verification," Int. J. Numer. Methods Eng., **41**(3), pp. 541–558.

[33] Saad, Y., 1996, *Iterative Methods for Sparse Linear Systems*, PWS, Boston.

[34] Wriggers, P., 2002, *Computational Contact Mechanics*, Wiley, New York.

An Alternative to F. Y. M. Wan's Single Equation for an Elastic Right Circular Conical Shell

J. G. Simmonds
Fellow ASME
Department of Civil Engineering,
University of Virginia,
Charlottesville, VA 22904-4742
e-mail: jgs@virginia.edu

*In 1970, F. Y. M. Wan derived a single, complex-valued ordinary differential equation for an elastically isotropic right circular conical shell ("On the Equations of the Linear Theory of Elastic Conical Shells," Studies Appl. Math., **49**, pp. 69–83). The unknown was the nth Fourier component of a complex combination of the midsurface normal displacement and its static-geometric dual, a stress function. However, an attempt to formally replace the Fourier index n by a partial derivative in the circumferential angle θ results in a partial differential equation, which is eighth order in θ. The present paper takes as unknowns the traces of the bending strain and stress resultant tensors, respectively, and derives static-geometric dual partial differential equations of fourth order in both the axial and circumferential variables. Because of the explicit appearance of Poisson ratios of bending and stretching, these two equations cannot be combined into a single complex-valued equation. Reduced equations for beamlike (axisymmetric and lateral) deformations are also derived.* [DOI: 10.1115/1.2875798]

1 Introduction

Attempts to reduce the homogeneous eight-order system of partial differential equations of the classical linear theory of elastic shells to a system with fewer unknowns go back at least to Goldenveiser [1] who showed that if the normal deflection of the reference surface and its static dual, a stress function, were taken as unknowns then, in general, they satisfy a coupled pair of *sixth-order* equations. Two notable exceptions are *spherical* shells—see, for example, Koiter [2]—and *circular cylindrical* shells. A history of various reductions of the equations for this latter shell may be found in Refs. [3,4].

In Ref. [5] Sanders attempted to reduce the linear Sanders–Koiter (SK) equations [6,7] for elastically isotropic shells with nondevelopable midsurfaces (i.e., midsurfaces of nonzero Gaussian curvature) to a single, complex-valued partial differential equation, free of Poisson's ratio ν (save for its appearance in a small parameter also containing the thickness of the shell and a typical radius of curvature of the reference surface). The complex unknown was $N+iK$, where N and K are, respectively, the traces of the stress resultant and bending strain tensors. The success of the scheme depended on being able to add certain small coupling terms to the stress-strain relations, these terms, in turn, having to satisfy certain auxiliary partial differential equations. Unfortunately, as Sanders himself noted in an addendum to Ref. [5], his scheme foundered on Cohen's example [8] of the (near) inextensional deformation of a right helicoidal shell where the factor $1-\mu$ is prominent, μ being Poisson's ratio of bending. A later analysis by Latta and Simmonds [9] showed that the SK equations for a shell with *any* minimal reference surface (of which the right helicoidal shell is a special case) could be reduced to *two* coupled fourth-order partial equations for the rotation about the normal and a stress function. The appearance of the factors $1-\mu$ and $1+\nu$, where ν is a Poisson ratio of stretching, prevents the two equations from being written as a single complex-valued equation (without a conjugate unknown), confirming Sanders observation.

However, as Novozhilov's earlier analysis shows—see Refs. [10,11]—Sanders' scheme works for general cylindrical shells. Finally, Wan showed [12] that the equations for an elastically isotropic *right* circular cone, after a *Fourier decomposition* in the polar angle θ, can be reduced to a single, complex-valued fourth-order ordinary differential equation. However, if one attempts to formally replace the Fourier index n by the differential operator $\partial/\partial\theta$, one obtains an equation of eight order in θ. Herein, we show, alternatively, that the SK equations for an elastically isotropic right circular cone can be reduced to static-geometric dual fourth-order partial differential equation for K and N, which because of the explicit appearance of Poisson ratios μ and ν of bending and stretching *cannot* be combined into a single complex-valued equation.

First, we present the general SK equations in tensor form to indicate concisely the type of acceptable approximations we can introduce into the stress-strain relations. Then, we specialize to shells with developable reference surfaces and, at the same time, introduce physical tensor components. Finally, we show that if the coordinate lines orthogonal to the generators of the developable reference surface have constant geodesic and normal curvature—implying that the reference surface is a right circular cone—then the governing equations can be reduced to two coupled fourth-order partial differential equations that are static-geometric duals.

2 Differential Geometry

Let $R\mathbf{x}(\theta^1,\theta^2)$ denote the twice differentiable position of the orientable shell reference surface $\mathcal{S}$, where (θ^1,θ^2) are the dimensionless Gaussian surface coordinates and R is a typical radius of curvature of $\mathcal{S}$. Furthermore, let $\mathbf{n}(\mathbf{x})$ denote a unit normal to $\mathcal{S}$ at $\mathbf{x}$. In standard notation, the dimensionless covariant base vectors on $\mathcal{S}$ are defined and denoted by $\mathbf{a}_\alpha \equiv \mathbf{x},_\alpha \equiv \partial\mathbf{x}/\partial\theta^\alpha$, $\alpha=1,2$; the covariant and contravariant components of the surface metric tensor by $a_{\alpha\beta}\equiv\mathbf{a}_\alpha\cdot\mathbf{a}_\beta$ and $a^{\alpha\beta}=\mathbf{a}^\alpha\cdot\mathbf{a}^\beta$, where $\mathbf{a}^\alpha\cdot\mathbf{a}_\beta=\delta^\alpha_\beta$, the Kronecker delta; the contravariant components of the dimensionless surface permutation tensor by $p^{\alpha\beta}$; and the covariant components of the dimensionless surface curvature by $b_{\alpha\beta}=\mathbf{n}\cdot\mathbf{x},_{\alpha\beta}$, where covariant differentiation on $\mathcal{S}$ will be denoted by a vertical bar. Indices, as usual, are raised or lowered with respect to the components of the metric tensor and $\mathbf{n},_\alpha=-b^\beta_\alpha\mathbf{a}_\beta$.

Contributed by the Applied Mechanics Division for publication in the JOURNAL OF APPLIED MECHANICS. Manuscript received June 10, 2007; final manuscript received September 15, 2007; published online May 19, 2008. Review conducted by Edmundo Corona.

3 Sanders–Koiter Shell Equations

The equilibrium-compatibility equations of SK theory, as presented in Ref. [13], may, in the absence of surface loads, be written in the concise form,

$$(\sqrt{a}\mathbf{T}^{\alpha})_{,\alpha}=\mathbf{0} \tag{1}$$

where $a=\det(a_{\alpha\beta})$ and

$$\begin{aligned}\mathbf{T}^{\alpha}&=\mathbf{N}^{\alpha}+i\mathbf{K}^{\alpha}\\ &=\left[N^{\alpha\beta}+\frac{1}{2}\varepsilon p^{\alpha\beta}S_{\lambda\mu}M^{\lambda\mu}+i\left(\widetilde{K}^{\alpha\beta}-\frac{1}{2}\varepsilon p^{\alpha\beta}S_{\lambda\mu}\widetilde{E}^{\lambda\mu}\right)\right]\mathbf{a}_{\beta}\\ &\quad-\varepsilon\,(M^{\alpha\beta}-i\widetilde{E}^{\alpha\beta})|_{\beta}\mathbf{n}\end{aligned} \tag{2}$$

is the reduced, complex-valued, stress-strain. Here, $\sigma hN^{\alpha\beta}$ and $\sigma h^2M^{\alpha\beta}$ are, respectively, the contravariant components of the (modified, symmetric) stress resultant and stress couple of SK theory [13], where σ is a typical stress level; $\varepsilon\equiv h/R$; $\widetilde{K}^{\alpha\beta}=p^{\alpha\lambda}p^{\beta\mu}K_{\lambda\mu}=a^{\alpha\beta}K^{\gamma}_{\gamma}-K^{\beta\alpha}$, etc.; $h^{-1}\lambda K^{\alpha\beta}$ and $\lambda E^{\alpha\beta}$ are, respectively, the contravariant components of the (modified, symmetric) bending and extensional strains of SK theory, where λ is to be chosen presently. Furthermore,

$$S_{\alpha\beta}=\frac{1}{2}(p_{\alpha\gamma}b^{\gamma}_{\beta}+p_{\beta\gamma}b^{\gamma}_{\alpha})=S_{\beta\alpha} \tag{3}$$

are the covariant components of Sanders' tensor. Note that

$$a^{\alpha\beta}S_{\alpha\beta}=b^{\alpha\beta}S_{\alpha\beta}=0 \tag{4}$$

From Eq. (2), the following pairs are static-geometric duals:

$$\{N^{\alpha\beta},M^{\alpha\beta}:\widetilde{K}^{\alpha\beta},-\widetilde{E}^{\alpha\beta}\} \tag{5}$$

Finally, we take the stress-strain relations in the isotropic form

$$\widetilde{E}^{\alpha\beta}=(A\sigma h/\lambda)[a^{\alpha\beta}N-(1+\nu)N^{\alpha\beta}+\mathrm{O}(\varepsilon\mathcal{K}^{\alpha\beta})],\quad N\equiv N^{\gamma}_{\gamma} \tag{6}$$

$$M^{\alpha\beta}=(\lambda D/\sigma h^3)[a^{\alpha\beta}K-(1-\mu)\widetilde{K}^{\alpha\beta}+\mathrm{O}(\varepsilon\mathcal{N}^{\alpha\beta})],\quad K\equiv K^{\gamma}_{\gamma} \tag{7}$$

where the order terms in Eqs. (6) and (7)—discussed in the following section—represent the inherent errors in the stress-strain relations of any classical shell theory. Here, we have allowed for an independent stretching compliance A and an independent bending stiffness D, as well as independent Poisson's ratios of stretching ν and bending μ. Conventionally,

$$A=\frac{1}{Eh},\quad D=\frac{Eh^3}{12(1-\nu^2)},\quad \nu=\mu \tag{8}$$

where E is Young's modulus. With $\lambda=\sigma h^2\sqrt{A/D}=\mathrm{O}(\sigma/E)$ and $c\equiv\sqrt{AD}/h=\mathrm{O}(1)$, we have $A\sigma h/\lambda=\lambda D/\sigma h^3=c$.

4 Errors in the Uncoupled Stress-Strain Relations

The error terms in Eqs. (6) and (7) come from making two types of approximations in the strain-energy density. First, coupling terms, of which $\varepsilon b^{\alpha}_{\beta}E^{\beta}_{\gamma}K^{\gamma}_{\alpha}$ and $\varepsilon^2 b^{\alpha\beta}|_{\gamma}E_{\alpha\beta}\Gamma^{\gamma}$ are typical, are neglected, where Γ^{γ} are the contravariant components of the transverse shearing strain. (Note that b^{α}_{β} must appear because both K^{γ}_{α} and Γ^{γ} undergo a sign change if the normal to $\mathcal{S}$ is replaced by $-\mathbf{n}$.) Second, when the three moment equilibrium equations—not displayed explicitly here—are multiplied by rotations ϕ_{α} and ω and the divergence theorem applied, one obtains the dimensionless expression $K_{\alpha\beta}=\frac{1}{2}(\phi_{\alpha|\beta}+\phi_{\beta|\alpha})+S_{\alpha\beta}\omega$. Shears and a shear-rotation strain, scaled by the factor $\varepsilon\lambda$, are then introduced by setting $\phi_{\alpha}=w_{,\alpha}+b^{\beta}_{\alpha}u_{\beta}-\varepsilon\Gamma_{\alpha}$ and $\omega=\frac{1}{2}\varepsilon^{\alpha\beta}u_{\beta|\alpha}-\varepsilon\Gamma$. Finally, all terms involving Γ_{α} or Γ are neglected in the resulting stress-strain relations. However, in a shear-deformation theory (where drilling moments are neglected), $\Gamma^{\alpha}=\mathrm{O}(\mathrm{K}^{\alpha\beta}|_{\beta})$ and $\Gamma=0$. Thus, in Eq. (6),

$$\mathcal{K}^{\alpha\beta}=\{b^{\alpha\beta}\langle K^{\alpha\beta},\ \varepsilon K^{\alpha\gamma}|^{\beta}_{\gamma}\rangle,\ \varepsilon b^{\alpha\beta}|_{\gamma}\langle K^{\alpha\beta}|_{\gamma}\rangle\} \tag{9}$$

where the notation means all possible products of the factors outside and inside the angular brackets ($\langle\ \rangle$) that form the contravariant components of a second-order tensor. Likewise, by the static-geometric duality,

$$\mathcal{N}^{\alpha\beta}=\{b^{\alpha\beta}\langle N^{\alpha\beta},\ \varepsilon N^{\alpha\gamma}|^{\beta}_{\gamma}\rangle,\ \varepsilon b^{\alpha\beta}|_{\gamma}\langle N^{\alpha\beta}|_{\gamma}\rangle\} \tag{10}$$

The form of these error terms is key to the reductions to follow. For further discussion on the errors in Love's uncoupled stress-strain relation, see Koiter [7] and Niordson [14].

5 Preliminary Simplifications

The substitution of Eq. (2) into Eq. (1) shows that

$$N^{\alpha\beta}|_{\alpha}=-\varepsilon\left[b^{\beta}_{\alpha}M^{\alpha\gamma}|_{\gamma}+\tfrac{1}{2}p^{\alpha\beta}(S_{\lambda\mu}M^{\lambda\mu})|_{\alpha}\right] \tag{11}$$

with an analogous expression for $\widetilde{K}^{\alpha\beta}|_{\alpha}$. Thus, Eqs. (6) and (7) yield

$$M^{\alpha\beta}|_{\beta}=c[K|^{\alpha}+\mathrm{O}(\varepsilon\mathcal{N}^{\alpha\beta}|_{\beta})]| \tag{12}$$

with an analogous expression for $\widetilde{E}^{\alpha\beta}|_{\alpha}$. Thus, with error terms omitted and by Eq. (4), Eq. (2) becomes

$$\begin{aligned}\mathbf{T}^{\alpha}=\Bigg\{&N^{\alpha\beta}-\frac{1}{2}\varepsilon_{*}(1-\mu)p^{\alpha\beta}S_{\lambda\mu}\widetilde{K}^{\lambda\mu}\\ &+i\left[\widetilde{K}^{\alpha\beta}+\frac{1}{2}\varepsilon_{*}(1+\nu)p^{\alpha\beta}S_{\lambda\mu}N^{\lambda\mu}\right]\Bigg\}\mathbf{a}_{\beta}-\varepsilon_{*}(K-iN)|^{\alpha}\mathbf{n}\end{aligned} \tag{13}$$

where $\varepsilon_{*}=\varepsilon c=\sqrt{AD}/R\ll 1$. Note that the static-geometric duality may be extended to the stress-strain relations as they manifest themselves as the coefficients of ε_{*} in Eq. (13) by appending to Eq. (5) the pairing $\{\varepsilon_{*},\mu:-\varepsilon_{*},-\nu\}$.

6 Shells With a Developable Reference Surface

From Ref. [15], the position $R\mathbf{x}$ of a point on a developable surface may be given the form

$$\mathbf{x}=\mathbf{y}(\xi)+\eta\mathbf{u}(\xi) \tag{14}$$

where η is dimensionless distance along a generator from the *reference curve* $\mathbf{y}(\xi)$ toward the edge of regression and

$$-\mathbf{u}=\mathbf{m}(\xi)\sin\psi(\xi)+\mathbf{b}(\xi)\cos\psi(\xi),\quad \psi'=\tau(\xi) \tag{15}$$

Here, from Ref. [16], $\mathbf{m}$ and $\mathbf{b}$ are the normal and binormal vectors that appear in the Serret–Frenet formulas

$$\mathbf{y}'=\mathbf{t},\quad \mathbf{t}'=\kappa\mathbf{m},\quad \mathbf{m}'=-\kappa\mathbf{t}+\tau\mathbf{b},\quad \mathbf{b}'=-\tau\mathbf{m} \tag{16}$$

κ and τ being the dimensionless curvature and torsion of $\mathbf{y}(\xi)$. (The notation used in Ref. [15] has been changed: $\mathbf{x}$ and $\mathbf{y}$ have been interchanged, $\mathbf{n}$ has been replaced by $\mathbf{m}$, and a sign error in the expression for $\mathbf{u}$ has been corrected.) Furthermore,

$$\mathbf{t}'=\kappa(-\sin\psi\mathbf{u}+\cos\psi\mathbf{n})=g\mathbf{u}+k\mathbf{n}\text{ and }\mathbf{u}'=\kappa\sin\psi\mathbf{t}=-g\mathbf{t} \tag{17}$$

where k and g are, respectively, the geodesic and normal curvatures of $\mathbf{y}(\xi)$. Thus, with $\theta^1=\xi,\theta^2=\eta$, and $f\equiv 1-g\eta$,

$$\begin{aligned}&\mathbf{a}_1=f\mathbf{t},\quad \mathbf{a}_2=\mathbf{u},\quad \sqrt{a}=f,\quad \mathbf{n}=\mathbf{t}\times\mathbf{u}=\mathbf{m}\cos\psi-\mathbf{b}\sin\psi,\\ &\qquad \mathbf{n}'=-k\mathbf{t}\end{aligned} \tag{18}$$

$$b_{11}=fk,\quad b_{12}=b_{22}=0,\quad S_{11}=S_{22}=0,\quad S_{12}=-\frac{1}{2}k \tag{19}$$

To introduce physical components of the stress resultant and bending strain tensors, we set

$$f\mathbf{T}^1 = (N_\xi + iK_\eta)\mathbf{t} + (\hat{S} - i\hat{U})\mathbf{u} - \varepsilon_* f^{-1}(K - iN)_{,\xi}\mathbf{n} \tag{20}$$

$$\mathbf{T}^2 = \{(\hat{S} - i\hat{U}) + \varepsilon_* f^{-1}k[(1-\mu)\hat{U} - i(1+\nu)\hat{S}]\}\mathbf{t} + (N_\eta + iK_\xi)\mathbf{u} - \varepsilon_*(K - iN)_{,\eta}\mathbf{n} \tag{21}$$

where

$$\hat{S} \equiv S - \left(\frac{1}{2}\right)\varepsilon_* f^{-1}k(1-\mu)\hat{U} \tag{22}$$

and where *we have taken advantage of the inherent errors in the stress-strain relations (6) and (7) to replace* S *by* $\hat{S}$ *and* U *by* $\hat{U}$ *in those terms with an* ε_* *factor, that is, those terms that come from the stress-strain relations.*

Substituting Eqs. (20) and (21) into Eq. (1), using the differentiation formulas in Eqs. (17) and (18), and taking the real part of the resulting vector equation, we find that the coefficients of the basis vectors $\mathbf{t},\mathbf{u},\mathbf{n}$, respectively, imply the three scalar equations

$$fN_{\xi,\xi} + (f^2\hat{S})_{,\eta} + \varepsilon_* k[(1-\mu)f\hat{U}_{,\eta} + K_{,\xi}] = 0 \tag{23}$$

$$gN_\xi + \hat{S}_{,\xi} + (fN_\eta)_{,\eta} = 0 \tag{24}$$

$$-\varepsilon_*\Delta K + f^{-1}kN_\xi = 0 \tag{25}$$

where

$$\Delta K = f^{-1}[(f^{-1}K_{,\xi})_{,\xi} + (fK_{,\eta})_{,\eta}] \tag{26}$$

is the Laplacian of K on $\mathcal{S}$. Note that if we set $N_\eta = N - N_\xi$ and recall that $g = -f_{,\eta}(\xi,\eta)$, we may replace Eq. (24) by

$$\hat{S}_{,\xi} + (fN)_{,\eta} - f^{-1}(f^2N_\xi)_{,\eta} = 0 \tag{27}$$

Using the static-geometric duality,

$$\{N_\xi, \hat{S}, N_\eta; \mu, \varepsilon_* : K_\eta, -\hat{U}, K_\xi; -\nu, -\varepsilon_*\} \tag{28}$$

we may easily infer from Eqs. (23)–(25) the three reduced compatibility equations.

7 Two Reduced Equations for a Right Circular Conical Shell

A general conical reference surface has arbitrary normal curvature k but constant geodesic curvature g so that $f = f(\eta)$. (In a *right circular* conical shell k is also constant; in a *general cylindrical* shell $g = 0$. This is readily seen if the reference surface is developed into a plane.)

Forming the combination $[\text{Eq. (23)}]_{,\xi} - [f^2\text{Eq. (27)}]_{,\eta}$ to eliminate $\hat{S}$, we have

$$f\Delta(f^2N_\xi) - [f^2(fN)_{,\eta}]_{,\eta} + \varepsilon_*\{k[(1-\mu)f\hat{U}_{,\eta} + K_{,\xi}]\}_{,\xi} = 0 \tag{29}$$

Now use Eq. (25) and its kinematic dual to express N_ξ and K_η in terms of K and N and again ignore terms of the same order as the inherent errors in the stress-strain relations. Because the geometric dual of Eq. (23) implies that

$$f\hat{U}_{,\eta} = 2g\hat{U} + \mathrm{O}(\varepsilon_*) \tag{30}$$

the Poisson ratio terms in Eq. (29) vanish for general cylindrical shells ($g = 0$), see Ref. [10] or [11]. On the other hand, if $g \neq 0$ and we carry out the ξ differentiation in the last term in Eq. (29), we are left with a factor $fk'\hat{U}_{,\eta}$ that cannot be eliminated unless $k = \text{const}$, *which we now assume*. That is, we assume that the reference surface $\mathcal{S}$ is a right circular cone.

Using the dual of Eq. (27) to set

$$\hat{U}_{,\xi} = (fK)_{,\eta} - \underline{\varepsilon_* k^{-1}f^{-1}(f^3\Delta K)_{,\eta}} \tag{31}$$

we have

$$f\hat{U}_{,\eta\xi} = f[(fK)_{,\eta} - \underline{\varepsilon_* k^{-1}f^{-1}(f^3\Delta K)_{,\eta}}]_{,\eta} \tag{32}$$

although in what follows, we ignore the underlined term as being of the same order as the error in the stress-strain relations. We note that for *axisymmetric deformation* it should be retained to obtain reduced equations that agree with the overall beamlike equations that we derive in the Appendix and which contain no Poisson ratio terms. Thus, the final form of Eq. (29) is

$$\varepsilon_*\{f\Delta(f^3\Delta K) + k^2[K_{,\xi\xi} + (1-\mu)f(fK)_{,\eta\eta}]\} = k[f^2(fN)_{,\eta}]_{,\eta} \tag{33}$$

By the static-geometric duality, the companion to Eq. (33) is

$$-\varepsilon_*\{f\Delta(f^3\Delta N) + k^2[N_{,\xi\xi} + (1+\nu)f(fN)_{,\eta\eta}]\} = k[f^2(fK)_{,\eta}]_{,\eta} \tag{34}$$

The factors $(1-\mu)$ and $(1+\nu)$ prevent the combining of Eqs. (33) and (34) into a single complex-valued equation.

8 (Seemingly Paradoxical) Simplification

Wan noted in Ref. [12] that the small parameter ε_* can be scaled out of the equations for a right circular conical shell. (This is also possible for general cones.) Thus, if we set

$$f = 1 - g\eta = \varepsilon_* x, \quad \partial/\partial\eta = -\varepsilon_*^{-1}g\,\partial/\partial x, \quad \vartheta \equiv x\partial/\partial x, \quad \mathcal{D} \equiv \partial/\partial\xi \tag{35}$$

and note the commutative and *pass-through* properties

$$(\vartheta + p)(\vartheta + q) = (\vartheta + q)(\vartheta + p), \quad \vartheta(x^pF) = x^p(\vartheta + p)F \tag{36}$$

then Eqs. (33) and (34) take the form

$$[\mathcal{Q} + (1-\mu)g^2k^2\vartheta(\vartheta+1)]K = g^2k\vartheta(\vartheta+1)(xN) \tag{37}$$

$$-[\mathcal{Q} + (1+\nu)g^2k^2\vartheta(\vartheta+1)]N = g^2k\vartheta(\vartheta+1)(xK) \tag{38}$$

where, because $g^2 + k^2 = 1$,

$$\mathcal{Q} \equiv [\mathcal{D}^2 + g^2(\vartheta+1)^2](\mathcal{D}^2 + g^2\vartheta^2) + k^2\mathcal{D}^2 = \mathcal{D}^2(\mathcal{D}^2 + 1) + g^2\vartheta(\vartheta+1)[g^2\vartheta(\vartheta+1) + 2\mathcal{D}^2] \tag{39}$$

The disappearance of the small parameter ε_* at first glance seems to invalidate our frequent neglect of terms of relative order ε_* in the stress-strain relations. However, $x = \mathrm{O}(1)$ means that we are within a thickness of the apex—a region where classical shell theory simply fails to hold.

Setting

$$\{K, N\} = \{K_n(x), N_n(x)\}\sin n\xi, \quad n = 0, 1, 2, \ldots \tag{40}$$

we obtain the ordinary differential equations

$$[Q_n(\vartheta) + (1-\mu)g^2k^2\vartheta(\vartheta+1)]K_n = g^2k\vartheta(\vartheta+1)(xN_n) \tag{41}$$

$$-[Q_n(\vartheta) + (1+\nu)g^2k^2\vartheta(\vartheta+1)]N_n = g^2k\vartheta(\vartheta+1)(xK_n) \tag{42}$$

where

$$Q_n \equiv n^2(n^2 - 1) + g^2\vartheta(\vartheta+1)[g^2\vartheta(\vartheta+1) - 2n^2] \tag{43}$$

9 Axisymmetric Solutions ($n = 0$)

These follow from Eqs. (A11) and (A13) and their kinematic duals or from Eqs. (25) and (27) and their duals. With the change of variables (35), Eq. (A11) and its dual may be combined into the single complex-valued equation

$$[g^2\vartheta(\vartheta+1)-ikx]P_0=xF_* \tag{44}$$

where $P_0 \equiv K_0+iN_0$ and F_* is the constant, real-valued, dimensionless axial force. Equation (44) is a nonhomogeneous Bessel equation whose solution, with the aid of Eqs. (127)–(129) of Ref. [17] and Chap. 12 of Ref. [18], may be expressed in terms of ber, bei, and Struve functions.

Equation (A13) and its dual are algebraic and readily yield the solution

$$S_0+\lambda U_0=\frac{x^{-1}T_*}{1+3ik\sqrt{(1-\mu)(1+\nu)}},\quad \lambda=i\sqrt{\frac{(1-\mu)}{(1+\nu)}} \tag{45}$$

where T_* is a dimensionless torque (moment about the axis of the cone).

10 Lateral Solutions ($n=1$)

Overall force and moment equilibrium, Eq. (A6), plus Eqs. (A15) and (A18) imply that $M''(\eta)=0$. Thus, using $g^2+k^2=1$ and Eq. (31) to set $U_1=-(fK_1)'+\mathrm{O}(\varepsilon_*)$, we have from Eq. (A18)

$$kf^2N_1+\varepsilon_*\{f[K_1+gfK_1'-\chi_1-(1-\mu)k^2K_1]\}=A_1+A_2\eta \tag{46}$$

or

$$kxN_1-[g^2\vartheta(\vartheta+1)-2+(1-\mu)k^2]K_1=A_1^*x^{-1}+A_2^* \tag{47}$$

where the various A's are constants. The dual of Eq. (47) is

$$kxK_1-[g^2\vartheta(\vartheta+1)-2+(1+\nu)k^2]N_1=0 \tag{48}$$

there being no constant terms because there are no gross dislocations. These equations agree with Eqs. (41) and (42) if $n=1$ and if integrated twice.

11 Solutions About $x=0$ (the Apex)

Looking for solutions of Eq. (37) the form

$$K_n=x^p\sum_0^\infty a_{2m}(p)x^{2m},\quad N_n=x^p\sum_0^\infty b_{2m+1}(p)x^{2m+1} \tag{49}$$

we find that p must satisfy the *indicial equation*

$$P_4(p;n,\mu)\equiv Q_n(p)-2(1-\mu)g^2k^2(p+1)=0 \tag{50}$$

If the conical shell includes its apex, then finite strain energy on any portion $0<x<l$ requires that $\int_0^l K^2xdx<\infty$ so that we must exclude solutions associated with values of $p<-1$.

Let the four roots of $P_4(p)$ be denoted by p_1, p_2, p_3, p_4. We now show that p_1, $p_2<-1$ and $-1<p_3$, p_4. To this end, note the following values of P_4:

$$P_4(\pm n/g;n,\mu)=-k^2\{n[1\pm(1-\mu)g]+(1-\mu)g^2\} \tag{51}$$

$$P_4(\pm n/g-1;n,\mu)=-k^2n[n\pm(1-\mu)g] \tag{52}$$

$$P_4(-1;n,\mu)=n^2(n^2-g^2-k^2) \tag{53}$$

If α is the (acute) apex angle of the conical reference surface, then $g=\sin\alpha$ and $k=-\cos\alpha$, and, since $n\geq 2$, we see that the right sides of Eqs. (51) and (52) are *negative* whereas the right side of Eq. (53) is *positive*. Thus, because $P_4(p;n)\sim g^4p^4$ as $p\to\infty$, there must be two roots of P_4 less than -1 and 2 greater.

By the static-geometric duality, two of the roots of $P_4(q;n,-\nu)$, call them q_1, q_2, will be less than -1 and 2, q_3, q_4 will be greater so that, altogether we obtain four formal solutions about the apex $x=0$, two of the form

$$K_n=x^{p_3,p_4}\sum_0^\infty a_{2m}(p_3,p_4)x^{2m},\quad N_n=x^{p_3,p_4}\sum_0^\infty b_{2m+1}(p_3,p_4)x^{2m+1} \tag{54}$$

with $a_0(p_3)$ and $a_0(p_4)$ arbitrary, and two of the form

$$N_n=x^{q_3,q_4}\sum_0^\infty b_{2m}(q_3,q_4)x^{2m},\quad K_n=x^{q_3,q_4}\sum_0^\infty a_{2m+1}(q_3,q_4)x^{2m+1} \tag{55}$$

with $b_0(q_3)$ and $b_0(q_4)$ arbitrary. The coefficients in these power series satisfy recurrence relations that are straightforward to set down but will not be given here.

12 Solutions About $x=\infty$

Because the point $x=\infty$ is an irregular singular point of the two ordinary differential equations (37) and (38), the *dominant term* of the solution is determined by the dominant term of the simplified, complex-valued differential equation

$$\vartheta(\vartheta+1)[g^2\vartheta(\vartheta+1)-ikx]\underline{T}=0 \tag{56}$$

where the dominant term in each of the four solutions of $\underline{T}$ are the dominant terms in $K+iN$ as $x\to\infty$.

Two integrations yield

$$[g^2\vartheta(\vartheta+1)-ikx]\underline{T}=C_1+C_2x^{-1} \tag{57}$$

where C_1 and C_2 are arbitrary complex constants. The dominant particular solutions of Eq. (57) are of the form $C_1^*x^{-1}+C_2^*x^{-2}$. The solution $\underline{T}\sim C_1^*x^{-1}$ leads to infinite strain energy on the interval $l<x<\infty$ and must be discarded. However, the solution $\underline{T}\sim C_2^*x^{-2}$ is acceptable.

According to Erdélyi p. 13 of Ref. [19], the two homogeneous solutions of the second-order differential equation in Eq. (57) have formal asymptotic solutions whose first (dominant) terms are $C_\pm\exp[\pm 2g^{-1}(ikx)^{1/2}]x^{-3/4}$, where $C_\pm$ are arbitrary complex constants. The growing exponential must be discarded.

Thus, with $T\equiv K+iN$, we can seek *asymptotic* solutions of the form

$$T=x^{-2}\sum_0^\infty c_mx^{-m}+\exp[-2g^{-1}(ikx)^{1/2}]x^{-3/4}\sum_0^\infty d_mx^{-m}\quad \text{as } x\to\infty \tag{58}$$

for the differential equation

$$\left\{Q_n(\vartheta)-g^2k^2(\vartheta+1)\left[1+\frac{1}{2}(\mu-\nu)\right]-i\vartheta(\vartheta+1)x\right\}T$$
$$-\frac{1}{2}(\mu+\nu)g^2k^2(\vartheta+1)\bar{T}=0 \tag{59}$$

where $\bar{T}=K-iN$ and the coefficients c_m and d_m in Eq. (58) are complex.

13 Conclusions

Wan's two equations (13) and (14) for a right circular conical shell in Ref. [12], derived in a totally different way than ours and involving the normal deflection of the reference surface and its dual, a stress function, do *not* contain the bending and stretching Poisson ratios factors $(1-\mu)$ and $(1+\nu)$ and thus, in contrast to our equations (37) and (38), can be combined into one equation for a complex-valued unknown. Because Wan does not explicitly give the algebraic details of his final reduction (simply mentioning that terms of order $\varepsilon=h/R$ have been omitted) it is not easy to determine if μ- and ν-terms have been consistently neglected.

For a finite conical shell with no apex, solutions that we have excluded because of unphysical behavior as $x\to 0$ or $x\to\infty$ must be considered. Of course, the two sets of eight solutions about these two singular points cannot be independent but must be related by (presently unknown) connection coefficients. However, for such a finite shell, it is probably much simpler in practice to use standard perturbation techniques to express the four boundary conditions at each edge in terms of four boundary layer and four interior solutions.

Because our equations are *intrinsic*, that is, because the unknowns are stresses and strains, there remains the task of determining the displacements. For the more general case of nonlinear shell equations, this problem has been treated recently by Pietraszkiewicz and Szwabowicz [20].

Acknowledgment

I thank Professor F. Y. M. Wan for his useful and penetrating comments.

Appendix: Beamlike Solutions

Let $\pi\sigma hR\mathbf{F}$ and $\pi\sigma hR^2\mathbf{M}$ denote, respectively, the net force and moment acting over any section η=const of a right circular conical shell of apex angle α. Then from Eq. (13),

$$\pi\mathbf{F}(\eta)=\int_0^{2\pi} f\mathcal{R}\mathbf{T}^2 d\xi, \quad \pi\mathbf{M}(\eta)=\int_0^{2\pi}(\mathbf{e}_\rho\times f^2\mathcal{R}\mathbf{T}^2+\varepsilon f\mathbf{M}^2)d\xi \tag{A1}$$

where $\mathcal{R}$ denotes "real part of," $\mathbf{e}_\rho=\cos\alpha\mathbf{n}-\sin\alpha\mathbf{u}=-(k\mathbf{n}+g\mathbf{u})$ is a radial vector, and

$$\mathbf{M}^2=M_\eta\mathbf{t}-H\mathbf{u}=c[\mu K\mathbf{t}-(1-\mu)\hat{U}\mathbf{u}+\mathrm{O}(\varepsilon_*)] \tag{A2}$$

is the dimensionless stress couple acting on the edge. Note that because $\mathbf{u}=\mathbf{n}\times\mathbf{t}, \mathbf{t}=\mathbf{e}_\rho'$, and $\mathbf{n}'=-k\mathbf{t}$, an integration by parts yields

$$\pi\mathbf{M}(\eta)=f\int_0^{2\pi}(\mathbf{e}_\rho\times f\bar{\mathbf{T}}^2+\varepsilon_* M_\eta\mathbf{t})d\xi \tag{A3}$$

From Eq. (25),

$$N_\eta=N-N_\xi=N-\varepsilon_* fk^{-1}\Delta K \tag{A4}$$

So, with the stress-strain relations (7), Eq. (21) yields

$$\begin{aligned} f\bar{\mathbf{T}}^2 &\equiv f\mathcal{R}\mathbf{T}^2-\varepsilon(H\mathbf{n})' \\ &=[f\hat{S}+2\varepsilon_*(1-\mu)k\hat{U}]\mathbf{t}+f(N-\varepsilon_* fk^{-1}\Delta K)\mathbf{u} \\ &\quad-\varepsilon_*[fK_{,\eta}+(1-\mu)\hat{U}_{,\xi}]\mathbf{n} \end{aligned} \tag{A5}$$

the "effective" Kirchhoff edge force [13].

Because $\eta\cos\alpha$ is the dimensionless distance along the axis of the cone *from* its apex and $k=-\cos\alpha$, overall force and moment equilibrium—beamlike equilibrium—require that

$$\mathbf{F}'=\mathbf{0}, \quad \mathbf{M}'-k\mathbf{k}\times\mathbf{F}=\mathbf{0} \tag{A6}$$

Let $\{\mathbf{i},\mathbf{j},\mathbf{k}\}$ denote the standard set of orthonormal Cartesian base vectors, with $\mathbf{i}$ horizontal, $\mathbf{j}$ vertical, and $\mathbf{k}$ along the axis of the cone pointing toward the (real or virtual) apex. Because $\sin\alpha=g, \cos\alpha=-k$,

$$\begin{aligned} &\mathbf{e}_\rho=\cos\xi\mathbf{i}+\sin\xi\mathbf{j}, \quad \mathbf{t}=-\sin\xi\mathbf{i}+\cos\xi\mathbf{j}, \quad \mathbf{u}=-(g\mathbf{e}_\rho+k\mathbf{k}), \\ &\mathbf{n}=-k\mathbf{e}_\rho+g\mathbf{k} \end{aligned} \tag{A7}$$

Furthermore, from Eqs. (26) and (38),

$$f\Delta K_0=(fK_0')', \quad f^2\Delta(K_1\sin\xi)=\chi\sin\xi, \quad \chi\equiv f(fK_1')'-K_1 \tag{A8}$$

Thus, with

$$\{\hat{S},\hat{U}\}=\{\hat{S}_0,\hat{U}_0\}+\{\hat{S}_1,\hat{U}_1\}\cos\xi \tag{A9}$$

Eqs. (A1) and (A4) imply that

$$\mathbf{F}\cdot\mathbf{j}\equiv V=f\hat{S}_1-gfN_1+\varepsilon_* k^{-1}[k^2(1-\mu)\hat{U}+\varepsilon_* f(gfK_1'+K_1)'] \tag{A10}$$

$$\mathbf{F}\cdot\mathbf{k}\equiv F=2f\{-kN_0+\varepsilon_*[(fK_0')'-gK_0']\} \tag{A11}$$

$$\mathbf{M}\cdot\mathbf{i}\equiv M=-kf^2N_1+\varepsilon_* f[\chi_1-K_1-gfK_1'+(1-\mu)(g\hat{U}_1+K_1)] \tag{A12}$$

$$\mathbf{M}\cdot\mathbf{k}\equiv T=2f[f\hat{S}_0+2\varepsilon_*(1-\mu)k\hat{U}_0] \tag{A13}$$

Equations (A10)–(A13) and their kinematic duals (for which the analogous constants are zero because there are no gross dislocations) yield four first integrals for $n=0$ and four for $n=1$.

We now simplify Eqs. (A10) and (A12) further—these represent first integrals for lateral ($n=1$) deformation—by exploiting the inherent errors in the stress-strain relations to express V and M in terms of the basic unknowns K_1 and N_1 only.

Beginning with Eq. (A10), we have from Eqs. (25), (27), and (A8), and their duals,

$$fS_1=f(fN_1)'-\varepsilon_* k^{-1}(f\chi_1)' \quad \text{and } U_1=-(fK_1)'+\mathrm{O}(\varepsilon_*) \tag{A14}$$

Thus,

$$V=\{(f^2N_1)+\varepsilon_* k^{-1}f[K_1+gfK_1'-\chi_1-(1-\mu)k^2K_1]\}' \tag{A15}$$

To reduce and simplify Eqs. (A12), note from Eqs. (23)–(25) and (A4) that

$$[f(\hat{S}_1-gN_1)]'=-\varepsilon_*[k(1-\mu)\hat{U}_1+k^{-1}g\chi_1+fK_1']' \tag{A16}$$

whose dual implies that

$$f(\hat{U}_1+gK_1)=C+\mathrm{O}(\varepsilon_*) \tag{A17}$$

where C is an arbitrary real constant. Thus, with $K_1=(g^2+k^2)K_1$, Eq. (A12) may be replaced by

$$M=-kf^2N_1-\varepsilon_*\{f[K_1+gfK_1'-\chi_1-(1-\mu)k^2K_1]+C_*\} \tag{A18}$$

where $C_*=g(1-\mu)C$. Obviously, Eqs. (A15) and (A18) imply that $M'+V=0$.

References

[1] Goldenveiser, A. L., 1957, "Equations of the Theory of Shells in Displacements and Stress Functions" Prikladnaia Mathematika i Mekhanika, **21**, pp. 801–814, in Russian.

[2] Koiter, W. T., 1963, "A Spherical Shell Under Point Loads at Its Poles," *Progress in Applied Mechanics (The Prager Anniversary Volume)*, Macmillan, New York.

[3] Simmonds, J. G., 1966, "A Set of Simple, Accurate Equations for Circular Cylindrical Elastic Shells," Int. J. Solids Struct., **2**, pp. 525–541.

[4] Sanders, J. L., Jr., 1983, "Analysis of Circular Cylindrical Shells," ASME J. Appl. Mech., **50**, pp. 1165–1170.

[5] Sanders, J. L., Jr., 1969, "On the Shell Equations in Complex Form," *Theory of Thin Shells, IUTAM Symposium Copenhagen, 1967*, F. I. Niordson, ed., Springer-Verlag, Berlin, pp. 135–156.

[6] Sanders, J. L., Jr., 1959, "An Improved First-Approximation Theory for Thin Shells," NASA Report No. 24.

[7] Koiter, W. T., 1960, "A Consistent First Approximation in the General Theory of Thin Elastic Shells," *Theory of Thin Elastic Shells*, Proceedings IUTAM Symposium, Delft, 1959, W. T. Koiter, ed., North-Holland, Amsterdam, pp. 12–33.

[8] Cohen, J. W., 1960, "The Inadequacy of the Classical Stress-Strain Relations for the Right Helicoidal Shell," *Theory of Thin Elastic Shells*, Proceedings IUTAM Symposium, Delft, 1959, W. T. Koiter, ed., North-Holland, Amster-

dam, pp. 415–433.

[9] Latta, G. E., and Simmonds, J. G., 1975, "The Sanders–Koiter Shell Equations can be Reduced to Two Coupled Equations for All Minimal Midsurfaces," Q. Appl. Math., **33**, pp. 170–174.

[10] Novozhilov, V. V., 1970, *Thin Shell Theory*, 2nd ed., Wolters-Noordhoff, Groningen.

[11] Simmonds, J. G., 2007, "The Hypercircle Theorem for Elastic Shells and the Accuracy of Novozhilov's Simplified Equations for General Cylindrical shells," Discrete Contin. Dyn. Syst., Ser. B, **7**, pp. 643–650.

[12] Wan, F. Y. M., 1970, "On the Equations of the Linear Theory of Elastic Conical Shells," Stud. Appl. Math., **49**, pp. 69–83.

[13] Budiansky, B., and Sanders, J. L., 1963, "On the 'Best' First-Order Linear Shell Theory," *Progress in Applied Mechanics (The Prager Anniversary Volume)*, Macmillan, New York, pp. 129–140.

[14] Niordson, F. I., 1971, "A Note on the Strain Energy of Elastic Shells," Int. J. Solids Struct., **7**, pp. 1573–1579.

[15] Libai, A., and Simmonds, J. G., 1979, "Exact Equations for the Inextensional Deformation of Cantilevered Plates," ASME J. Appl. Mech., **46**, pp. 631–636.

[16] Struik, D. J., 1961, *Differential Geometry*, 2nd ed., Addison-Wesley, Reading MA.

[17] Hildebrand, F., 1976, *Advanced Calculus for Applications*, 2nd ed., Prentice-Hall, Englewood Cliffs, NJ.

[18] Abramowitz, M., and Stegun, I., 1964, *Handbook of Mathematical Functions*, U.S. Government Printing Office, Washington, DC.

[19] Erdélyi, A., 1956, *Asymptotic Expansions*, Dover, New York.

[20] Pietraszkiewicz, W., and Szwabowicz, M. L., 2007, "Determination of the Midsurface of a Deformed Shell From Prescribed Fields of Surface Strains and Bendings," Int. J. Solids Struct., **44**, pp. 6163–6172.

Aeroelastic Stability of Wide Webs and Narrow Ribbons in Cross Flow

Rahul A. Bidkar
Graduate Student

Arvind Raman
Associate Professor
e-mail: raman@ecn.purdue.edu

Anil K. Bajaj
Professor

Dynamic Systems and Stability Laboratory,
School of Mechanical Engineering,
Purdue University,
585 Purdue Mall,
West Lafayette, IN 47907

Aeroelastic flutter can lead to large amplitude oscillations of tensioned wide webs and narrow ribbons commonly used in the paper-handling, textile, sheet-metal, and plastics industries. In this article, we examine the aeroelastic stability of a web or a ribbon, which is submerged in an incompressible and inviscid fluid flow across its free edges. The web or ribbon is modeled as a uniaxially tensioned Kirchhoff plate with vanishingly small bending stiffness. A Galerkin discretization for the structural dynamics together with panel methods for the unsteady three dimensional potential flow are used to cast the coupled system into the form of a gyroscopic, nonconservative dynamical system. It is found that wide webs mainly destabilize through a divergence instability due to the cross-flow-induced conservative centrifugal effects. However, for certain values of applied tension, the wake-induced nonconservative effects can destabilize the web via a weak flutter instability. Contrarily, narrow ribbons in cross flow are nearly equally likely to undergo flutter or divergence instability depending on the value of applied tension.

[DOI: 10.1115/1.2871192]

1 Introduction and Background

The term *web* refers to thin uniaxially tensioned flexible media transported through a series of rollers while remaining unsupported at the remaining edges. *Ribbons* are narrow webs with small width to length ratio. Wide webs and narrow ribbons find wide use in industrial settings such as in the paper, textile, sheet metal, and plastics manufacturing industries, as well as in data storage tapes. Large amplitude web vibrations characterized as aeroelastic flutter have been known to occur especially in high-speed lines handling lightweight materials. Large amplitude vibrations increase the probability of breakage and lead to poor manufacturing quality and considerable financial losses due to machine downtimes. The commonly observed phenomenon of flow-induced instabilities of tensioned barricade or caution tapes is yet another example of this category of problems. In this article, we focus on the influence of cross flow on the aeroelastic stability of webs and ribbons.

Compared to the classical panel flutter problems [1] in the literature, a distinguishing feature of webs and ribbons is their vanishingly small bending stiffness and the application of tension only along the web or ribbon axis. This results in very close frequency spacing of a large number of cross-span modes, a phenomenon referred to as frequency clustering [2] in the literature. Such clustered modes present the possibility of complex modal interactions and rich dynamical behavior in uniaxially tensioned webs that are not possible in biaxially tensioned or stiff plates.

Air flows are generated around the web (in the axial as well as the cross-span direction) by the interaction of the moving web and surrounding air or are sometimes generated externally. For example, in a printing process, when the web passes through a dryer, air is blown over the web, thus providing a steady flow parallel to the web. When studying web dynamics, several interesting cases involving moving and stationary webs coupled to either a quiescent fluid or a steady fluid flow (axial or cross flow) can be considered. However, experimentally, it has been observed [3,4] that webs are most susceptible to cross-flow-induced flutter, even at zero or low web transport speeds. Moreover, cross flow over the free edges of the web gives rise to wake vortices. These wake vortices can lead to complex interactions between the clustered cross-span modes. For these reasons, the primary goal of this article is to model and investigate the aeroelastic stability of stationary webs and ribbons in cross flows.

Comprehensive literature reviews on the aeroelasticity of plates and shells can be found in the monographs by Dowell [5] and Paidoussis [6]. However, the aeroelasticity of webs and ribbons remains a sparsely studied topic. Raman et al. [2] study the effect of surrounding incompressible and inviscid fluid on axially moving paper webs. Guo and Paidoussis [7] investigate the linear stability of a plate immersed in a channel flow. Tang et al. [8] study the aeroelastic flutter of elastic panels (clamped at the leading edge) using a theoretical model with structural nonlinearities and reduced-order linear aerodynamics. Niemi and Pramila [9] present the finite element method (FEM) analysis of a linear membrane (with artificial tension along the cross-span direction) coupled to an incompressible, inviscid, and initially quiescent flow. Frondelius et al. [10] present the vibration characteristics of a moving band coupled to a viscous air flow using an analytical boundary layer model. Chang and Moretti [11] present a theoretical study by modeling the web as a tensioned infinitely wide Kirchhoff plate with base flow in the cross machine direction. The theoretical model in the work of Watanabe et al. [12] predicts the onset of flow-induced instabilities with a 1D beam model of the plate with clamped-free boundary conditions. Watanabe et al. [4] present flutter experiments on stationary paper sheets clamped at the leading edge and uniaxially tensioned webs with cross flow. Experimentally observed flutter in webs is also reported in the work of Hill [3], Chang and Moretti [13], and Chang et al. [14]. Finally, Vaughan and Raman [15] and Vaughan [29] model the web as a Kirchhoff plate surrounded by incompressible and inviscid fluid, but the fluid flow model does not include the effects of a trailing edge wake. These effects could be important for the cross flow problem considered in the current work.

In this article, the vibrations of a uniaxially tensioned stationary web coupled to a surrounding incompressible inviscid fluid flowing in the cross span direction are investigated. The focus is placed on understanding the influence of nonconservative effects of trailing edge wakes on the clustered modes of tensioned webs, and on the role of aspect ratios and the applied tension in sup-

---

Contributed by the Applied Mechanics Division of ASME for publication in the JOURNAL OF APPLIED MECHANICS. Manuscript received June 26, 2007; final manuscript received October 30, 2007; published online May 19, 2008. Review conducted by Robert M. McMeeking.

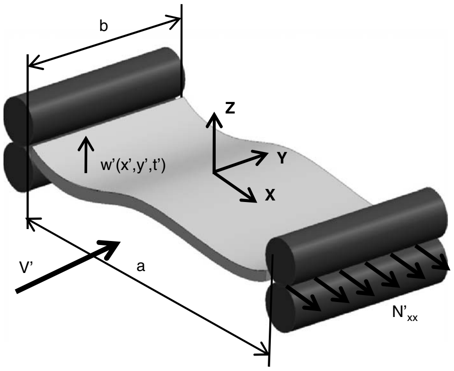

Fig. 1 A Schematic for the uniaxially tensioned stationary web subjected to cross flow

pressing or enhancing aeroelastic stability. The article is organized in the following fashion. In Sec. 2, the details of the web and fluid models are presented. In Sec. 3, the equations of motion are discretized using Galerkin's method. The solution of the fluid flow problem using the vortex-lattice method and the details of the coupled eigenvalue problem are presented in Sec. 4. A discussion on the computational issues is presented in Sec. 5. In Sec. 6, we present numerical results for the different cases of interest. Finally, in Sec. 7, we summarize the main results of the present work.

2 Modeling

Figure 1 shows the system under consideration. The rectangular web is modeled as a flat, isotropic, linearly elastic, and uniaxially tensioned Kirchhoff plate. The web has a length a (along the X axis), width b (along the Y axis), thickness h, and is supported at $x=-a/2$ and $x=a/2$ by two rollers such that the right-handed Cartesian coordinate system XYZ has its origin at the center of the web.

A steady flow of velocity V' is incident on the web along the Y axis. The fluid flow in the three dimensional infinite domain surrounding the web is assumed to be incompressible and inviscid. In the X-Y plane, a linearized wake (having width a and negligible thickness) [16] emanating from the trailing edge of the web and extending to infinity downstream is assumed to exist. For small amplitudes of web oscillation, it can be shown that the flow remains attached to the web near the leading edge and a leading edge wake is absent [7,17,18]. The effects of the drag force (due to the viscous boundary layer) along the Y direction are not considered in this model.[1] It is assumed that the fluid flow comprises of a steady base flow and small perturbations to this base flow caused by the web motion. These assumptions give the following set of *dimensionless* equations for the coupled fluid-structure problem:

$$w_{,tt} + \epsilon\nabla^4 w - w_{,xx} = 2\Lambda[\phi(x,y,0^+,t)_{,t} + V\phi(x,y,0^+,t)_{,y}]$$
$$\nabla^2\phi = 0 \tag{1}$$

where

$$w = \frac{w'}{a}, \quad x = \frac{x'}{a}, \quad y = \frac{y'}{a}, \quad z = \frac{z'}{a}$$

$$t = \frac{t'}{a}\sqrt{\frac{N'_{xx}}{\rho}}, \quad \phi(x,y,z,t) = \frac{\phi'(x',y',z',t')}{a\sqrt{N'_{xx}/\rho}}, \quad V = \frac{V'}{\sqrt{N'_{xx}/\rho}} \tag{2}$$

$$\epsilon = \frac{D}{a^2 N'_{xx}}, \quad \Lambda = a\frac{\rho_{\text{fluid}}}{\rho}, \quad \kappa = \frac{a}{b}$$

In Eqs. (1) and (2), the *primed* variables denote *dimensional* quantities, whereas the unprimed variables are the corresponding dimensionless quantities. w represents the out-of-plane web displacement and $\phi(x,y,z,t)$ is the antisymmetric (about the X-Y plane) part of the perturbation aerodynamic potential. ρ is the mass per unit area of the web, ρ_{fluid} is the fluid density, and $D=Eh^3/12(1-\mu^2)$ is the bending stiffness of the web. E is Young's modulus of elasticity and μ is Poisson's ratio. N'_{xx} is the axial tension per unit width of the web applied along the X axis. From Eq. (2), it can be seen that four nondimensional numbers ϵ, Λ, κ, and V govern the dynamics of tensioned webs and ribbons subjected to cross flow. ϵ is the bending stiffness to tension ratio, Λ is the density ratio, κ is the web aspect ratio, and V is the nondimensional cross flow velocity.

For small amplitude oscillations, the roller supports can be suitably modeled as simple supports [19]. Accordingly, the web boundary conditions are simply supported at the edges $x=1/2$ and $x=-1/2$ and free at the edges $y=1/(2\kappa)$ and $y=-1/(2\kappa)$. The boundary conditions for the fluid flow equations are derived by matching the normal velocity of the web with the velocity of the fluid particle at that location. Thus, on the web surface, the following must be true:

$$\phi_{,z}|_{\text{on the web}} = w_{,t} + Vw_{,y} \tag{3}$$

where this boundary condition can be enforced on the $Z=0$ plane for linear stability studies. Additionally, it is required that the far field conditions be satisfied, that is,

$$\phi_{,n}|_{\text{as } r\to\infty} = 0 \tag{4}$$

where $r=\sqrt{x^2+y^2+z^2}$, $(\cdot)_{,n}$ represents $\partial(\cdot)/\partial n$, and n denotes any radial normal direction. Apart from the purely kinematical boundary conditions specified in Eqs. (3) and (4), the Kutta condition [16,18] is enforced at the trailing edge of the web. The Kutta condition (which is used to find the value of the trailing edge vorticity shed into the wake) ensures that the solution to the fluid flow equations is unique. In the case of flow behind an oscillating web, the Kutta condition can be interpreted [18] as requiring the pressure jump at the trailing edge of the web to be zero, that is,

$$\Delta p|_{\text{at the trailing edge}} = 0 \tag{5}$$

where the pressure $p(x,y,z,t)=\rho_{\text{fluid}}(\phi_{,t}+V\phi_{,y})$ is obtained by using the linearized Bernoulli equation and the symbol Δp refers to the difference between the values of pressure above and below the web.

3 Discretized Model

The Galerkin method, which is used to discretize Eq. (1), employs the mass normalized in-vacuo eigenfunctions of a Kirchhoff plate (with no applied tension) as its basis functions. Thus, we can write the transverse web displacement as

$$w(x,y,t) = \sum_{m=0}^{\infty}\sum_{n=0}^{\infty} q_{mn}(t)\Psi_{mn}(x,y) \tag{6}$$

where $q_{mn}(t)$ represents the generalized coordinate of a basis function and the basis function $\Psi_{mn}(x,y)$ is given by:

$$\begin{aligned}\Psi_{mn}(x,y) &= C_{mn}\sin((m+1)\pi(x+1/2))[\cosh(\alpha_{mn}y) \\ &\quad + \gamma_{mn}\cosh(\beta_{mn}y)] \quad m=0,1,2,\ldots \quad n=0,2,4,\ldots \\ \Psi_{mn}(x,y) &= C_{mn}\sin((m+1)\pi(x+1/2))[\sinh(\alpha_{mn}y) \\ &\quad + \gamma_{mn}\sinh(\beta_{mn}y)] \quad m=0,1,2,\ldots \quad n=1,3,5,\ldots\end{aligned} \tag{7}$$

The values of coefficients α_{mn}, β_{mn}, and γ_{mn} depend on the eigenvalues of the boundary-value problem defined by the first equation

---

[1] See Sec. 6 for a discussion on the validity of this assumption.

in (1) (with $\Lambda = 0$, and the $w,_{xx}$ term neglected) and its corresponding boundary conditions.

In order to solve the coupled fluid-structure equations in (1), we first compute the fluid flow solution corresponding to each structural basis function $\Psi_{mn}(x,y)$. For small amplitude motion of the web, all these fluid flow solutions can be superimposed to obtain an expansion for the perturbation aerodynamic potential. Using this discretization approach, an expansion for the perturbation aerodynamic potential $\phi(x,y,z,t)$ is obtained under the assumption that the web motion is purely oscillatory (which is also justified when the web motion has a very small rate of decay or growth such as near the critical values of cross flow velocity corresponding to the onset of flutter instability [20,21]). Thus, $q_{mn}(t) = \xi_{mn} e^{j\omega t}$, where ξ_{mn} are complex numbers representing the amplitude and phase of the mnth basis function and ω is the frequency of oscillation of the web. Substituting the expansion in (6) into the right-hand side of Eq. (3) and assuming that the time dependence of the perturbation aerodynamic potential $\phi(x,y,z,t)$ is the same as that of the web velocities, from Eqs. (1) and (3) for each basis function Ψ_{mn}, we obtain

$$\nabla^2 \phi_{mn} = 0 \tag{8a}$$

$$\phi_{mn,z} e^{j\omega t} = j\omega \xi_{mn} \Psi_{mn} e^{j\omega t} + V \xi_{mn} \Psi_{mn,y} e^{j\omega t} \tag{8b}$$

Equation (8*a*) and the associated boundary condition (8*b*) can be subdivided into two boundary-value problems corresponding to the perturbation aerodynamic potentials $\phi_{mn1}(x,y,z)$ and $\phi_{mn2}(x,y,z)$; $\phi_{mn1}(x,y,z)$ satisfies the first term on the right-hand side of Eq. (8*b*) and $\phi_{mn2}(x,y,z)$ satisfies the second term on the right-hand side of Eq. (8*b*). Specifically, the two boundary-value problems arising from each basis function $\Psi_{mn}(x,y)$ are

$$\nabla^2 \phi_{mn1} = 0 \tag{9a}$$

$$\phi_{mn1,z}(x,y,0) = \Psi_{mn}(x,y) \tag{9b}$$

and

$$\nabla^2 \phi_{mn2} = 0 \tag{10a}$$

$$\phi_{mn2,z}(x,y,0) = \Psi_{mn,y}(x,y) \tag{10b}$$

The solutions of Eqs. (9*a*) and (10*a*) for all the values of m and n can be added to obtain the expansion for perturbation aerodynamic potential as

$$\phi(x,y,z,t) = \sum_{m=0}^{\infty} \sum_{n=0}^{\infty} [j\omega \xi_{mn} \phi_{mn1}(x,y,z) e^{j\omega t} + V \xi_{mn} \phi_{mn2}(x,y,z) e^{j\omega t}] \tag{11}$$

Using the expansion in Eq. (11), the pressure differential $\Delta p(x,y,t)$ acting on the web (the right hand side of the first equation in Eq. (1)) is

$$\begin{aligned}\Delta p(x,y,t) &= \sum_{m=0}^{\infty} \sum_{n=0}^{\infty} 2\Lambda \xi_{mn} [-\omega^2 \phi_{mn1} + j\omega V(\phi_{mn1,y} + \phi_{mn2}) \\ &\quad + V^2 \phi_{mn2,y}] e^{j\omega t} \\ &= \sum_{m=0}^{\infty} \sum_{n=0}^{\infty} \xi_{mn} [2\Lambda (A_{mn})_{\text{real}} + j 2\Lambda (A_{mn})_{\text{imag}}] e^{j\omega t} \\ &= \sum_{m=0}^{\infty} \sum_{n=0}^{\infty} 2\Lambda \left[q_{mn}(t)((A_{mn})_{\text{real}}) + \dot{q}_{mn}(t) \left(\frac{(A_{mn})_{\text{imag}}}{\omega} \right) \right]\end{aligned} \tag{12}$$

The real part $2\Lambda(A_{mn})_{\text{real}}$ of the complex pressure differential acts in phase with the web displacement, while the imaginary part $2\Lambda(A_{mn})_{\text{imag}}$ acts in phase with the web velocity. Furthermore, the pressure differential terms $\omega^2 \phi_{mn1}$, $j\omega V(\phi_{mn1,y} + \phi_{mn2})$, and $V^2 \phi_{mn2,y}$ in Eq. (12) represent, respectively, the aerodynamic inertia, the aerodynamic damping, and the aerodynamic stiffness. All these pressure differential terms play different roles in the onset of instabilities. Specifically, the aerodynamic stiffness or the $V^2 \phi_{mn2,y}$ term is a centrifugal pressure term. In the discretized fluid-web system, the symmetric matrix representing the $V^2 \phi_{mn2,y}$ term is responsible for the fluid-induced reduction in stiffness of the coupled fluid-web system. The antisymmetric matrix representing the $V^2 \phi_{mn2,y}$ term, which forms the circulatory terms in the discretized system, leads to the onset of flutter instabilities in webs and ribbons.

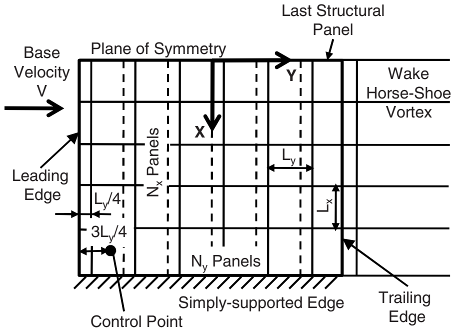

Fig. 2 A schematic representation showing the arrangement of panels and vortex rings on the half-web and in the wake

For discretizing the equations by Galerkin's method, $M \times N$ structural basis functions and their perturbation aerodynamic potentials are retained and substituted into Eq. (1). The resulting residual terms are weighted by using the basis functions $\Psi_{mn}(x,y)$ and integrated over the domain, leading to the following discretized system of $M \times N$ equations:

$$[I]\{\ddot{q}\} + [[K_1] + \epsilon [K_2]]\{q\} = 2\Lambda \left([A_{\text{real}}]\{q\} + \frac{[A_{\text{imag}}]}{\omega}\{\dot{q}\} \right) \tag{13}$$

In Eq. (13), $[I]$ is the identity matrix, which accounts for the web inertia. The matrices $[K_1]$ and $[K_2]$ represent the structural membrane stiffness and the bending stiffness, respectively. The matrices $[A_{\text{real}}]$ and $[A_{\text{imag}}]$: (a) represent, respectively, the real and imaginary parts of the pressure differential acting on the web, (b) are functions of the reduced frequency $k = (\omega b)/(2V)$ [22], and (c) are nonsymmetric as a direct consequence of the inclusion of a trailing edge wake in the fluid flow model. As a result, the coupled fluid-structure system is a nonconservative dynamical system with gyroscopic and circulatory forces. The definitions of the various matrices in Eq. (13) are given in the Appendix.

4 Vortex-Lattice Method and the Coupled Eigenvalue Problem

The perturbation aerodynamic potentials are numerically evaluated for each structural basis function by using the vortex-lattice method [18]. The solution methodology consists of dividing the web into a series of panels, distributing vortex rings of unknown strength in the panels on the web surface, and then evaluating their strength so that the boundary conditions in Eqs. (9*b*) and (10*b*) are satisfied.

In what follows, the arrangement of vortex rings on the web, the resulting system of linear equations, and its solution to obtain the perturbation aerodynamic potentials is described. A total of $R = 2N_x \times N_y$ rectangular panels ($2N_x$ along the X direction and N_y panels along the Y direction) are arranged on the surface of the web (see Fig. 2) in the X-Y plane. A vortex ring of unknown strength is placed on each panel at a distance of $L_y/4$ from the leading edge of the panel, and the control point (i.e., the point where the structural and fluid velocities are matched) is located at a distance of $3L_y/4$ from the leading edge of each panel. Apart from this, horseshoe vortices are located in the wake region starting at a distance of $L_y/4$ from the trailing edge and extending until infinity downstream.

The unknown strengths of the R web vortex ring panels described above are determined by fluid-structure velocity matching enforced at the R control points. This velocity matching results in a system of linear equations:

$$\begin{bmatrix} \beta_{11} & \cdots & \beta_{1R} \\ \vdots & \ddots & \vdots \\ \beta_{R1} & \cdots & \beta_{RR} \end{bmatrix} \begin{Bmatrix} \Gamma_1 \\ \vdots \\ \Gamma_R \end{Bmatrix} = \begin{Bmatrix} \nu_1 \\ \vdots \\ \nu_R \end{Bmatrix} \tag{14}$$

where $\Gamma_i (i=1,2,\ldots,R)$ denote the unknown vortex strengths of the R panels and $\beta_{ij}(i,j=1,2,\ldots,R)$ represents the velocity induced at the ith control point by a unit strength vortex ring at the j^{th} panel. The expression for the coefficient β_{ij} can be found in Ref. [18]. $\nu_i(i=1,2,\ldots,R)$ on the right-hand side of Eq. (14) represent the Z-direction velocity of the fluid at the ith control point. The Kutta condition is enforced by assuming that the strength of the wake horse shoe vortex is equal to the last structural panel (see Fig. 2). The linear system described in Eq. (14) is used to solve the boundary-value problem of Eqs. (9*a*) and (9*b*) (the solution of the boundary-value problem of Eqs. (10*a*) and (10*b*) follows an identical procedure). This procedure is presented next.

Given the structural basis function $\Psi_{mn}(x,y)$, the goal is to use Eq. (14) to find the perturbation aerodynamic potential $\phi_{mn1}(x,y,z)$. Following the work of Von Kármán and Sears [23], $\phi_{mn1}(x,y,z)$ is divided in two parts: the quasisteady solution $(\phi_{mn1})_{\text{quasisteady}}$ and the correction $(\phi_{mn1})_{\text{wake}}$ due to the harmonic vortex shedding in the wake. The velocity potential $(\phi_{mn1})_{\text{quasisteady}}$ can be thought of as the instantaneous response of the fluid to the structural motion. Then, in order to evaluate $(\phi_{mn1})_{\text{quasisteady}}$, the basis function $\Psi_{mn}(x,y)$ is evaluated at the R control points and these values form the right-hand side of Eq. (14). The solution of Eq. (14) yields $\Gamma_i(i=1,2,\ldots,R)$, which is mapped to obtain $\Gamma(x,y)$. Moreover, $(\phi_{mn1})_{\text{quasisteady}}$ is obtained by using $(\phi_{mn1})_{\text{quasisteady}}(x,y,0^+)=\Gamma(x,y)/2$. The quasisteady solution $(\phi_{mn1})_{\text{quasisteady}}$ determined above gives rise to harmonically varying wake vortices [23]. The image vortices (formed on the web) that nullify the effect of this harmonically varying wake result in $(\phi_{mn1})_{\text{wake}}$. The procedure to find $(\phi_{mn1})_{\text{wake}}$ involves applying Kelvin's theorem [23] and solving Eq. (14) such that the normal flow (at the R control points) caused by the wake is nullified. Once the solution $(\phi_{mn1})_{\text{wake}}$ is known, the perturbation aerodynamic potential caused by the basis function $\Psi_{mn}(x,y)$ is simply the sum of $(\phi_{mn1})_{\text{quasisteady}}$ and $(\phi_{mn1})_{\text{wake}}$.

The perturbation aerodynamic potentials obtained with the above procedure are used to evaluate the pressure differential (see Eq. (12)) and then substituted in Eq. (13) to obtain the coupled eigenvalue problem. The complex eigenvalues (which represent decaying or growing oscillatory web motion) of the coupled eigenvalue problem need to be evaluated using an iterative method known as the p-k method [20]. The numerical results obtained by using the p-k method are presented in Sec. 6 after a discussion of the computational issues in Sec. 5.

5 Computational Issues

The perturbation aerodynamic potential solutions $\phi_{mn1}(x,y,z)$ and $\phi_{mn2}(x,y,z)$ are evaluated numerically using computer programs written in the C++ language. The linear system of Eq. (14) is column block partitioned and solved by using the *LU* decomposition method. The computations were performed by using the parallel computing machines at the Rosen Center for Advanced Computing, Purdue University, West Lafayette, IN.

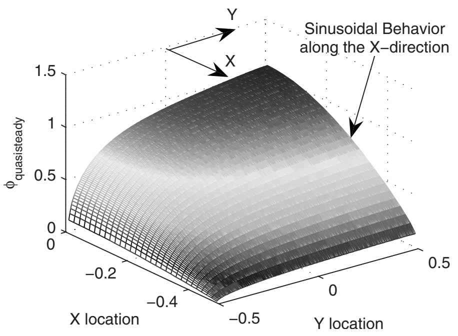

Fig. 3 Behavior of the perturbation aerodynamic potential along the *X* and *Y* axes

The vortex-lattice fluid solver developed here is bench-marked with the results in the work of Lawrence and Gerber [24] (error of less than 2% in the lift coefficient and error of less than 0.5% in the phase angle for a 3D plate performing heaving motion were obtained). Certain simplifications to reduce the computational effort can be made while numerically solving the fluid flow problem. First, symmetry of the fluid domain about the Y-Z plane is invoked. Symmetry reduces the number of unknowns in Eq. (14) to just $R=N_x \times N_y$. Second, it is observed in the full three dimensional solution (see Fig. 3) that the vortex ring strength varies sinusoidally along the X direction (a direct consequence of all structural basis functions behaving sinusoidally along the X direction). This implies that for a given panel row along the X direction (see Fig. 2), the unknown strengths are simply $\sin((m+1)\pi(x+1/2))(m=0,1,2,\ldots)$ multiples of the first panel. This provides an additional $(N_x-1)\times N_y$ constraint equations in conjunction with the linear system in Eq. (14). It should be noted that this simplification does not reduce the dimension of the fluid flow problem from 3 to 2, but simply reduces the number of unknowns in Eq. (14) from $R=N_x \times N_y$ to $R=N_y$.

Variation in the predicted web frequencies with (a) change in the number of vortex ring panels and (b) change in the number of basis functions in the Galerkin expansion is studied in order to ensure converged numerical results. It was found that the predicted web frequencies and the predicted rates of growth change by less than 1% when more than $N_y=5000$ vortex panels were used. Moreover, up to 27 *structural* basis functions along the Y direction are needed to obtain converged web frequencies and rates of growth (relative percentage change of less than 1%). These convergence studies were performed over a range of cross flow velocities V both near and away from the point of onset of instabilities.

6 Aeroelastic Stability

We now turn our attention to the predictions of the aeroelastic stability of webs and ribbons as a function of cross flow speed V, the aspect ratio κ (the length to width ratio), and the ratio ϵ of web bending stiffness to the applied tension. The computations performed below use realistic web properties. Young's modulus and Poisson's ratio are estimates for paper web properties from the literature [11]. The spanwise length, thickness, tension, and area density of the web are taken from Vaughan [29]. The following numerical values were used for the web dimensions and material properties:

$$a = 1.372 \text{ m}, \quad h = 25.4 \times 10^{-6} \text{ m}, \quad \rho = 40 \text{ g/m}^2$$

$$E = 6.8 \text{ GPa}, \quad \mu = 0.3, \quad \rho_{\text{fluid}} = 1.225 \text{ kg/m}^3$$

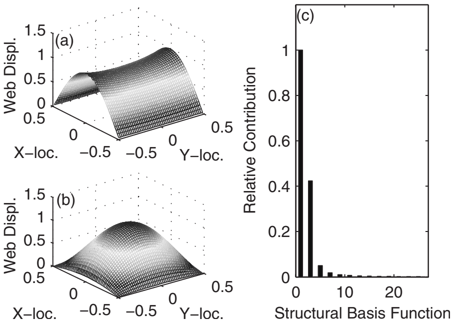

Fig. 4 The first mode shape at zero cross flow velocity for (*a*) in vacuo web, (*b*) web with surrounding air, and (*c*) relative contributions of the structural basis functions to the first mode of the fluid-web system

Furthermore, the width ranges from $b=0.0457$ m to 1.372 m and the applied tension ranges from $N'_{xx}=1.08$ N/m to 985.64 N/m. This corresponds to nondimensional numbers of $\Lambda=42$, κ varying from 1 to 30, and ϵ varying from 5.5×10^{-9} to 5×10^{-6}.

In all the calculations presented, the Galerkin expansion uses $M=1$ and $N=27$. For a given cross flow velocity V, the frequencies and the rates of growth of the web or ribbon displacement are obtained by solving the coupled fluid-web eigenvalue problem using the p-k method. The components of the resulting eigenvector are used to weight the structural basis functions to yield the complex mode shape of the web or the ribbon. Flutter instability is said to occur whenever the rate of growth associated with the nonzero frequency of a mode becomes positive. Divergence instability is said to occur when the frequency associated with a particular mode is zero and the rate of growth has a positive sign. First, the results on aeroelastic stability of webs are presented, which are followed by the aeroelastic stability of ribbons. Finally, a comparison between the aeroelastic characteristics of webs and ribbons is provided.

6.1 Aeroelastic Stability of Webs.

For the numerical results presented in this section, a web aspect ratio of $\kappa=1$ was chosen. Unless otherwise mentioned, all web calculations assume $\Lambda=42$ and $\epsilon=5\times10^{-6}$ (corresponding to $a=1.372$ m and $N'_{xx}=1.08$ N/m).

6.1.1 Web Mode Shape Dependence on the Cross Flow Velocity. At zero cross flow velocity, the effect of the surrounding air is that of an added mass on the web. Figures 4(*a*) and 4(*b*) show the first in-vacuo mode of the web and the first mode of the coupled fluid-web system, respectively. The added mass effect of the surrounding fluid near the free edges of the web causes significant reduction in the displacement of the free edges. The relative contributions of the structural basis functions to this mode of the coupled fluid-web system are shown in Fig. 4(*c*). The first mode shape of the fluid-web system comprises only of those structural basis functions that are symmetric about the *X*-*Z* plane.

With increasing cross flow velocity V, the relative contributions of the structural basis functions start changing. At nonzero cross flow velocities, the mode shapes of the coupled fluid-web system are complex. These complex mode shapes are represented by plotting the envelope, the phase, and the relative contribution of the structural basis functions. Note that only the dependence along the Y direction is shown (while the dependence along the X direction is sinusoidal). Figure 5 shows the envelope, the phase, and the structural basis content of the first web mode at cross flow velocities of $V=0.035$, 0.045, and 0.055. As the cross flow velocity V is increased, the relative contributions from the higher basis functions increase, while those from the lower basis functions decrease. This is due to the flow-induced loss in stiffness associated with the higher basis functions.[2] With increasing cross flow velocity V, the first web mode shape increasingly localizes near the leading edge. It is interesting to note that unlike the first mode, the higher modes (not shown here) do not show edge localization with increasing cross flow velocity.

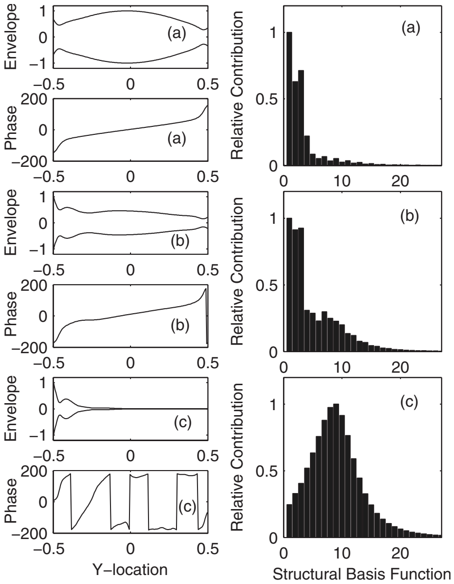

Fig. 5 The envelope and the phase of the first mode of the coupled fluid-web system along with the relative contributions of the structural basis functions at (*a*) $V=0.035$, (*b*) $V=0.045$, and (*c*) $V=0.055$

6.1.2 Web Frequency Dependence on the Cross Flow Velocity. Consider the behavior of the natural frequencies as a function of the cross flow velocity. The natural frequencies and the corresponding rates of growth of the first five modes of the web are shown in Fig. 6. As the flow velocity is increased, all the natural frequencies decrease. For such small values of ϵ, a notable feature of these frequency loci[3] is that the frequencies of the higher modes decrease at a faster rate compared to the lower modes (again the reason is large pressure differentials associated with the higher basis functions). As a consequence, the frequency loci either appear to cross (the apparent frequency crossing *does not* imply curve intersection because of the different rates of growth associated with each curve) or exhibit the frequency curve veering phenomenon [26] accompanied by the exchange of mode shapes. For example, in Fig. 6, veering occurs between the first and the second, and the second and the fourth mode. These instances of frequency curve veering are accompanied by exchange of mode shapes. Furthermore, as shown in Fig. 6, the frequency of the first mode becomes zero at a nondimensional velocity of $V\cong0.0585$ and the coupled system loses stability by divergence. The corresponding rate of growth of the first mode splits into a positive real and a negative real part.

Interestingly, the coupling between the third and the fifth mode leads to a *weak flutter instability* (see Fig. 6 and the inset) for a small velocity range of $V\cong0.0523$–0.0529, when the rate of growth of the third mode becomes positive. This indicates the appearance and the disappearance of the flutter instability *before*

---

[2] For higher basis functions, a fluid particle traveling tangentially to the web surface turns through smaller radii of curvature, giving rise to larger centrifugal pressures, which in turn leads to a more rapid fluid-induced reduction in stiffness compared to the lower basis functions.

[3] Based on the large Reynolds number and the small web oscillation amplitude, the use of the unsteady Kutta condition is valid [18,25] even at such high reduced frequencies $k=(\omega b)/(2V)$ ranging from 0 to 15.

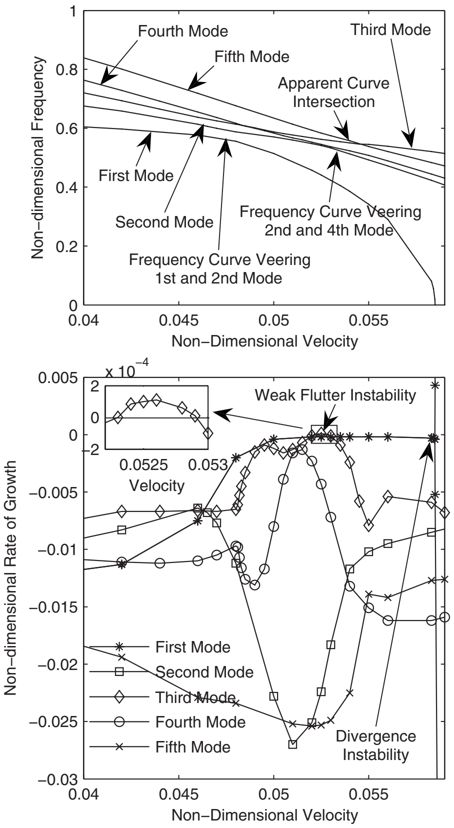

Fig. 6 Nondimensional frequencies and rates of growth of the first five modes of a fluid-web system of aspect ratio κ=1 and tension ratio ϵ=5×10^{-6}

the occurrence of the divergence instability. In the absence of wake-induced nonconservative effects, flutter instability can only occur after the divergence instability. This implies that the nonconservative effects caused by the trailing edge wake are responsible for this flutter instability. The flutter instability is termed *weak* because the corresponding rate of growth is very small.

6.1.3 Effect of Applied Tension on the Onset of Instabilities in Webs. The results presented so far have been for a fixed, realistic value of ϵ. To study the effect of tension on the onset of instability, the ratio ϵ is varied from 2×10^{-6} to 6×10^{-6}. Figure 7 shows the graph of the dimensional critical flow velocity V versus the parameter ϵ. It can be seen that increased values of applied tension (decreased values of ϵ) lead to occurrence of divergence instability at higher cross flow velocities. The reason for this behavior is that increasing the applied tension increases the stiffness of the web and makes it more resistant to the divergence instability.

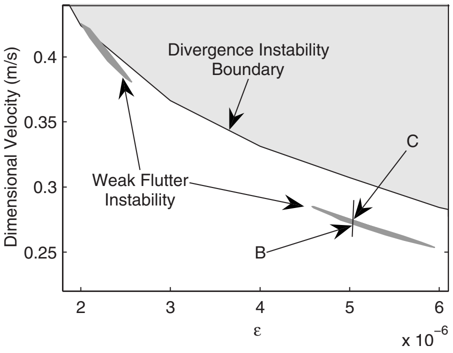

Fig. 7 Stability regions in the V-ϵ plane for a fluid-web system of aspect ratio κ=1

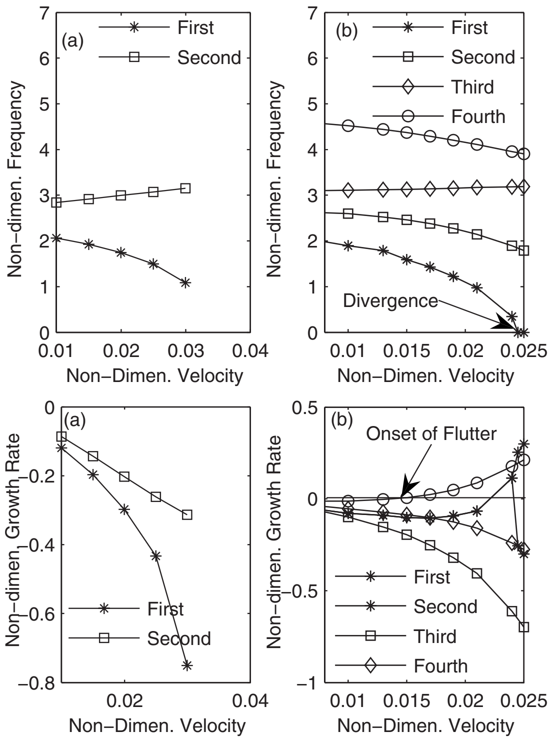

Fig. 8 Nondimensional frequencies and rates of growth for a ribbon of aspect ratio κ=30 with (*a*) ϵ=5×10^{-6} and (*b*) ϵ=5.5×10^{-9}

The occurrence of flutter over a small velocity interval between points B and C is attributed to the coupling between the third and the fifth mode. An interesting aspect of this flutter instability caused by the interaction of the third and fifth modes is that it does not occur for all values of ϵ, but only over a small range of $\epsilon=4.5\times10^{-6}$–$5.9\times10^{-6}$. At even lower values of ϵ, flutter instability disappears. Further reduction of ϵ causes the flutter instability to reappear, but now due to coupling between a pair of higher modes.

An important conclusion from this behavior is that the spanwise applied tension plays a crucial role in the occurrence of flutter. For most ϵ values, the web loses stability via divergence instability. However, for some ranges of ϵ values, two closely spaced modes under the influence of the nonconservative wake effects can interact to produce flutter instability prior to divergence. These conclusions are valid for wide webs with free leading and trailing edges, with fluid flow across the free edges. For webs with constrained leading edges [13], the aeroelastic stability predictions can be different from the ones presented above.

6.2 Aeroelastic Stability of Ribbons. Next, the aeroelastic stability characteristics of a narrow ribbon are investigated. A ribbon of length a=1.372 m (which corresponds to Λ=42) and an aspect ratio of κ=30 is chosen. Two sets of results corresponding to $\epsilon=5\times10^{-6}$ (the same ϵ value as used for wide webs) and $\epsilon=5.5\times10^{-9}$ (an ϵ value corresponding to significantly increased applied tension) are presented.

6.2.1 Frequencies and Mode Shapes of a Narrow Ribbon. For a ribbon with $\epsilon=5\times10^{-6}$, the frequencies and the rates of growth of the lowest two modes are shown in Fig. 8(*a*). The frequencies of the third and higher modes are spaced away from these two frequency curves and are not shown in this figure. The motion

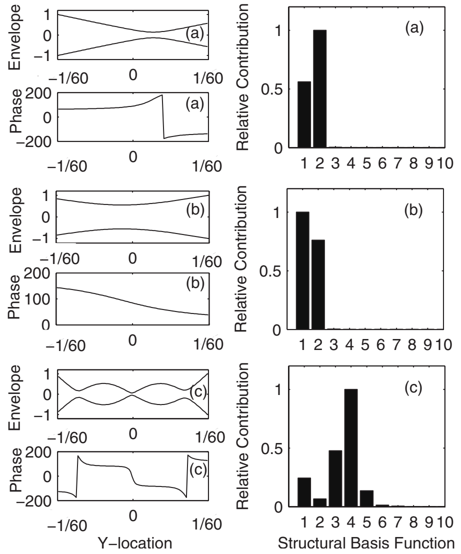

Fig. 9 Mode shapes of a narrow ribbon of $\kappa=30$: (*a*) first mode at $V=0.03$ and $\epsilon=5\times10^{-6}$, (*b*) second mode at $V=0.03$ and $\epsilon=5\times10^{-6}$, and (*c*) fourth mode at $V=0.0139$ and $\epsilon=5.5\times10^{-9}$

corresponding to the lower frequency is dominated by the in-vacuo torsional mode of the ribbon (pitching motion about the X axis with a sinusoidal shape along the X direction). The envelope, the phase, and the relative contributions of the two participating structural basis functions for the first ribbon mode (at $V=0.03$) are shown in Fig. 9(*a*).

The larger of the two frequencies in Fig. 8(*a*) corresponds to the heaving-motion-dominated mode of the ribbon (see Fig. 9(*b*) for the envelope, the phase, and the structural basis function content at $V=0.03$). With increasing cross flow velocity, the frequency for this mode remains approximately constant. This is expected because the heaving motion does not produce significant flow gradients along the Y direction, thereby not producing the associated aerodynamic pressure differentials. This causes the frequency of the heaving-motion-dominated mode to remain approximately constant as cross flow velocity increases, while that corresponding to the torsional-motion-dominated mode reduces with increasing cross flow velocity.

The frequencies and the rates of growth for the lowest four modes for a high tension ribbon with $\epsilon=5.5\times10^{-9}$ are shown in Fig. 8(*b*). At a nondimensional velocity $V\cong0.0139$, the rate of growth of the fourth mode becomes positive, indicating flutter instability. At yet larger flow velocity $V\cong0.022$, the first mode starts fluttering followed by divergence instability of the first mode at $V\cong0.0245$. The envelope, the phase, and the structural basis function content corresponding to the fluttering mode at $V=0.0139$ are shown in Fig. 9(*c*).

6.2.2 Effect of Applied Tension on the Onset of Instabilities in Ribbons. It is clear from Figs. 8(*a*) and 8(*b*) that for high tension (low ϵ), the initial ribbon frequencies are closely spaced while for lower tension, the ribbon frequencies move apart. The spanwise applied tension changes the relative spacing between different ribbon frequencies, thereby changing the modal coupling. Increased modal coupling (due to increased applied tension) can lead to the occurrence of flutter instability. Consequently, low tension ribbons destabilize via divergence (flutter instability cannot occur due to the low modal coupling), while high tension ribbons appear to destabilize via flutter prior to their onset of divergence. Thus, changing the applied tension can lead to a change in the type of instability exhibited by the ribbon. The role of applied tension in the occurrence of instability for a ribbon can be investigated by plotting the stability boundaries on the V-ϵ plane.

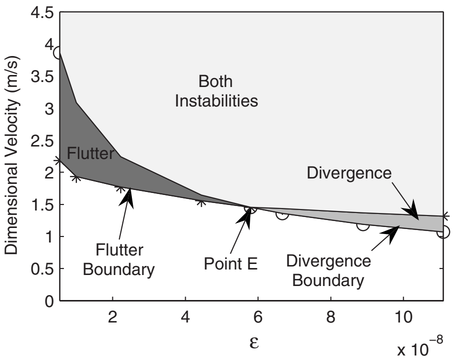

Fig. 10 Stability regions in the V-ϵ plane for a narrow ribbon of aspect ratio $\kappa=30$

As shown in Fig. 10, for the values of $\epsilon\cong5.8\times10^{-8}$ and above, the ribbon loses stability through divergence of the first mode. For values of ϵ less than 5.8×10^{-8}, flutter instability occurs before the occurrence of the divergence instability. In the V-ϵ plane, at point E, both the flutter and divergence instabilities occur simultaneously. The shaded regions in Fig. 10 signify the occurrence of flutter instability or divergence instability or the simultaneous occurrence of both instabilities.

6.3 Comparison of Wide Webs and Narrow Ribbons. The aspect ratio κ, and ϵ, the ratio of bending stiffness to applied tension of the web, play a crucial role in the modal interactions and the onset of divergence or flutter instability. In order to point out the important differences between wide webs and narrow ribbons, consider the frequency loci of three representative webs having the same length $a=1.372$ m, the same ratio $\epsilon=5\times10^{-6}$, but different aspect ratios $\kappa=1$, 5, and 30. These loci are shown in Fig. 11. At $\epsilon=5\times10^{-6}$, the narrow ribbon ($\kappa=30$) does not show a flutter instability, while the wide ribbon ($\kappa=5$) loses stability by flutter. The wide web ($\kappa=1$) shows a weak flutter instability before the occurrence of divergence instability.

The differences between the behavior of wide webs and narrow ribbons are as follows:

- For a fixed value of ϵ, the frequencies of wide webs are clustered closely while they are further apart for narrow ribbons. As a consequence, the possibility of modal interactions due to nonconservative wake effects is greater in wide webs.

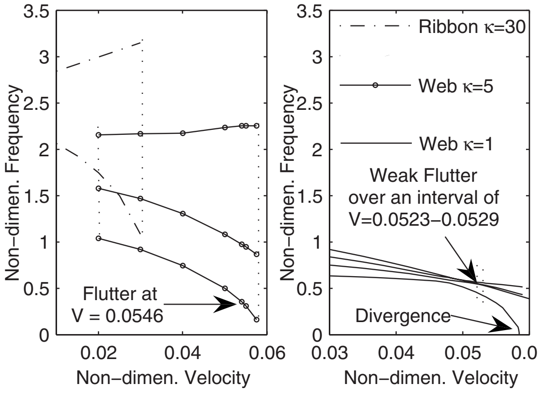

Fig. 11 Comparison of the frequencies of a narrow ribbon ($\kappa=30$), a wide ribbon ($\kappa=5$), and a wide web ($\kappa=1$)

- The flow-induced change in frequencies for a wide web is small when compared to change in frequencies for a narrow ribbon.
- The flutter instability exhibited by wide webs is weak and occurs only over small intervals of velocity. Narrow ribbons and intermediate aspect ratio webs do not exhibit this behavior.
- For narrow ribbons, when ϵ is below a critical value, the ribbon destabilizes by flutter (see Fig. 10). This behavior is absent in the case of wide webs (see Fig. 7).

6.4 Discussion of Results. Wide webs and narrow ribbons of the same length but different widths exhibit different behaviors (see Figs. 6, 8, and 11). The differences between the behavior of a wide web ($\kappa=1$) and a narrow ribbon (some $\kappa>1$) can be explained by writing the *discretized* equations of motion[4] as follows:

$$\underbrace{[I]\{\ddot{q}_{\text{web}}\}}_{\text{struct inertia}} + \underbrace{[K_1]\{q_{\text{web}}\}}_{\text{memb stiff}} + \underbrace{\epsilon[K_2]\{q_{\text{web}}\}}_{\text{bend stiff}}$$

$$= \underbrace{2\Lambda([M] + V[G_1] + V[G_2] + V^2[K])\{q_{\text{web}}\}}_{\text{aerodyn press}} \qquad (15a)$$

$$\underbrace{[I]\{\ddot{q}_{\text{rib}}\}}_{\text{struct inertia}} + \underbrace{[K_1]\{q_{\text{rib}}\}}_{\text{memb stiff}} + \underbrace{\epsilon[K_2]\{q_{\text{rib}}\}}_{\text{bend stiff}}$$

$$= \underbrace{2\Lambda\left(\frac{1}{\kappa}[M] + V[G_1] + V[G_2] + \kappa V^2[K]\right)\{q_{\text{rib}}\}}_{\text{aerodyn press}} \qquad (15b)$$

Equation (15*a*) is a special case of Eq. (15*b*) when $\kappa=1$. Since the basis functions are mass normalized, the membrane stiffness scales as $[K_1]^{\text{web}} \sim [K_1]^{\text{rib}}$. However, the bending stiffness for ribbons scales such that $[K_2]^{\text{rib}} \gg [K_2]^{\text{web}}$ because for a ribbon, the curvature of the structural basis functions along the Y direction is large. Moreover, the aerodynamic pressure differential matrices scale, as shown in Eq. (15*b*). Specifically, compared to a web, the $V^2[K]$ pressure differential matrix is κ times larger for a ribbon due to the large flow gradients along the Y direction.

For a fixed value of applied tension (represented by ϵ), it is interesting to note that as the width is reduced (κ is increased), there are two competing effects governing the occurrence of flutter: (a) the increased bending stiffness *reduces* the modal interactions by increasing the frequency spacing, and (b) the $V^2[K]$ pressure differential term *increases* the modal interactions by increasing the antisymmetric stiffness terms (i.e., the circulatory terms responsible for flutter instability). The actual rate of growth associated with a flutter instability is, however, decided by the relative magnitudes of the membrane stiffness term and the $V^2[K]$ pressure differential term. Thus, for a wide web, clustered frequencies lead to flutter, but the instability is weak due to the small magnitudes of the $V^2[K]$ pressure differential terms. For a narrow ribbon, as seen in Fig. 11, although the $V^2[K]$ pressure differential terms are large, the widely spaced frequencies lead to low modal interactions and the absence of flutter. For the intermediate case of $\kappa=5$, where flutter does occur, the rate of growth is large because the $V^2[K]$ pressure differential terms are large compared to the membrane stiffness terms.

The theoretical model presented in this article does not include a viscous drag force. If included, this viscous drag force introduces a follower force term $\frac{1}{2}\rho_{\text{fluid}}V^2C_D w_{,y}$ on the right-hand side of Eq. (1), where C_D is the viscous drag coefficient calculated based on the Blasius boundary layer [27,28]. Preliminary calculations after including this viscous drag force show that (a) for wide webs with extremely small bending stiffness, the aeroelastic stability predictions change qualitatively when compared to the predictions in the current article, (b) the predictions for narrow ribbons also change qualitatively, though narrow ribbons are less affected compared to wide webs, (c) the quantitative shift in the eigenvalue (oscillation frequencies and growth rates) predictions of stability for wide webs as well as narrow ribbons is small, and (d) webs and ribbons with large bending stiffness D are relatively less affected by the drag force when compared to webs and ribbons with smaller D. Thus, the inclusion of the drag force could become important for wide webs with extremely small bending stiffness, while for wide webs with moderately large bending stiffness, the predictions of the current article are valid.

The theoretical predictions from the current work cannot be directly compared with the experimental data available in the literature. Experimental data on uniaxially tensioned webs in cross flow have been reported in the works of Chang and Moretti [11] and Watanabe et al. [4]. Specifically, it has been shown by Watanabe et al. [4] (see Fig. 17 of this reference) that the experimental data collapse on a straight line in the $\log(V\sqrt{\Lambda/\epsilon})$ versus $\log(\epsilon/\Lambda)$ plane. However, the leading edge of the web is constrained in the experiments of Chang and Moretti [11] (see Fig. 5 of this reference) and Watanabe et al. [4] (see Fig. 14 of this reference). The situation of a web with fluid flow across its *two free* edges is more complicated when compared to the experiments in the existing literature. Experiments with these practically important boundary conditions need to be performed in order to verify the findings in this work.

7 Conclusions

Tensioned wide webs and narrow ribbons are widely used in the paper-handling, textile, plastics, and sheet metal industries. These webs are often subjected to air flows that lead to aeroelastic flutter problems. The work presented in this article addresses this broad category of problems by tackling a specific problem of flow-induced vibrations of stationary wide webs and narrow ribbons in cross flow.

For wide webs, the clustered modes interact with one another and give rise to frequency veering. The nonconservative effects caused by the trailing edge wake destabilize the webs near the occurrence of frequency curve veering and apparent frequency curve intersections. However, this flutter instability in wide webs is weak and wide webs mainly lose stability by divergence. On the other hand, depending on the value of applied tension, narrow ribbons can lose stability either through flutter or divergence.

Acknowledgment

Financial support from the author's (A.R.) group of industrial sponsors and from the National Science Foundation (CAREER Award No. 0116414-CMS) is gratefully acknowledged. This research was supported through the computing resources provided by Information Technology at Purdue—the Rosen Center for Advanced Computing, West Lafayette, IN.

Appendix

The definition of various matrices in Eqs. (13), (15*a*), and (15*b*) are as follows:

$$(\mathbf{K}_1)_{ij;mn} = \int_{x=-1/2}^{1/2}\int_{y=-1/(2\kappa)}^{1/(2\kappa)} \Psi_{ij,x}(x,y)\Psi_{mn,x}(x,y)\,dydx$$

---

[4] See the Appendix for the definition of the various matrices.

$$(\mathbf{K}_2)_{ij;mn} = \int_{x=-1/2}^{1/2}\int_{y=-1/(2\kappa)}^{1/(2\kappa)} \left\{ \begin{array}{c} \Psi_{ij,xx}(x,y)\Psi_{mn,xx}(x,y) \\ +\Psi_{ij,yy}(x,y)\Psi_{mn,yy}(x,y) \\ +2(1-\mu)\Psi_{ij,xy}(x,y)\Psi_{mn,xy}(x,y) \\ +\mu\Psi_{ij,xx}(x,y)\Psi_{mn,yy}(x,y) \\ +\mu\Psi_{ij,yy}(x,y)\Psi_{mn,xx}(x,y) \end{array} \right\} dydx$$

$$(\mathbf{A}_{\text{real}})_{ij;mn} = \text{Re}\left[\int_{x=-1/2}^{1/2}\int_{y=-1/(2\kappa)}^{1/(2\kappa)} \Psi_{ij}(x,y) \times \left\{ \begin{array}{c} -\omega^2\phi_{mn1}(x,y) + j\omega V\phi_{mn1,y}(x,y) \\ + j\omega V\phi_{mn2}(x,y) + V^2\phi_{mn2,y}(x,y) \end{array} \right\} dydx \right]$$

$$(A_{\text{imag}})_{ij;mn} = \text{Im}\left[\int_{x=-1/2}^{1/2}\int_{y=-1/(2\kappa)}^{1/(2\kappa)} \Psi_{ij}(x,y) \times \left\{ \begin{array}{c} -\omega^2\phi_{mn1}(x,y) + j\omega V\phi_{mn1,y}(x,y) \\ + j\omega V\phi_{mn2}(x,y) + V^2\phi_{mn2,y}(x,y) \end{array} \right\} dydx \right]$$

$$(\mathbf{M})_{ij;mn} = \int_{x=-1/2}^{1/2}\int_{y=-1/2}^{1/2} \Psi_{ij}(x,y)\{-\omega^2\phi_{mn1}(x,y)\}dydx$$

$$(\mathbf{G}_1)_{ij;mn} = \int_{x=-1/2}^{1/2}\int_{y=-1/2}^{1/2} \Psi_{ij}(x,y)\{j\omega\phi_{mn1,y}(x,y)\}dydx$$

$$(\mathbf{G}_2)_{ij;mn} = \int_{x=-1/2}^{1/2}\int_{y=-1/2}^{1/2} \Psi_{ij}(x,y)\{j\omega\phi_{mn2}(x,y)\}dydx$$

$$(\mathbf{K})_{ij;mn} = \int_{x=-1/2}^{1/2}\int_{y=-1/2}^{1/2} \Psi_{ij}(x,y)\{\phi_{mn2,y}(x,y)\}dydx$$

References

[1] Dowell, E. H., 1966, "Nonlinear Oscillations of a Fluttering Plate," AIAA J., **4**(7), pp. 1267–1275.

[2] Raman, A., Wolf, K., and Hagedorn, P., 2001, "Observations on the Vibrations of Paper Webs," *Proceedings of the International Conference on Web Handling*, Stillwater, OK.

[3] Hill, K. C., 1988, "Dryer Sheet Stability for Older Paper Machines," Tappi J., **71**, pp. 55–59.

[4] Watanabe, Y., Suzuki, S., Sugihara, M., and Sueoka, Y., 2002, "An Experimental Study of Paper Flutter," J. Fluids Struct., **16**(4), pp. 529–542.

[5] Dowell, E. H., 1975, *Aeroelasticity of Plates and Shells*, Noordhoff, Leyden.

[6] Paidoussis, M. P., 2004, *Fluid-Structure Interactions: Slender Structures and Axial Flow*, Vol. 2, Elsevier Academic, London.

[7] Guo, C. Q., and Paidoussis, M. P., 2000, "Stability of Rectangular Plates With Free Side-Edges in Two Dimensional Inviscid Channel Flow," ASME J. Appl. Mech., **67**(1), pp. 171–176.

[8] Tang, D. M., Yamamoto, H., and Dowell, E. H., 2003, "Flutter and Limit Cycle Oscillations of Two-Dimensional Panels in Three-Dimensional Axial Flow," J. Fluids Struct., **17**, pp. 225–242.

[9] Niemi, J., and Pramila, A., 1987, "FEM-Analysis of Transverse Vibrations of an Axially Moving Membrane Immersed in Ideal Fluid," Int. J. Numer. Methods Eng., **24**(12), pp. 2301–2313.

[10] Frondelius, T., Koivurova, H., and Pramila, A., 2006, "Interaction of an Axially Moving Band and Surrounding Fluid by Boundary Layer Theory," J. Fluids Struct., **22**(8), pp. 1047–1056.

[11] Chang, Y. B., and Moretti, P. M., 2002, "Flow-Induced Vibration of Free Edges of Thin Films," J. Fluids Struct., **16**(7), pp. 989–1008.

[12] Watanabe, Y., Isogai, K., Suzuki, S., and Sugihara, M., 2002, "A Theoretical Study of Paper Flutter," J. Fluids Struct., **16**(4), pp. 543–560.

[13] Chang, Y. B., and Moretti, P. M., 1992, "An Experimental Study on Edge Flutter in Webs," *Web Handling*, J. K. Good, ed., American Society of Mechanical Engineers, New York, Vol. AMD-149, pp. 67–78.

[14] Chang, Y. B., Cho, H. C., and Moretti, P. M., 1999, "Edge Flutter," *Noise Control and Acoustics Division Proceedings of the ASME*, Vol. 26, pp. 413–423.

[15] Vaughan, M., and Raman, A., "Aeroelastic Stability of Axially Moving Webs Coupled to Incompressible Flows," ASME J. Appl. Mech., in press.

[16] Bassanini, P., Casciola, C. M., Lancia, M. R., and Piva, R., 1996, "On the Trailing Edge Singularity and Kutta Condition for 3D Airfoils," Eur. J. Mech. B/Fluids, **15**(6), pp. 809–830.

[17] VanDyke, M. D., 1956, "Second-Order Subsonic Airfoil Theory Including Edge Effects," NACA Report No. 1274.

[18] Katz, J., and Plotkin, A., 2001, *Low Speed Aerodynamics*, 2nd ed., Cambridge University Press, New York.

[19] Turnbull, P. F., Perkins, N. C., and Schultz, W. W., 1995, "Contact-Induced Nonlinearity in Oscillating Belts and Webs," J. Vib. Control, **1**, pp. 459–479.

[20] Hassig, H. J., 1971, "An Approximate True Damping Solution of the Flutter Equation by Determinant Iteration," J. Aircr., **8**(11), pp. 885–889.

[21] Rodden, W. P., Harder, R. L., and Bellinger, E. D., 1979, "Aeroelastic Addition to NASTRAN," NASA Contractor Report No. 3094.

[22] Theodorson, T., 1935, "General Theory of Aerodynamic Instability and the Mechanism of Flutter," NACA Report No. 496.

[23] Von Kármán, T., and Sears, W. R., 1938, "Airfoil Theory for Non-Uniform Motion," J. Aeronaut. Sci., **5**(10), pp. 379–390.

[24] Lawrence, H. R., and Gerber, E. H., 1952, "The Aerodynamic Forces on Low Aspect Ratio Wings Oscillating in an Incompressible Flow," J. Aeronaut. Sci., **19**, pp. 769–781.

[25] Crighton, D. G., 1985, "The Kutta Condition in Unsteady Flow," Annu. Rev. Fluid Mech., **17**, pp. 411–445.

[26] Perkins, N. C., and Mote, Jr., C. D., 1986, "Comments on Curve Veering in Eigenvalue Problems," J. Sound Vib., **106**(3), pp. 451–463.

[27] Argentina, M., and Mahadevan, L., 2005, "Fluid-Flow-Induced Flutter of a Flag," Proc. Natl. Acad. Sci. U.S.A., **102**(6), pp. 1829–1834.

[28] Paidoussis, M. P., 1973, "Dynamics of Cylindrical Structures Subjected to Axial Flow," J. Sound Vib., **29**(3), pp. 365–385.

[29] Vaughan, M., 2003, "Aeroelastic Stability of Axial Moving Webs Coupled to Incompressible Flows," Master's thesis, Purdue University, West Lafayette, IN.

Snapping of a Planar Elastica With Fixed End Slopes

Jen-San Chen[1]
Professor
e-mail: jschen@ntu.edu.tw

Yong-Zhi Lin
Graduate Student

Department of Mechanical Engineering,
National Taiwan University,
Taipei 10617, Taiwan

In this paper, we study the deformation and stability of a planar elastica. One end of the elastica is clamped and fixed in space. The other end of the elastica is also clamped, but the clamp itself is allowed to slide along a linear track with a slope different from that of the fixed clamp. The elastica deforms after it is subjected to an external pushing force on the moving clamp. It is observed that when the pushing force reaches a critical value, snapping may occur as the elastica jumps from one configuration to another remotely away from the original one. In the theoretical investigation, we calculate the static load-deflection curve for a specified slope difference between the fixed clamp and the moving clamp. To study the stability of the equilibrium configuration, we superpose the equilibrium configuration with a small perturbation and calculate the natural frequencies of the deformed elastica. An experimental setup is designed to measure the load-deflection curve and the natural frequencies of the elastica. The measured load-deflection relation agrees with the theoretical prediction very well. On the other hand, the measured natural frequencies do not agree very well with the theoretical prediction, unless the mass of the moving clamp is taken into account. [DOI: 10.1115/1.2871207]

1 Introduction

Snap-through buckling in structures is a violent transition from one stable equilibrium position to another equilibrium position remotely away from the original one. For instance, a shallow arch with both ends fixed in space and under transverse loading may undergo snap-through buckling when certain conditions on the arch height and load are met; see the pioneering works of Timoshenko [1] and Bruce and Hoff [2]. Similar snap-through buckling phenomena can also be observed in the case of a shallow shell under lateral load; see the work of Budiansky and Roth [3]. Many more references on the snap-through phenomena in structures, such as shallow arches, shallow spherical caps, and cylindrical shells, can be found in the book by Simitses [4]. The term "snap through" is adopted because during buckling the structures snap from one side of the base plane "through" to the other side.

In this paper, we present a new snapping phenomenon observed in a clamped-clamped planar elastica, in which one clamp is fixed in space while the other is sliding along a linear track with a slope different from the one at the other end. Both theoretical and experimental results are presented. This structure may be used as a compliant mechanism in mechanical design [5,6]. In transmission of motion or force between two locations, compact space such as in miniature devices usually makes the conventional rigid body joint pairs impractical. In such a case, a flexible elastica capable of large deformation may be the only choice.

2 Problem Formulation

We consider a uniform beam with length L and flexural rigidity EI. The two ends of the beam are denoted as A and B, as shown in Fig. 1. An xy-coordinate system with origin attached to End A is chosen to describe the geometry of the beam. The rotation angles of the beam at Ends A and B with respect to the x axis are specified as $\theta_A=0$ and θ_B, respectively. End B is clamped and fixed in space. End A is also clamped, but the clamp itself is allowed to slide on a straight line. In its initial configuration without any external pushing force in the longitudinal direction at End A, the neutral axis of the beam is a circular arc with radius r. The bending moment along the deformed beam is a constant in this initial configuration. It is noted that the beam may be termed an elastica, whose mechanics investigation was initiated by Euler and Lagrange over two centuries ago [7]. The relations between some geometric parameters are

$$L = r\theta_B, \quad x_B = r\sin\theta_B, \quad y_B = r(1-\cos\theta_B) \tag{1}$$

where x_B and y_B are the x, y coordinates of Point B. The equations governing the motion of the elastica will be formulated first.

Figure 2 shows the free body diagram of an element ds of the elastica after End A is pushed in a distance δ_A. Forces F_x and F_y are in the x and y directions, and M is the bending moment. θ is the rotation angle of the tangent. First of all, from geometric relation we can write

$$\frac{\partial x}{\partial s} = \cos\theta \tag{2}$$

$$\frac{\partial y}{\partial s} = \sin\theta \tag{3}$$

where s is the length of the elastica measured from Point A. From the balance of moment and forces in the x and y directions, we can derive the following three equations:

$$\frac{\partial M}{\partial s} = F_x\sin\theta - F_y\cos\theta \tag{4}$$

$$\frac{\partial F_x}{\partial s} = \mu\frac{\partial^2 x}{\partial t^2} \tag{5}$$

$$\frac{\partial F_y}{\partial s} = \mu\frac{\partial^2 y}{\partial t^2} \tag{6}$$

where μ is the mass per unit length of the elastica. $x(s,t)$ and $y(s,t)$ represent the deformed shape of the elastica. The moment-curvature equation from Euler–Bernoulli beam model is

$$\frac{\partial \theta}{\partial s} = \frac{M}{EI} \tag{7}$$

The six equations (2)–(7) govern the motion of the elastica. In the case when only static deformation is of interest, the terms involv-

---

[1] Corresponding author.

Contributed by the Applied Mechanics Division for publication in the JOURNAL OF APPLIED MECHANICS. Manuscript received July 30, 2007; final manuscript received November 8, 2007; published online May 20, 2008. Review conducted by Edmundo Corona.

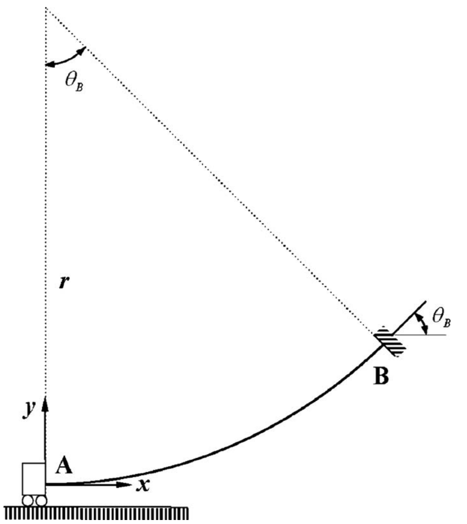

Fig. 1 A beam placed between the two clamps with specified directions. End *A* of the beam is pushed in a distance along the horizontal direction, while End *B* is fixed in space.

ing differentiation with respect to time in Eqs. (5) and (6) can be neglected.

3 Static Deformation

We first study the static deformation of the elastica after End A is pushed in a distance δ_A. There exist three different types of deformation configurations; they are the deformations with zero, one, and two inflection points. In this paper, we present the solution procedure for the deformation with two inflection points. The solution procedures for the other two simpler cases with zero and one inflection point are similar and can be found in the thesis of the second author [8].

Figure 3 shows an elastica with two inflection Points C and D. End A is under longitudinal force P_A and is pushed in a distance δ_A in the horizontal direction. The shear force and bending moment at End A are Q_A and M_A, respectively. It is noted that in this static analysis we use the tangential component P (longitudinal force) and the normal component Q (shear force) on the cross section instead of using F_x and F_y, as depicted in Fig. 2. F_x and F_y will be used in dynamic analysis later. P and Q can be related to F_x and F_y in the following relations:

$$P = -F_x \cos\theta - F_y \sin\theta, \quad Q = -F_x \sin\theta + F_y \cos\theta \tag{8}$$

The moment equation at any point (x,y) of the elastica can be written as

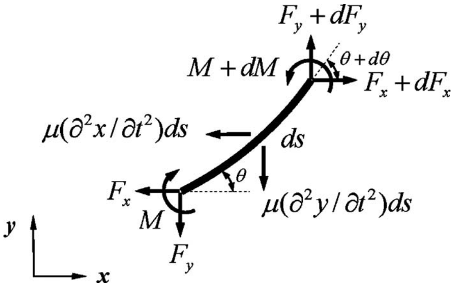

Fig. 2 The free body diagram of a small element *ds*

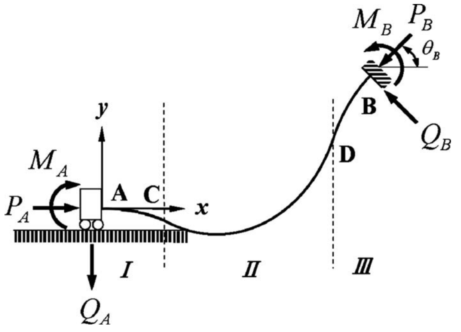

Fig. 3 Elastica deformation with two inflection points

$$EI\frac{d\theta}{ds} = M_A - P_A y - Q_A x \tag{9}$$

For convenience, we introduce the following dimensionless parameters (with asterisks):

$$(s^*, x^*, y^*, \delta_A^*) = \frac{(s, x, y, \delta_A)}{L},$$

$$(P^*, Q^*, F_x^*, F_y^*) = \frac{L^2}{4\pi^2 EI}(P, Q, F_x, F_y)$$

$$M^* = \frac{L}{4\pi^2 EI}M, \quad t^* = \frac{1}{L^2}\sqrt{\frac{EI}{\mu}}t, \quad \omega^* = L^2\sqrt{\frac{\mu}{EI}}\omega, \quad m_c^* = \frac{1}{\mu L}m_c$$

where ω is a circular frequency of the elastica. m_c is the mass of the moving clamp, which will be used in dynamic analysis later. It is noted that $P^* = 1$ corresponds to the Euler buckling load of a clamped-clamped straight beam. After substituting the above relations into Eq. (9) and dropping the asterisks thereafter for simplicity, Eq. (9) can be written in dimensionless form as

$$\frac{d\theta}{ds} = 4\pi^2(M_A - P_A y - Q_A x) \tag{10}$$

Similarly, Eqs. (5)–(7) can be rewritten in the following forms:

$$\frac{\partial F_x}{\partial s} = \frac{1}{4\pi^2}\frac{\partial^2 x}{\partial t^2} \tag{5'}$$

$$\frac{\partial F_y}{\partial s} = \frac{1}{4\pi^2}\frac{\partial^2 y}{\partial t^2} \tag{6'}$$

$$\frac{\partial \theta}{\partial s} = 4\pi^2 M \tag{7'}$$

It is noted that the dimensionless versions of Eqs. (2)–(4) remain the same as the dimensional versions. By differentiating Eq. (10) with respect to s once, and using the relations (2) and (3), we obtain

$$\frac{d^2\theta}{ds^2} = -4\pi^2(P_A \sin\theta + Q_A \cos\theta) \tag{11}$$

We multiply Eq. (11) by $d\theta$ and integrate to obtain

$$\left(\frac{d\theta}{ds}\right)^2 = 8\pi^2(P_A \cos\theta - Q_A \sin\theta + K) \tag{12}$$

where K is an integration constant. The sign of the curvature $d\theta/ds$ can be positive or negative, depending on the deformation pattern. The slopes of the elastica at Points C and D are denoted as α and β, respectively. We divide the domain of the elastica into three segments as separated by Points C and D. In Segments I and

III, the curvature of the elastica is negative, while in Segment II, the curvature is positive.

Segment I must satisfy the condition $d\theta/ds=0$ when $\theta=\alpha$. Therefore, for Segment I the integration constant K can be found as

$$K = Q_A \sin\alpha - P_A \cos\alpha \tag{13}$$

As a consequence, Eq. (12) can be written as

$$\left(\frac{d\theta}{ds}\right)_{\mathrm{I}}^2 = 8\pi^2[P_A(\cos\theta-\cos\alpha) - Q_A(\sin\theta-\sin\alpha)] \tag{14}$$

After taking square root, we have the curvature in Segment I,

$$\left(\frac{d\theta}{ds}\right)_{\mathrm{I}} = -2\sqrt{2}\pi[P_A(\cos\theta-\cos\alpha) - Q_A(\sin\theta-\sin\alpha)]^{1/2} \tag{15}$$

From Eq. (15), the length of the elastica in Segment I can be calculated as

$$l_{\mathrm{I}} = -\int_0^{\alpha} \frac{d\theta}{2\sqrt{2}\pi\sqrt{P_A(\cos\theta-\cos\alpha) - Q_A(\sin\theta-\sin\alpha)}} \tag{16}$$

The x and y coordinates of Point C relative to A can be calculated as

$$x_{C/A} = -\int_0^{\alpha} \frac{\cos\theta d\theta}{2\sqrt{2}\pi\sqrt{P_A(\cos\theta-\cos\alpha) - Q_A(\sin\theta-\sin\alpha)}} \tag{17}$$

$$y_{C/A} = -\int_0^{\alpha} \frac{\sin\theta d\theta}{2\sqrt{2}\pi\sqrt{P_A(\cos\theta-\cos\alpha) - Q_A(\sin\theta-\sin\alpha)}} \tag{18}$$

The situation in Segment III is similar to the one in Segment I. The equation for curvature $(d\theta/ds)_{\mathrm{III}}$ is the same as in Eq. (15) except that α is replaced by β. The formulas for l_{III}, $x_{B/D}$, and $y_{B/D}$ are the same as in Eqs. (16)–(18), except that α is replaced by β in all the integrands, and the integration limits are changed to from β to θ_B.

Segment II must satisfy the condition $d\theta/ds=0$ when $\theta=\alpha$ and β. Therefore, the integration constant K can be found as

$$K = Q_A\sin\alpha - P_A\cos\alpha = Q_A\sin\beta - P_A\cos\beta \tag{19}$$

As a consequence, Q_A and P_A must satisfy the relation

$$Q_A = P_A\frac{\cos\alpha-\cos\beta}{\sin\alpha-\sin\beta} \tag{20}$$

The formulas for l_{II}, $x_{D/C}$, and $y_{D/C}$ are the same as in Eqs. (16)–(18), except that α is replaced by β, and the integration limits are changed to from β to α.

We assume that the elastica is inextensible. As a consequence, we have the relation

$$l_{\mathrm{I}} + l_{\mathrm{II}} + l_{\mathrm{III}} = 1 \tag{21}$$

The relative position between Ends B and A in the y direction is fixed; therefore, we have

$$y_{B/D} + y_{D/C} + y_{C/A} = y_{B/A} = \frac{1-\cos\theta_B}{\theta_B} \tag{22}$$

By specifying P_A and θ_B, and using Eqs. (20)–(22), we can solve for the three unknowns Q_A, α, and β. The displacement δ_A of End A in the horizontal direction can then be calculated from

$$\delta_A = \frac{\sin\theta_B}{\theta_B} - (x_{B/D} + x_{D/C} + x_{C/A}) \tag{23}$$

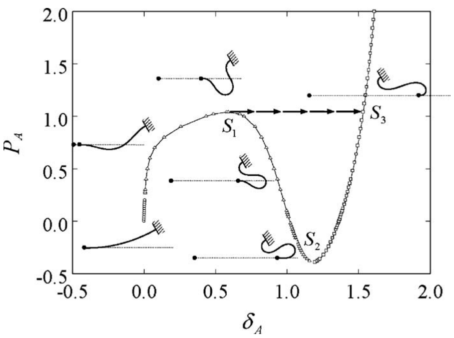

Fig. 4 Load-deflection curve for θ_B=30 deg. The symbols ○, □, and △ represent deformations without, with one, and with two inflection points, respectively.

4 Load-Deflection Curve When $\theta_B = 30$ deg

Figure 4 shows the relation between the longitudinal force P_A and end movement δ_A for the case when $\theta_B=30$ deg. This curve is also called the load-deflection curve. The symbols ○, □, and △ represent deformations without, with one, and with two inflection points, respectively. The deformed configurations of the elastica at various stages are also depicted. The two black dots on the dashed horizontal line represent the starting point and the stop point of End A. The elastica is originally in the circular arc shape when P_A is zero, which has no inflection point. The elastica deformation experiences a transition from no inflection point to two inflection points when $(P_A, \delta_A)=(0.25, 0.006)$, and experiences a transition from two inflection points to one inflection point when $(P_A, \delta_A)=(-0.39, 1.19)$. The load-deflection curve approaches a local maximum S_1 at $(P_A, \delta_A)=(1.04, 0.58)$ and hits a local minimum S_2 at $(P_A, \delta_A)=(-0.4, 1.19)$. It is noted that a negative P_A means that a pulling force is required to maintain equilibrium of the elastica. The load-deflection curve between S_1 and S_2 has negative slope.

It is noted that the above static analysis does not say anything about the stability of the equilibrium positions. Previous experience with shallow arches and shallow shells suggests that the equilibrium positions corresponding to the load-deflection curve with negative slope are unstable [9]. Therefore, the equilibrium positions corresponding to the deflection curve with negative slope cannot be realized in the laboratory. As a consequence, if we follow the load-deflection curve by increasing the external pushing force P_A to slightly beyond the local maximum S_1, the elastica will snap, as indicated by the arrows, to an equilibrium position corresponding to a Point S_3 on the load-deflection curve. This conjecture will be examined by a dynamic analysis in the next section.

5 Natural Frequencies and Stability Analysis

In this section, we study the natural frequencies and stability of the elastica when it is pushed in by a distance δ_A. We first solve for the static deformation of the elastica as described in Secs. 3 and 4, and denote the static solution as $x_e(s)$, $y_e(s)$, $\theta_e(s)$, $M_e(s)$, $F_{xe}(s)$, and $F_{ye}(s)$. We superpose the static solution with small perturbation, for instance,

$$x(s,t) = x_e(s) + x_d(s)\sin\omega t \tag{24}$$

where ω is a natural frequency. The other variables $y(s,t)$, $\theta(s,t)$, $M(s,t)$, $F_x(s,t)$, and $F_y(s,t)$ are treated in the same manner.

By substituting the above perturbed variables into Eqs. (2)–(4) and (5′)–(7′) and ignoring the higher order terms, we arrive at the following linear equations for the six unknowns $x_d(s)$, $y_d(s)$, $\theta_d(s)$, $M_d(s)$, $F_{xd}(s)$, and $F_{yd}(s)$:

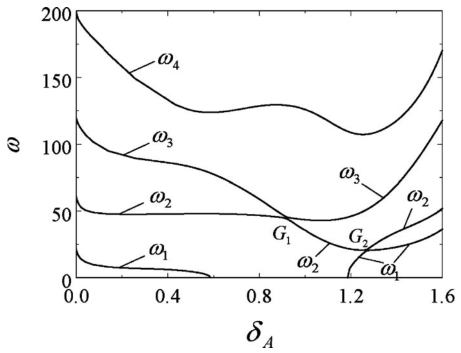

Fig. 5 The first four natural frequencies as functions of δ_A for θ_B=30 deg

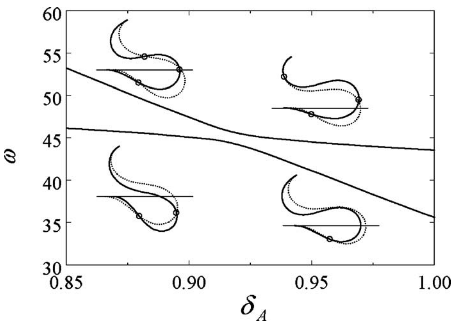

Fig. 6 Magnification of the frequency loci near location G_1 in Fig. 5. The mode shapes corresponding to the natural frequencies are also shown.

$$\frac{\partial x_d}{\partial s} = -\theta_d \sin\theta_e, \quad \frac{\partial y_d}{\partial s} = \theta_d \cos\theta_e, \quad \frac{\partial \theta_d}{\partial s} = 4\pi^2 M_d \qquad (25)$$

$$\frac{\partial M_d}{\partial s} = (F_{xe}\theta_d - F_{yd})\cos\theta_e + (F_{xd} + F_{ye}\theta_d)\sin\theta_e \qquad (26)$$

$$\frac{\partial F_{xd}}{\partial s} = -\frac{1}{4\pi^2}\omega^2 x_d, \quad \frac{\partial F_{yd}}{\partial s} = -\frac{1}{4\pi^2}\omega^2 y_d \qquad (27)$$

The boundary conditions at $s=1$ are

$$x_d(1) = y_d(1) = \theta_d(1) = 0 \qquad (28)$$

It is noted that while End A is subjected to a prescribed pushing force P_A, it is allowed to slide freely when the elastica vibrates. As a consequence, the boundary conditions at $s=0$ are

$$F_{xd}(0) = y_d(0) = \theta_d(0) = 0 \qquad (29)$$

In other words, this is a load-control procedure. It is noted that ω in linear equations (25)–(27) only appears in the form of ω^2. Therefore, if the characteristic value ω^2 is positive, it means that the corresponding mode is stable with natural frequency ω. On the other hand, if ω^2 is negative, it means that the equilibrium position is unstable. The Newton–Raphson method is used to solve for the characteristic values ω^2. The details of the numerical procedure can be found in Ref. [8].

Figure 5 shows the first four natural frequencies as functions of the end movement δ_A for the case when θ_B=30 deg. Two important features should be noted here. First of all, we notice that the lowest natural frequency ω_1 is 21 when δ_A=0. As δ_A increases to 0.58, ω_1 decreases to zero. Between δ_A=0.58 and 1.19, ω_1 is purely imaginary, and the elastica is unstable. This range of δ_A corresponds to the load-deflection curve between S_1 and S_2 in Fig. 4. This analysis validates the conjecture we made in Sec. 4 that the load-deflection curve between S_1 and S_2 in Fig. 4 represents the unstable equilibrium positions.

The second feature worthy of a closer look is that the frequency loci in Fig. 5 appear to be crossing each other at locations G_1 (δ_A=0.92) and G_2 (δ_A=1.27). However, if we magnify the frequency loci near the neighborhood of these two locations, the frequency loci are actually veering away from each other. Figure 6 shows the magnification of the frequency loci near G_1. In the same figure, we also show the mode shapes corresponding to the four natural frequencies in the neighborhood. The dotted lines represent the equilibrium shapes. The solid lines represent the mode shapes. The intersections of the dotted lines and the solid lines are the nodal points of the mode shapes, as noted by the open circles. It is noted that the two mode shapes on the top possess the three nodal points. The left mode shape on the bottom possesses two nodal points, while the one on the right possesses only one nodal point. It is interesting to note that a similar frequency loci veering phenomenon occurs in other totally different structures, such as in rotating flexible disks [10].

6 Experiments

Figure 7 shows a schematic diagram of the experimental setup we use to examine the theoretical predictions. The elastica is made of a stainless steel strip (AISI type 420) with Young's modulus 200 GPa and a mass density of 7800 kg/m^3. The length L of the strip is 60 cm and the cross section is 60×0.3 mm^2. One end of the strip is fixed in an aluminum clamp, while the other aluminum clamp on the other end is allowed to slide on a guide rail. The angle between the fixed clamp and the sliding clamp is adjustable. For the time being, we set the angle to be 30 deg. The sliding clamp is attached by a cotton string. The string passes through a pulley with a bucket attached to the other end. In the bucket, we put in small steel screws as dead load. Each small screw weighs 11.2 g. The displacement of the sliding clamp can be recorded by using a ruler. In order to measure the natural frequencies of the elastica under fixed load, we point a photonic probe (MTI 2000) normal to one point of the elastica. After hitting the elastica manually, we can obtain the natural frequencies of the system.

The cross marks (×) in Fig. 8 represent the measured load-deflection relation. For convenient reference, we present the measured results with both dimensionless parameters (left and bottom sides) and the physical ones (right and top sides). The same labeling style is adopted in Fig. 9 as well. The solid line represents the theoretical prediction, as shown in Fig. 4. We found that the measured deflections agree with the theoretical predictions reasonably well.

The natural frequencies are obtained from a power spectrum measurement by hitting the elastica at about one-third of the length from the moving end (End A) and measuring the displacement of the elastica at a location close to the fixed end (End B). Figure 9 shows the power spectrum when the elastica is free from

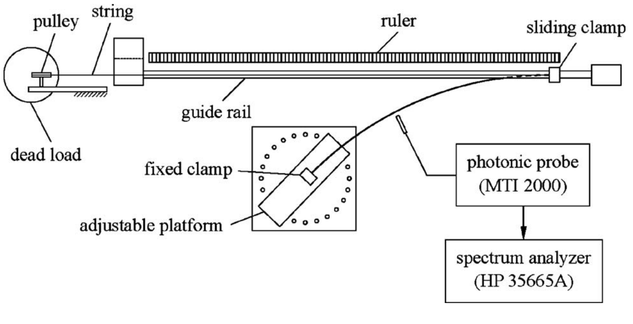

Fig. 7 Schematic diagram of the experimental setup

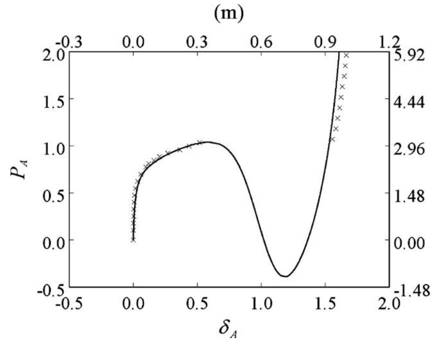

Fig. 8 Experimental measurement of load-deflection curve

external pushing force. Four natural frequencies can be observed within the range of 50 Hz. The lowest natural frequency is 3.4 Hz. As δ_A increases, this lowest natural frequency approaches zero quickly and is difficult to measure. In Fig. 10, we record the variation of these four natural frequencies with cross marks ($\times$) as δ_A changes due to the external load. To compare these measured natural frequencies with the theoretical predictions, we replot the theoretical natural frequency loci from Fig. 5 as dashed lines. It is found that the measured natural frequencies do not agree with the theoretical curves from Fig. 5 very well. To account for this discrepancy, we have to take into account the mass of the moving clamp.

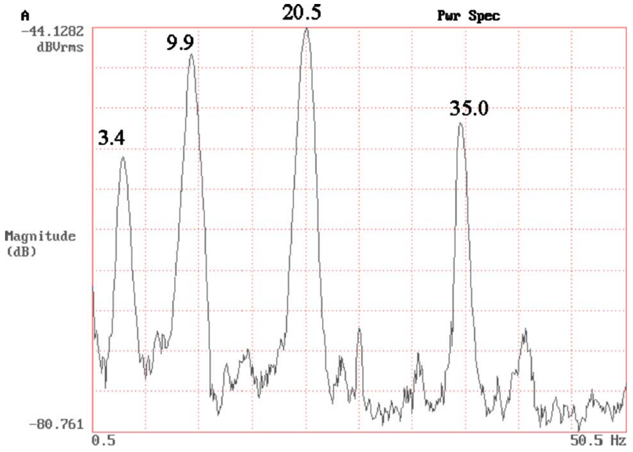

Fig. 9 Power spectrum when the elastica is free from external pushing force

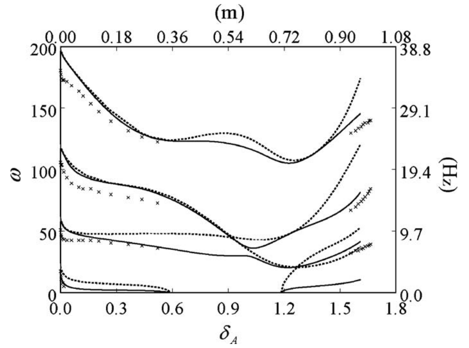

Fig. 10 The measured natural frequencies are recorded with cross marks. The dashed and solid curves are the theoretical predictions neglecting and including the clamp mass, respectively.

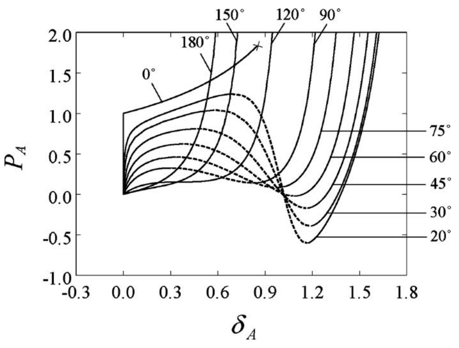

Fig. 11 Load-deflection curves for various values of θ_B

7 Effect of Clamp Mass on the Natural Frequencies

In Sec. 5, we calculate the natural frequencies of the elastica by ignoring the mass of the sliding clamp. In the experiment, the mass of the sliding clamp is 483 g. This mass is quite significant compared to the mass of the elastica, 84 g. In order to take into account the mass of the clamp, the boundary condition (with dimension) at the moving end must be modified as

$$F_x(0,t) = m_c \frac{\partial^2 x(0,t)}{\partial t^2} - P_A \tag{30}$$

where $P_A = -F_{xe}(0)$. m_c is the mass of the moving clamp. After following the same linearization procedure as in Sec. 5, the dimensionless boundary condition on $F_{xd}(0)$ in Eq. (29) can be replaced by

$$F_{xd}(0) = -\frac{1}{4\pi^2} m_c \omega^2 x_d(0) \tag{31}$$

After this modification, the predicted natural frequencies are plotted as the solid lines in Fig. 10. Generally speaking, the clamp mass lowers the natural frequencies. Besides, the clamp mass does not affect the range in which ω_1 becomes imaginary. It is observed that the agreement between the measured natural frequencies and the theoretical prediction is improved by taking into account the clamp mass. It is noted that after snapping, we are unable to measure the lowest natural frequency because the friction force is too large due to the large shear force from the clamp. This sticking phenomenon from the friction force prevents the free movement of the moving clamp, which is essential to the fundamental mode. In this paper, we do not consider friction in our formulation.

8 Effects of θ_B

Having experimentally confirmed the theoretical predictions, we are ready to investigate the effect of θ_B on the load-deflection relations. Figure 11 shows the theoretical load-deflection curves for various θ_B. In this figure, we identify the unstable equilibrium positions with dashed lines. The load-deflection curve for $\theta_B = 0$ deg is a special case and deserves more attention. For this case, End A will not move until P_A reaches the critical load $P_A = 1$, at which the natural frequency ω_1 is zero. The first four natural frequencies as functions of δ_A are shown in Fig. 12. It is noted that this elastica becomes unsable when δ_A reaches 1. It means that Ends A and B coincide. However, it is impossible to produce this equilibrium position in the laboratory without dismantling Clamp A and reversing its direction [11]. Furthermore, before δ_A reaches 1 the elastica will contact itself when $\delta_A = 0.85$. This self-contact phenomenon prevents Clamp A from moving beyond $\delta_A = 0.85$[11,12]. The deformation configurations corresponding to

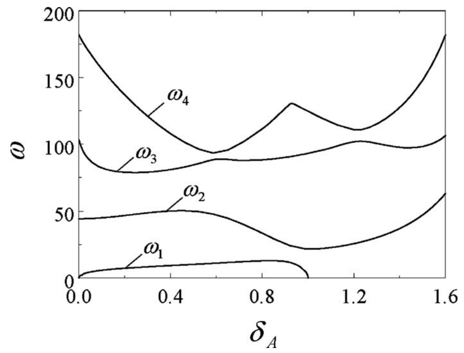

Fig. 12 The first four natural frequencies as functions of δ_A for $\theta_B=0$ deg

$\delta_A=0.85$ and 1 are depicted in Figs. 13(*a*) and 13(*b*). The load-deflection curve for $\theta_B=0$ deg in Fig. 11 is terminated with a cross mark when self-contact occurs. To avoid self-contact, θ_B must be greater than 18 deg. It is noted that for $\theta_B=120$ deg, 150 deg, and 180 deg no snapping will occur.

For the load-deflection curves in Fig. 11 with local maximum and local minimum, we denote the external force P_A corresponding to the local maximum as $P^+_{A(\mathrm{cr})}$ and the local minimum as $P^-_{A(\mathrm{cr})}$. If Clamp A is pushed in from the original position, the elastica will snap when P_A reaches $P^+_{A(\mathrm{cr})}$. On the other hand, if we trace the load-deflection curve in the opposite direction by reducing P_A, then a reverse snapping may occur when P_A reaches $P^-_{A(\mathrm{cr})}$. Figure 14 shows these two critical loads as functions of θ_B. It is noted that snapping can occur only when θ_B is in the range from 18 deg to 119 deg. The gap between $P^+_{A(\mathrm{cr})}$ and $P^-_{A(\mathrm{cr})}$ decreases as θ_B increases.

9 Conclusions

In this paper, we study, both theoretically and experimentally, the deformation and stability of a clamped-clamped planar elastica, with one clamp fixed in space and the other allowed to slide along a straight line when it is under a longitudinal pushing force. Several conclusions can be summarized as follows.

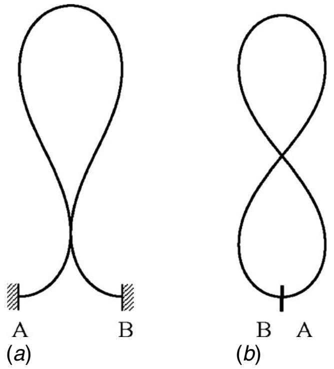

(*a*) (*b*)

Fig. 13 (*a*) Self-contact occurs when $\delta_A=0.85$. (*b*) Clamp reverse is required for this deformation configuration when $\delta_A=1$.

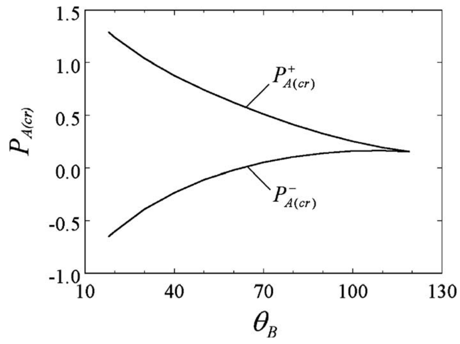

Fig. 14 Critical loads $P^+_{A(\mathrm{cr})}$ and $P^-_{A(\mathrm{cr})}$ as functions of θ_B

(1) The deformation of the elastica can have zero, one, and two inflection points, depending on the slope difference between the two ends and the magnitude of the external longitudinal force.
(2) When the pushing force reaches a critical value, snapping may occur as the elastica jumps from one configuration to another remotely away from the original one. The equilibrium configuration corresponding to a negative slope in the load-deflection curve is unstable.
(3) Natural frequency loci veering phenomena are observed when the natural frequencies of the elastica are plotted as functions of the sliding clamp movement.
(4) The measured static load-deflection relation agrees with the theoretical prediction very well. On the other hand, the measured natural frequencies do not agree very well with the theoretical prediction, unless the mass of the moving clamp is taken into account.

References

[1] Timoshenko, S. P., 1935, "Buckling of Flat Curved Bars and Slightly Curved Plates," ASME J. Appl. Mech., **2**, pp. 17–20.
[2] Hoff, N. J., and Bruce, V. G., 1954, "Dynamic Analysis of the Buckling of Laterally Loaded Flat Arches," J. Math. Phys. (Cambridge, Mass.), **32**, pp. 276–288.
[3] Budiansky, B., and Roth, R. S., 1962, "Axisymmetric Dynamic Buckling of Clamped Shallow Spherical Caps," Collected Papers on Instability of Shells Structures, NASA Paper No. TND-1510, pp. 597–606.
[4] Simitses, G. J., 1990, *Dynamic Stability of Suddenly Loaded Structures*, Springer-Verlag, New York.
[5] Kimball, C., and Tsai, L.-W., 2002, "Modeling of Flexural Beams Subjected to Arbitrary End Loads," ASME J. Mech. Des., **124**, pp. 223–235.
[6] Venanzi, S., Giesen, P., and Parenti-Castelli, V., 2005, "A Novel Technique for Position Analysis of Planar Compliant Mechanisms," Mech. Mach. Theory, **40**, pp. 1224–1239.
[7] Love, A. E., 1944, *A Treatise on the Mathematical Theory of Elasticity*, Dover, New York.
[8] Lin, Y.-Z., 2007, *Longitudinal Force Transmission and Vibration of a Planar Elastica*, Master thesis, Department of Mechanical Engineering, National Taiwan University.
[9] Simitses, G. J., 1976, *An Introduction to the Elastic Stability of Structures*, Prentice-Hall, Englewood Cliffs, NJ.
[10] Chen, J.-S., and Bogy, D. B., 1992, "Mathematical Structure of Modal Interactions in a Spinning Disk-Stationary Load System," ASME J. Appl. Mech., **59**, pp. 390–397.
[11] Van der Heijden, G. H. M., Neukirch, S., Goss, V. G. A., and Thompson, J. M. T., 2003, "Instability and Self-Contact Phenomena in the Writhing of Clamped Rods," Int. J. Mech. Sci., **45**, pp. 161–196.
[12] Plaut, R. H., Taylor, R. P., and Dillard, D. A., 2004, "Postbuckling and Vibration of a Flexible Strip Clamped at its Ends to a Hinged Substrate," Int. J. Solids Struct., **41**, pp. 859–870.

A Micromechanics Model for the Thermal Conductivity of Nanotube-Polymer Nanocomposites

Gary D. Seidel

Dimitris C. Lagoudas[1]
e-mail: lagoudas@aero.tamu.edu

Department of Aerospace Engineering,
Texas A&M University,
College Station, TX 77843-3141

A micromechanics approach for assessing the impact of an interfacial thermal resistance, also known as the Kapitza resistance, on the effective thermal conductivity of carbon nanotube-polymer nanocomposites is applied, which includes both the effects of the presence of the hollow region of the carbon nanotube (CNT) and the effects of the interactions amongst the various orientations of CNTs in a random distribution. The interfacial thermal resistance is a nanoscale effect introduced in the form of an interphase layer between the CNT and the polymer matrix in a nanoscale composite cylinder representative volume element to account for the thermal resistance in the radial direction along the length of the nanotube. The end effects of the interfacial thermal resistance are accounted for in a similar manner through the use of an interphase layer between the polymer and the CNT ends. Resulting micromechanics predictions for the effective thermal conductivity of polymer nanocomposites with randomly oriented CNTs, which incorporate input from molecular dynamics for the interfacial thermal resistance, demonstrate the importance of including the hollow region in addition to the interfacial thermal resistance, and compare well with experimental data. [DOI: 10.1115/1.2871265]

Keywords: carbon nanotube, nanocomposite, thermal conductivity, micromechanics, composite cylinders

1 Introduction

Carbon nanotubes (CNTs) have been proposed as nanoscale inclusions capable of imparting multifunctionality to composites in which they are a constituent. This is due to the reported high stiffness (~1 TPa [1]), high strength (~150 GPa [2]), as well as high thermal and electrical conductivities (~2000 W/m K [3] and 1000–200,000 S/cm [4], respectively) of CNTs. Experimental measurements of the electrical conductivity of polymers containing CNTs, or nanocomposites, have shown substantial increase (seven or more orders of magnitude) in electrical conductivity at very low volume fractions (~1 wt. %) of CNTs [5–10]. However, measurements of the impact of CNTs on the thermal conductivity of polymer nanocomposites have not found as significant of an increase in the nanocomposite conductivity, a factor of 3 or less relative to the neat polymer at 1 wt. % [11–15]. It was observed further that theoretical estimates for the nanocomposite thermal conductivity in the form of micromechanics modeling yielded predictions more than a factor of 10 larger than the measured values [16,17].

It has been proposed that despite the high thermal conductivity of nanotubes, it is a nanoscale effect at the interface between the nanotube and the polymer that governs the composite thermal conductivity [18,19] due to the presence of an interface thermal resistance often referred to as the Kapitza resistance. However, at present, it is difficult to directly measure the interfacial thermal resistance between the nanotube and the polymer. As an alternative, molecular dynamics simulations have been used to estimate the interfacial thermal resistance of CNTs embedded in a polymer [19,20]. Based on temperature decay times on the order of tens of picoseconds, such efforts have yielded estimates for the interfacial thermal resistance on the order of 10^{-8} $\mathrm{m}^2\,\mathrm{K/W}$.

Using molecular dynamics estimates of the interfacial thermal resistance as a starting point, effective medium approaches (EMAs) [21] have been used in parametric studies to theoretically assess the potential impact of the interfacial thermal resistance on the effective nanocomposite thermal conductivity [12,16,20,22–24]. These models consider the nanotubes as straight isotropic solid circular cylinders, and subsequently define a Kapitza radius based on an estimate of the Kapitza resistance, which is used to scale the conductivity of the nanotubes resulting in anisotropic effective circular solid cylinders for the micromechanics modeling. These anisotropic circular cylinders are then taken as randomly oriented and well dispersed in the matrix material. By varying the nanotube aspect ratio (L/d, where L and d are the CNT length and diameter, respectively), initial nanotube conductivity, and the Kapitza resistance values, these models can obtain good agreement with a given set of measured data. For example, using a Kapitza resistance obtained from molecular dynamics (MD) simulations [19] of 8×10^{-8} $\mathrm{m}^2\,\mathrm{K/W}$, Nan et al. [16] applied the EMA and varied the nanotube diameter for a fixed aspect ratio of 2000, obtaining good agreement with the data from Choi et al. [25] with a CNT diameter of 15 nm (and therefore length of 30 μm). In contrast, Bryning et al. [12] applied EMA and varied the Kapitza resistance, obtained good agreement with their measured data using a Kapitza resistance of 2.6×10^{-8} $\mathrm{m}^2\,\mathrm{K/W}$ and nanotube diameter and length of 1.1 nm and 167 nm, respectively, or an aspect ratio of 150.

In an alternative approach, Chen et al. [17] introduced the interfacial thermal resistance in the form of a jump factor [26] in conjunction with a Mori–Tanaka [27–29] micromechanics averaging method, which also considered the CNTs to be randomly oriented, well-dispersed isotropic solid circular cylinders. There it was observed that the interfacial thermal resistance had little impact on the effective thermal conductivity of the nanocomposite as

---

[1] Corresponding author.

Contributed by the Applied Mechanics Division of ASME for publication in the JOURNAL OF APPLIED MECHANICS. Manuscript received August 9, 2007; final manuscript received November 7, 2007; published online May 20, 2008. Review conducted by Yonggang Huang.

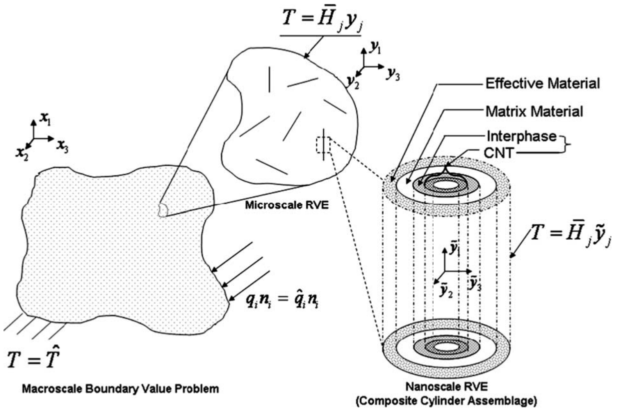

Fig. 1 Schematic representation of CNT-polymer nanocomposite consisting randomly oriented high aspect ratio composite cylinder assemblages

the jump factor only accounted for the thermal resistance along the lateral surface of the nanotubes. Instead, it was argued that the thermal transport across the tube ends played a larger role, which was demonstrated through the introduction of anisotropy in the nanotube conductivity by taking the axial conductivity of the nanotube as an average of the isotropic nanotube and matrix conductivities.

In the present work, a micromechanics approach based on the composite cylinder model [30,31] is applied as an alternate approach for assessing the impact of an interfacial thermal resistance on the effective thermal conductivity of nanocomposites. The present model considers the nanotubes as isotropic, hollow circular cylinders well dispersed in the matrix, but uses a different approach for considering the effects of random orientation. This approach applies the Mori–Tanaka method in a consistent manner, which accounts for the interactions amongst the various nanotube orientations. In addition, the generalized self-consistent composite cylinder method is used for the nanoscale representative volume element (RVE) as it allows for the introduction of interphase layers in a manner which enforces concentric heat flux through each layer, and accounts for the hollow interior of the nanotube. As such, the effects of the interfacial thermal resistance are accounted for through the incorporation of an interphase layer in the composite cylinder assemblage, which is of sufficiently small, but finite thickness, and which has a thermal conductivity determined based on the Kapitza resistance value in accordance with MD simulations [19,20]. The end effects of the Kapitza resistance are accounted for in a similar manner through the use of an interphase layer between the polymer and the CNT ends using a simple series model, the effective conductivity of which is used to introduce anisotropy into the CNTs by altering the axial conductivity of the CNT annulus.

The micromechanics model is described in detail in the subsequent section, where in addition the influence of the hollow region of the CNT and interactions between CNTs is discussed, and results for effective thermal conductivity in the absence of the Kapitza resistance are put into context with current experimental data in the literature. In Sec. 3, the details of including both the lateral and end effects of the Kapitza resistance are provided, with results for the effective thermal conductivity of polymer nanocomposites provided in Sec. 4 where they are discussed in comparison to other micromechanics models for polymer nanocomposites in the literature as well as in comparison with measured data also available in the literature.

2 Micromechanics Model

For modeling purposes, the CNT-polymer nanocomposite is idealized, as shown in Fig. 1. The macroscale boundary value problem of engineering interest is shown there to depend on microstructure consisting of randomly oriented, straight, high aspect ratio, interphase coated CNTs. For a given set of boundary conditions at the macroscale, the temperature T, for example, can be determined for the steady-state heat conduction case from the following equation:

$$\nabla \cdot \mathbf{q} = 0 \tag{1}$$

where the heat flux $\mathbf{q}$ is assumed to obey Fourier's law of heat conduction given by

$$\mathbf{q} = -\mathbf{k}^{\text{eff}} \nabla T \tag{2}$$

In Eq. (2) above, $\mathbf{k}^{\text{eff}}$ is the effective thermal conductivity for the nanocomposite determined from the microscale RVE, with input from the nanoscale RVE. As such, the boundary conditions on the microscale RVE are homogeneous, and correspond to the average thermal gradient in the macroscale boundary value problem.

2.1 Microscale RVE.

The key assumption for the microscale RVE is that the CNTs are well dispersed and randomly oriented in a matrix material. The effective thermal conductivity for the microscale RVE is determined by treating each orientation of a given CNT as a separate material phase, and consistently averaging over all possible orientations (see, for example, Refs. [32–34]). As such, the nanocomposite effective thermal conductivity can be expressed as

$$\mathbf{k}^{(\text{eff})} = \mathbf{k}^{(M)} + \frac{1}{4\pi}\int_0^{2\pi}\int_0^{\pi}\{c_f(\mathbf{k}^{(f)} - \mathbf{k}^{(M)})\mathbf{A}^{(f)}\}\sin(\varphi)d\varphi d\psi \tag{3}$$

where c_f is the total volume fraction of CNTs, including all interphase layers; φ and ψ are angles identifying a given CNT orientation; $\mathbf{k}^{(M)}$ is the matrix conductivity tensor; $\mathbf{k}^{(f)}$ is the CNT conductivity tensor, including all interphase layers; and $\mathbf{A}^{(f)}$ is the thermal gradient concentration tensor, which accounts for interactions among the various orientations of CNTs.

In order to account for the hollow nature of the CNTs and for the presence of interphase regions, the thermal conductivity is determined from the nanoscale RVE consisting of a composite cylinder assemblage, as depicted in Fig. 1. As such, the CNT conductivity ($\mathbf{k}^{(f)}$) in Eq. (3) is obtained using the generalized self-consistent composite cylinder method [31]. As all of the CNTs are assumed to be identical, the generalized self-consistent composite cylinder method need only be applied to a single composite cylinder assemblage at an arbitrary orientation (with local coordinate system $\tilde{y}_i$), and then expressed in the global microscale RVE coordinate system (y_i) by a change of basis, i.e.,

$$k_{ij}^{(\text{CCA})} = Q_{im}\tilde{k}_{mn}^{(\text{CCA})}Q_{jn} \tag{4}$$

where the tilde denotes quantities in the local composite cylinder assemblage coordinate system and the components of the rotation matrix $[\mathbf{Q}]$ are given in terms of the direction cosines for the 2-1-3 Euler angles (with the angle for the 1-rotation specified to be zero)[2] by

$$[\mathbf{Q}] = \begin{bmatrix} \cos(\psi)\sin(\varphi) & \sin(\psi)\sin(\varphi) & \cos(\varphi) \\ -\sin(\psi) & \cos(\psi) & 0 \\ -\cos(\psi)\cos(\varphi) & -\sin(\psi)\cos(\varphi) & \sin(\varphi) \end{bmatrix} \tag{5}$$

While Eq. (3) is valid for a variety of micromechanics approximations (e.g., the Mori–Tanaka, self-consistent, and generalized self-consistent methods), for the Mori–Tanaka method [27–29], the specific form of the thermal gradient concentration tensor is given by

---

[2] In Ref. [33], the rotation matrix corresponds to a 3-1-3 set of Euler angles with the 1-rotation specified to be $\pi/2$, and is an equivalent change of basis, but different parametrization.

$$A_{ij}^{(f)} = Q_{im}\widetilde{T}_{mn}^{(\mathrm{MT})}Q_{\ln}\left\{(1-c_f)I_{jl} + \frac{c_f}{4\pi}\right.$$

$$\left.\times \int_0^{2\pi}\int_0^{\pi}\{Q_{lr}\widetilde{T}_{rs}^{(\mathrm{MT})}Q_{js}\}\sin(\varphi)d\varphi d\psi\right\}^{-1} \qquad (6)$$

where $\widetilde{T}_{ij}^{(\mathrm{MT})}$ is given by

$$\widetilde{T}_{ij}^{(\mathrm{MT})} = \{\delta_{ji} + S_{jm}(k_{nm}^{(M)})^{-1}(\widetilde{k}_{ni}^{(\mathrm{CCA})} - k_{ni}^{(M)})\}^{-1} \qquad (7)$$

In Eq. (7) above, δ_{ij} is the Kronecker delta and S_{ij} is the thermal equivalent of the Eshelby tensor. The details of the generalized self-consistent composite cylinder method for determining $\widetilde{k}_{ij}^{(\mathrm{CCA})}$ are discussed in the subsequent section. The use of Eq. (6) with the composite cylinder method for the nanoscale RVE results in a what is termed a two-step process. However, it is noted that, through the use of the composite cylinder method, one can define concentration tensors for each layer in accordance with the generalized self-consistent, the self-consistent, or even the Mori–Tanaka method. Such an approach was not employed here in order to isolate the effects of interactions amongst the various orientations of CNTs from the effects of the hollow region, as will be discussed in Sec. 2.3.

2.2 Nanoscale RVE. The generalized self-consistent composite cylinder method consists of the application of a set of homogeneous boundary conditions relating the nanoscale RVE to the microscale RVE. An energy equivalency is established between the generalized self-consistent composite cylinder assemblage shown in Fig. 1 and a homogeneous effective medium [31]. In accordance with a given homogeneous boundary condition, an admissible temperature field is assumed for each layer of the generalized self-consistent composite cylinder assemblage. The admissible temperature fields satisfy both the boundary conditions and the steady-state thermal energy equation expressed in the local assemblage coordinate system ($\widetilde{y}_i$) by

$$\nabla \cdot \widetilde{\mathbf{q}} = 0 \qquad (8)$$

Defining the intensity in terms of the temperature $\widetilde{T}$ as

$$\widetilde{\mathbf{H}} = -\nabla\widetilde{T} \qquad (9)$$

and applying Fourier's law

$$\widetilde{\mathbf{q}} = \widetilde{\mathbf{k}}\widetilde{\mathbf{H}} \qquad (10)$$

Eq. (8) can be expressed in cylindrical coordinates for spatially homogeneous, transversely isotropic materials as

$$\widetilde{k}_{22}\frac{\partial^2\widetilde{T}}{\partial r^2} + \widetilde{k}_{22}\left(\frac{1}{r^2}\frac{\partial^2\widetilde{T}}{\partial\theta^2} + \frac{1}{r}\frac{\partial\widetilde{T}}{\partial r}\right) + \widetilde{k}_{11}\frac{\partial^2\widetilde{T}}{\partial z^2} = 0 \qquad (11)$$

which has admissible solutions

$$\widetilde{T} = D_1 z + D_2 \qquad (12a)$$

$$\widetilde{T} = \left(D_1 r + \frac{1}{r}D_2\right)\cos(\theta) \qquad (12b)$$

where D_1 and D_2 are constants. The two admissible solutions correspond to uniform heat flow in the axial and transverse directions, respectively, and are applied in all layers of the generalized self-consistent composite cylinder assemblage. For example, if the innermost layer (the CNT) is identified as layer one, and the matrix layer identified as layer N, then the temperature fields in each layer can be expressed as

$$\widetilde{T}^{(i)} = D_1^{(i)}z + D_2^{(i)} \quad \text{for } r_{i-1} \leqslant r \leqslant r_i \qquad (13a)$$

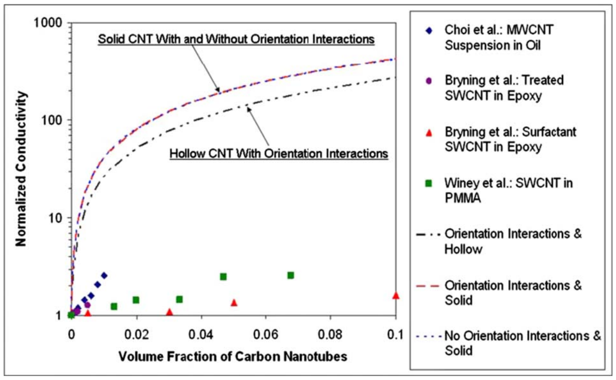

Fig. 2 Initial comparison of micromechanics modeling approaches with the measured data from Choi et al. [25], Bryning et al. [12], and Guthy et al. [13]

$$\widetilde{T}^{(i)} = \left(D_1^{(i)}r + D_2^{(i)}\frac{1}{r}\right)\cos(\theta) \quad \text{for } r_{i-1} \leqslant r \leqslant r_i \qquad (13b)$$

where i ranges from 1 to $N+1$, the effective material layer. The constants in Eq. (13a) are determined from the application of the homogeneous boundary conditions corresponding to axial heat flow given by

$$\widetilde{T}^{(i)}\left(z = -\frac{L}{2}\right) = \widetilde{T}_0 \qquad (14a)$$

$$\widetilde{T}^{(i)}\left(z = \frac{L}{2}\right) = \widetilde{T}_0 + \Delta\widetilde{T} \qquad (14b)$$

while the constants in Eq. (13b) are determined from the homogeneous boundary conditions corresponding to transverse heat flow and insulated internal surface given by

$$\widetilde{T}^{(N)}(r = r_N, \theta) = \widetilde{H}_0 r_N \cos(\theta) \qquad (15a)$$

$$\widetilde{q}_r^{(1)}(r = r_0, \theta) = 0 \qquad (15b)$$

and the continuity of temperature and heat flux conditions across an ideal interface given by

$$\widetilde{T}^{(j)}(r = r_j, \theta) = \widetilde{T}^{(j+1)}(r = r_j, \theta) \qquad (16a)$$

$$\widetilde{q}_r^{(j)}(r = r_j, \theta) = \widetilde{q}_r^{(j+1)}(r = r_j, \theta) \qquad (16b)$$

where j ranges from 1 to N.

Following the approach of Hashin [30], we define "energy" integrals over the total volume of the assemblage, which require the same energy transfer by the same thermal gradient as

$$W = \frac{1}{V}\int_V \frac{1}{2}(\widetilde{\mathbf{q}} \cdot \widetilde{\mathbf{H}})dV \qquad (17)$$

and equating the energy integral for the total composite cylinder assemblage to that of an effective homogeneous material, expressions for the effective axial and transverse conductivities for the total composite cylinder assemblage are obtained as

$$\widetilde{k}_{11}^{(\mathrm{total})} = \sum_{i=1}^{N}\widetilde{k}_{11}^{(i)}\frac{(r_i^2 - r_{i-1}^2)}{r_N^2} \qquad (18a)$$

Table 1 Input data for the three micromechanics models for randomly oriented CNTs in an epoxy matrix, the resulting effective conductivities of which are provided in Fig. 2. All conductivities are in W/m K, and all dimensions are in nanometers. Values for the CNT conductivity are taken from Ref. [3] and are within the range of values reported in Ref. [12]. Epoxy matrix conductivity is reflective of the value from Ref. [13]. The thickness of 0.34 nm for the hollow case is a commonly accepted value [38–41] consistent with the interlayer spacing of graphite.

	$\tilde{k}^{(\mathrm{CNT})}$	r_{CNT}	t_{CNT}	$\tilde{k}_{11}^{(f)}$	$\tilde{k}_{22}^{(f)}$	$\tilde{k}^{(M)}$
No interactions, solid	2000	0.85	N/A	2000	2000	0.16725
With interactions, solid	2000	0.85	N/A	2000	2000	0.16725
With interactions, hollow	2000	0.85	0.51	1267	32	0.16725

$$\tilde{k}_{22}^{(\mathrm{total})} = \frac{1}{r_N^2 H_0^2}\sum_{i=1}^{N} k_{22}^{(i)}\left[(D_1^{(i)})^2(r_i^2 - r_{i-1}^2) - (D_2^{(i)})^2\left(\frac{1}{r_i^2} - \frac{1}{r_{i-1}^2}\right)\right] \tag{18b}$$

where it is noted that the radius of the Nth layer is given in terms of the volume fraction of the innermost layer in the assemblage as $r_N = r_1/\sqrt{v_f}$. The conductivities obtained from Eqs. (18*a*) and (18*b*) correspond to the effective properties for aligned CNTs of a single type at a given volume fraction. However, as we are interested in randomly oriented CNTs, we identify the critical volume fraction as $\hat{v}_f = r_1^2/r_{N-1}^2$, which corresponds to the volume fraction at which there is not longer a matrix phase enveloping the composite cylinder assemblage so that the effective properties obtained are for the CNT plus the interphase region(s). As such, the axial component for the conductivity of the composite cylinder assemblage in Eqs. (3) and (6) is obtained as

$$\tilde{k}_{11}^{(\mathrm{CCA})} = \tilde{k}_{11}^{(\mathrm{total})}\big|_{v_f = \hat{v}_f} \tag{19}$$

and the transverse components from

$$\tilde{k}_{22}^{(\mathrm{CCA})} = \tilde{k}_{22}^{(\mathrm{total})}\big|_{v_f = \hat{v}_f} \tag{20}$$

If there are no interphase regions, the values obtained correspond to the effective properties of the CNT, having accounted for its hollow nature.

It is noted that, in order to be consistent with the average fields at the microscale RVE, the boundary conditions on the nanoscale RVE should account for the interactions amongst the various orientations. However, in considering linear materials, it is observed that the effective properties obtained from the generalized self-consistent composite cylinder are independent of the boundary conditions applied. This means that the generalized self-consistent composite cylinder method, in which the effective material layer of the composite cylinder assemblage is taken to extend to infinity and to account for interactions amongst the various CNTs, is equivalent to the composite cylinder method in which the boundary conditions are applied directly to the Nth layer of the composite cylinder assemblage, as the bounds for both methods are equal and coincident.

2.3 Micromechanics Modeling Results. Initial micromechanics predictions for the effective thermal conductivity of CNT-polymer nanocomposites, which do not include the effects of the Kapitza resistance, are provided in Fig. 2. Three micromechanics models are presented, all of which make use the Mori–Tanaka method [27–29] in considering random orientation, i.e., all methods make use of the Eshelby solution [35] for an ellipsoid in an infinite matrix subject to a homogeneous displacement, which is dependent on the average macroscale thermal gradient and a perturbation thermal gradient in approximating the thermal gradient concentration tensor in Eq. (3). The differences lie first in how interactions are accounted for, which is dependent on the definitions of the average and perturbation thermal gradients applied in the Eshelby solution, and second on the inhomogeneity considered in the Eshelby solution.

The first model considers the CNTs to be randomly oriented, solid, isotropic cylinders and does not consider the interactions amongst the various orientations of CNTs in applying the Mori–Tanaka consistency condition, i.e., in solving for the perturbation thermal gradient. Instead, the effective properties for an aligned CNT are averaged over all orientations as described for effective elastic properties in Ref. [36]. As such, the Mori–Tanaka consistency condition is applied for the aligned case, so that Eq. (6) is instead expressed as

$$\tilde{A}_{ij}^{(f)} = \tilde{T}_{ik}^{(\mathrm{MT})}\{(1-c_f)I_{jk} + c_f\tilde{T}_{jk}^{(\mathrm{MT})}\}^{-1} \tag{21}$$

and the effective nanocomposite properties obtained as

$$\mathbf{k}^{(\mathrm{eff})} = \frac{1}{4\pi}\int_0^{2\pi}\int_0^{\pi}\{\mathbf{Q}\tilde{\mathbf{k}}^{\mathrm{aligned}}\mathbf{Q}^T\}\sin(\varphi)\,d\varphi\,d\psi \tag{22}$$

where

$$\tilde{\mathbf{k}}^{\mathrm{aligned}} = \tilde{\mathbf{k}}^{(M)} + c_f(\tilde{\mathbf{k}}^{(f)} - \tilde{\mathbf{k}}^{(M)})\tilde{\mathbf{A}}^{(f)} \tag{23}$$

This model is equivalent to the Maxwell–Garnett EMA (MG-EMA) used by Nan et al. [16] and to the Mori–Tanaka method used by Chen et al. [17] in the absence of the Kapitza resistance.[3]

The second model also considers the CNTs to be randomly oriented, solid, isotropic cylinders, but *does* consider the interactions amongst the various orientations in applying the Mori–Tanaka consistency condition, as described for effective elastic properties in Refs. [32–34], resulting in the additional integration over all orientations contained in the global concentration tensor of Eq. (6). From Fig. 2, it is observed that whether or not the interactions between the various orientations are considered in a consistent manner or not has little impact on the effective properties predicted. This is consistent with what has similarly been noted for the effective elastic properties or randomly oriented fibers using both methods, and is likely to be the case for all composites containing only linear materials.

The third micromechanics model provided in Fig. 2 considers the CNTs to be randomly oriented, hollow cylinders, with the annulus of material having the same isotropic properties as in the previous two models (see Table 1). The model proceeds in a two-step approach using the generalized self-consistent composite cylinder method to account for the hollow region of the CNT before using the Mori–Tanaka method (with consistent orientation interactions) to account for random orientation distribution as described above (with $N=2$). In contrast to the previous two models, the effective CNT used in the Mori–Tanaka method is therefore

---

[3] Upon closer inspection of the theory behind the MG-EMA (see, for example, Ref. [37]), it is found that the MG-EMA and Mori–Tanaka methods are rooted in the same philosophy of using single inclusions embedded in an infinite matrix material subject to a perturbation in the thermal gradient to obtain effective thermal conductivities and that both methods account for random orientations of inclusions in exactly the same manner. For aspect ratios of 200 or greater, it can be shown that the geometrical factors in Ref. [37] are equal to the Eshelby tensor components of the Mori–Tanaka method for circular cylinders.

transversely isotropic due to the influence of the hollow region. From Fig. 2, it is observed that even for CNTs with a small radius (the value here corresponds to a (10,10) CNT), the effect of the hollow region on the effective thermal conductivity of the nanocomposite is significant, resulting in decreases in conductivities of 14%, 37%, and 45% at volume fractions of 0.0001, 0.001, and 0.1 CNTs, respectively.

It is noted that, while the Mori–Tanaka method has been used here to account for the random orientation distribution, similar approaches can be taken to consistently apply the self-consistent [42] and generalized self-consistent micromechanics methods. However, in these methods, the consistency comes from the application of homogeneous boundary conditions reflective of the average thermal gradient in the macroscale RVE as applied to the effective material, which envelopes the inhomogeneity, and as such, result in a nonlinear set of equations. However, as the bounds are coincident for linear materials, this extra complexity is not expected to be largely different from the thermal conductivities obtained from the Mori–Tanaka method, particularly for the generalized self-consistent case. As such, the Mori–Tanaka method is considered sufficiently accurate and is for its ease of implementation.

It is also of interest to note that included in Fig. 2 is a collection of measured data from the literature for CNTs dispersed in different matrix materials, including polymethylmethacrylate (PMMA) and epoxy, i.e., non-cross-linked and cross-linked polymers [12,13,25]. Of particular note is the measured data for the thermal conductivity of a suspension of CNTs in a synthetic poly(α-olefin) oil obtained by Choi et al. [25]. These data have been used by both Nan et al. [16] and Chen et al. [17] to demonstrate that micromechanics methods overpredict experimental measurements, which continues to be the case even with accounting for the hollow region as in the present model. Nan et al. [18,16] and others have attributed the difference between measured values and the predicted values of micromechanics models as the result of an interface thermal resistance layer known as the Kapitza resistance. In order to include the Kapitza resistance in the MG-EMA, Nan et al. [16] used the rule of mixtures to first define an effective CNT with transversely isotropic properties due to the Kapitza resistance, and then used the MG-EMA to determine the effective properties of the nanocomposite. The transversely isotropic properties of the effective CNT are obtained by using the Kapitza resistance R_K to define a Kapitza radius a_k, which is then used with the CNT length and diameter to scale the CNT conductivity in defining effective axial ($\tilde{k}_{11}^{(f)}=\tilde{k}_{11}^{(\mathrm{RoM})}$) and transverse ($\tilde{k}_{22}^{(f)}=\tilde{k}_{22}^{(\mathrm{RoM})}$) conductivities, respectively. In contrast, Chen et al. [17] retained the solid, isotropic CNT and introduced the Kapitza resistance in the form of a jump factor [26] using a flux condition based on the Kapitza conductivity ($\beta=1/R_K$) (see Eq. (1) of Ref. [17]). In the present work, the Kapitza conductivity is used with a total heat flow condition to define the conductivity of a thin interphase layer in the construction of an $N=3$ total composite cylinder assemblage consisting of the hollow CNT, the Kapitza interphase layer, and the matrix. The details of how the conductivity of the Kapitza interphase layer are determined are provided in the subsequent section.

3 Accounting for Interface Thermal Resistance

In accounting for the interface thermal resistance using the composite cylinder model, the effects of the resistance layer (Kapitza resistance) on radial heat flow are accounted for separately from the end effects of the thermal resistance.

3.1 Accounting for Interface Thermal Resistance: Radial Effects. An $N=3$ total composite cylinder assemblage consisting of the CNT ($r_1=r_{\mathrm{CNT}}$, $\tilde{k}^{(1)}=\tilde{k}^{(\mathrm{CNT})}$, t_{CNT}), the Kapitza interphase layer ($r_2=r_{\mathrm{CNT}}+t_{\mathrm{Kap}}$, $\tilde{k}^{(2)}=\tilde{k}^{(\mathrm{Kap})}$), and the matrix ($\tilde{k}^{(3)}=\tilde{k}^{(M)}$) is used to introduce the Kapitza resistance into the micromechanics model as a thin interphase region enveloping the nanotube. The conductivity of the interphase region is taken to be isotropic with the value of the conductivity determined from the energy balance condition that

$$\begin{aligned}\tilde{Q}^{(\mathrm{CNT})}\big|_{r=r_{\mathrm{CNT}}} &= \int\int \beta\left(\tilde{T}^{(\mathrm{CNT})}\big|_{r=r_{\mathrm{CNT}}} - \tilde{T}^{(M)}\big|_{r=r_{\mathrm{Kap}}}\right) r_{\mathrm{CNT}}\, d\theta dz \\ &= \tilde{Q}^{(M)}\big|_{r=r_{\mathrm{Kap}}}\end{aligned} \tag{24}$$

where the $\tilde{T}^{(i)}$ are from Eq. (13*b*) and where the total heat fluxes $\tilde{Q}^{(i)}$ are given by

$$\tilde{Q}^{(i)}\big|_{r=r_i} = \int\int \tilde{q}_r^{(i)}\big|_{r=r_i} r_i\, d\theta dz \tag{25}$$

The parameter β is the inverse of the Kapitza resistance (i.e., the Kapitza conductivity) and is analogous to a convection constant. It is used to determine the conductivity of the thin interphase layer representing the Kapitza resistance. From the continuity conditions in Eqs. (16*a*) and (16*b*) applied at r_{CNT} and r_{Kap}, Eq. (24) can be written as

$$\begin{aligned}\tilde{Q}^{(\mathrm{Kap})}\big|_{r=r_{\mathrm{CNT}}} &= \tilde{Q}^{(\mathrm{Kap})}\big|_{r=r_{\mathrm{Kap}}} \\ &= \int\int \beta\left(\tilde{T}^{(\mathrm{Kap})}\big|_{r=r_{\mathrm{CNT}}} - \tilde{T}^{(\mathrm{Kap})}\big|_{r=r_{\mathrm{Kap}}}\right) r_{\mathrm{CNT}}\, d\theta dz\end{aligned} \tag{26}$$

allowing the conductivity of the interphase layer representing the Kapitza resistance to be given by

$$\tilde{k}^{(\mathrm{Kap})} = \frac{\beta\left[D_1^{(\mathrm{Kap})}(r_{\mathrm{CNT}} - r_{\mathrm{Kap}}) + D_2^{(\mathrm{Kap})}\left(\frac{1}{r_{\mathrm{CNT}}} - \frac{1}{r_{\mathrm{Kap}}}\right)\right]}{\left(D_1^{(\mathrm{Kap})} - \frac{1}{r_{\mathrm{CNT}}^2} D_2^{(\mathrm{Kap})}\right)} \tag{27}$$

where the constants $D_1^{(\mathrm{Kap})}$ and $D_2^{(\mathrm{Kap})}$ are determined from the application of the boundary and continuity conditions in Eqs. (15*a*), (15*b*), (16*a*), and (16*b*) to the composite cylinder assemblage. The resulting simplified expression for the Kapitza layer conductivity is then given as

$$\tilde{k}^{(\mathrm{Kap})} = \frac{\beta \tilde{k}^{(\mathrm{CNT})} t_{\mathrm{CNT}} t_{\mathrm{Kap}} \gamma_1}{\gamma_2 t_{\mathrm{Kap}}^2 \beta + \gamma_3 t_{\mathrm{CNT}} \tilde{k}^{(\mathrm{CNT})}} \tag{28}$$

where

$$\begin{aligned}\gamma_1 &= (t_{\mathrm{CNT}} - 2r_{\mathrm{CNT}})(2r_{\mathrm{CNT}} + t_{\mathrm{Kap}}) \\ \gamma_2 &= 2r_{\mathrm{CNT}}^2 - 2r_{\mathrm{CNT}} t_{\mathrm{CNT}} + t_{\mathrm{CNT}}^2 \\ \gamma_3 &= (2t_{\mathrm{CNT}} - 4r_{\mathrm{CNT}})(t_{\mathrm{Kap}} + r_{\mathrm{CNT}})\end{aligned} \tag{29}$$

As only of the $\tilde{Q}^{(i)}$ conditions in Eq. (26) is needed to determine the conductivity of the Kapitza layer, the other is used to evaluate the error associated with a chosen thickness of the Kapitza layer. In the results that follow, the thickness of the interphase region is set to a value less than 1% the radius of the nanotube, e.g., $t_{\mathrm{Kap}}=0.005r_{\mathrm{CNT}}$, which results in an evaluated error of one one-thousandth of a percent.

However, it is noted that accounting for the Kapitza resistance in this way will only introduce the effects of the Kapitza resistance on the effective transverse conductivity of the CNT. In the approach employed by Chen et al. [17], they observed that the method they used to account for the thermal resistance effect did not have a significant impact on the predicted effective thermal conductivities. Instead, using different mean values of the nanotube and matrix conductivities to replace the axial conductivity of

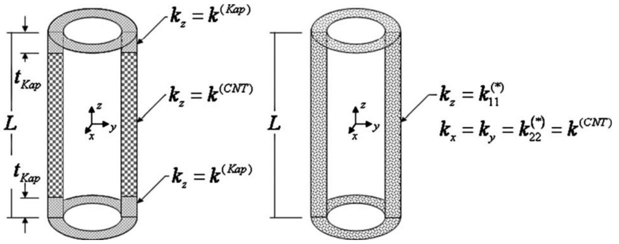

Fig. 3 Schematic representation of how the Kapitza layer conductivity is used to introduce anisotropy into the nanotube conductivity

the nanotube, they have argued that the tube end transport plays a larger role. As such, a simple model is used to effectively account for the interface thermal resistance end effects.

3.2 Accounting for Interface Thermal Resistance: End Effects. As a result of modeling the CNTs with high aspect ratio composite cylinder assemblages, the transfer of heat from the ends of the nanotube to the polymer matrix is ignored. As such, incorporating the lateral interface thermal resistance as a thin interphase region does not reflect the inclusion of the interface thermal resistance at the nanotube ends. A simple model for including such effects is instead applied in which the nanotube axial conductivity, $k_{11}^{(1)}=k_{11}^{(\mathrm{CCA})}=k^{(\mathrm{CNT})}$, is replaced by an effective value, $k_{11}^{(1)}=k_{11}^{(*)}$, determined from a simple series model shown in Fig. 3. Looking at a θ cross section of the nanotube (see Fig. 3), the lengthwise ends of the nanotube are replaced by regions with conductivity equal to that determined for the Kapitza layer interphase and with the same thickness as the Kapitza layer. Applying the general solution for the axial heat flow potential (Eq. (12*a*)) for each phase in this column, we obtain

$$\tilde{T}^{(2a)} = D_1^{(2a)} z + D_2^{(2a)} \quad \text{for } -\frac{L}{2} \leq z \leq -\frac{L}{2} + t_{\mathrm{Kap}} \tag{30a}$$

$$\tilde{T}^{(1)} = D_1^{(1)} z + D_2^{(1)} \quad \text{for } -\frac{L}{2} + t_{\mathrm{Kap}} \leq z \leq \frac{L}{2} - t_{\mathrm{Kap}} \tag{30b}$$

$$\tilde{T}^{(2b)} = D_1^{(2b)} z + D_2^{(2b)} \quad \text{for } \frac{L}{2} - t_{\mathrm{Kap}} \leq z \leq \frac{L}{2} \tag{30c}$$

where t_{Kap} is the thickness of the Kapitza interphase layer and L is the length of the nanotube. The constants $D_1^{(i)}$ and $D_2^{(i)}$ are determined from the boundary and matching conditions given by

$$\tilde{T}^{(2a)}|_{z=-L/2} = \hat{T}_1 \tag{31a}$$

$$\tilde{T}^{(2b)}|_{z=(L/2)} = \hat{T}_2 \tag{31b}$$

$$\tilde{T}^{(2a)}|_{z=-(L/2)+t_{\mathrm{Kap}}} = \tilde{T}^{(1)}|_{z=-(L/2)+t_{\mathrm{Kap}}} \tag{31c}$$

$$\tilde{q}_z^{(2a)}|_{z=-(L/2)+t_{\mathrm{Kap}}} = \tilde{q}_z^{(1)}|_{z=-(L/2)+t_{\mathrm{Kap}}} \tag{31d}$$

$$\tilde{T}^{(2b)}|_{z=(L/2)-t_{\mathrm{Kap}}} = \tilde{T}^{(1)}|_{z=(L/2)-t_{\mathrm{Kap}}} \tag{31e}$$

$$\tilde{q}_z^{(2b)}|_{z=(L/2)-t_{\mathrm{Kap}}} = \tilde{q}_z^{(1)}|_{z=(L/2)-t_{\mathrm{Kap}}} \tag{31f}$$

The cross section is then taken as equivalent to a homogeneous cross section with axial conductivity k_{11}^{*} and with axial heat flow potential given by

$$\tilde{T}^{(*)} = D_1^{(*)} z + D_2^{(*)} \quad \text{for } -\frac{L}{2} \leq z \leq \frac{L}{2} \tag{32}$$

where the constants $D_1^{(*)}$ and $D_2^{(*)}$ are determined through application of the boundary conditions identical to those applied in Eqs. (31*a*) and (31*b*). Equating the thermal energies, an expression for the effective axial conductivity of the nanotube is obtained as

$$k_{11}^{(*)} = \frac{2k^{(\mathrm{Kap})}(D_1^{(2a)})^2 t_{\mathrm{Kap}} + k^{(\mathrm{CNT})}(D_1^{(1)})^2 (L - 2t_{\mathrm{Kap}})}{(D_1^{(*)})^2 L} \tag{33}$$

where $k^{(\mathrm{Kap})}$ is the conductivity of the interface thermal resistance interphase layer determined from Eq. (27) and $k^{(\mathrm{CNT})}$ is the original isotropic nanotube conductivity in which the nanotube retains in the transverse direction, i.e., $k_{22}^{(1)}=k^{(\mathrm{CNT})}$. Substituting the values for the constants into Eq. (33), the expression for the effective axial conductivity of the nanotube can be expressed as

$$k_{11}^{(*)} = \frac{k^{(\mathrm{CNT})} k^{(\mathrm{Kap})} L}{k^{(\mathrm{CNT})} 2t_{\mathrm{Kap}} + k^{(\mathrm{Kap})}(L - 2t_{\mathrm{Kap}})} \tag{34}$$

It is of interest to note from Eq. (34) that as $k^{(\mathrm{Kap})}$ goes to zero, $k_{11}^{(*)}$ goes to zero indicative of the Kapitza layer being a perfect insulator. If $k^{(\mathrm{Kap})}$ goes to infinity, then $k_{11}^{(*)}=k^{(\mathrm{CNT})}L/(L-2t_{\mathrm{Kap}})$, which means that for small thicknesses, $k_{11}^{(*)}$ approaches $k^{(\mathrm{CNT})}$ returning the perfect interface assumption.

4 Results and Discussion

MD simulations have been used by many to quantify Kapitza resistance/conductance values for CNTs in a variety of matrix materials using transient heat flow analysis. Huxtable et al. [19] obtained a value of 12.5 $\mathrm{MW/m^2\,K}$ for the Kapitza conductance of a (5,5) single walled CNT (SWCNT) in an octane liquid. This value has been used by Nan et al. [16] and others in EMA micromechanics models, which include thermal resistance effects in predicting effective thermal conductivities. Focusing on functionalized CNTs in poly(ethylene vinyl acetate), Clancy and Gates [20] also used MD simulations to study the effects grafting density of functional groups on the Kapitza resistance. There it was noted that functionalization could reduce the Kapitza resistance from the pristine value of $\sim 9.5 \times 10^{-8}\ \mathrm{m^2\,K/W}$ (i.e., a conductance comparable to the value in Ref. [19]) to a value of $\sim 2 \times 10^{-8}\ \mathrm{m^2\,K/W}$ for a (6,6) SWCNT.

Micromechanics estimates for the effective thermal conductivity of CNT-polymer nanocomposites using values for the Kapitza resistance obtained by MD simulations [19] for both the EMA model and the two-step composite cylinders/Mori–Tanaka model described herein are provided in Fig. 4. Micromechanics predictions using the Kapitza conductance jump factor were noted by Chen et al. [17] to demonstrate negligible difference relative to initial micromechanics estimates (i.e., no Kapitza resistance), and are in effect represented by the no Kapitza EMA results also included in the figure. However, for the two-step CCM/MT and EMA models, the effects of including the Kapitza resistance are observed to quite significant, with decreases in thermal conductivity from no Kapitza cases of 20%, 71%, and 99% at volume fractions of 0.0001, 0.001, and 0.1 CNTs, respectively, for the two-step composite cylinders method/Mori–Tanaka (CCM/MT) results. Also, from Fig. 4, the percent differences between the two-step CCM/MT model and EMA are observed to be 0.06%, 0.6%, and 28% at volume fractions of 0.0001, 0.001, and 0.1 CNTs, respectively.

This reduction in the difference between the two model predictions is noted to be the result of the competing influences of the interface thermal resistance and the hollow region of the CNT. For example, for a CNT radius of 0.85 nm (as used in Fig. 4 corresponding to a (10,10) SWCNT), the surface area to volume ratio

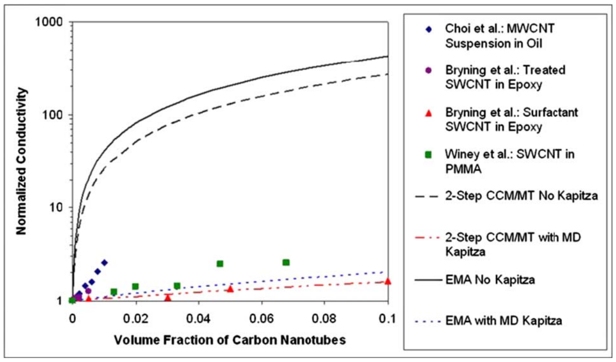

Fig. 4 Comparison of two-step CCM/MT effective thermal conductivities that include the effects of the interface thermal resistance with EMA effective thermal conductivities and with measured data from Choi et al. [25], Bryning et al. [12], and Guthy et al. [13] for values of the Kapitza conductivity parameter β obtained from MD studies [19]

of the CNT is 1.17 nm^{-1} and the volume fraction of the hollow region within the CNT is 0.36. However, for a CNT radius of 5 nm (as used in Ref. [16] corresponding to a (74,74) SWCNT), the surface area to volume ratio of the CNT is reduced to 0.2 nm^{-1} while the volume fraction of the hollow region within the CNT is increased to 0.86, resulting in percent differences between the two-step CCM/MT model and EMA of 2%, 16%, and 84% at volume fractions of 0.0001, 0.001, and 0.1 CNTs, respectively. As illustrated in Fig. 5, the rule of mixtures approach utilized by Nan et al. [16] to account for Kapitza resistance neglects the effects of the hollow region, which becomes increasingly significant at larger radii, and therefore makes rule of mixtures estimates increasingly less accurate.

The same is true in the axial direction, which for the rule of mixtures approach can be represented by changing the d_{CNT} in Fig. 5(*a*) to L_{CNT}, while the composite cylinder model considers the effect of the hollow region in addition to the end effects of the Kapitza resistance when determining the effective conductivity of CNT, as shown schematically in Fig. 3.

It is also of interest to note from Fig. 4 that the two-step CCM/MT model predictions using the Kapitza resistance value from the MD simulations of Huxtable et al. [19] compare well with the measured data obtained by Bryning et al. [12] for surfactant dispersed SWCNTs in epoxy EPON 828. While the MD simulations of Huxtable et al. are for a different matrix material (D_2O or heavy water), both the MD simulations and the measured data from Bryning et al. are for surfactant dispersed SWCNTs. Further, the measured value for the mean radius of CNTs reported by Bryning et al. is comparable to the radius of the CNT used in the MD simulation and the radius used in the present model. In contrast, Nan et al. [16] used this same MD value for the Kapitza resistance and a radius of 5 nm in obtaining EMA results, which compared favorably with measured data from Choi et al. [25]. However, as previously mentioned, these results neglected the significant effect of the hollow region, and when corrected for this using the two-step CCM/MT model, the results underpredict the data of Choi et al. by 200% at a volume fraction of 0.01 CNTs. If instead the radius of 0.85 nm is used in the EMA model, the resulting thermal conductivities (as shown in Fig. 4) are only slightly larger than those predicted using the two-step CCM/MT method. As such, despite not including the influence of the hollow region of the CNT, Bryning et al. were able to obtain an equally good comparison with their measured surfactant dispersed CNT data using EMA by treating the Kapitza resistance as a free parameter and using a much lower aspect ratio (below the aspect ratio of 200, above which the ellipsoid is equivalent to a fiber). However, the two-step CCM/MT model presented herein not only compares favorably with measured date but does so using Kapitza resistance values obtained from MD simulations while retaining both the influence of the hollow region and the high CNT aspect ratio (a value of 588 corresponding to an ~1 μm long CNT[4]).

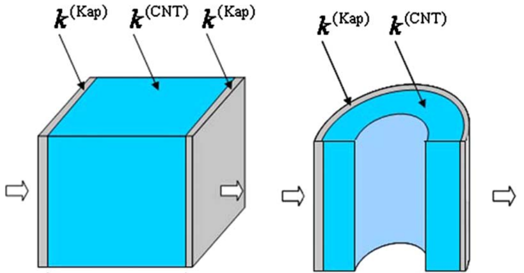

(a) Wall Model for Rule of Mixtures

(b) Composite Cylinder Model

Fig. 5 Schematic representation of the difference between the rule of mixtures approach employed by Nan et al. [16] to account for the Kaptiza resistance and the composite cylinder model approach applied herein

Additional MD simulations performed by Clancy and Gates [20] have studied the effects of functionalization on the Kapitza conductance for a SWCNT dispersed in poly(ethylene vinyl acetate) (EVA) polymer. For the unfunctionalized CNT, a value for Kapitza conductance of 10 MW/m^2 K was obtained for the CNT-EVA interface. While this value is on the same order as the value obtained by Huxtable et al. [19] of 12.5 MW/m^2 K for the CNT-surfactant interface in D_2O, it implies that there can be a difference in Kapitza conductance between different matrix materials. Further, Clancy and Gates obtained values for the Kapitza conductance, which increased with increasing functional group grafting density (increasing faster for longer functional groups), starting from the unfunctionalized value of 10 MW/m^2 K and increasing to values even larger than 200 MW/m^2 K. While at present the authors are unaware of measured data for thermal conductivity for CNT-EVA nanocomposites corresponding to the Clancy and Gates system, the variations in Kapitza conductance which they obtained can be used to motivate a parametric study on Kapitza conductance. Such a parametric study is provided in Fig. 6 for a range of Kapitza conductivity values between 10 MW/m^2 K and 300 MW/m^2 K.

In addition to the aforementioned good agreement between the effective thermal conductivities obtained from the two-step CCM/MT model using a Kapitza conductance of 12.5 MW/m^2 K and the measured data of Bryning et al. for surfactant dispersed CNTs, it is observed that Kapitza conductance values of 40 MW/m^2 K and 90 MW/m^2 K yield effective thermal conductivities, which compare favorably with the measured data of Guthy et al. for dimethylformamide (DMF) dispersed SWCNTs in PMMA [13] and of Bryning et al. [12] for DMF dispersed SWCNTs in epoxy, respectively. Unlike with the surfactant case, the DMF is not expected to be at the CNT interface in the final prepared nanocomposite [13], and as such, these two sets of data represent interfaces between CNTs and different materials, and thus, may have different Kapitza resistances, reflecting the varying degree of phonon scattering at the nanotube-matrix interface. However, in order to further assess the micromechanics model, MD simulations for SWCNTs in these matrix materials are needed.

Table 2 provides a summary of the influence of the Kapitza resistance on the effective CNT properties for a range of β values.

---

[4] Nan et al. use a 5 nm radius and aspect ratio of 2000 corresponding to a 20 μm long CNT.

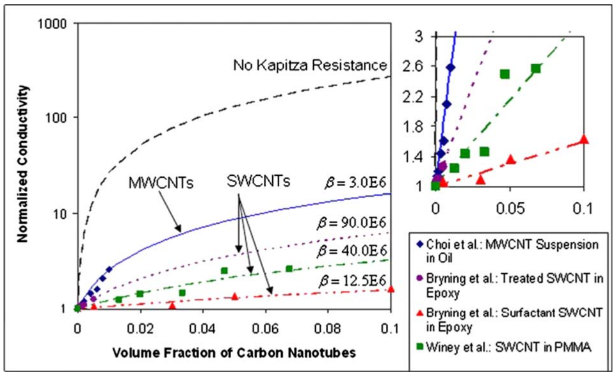

Fig. 6 Parametric study on the influence of the Kapitza resistance using the two-step CCM/MT effective thermal conductivities in comparison with measured data from Choi et al. [25], Bryning et al. [12], and Guthy et al. [13] for a range of values of the Kapitza conductivity parameter β obtained from MD studies [19,20]

It is observed that, over a four order of magnitude range of the Kapitza conductance, the axial and transverse conductivities of the effective CNT increase from values which are a factor of 0.003 of their respective no Kapitza values obtained using $\beta = 12.5\ \mathrm{MW/m^2\,K}$ to nearly equal to their no Kapitza values when $\beta = 10\ \mathrm{GW/m^2\,K}$. Over this same range, the conductivity of the Kapitza layer $k^{(\mathrm{Kap})}$ also increases by four orders of magnitude from a value of 53 μW/m K to 0.4 W/m K, while the value of the effective axial conductivity of the CNT annulus, $k_{11}^{(*)}$, increases by three orders of magnitude to nearly return the CNT input value of 2000 W/m K. In order to further illustrate the importance of including the hollow region of the CNT, effective CNT conductivities as obtained by the rule of mixtures approach employed by Nan et al. [16] are also included. Both the composite cylinder model and the rule of mixtures model use equivalent values for $k^{(\mathrm{Kap})}$ and $k_{11}^{(*)}$. Here, it is observed that the largest difference between the two methods is seen in the effective axial CNT conductivity ($\tilde{k}_{11}^{(\mathrm{CCA})}$ versus $\tilde{k}_{11}^{(\mathrm{RoM})}$).

Also included in Fig. 6 are two-step CCM/MT micromechanics estimates for the effective thermal conductivity of multiwalled CNTs (MWCNTs) intended for comparison with the measured data of Choi et al. [25]. In order to be consistent with the high resolution scanning electron microscopy (SEM) results reported by Choi et al., the CNT radius used in these micromechanics estimates was set to 12.5 nm, the CNT length was set to 50 μm (resulting in an aspect ratio of 2000), and the thickness of the CNT was set to 10.2 nm to be consistent with the reported 30 walls of MWCNT, each wall having a thickness of 0.34 nm. Using a value of the Kapitza conductivity of 12.5 MW/m^2 K from the MD simulations of Huxtable et al. [19] (as used by Nan et al. [16]) was observed to overestimate the measured data by as much as 160% at a volume fraction of 0.01 MWCNT. Instead, in order to obtain relatively good agreement with the MWCNT-oil data of Choi et al., a Kapitza conductance of 3 MW/m^2 K (within a range of MD values reported for EVA by Clancy and Gates [20]) is used. From the point of view of surface to volume ratio (which for MWCNT is 93% smaller than for SWCNTs) and of hollow region volume fraction (which for 30 layers in a 12.5 nm radius MWCNT is 0.03), it is clear why such a low Kapitza conductance yields effective thermal conductivities that are much larger than for the SWCNT cases. However, it is again noted that in order to further assess the micromechanics predictions, additional MD simulations are required to quantify the Kapitza conductance at both a CNT-synthetic poly(α-olefin) oil interface and at a CNT-CNT interface.

5 Conclusions

A micromechanics model for CNT-polymer nanocomposites, which accounts for interactions amongst the various orientations of CNTs in a random distribution, and includes the effects of both the hollow region of the CNT and of the Kapitza conductance, has been developed. It has been shown that accounting for interactions amongst the various orientations in a consistent manner does not yield large differences from methods that average aligned properties over all orientations. In contrast, accounting for the hollow region of the CNT has been shown to have a significant impact on the effective thermal conductivities predicted, especially for SWCNTs with large radii. Furthermore, it has been shown that including the effects of the Kapitza conductance, as obtained from MD simulations for surfactant treated SWCNTs, in micromechanics predictions yields effective properties that compare well with measured data for surfactant dispersed SWCNTs. Values for the Kapitza conductance for a variety of nonsurfactant dispersed SWCNTs and for MWCNTs have been estimated through micromechanics parametric studies and await validation from additional MD simulations.

Table 2 Values for the Kapitza conductivity ($\beta = 1/R_K$) and the effective CNT axial and transverse conductivities obtained from the composite cylinder method (Eqs. (19) and (20)) for $N = 3$, where the second layer is the Kapitza interphase layer. Also included are the corresponding Kapitza interphase layer conductivity ($k^{(\mathrm{Kap})}$ given by Eq. (27)) and effective axial conductivity of the CNT annulus ($k_{11}^{(*)}$ given by Eq. (34)) used in the parametric study on the influence of the Kapitza conductivity on the effective nanocomposite conductivities. Also provided are the effective CNT axial and transverse conductivities obtained from the rule of mixtures approach (Eq. (3) of Ref. [16]). Units for the Kapitza conductance are in W/m^2 K, while conductivities are reported in W/m K.

	Effective CNT from CCM		Effective CNT from RoM		Kapitza layer effects	
β	$\tilde{k}_{11}^{(\mathrm{CCA})}$	$\tilde{k}_{22}^{(\mathrm{CCA})}$	$\tilde{k}_{11}^{(\mathrm{RoM})}$	$\tilde{k}_{22}^{(\mathrm{RoM})}$	$k^{(\mathrm{Kap})}$	$k_{11}^{(*)}$
1.25E+07	3.90E+00	1.15E−02	6.23E+00	1.06E−02	5.30E−05	6.22E+00
4.00E+07	1.24E+01	3.48E−02	1.98E+01	3.40E−02	1.70E−04	1.98E+01
9.00E+07	2.75E+01	7.72E−02	4.40E+01	7.65E−02	3.82E−04	4.39E+01
2.80E+08	8.19E+01	2.37E−01	1.31E+02	2.38E−01	1.19E−03	1.31E+02
1.00E+11	1.21E+03	2.33E+01	1.92E+03	8.15E+01	4.24E−01	1.92E+03
∞	1267.202	32.146	2000	2000	N/A	N/A

Acknowledgment

The authors graciously acknowledge the support provided by Sandia National Laboratories and Texas A&M University through the Sandia National Laboratories/Texas A&M University Doctoral Fellowship in Engineering, as well as the support of the Texas Institute for Intelligent Bio-Nano Materials and Structures for Aerospace Vehicles, funded by NASA Cooperative Agreement No. NCC-1-02038, and of the National Science Foundation under contract No. DMI-0626460.

References

[1] Yakobson, B., and Avouris, P., 2001, "Mechanical Properties of Carbon Nanotubes," Top. Appl. Phys., **80**, pp. 287–327.
[2] Demczyk, B., Wang, Y., Cumings, J., Hetman, M., Han, W., Zettl, A., and Ritchie, R., 2002, "Direct Mechanical Measurement of the Tensile Strength and Elastic Modulus of Multiwalled Carbon Nanotubes," Mater. Sci. Eng., A, **334**, pp. 173–178.
[3] Hone, J., Whitney, M., Piskoti, C., and Zettl, A., 1999, "Thermal Conductivity of Single-Walled Carbon Nanotubes," Phys. Rev. B, **59**(4), pp. R2514-R2516.
[4] Ebbesen, T., Lezec, H., Hiura, H., Bennett, J., Ghaemi, H., and Thio, T., 1996, "Electrical Conductivity of Individual Carbon Nanotubes," Nature (London), **382**, pp. 54–56.
[5] Allaoui, A., Bai, S., Cheng, H., and Bai, J., 2002, "Mechanical and Electrical Properties of a Mwnt/Epoxy Composite," Compos. Sci. Technol., **62**, pp. 1993–1998.
[6] Potschke, P., Bhattacharyya, A., and Janke, A., 2004, "Carbon Nanotube-Filled Polycarbonate Composites Produced by Melt Mixing and Their use in Blends With Polyethylene," Carbon, **42**, pp. 965–969.
[7] Meincke, O., Kaempfer, D., Weickmann, H., Friedrich, C., Vathauer, M., and Warth, H., 2004, "Mechanical Properties and Electrical Conductivity of Carbon-Nanotube Filled Polyamide-6 and its Blends With Acrylonitrile/Butadiene/Styrene," Polymer, **45**, pp. 739–748.
[8] McNally, T., Potschke, P., Halley, P., Murphy, M., Martin, D., Bell, S., Brennan, G., Bein, D., Lemoine, P., and Quinn, J., 2005, "Polyethylene Multiwalled Carbon Nanotube Composites," Polymer, **46**, pp. 8222–8232.
[9] Gojny, F., Wichmann, M., Fiedler, B., Kinloch, I., Bauhofer, W., Windle, A., and Schulte, K., 2006, "Evaluation and Identification of Electrical and Thermal Conduction Mechanisms in Carbon Nanotube/Epoxy Composites," Polymer, **47**, pp. 2036–2045.
[10] Hu, G., Zhao, C., Zhang, S., Yang, M., and Wang, Z., 2006, "Low Percolation Thresholds of Electrical Conductivity and Rheology in Poly(Ethylene Terephthalate) Through the Networks of Multi-Walled Carbon Nanotubes," Polymer, **47**, pp. 480–488.
[11] Song, Y., and Youn, J., 2006, "Evaluation of Effective Thermal Conductivity for Carbon Nanotube/Polymer Composites Using Control Volume Finite Element Method," Carbon, **44**, pp. 710–717.
[12] Bryning, M., Milkie, D., Islam, M., Kikkawa, J., and Yodh, A., 2005, "Thermal Conductivity and Interfacial Resistance in Single-Wall Carbon Nanotube Epoxy Composites," Appl. Phys. Lett., **87**, p. 161909.
[13] Guthy, C., Du, F., Brand, S., Fischer, J., and Winey, K., 2005, "Thermal Conductivity of Single-Walled Carbon Nanotube/Pmma Nanocomposites," Mater. Res. Soc. Symp. Proc., **858E**, p. hH3.31.1.
[14] Du, F., Guthy, C., Kashiwagi, T., Fischer, J., and Winey, K., 2006, "An Infiltration Method for Preparing Single-Wall Nanotube/Epoxy Composites With Improved Thermal Conductivity," J. Polym. Sci., Part B: Polym. Phys., **44**, pp. 1513–15196.
[15] Xu, Y., Ray, G., and Abdel-Magid, B., 2006, "Thermal Behavior of Single-Walled Carbon Nanotube Polymer-Matrix Composites, Part A," Composites, Part A, **37**, pp. 114–1216.
[16] Nan, C.-W., Liu, G., Lin, Y., and Li, M., 2004, "Interface Effect on Thermal Conductivity of Carbon Nanotube Composites," Appl. Phys. Lett., **85**(16), pp. 3549–3551.
[17] Chen, T., Weng, G., and Liu, W.-C., 2005, "Effect of Kapitza Contact and Consideration of Tube-End Transport on the Effective Conductivity in Nanotube-Based Composites," J. Appl. Phys., **97**, p. 104312.
[18] Nan, C.-W., Shi, Z., and Lin, Y., 2003, "A Simple Model for Thermal Conductivity of Carbon Nanotube-Based Composites," Chem. Phys. Lett., **375**, pp. 666–6693.
[19] Huxtable, S., Cahill, D., Shenogin, S., Xue, L., Ozisik, R., Barone, P., Usrey, M., Strano, M., Siddons, G., Shim, M., and Keblinski, P., 2003, "Interfacial Heat Flow in Carbon Nanotube Suspensions," Nat. Mater., **2**, pp. 731–734.
[20] Clancy, T., and Gates, T., 2006, "Modeling of Interfacial Modification Effects on Thermal Conductivity of Carbon Nanotube Composites," Polymer, **47**, pp. 5990–5996.
[21] Nan, C.-W., Birringer, R., Clarke, D., and Gleiter, H., 1997, "Effective Thermal Conductivity of Particulate Composites With Interfacial Thermal Resistance," J. Appl. Phys., **81**(10), pp. 6692–6699.
[22] Shenogin, S., Bodapati, A., Xue, L., Ozisik, R., and Keblinski, P., 2004, "Effect of Chemical Functionalization on Thermal Transport of Carbon Nanotube Composites," Appl. Phys. Lett., **85**(12), pp. 2229–2231.
[23] Yang, R., Chen, G., and Dresselhaus, M., 2005, "Thermal Conductivity of Simple and Tubular Nanowire Composites in the Longitudinal Direction," Phys. Rev. B, **72**, p. 125418.
[24] Hung, M.-T., Choi, O., Ju, Y., and Hahn, H., 2006, "Heat Conduction in Graphite-Nanoplatelet-Reinforced Polymer Nanocomposites," Appl. Phys. Lett., **89**, p. 023117.
[25] Choi, S., Zhang, Z., Yu, W., Lockwood, F., and Grulke, E., 2001, "Anomalous Thermal Conductivity Enhancement in Nanotube Suspensions," Appl. Phys. Lett., **79**(14), pp. 2252–2254.
[26] Benveniste, Y., and Miloh, T., 1986, "The Effective Conductivity of Composites With Imperfect Thermal Contact at Constituent Interfaces," Int. J. Eng. Sci., **24**(9), pp. 1537–1552.
[27] Mori, T., and Tanaka, K., 1973, "Average Stress in Matrix and Average Elastic Energy of Materials With Misfitting Inclusions," Acta Metall., **21**, pp. 571–574.
[28] Hatta, H., and Taya, M., 1985, "Effective Thermal Conductivity of a Misoriented Short Fiber Composite," J. Appl. Phys., **58**(7), pp. 2478–2486.
[29] Hatta, H., and Taya, M., 1986, "Equivalent Inclusion Method for Steady State Heat Conduction in Composites," Int. J. Eng. Sci., **24**(7), pp. 1159–1172.
[30] Hashin, Z., 1968, "Assessment of the Self Consistent Scheme Approximation: Conductivity of Particulate Composites," J. Compos. Mater., **2**(3), pp. 284–300.
[31] Hashin, Z., 1990, "Thermoelastic Properties and Conductivity of Carbon/Carbon Fiber Composites," Mech. Mater., **8**, pp. 293–308.
[32] Marzari, N., and Ferrari, M., 1992, "Textural and Micromorphological Effects on the Overall Elastic Response of Macroscopically Anisotropic Composites," ASME J. Appl. Mech., **59**, pp. 269–275.
[33] Entchev, P., Lagoudas, D., 2002, "Modeling Porous Shape Memory Alloys Using Micromechanical Averaging Techniques," Mech. Mater., **34**, pp. 1–24.
[34] Odegard, G., Gates, T., Wise, K., Park, C., and Siochi, E., 2003, "Constitutive Modeling of Nanotube-Reinforced Polymer Composites," Compos. Sci. Technol., **63**, pp. 1671–1687.
[35] Eshelby, J., 1957, "The Determination of the Elastic Field of an Ellipsoidal Inclusion, and Related Problems," Proc. R. Soc. London, **241**(1226), pp. 376–396.
[36] Christensen, R. M., 1979, *Mechanics of Composite Materials*, Krieger, Malabar, FL.
[37] Levy, O., and Stroud, D., 1997, "Maxwell Garnett Theory for Mixtures of Anisotropic Inclusions: Application to Conducting Polymers," Phys. Rev. B, **56**(13), pp. 8035–8046.
[38] Yu, M.-F., Files, B. S., Arepalli, S., and Ruoff, R., 2000, "Tensile Loading of Ropes of Single Wall Carbon Nanotubes and Their Mechanical Properties," Phys. Rev. Lett., **84**(24), pp. 5552–5555.
[39] Ruoff, R. S., Lorents, and D. C., 1995, "Mechanical and Thermal Properties of Carbon Nanotubes," Carbon, **33**, pp. 925–930.
[40] Qian, D., Liu, W. K., Ruoff, and R. S., 2003, "Load Transfer Mechanisms in Carbon Nanotube Ropes," Compos. Sci. Technol., **63**, pp. 1561–1569.
[41] Yu, M.-F., Lourie, O., Dyer, M. J., Maloni, K., Kelly, T. F., and Ruoff, R. S., 2000, "Strength and Breaking Mechanism of Multi-Walled Carbon Nanotubes Under Tensile Load," Science, **287**(28), pp. 637–640.
[42] Hill, R., 1965, "A Self-Consistent Mechanics of Composite Materials," J. Mech. Phys. Solids, **13**, pp. 213–222.

Analytical Solutions for the Modeled k Equation

Rafik Absi
EBI, 32 Boulevard du Port,
95094 Cergy-Pontoise Cedex, France
e-mail: r.absi@ebi-edu.com

The semitheoretical function of Nezu and Nakagawa (1993, Turbulence in Open-Channel Flows, A. A. Balkema, ed., Rotterdam, The Netherlands) for the turbulent kinetic energy k is valid only where local equilibrium is a good approximation. From an estimation of the difference between the energy production and its dissipation $G-\epsilon$*, we present in this study an analytical solution for the modeled k equation. Comparisons with direct numerical simulation data of turbulent channel flows show good agreement. A universal function for* k^+ *is deducted for* $y^+<20$*.*

[DOI: 10.1115/1.2912722]

1 Introduction

The development of theoretical and semitheoretical analytical methods for turbulent flows is of great importance in both practical engineering applications and basic turbulence research.

For steady open-channel flows in local equilibrium, where the energy production G is balanced by the dissipation ϵ, Nezu and Nakagawa [1] suggested an analytical solution for the modeled k equation, based on an approximation that allows to write the eddy viscosity ν_t as $1/k$. Even if this approximation is not completely realistic, their solution, which is represented by a function that exponentially decreases with y the distance from the bed, is valid far from the bed, where local equilibrium seems to be a good approximation. However, it is not adapted in the near-bed region. In the immediate vicinity of a wall, from expanding the fluctuating velocity components in Taylor series about the normal distance y from the wall, Hanjalić and Launder [2] obtained an equation where the turbulent kinetic energy k is proportional to square of y. However, this quadratic variation of k is valid only in the viscous sublayer.

In this study, we will first improve the demonstartion of Nezu and Nakagawa for the equilibrium solution for k by a more rigorous approximation for ν_t. Based on our demonstration, with an estimation of $G-\epsilon$, we will present a more general solution for the modeled k equation, which improves the description of k in the near-wall region. This near-wall solution will be validated and calibrated by direct numerical simulation (DNS) data of turbulent channel flows.

2 Analytical Solution for Local Equilibrium

We write the modeled k-equation as [1]

$$\frac{\partial k}{\partial t}=G+\frac{\partial}{\partial y}\left(\nu_t\frac{\partial k}{\partial y}\right)-\epsilon \tag{1}$$

where G is the energy production, ϵ the dissipation, and ν_t the eddy viscosity. For steady open-channel flows, Eq. (1) becomes

$$\frac{\partial}{\partial y}\left(\nu_t\frac{\partial k}{\partial y}\right)=-(G-\epsilon) \tag{2}$$

In local equilibrium, where the energy production is balanced by the dissipation ($G=\epsilon$), it is possible to write Eq. (2) as

$$\nu_t\frac{dk}{d\xi}=\text{const}\equiv-2C_1 \tag{3}$$

where $\xi=y/h$ and h is the scale of the flow (can represent either the turbulent flow depth or the boundary layer thickness).

2.1 Nezu and Nakagawa's Demonstration. Nezu and Nakagawa [1] wrote an approximation for the eddy viscosity ν_t as

$$\nu_t\approx\frac{k^2}{\epsilon}\approx\frac{l}{k}\left(\frac{k}{u'}\right)^3\approx\left(\frac{u_\tau^2}{k}\right)(u_\tau h)\approx\frac{1}{k},\quad \nu_t=C'_{\nu_t}\frac{1}{k} \tag{4}$$

where l is a turbulent length scale, u_τ the friction velocity, u' the root-mean-square of turbulent velocity fluctuations, and C'_{ν_t} a constant. Inserting Eq. (4) into Eq. (3) and by integrating, they obtained [1]

$$\frac{k}{u_\tau^2}=D_1e^{(-2C'_1\xi)} \tag{5}$$

where D_1 is a coefficient, and $C'_1=C_1/C'_{\nu_t}$. Equation (5) can be expressed as

$$\sqrt{k}=\sqrt{k_0}e^{[-C'_1(\xi-\xi_0)]} \tag{6}$$

where $k_0=k(y_0)$, $\xi_0=y_0/h$ is the relative roughness (y_0 is the hydrodynamic roughness), and $D_1=(k_0e^{2C'_1\xi_0})/u_\tau^2$.

2.2 Proposed Demonstration. The approximation $\nu_t\approx1/k$ seems not completely realistic. If we assume a shape given by a dimensionless function $f(\xi)$ as

$$\frac{k}{u_\tau^2}=D_1f^2(\xi) \tag{7}$$

and

$$\frac{u'}{u_\tau}=D_uf(\xi) \tag{8}$$

a more rigorous approximation for ν_t is [3]

$$\nu_t\approx\frac{k^2}{\epsilon}\approx\frac{l}{k}\left(\frac{k}{u'}\right)^3\approx\frac{l(\xi)}{k}u_\tau^3f(\xi)^3\approx\frac{g}{k} \tag{9}$$

where

$$g(\xi)=l(\xi)u_\tau^3f(\xi)^3 \tag{10}$$

With g, Eq. (9) is dimensionally valid and with a dimensionless constant C_{ν_t}, we write ν_t as

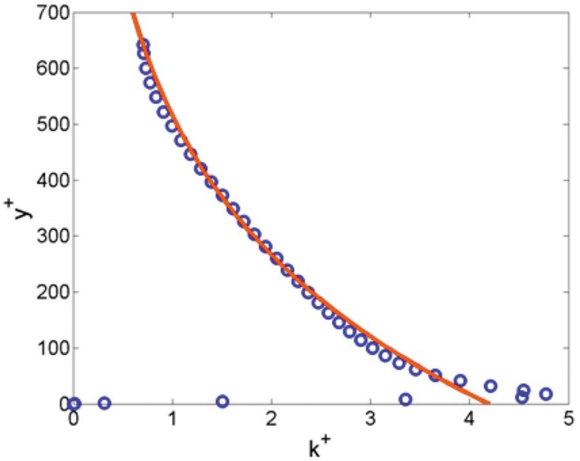

Fig. 1 Turbulent kinetic energy. ○, DNS data [4] for $Re_\tau=642$; curve, Eq. (17) with $A_1^+=360$ and $D_1=4.2$.

Contributed by the Applied Mechanics Division of ASME for publication in the JOURNAL OF APPLIED MECHANICS. Manuscript received February 20, 2006; final manuscript received March 27, 2007; published online May 13, 2008. Review conducted by Bassam A. Younis.

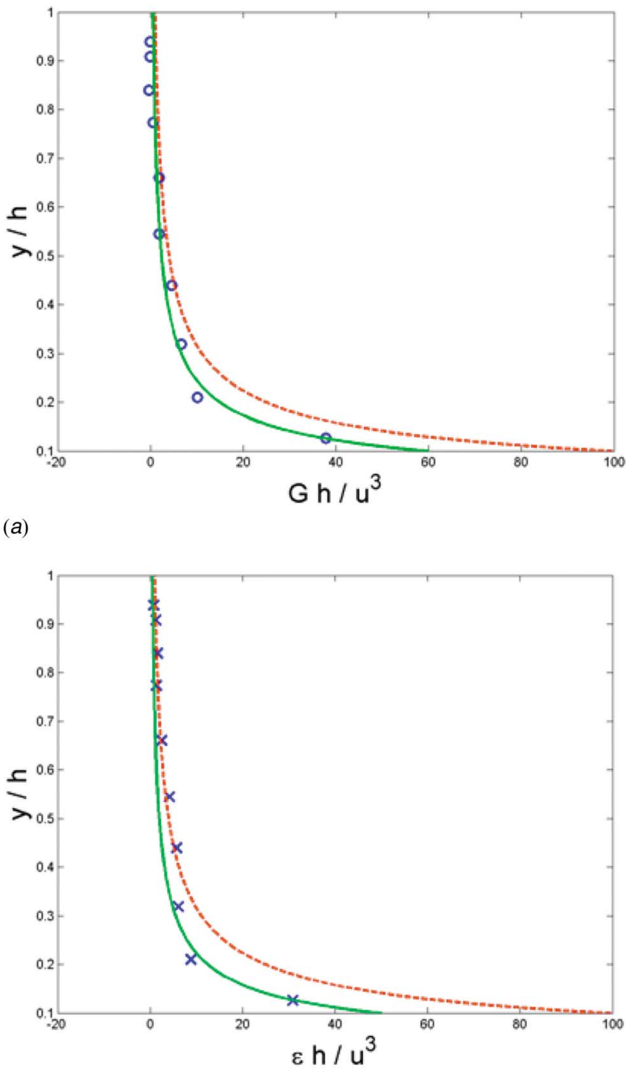

(*a*)

(*b*)

Fig. 2 Dimensionless turbulence generation and dissipation rate versus dimensionless distance. (*a*) Turbulence generation. ○, measurements [5] (Profile 3). Curves, approximation (18); dashed line, with $C_G=1$; solid line, with $C_G=0.6$. (*b*) Turbulence dissipation rate. ×, measurements [5] (Profile 3). Curves, approximation (19); dashed line, with $C_\epsilon=1$; solid line, with $C_\epsilon=0.5$.

$$\nu_t = C_{\nu_t}\frac{g}{k} \tag{11}$$

From Eqs. (4) and (11), we have $C'_{\nu_t}=C_{\nu_t}g$. Inserting Eq. (11) into Eq. (3), we obtain

$$\frac{g(\xi)}{k}\frac{dk}{d\xi} = -2C_n \tag{12}$$

where $C_n=C_1/C_{\nu_t}$. Equation (12) can be expressed as

$$\left(\frac{g(\xi)}{\sqrt{k}}\right)\frac{d\sqrt{k}}{d\xi} = -C_n \tag{13}$$

By integrating Eq. (13) between ξ_0 and ξ, we obtain [3]

$$\sqrt{k} = \sqrt{k_0}\exp\left[-C_n\int_{\xi_0}^{\xi}\frac{d\xi}{g(\xi)}\right] \tag{14}$$

From this equation, we find Eq. (6) only in the case where

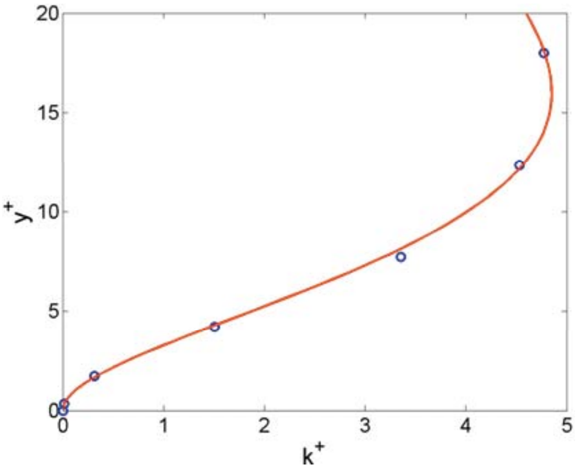

Fig. 3 Turbulent kinetic energy. ○, DNS data [4] for $Re_\tau=642$; curves, proposed analytical solution (26) with $C=1$, $A^+=8$ and $B=0.14$ for $y^+\leq 20$.

$$g = \text{const} \tag{15}$$

since $C'_1=C_1/C'_{\nu_t}=C_1/(C_{\nu_t}.g)=C_n/g$. Condition (15) allows therefore to obtain for steady open-channel flows in local equilibrium an analytical solution for the modeled k equation.

We can notice finally that in Nezu and Nakagawa's demonstration

$$g \approx u_\tau^3 h = \text{const} \tag{16}$$

2.3 Interest and Limits of the Equilibrium Analytical Solution. We write Eq. (5) in wall units as

$$k^+ = D_1 e^{[-y^+/A_1^+]} \tag{17}$$

where $y^+=u_\tau y/\nu$ is the dimensionless wall distance (where u_τ is the wall friction velocity and ν the kinematic viscosity), $k^+=k/u_\tau^2$, and $A_1^+=(hu_\tau)/(2C'_1\nu)$. Figure 1 presents a comparison between the analytical solution (17) and DNS of turbulent channel flow of Iwamoto et al. [4] for $Re_\tau=642$ (hereafter, Re_τ denotes the friction Reynolds number defined based on u_τ, ν, and the channel half-width δ). With $D_1=4.2$ and $A_1^+=360$, this solution represents well the DNS data. However, the solution (17) is not appropriated near the wall. In fact, for $y^+<20$, k^+ decreases to 0 and Eq. (17) is not able to represent this decrease.

The solution (17) is therefore valid only where local equilibrium is a good approximation. In order to provide a more accurate solution, we need an estimation of the difference between G and ϵ. We will first suggest an approximation for $G-\epsilon$ and then we will present a more general solution. This solution will allow to improve the k profile in the near-wall region.

3 Proposed Analytical Solution for *k*

3.1 Approximation for $G-\epsilon$. From measurements of Sukhodolov et al. [5] (Fig. 2(*a*)), we notice that the approximation $Gh/u_\tau^3=C_G/(y/h)^2$ (where C_G is a dimensionless constant), which can be expressed as follows:

$$G = C_G\frac{u_\tau^3 h}{y^2} \tag{18}$$

represents well, with $C_G=1$ (dashed line), the experimental data [5]. An appropriate fit for G (Fig. 2(*a*)) gives $C_G=0.6$ (solid line). Equation (16) shows that Eq. (18) is in the form of $G\approx g/y^2$.

We notice from these experimental data [5] (Fig. 2) that ϵ has a shape similar to G, we write therefore

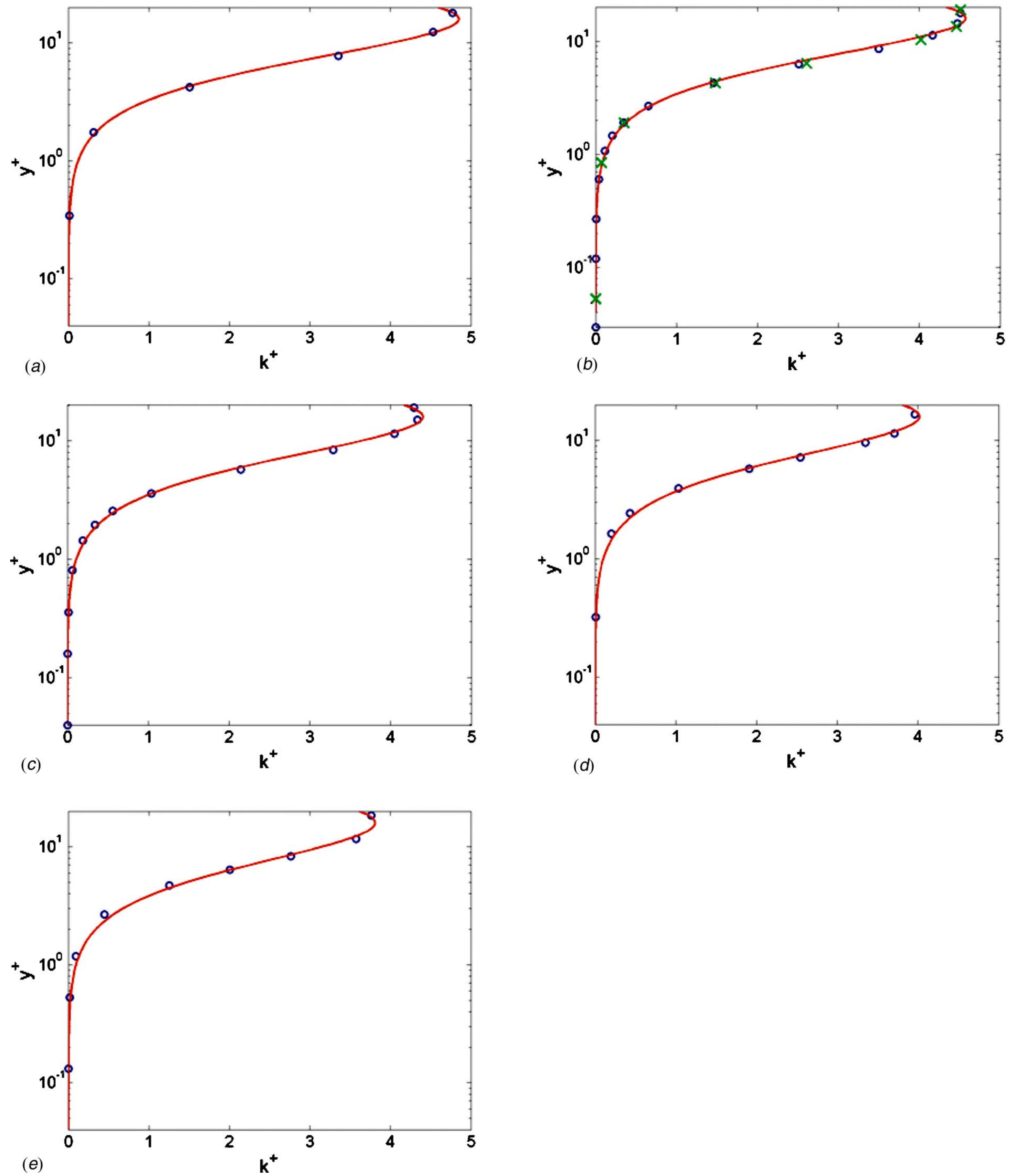

Fig. 4 Turbulent kinetic energy for $y^+ \leqslant 20$. ○, DNS data of Iwamoto et al. [4]; ×, DNS data of Kim [7]; curves, proposed analytical solution (27). (*a*) $\mathrm{Re}_\tau = 642$; curve, $A^+ = 8$ and $B = 0.14$; (*b*) $\mathrm{Re}_\tau = 395$; curve, $A^+ = 8$ and $B = 0.132$; (*c*) $\mathrm{Re}_\tau = 298$; curve, $A^+ = 8$ and $B = 0.127$; (*d*) $\mathrm{Re}_\tau = 150$; $A^+ = 8$ and $B = 0.116$; (*e*) $\mathrm{Re}_\tau = 109$; $A^+ = 8$ and $B = 0.11$.

$$\epsilon = C_\epsilon \frac{u_\tau^3 h}{y^2} \tag{19}$$

where C_ϵ is a constant. As for G, this equation is in the form $\epsilon \approx g/y^2$. With $C_\epsilon = 1$ (dashed line), Eq. (19) represents the shape of experimental data [5]. An appropriate fit for ϵ (Fig. 2(*b*)) gives $C_\epsilon = 0.5$ (solid line).

This shape for G and ϵ is confirmed by wind tunnel experiments of Krogstad and Antonia [6] over rough walls (mesh surface and rod surface).

From Eqs. (18), (19), and (16), we are able to write $G\text{-}\epsilon \approx g/y^2$. Therefore, $G - \epsilon$ can be approximated by

$$G - \epsilon = C_d \frac{g}{y^2} \tag{20}$$

where C_d is a dimensionless coefficient. With Eqs. (11) and (20), we write Eq. (2) as

$$\frac{d}{d\xi}\left(C_{\nu_t} \frac{g}{k} \frac{dk}{d\xi} \right) = - C_d \frac{g}{\xi^2} \tag{21}$$

Table 1 Coefficient B for different Re_τ

Re_τ	109	150	298	395	642
B	0.11	0.116	0.127	0.132	0.14

The assumption $d(\nu_t dk/dy)/dy \approx 1/y^2$ of Eq. (21), which is valid for rough beds, seems to be valid even for smooth walls, since even if G decreases very close to a wall, the term of molecular viscosity in the k equation increases there.

3.2 Proposed Analytical Solution. We are able to integrate Eq. (21), and therefore to find an analytical solution, only in the case where g=const. We will assume, like for the first solution in local equilibrium, that g=const.

By integrating Eq. (21) with the assumption of condition (15), we obtain

$$\frac{g}{k}\frac{dk}{d\xi}=\frac{C_d}{C_{\nu_t}}g\left(\frac{1}{\xi}+\text{const}\right) \tag{22}$$

We write Eq. (22) as

$$\frac{1}{\sqrt{k}}\frac{d\sqrt{k}}{d\xi}=\left(\frac{C}{\xi}-C_2\right) \tag{23}$$

where $C=C_d/2C_{\nu_t}$ and $C_2=-\text{const}C$. By integrating Eq. (23), we obtain

$$\frac{k}{k_0}=\left(\frac{\xi}{\xi_0}\right)^{2C}e^{[-2C_2(\xi-\xi_0)]} \tag{24}$$

which can be expressed as

$$\frac{k}{u_\tau^2}=D\left(\frac{y}{y_0}\right)^{2C}e^{(-y/A)} \tag{25}$$

where $D=(k_0e^{2C_2\xi_0})/u_\tau^2$ and $A=h/(2C_2)$. As for the first solution in local equilibrium, the condition (15) allows to obtain an analytical solution for the modeled k equation.

With the dimensionless wall distance $y^+=u_\tau y/\nu$ (wall unit), we write Eq. (25) as

$$k^+=B(y^+)^{2C}e^{[-y^+/A^+]} \tag{26}$$

where $A^+=Au_\tau/\nu$, $k^+=k/u_\tau^2$, $B=D/(y_0^+)^{2C}$, and $y_0^+=y_0u_\tau/\nu$.

We notice that we find Eq. (17) from our solution (26) for $C=0$. This confirms that Eq. (17) is a particular case of our solution (26), when $G=\epsilon$. Indeed, coefficient C is related to C_d and therefore to $G-\epsilon$.

3.3 Interest and Calibration of the Proposed Solution in the Near-Wall Region. The proposed analytical solution (26) is examined by DNS data of Iwamoto et al. [4]. Figure 3 shows that our analytical solution with $C=1$, $A^+=8$, and $B=0.14$ reproduces well the DNS data [4] for $y^+ \leqslant 20$. The coefficient C seems therefore to be equal to 1 in the near-wall region, where we write k^+ as

$$k^+=By^{+2}e^{[-y^+/A^+]} \tag{27}$$

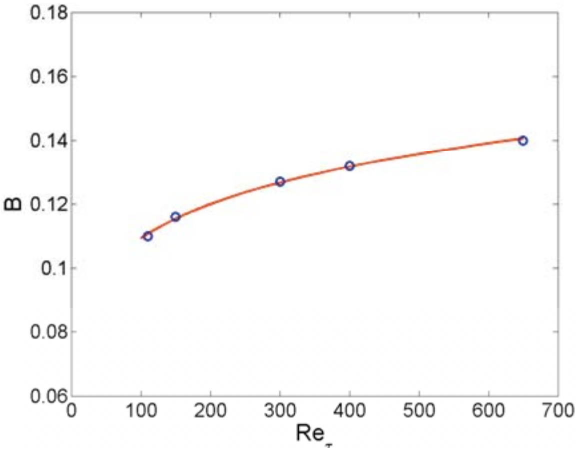

Fig. 5 Dependency of the coefficient B on the Reynolds number Re_τ. ○, values obtained from DNS data [4]; curve, proposed function (28).

In order to verify the universality of this function (27), we validate the proposed equation with other DNS data. Figure 4 presents a comparison between our proposed solution (27) and DNS data of Iwamoto et al. [4] for different values of Re_τ. Figure 4(*b*) shows also a comparison with DNS data of Kim [7] for $\mathrm{Re}_\tau=395$. These figures confirm the ability of this equation to represent k^+, with $C=1$ and $A^+=8$. However, B seems to depend on Re_τ.

We notice that the series expansion of the exponential at the first order in Eq. (27) gives $k^+=By^{+2}-(B/A^+)y^{+3}$. This is similar to the equation obtained from expanding the fluctuating velocity components in Taylor series [2] (p. 608) which is valid only in the immediate vicinity of a wall (~y+<5).

Table 1 gives some values of B for different Re_τ obtained from DNS data.

We propose a function (28) for the coefficient B as

$$B(\mathrm{Re}_\tau)=C_{B1}\,\mathrm{Re}_\tau^{C_{B2}} \tag{28}$$

where C_{B1} and C_{B2} are constants. The calibration (Fig. 5) gives $C_{B1}=0.0588$ and $C_{B2}=0.1346$.

4 Conclusion

In summary, we proposed a more realistic demonstration of the equilibrium solution (17) for k and we presented its interest and limits. Based on our demonstration, with an estimation of $G-\epsilon$, we suggested a more general solution (26) for k, which allows to find Eq. (17) for $C=0$ (when $G=\epsilon$) and gives Eq. (27) for $C=1$ in the near-wall region. This near-wall solution (27) was calibrated by DNS data ($A^+=8$ and B is given by Eq. (28)). The matching procedure between the two solutions (17) and (27) will allow to provide a link between the coefficients D_1 of Eq. (17) and B of Eq. (27) and therefore to write $D_1(\mathrm{Re}_\tau)$. Finally, our main assumptions, which concern the approximation $d(\nu_t dk/dy)/dy \approx 1/y^2$ and the condition g=const, need to be investigated.

References

[1] Nezu, I., and Nakagawa, H., 1993, *Turbulence in Open-Channel Flows*, A. A. Balkema, ed., Rotterdam, The Netherlands.
[2] Hanjalić, K., and Launder, B. E., 1976, "Contribution Towards a Reynolds-Stress Closure for Low-Reynolds-Number Turbulence," J. Fluid Mech., **74**, pp. 593–610.
[3] Absi, R., 2005, "Comment on Turbulent Diffusion of Momentum and Suspended Particles: A Finite-Mixing-Length-Theory," Phys. Fluids, **17**, 079101.
[4] Iwamoto, K., Suzuki, Y., and Kasagi, N., 2002, "Reynolds Number Effect on Wall Turbulence: Toward Effective Feedback Control," Int. J. Heat Fluid Flow, **23**, pp. 678–689.
[5] Sukhodolov, A., Thiele, M., and Bungartz, H., 1998, "Turbulence Structure in a River Reach With Sand Bed," Water Resour. Res., **34**, pp. 1317–1334.
[6] Krogstad, P.-A., and Antonia, R. A., 1999, "Surface Roughness Effects in Turbulent Boundary Layers," Exp. Fluids, **27**, pp. 450–460.
[7] Kim, J., 1989, unpublished data for $\mathrm{Re}_\tau=395$.

Stationary Response of MDOF Dissipated Hamiltonian Systems to Poisson White Noises

Y. Wu

W. Q. Zhu[1]
e-mail: wqzhu@yahoo.com

Department of Mechanics,
State Key Laboratory of Fluid Power Transmission
and Control,
Zhejiang University,
Hangzhou 310027, P.R.C.

The stationary response of multi-degree-of-freedom dissipated Hamiltonian systems to random pulse trains is studied. The random pulse trains are modeled as Poisson white noises. The approximate stationary probability density function and mean-square value for the response of MDOF dissipated Hamiltonian systems to Poisson white noises are obtained by solving the fourth-order generalized Fokker–Planck–Kolmogorov equation using perturbation approach. As examples, two nonlinear stiffness coupled oscillators under external and parametric Poisson white noise excitations, respectively, are investigated. The validity of the proposed approach is confirmed by using the results obtained from Monte Carlo simulation. It is shown that the non-Gaussian behavior depends on the product of the mean arrival rate of the impulses and the relaxation time of the oscillator.

[DOI: 10.1115/1.2912987]

1 Introduction

While Gaussian random processes provide efficient models of various environmental actions, for a broader class of random excitations, such as random pulse trains, the assumption of Gaussianity is not justified by the experimental evidence. So, there has been sustained interest in the response of nonlinear dynamical systems to non-Gaussian random excitations in the past two decades. Very important contributions to such a problem are due to Roberts [1], who considered a Poisson impulse process and proposed a perturbation solution to solve the generalized Fokker–Planck–Kolmogorov (FPK) equation. An improved perturbation scheme was devised by Cai and Lin to obtain an approximate stationary probability density function (PDF) of the response of a nonlinear oscillator to Poisson white noises [2]. The Itô differential rule was extended by Di Paola and Falsone to the case of external and parametric non-Gaussian delta-correlated excitation including Poisson white noise [3]. Linear system excited by polynomials of filtered Poisson pulses was studied by Di Paola [4]. A new approach was proposed by Di Paola and Pirrotta to transform the FPK equation for the original system driven by external input into that governing the PDF of the new state variable [5].

Although significant progress has been made in this area, to the present authors' knowledge, all known techniques to date are applicable only to the single-degree-of-freedom (SDOF) systems [6–9]. Much more efforts are needed to solve higher dimensional generalized FPK equations.

In the present paper, the approximate stationary PDF and mean-square value for the response of multi-degree-of-freedom (MDOF) dissipated Hamiltonian systems to Poisson white noises are obtained by using the perturbation approach. Two specific nonlinearly coupled oscillators under external and parametric Poisson white noise excitations, respectively, are investigated. The numerical results are compared to those obtained from Monte Carlo simulations, and some useful conclusions are made.

2 Poisson White Noise

One versatile model for random pulse train is Poisson white noise

$$\xi(t) = \sum_{k=1}^{N(t)} Y_k \delta(t - t_k) \tag{1}$$

where $\delta(\cdot)$ is the Dirac delta function and $N(t)$ denotes a Poisson counting process giving the number of pulses that arrive in the time interval $[0,t]$; $\{Y_k, k \geq 1\}$ is a collection of real-valued identically distributed independent random variables; Y_k represents the random magnitude of the impulse, which is independent of the pulse arrival time t_k.

The Poisson white noise $\xi(t)$ can be considered as the formal derivative of a homogeneous compound Poisson process defined as

$$C(t) = \sum_{k=1}^{N(t)} Y_k U(t - t_k) \tag{2}$$

where $U(t)$ being the unit step function. The increments $dC(t) = C(t+dt) - C(t)$ hold the following relationship [3] (neglecting infinitesimals of higher order than dt):

$$E[(dC(t))^r] = \lambda E[Y^r] dt \tag{3}$$

where $E[\cdot]$ denotes the mathematical expectation and $\lambda > 0$ is the mean arrival rate of the Poisson counting process $N(t)$. For the limiting case when λ approaches infinity and, at the same time, the intensity $\lambda E[Y^2]$ keeps a constant value, the Poisson white noise $\xi(t)$ tends to a Gaussian one [3]. For the present study, we confine ourselves to a restricted class of problems for which λ and $\lambda E[Y^2]$ are constants.

3 Generalized FPK Equation

Consider a MDOF dissipated Hamiltonian system excited by Poisson white noise. The equations of motion of the system are of the form [10]

$$\dot{Q}_i = \frac{\partial H}{\partial P_i} \tag{4a}$$

$$\dot{P}_i = -\frac{\partial H}{\partial Q_i} - c_{ij}(\mathbf{Q},\mathbf{P})\frac{\partial H}{\partial P_j} + f_{ik}(\mathbf{Q},\mathbf{P})\xi_k(t) \tag{4b}$$

$$(i,j = 1,2, \ldots ,n;\ k = 1,2, \ldots ,\alpha)$$

where Q_i and P_i are the generalized displacements and momenta, respectively. $H=H(\mathbf{Q},\mathbf{P})$ is a Hamiltonian with continuous infinite-order partial derivatives. Equations (4a) and (4b) can be converted into the following Itô stochastic differential equations [5,10]:

$$dQ_i = \frac{\partial H}{\partial P_i} dt \tag{5a}$$

---

[1] Corresponding author.

Contributed by the Applied Mechanics Division of ASME for publication in the JOURNAL OF APPLIED MECHANICS. Manuscript received May 25, 2007; final manuscript received February 22, 2008; published online May 14, 2008. Review conducted by N. Sri Namachchivaya.

$$dP_i = \left(-\frac{\partial H}{\partial Q_i} - c_{ij}(\mathbf{Q},\mathbf{P})\frac{\partial H}{\partial P_j} + \frac{\lambda}{m!}E[Y_{k_1}Y_{k_2}\cdots Y_{k_m}]S^{(m)}_{k_1k_2\cdots k_m}\right)dt + f_{ik}(\mathbf{Q},\mathbf{P})dC_k(t) \tag{5b}$$

$$(i,j=1,2,\ldots,n;\ m=2,\ldots,\infty;\ k,k_1,k_2,\ldots,k_m=1,2,\ldots,\alpha)$$

where $\lambda/m!E[Y_{k_1}Y_{k_2}\cdots Y_{k_m}]S^{(m)}_{k_1k_2\cdots k_m}$ are known as the Wong–Zakai–Di Paola–Falsone (WZDF) correction terms, and $S^{(m)}_{k_1k_2\cdots k_m}$ may be recursively evaluated as follows:

$$S^{(m)}_{k_1k_2\cdots k_m} = \frac{\partial S^{(m-1)}_{k_1k_2\cdots k_{m-1}}}{\partial P_j}f_{jk_m}(\mathbf{Q},\mathbf{P}), \quad S^{(1)}_{k_1} = f_{ik_1}(\mathbf{Q},\mathbf{P}) \tag{6}$$

The WZDF correction terms disappear if the functions f_{ij} depend on $\mathbf{Q}$ only, and then the stationary PDF $p(\mathbf{q},\mathbf{p})$ is governed by the following reduced generalized FPK equation [2,5]:

$$\begin{aligned} &-\frac{\partial}{\partial q_i}\left(\frac{\partial H}{\partial p_i}p\right) - \frac{\partial}{\partial p_i}\left[\left(-\frac{\partial H}{\partial q_i} - c_{ij}\frac{\partial H}{\partial p_j}\right)p\right] \\ &+ \frac{1}{2}\delta_{mn}\lambda E[Y_mY_n]f_{im}f_{jn}\frac{\partial^2 p}{\partial p_i\partial p_j} \\ &- \frac{1}{3!}\delta_{mn}\delta_{mp}\lambda E[Y_mY_nY_p]f_{im}f_{jn}f_{kp}\frac{\partial^3 p}{\partial p_i\partial p_j\partial p_k} \\ &+ \frac{1}{4!}\delta_{mn}\delta_{mp}\delta_{mq}\lambda E[Y_mY_nY_pY_q]f_{im}f_{jn}f_{kp}f_{lq}\frac{\partial^4 p}{\partial p_i\partial p_j\partial p_k\partial p_l} \\ &- \cdots = 0 \quad (i,j,k,l=1,2,\ldots,n;\ m,n,p,q=1,2,\ldots,\alpha) \end{aligned} \tag{7}$$

where δ_{ij} is the Kronecker delta.

4 Perturbation Approach

We now employ a perturbation approach to extract a hierarchy of partial differential equations for $p(\mathbf{q},\mathbf{p})$, from Eq. (7). In view of the fact that the excitation process tends to a Gaussian process as $\lambda \to \infty$, we select $\varepsilon = (\zeta/\lambda)^{1/2}$ as a dimensionless perturbation parameter. Since the intensity $\lambda E[Y^2]$ must be finite, it can be inferred that $\zeta E[Y^2] \sim O(\varepsilon^2)$, $\zeta^{3/2}E[Y^3] \sim O(\varepsilon^3)$, $\zeta^2 E[Y^4] \sim O(\varepsilon^4)$, etc. Let

$$\varepsilon^n I_n = \zeta^{n/2}\lambda E[Y^{n+2}] \tag{8}$$

The solution of Eq. (7) can be written in the following form:

$$p(\mathbf{q},\mathbf{p}) = p_0(\mathbf{q},\mathbf{p})[1 + \varepsilon Q_1(\mathbf{q},\mathbf{p}) + \varepsilon^2 Q_2(\mathbf{q},\mathbf{p}) + \ldots] \tag{9}$$

On substituting Eqs. (8) and (9) into Eq. (7) and grouping terms of the same power of ε, the following set of second-order partial differential equations is obtained.

In ε^0,

$$-\frac{\partial}{\partial q_i}\left(\frac{\partial H}{\partial p_i}p_0\right) + \frac{\partial}{\partial p_i}\left[\left(\frac{\partial H}{\partial q_i} + c_{ij}\frac{\partial H}{\partial p_j}\right)p_0\right] + \frac{I_0}{2}\delta_{mn}f_{im}f_{jn}\frac{\partial^2 p_0}{\partial p_i\partial p_j} = 0 \tag{10}$$

In ε^1,

$$\begin{aligned} &-\frac{\partial H}{\partial p_i}\frac{\partial Q_1}{\partial q_i} + \left(\frac{\partial H}{\partial q_i} + c_{ij}\frac{\partial H}{\partial p_j} + 2I_0\delta_{mn}f_{jn}\frac{\partial f_{im}}{\partial p_j} + \frac{I_0}{p_0}\delta_{mn}f_{im}f_{jn}\frac{\partial p_0}{\partial p_j}\right)\frac{\partial Q_1}{\partial p_i} \\ &+ \frac{I_0}{2}\delta_{mn}f_{im}f_{jn}\frac{\partial^2 Q_1}{\partial p_i\partial p_j} = \frac{I_1}{3!\zeta^{1/2}p_0}\delta_{mn}\delta_{mp}f_{im}f_{jn}f_{kp}\frac{\partial^3 p_0}{\partial p_i\partial p_j\partial p_k} \end{aligned} \tag{11}$$

In ε^2,

$$\begin{aligned} &-\frac{\partial H}{\partial p_i}\frac{\partial Q_2}{\partial q_i} + \left(\frac{\partial H}{\partial q_i} + c_{ij}\frac{\partial H}{\partial p_j} + 2I_0\delta_{mn}f_{jn}\frac{\partial f_{im}}{\partial p_j} + \frac{I_0}{p_0}\delta_{mn}f_{im}f_{jn}\frac{\partial p_0}{\partial p_j}\right)\frac{\partial Q_2}{\partial p_i} \\ &+ \frac{I_0}{2}\delta_{mn}f_{im}f_{jn}\frac{\partial^2 Q_2}{\partial p_i\partial p_j} \\ &= \frac{I_1}{3!\zeta^{1/2}p_0}\delta_{mn}\delta_{mp}f_{im}f_{jn}f_{kp}\frac{\partial^3 p_1}{\partial p_i\partial p_j\partial p_k} \\ &- \frac{I_2}{4!\zeta p_0}\delta_{mn}\delta_{mp}\delta_{mq}f_{im}f_{jn}f_{kp}f_{lq}\frac{\partial^4 p_0}{\partial p_i\partial p_j\partial p_k\partial p_l} \\ &\vdots \\ &(i,j,k,l=1,2,\ldots,n;\ m,n,p,q=1,2,\ldots,\alpha) \end{aligned} \tag{12}$$

Equation (10) is well known as a usual FPK equation for Gaussian white noise excitation, which is exactly solvable if it belongs to the class of generalized stationary potential [11]. The functional form of the solution depends on the integrability and resonance of the associated Hamiltonian system [10].

The solution to Eq. (10) $p_0(\mathbf{q},\mathbf{p})$ enables Eq. (11) to be formulated. Attempts to solve Eq. (11) generally for arbitrary H and f_{ij} have proved to be extremely difficult. However, in most of the practical cases, H is a polynomial of q_i and p_i. If f_{ij} is a constant or a linear function of q_i, then replace the nonlinear coefficient of $\partial Q_1/\partial p_i$ by the linear form $A_iq_i+B_ip_i$; we can obtain the approximate solution in polynomial form. The following equivalence criterion, minimization of the mean-square error, is considered

$$E[\Delta^2] = \text{minimum} \tag{13}$$

where

$$\Delta = A_iq_i + B_ip_i - \left(\frac{\partial H}{\partial q_i} + c_{ij}\frac{\partial H}{\partial p_j} + 2I_0\delta_{mn}f_{jn}\frac{\partial f_{im}}{\partial p_j} + \frac{I_0}{p_0}\delta_{mn}f_{im}f_{jn}\frac{\partial p_0}{\partial p_j}\right) \tag{14}$$

The linearization coefficients are

$$A_i = E\left[q_i\left(\frac{\partial H}{\partial q_i} + c_{ij}\frac{\partial H}{\partial p_j} + \frac{3I_0}{2}f_{jn}\frac{\partial f_{im}}{\partial p_j} + \frac{I_0}{p_0}\delta_{mn}f_{im}f_{jn}\frac{\partial p_0}{\partial p_j}\right)\right](E[q_i^2])^{-1} \tag{15a}$$

$$B_i = E\left[p_i\left(\frac{\partial H}{\partial q_i} + c_{ij}\frac{\partial H}{\partial p_j} + \frac{3I_0}{2}f_{jn}\frac{\partial f_{im}}{\partial p_j} + \frac{I_0}{p_0}\delta_{mn}f_{im}f_{jn}\frac{\partial p_0}{\partial p_j}\right)\right](E[p_i^2])^{-1} \tag{15b}$$

The left-hand side of Eq. (12) is exactly the same as that of Eq. (11); therefore, it can be approximately solved in the same manner.

To estimate the optimal A_i and B_i values, one may apply the perturbation procedure iteratively outlined above. The initial estimates for A_i and B_i may impose upon $p_0(\mathbf{q},\mathbf{p})$, the exact solution to Eq. (10). Then $p(\mathbf{q},\mathbf{p})$ given in Eq. (9) is used for further calculation for the improved A_i, B_i, etc. The iterative process continues until it converges.

It is well known that the non-Gaussian probabilistic characterization of the stationary response is verified to be depending mainly on two coefficients, namely, the skewness and kurtosis, which are associated with Q_1 and Q_2, respectively [12]. For the case in which the random amplitude Y_i is symmetrically distributed, then $I_1=0$ and Eq. (11) gives rise to a trivial solution $Q_1=0$, and so does the skewness coefficient. Hence, the second-order term $\varepsilon^2 Q_2$ becomes the leading correction term for non-Gaussianity, and kurtosis becomes the most significant characteristic depart from normal distribution.

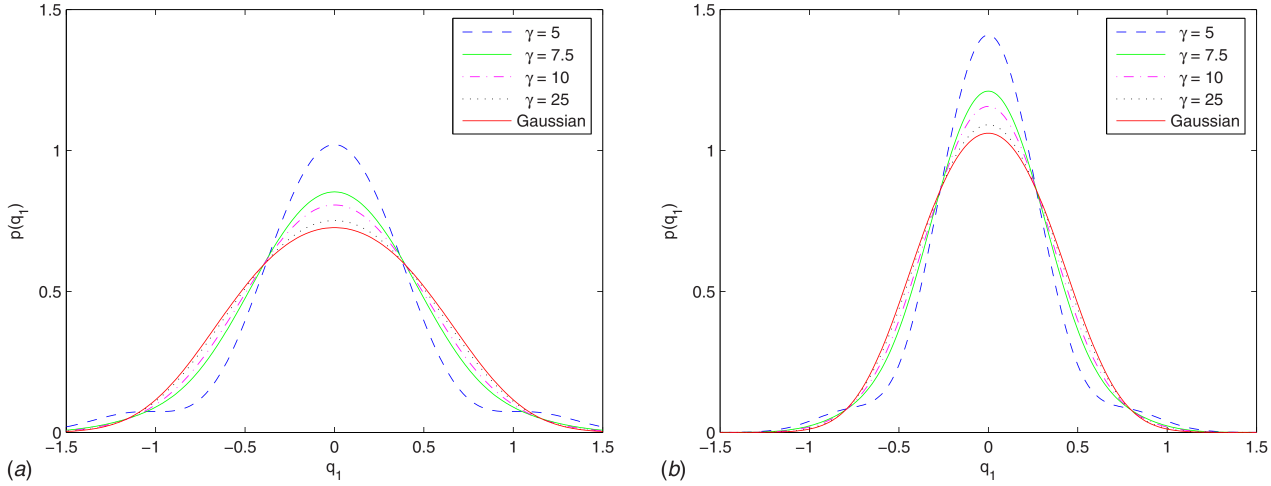

Fig. 1 Approximate stationary probability density of displacement q_1 of system (16). (*a*) $b=0.1$; (*b*) $b=1$.

5 Example

5.1 Example 1. To illustrate the foregoing general procedure, consider two linearly and nonlinearly stiffness coupled Duffing oscillators subject to external Poisson white noise. The equation of motion of the system is of the form

$$\ddot{X}_1 + 2\zeta_1\dot{X}_1 + k_1X_1 + aX_2 + b(X_1 - X_2)^3 = \xi_1(t) \tag{16a}$$

$$\ddot{X}_2 + 2\zeta_2\dot{X}_2 + k_2X_2 + aX_1 + b(X_2 - X_1)^3 = \xi_2(t) \tag{16b}$$

where $\xi_1(t)$ and $\xi_2(t)$ are the two independent Poisson white noises. Equations (16*a*) and (16*b*) can be formulated as the following stochastically excited and dissipated Hamiltonian system [10]:

$$\dot{Q}_1 = \frac{\partial H}{\partial P_1}, \quad \dot{P}_1 = -\frac{\partial H}{\partial Q_1} - 2\zeta_1\frac{\partial H}{\partial P_1} + \xi_1(t) \tag{17a}$$

$$\dot{Q}_2 = \frac{\partial H}{\partial P_2}, \quad \dot{P}_2 = -\frac{\partial H}{\partial Q_2} - 2\zeta_2\frac{\partial H}{\partial P_2} + \xi_2(t) \tag{17b}$$

where the associated Hamiltonian is the total energy

$$H(q_1,q_2,p_1,p_2) = \frac{p_1^2}{2} + \frac{p_2^2}{2} + \frac{1}{2}k_1q_1^2 + \frac{1}{2}k_2q_2^2 + aq_1q_2 + \frac{b}{4}(q_1 - q_2)^4 \tag{18}$$

which is nonintegrable for $a, b \neq 0$. It further assumed that $\zeta_1 = \zeta_2 = \zeta$, and the random pulse amplitude Y is symmetrically distributed, then $I_1=0$, $Q_1=0$; only second-order correction term ε^2Q_2 needs to be taken into consideration. Following the aforementioned perturbation procedure, the following approximate PDF for the system stationary response is found:

$$\begin{aligned} p(\mathbf{q},\mathbf{p}) &= p_0(\mathbf{q},\mathbf{p})[1 + \varepsilon^2Q_2(\mathbf{q},\mathbf{p})] \\ &= C_1 \exp\left[-\frac{4\zeta}{I_0}\left(\frac{p_1^2}{2} + \frac{p_2^2}{2} + \frac{1}{2}k_1q_1^2 + \frac{1}{2}k_2q_2^2 + aq_1q_2\right.\right. \\ &\quad \left.\left. + \frac{b}{4}(q_1 - q_2)^4\right)\right]\left\{1 + \frac{\zeta^2}{3\lambda I_0^2}\left[-18I_0(p_1^2 + p_2^2)\right.\right. \\ &\quad + 8(Ap_1^3q_1 + Bp_2^3q_2) + 12(p_1^4 + p_2^4)\zeta \\ &\quad + \frac{A}{A + 3\zeta^2}(9A^2q_1^4\zeta - 3p_1(p_1^3 + 6I_0q_1)\zeta + 2Aq_1(-4p_1^3 \\ &\quad - 9I_0q_1 + 9p_1^2q_1\zeta)) + \frac{B}{B + 3\zeta^2}(9B^2q_2^4\zeta - 3p_2(p_2^3 + 6I_0q_2)\zeta \\ &\quad \left.\left. + 2Bq_2(-4p_2^3 - 9I_0q_2 + 9p_2^2q_2\zeta))\right]\right\} \end{aligned} \tag{19}$$

where the linearization coefficients A and B are obtained by solving Eqs. (15*a*) and (15*b*).

For illustrative purpose, the system parameters $\zeta=0.04$, $k_1=1$, $k_2=1.5$, $a=1$ were assigned, and the numerical results were obtained. The random pulse amplitude is assumed to be Gaussian distributed with zero mean and the intensity of the Poisson white noise is chosen as $I_0=0.03$. Figures 1 and 2 show the stationary probability densities of the generalized displacements q_1 and q_2 obtained by integrating Eq. (19). Two different intensities of system nonlinearity, $b=0.1$ and 1, are considered.

It is no doubt that the response of the system depends on the mean arrival rate of impulses. However, the inherent characteristic of the system should also be taken into account. Cai and Lin suggested that a suitable measure for the closeness to a Gaussian excitation is the product of λ and the relaxation time t_r of the system, i.e., $\gamma=\lambda t_r$ [2]. It is convenient to assume, for simplicity, that the relaxation time of the system is near to that of the corresponding linear system ($b=0$), for which $t_r=1/\zeta=25$. Four different cases corresponding to $\gamma=5$, 7.5, 10, and 25, as well as the case of Gaussian white noise excitation, are plotted in Figs. 1 and 2. It is seen that for the PDF of all the cases, the departure from that of the Gaussian excitation decreases as γ increases. The results show that the response approaches to Gaussian process when $\gamma > 25$.

The approximate stationary mean-square values $E[Q_i^2] = \int_{-\infty}^{\infty}\int_{-\infty}^{\infty} q_i^2 p(\mathbf{q},\mathbf{p})d\mathbf{q}d\mathbf{p}$ are shown in Figs. 3(*a*) and 3(*b*) for different cases $b=0$, 0.1, and 1. For nonlinear cases $b=0.1$ and 1, the stationary mean-square response increases as γ increases.

For substantiation purpose, the results from Monte Carlo simulations are also included in Fig. 3 as circles. It is seen that they extremely agree well with the analytical results obtained by the proposed perturbation approach in the region $\gamma > 7.5$.

5.2 Example 2. Another example selected for consideration is governed by

$$\ddot{X}_1 + 2\zeta_1X_1^2\dot{X}_1 + k_1X_1 + aX_2 + b(X_1 - X_2)^3 = X_1\xi_1(t) \tag{20a}$$

$$\ddot{X}_2 + 2\zeta_2X_2^2\dot{X}_2 + k_2X_2 + aX_1 + b(X_2 - X_1)^3 = X_2\xi_2(t) \tag{20b}$$

which are the two stiffness coupled oscillators subject to parametric Poisson white noise excitations. The Hamiltonian formulations of the system are [10]

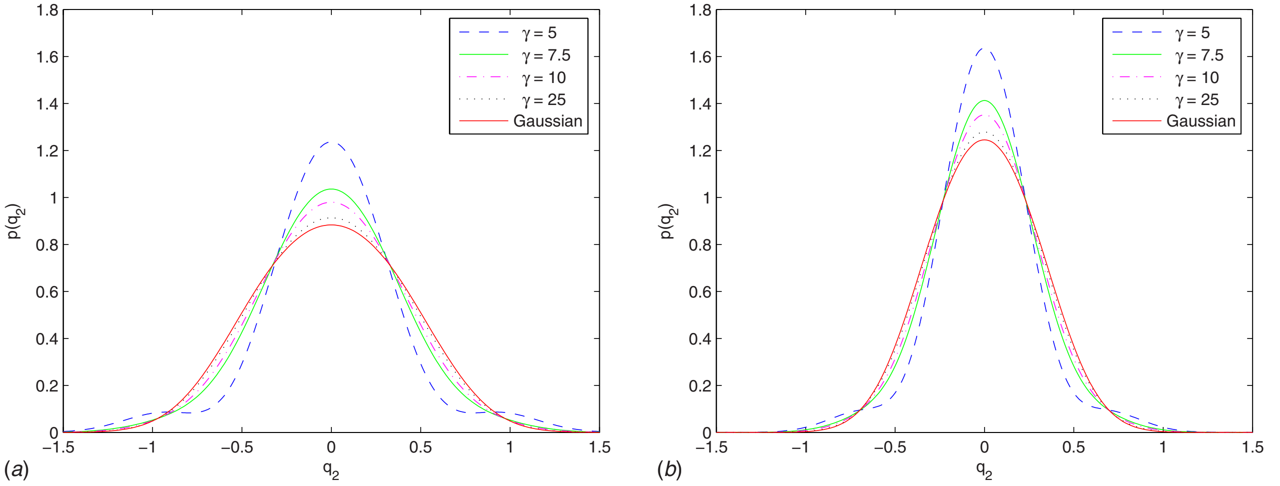

Fig. 2 Approximate stationary probability density of displacement q_2 of system (16). (*a*) $b=0.1$; (*b*) $b=1$.

$$\dot{Q}_1 = \frac{\partial H}{\partial P_1}, \quad \dot{P}_1 = -\left(\frac{\partial H}{\partial Q_1} + 2\zeta_1 Q_1^2 \frac{\partial H}{\partial P_1}\right) + Q_1 \xi_1(t) \qquad (21a)$$

$$\dot{Q}_2 = \frac{\partial H}{\partial P_2}, \quad \dot{P}_2 = -\left(\frac{\partial H}{\partial Q_2} + 2\zeta_2 Q_2^2 \frac{\partial H}{\partial P_2}\right) + Q_2 \xi_2(t) \qquad (21b)$$

in which the Hamiltonian is the same as that in Eq. (18). By making the same assumptions as those in the foregoing example, it shares the same stationary PDF with system (17*a*) and (17*b*) when $\xi_{1,2}(t)$ are Gaussian white noises. The approximate PDF for the stationary response can be deduced by the same perturbation procedure.

The numerical results are obtained and the stationary PDFs of displacements q_1 and q_2 for strongly nonlinear case ($b=5$) are shown in Figs. 4(*a*) and 4(*b*), respectively, along with the Monte Carlo simulation results. The specified case in which $\gamma=3$, corresponding to sparse pulses, is compared to the case of Gaussian white noise excitation. It is worthy to note that, even for this highly non-Gaussian excitation process ($\gamma=3$), the non-Gaussianity of the excitation has little influence on the response non-Gaussianity. A comparison of Figs. 1, 2, and 4 shows that the effect of excitation non-Gaussianity on the response non-Gaussianity for parametric excitation system is much weaker than that for external excitation system.

6 Discussion on the Criterion

It is reasonable for the present study to adopt $\gamma=\lambda t_r$ as the criterion for the departure from a Gaussian excitation. The following two aspects are taken into consideration.

First, we can see this from the viewpoint of the measure of the denseness of the pulse trains. So γ comes to be the ratio of the relaxation time of the system to the interarrival interval of the excitation, $\gamma=t_r/(1/\lambda)=\lambda t_r$, which stands for the measure of the "comparative" denseness of the pulse train with respect to the specified system. The pulses tend toward comparative sparseness with a decreasing γ.

Second, we can also explain this in the aspect of a single impulse. According to the following relationship, $\gamma=\lambda t_r=\lambda/\zeta=(I_0/\zeta)/E[Y^2]$, it is seen that $\gamma \propto (E[Y^2])^{-1}$ for a fixed intensity I_0. The mean-square value $E[Y^2]$ denotes the average intensity of each single impulse (distinguishes from the intensity of the impulsive noise), the rising value of which may give rise to the effects of geometric nonlinearity (e.g., large deflections) and/or nonlinear material behavior and is likely to increase the probability of the first-passage failure for the pulse excited system, in view of the fact that the dissipating ability is not infinite for a restricted damping coefficient ζ.

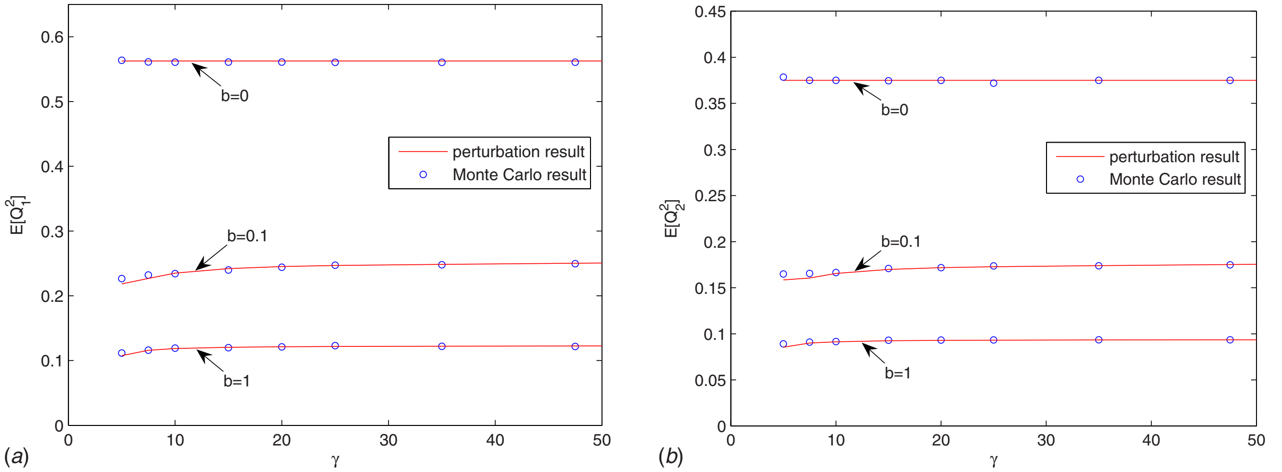

Fig. 3 Mean-square response of displacements q_1 and q_2 of 2DOF Duffing oscillator excited by external Poisson white noise. (*a*) $E[Q_1^2]$; (*b*) $E[Q_2^2]$.

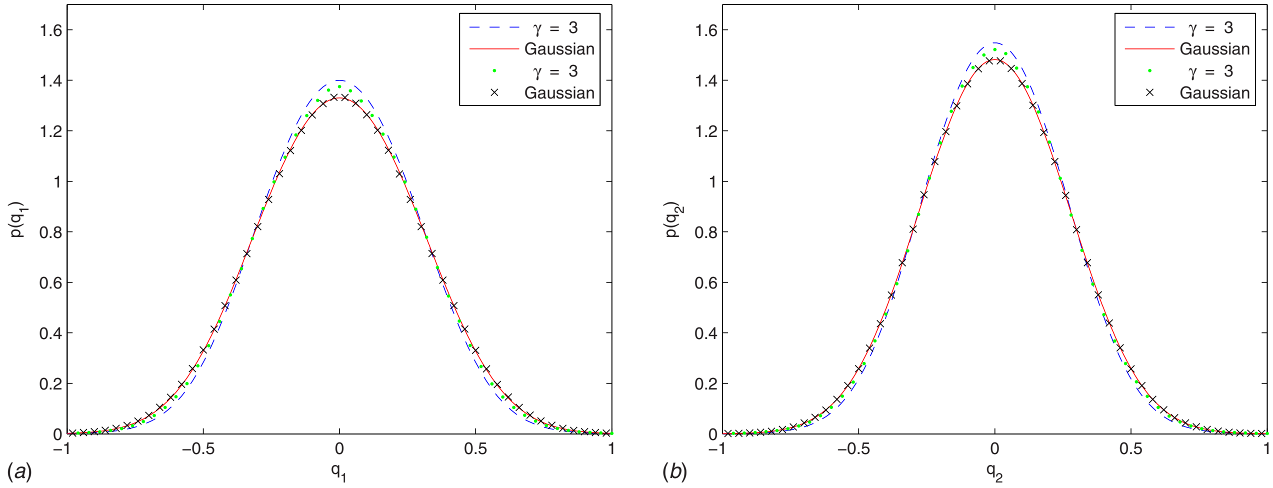

Fig. 4 Approximate stationary probability density of displacements q_1 and q_2 of 2DOF Duffing oscillator excited by parametric Poisson white noise. ---, ——: perturbation solution; ●, ×: Monte Carlo simulation. $\zeta=0.05$, $k_1=1$, $k_2=1.5$, $a=1$, $b=5$, $I_0=0.04$.

7 Concluding Remarks

In the present paper, the stationary response of MDOF dissipated Hamiltonian systems to Poisson white noises has been studied. A perturbation approach has been adopted to get an approximate stationary solution for the generalized FPK equation, thereby the stationary PDF and the mean-square value for the system response have been obtained. The effects of non-Gaussianity of the excitation on the system response have been investigated by using two specific examples. Both the analytical results and those from Monte Carlo simulations show that the effect of excitation non-Gaussianity is significant for the externally excited system, but negligible for the parametrically excited system. A suitable criterion for identifying departure from Gaussianity is the comparative denseness of the pulse train with respect to the specified system, which is defined as the product of the mean arrival rate of the impulses and the relaxation time of the oscillator, i.e., $\gamma=\lambda t_r$. The non-Gaussianity of excitation intensifies as γ decreases. For practical purposes, it is convenient to treat Poisson white noises as Gaussian white noises if $\gamma > 25$.

It is possible to further extend the proposed procedures to predict the response of MDOF nonlinear systems to Poisson white noises with nonsymmetrically distributed random amplitudes.

Acknowledgment

The authors gratefully acknowledge the financial support of the National Natural Science Foundation of China under key Grant Nos. 10332030 and 10772159 and the Specialized Research Fund for the Doctoral Program of Higher Education of China under Grant No. 20060335125. The authors are indebted to Professor G. Q. Cai of Florida Atlantic University for pertinent and kind suggestions.

References

[1] Roberts, J. B., 1972, "System Response to Random Impulses," J. Sound Vib., **24**(1), pp. 23–34.

[2] Cai, G. Q., and Lin, Y. K., 1992, "Response Distribution of Non-Linear Systems Excited by Non-Gaussian Impulsive Noise," Int. J. Non-Linear Mech., **27**(6), pp. 955–967.

[3] Paola, M. D., and Falsone, G., 1993, "Itô and Stratonovich Integrals for Delta-Correlated Processes," Probab. Eng. Mech., **8**, pp. 197–208.

[4] Paola, M. D., 1997, "Linear Systems Excited by Polynomials of Filtered Poisson Pulses," ASME J. Appl. Mech., **64**(3), pp. 712–717.

[5] Paola, M. D., and Pirrotta, A., 2004, "Direct Derivation of Corrective Terms in SDE Through Nonlinear Transformation on Fokker–Planck Equation," Nonlinear Dyn., **36**, pp. 349–360.

[6] Vasta, M., 1995, "Exact Stationary Solution for a Class of Non-Linear Systems Driven by a Non-Normal Delta-Correlated Process," Int. J. Non-Linear Mech., **30**(4), pp. 407–418.

[7] Köylüoğlu, H. U., Nielsen, S. R. K., and Iwankiewicz, R., 1995, "Response and Reliability of Poisson Driven Systems by Path Integration," J. Eng. Mech., **121**(1), pp. 117–130.

[8] Iwankiewicz, R., and Nielsen, S. R. K., 2000, "Solution Techniques for Pulse Problems in Non-Linear Stochastic Dynamics," Probab. Eng. Mech., **15**, pp. 25–36.

[9] Zhu, W. Q., and Cai, G. Q., 2002, "Nonlinear Stochastic Dynamics: A Survey of Recent Developments," Acta Mech. Sin., **18**(6), pp. 551–566.

[10] Zhu, W. Q., *Nonlinear Stochastic Dynamics and Control: Hamiltonian Framework*, 1st ed., Science, Beijing.

[11] Lin, Y. K., and Cai, G. Q., 1988, "Exact Stationary-Response Solution for Second-Order Nonlinear Systems Under Parametric and External White-Noise Excitations: Part II," ASME J. Appl. Mech., **55**, pp. 702–705.

[12] Grigoriu, M., 2004, "Dynamic Systems With Poisson White Noise," Nonlinear Dyn., **36**, pp. 255–266.

An Alternative Two-Variable Model for Bending Problems of Multilayered Beams

Neng-Hui Zhang[1]
e-mail: nhzhang@shu.edu.cn

Jian-Zhong Chen

Department of Mechanics,
College of Sciences,
Shanghai University,
Shanghai 200444, P.R.C.;
Shanghai Institute of Applied Mathematics and Mechanics,
Shanghai 200072, P.R.C.

A closed-form analytical solution to thermoelastic bending problems of multilayered beams is obtained by an alternative two-variable method. There are only two unknowns to be solved and two equilibrium conditions to be satisfied in the present analysis. Differences among zero-strain axis, zero-stress axis, bending axis and centroidal axis are compared. [DOI: 10.1115/1.2912994]

Keywords: multilayered beam, stress, thermoelasticity

1 Introduction

Film/substrate structures have been widely used in surface engineering, semiconductor industry, etc. Residual stresses and bending are inevitably generated by external moments or/and internal stresses such as due to differential thermal expansion or lattice mismatch. For example, in 1865, Rosse [1] tried to make flat bimetallic mirrors for a Newtonian telescope by coating glass with silver and copper. Up until now, many efforts have been devoted to the analysis of residual stresses in multilayered systems. There are two approaches to tackle the problem: One is based on beam-bending theory [2–15]; the other is based on physical superposition method [16–24].

The "neutral axis" has been studied by Beeckman early in 1620, which is defined in bending theory as the line in the cross section of a beam where the normal strain is zero. Until 1826, Navier proved that the location of the neutral axis passes through the centroid of the cross section for pure bending problems of single-layered beams. When the beam is subjected to external moments only, the zero-stress axis coincides with the zero-strain axis [5–7], so the neutral axis can be obtained by finding the location with zero normal stress after solving the stress distribution in the system. However, when subjected to internal stresses, the conclusion is not valid, because multiple zero-stress axes may exist for multilayered beams, which depends on material properties and geometrical sizes [18,19]. A simple relationship was formulated by Stoney [2] in 1909 to predict residual stresses when the film is ultrathin, which has been widely used in many applications. However, his assumption on a neutral axis for zero bending moment does not exist in a bilayer system bent by internal stresses. A general solution for the bending of bilayers due to thermal stresses was derived by Timoshenko [3]. Furthermore, both layers were assumed to have the same curvature and there were three unknowns for the bilayer cases. Moreover, the numbers of both the unknowns and continuity conditions at interfaces increase with the number of layers [8–11]. As a result, obtaining a closed-form solution is a formidable task. Nevertheless, Freund [12,13] presented a two-variable model for multilayered structures, in which there are only two unknowns: a reference strain and a reference curvature for the same reference plane. Furthermore, Freund's reference plane can be arbitrarily defined. The approach has been adopted by others by assuming either the midplane of the system [14] or the midplane of the graded layer [15] as the reference plane.

For the existence of dual zero-stress axes for residual stress problems of bilayers, the definition of the neutral axis for zero normal stress cannot be used in the cases. Hsueh and Evans [16] and Townsend et al. [17] found that if the neutral axis were defined as the line in the cross section of the bilayer where the bending strain component is zero, the definition could be readily used to solve the bending problem. Subsequently, Hsueh et al. extended their approach to multilayers [20–22] and graded layers [23,24]. The approach was achieved by decomposing the total strain into a uniform strain component and a bending strain component. So, there are still only three unknowns to be solved. In order to supply three equations, the original axial force equilibrium condition is divided into the following two conditions [22]: The resultant axial force due to the uniform strain component is zero; the resultant axial force due to the bending strain component is zero. Another parallel physical approach to bending problems of bilayers was developed by Chu [18] and Chuang and Lee [19] via a thought experiment. Compared to Hsueh's model, the virtual force in the later approach should be solved by the continuous condition at the interface. As Chuang and Lee [19] pointed out that the source of error for Chu's analysis comes from the derivation of virtual force that was solved by satisfying the force balance condition not the displacement continuous condition.

Recently, Zhang and Xing [25] provided an alternative model for residual stresses of multilayered beams, in which the centroidal principal axis was taken as the coordinate axis and the two unknowns are the curvature radius of the zero-strain axis (i.e., the neutral axis) and the normal strain at the centroidal principal axis. That is to say, there are two reference planes in Zhang and Xing's model [25], which is a little different from Freund's model [12–15]. As a complement, the present study examines the differences among zero-stress axis, zero-strain axis, bending axis, centroidal axis, and the extent to which it is useful for bending problems if multilayers are subjected to both residual stresses and external moments. It should be noted that the coordinate axis is relocated at the interface between the substrate and the film, which is the same as Hsueh's model [20–22], and the two unknowns are the curvature radius of the zero-strain axis and the normal strain at the interface between the substrate and the film. First, an alternative exact solution to stress distribution in multilayer beams subjected to both residual stresses and external moments is derived. Then, the solution is reduced to that of bilayers and compared to existing solutions. Finally, a comparison among the zero-strain stress, the zero-stress axis, the bending axis, and the centroidal axis is made by considering a bilayered beam subjected to external moments or residual stresses.

2 Two-Variable Model for Multilayered Beams

As shown in Fig. 1, an elastic multilayered beam with length l and width b is subjected to the external moment M and the temperature variation ΔT, where n layers of the film with individual thickness, h_i, $(i=1,2,\ldots,n)$, are sequentially bonded to a substrate with thickness h_s. The interface between the substrate and layer 1 of the film is taken as the coordinate axis x. The thermoelastic properties of the substrate and the film are E_s, α_s and E_i, α_i, where E is Young's modulus and α is the thermal expansion coefficient. Assume that the plane cross-section assumption and

---

[1] Corresponding author.

Contributed by the Applied Mechanics Division of ASME for publication in the JOURNAL OF APPLIED MECHANICS. Manuscript received July 28, 2007; final manuscript received December 26, 2007; published online May 16, 2008. Review conducted by Edmundo Corona.

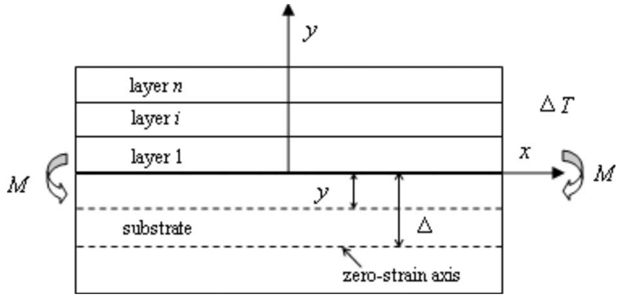

Fig. 1 Longitudinal section of a multilayered beam and the coordinate system

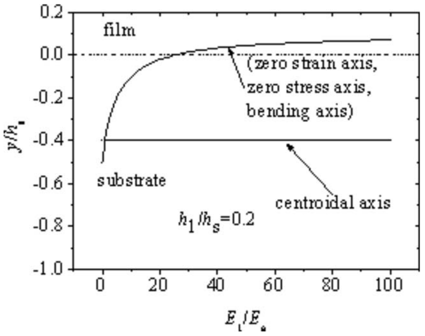

Fig. 2 Comparison among different axes of a bilayered beam subjected to external moments only

the uniaxial stress assumption are still valid. If Δ is the distance from the zero-strain axis to the coordinate axis x, and ρ is the curvature radius of the zero-strain axis, then the normal strain at the location y is

$$\varepsilon = [(\rho + \Delta + y)d\theta - \rho d\theta]/(\rho d\theta) \tag{1}$$

in which $d\theta$ is the relative rotation angle of the two adjacent cross sections. Similarly, the normal strain at the coordinate axis x is

$$\varepsilon_0 = [(\rho + \Delta)d\theta - \rho d\theta]/(\rho d\theta) \tag{2}$$

From Eqs. (1) and (2), one can get

$$\varepsilon = \varepsilon_0 + y/\rho \tag{3}$$

The stress-strain relations for thermoelastic problems are given as

$$\sigma_s = E_s\varepsilon - E_s\alpha_s\Delta T \tag{4a}$$

$$\sigma_i = E_i\varepsilon - E_i\alpha_i\Delta T \tag{4b}$$

where σ_s and σ_i are the normal stresses in the substrate and the film, respectively. From Eqs. (3), (4*a*), and (4*b*), one can get

$$\sigma_s = E_s y/\rho + E_s\varepsilon_0 - E_s\alpha_s\Delta T \tag{5a}$$

$$\sigma_i = E_i y/\rho + E_i\varepsilon_0 - E_i\alpha_i\Delta T \quad (\text{for } i = 1 - n) \tag{5b}$$

For zero axial force, the balance equations of the multilayered beam are given as

$$\int_{A_s} \sigma_s dA_s + \sum_{i=1}^{n} \int_{A_i} \sigma_i dA_i = 0 \tag{6a}$$

$$\int_{A_s} \sigma_s y dA_s + \sum_{i=1}^{n} \int_{A_i} \sigma_i y dA_i = M \tag{6b}$$

where A_s and A_i are, respectively, the cross-section areas of the substrate and the film. Substituting Eqs. (5*a*) and (5*b*) into Eqs. (6*a*) and (6*b*) yields

$$\varepsilon_0 = \left[\left(E_s\alpha_s A_s + \sum_{i=1}^{n} E_i\alpha_i A_i\right)\Delta T - (M + M^T)C_1/C_3\right] \Big/ C_2 \tag{7a}$$

$$1/\rho = (M + M^T)/C_3 \tag{7b}$$

in which

$$C_1 = E_sS_s + \sum_{i=1}^{n} E_iS_i, \quad C_2 = E_sA_s + \sum_{i=1}^{n} E_iA_i,$$

$$C_3 = \left(E_sI_s + \sum_{i=1}^{n} E_iI_i\right) - C_1^2/C_2$$

$$M^T = \left(E_s\alpha_sS_s + \sum_{i=1}^{n} E_i\alpha_iS_i\right)\Delta T - \left(E_s\alpha_sA_s + \sum_{i=1}^{n} E_i\alpha_iA_i\right)\Delta T C_1/C_2$$

in which S_s, S_i and I_s, I_i are the geometrical properties of the substrate and the film, where S is the static moment and I is the second axial moment of the cross section with regard to the coordinate axis x.

3 Results for a Bilayered Beam

A special case of one layer of film on a substrate (i.e., $n=1$) is considered to compare with existing solutions. Assume that the film is much thinner than the substrate. When the bilayered beam is subjected to residual stresses only (i.e., $M=0$), the zero-order approximate solution for stress distribution can be given as

$$\sigma_1 = -E_sh_s^2/(6\rho h_1) \tag{8a}$$

$$\sigma_s = E_s(y + 2h_s/3)/\rho \tag{8b}$$

$$1/\rho = 6E_1h_1(\alpha_1 - \alpha_s)\Delta T/(E_sh_s^2) \tag{8c}$$

Equation (8*a*) is the same as the well-known Stoney equation [2]. From Eq. (8*b*), the zero-stress axis is located at 2/3 of the substrate thickness underneath the film/substrate interface, which has also been obtained by Townsend et al. [17] and Hsueh [21,22]. Conversely, under the external moments only (i.e., $\Delta T=0$), the approximate stresses become

$$\sigma_1 = 6ME_1/(E_sbh_s^2) = E_1h_s/(2\rho) \tag{9a}$$

$$\sigma_s = 6(2y + h_s)/(bh_s^3) \tag{9b}$$

$$1/\rho = 12M/(E_sbh_s^3) \tag{9c}$$

From Eq. (9*b*), the zero-stress axis is located at $y=-h_s/2$. Hsueh et al. [18,19,22] pointed out that there is an improper tendency to locate the zero-stress axis at the centroid of the substrate in residual stress analysis of bilayers. In addition, the zero-stress axis is often taken as the neutral axis in some cases.

Next, in Figs. 2 and 3, the location differences among zero-strain axis, zero-stress axis, bending axis, and centroidal axis are compared by Eqs. (3), (5*a*), (5*b*), (7*a*), and (7*b*) as well as the following bending axis formula [22]: $y_b = (-E_sh_s{}^2 + E_1h_1{}^2)/[2(E_sh_s + E_1h_1)]$. It should be pointed out that the centroidal axis in this paper is geometrically defined by $y_c = (h_1\text{-}h_s)/2$. As shown in Fig. 2, when the bilayered beam ($h_1/h_s=0.2$) is subjected to external moments only, the zero-strain axis coincides with the zero-stress axis and the bending axis, but does not pass through the centroidal axis for the cross section of the beam. However, the bending axis passes through the centroid of the equivalent cross section of the beam [22]. In addition, the

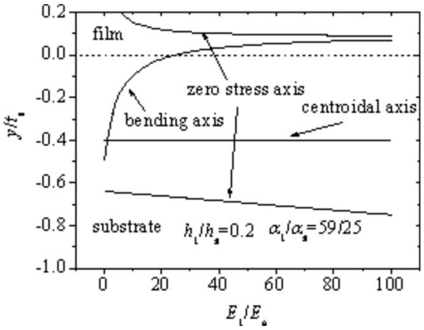

Fig. 3 Comparison among different axes of a bilayered beam subjected to residual stresses only

location of the zero-strain axis, the zero-stress axis, and the bending axis ascends from the substrate to the film with the increase in the modulus ratio E_1/E_s.

As shown in Fig. 3, when the bilayered beam ($h_1/h_s=0.2$, $\alpha_1/\alpha_s=59/25$) is subjected to residual stresses only, the locations of the zero-stress axis, the bending axis, and the centroidal axis apparently diverge. The zero-strain axis disappears in the beam in that case. The number of the bending axis is unique, and its location rises up from the substrate to the film with the increase in the modulus ratio E_1/E_s. However, the number and the location of zero-stress axes vary with the modulus ratio E_1/E_s. The zero-stress axis in the substrate always exists and its location descends with the increase in the modulus ratio E_1/E_s. However, the zero-stress axis in the film emerges only when $E_1/E_s > 6.35$; furthermore, its location also descends with the increase in the modulus ratio E_1/E_s, and finally approaches a value of 0.11. Obviously, in order to avoid interface stress problem, the zero-stress axis of the substrate should be closer to that of the film, but it does not mean that the interface strain takes the least value. It should be pointed out that the locations of the zero-strain axis and the zero-stress axis are not related to the magnitude of external moments or temperature variation when the bilayer beam is subjected to external moments or residual stresses.

4 Conclusions

In classical beam-bending theory, the neutral axis (i.e., zero-strain axis) is often taken as the coordinate axis. So, it is necessary to find its location after the stress distribution in the beam is solved. However, the zero-strain axis does not coincide with the zero-stress axis any longer, and the number of the zero-stress axis varies with the parameters (Fig. 3) when the multilayered beam is subjected to residual stresses. Compared to Timoshenko's model and Hsueh's model, there are only two unknowns in the present model Eqs. (7*a*) and (7*b*), and the step for locating the neutral axis or the bending axis is abandoned. Compared to Freund's model, there are two reference planes in the present model, and the geometrical relation (3) is precisely obtained in the sense of the plane cross-section assumption and the uniaxial stress assumption. However, if the radius of the curvature can be regarded as the same throughout the thickness, the present model is the same to Freund's model numerically.

Acknowledgment

The authors thank Professor C. H. Hsueh and Professor S. Lee for providing their PDF papers. The research was sponsored by the National Outstanding Young Scientists Foundation of China (No. 10725209), the Natural Science Foundation of Shanghai Municipality (No. 07ZR14037), the Multiscale Material Mechanics Fellowship, and the Shanghai Leading Academic Discipline Project under Grant No. Y0103.

References

[1] Rosse, 1908, "Bimetallic Mirrors Made by Electro-Depositions," Nature (London), **78**(2025), pp. 366–367.
[2] Stoney, G. G., 1909, "The Tension of Metallic Films Deposited by Electrolysis," Proc. Phys. Soc. London, **82**, pp. 172–175.
[3] Timoshenko, S., 1925, "Analysis of Bi-Metal Thermostats," J. Opt. Soc. Am., **11**, pp. 233–255.
[4] Sun, C. T., Achenbach, J. D., and Hermann, G., 1968, "Continuum Theory for a Laminated Medium," ASME J. Appl. Mech., **28**, pp. 467–475.
[5] Timoshenko, S., 1955, *Strength of Materials, Part I: Elementary Theory and Problems*, Van Nostrand, New York.
[6] Hearn, E. J., 1977, *Mechanics of Materials*, Pergamon, Oxford, UK.
[7] Beer, F. P., and Johnston, Jr., E. R., 1981, *Mechanics of Materials*, McGraw-Hill, New York.
[8] Saul, R. H., 1969, "Effect of a $GaAs_xP_{1-x}$ Transition Zone on the Perfection of GaP Crystals Grown by Deposition Onto GaAs Substrates," J. Appl. Phys., **40**(8), pp. 3273–3279.
[9] Olsen, G. H., and Ettenberg, M., 1977, "Calculated Stresses in Multilayered Heteroepitaxial Structures," J. Appl. Phys., **48**(6), pp. 2543–2547.
[10] Feng, Z. C., and Liu, H. D., 1983, "Generalized Formula for Curvature Radius and Layer Stresses Caused by Thermal Strain in Semiconductor Multilayer Structures," J. Appl. Phys., **54**(1), pp. 83–85.
[11] Liu, H. C., and Murarka, S. P., 1992, "Elastic and Viscoelastic Analysis of Stress in Thin Films," J. Appl. Phys., **72**(8), pp. 3458–3463.
[12] Freund, L. B., 1993, "The Stress Distribution and Curvature of a General Compositionally Graded Semiconductor Layer," J. Cryst. Growth, **132**(1–2), pp. 341–344.
[13] Freund, L. B., 1996, "Some Elementary Connections Between Curvature and Mismatch Strain in Compositionally Graded Thin Films," J. Mech. Phys. Solids, **44**(5), pp. 723–736.
[14] Sorensen, B. F., Sarraute, S., Jorgensen, O., and Horsewell, A., 1998, "Thermally Induced Delamination of Multilayers," Acta Mater., **46**(8), 2603–2615.
[15] Pitakthapanaphong, S., and Busso, E. P., 2002, "Self-Consistent Elastoplastic Stress Solutions for Functionally Graded Material Systems Subjected to Thermal Transients," J. Mech. Phys. Solids, **50**(4), 695–716.
[16] Hsueh, C. H., and Evans, A. G., 1985, "Residual Stresses in Metal/Ceramic Bonded Strips," J. Am. Ceram. Soc., **68**(5), pp. 241–248.
[17] Townsend, P. H., Barnett, D. M., and Brunner, T. A., 1987, "Elastic Relationships in Layered Composite Media With Approximation for the Case of Thin Films on a Thick Substrate," J. Appl. Phys., **62**(11), pp. 4438–4444.
[18] Chu, S. N. G., 1998, "Elastic Bending of Semiconductor Wafer Revisited and Comments on Stoney's Equation," J. Electrochem. Soc., **145**(10), pp. 3621–3627.
[19] Chuang, T. J., and Lee, S., 2000, "Elastic Flexure of Bilayered Beams Subjected to Strain Differentials," J. Mater. Res., **15**(12), pp. 2780–2788.
[20] Hsueh, C. H., 2002, "Modeling of Elastic Deformation of Multilayers Due to Residual Stresses and External Bending," J. Appl. Phys., **91**(12), pp. 9652–9656.
[21] Hsueh, C. H., 2002, "Thermal Stresses in Elastic Multilayer Systems," Thin Solid Films, **418**(2), pp. 182–188.
[22] Hsueh, C. H., Lee, S., and Chuang, T. J., 2003, "An Alternative Method of Solving Multilayered Bending Problems," ASME J. Appl. Mech., **70**(1), pp. 151–154.
[23] Hsueh, C. H., and Lee, S., 2003, "Modeling of Elastic Thermal Stresses in Two Materials Joined by a Graded Layer," Composites, Part B, **34**(8), pp. 747–752.
[24] Hsueh, C. H., 2003, "Stress Distribution and Curvature in Graded Semiconductor Layers," J. Cryst. Growth, **258**(3–4), pp. 302–309.
[25] Zhang, N. H., and Xing, J. J., 2006, "An Alternative Model for Elastic Bending Deformation of Multilayered Beams," J. Appl. Phys., **100**, pp. 103519.

Transient Response of Submerged Plates Subject to Underwater Shock Loading: An Analytical Perspective

Zhanke Liu
e-mail: zhankel@princeton.edu

Yin L. Young
e-mail: yyoung@princeton.edu

Department of Civil and Environmental Engineering,
Princeton University,
Princeton, NJ 08544

In this paper, Taylor's floating air-backed plate (ABP) model is extended to the case of a submerged water-backed plate (WBP) within the acoustic range. The solution of the WBP is cast into the same format as that of the ABP with a modified fluid-structure interaction (FSI) parameter, which allows a unified analysis of the ABP and WBP using the same set of formulas. The influence of back conditions on fluid and structural dynamics, including fluid cavitation, is systematically investigated. Asymptotic limits are mathematically identified and physically interpolated. Results show that the WBP experiences lower equivalent pressure loading, reduced structural response, and hence lower peak momentum gaining. The time to reach peak momentum is shorter for the WBP than for the ABP. Cavitation is found to be almost inevitable for the ABP, while relevant to the WBP only for a small range of the FSI parameter. Implications to shock response of submerged structures are briefly discussed. [DOI: 10.1115/1.2871129]

1 Introduction

In his pioneering work, Taylor [1] studied the fluid-structure interactions (FSIs) between an exponentially decaying plane shock wave and an infinite rigid flat plate. Closed-form solution for the wetted surface pressure and plate response histories were obtained for air-backed plates with elastic constraints. It was shown that the influence of elastic constraints is small for practical configurations. By neglecting the elastic constraint, elegant formulations were derived for a freestanding air-backed plate (ABP). It was shown that the peak momentum transmitted to a freestanding plate decreases significantly with increasing FSI effects.

Taylor's model of a floating ABP remains the foundation for the understanding of FSI between underwater shock and floating structures. It was adopted in the three-stage model proposed in Ref. [2] to estimate the momentum input via decoupling the FSI stage from the core compression and structural bending stages of sandwich constructions. The special properties of shock-structure interaction have been extensively demonstrated and utilized, theoretically and experimentally, in the enhanced design of air-backed sandwich structures against underwater shock loading [3–12].

An enhancement of Taylor's treatment was presented in Ref. [13] to account for the yield strength of the core to improve the estimation of momentum transmission to sandwich constructions. The extension of Taylor's model for air blast loading was accomplished in Refs. [14–16], where nonlinear compressibility effects are important [17]. The extended model for air blast loading was utilized in Ref. [18] to study the transient response of metal sandwich plates subject to intense air shocks. In Ref. [19], the dynamic response of two plates separated by a column of water subject to an incident pressure pulse was investigated for a specific choice of parameter values with the purpose of simulating the sail appendage of a submarine. In addition to Taylor-type models, there is another important class of analytical work that investigated the dynamic response of elastic shell structures subject to underwater shock loading [20–26].

The objective of the current work is to extend Taylor's floating ABP model for the analysis of submerged water-backed plate (WBP) to characterize the transient FSI response and to identify asymptotic limits. The motivation is to gain insights for the design of submerged structures (e.g., marine propellers, rudders, offshore piles, etc.) against underwater blast loads.

2 Formulation

2.1 Governing Equations. Similar to the assumptions used in Refs. [1,2], a rigid (neglect the elastic deformation and wave propagation) but freestanding plate of mass per unit area $m=\rho_s h_s$ is considered, where ρ_s and h_s are, respectively, the density and thickness of the solid plate. The plate model adopted in Refs. [1,2] has only one wetted surface with water on the left side Ω_L and air on the right side Ω_R. In the current work, the plate is fully submerged in water so that it has two wetted surfaces Ω_L and Ω_R, as shown in Fig. 1. Consider an incident plane pressure wave from the left hand side,

$$p^i(x,t) = p_0 e^{-(t-x/c)/\theta} \tag{1}$$

where c is the sound speed in the water, p_0 is the peak pressure, and θ is the pressure decay time. The origin of the coordinate is taken to be on the plate, with the positive direction to be the same as the traveling direction of the incident wave. The plate is assumed to be able to freely translate in the x direction. Hence, the problem is essentially one dimensional (1D). Upon arrival of the incident wave on the left side of the structural surface Ω_L, it is only partially reflected back due to the translation of the plate in the x direction. The wetted pressure on Ω_L is the sum of the contribution from the incident wave $p_L^i(t)=p_0e^{-t/\theta}$ and from the reflected wave $p_L^r(t)=p_0\varphi(t)$,

$$p_L(t) = p_0[e^{-t/\theta} + \varphi(t)] \tag{2}$$

where $\varphi(t)$ is a functional to be determined. Let $u(t)$, $\dot{u}(t)$, and $\ddot{u}(t)$ be the displacement, velocity, and acceleration of the plate, respectively. Mass and momentum balance near the left surface Ω_L requires

$$\dot{u}(t) = \frac{p_0}{\rho c}[e^{-t/\theta} - \varphi(t)] \tag{3}$$

where $p_0e^{-t/\theta}/\rho c$ and $-p_0\varphi(t)/\rho c$ are the particle velocities due to the incident and reflected waves, respectively. Notice that the nonlinear compressibility effects have been neglected. Combining Eqs. (2) and (3), a relation between the wetted pressure on Ω_L and the plate velocity can be obtained as

$$p_L(t) = 2p_0e^{-t/\theta} - \rho c\dot{u}(t) \tag{4}$$

For a fixed rigid surface, the incident wave will be fully reflected and the resultant pressure will be doubled at the surface. However, axial translation of the plate leads to a partial reflection of the incident wave, and the pressure reduction as compared to a fixed surface is $\rho c\dot{u}(t)$, as shown in Eq. (4). Similarly, mass and moment balance near the right side of the structural surface Ω_R requires

---

Contributed by the Applied Mechanics Division of ASME for publication in the JOURNAL OF APPLIED MECHANICS. Manuscript received May 29, 2007; final manuscript received September 24, 2007; published online May 19, 2008. Review conducted by Robert M. McMeeking.

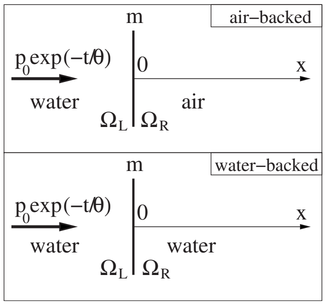

Fig. 1 Schematic drawing for the ABP and WBP subject to an exponentially decaying shock wave from the left hand side

$$\dot{u}(t) = \frac{p_R(t)}{\rho c} \tag{5}$$

where $p_R(t)$ is the wetted pressure on Ω_R. The plate is subjected to $p_L(t)$ on Ω_L and $p_R(t)$ on Ω_R simultaneously. Hence, the equation of motion for the plate can be expressed as

$$m\ddot{u}(t) = p_L(t) - p_R(t) \tag{6}$$

Combining Eqs. (4)–(6), we obtain the governing ordinary differential equation (ODE) for the plate motion as

$$m\ddot{u}(t) + 2\rho c\dot{u}(t) - 2p_0 e^{-t/\theta} = 0 \tag{7}$$

2.2 Transient Response. Applying initial conditions $u(0) = \dot{u}(0) = 0$ to solve for the plate displacement from Eq. (7),

$$u(t) = \frac{2p_0\theta^2}{m(\phi-1)\phi}[(\phi-1) + e^{-\phi t/\theta} - \phi e^{-t/\theta}] \tag{8}$$

where ϕ is the FSI parameter for the WBP,

$$\phi \equiv \frac{2\rho c\theta}{m} \tag{9}$$

Notice that the FSI parameter for the ABP is $\psi \equiv \rho c\theta/m(=\phi/2)$, as defined in Refs. [1,2]. Based on the definition, $\psi, \phi \in (0,\infty)$, where they both approach zero for an extremely heavy plate ($m \to \infty$) or an extremely short shock event ($\theta \to 0$), and infinity for an extremely light plate ($m \to 0$) or an extremely long shock event ($\theta \to \infty$). The FSI parameter can be interpolated as the relative duration of the incident shock wave θ and the duration of the FSI interaction process ϑ: $\psi, \phi \sim \theta/\vartheta$. For the ABP, $\vartheta^a = m/\rho c$ as defined in Ref. [14]; for the WBP, $\vartheta^w = m/2\rho c$. Note that $\vartheta^w = \vartheta^a/2$ since the WBP interacts with water on both sides while the ABP interacts with water only on one side.

The plate velocity and acceleration can be obtained from Eq. (8) as

$$\dot{u}(t) = \frac{2p_0\theta}{m(\phi-1)}(e^{-t/\theta} - e^{-\phi t/\theta}) \tag{10}$$

$$\ddot{u}(t) = \frac{2p_0}{m(\phi-1)}(\phi e^{-\phi t/\theta} - e^{-t/\theta}) \tag{11}$$

The wetted pressures on Ω_L and on Ω_R can be obtained by combining Eqs. (4), (5), and (10),

$$p_L(t) = 2p_0 e^{-t/\theta} - \frac{p_0\phi}{\phi-1}(e^{-t/\theta} - e^{-\phi t/\theta}) \tag{12}$$

$$p_R(t) = \frac{p_0\phi}{\phi-1}(e^{-t/\theta} - e^{-\phi t/\theta}) \tag{13}$$

The net pressure acting on the plate is the difference between $p_L(t)$ and $p_R(t)$,

$$p_T(t) = p_L(t) - p_R(t) = 2p_0 e^{-t/\theta} - \frac{2p_0\phi}{\phi-1}(e^{-t/\theta} - e^{-\phi t/\theta}) \tag{14}$$

When $p_L(t)$ decreases to zero, cavitation will set in on Ω_L (assuming the fluid cavitation pressure to be zero). The cavitation inception time τ_c can be estimated by solving for $p_L(t)=0$. Notice that there is no real solution to this equation if $\phi > 2$. This means that cavitation is only relevant when $\phi < 2$, where the real solution takes the form

$$\tau_c = \theta\left[\frac{\ln\phi}{\phi-1} - \frac{\ln(2-\phi)}{\phi-1}\right] \quad (\phi < 2) \tag{15}$$

When $p_T(t)$ decreases to zero at time τ_p, the plate will reach its peak response with momentum I_p,

$$\tau_p = \theta\frac{\ln\phi}{\phi-1} \tag{16}$$

$$I_p = m\dot{u}(\tau_p) = \zeta I \tag{17}$$

where $I = \int_o^\infty 2\exp(-t/\theta)dt = 2p_0\theta$ is the maximum achievable momentum (in the limit of a fixed rigid plate) and ζ is the momentum transmission coefficient for the WBP,

$$\zeta \equiv \phi^{\phi/(1-\phi)} \tag{18}$$

Equation (18) provides a quantitative measure of the percentage of momentum transfer from the fluid to the structure during the FSI process. Based on the definition, the momentum transmission coefficient ζ is dependent on a sole FSI parameter $\phi \equiv 2\rho c\theta/m$ and is bounded by zero and unity. For an extremely light plate or an extremely long shock event, $\zeta \to 0$; for an extremely heavy plate or an extremely short shock event, $\zeta \to 1$.

The dynamics of the ABP subject to the same planar shock has been derived in Refs. [1,2]. The results are summarized below for comparison with the WBP solution (Eqs. (8), (10), (11), (14)–(16), and (18)). For the presentation hereafter, superscripts a and w will be used to represent the air-backed and water-backed conditions, respectively,

$$u^a(t) = \frac{2p_0\theta^2}{m(\psi-1)\psi}[(\psi-1) + e^{-\psi t/\theta} - \psi e^{-t/\theta}] \tag{19}$$

$$\dot{u}^a(t) = \frac{2p_0\theta}{m(\psi-1)}(e^{-t/\theta} - e^{-\psi t/\theta}) \tag{20}$$

$$\ddot{u}^a(t) = \frac{2p_0}{m(\psi-1)}(\psi e^{-\psi t/\theta} - e^{-t/\theta}) \tag{21}$$

$$p_T^a(t) = p_L^a(t) = 2p_0 e^{-t/\theta} - \frac{2p_0\psi}{\psi-1}(e^{-t/\theta} - e^{-\psi t/\theta}) \tag{22}$$

$$\tau_c^a = \tau_p^a = \theta\frac{\ln\psi}{\psi-1} \tag{23}$$

$$\zeta^a = \psi^{\psi/(1-\psi)} \tag{24}$$

where $\psi \equiv \rho c\theta/m$ is the FSI parameter for the ABP. In these expressions, the pressure on the dry surface of the ABP, p_L^a, has been taken to be zero for simplicity.

The solution to the WBP has the same form as that for the ABP except for the FSI parameter and the cavitation inception time. The FSI parameter $\phi \equiv 2\rho c\theta/m$ for the WBP is two times that of $\psi \equiv \rho c\theta/m$ for the ABP. The cavitation inception time τ_c^a and the

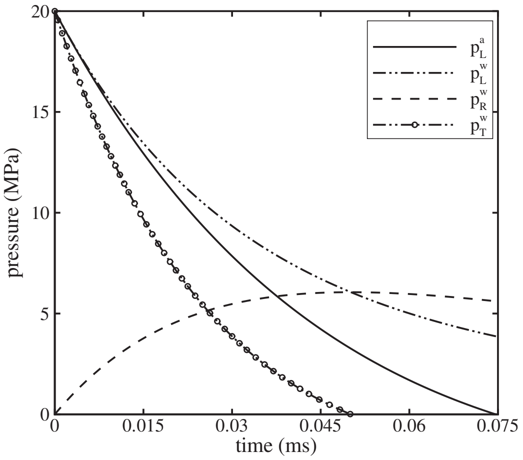

Fig. 2 Comparison of pressure histories between the ABP (ψ =1.75) and the WBP (ϕ=3.5)

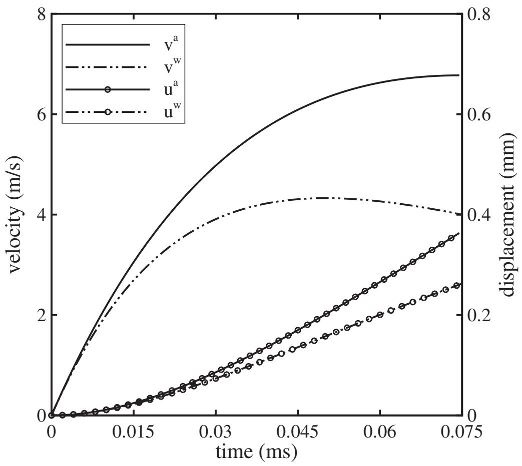

Fig. 3 Comparison of velocity and displacement histories between the ABP (ψ=1.75) and the WBP (ϕ=3.5)

peak response time τ_p^a are equal for the ABP because it has only one wetted surface and $p_T^a = p_L^a - p_R^a = p_L^a$ since $p_R^a = 0$. However, τ_c^w is different from τ_p^w for the WBP because it has two wetted surfaces and $p_T^w = p_L^w - p_R^w < p_L^w$ since $p_R^w > 0$. In addition, Eqs. (23) and (15) indicate that cavitation inception is consistently relevant to the ABP for all $\psi > 0$, while it is only relevant to the WBP for $\phi < 2$.

3 Results

3.1 Fluid Pressure and Structural Response: A Case Study. In order to investigate the influence of different back conditions on the transient response characteristics, a freestanding steel plate with either air-backed or water-backed conditions is chosen as a case study. The water density, sound speed, and steel density are $\rho = 1000\ \mathrm{kg/m^3}$, $c = 1400\ \mathrm{m/s}$, and $\rho_s = 8000\ \mathrm{kg/m^3}$, respectively. The incident shock wave has peak pressure $p_0 = 10$ MPa and decay time $\theta = 0.1$ ms. A typical plate thickness is taken to be $h_s = 0.01$ m, which leads to the FSI parameter $\psi \equiv \rho c\theta/m = \rho c\theta/\rho_s h_s = 1.75$ for the ABP and $\phi \equiv 2\rho c\theta/m = 3.5$ for the WBP. Notice that for this specific configuration, cavitation is only relevant for the ABP, but not for the WBP, as analyzed in Sec. 2.2 since $\phi > 2$.

3.1.1 Fluid Pressure. The time histories of p_L^a, p_L^w, p_R^w, and p_T^w are plotted in Fig. 2, where p_L^a is the wetted pressure on Ω_L of the ABP; p_L^w, p_R^w, and p_T^w are the wetted pressure on Ω_L, wetted pressure on Ω_R, and net pressure, respectively, of the WBP. Notice that the atmosphere pressure on the dry surface Ω_R of the ABP has been neglected; hence, $p_T^a = p_L^a$. In the history plots, the time period is chosen to be equal to 0.075 ms, during which the plates have achieved their peak momentum. Observations can be summarized as follows.

- p_L^w is higher than p_L^a during the time period of interest because a water-backed condition provides more resistance to the plate motion. Hence, the WBP is less yielding and is subjected to higher pressure loading on Ω_L.
- $p_T^w \equiv (p_L^w - p_R^w)$ is lower than $p_T^a = p_L^a$ during the time period of interest due to the fact that p_R^w acts in the opposite direction and hence partially cancels the effect of p_L^w.
- p_T^a and p_T^w become negative after $t > \tau_p^a$ and $t > \tau_p^w$, respectively. Once the net pressure loading becomes negative, the plate starts to decelerate. Hence, τ_p^a and τ_p^w are the time corresponding to peak momentum, respectively, for the ABP and WBP.

3.1.2 Structural Response. The plate velocity ($v^a = \dot{u}^a$ and $v^w = \dot{u}^w$) and displacement (u^a and u^w) time histories are plotted in Fig. 3. The following observations can be summarized.

- The WBP experiences lower velocity and less displacement than the ABP due to the lower net pressure loading.
- The plate velocity reaches its peak value when the net pressure becomes negative, at time τ_p^a and τ_p^w, respectively, for the ABP and WBP. Since $\tau_p^w < \tau_p^a$, the WBP reaches its peak velocity earlier than the ABP.
- The displacement for both plates has not yet reached its peak value since the plate velocity is still positive during the time period of interest.

3.2 Momentum Transmission and Cavitation Inception: A Parametric Study. In order to investigate the influence of the FSI parameter (ψ for the ABP and ϕ for the WBP), a parametric study is presented in this section for the momentum transmission and cavitation inception. General trends are observed. Asymptotic limits are mathematically identified and physically interpolated.

3.2.1 Momentum Transmission. The momentum transmission coefficient, ζ, as a function of the FSI parameter $\psi \equiv \rho c\theta/m (= \phi/2)$ is plotted in Fig. 4 for both the ABP ($\zeta^a = \psi^{\psi/1-\psi}$) and

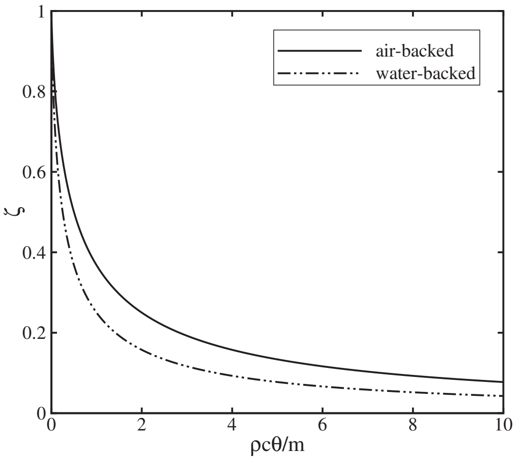

Fig. 4 Comparison of momentum transmission coefficient ζ as a function of the FSI parameter $\rho c\theta/m$ between the ABP and WBP

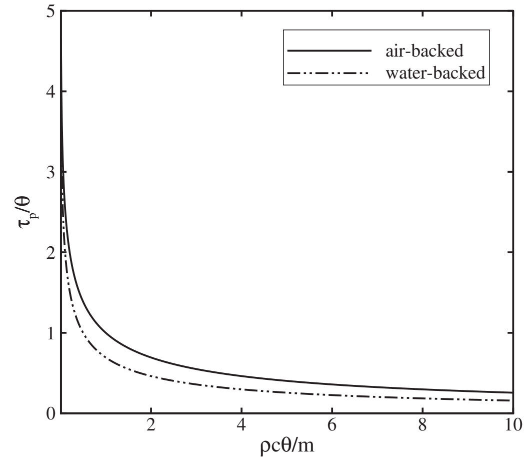

Fig. 5 Comparison of the dimensionless peak response time τ_p/θ as a function of the FSI parameter $\rho c\theta/m$ between the ABP and WBP.

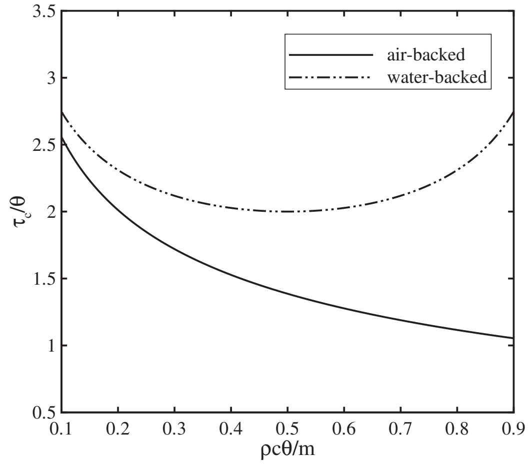

Fig. 6 Comparison of dimensionless cavitation inception time τ_c/θ as a function of the FSI parameter $\rho c\theta/m$ between the ABP and WBP

WBP ($\zeta^w=\phi^{\phi/1-\phi}$). The following general trends are observed.

- ζ asymptotically decreases with increasing ψ values for both the ABP and WBP. This is due to the fact that an increase in FSI effects leads to more pressure reduction and, hence, less momentum transmission. It can be formally proven that $\lim_{\psi\to 0}\zeta=1$, which corresponds to the maximum achievable momentum transfer for an extremely heavy plate or an extremely short shock event, and $\lim_{\psi\to\infty}\zeta=0$, which corresponds to the vanishing momentum transfer for an extremely light plate or an extremely long shock event.
- ζ is consistently lower for the WBP than for the ABP, except at vanishing ψ, due to the lower net pressure loading on the WBP than on the ABP. The influence of back conditions vanishes for an extremely heavy plate or an extremely short shock event, i.e., $\lim_{\psi\to 0}\zeta^w/\zeta^a=1$. On the other extremity, it can be shown that $\lim_{\psi\to\infty}\zeta^w/\zeta^a=0.5$, which indicates that the rate of $\zeta^w\to 0$ is two times faster than $\zeta^a\to 0$ in the limit of $\psi\to\infty$ (extremely light plate or extremely long shock event).

As mentioned in Sec. 3.1.2, the time to reach the peak velocity or, equivalently, the peak momentum, τ_p, is shorter for the WBP than for the ABP. To further investigate this point, the dimensionless time τ_p/θ is plotted against ψ in Fig. 5 for both the ABP and WBP. The following general trends are observed.

- τ_p/θ asymptotically decreases with increasing ψ for both the ABP and WBP. It can be formally proven that $\lim_{\psi\to 0}\tau_p/\theta\to\infty$ and $\lim_{\psi\to\infty}\tau_p/\theta=0$.
- τ_p/θ is consistently smaller for the WBP than for the ABP except at vanishing ψ. The influence of back conditions on the peak response time vanishes for an extremely heavy plate or an extremely short shock event, i.e., $\lim_{\psi\to 0}\tau_p^w/\tau_p^a=1$. On the other extremity, $\lim_{\psi\to\infty}\tau_p^w/\tau_p^a=0.5$, which indicates that the rate of $\tau_p^w/\theta\to 0$ is two times faster than $\tau_p^a/\theta\to 0$ in the limit of $\psi\to\infty$ (extremely light plate or extremely long shock event).

3.2.2 Cavitation Inception. When a plane shock impacts a plate on the left side Ω_L, cavitation may occur due to wave reflection and rarefaction. The current mathematical model is able to identify the cavitation inception time τ_c, as shown in Sec. 2.2. It has been shown that cavitation is relevant to the WBP only for $0<\phi<2$, but to the ABP for all $\psi>0$. The dimensionless cavitation inception time τ_c/θ is plotted against the FSI parameter $\psi\in[0.1,0.9]$ for both the ABP and WBP in Fig. 6. A region of $[0.1,0.9]$ is chosen since τ_c^a and τ_c^w quickly approach ∞ for $\psi<0.1$, and there is no real solution for τ_c^w if $\psi>1$ ($\phi>2$). The following observations can be summarized.

- For the ABP, τ_c^a/θ monotonically decreases with increasing ψ. This implies that the fluid is more susceptible to cavitation for a larger value of ψ. It can be formally proven that $\lim_{\psi\to 0}\tau_c^a/\theta\to\infty$ and $\lim_{\psi\to\infty}\tau_c^a/\theta=0$. Notice that $\tau_c^a=\tau_p^a$ for the ABP, as shown in Eq. (23), which implies that cavitation immediately sets in when the plate has achieved its peak momentum.
- For the WBP, the relation between τ_c/θ and ψ is not monotonic. In fact, $(\tau_c^w/\theta)_{\min}=2$ when $\psi=0.5$ ($\phi=1$). Notice that $\tau_c^w\neq\tau_p^w$ for the WBP, as shown in Eqs. (15) and (16). In fact, $\tau_c^w>\tau_p^w$, which implies that cavitation sets in after the plate has achieved its peak momentum if cavitation is indeed relevant.
- Cavitation inception time is larger, or, equivalently, cavitation sets in later for the WBP than for the ABP because the resistance provided by the water-backed condition tends to weaken the rarefaction wave for the WBP.

4 Conclusion

In this paper, Taylor's freestanding plate model is reformulated for the case of a submerged WBP within the acoustic range. The solution of the WBP is cast into the same format as that of the ABP using a doubled FSI parameter. The influence of the water-backed condition to fluid and structural dynamics is systematically investigated in terms of peak momentum transmission, peak response time, and cavitation inception time. Asymptotic limits are mathematically identified and physically interpolated. Results show that the WBP experiences lower net pressure loading, reduced structural response, and, hence, lower peak momentum gaining, when compared to an equivalent ABP. In addition, the peak response time is shorter for the WBP than for the ABP. Cavitation is found to be almost inevitable for the ABP, while only relevant to the WBP over a small range of FSI parameters. The cavitation inception time, if relevant, is longer for the WBP than for the ABP.

It should be mentioned that the current analytical model assumes a rigid body motion and a 1D system behavior. The effect of nonlinear fluid compressibility has also been neglected. Additional studies are needed to improve the understanding of interactions between multidimensional deformable structures and underwater blast loadings with complex fluid cavitation.

Acknowledgment

The authors are grateful to the Office of Naval Research (ONR) and Dr. Ki-Han Kim (program manager) for their financial support through Grant Nos. N00014-05-1-0694 and N00014-07-1-0491.

References

[1] Taylor, G. I., 1941, "The Pressure and Impulse of Submarine Explosion Waves on Plates," *Scientific Papers of G. I. Taylor III*, Cambridge University Press, Cambridge, UK, pp. 287–303.

[2] Fleck, N. A., and Deshpande, V. S., 2004, "The Resistance of Clamped Sandwich Beams to Shock Loading," ASME J. Appl. Mech., **71**, pp. 386–401.

[3] Rabczuk, T., Kim, J. Y., Samaniego, E., and Belytschko, T., 2004, "Homogenization of Sandwich Structures," Int. J. Numer. Methods Eng., **61**, pp. 1009–1027.

[4] Rabczuk, T., Samaniego, E., and Belytschko, T., 2007, "Simplified Model for Predicting Impulsive Loads on Submerged Structures to Account for Fluid-Structure Interaction," Int. J. Impact Eng., **34**, pp. 163–177.

[5] Qiu, X., Deshpande, V. S., and Fleck, N. A., 2004, "Dynamic Response of a Clamped Circular Sandwich Plate Subject to Shock Loading," ASME J. Appl. Mech., **71**, pp. 637–645.

[6] Deshpande, V. S., and Fleck, N. A., 2005, "One-Dimensional Response of Sandwich Plates to Underwater Shock Loading," J. Mech. Phys. Solids, **53**, pp. 2347–2383.

[7] Deshpande, V. S., Heaver, A., and Fleck, N. A., 2006, "An Underwater Shock Simulator," Proc. R. Soc. London, Ser. A, **462**, pp. 1021–1041.

[8] Xue, Z., and Hutchinson, J. W., 2004, "A Comparative Study of Impulse-Resistant Metal Sandwich Plates," Int. J. Impact Eng., **30**, pp. 1283–1305.

[9] Espinosa, H. D., Lee, S., and Moldovan, N., 2006, "A Novel Fluid Structure Interaction Experiment to Investigate Deformation of Structural Elements Subjected to Impulsive Loading," Exp. Mech., **46**, pp. 805–824.

[10] Wadley, H. N. G., 2006, "Multifunctional Periodic Cellular Metals," Proc. R. Soc. London, Ser. A, **364**, pp. 31–68.

[11] Liang, Y., Spuskanyuk, A. V., Flores, S. E., Hayhurst, D. R., Hutchinson, J. W., McMeeking, R. M., and Evans, A. G., 2007, "The Response of Mettalic Sandwich Panels to Water Blast," ASME J. Appl. Mech., **74**, pp. 81–99.

[12] Xie, W., Liu, Z., Young, Y. L., and Liu, T., "Modeling of Interactions Between Cavitating Flows and Elastic Structures," Int. J. Numer. Methods Eng. submitted.

[13] Hutchinson, J. W., and Xue, Z., 2005, "Metal Sandwich Plates Optimized for Pressure Impulses," Int. J. Mech. Sci., **47**, pp. 545–569.

[14] Kambouchev, N., Noels, L., and Radovitzky, R., 2006, "Nonlinear Compressibility Effects in Fluid-Structure Interaction and Their Implications on the Air-Blast Loading of Structures," J. Appl. Phys., **100**, pp. 063519.

[15] Kambouchev, N., and Radovitzky, R., 2007, "Fluid-Structure Interaction Effects in the Dynamic Response of Free-Standing Plates to Uniform Shock Loading," ASME J. Appl. Mech., **74**, pp. 1042–1045.

[16] Kambouchev, N., Noels, L., and Radovitzky, R., 2007, "Numerical Simulation of the Fluid-Structure Interaction Between Air Blast Waves and Free-Standing Plates," Comput. Struct., **85**, pp. 923–931.

[17] Tan, P. J., Reid, S. R., and Harrigan, J. J., 2005, "Discussion: The Resistance of Clamped Sandwich Beams to Shock Loading," ASME J. Appl. Mech., **72**, pp. 978–979.

[18] Vaziri, V., and Hutchinson, J. W., 2004, "Metal Sandwich Plates Subject to Intense Air Shocks," Int. J. Solids Struct., **44**, pp. 2021–2035.

[19] Schechter, R. S., and Bort, R. L., 1981, "The Response of Two Fluid-Coupled Plates to an Incident Pressure Pulse," Naval Research Laboratory, Technical Report No. 4647.

[20] Mindlin, R. D., and Bleich, H. H., 1953, "Response of an Elastic Cylindrical Shell to a Transverse Step Shock Wave," ASME J. Appl. Mech., **26**, pp. 189–195.

[21] Haywood, J. H., 1958, "Response of an Elastic Cylindrical Shell to a Pressure Pulse," Q. J. Mech. Appl. Math., **11**, pp. 129–141.

[22] Huang, H., 1969, "Transient Interaction of Plane Acoustic Waves With a Spherical Elastic Shell," J. Acoust. Soc. Am., **45**, pp. 661–670.

[23] Huang, H., 1970, "An Exact Analysis of the Transient Interaction of Acoustic Plane Waves With a Cylindrical Elastic Shell," ASME J. Appl. Mech., **37**, pp. 1091–1099.

[24] Huang, H., 1979, "Transient Response of Two Fluid-Coupled Spherical Elastic Shells to an Incident Pressure Pulse," J. Acoust. Soc. Am., **65**, pp. 881–887.

[25] Zhang, P., and Geers, T., 1993, "Excitation of a Fluid-Filled, Submerged Spherical Shell by a Transient Acoustic Wave," J. Acoust. Soc. Am., **93**, pp. 696–705.

[26] Jones-Oliveira, J., 1996, "Transient Analytic and Numerical Results for the Fluid-Solid Interaction of Prolate Spheroidal Shells," J. Acoust. Soc. Am., **99**, pp. 392–407.

Discussion: "A Greenwood–Williamson Model of Small-Scale Friction" (Jones, R. E., 2007, ASME J. Appl. Mech., 74, pp. 31–40)

Izhak Etsion
Fellow ASME
Department of Mechanical Engineering,
Technion,
Haifa 32000, Israel
e-mail: etsion@technion.ac.il

The author is to be commended for his attempt to cope analytically with the complex problem of friction. A few comments regarding the present paper are in place. The present simplified friction model is essentially based on the 1949 Mindlin approach (see Ref. [1]). According to this concept, it is assumed that the contact area of an elastic spherical asperity is given by the frictionless Hertz solution (see Eq. (2)) and that slip of such an asperity will ensue when the average shear stress at its contact area reaches a critical value (see Eq. (6)). These simplifying assumptions may lead to some unrealistic situations where the local equivalent von Mises stress in the contact interface can exceed the yield strength of the sphere material. Additional shortcomings of the Mindlin concept is that an increase of the contact area due to the tangential load is completely excluded, and that sliding inception always occurs in the contact interface of each asperity regardless of its level of normal loading. This would contradict the well known phenomena of junction growth and material transfer, where the latter requires slip below the contact interface. In this regard, it is worthwhile mentioning a different approach to sliding inception of a single spherical asperity [2] and to modeling of static friction of contacting rough surfaces [3]. These papers are not limited to elastically deformed asperities, and in Ref. [3] adhesion effect was also considered. However, these two models still assume, like in the present paper, that the contact area resulting from a frictionless normal loading is unaffected by the additional tangential load. A more realistic model was recently presented in two papers by Brizmer et al. assuming full stick contact condition for both normal and tangential loadings (see Refs. [4,5]). The full stick contact condition captures very well the concept of an adhesive joint formed in the contact interface. It does not require simplifying assumptions regarding the size of the contact area and the location of slip at the contact interface; therefore, it never violates the von Mises yield criterion. Furthermore, it utilizes first principles to predict the sliding inception at the instant of vanishing tangential stiffness (as shown in Fig. 1 of the present paper) and to obtain the resulting corresponding static friction and junction growth. Since the full stick contact condition does not impose slip at the contact interface, it allows for the possibility of material transfer under severe normal loads. Additionally, the results of Refs. [4,5] correlate well with some preliminary experimental results obtained by Ovcharenko et al. [6].

References

[1] Mindlin, R. D., 1949, "Compliance of Elastic Bodies in Contact," ASME J. Appl. Mech., **16**, pp. 259–268.
[2] Kogut, L., and Etsion, I., 2003, "A Semi-Analytical Solution for the Sliding Inception of a Spherical Contact," ASME J. Tribol., **125**, pp. 499–506.
[3] Kogut, L., and Etsion, I., 2004, "A Static Friction Model for Elastic-Plastic Contacting Rough Surfaces," ASME J. Tribol., **126**, pp. 34–40.
[4] V. Brizmer, Y. Kligerman, and Etsion, I., 2007, "Elastic-Plastic Spherical Contact Under Combined Normal and Tangential Loading in Full Stick," Tribol. Lett., **25**, pp. 61–70.
[5] Brizmer, V., Kligerman, Y., and Etsion, I., 2007, "A Model for Junction Growth of a Spherical Contact Under Full Stick Condition," ASME J. Tribol., **129**, pp. 783–790.
[6] Ovcharenko, A., Halperin, G., Etsion, I., and Varenberg, M., 2006, "A Novel Test Rig for *In Situ* and Real Time Optical Measurement of the Contact Area Evolution During Pre-Sliding of a Spherical Contact," Tribol. Lett., **23**, pp. 55–63.

Contributed by the Applied Mechanics Division of ASME for publication in the JOURNAL OF APPLIED MECHANICS. Manuscript received April 9, 2007; final manuscript received September 24, 2007; published online May 15, 2008. Review conducted by Robert M. McMeeking.

Closure to "Discussion of 'A Greenwood–Williamson Model of Small-Scale Friction' " (2008, ASME J. Appl. Mech., 75, p. 045501)

Reese Jones
Sandia National Laboratories,
Livermore, CA 94551

I appreciate the comments made about the paper and the additional references. It is true that Eq. (4), taken from Johnson's book, is Mindlin's solution from his 1949 paper, and due credit should have been given. Moreover, as Johnson pointed out, a full stick solution for a Hertzian contact problem will have singularities. However, as stated in the paper: "This work is an attempt to obtain the representative qualitative features and scaling of the PSTD phenomenon without modeling the details of the single asperity solution, i.e., the traction fields on the asperity-asperity interface." The assumption that, on average, the behavior follows the Mindlin-based solution is admittedly crude, but tractable analytically. This simple relationship minimized the complexity of the resulting expressions as compared to ones based on empirical relationships, e.g., Tabor's work, and allowed for a clearer analysis of the basic mechanisms and population dynamics. More specifically, the need for substantial assumptions about the details of the asperity-asperity constitutive interaction are in counterpoint with the assumptions of smooth asperity surface geometry with well-defined radii of curvature. I assume that most researchers would agree that there are no precisely hemispherical asperities identifiable outside of the realm of theory and some artificial geometries created in the laboratory. So, given the lack of characterization of the details of asperity behavior, I think it is best to view asperities as merely actors in an ensemble, with the ensemble determining the observable behavior. Extension of the work to more detailed interactions, including those cited in the Discussion, is straightforward and is left for future work.

Contributed by the Applied Mechanics Division of ASME for publication in the Journal of Applied Mechanics. Manuscript received September 6, 2007; final manuscript received September 26, 2007; published online May 15, 2008. Review conducted by Robert M. McMeeking.

Discussion: "New First-Order Shear Deformation Plate Theories" (Shimpi, R. P., Patel, H. G., and Arya, H., 2007, ASME J. Appl. Mech., 74, pp. 523–533)

J. G. Simmonds
ASME Fellow
Department of Civil Engineering,
University of Virginia,
Charlottesville, VA 22904-4742
e-mail: jgs@virginia.edu

This paper joins a host of others, beginning with the seminal papers of Reissner [1,2], that attempt to improve the accuracy of classical (Kirchhoff) plate theory *without* a concomitant refinement of the classical boundary conditions—a refinement that necessitates using the equations of three-dimensional elasticity to examine edge layers whose thicknesses are of the order of the plate thickness. Without such a refinement, improvements to Kirchhoff's theory are, in general, illusory, as many authors over the past 50 years have emphasized, especially Goldenveiser. See, for example, Refs. [3–9], where many other relevant references will be found.

Often, authors of "improved" plate theories compare solutions of their equations under simple support either to other theories or to exact three-dimensional elasticity solutions. However, because such solutions are mathematically equivalent to those of an infinite plate under periodic surface loads, no edge layers arise so that such comparisons are virtually useless.

References

[1] Reissner, E., 1944, "On the Theory of Bending of Elastic Plates," J. Math. Phys. (Cambridge, Mass.), **23**, pp. 184–191.
[2] Reissner, E., 1945, "The Effect of Transverse-Shear Deformation on the Bending of Elastic Plates," ASME J. Appl. Mech., **12**, pp. A69–A77.
[3] Goldenveiser, A. L., 1997, "On Approximate Methods for Analyzing Thin Elastic Shells and Plates," Mech. Solids, **32**, pp. 115–126.
[4] Goldenveiser, A. L., 1995, "Internal and Boundary Calculations of Thin Elastic Bodies," J. Appl. Math. Mech., **59**, pp. 973–985.
[5] Wan, F. Y. M., 2003, "Stress Boundary Conditions for Plate Bending," Int. J. Solids Struct., **40**, pp. 4107–4123.
[6] Ladevèze, P., and Précastaings, F., 1988, "The Optimal Version of Reissner's Theory," ASME J. Appl. Mech., **55**, pp. 413–418.
[7] Gregory, R. D., and Wan, F. Y. M., 1988, "The Interior Solution for Linear Problems of Elastic Plates," ASME J. Appl. Mech., **55**, pp. 551–559.
[8] 1985, *Local Effects in the Analysis of Structures*, P. Ladevèze, ed., Elsevier, Amsterdam.
[9] Simmonds, J. G., 1976, "Recent Advances in Shell Theory," *Advances in Engineering Science*, Proceedings 13th Annual Meeting Society of Engineering Science, NASA CP-2001, pp. 617–626.

Contributed by the Applied Mechanics Division for publication in the Journal of Applied Mechanics. Manuscript received August 4, 2007; final manuscript received December 28, 2007; published online May 20, 2008. Review conducted by Robert M. McMeeking.

Closure to "Discussion of 'New First-Order Shear Deformation Plate Theories'" (2008, ASME J. Appl. Mech., 75, p. 045503)

R. P. Shimpi
Professor
e-mail: rpshimpi@aero.iitb.ac.in

H. G. Patel
Research Scholar

H. Arya
Assistant Professor

Aerospace Engineering Department,
Indian Institute of Technology Bombay,
Powai, Mumbai 400076, India

The authors are grateful to Professor Simmonds for giving his observations on the paper under discussion. They would like to present their comments on his observations.

1. The authors' comments on the first paragraph (which starts with "This paper joins a host of others,…") of observations by Professor Simmonds:
   (a) The observations in the just mentioned paragraph are not specifically directed toward the paper under discussion, but are directed, in general, toward host of papers (beginning with the seminal papers of Reissner) wherein boundary edge effects are not specifically taken into account.
   (b) The observations imply that as Reissner does not address the boundary edge effects, refinement brought in by his work is illusory. However, at the same time, the papers of Reissner are referred to as "seminal papers." The authors detect contradiction in the observations.
   (c) The authors do feel that the works of Reissner and host of others (including the work of Mindlin) have positively contributed to the research in the area of theory of plates. All these theories, in general, have their own importance and are useful in practice.

2. The authors' comments on the second paragraph (which starts with "Often, authors of "improved" plate theories compare solutions…") of observations by Professor Simmonds:
   (a) The observations in the just mentioned paragraph are also not specifically directed toward the paper under discussion, but are directed, in general, toward "all authors of 'improved' plate theories who compare solutions of their equations under simple support either to other theories or to exact three-dimensional elasticity solutions."
   (b) The observations, in the mentioned paragraph, do not deny that exact three-dimensional elasticity solution for a simply supported plate does exist.
   It is well known that, in the domain of linear theory of elasticity, there cannot be a more accurate solution for a given problem than the solution given by exact three-dimensional elasticity.
   It is just a sheer coincidence, and it is also just incidental, that the exact three-dimensional elasticity solution for a simply supported plate also happens to be the solution for an infinite plate under periodic surface loads. As a result, authors of various theories cannot be faulted for comparing their results with the exact results, wherever available, for validating their theories.

The authors would like to stress that they have named their theories as "New First-Order Shear Deformation Plate Theories," and as such they would like the theories presented to be viewed only as simple alternatives to Reissner's theory and to Mindlin's theory. The advantages of the new theories presented have been clearly brought out in the paper under discussion.

Contributed by the Applied Mechanics Division of ASME for publication in the Journal of Applied Mechanics. Manuscript received November 27, 2007; final manuscript received December 26, 2007; published online May 20, 2008. Review conducted by Robert M. McMeeking.

Erratum: “Reynolds-Stress Modeling of Three-Dimensional Secondary Flows With Emphasis on Turbulent Diffusion Closure” [Journal of Applied Mechanics, 2007, 74(6), pp. 1142–1156]

I. Vallet

Equation (31) in the published paper contains a coefficient value error. The corrected equation is written below:

$$\frac{1}{\rho}\overline{p'u_i'}^{(2)} = -C_{\mathrm{SP}}\left\{-(2C_{r1}+10C_{r2})\frac{\mathrm{k}^3}{\varepsilon^2}\left[\bar{S}_{ik}\frac{\partial \mathrm{k}}{\partial x_k}+\bar{S}_{pk}\frac{\partial \overline{u_i'u_p'}}{\partial x_k}\right]\right\}$$

$$C_{r1}=0.0001;\quad C_{r2}=0.0001;\quad C_{\mathrm{SP}}=0.085\left[1+\min\left(0.5,A^{\max(0.25,2(1-6A))}\right)\right] \tag{31}$$